Diagnostics Optiques des Milieux Multiphasiques

Fabrice R. A. Onofri

UNIVERSITE DE PROVENCE
(AIX-MARSEILLE I)
Ecole Doctorale : Mécanique, Physique et Modélisation

MEMOIRE
de synthèse des travaux scientifiques et d'encadrement
en vue de l'obtention du diplôme d'

HABILITATION A DIRIGER DES RECHERCHES

Discipline : Physique
Spécialité : Mécanique-Energétique

« DIAGNOSTICS OPTIQUES DES MILIEUX MULTIPHASIQUES »

Présenté par :

Fabrice ONOFRI
IUSTI, UMR n°6595-CNRS-Université de Provence

Soutenance prévue le **22 juin 2005**

Devant le jury composé de

Gérard Gouesbet	Professeur à l'INSA de Rouen, CORIA	Rapporteur
Stefan Radev	Professeur à l'Académie des sciences de Bulgarie, IMECH	Rapporteur
Richard Saurel	Professeur à l'université de Provence, IUSTI Membre de l'Institut Universitaire de France	Rapporteur
Fabrice Lemoine	Professeur à l'université Henri Poincaré, LEMTA	Examinateur
Roger Martin	Professeur à l'université de Provence, IUSTI	Examinateur
Daniel Maystre	Directeur de Recherche au CNRS, Institut Fresnel	Examinateur
Paul-Henri Guering	Chef de service à Saint-Gobain Recherche	Invité

Tables de matières

Abréviations et symboles

α	Angle entre deux faisceaux ou paramètre de taille
δ	Interfrange ou distribution de Dirac
λ	Longueur d'onde
Ω	Angle d'intégration, angle solide
$\omega,\ \nu$	Pulsation et fréquence
ω_0	Diamètre au col du faisceau laser
$\psi_n,\ \chi_n,\ \xi_n$	Fonction de Ricatti-Bessel (sphère)
$\phi,\ \phi_{ab}$	Phase et déphasage (signal Doppler)
θ	Angle de diffusion
$a,\ r$	Rayon d'une particule
$A_n, B_n / a_n, b_n$	Coefficients de diffusion externe, onde plane, particule homogène/multicouche
A_n^m, B_n^m	Idem, pour une sphère multicouche éclairée par une onde de forme arbitraire (GLMT)
C_v	Concentration volumique (en particules).
$E,\ H$	Champs électrique et magnétique
D	Diamètre
DBT	Technique Dual Bursts
DM	Technique Dual Mode
F	Tension
GLMT	Théorie de Lorenz-Mie Généralisée
OG	Optique géométrique
$g_{n,TM}^m,\ g_{n,TE}^m$	Coefficients utilisés pour la description du faisceau incident (GLMT)
I	Intensité diffusée
IUSTI	Institut Universitaire des Systèmes Thermiques Industriels, Marseille.
$J_n,\ Y_n,\ H_n^{(1)}$	Fonctions de Bessel cylindriques (cylindre)
$K,\ k$	Absorptivité et partie imaginaire de l'indice, vecteur d'onde
L	Nombre de couches (discrétisation du profil d'indice)
LFC	Lit Fluidisé Circulant
LMT	Théorie de Lorenz-Mie
m	Indice de réfraction (réel ou complexe)
MDR	Résonances Morphologico-Dépendantes
$P,\ S$	Vecteur de Poynting
P	Piédestal (signal Doppler)
p=0,1,2,3…	Ordre de diffusion (optique géométrie et séries de Debye)
PIV	Vélocimétrie par Images de Particules
POA	Approximation d'optique physique
PSB	Potentiel Scalaire de Bromwich
$Q_{ext}, Q_{sca}, Q_{abs}$	Coefficients d'extinction, de diffusion et d'absorption

S_1, S_2, T_1, T_2	Fonctions d'amplitude des champs diffusés 2 : onde TM (//) ; 1 : onde TE ($\perp$)
SGR	Saint-Gobain Recherche
T, T_0	Température, température initiale de fibrage
TE, TM	Transversale Electrique et Magnétique
V	Visibilité (signal Doppler)
V_f	Vitesse de fibrage
z, Z	Axe optique ou axe du cylindre

Notations pour les références et les légendes des vignettes

Notations pour les références

Les références de mes propres travaux sont précédées d'une à deux lettres : **A** pour article, **B** pour brevets, **C** pour article de congrès, **L** pour logiciel, **RC** pour rapport de contrat, **RI** pour rapport interne, **S** pour séminaire et **T** pour thèse. Ces références sont listées dans la section § 8.2 du Chapitre 8. (pages 107 à 113). Les reproductions de dix articles sont incluses dans le Chapitre 9.

Les Références concernant les travaux d'autres auteurs sont numérotées de façon classique [entre crochets]. Elles sont détaillées dans le Chapitre 7 (à partir de la page 100).

Légendes des vignettes des têtes de chapitre

Chaque tête de chapitre est illustrée par une vignette (petite figure) dont voici les légendes :

Chapitre 1, page 11 : Intensité des champs électromagnétiques : incident, interne et diffusé par une goutte d'eau éclairée par une onde plane. Cette simulation a été réalisée *à partir* des codes de calcul de Barber et Hill [1].

Chapitre 2, page 15 : Diagrammes de diffusion arrière de fibres de verre de différents diamètres. Pour ce calcul, seules les ondes partielles ayant subi deux réflexions internes sont prises en compte (série de Debye, p=3), § 2.3.

Chapitre 3, page 41 : Evolution temporelle des diagrammes de diffraction expérimentaux d'une fibre de verre dont le diamètre fluctue, § 3.1.4.

Chapitre 4, page 65 : Photographie de la tête optique de l'interféromètre rétro diffusion FIB, §3.1.3.

Chapitre 5, page 96 : Tomographie laser de la distribution des solides dans un Lit Fluidisé Circulant gaz-solide, §4.4.1.

Chapitre 6, page 100 : Champ de vitesse de la phase dispersée d'un Lit Fluidisé Circulant gaz-solide, lors du passage d'une poche de gaz (en rotation, vue en coupe), § 4.4.1.

Chapitre 7, page 100 : Copie d'écran du logiciel d'acquisition et de traitement de l'interféromètre FIBS, § 4.3.3.

Chapitre 8, page 106 : Simulation par méthode de Monte Carlo de la diffusion de la lumière par un jet li quide fortement chargé en micro particules, § 2.4.3.

Chapitre 9, page 120 : Principe de la technique de mesure d'indice par faisceaux focalisés : les signaux lumineux réfléchis et réfractés apparaissent décalés dans le temps, § 3.2.1.

Chapitre 1

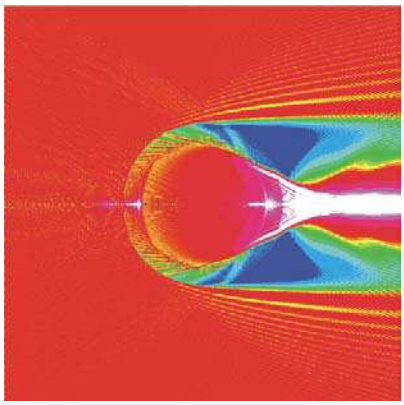

INTRODUCTION

Ce *mémoire d'habilitation* présente l'essentiel de mes travaux sur la *caractérisation optique de particules et fluides en écoulement*. J'ai démarré cette *activité de recherche* au cours de la deuxième partie de ma thèse [T1][1] dans la mesure où mon sujet de thèse initial, sur les effets de trajectoires, bien que très riche [A1, A3, A6-7], a été considéré comme pratiquement bouclé après seulement deux ans de thèse et le dépôt de deux brevets [B1, B2]. Depuis ma nomination comme Chargé de Recherche au CNRS en novembre 1996, je développe cette activité dans le cadre d'une opération de recherche sur les « *Diagnostics Optiques des Milieux Multiphasiques* » de l'IUSTI-UMR n°6595 CNRS-Université de Provence. Mes activités sont transverses à deux des trois thématiques de recherche de mon laboratoire d'affectation : «*Physique des Transferts*» et «*Ecoulements*». Cette transversalité tient moins à l'objet de mon étude, *les écoulements diphasiques et multiphasiques*, qu'à mon outil d'analyse : la «lumière». Cet outil est puissant mais il est également complexe et coûteux… et, depuis ma nomination, il m'a fallu de nombreux efforts pour parvenir à équiper un laboratoire et ainsi, développer mes travaux de recherche.

Les *écoulements diphasiques ou multiphasiques* sont des milieux extrêmement *complexes* dans lesquels une ou plusieurs phases dispersées sont transportées ou mises en suspension par une phase fluide. La complexité de ces milieux, que l'on s'intéresse à leurs modes de production[2], à leurs propriétés de transport[3] ou à leur réactivité[4], tient pour l'essentiel à la multiplicité et à la complexité des phénomènes physiques mis en jeu (turbulence, évaporation, coalescence, physico-chimie, rayonnement…). L'étude de ces milieux revêt de ce fait un caractère fortement *pluridisciplinaire*. La modélisation et le contrôle expérimental de ceux-ci imposent que nous en développions nos connaissances fondamentales et nos *capacités de diagnostics*. Expérimentalement, le « mécanicien des fluides » cherche caractériser trois types de propriétés de ces milieux : *i)* vi-

[1] LESP/CORIA-UMR n°6614-CNRS-Université et INSA de Rouen
[2] Cavitation, pulvérisation, granulation, séchage, enrobage, polymérisation catalytique …
[3] Sédimentation, fluidisation; dépôts céramiques, aérosols marins, boues, sang…
[4] Combustion diphasique, incinération, polymérisation…

tesses moyennes et fluctuations, corrélations spatiales et temporelles, les flux en masse… ; *ii)* compositions, taux de mélange, températures... et *iii)* forme, la granulométrie, la concentration en masse… des phases dispersées.

Les techniques laser, non intrusives, sont particulièrement bien adaptées à l'étude de ces *milieux* parfois *hostiles,* où les *échelles* temporelles et spatiales à résoudre sont très *critiques*. Cependant, il n'existe aucune technique de mesure capable d'obtenir de manière corrélée les trois types propriétés précédemment citées [C40]. *Les systèmes actuels* de *granulométrie optique de particules* en écoulement sont, par exemple, *incapables de distinguer le matériau et donc la nature des particules* qu'ils détectent. Ceci conduit, dans l'étude des écoulements réactifs en lit fluidisé, à ce que l'on ne puisse pas distinguer les particules combustibles, des particules utilisées pour fixer les polluants ou de celles issues de la combustion… On pourrait multiplier les exemples *d'applications industrielles*, ou de *recherches fondamentales*, où la *caractérisation du matériau* des particules en écoulement pourrait contribuer à la réalisation de *progrès fondamentaux*.

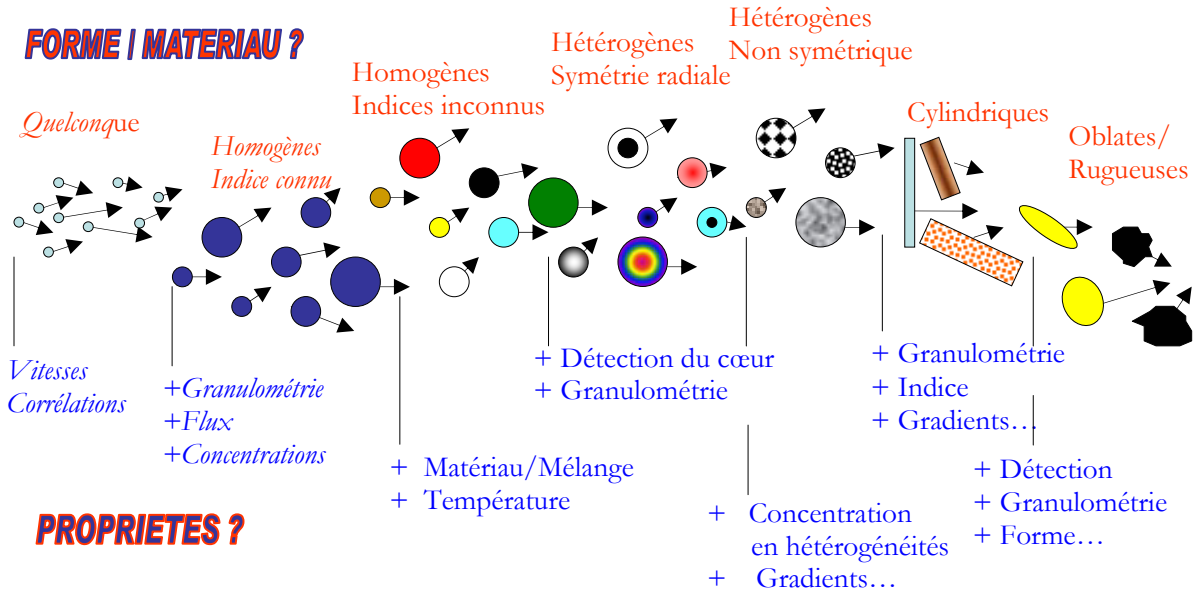

Figure 1 L'étude des milieux multiphasiques nécessite la caractérisation de particules de forme et de composition variées, ainsi que leurs propriétés dynamiques et celles du fluide qui les transporte.

Partant de ce constat, mon activité de recherche porte sur la mise au point de nouveaux outils (ou l'amélioration d'outils existants) pour l'étude des milieux multiphasiques, à partir de l'analyse des propriétés de diffusion de la lumière des particules présentes dans ces écoulements.
A l'image de mes activités de recherche, ce mémoire est composé de trois parties que je qualifierais de « symbiotiques » :

Théories et modèles de diffusion de la lumière par les particules sub-millimétriques :

Cet axe sous-tend aussi bien les axes expérimentaux qu'il les devance. Il consiste à développer des outils théoriques et numériques pour prédire les propriétés de diffusion de la lumière de différentes particules. Ceci, afin de pouvoir déterminer une « signature optique » de ces particules et, au final, proposer le principe d'une technique optique susceptible d'améliorer la caractérisation des milieux en écoulement, Chapitre 2.

Caractérisation optique de particules en écoulement :

Cet axe vise à réaliser des *expériences* de validation des modèles développés ou à valider expérimentalement le concept de *techniques* de mesure *originales*, pouvant répondre à un besoin actuel de la communauté ou, prévisible à terme. Diverses techniques ont ainsi été développées pour l'amélioration de la *granulométrie optique* de particules en écoulement, ou la *caractérisation simultanée* de leur *vitesse*, de leur *taille* et de leur *matériau*, Chapitre 3.

Collaborations & Applications :

J'ai été amené à développer différents *partenariats industriels et universitaires*, pour développer et financer mes acticités de recherches. Cette démarche fait partie intégrante des missions du département *Sciences Pour l'Ingénieur* du CNRS. Aussi, en essayant de garder une juste proportion entre recherche amont, applications *contractuelles* et *collaborations interdisciplinaires*, ceci m'a conduit à *aborder* des domaines aussi variés que la biophysique, la combustion, la fluidisation et le traitement des poudres, la micro fluidique, les instabilités de jets capillaires, les procédés de fibrage du verre…, Chapitre 4.

Ce mémoire comprend également une **Annexe,** Chapitre 5. Celle-ci rassemble différents développements analytiques, inutiles pour la compréhension du problème physique absorbé dans le texte, mais néanmoins importants et encore non publiés.

Des **Conclusions et Perspectives** sur mes activités de recherche sont présentées dans le Chapitre 6.

Les **Références** des travaux d'autres auteurs, utiles à la compréhension de ce mémoire, sont listées dans le Chapitre 7.

Conformément aux réglementations sur le diplôme d'Habilitation à Diriger des Recherches (HDR), ce mémoire comprend également un résumé de mes autres activités liées à la recherche : **enseignement et encadrement, gestion de projets de recherche, transferts technologiques**…, Chapitre 8. Ce dernier rassemble également la liste de mes publications.

Au final, ce mémoire regroupe des **Reproductions d'Articles** qui présentent de façon plus détaillée certains aspects de mes travaux de recherche, Chapitre 9.

Chapitre 2

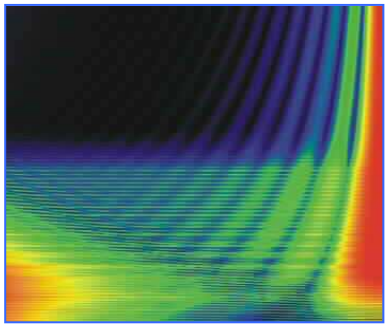

THEORIES ET MODELES DE DIFFUSION DE LA LUMIERE PAR DES PARTICULES SUB-MILLIMETRIQUES

Ce chapitre présente les théories et modèles de diffusion de lumière élaborés pour simuler les propriétés de diffusion de différentes particules rencontrées dans les écoulements. Les particules multicouches (stratification radiale de l'indice de réfraction) occupent une place importante dans mes travaux. En effet, ces dernières permettent de modéliser l'influence de nombreux phénomènes physiques et « particules » produites par l'industrie, Figure 2.

D'une manière générale, ces travaux sont ordonnés par type de particules et en distinguant les théories, parfaitement exactes, des modèles, qui sont généralement des approximations asymptotiques. Ces travaux ont été à l'origine de différentes applications et collaborations. Les autres chapitres de ce mémoire y font donc souvent référence.

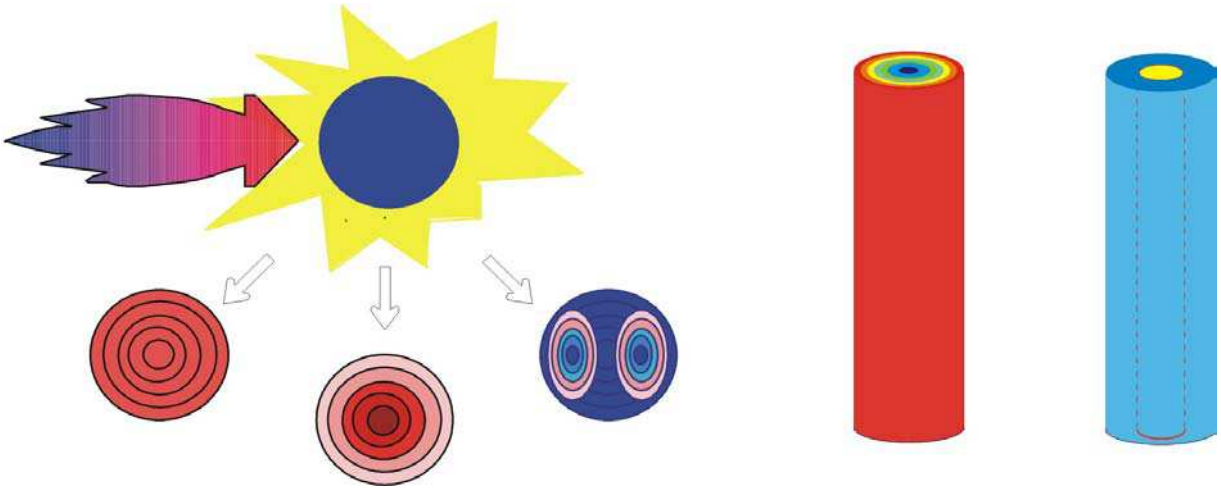

Figure 2 Différents phénomènes physiques et procédés industriels sont à l'origine de la formation de gradients radiaux d'indice à l'intérieur des particules : gouttes multi composant soumises à un choc thermique, formation des cénosphères, fibres optiques…

2.1 Théorie de Lorenz-Mie : cylindre homogène et multicouche

Cette section traite du calcul de la diffusion d'une onde électromagnétique plane, harmonique, par un cylindre infini, de section circulaire, à stratification radial d'indice et biréfringence uniaxe [A18].

2.1.1 Théorie

On considère un cylindre infini de section circulaire composé de L couches concentriques, $j = 1, 2 \ldots . L-1, L$. Chaque couche est caractérisée par son indice de réfraction complexe $m_j = \sqrt{\varepsilon_j}$, sa constante de perméabilité magnétique μ_j et son rayon r_j, voir la Figure 3. Ce cylindre, placé dans un milieu d'indice réel m_{ext}, est éclairé sous incidence normale par une onde plane harmonique de vecteur d'onde $\mathbf{k} = k\mathbf{e}_x = (2\pi m_{ext}/\lambda)\mathbf{e}_x$. La géométrie du modèle et les notations sont les mêmes que celles introduites par Bohren et Huffman [2], pour le calcul de la diffusion par un cylindre homogène.

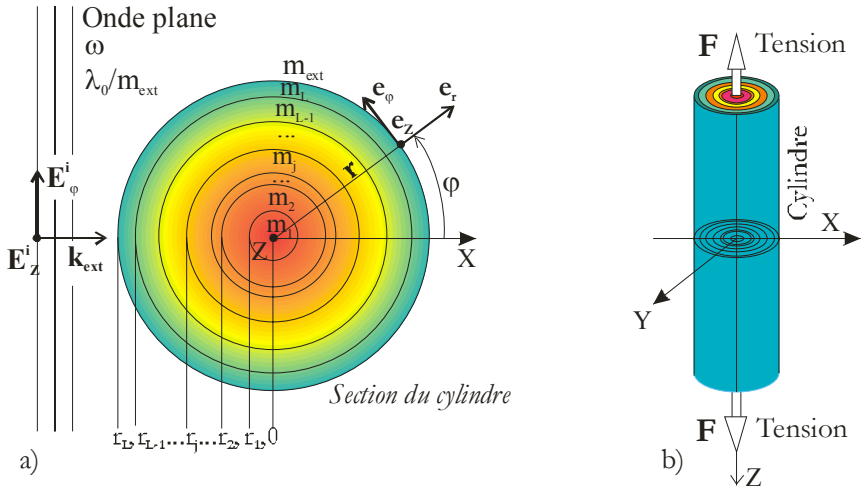

Figure 3 Géométrie du modèle de diffusion d'une onde électromagnétique plane par un cylindre infini à stratification radial d'indice et biréfringence uniaxe.

La solution du problème est obtenue [RI7, C37, A18] en résolvant l'équation d'onde, Eq. (2.1), pour les conditions limites du problème : décroissance de l'intensité diffusée en $1/r$ dans le champ lointain, champs interne et incident finis au centre de la particule, continuité des composantes tangentielles des champs (électrique et magnétique) à la traversée de la surface externe de la particule et de chaque couche *j*.

$$\nabla^2\Psi + k^2\Psi = 0 \tag{2.1}$$

L'équation d'onde s'écrit en coordonnées cylindriques :

$$\frac{1}{r}\frac{\partial}{\partial r}\left(r\frac{\partial \psi}{\partial r}\right) + \frac{1}{r^2}\frac{\partial^2 \psi}{\partial \phi^2} + \frac{\partial^2 \psi}{\partial z^2} + k^2\psi = 0 \tag{2.2}$$

Elle peut être résolue par une méthode de séparation des variables (i .e. Théorie de Lorenz-Mie) :

$$\Phi_n(\rho,\varphi) = Z_n(\rho)e^{in\varphi} \qquad (\mathrm{n}=0,\pm 1,\ldots,\infty) \tag{2.3}$$

Pour la fonction radiale $Z_n(\rho)$, l'argument $\rho = kr$ est solution de l'équation de Bessel :

$$\rho\frac{d}{d\rho}\left(\rho\frac{dZ_n}{d\rho}\right) + \left(\rho^2 - n^2\right)Z_n = 0 \tag{2.4}$$

Avec $k = 2\pi m/\lambda$ pour le vecteur d'onde, les solutions de l'équation précédente sont les composantes des harmoniques cylindriques :

$$\mathbf{M}_n^{(p)} = -kZ_n^{'(p)}(\rho)e^{in\varphi}\mathbf{e}_\varphi \qquad \mathbf{N}_n^{(p)} = kZ_n^{(p)}(\rho)e^{in\varphi}\mathbf{e}_z \tag{2.5}$$

Toute combinaison linéaire de ces harmoniques est, a priori, une solution de l'équation précédente. Les fonctions $Z^{(p)}$ et leurs dérivées $Z^{'(p)}$ sont les fonctions de Bessel d'ordre n entier ($n \in \mathbb{Z}$) : $J_n(\rho)$, du premier ordre; $Y_n(\rho)$, du second ordre (ou encore fonction de « Neumann »); et la fonction de Hankel, $H_n(\rho)$, avec $\rho \in \mathbb{C}$:

$$Z_n^{(p=1)}(\rho) = J_n(\rho) \quad Z_n^{(p=2)}(\rho) = Y_n(\rho) \quad Z_n^{(p=3)}(\rho) = H_n^{(1)}(\rho) = J_n(\rho) + iY_n(\rho) \tag{2.6}$$

Expressions des champs TM :

On s'intéresse ici au cas d'une onde incidente plane harmonique, linéairement polarisée, Transversale Magnétique (TM, i.e. champ électrique parallèle à l'axe z de la fibre).

Champs incidents : $\mathbf{E}_{TM}^i, \mathbf{H}_{TM}^i$

Le champ incident doit être de dimension finie au centre de la particule. Ceci conduit à éliminer la fonction de Bessel du second ordre $Y_n(\rho \to 0) \to -\infty$, de la combinaison linéaire des solutions possibles de l'Eq. (2.4). De même que pour un cylindre homogène [2], le système (2.5) se réduit alors à :

$$\begin{aligned} \mathbf{E}_{TM}^i &= \sum_{n=-\infty}^{\infty} E_n \mathbf{N}_n^{(1)} \\ \mathbf{H}_{TM}^i &= \frac{-ik_{ext}}{\omega\mu_{ext}} \sum_{n=-\infty}^{\infty} E_n \mathbf{M}_n^{(1)} \end{aligned} \tag{2.7}$$

Avec pour le vecteur d'onde de l'onde incidente: $k_{ext} = 2\pi m_{ext}/\lambda_0$, où λ_0 est la longueur d'onde de l'onde incidente « dans l'air » ; $E_n = E_0(-i)^n/k_{ext}$, où E_0 est l'amplitude du champ incident.

Les composantes des harmoniques se réduisent alors à :

$$\mathbf{M}_n^{(1)}(m_{ext}x_L) = -k_{ext}J_n'(m_{ext}x_L)\mathbf{e}_\varphi \qquad \mathbf{N}_n^{(1)}(m_{ext}x_L) = k_{ext}J_n(m_{ext}x_L)\mathbf{e}_z \tag{2.8}$$

Ce qui donne pour les composantes des champs électrique et magnétique sur la surface de la particule :

$$\begin{aligned} E_z^i(m_{ext}x_L) &= k_{ext}\sum_{n=-\infty}^{\infty} E_n J_n(m_{ext}x_L) \\ H_z^i(m_{ext}x_L) &= E_\varphi^i(m_{ext}x_L) = 0 \\ H_\varphi^i(m_{ext}x_L) &= \frac{i(k_{ext})^2}{\omega\mu_{ext}} \sum_{n=-\infty}^{\infty} E_n J_n'(m_{ext}x_L) \end{aligned} \tag{2.9}$$

Champs diffusés : $\mathbf{E}_{TM}^s, \mathbf{H}_{TM}^s$

Dans le cas du champ diffusé par la particule $\rho \geq r$, seule la fonction de Hankel, qui permet d'obtenir une intensité diffusée qui décroît en $1/r$ quand r tend vers l'infini $I(r) \propto H_n(r)\bar{H}_n(r) \to \alpha/r,\ r \to \infty$, peut être retenue comme solution de l'Eq. (2.4). De ce fait, on obtient que :

$$\begin{aligned} \mathbf{E}_{TM}^s &= -\sum_{n=-\infty}^{\infty} E_n b_{nI} \mathbf{N}_n^{(3)} \\ \mathbf{H}_{TM}^s &= \frac{ik_{ext}}{\omega\mu_{ext}} \sum_{n=-\infty}^{\infty} E_n b_{nI} \mathbf{M}_n^{(3)} \end{aligned} \tag{2.10}$$

Les champs diffusés se propagent dans le milieu extérieur, d'indice m_{ext}, depuis la surface de la particule ($\rho = m_{ext} x_L$) vers l'infini. $x_L = 2\pi r_L / \lambda_0$ est le paramètre de taille de la particule (correspondant à celui de la couche externe, $j = L$).

A la surface de la particule les composantes des harmoniques s'écrivent :

$$\mathbf{M}_n^{(3)}\left(m_{ext}x_L\right) = -k_{ext}H_n^{(1)'}\left(m_{ext}x_L\right)\mathbf{e}_\varphi \qquad \mathbf{N}_n^{(3)}\left(m_{ext}x_L\right) = k_{ext}H_n^{(1)}\left(m_{ext}x_L\right)\mathbf{e}_z \tag{2.11}$$

Ce qui donne pour les composantes tangentielles des champs diffusés :

$$\begin{aligned} E_z^s &= -k_{ext}\sum_{n=-\infty}^{\infty} E_n b_{nI} H_n^{(1)}\left(m_{ext}x_L\right) \\ H_z^s &= E_\varphi^s = 0 \\ H_\varphi^s &= \frac{-i\left(k_{ext}\right)^2}{\omega\mu_{ext}} \sum_{n=-\infty}^{\infty} E_n b_{nI} H_n^{(1)'}\left(m_{ext}x_L\right) \end{aligned} \tag{2.12}$$

Dans l'Eq. (2.12), les expressions des champs électrique et magnétique sont strictement identiques à celles obtenues pour un cylindre homogène. Seule l'expression du coefficient de diffusion externe b_{nI} diffère.

Calcul des champs internes $\mathbf{E}_{TM}^{(j)}, \mathbf{H}_{TM}^{(j)}$

Pour une onde incidente TM, les champs électrique et magnétique, internes à la couche *j*, sont de la forme :

$$\begin{aligned} \mathbf{E}_{TM}^{(j)} &= \sum_{n=-\infty}^{\infty} E_n\left[c_n^{(j)}\mathbf{N}_n^{(1)} - e_n^{(j)}\mathbf{N}_n^{(2)}\right] \\ \mathbf{H}_{TM}^{(j)} &= \frac{ik_{ext}}{\omega\mu_{ext}} \sum_{n=-\infty}^{\infty} E_n\left[c_n^{(j)}\mathbf{M}_n^{(1)} - e_n^{(j)}\mathbf{M}_n^{(2)}\right] \end{aligned} \tag{2.13}$$

Les coefficients de diffusion interne $c_n^{(j)}$ et $e_n^{(j)}$ sont a priori non nuls. Les composantes des harmoniques s'écrivent avec $k_j = 2\pi m_j / \lambda_0$ et $\rho = m_j x_j$:

$$\mathbf{M}_n^{(p)}\left(\rho\right) = -k_j Z_n^{'(p)}\left(\rho\right)\mathbf{e}_\varphi \qquad \mathbf{N}_n^{(p)}\left(\rho\right) = k_j Z_n^{(p)}\left(\rho\right)\mathbf{e}_z \tag{2.14}$$

Comme pour les champs incidents, la fonction de Bessel du second ordre Y_n ne peut être solution de l'Eq. (2.4). Dans le cas du cylindre multicouche, la condition «de dimension» finie n'est critique que pour la première couche (qui est en fait un cylindre homogène), $j = 1$. Pour les autres couches, $j = 2 \ldots L$, cette restriction n'a pas lieu d'être. C'est pourquoi, on doit exprimer les champs internes, pour chaque couche *j*, comme une combinaison linéaire des deux fonctions de Bessel, J_n, Y_n avec $\rho = m_j x_j$:

$$\begin{aligned} E_{n,z}^{(j)} &= = k_j \sum_{n=-\infty}^{\infty} E_n\left[c_n^{(j)} J_n\left(m_j x_j\right) - e_n^{(j)} Y_n\left(m_j x_j\right)\right] \\ H_{n,z}^{(j)} &= E_{n,\varphi}^{(j)} = 0 \\ H_{n,\varphi}^{(j)} &= = \frac{i\left(k_j\right)^2}{\omega\mu_j} \sum_{n=-\infty}^{\infty} E_n\left[c_n^{(j)} J_n'\left(m_j x_j\right) - e_n^{(j)} Y_n'\left(m_j x_j\right)\right] \end{aligned} \tag{2.15}$$

Pour les cas particuliers de la première couche : $e_n^{(1)} = 0$ et de la couche externe *j=L* (i.e. $\rho = m_L x_L$) on a :

$$\begin{aligned} E_{n,z}^{(L)} &= k_L \sum_{n=-\infty}^{\infty} E_n\left[c_n^{(L)} J_n\left(m_L x_L\right) - e_n^{(L)} Y_n\left(m_L x_L\right)\right] \\ H_{n,z}^{(L)} &= E_{n,\varphi}^{(L)} = 0 \\ H_{n,\varphi}^{(L)} &= \frac{i\left(k_L\right)^2}{\omega\mu_L} \sum_{n=-\infty}^{\infty} E_n\left[c_n^{(L)} J_n'\left(m_L x_L\right) - e_n^{(L)} Y_n'\left(m_L x_L\right)\right] \end{aligned} \tag{2.16}$$

Le calcul des champs TM internes nécessite, a priori, la détermination d'une infinité de coefficients : $c_n^{(j)}$ et $e_n^{(j)}$. Pour un ordre d'expansion donné, ils sont au nombre de $2n(L-1)$.

Récurrence ascendante sur les coefficients internes

Pour le calcul des coefficients de diffusion externe, nous allons transposer le principe de la méthode de *résolution par récurrence* introduite par Wu et Wang [3] dans le cas de la diffusion d'une onde plane par une sphère multicouches[5].

Conditions de continuité des champs internes

La méthode de résolution par récurrence conduit, dans un premier temps, à écrire les équations de continuité des composantes tangentielles des champs à la traversée des interfaces $j-1 \to j$:

$$V_\Theta^{(j)}\left(m_j x_{j-1}\right) = V_\Theta^{(j-1)}\left(m_{j-1} x_{j-1}\right) \quad \text{avec } \Theta = \varphi \text{ et z; V=E et H} \tag{2.17}$$

Ce qui donne, en remplaçant dans l'Eq. (2.17) les champs par leur expression donnée par l'Eq. (2.16), et après simplification :

$$m_j c_n^{(j)}\left[J_n\left(m_j x_{j-1}\right) - \frac{e_n^{(j)}}{c_n^{(j)}} Y_n\left(m_j x_{j-1}\right)\right] = m_{j-1} c_n^{(j-1)}\left[J_n\left(m_{j-1} x_{j-1}\right) - \frac{e_n^{(j-1)}}{c_n^{(j-1)}} Y_n\left(m_{j-1} x_{j-1}\right)\right] \tag{2.18}$$

$$\frac{\left(m_j\right)^2}{\mu_j} c_n^{(j)}\left[J_n'\left(m_j x_{j-1}\right) - \frac{e_n^{(j)}}{c_n^{(j)}} Y_n'\left(m_j x_{j-1}\right)\right] = \frac{\left(m_{j-1}\right)^2}{\mu_{j-1}} c_n^{(j-1)}\left[J_n'\left(m_j x_{j-1}\right) - \frac{e_n^{(j-1)}}{c_n^{(j-1)}} Y_n'\left(m_j x_{j-1}\right)\right] \tag{2.19}$$

Plutôt que de calculer les $2n(L-1)$ coefficients internes, on peut se limiter au calcul des $n(L-1)$ quotients suivants (avec $B_n^{(1)} = 0$) :

$$\mathrm{B}_n^{(j)} = \frac{e_n^{(j)}}{c_n^{(j)}} \tag{2.20}$$

Ce qui permet, avec le calcul du rapport Eq. (2.19)/Eq. (2.18), d'éliminer une série d'inconnues :

$$\frac{J_n'\left(m_j x_{j-1}\right) - B_n^{(j)} Y_n'\left(m_j x_{j-1}\right)}{J_n\left(m_j x_{j-1}\right) - B_n^{(j)} Y_n\left(m_j x_{j-1}\right)} = \frac{\mu_j m_{j-1}}{\mu_{j-1} m_j}\left[\frac{J_n'\left(m_{j-1} x_{j-1}\right) - B_n^{(j-1)} Y_n'\left(m_{j-1} x_{j-1}\right)}{J_n\left(m_{j-1} x_{j-1}\right) - B_n^{(j-1)} Y_n\left(m_{j-1} x_{j-1}\right)}\right] \tag{2.21}$$

En introduisant la fonction ou « quotient intermédiaire » $H_{b,n}^j$:

$$H_{b,n}^{(j-1)} = \frac{J_n'\left(m_{j-1} x_{j-1}\right) - B_n^{(j-1)} Y_n'\left(m_{j-1} x_{j-1}\right)}{J_n\left(m_{j-1} x_{j-1}\right) - B_n^{(j-1)} Y_n\left(m_{j-1} x_{j-1}\right)} \tag{2.22}$$

L'équation (2.21) devient alors :

$$J_n'\left(m_j x_{j-1}\right) - B_n^{(j)} Y_n'\left(m_j x_{j-1}\right) = \frac{\mu_j}{\mu_{j-1}} \frac{m_{j-1}}{m_j} H_{b,n}^{(j-1)}\left[J_n\left(m_j x_{j-1}\right) - B_n^{(j)} Y_n\left(m_j x_{j-1}\right)\right] \tag{2.23}$$

De cette dernière expression on peut tirer la forme récurrente du quotient $B_n^{(j)}$:

$$B_n^{(j)} = \frac{m_{j-1}\mu_j J_n\left(m_j x_{j-1}\right) H_{b,n}^{(j-1)} - m_j \mu_{j-1} J_n'\left(m_j x_{j-1}\right)}{m_{j-1}\mu_j Y_n\left(m_j x_{j-1}\right) H_{b,n}^{(j-1)} - m_j \mu_{j-1} Y_n'\left(m_j x_{j-1}\right)} \tag{2.24}$$

[5] Il a noter que j'ai également généralisé cette méthode au cas de la diffusion d'une onde incidente de forme arbitraire par une sphère stratifiée, voir à ce sujet l'article [A2] et le paragraphe § 2.2.

Conditions de continuité à la traversée de la surface externe

La condition de continuité des composantes tangentielles des champs électrique et magnétique, à la traversée de la surface externe de la particule s'écrit :

$$V_\Theta^i\left(m_{ext}x_L\right)+V_\Theta^s\left(m_{ext}x_L\right)=V_\Theta^L\left(m_Lx_L\right),\quad \text{avec } \Theta=\varphi \text{ et z; V=E et H} \tag{2.25}$$

En remplaçant dans l'Eq. (2.25), les champs par leur expression sur l'interface externe, et en simplifiant, on obtient le système suivant :

$$\frac{i\left(k_{ext}\right)^2}{\omega\mu_{ext}}E_n\left[J_n^{'}\left(m_{ext}x_L\right)\text{-}b_{nI}H_n^{(1)'}\left(m_{ext}x_L\right)\right]=\frac{i\left(k_L\right)^2}{\omega\mu_L}c_n^{(L)}E_n\left[J_n^{'}\left(m_Lx_L\right)-B_n^{(L)}Y_n^{'}\left(m_Lx_L\right)\right] \tag{2.26}$$

$$k_{ext}E_n\left[J_n\left(m_{ext}x_L\right)\ -b_{nI}H_n^{(1)}\left(m_{ext}x_L\right)\right]=k_Lc_n^{(L)}E_n\left[J_n\left(m_Lx_L\right)-B_n^{(L)}J_n\left(m_Lx_L\right)\right] \tag{2.27}$$

Le calcul du rapport des Eqs. (2.26)/ (2.27) permet d'éliminer le coefficient de diffusion interne $c_n^{(L)}$ et la constante E_n :

$$\frac{k_{ext}}{\mu_{ext}}\frac{J_n^{'}\left(m_{ext}x_L\right)-b_{nI}H_n^{(1)'}\left(m_{ext}x_L\right)}{J_n\left(m_{ext}x_L\right)-b_{nI}H_n^{(1)}\left(m_{ext}x_L\right)}=\frac{k_L}{\mu_L}\frac{J_n^{'}\left(m_Lx_L\right)-B_n^{(L)}Y_n^{'}\left(m_Lx_L\right)}{J_n\left(m_Lx_L\right)-B_n^{(L)}J_n\left(m_Lx_L\right)}=\frac{k_L}{\mu_L}H_{b,n}^L \tag{2.28}$$

Dans le 2ème membre de l'expression précédente on reconnaît l'expression du rapport $H_{b,n}^L$, introduite par l'Eq. (2.22). En remplaçant $H_{b,n}^L$ par son expression et en simplifiant on obtient :

$$k_{ext}\mu_LJ_n^{'}\left(m_{ext}x_L\right)-k_{ext}\mu_Lb_{nI}H_n^{(1)'}\left(m_{ext}x_L\right)=k_L\mu_{ext}H_{b,n}^LJ_n\left(m_{ext}x_L\right)-k_L\mu_{ext}H_{b,n}^Lb_{nI}H_n^{(1)}\left(m_{ext}x_L\right) \tag{2.29}$$

On en déduit l'expression du coefficient de diffusion externe des champs TM, b_{nI} :

$$b_{nI}=\frac{m_L\mu_{ext}H_{b,n}^L\left(m_Lx_L\right)J_n\left(m_{ext}x_L\right)-m_{ext}\mu_LJ_n^{'}\left(m_{ext}x_L\right)}{m_L\mu_{ext}H_{b,n}^L\left(m_Lx_L\right)H_n^{(1)}\left(m_{ext}x_L\right)-m_{ext}\mu_LH_n^{(1)'}\left(m_{ext}x_L\right)} \tag{2.30}$$

On procède de même pour le champ TE, voir à ce propos le paragraphe § 5.1.1 placé en annexe.

La façon dont nous prenons en compte la biréfringence uniaxe, est décrite dans l'article [A13] et la référence [4].

2.1.2 Résolution numérique et expressions des fonctions de diffusion

Résolution numérique

Le calcul des fonctions de Bessel, pour de grands arguments complexes et de grands ordres, pose de nombreux problèmes numériques. Pour pallier au manque de stabilité de ce calcul, il faut réécrire les fonctions de Bessel sous la forme de dérivées logarithmiques et faire apparaître, dans les différentes expressions précédentes, des rapports de ces fonctions plutôt que les fonctions elles-mêmes. Ce travail analytique permet d'obtenir des expressions qui se prêtent mieux aux calculs numériques, voir à ce propos le paragraphe § 5.1.2.

Numériquement, le profil d'indice du cylindre multicouche est introduit sous la forme d'un profil en rayon, adimensionnalisé par le rayon externe du cylindre r_L, et d'un profil d'indice complexe (indice du matériau pour λ_0) :

$$\begin{aligned} &r_1/r_L \quad \left[\mathrm{Re}\left(\mathrm{m_1}\right),\mathrm{Im}\left(\mathrm{m_1}\right)\right]\\ &r_2/r_L \quad \left[\mathrm{Re}\left(\mathrm{m_2}\right),\mathrm{Im}\left(\mathrm{m_2}\right)\right]\\ &\ldots\\ &r_L/r_L \quad \left[\mathrm{Re}\left(\mathrm{m_L}\right),\mathrm{Im}\left(\mathrm{m_L}\right)\right] \end{aligned} \tag{2.31}$$

Dans les codes de calcul, ce profil est pris en compte en le redimensionnant: $x_j = 2\pi\left(r_1 / r_L\right)/\left(\lambda_0 / m_{ext}\right)$. Ce qui permet d'itérer facilement sur le diamètre externe de la particule. On pose par ailleurs $m_{L+1} = m_{ext}$, $m_{ext} \in \mathbb{R}$. De manière classique maintenant [2], comme pour une particule homogène (sphère ou cylindre), les séries infinies sont tronquées à partir de :

$$n_{stop} = x_L + 4x_L^{1/3} + 2 \tag{2.32}$$

Remarque : selon le principe de l'approximation localisée de Van de Hulst [5], le rayon de la particule correspond à la valeur : $n + 1/2 = x_L = \pi D / \lambda$. D'où une décroissance très forte des coefficients de diffusion externe pour $n > x_L - 1/2$.

Sections efficaces et fonctions d'amplitude

Nous sommes à présent en mesure de calculer des quantités intégrales, comme les sections efficaces de diffusion, ou les fonctions d'amplitude d'un cylindre multicouche. Pour ce faire, dans les expressions dérivées pour le cylindre homogène [2], il suffit de remplacer les coefficients de diffusion externe du cylindre homogène par ceux que nous venons d'établir pour le cylindre multicouche :

Pour les coefficients d'efficacité de diffusion:

$$\begin{aligned} Q_I^{sca} &= \frac{2}{x}\left(\left|b_{0I}\right|^2 + 2\sum_{n=1}^{\infty}\left|b_{0I}\right|^2\right), \qquad Q_I^{ext} = \frac{2}{x}\mathrm{Re}\left(b_{0I} + 2\sum_{n=1}^{\infty} b_{0I}\right) \\ Q_{II}^{sca} &= \frac{2}{x}\left(\left|a_{0II}\right|^2 + 2\sum_{n=1}^{\infty}\left|a_{0II}\right|^2\right), \quad Q_I^{ext} = \frac{2}{x}\mathrm{Re}\left(a_{0II} + 2\sum_{n=1}^{\infty} a_{0II}\right) \end{aligned} \tag{2.33}$$

Où $Q_I^{abs} = Q_I^{ext} - Q_I^{sca}$ et $Q_{II}^{abs} = Q_{II}^{ext} - Q_{II}^{sca}$, avec *Ext.* pour l'extinction, *Sca.* pour la diffusion et *Abs.* pour l'absorption).

Pour les expressions des champ diffusés et des fonctions d'amplitude:

$$\begin{pmatrix} E_z^s(r,\theta,t) \\ E_\varphi^s(r,\theta,t) \end{pmatrix} = \exp\left[\frac{3\pi i}{4}\right]\sqrt{\frac{2}{\pi k r}}\begin{pmatrix} T_1(\theta) & 0 \\ 0 & T_2(\theta) \end{pmatrix}\begin{pmatrix} E_{0,z}^i \\ E_{0,\varphi}^i \end{pmatrix}\exp\left[k_{ext} r - 2\pi\nu t\right] \tag{2.34}$$

$$\begin{aligned} T_1(\theta) &= \sum_{-\infty}^{+\infty} b_{nI}\exp\left[-in\theta\right] = b_{0I} + 2\sum_{n=1}^{+\infty} b_{nI}\cos\left(n\theta\right) \\ T_2(\theta) &= \sum_{-\infty}^{+\infty} a_{nII}\exp\left[-in\theta\right] = a_{0II} + 2\sum_{n=1}^{+\infty} a_{nII}\cos\left(n\theta\right) \end{aligned} \tag{2.35}$$

$\theta = \pi - \varphi$ est l'angle de diffusion, voir la Figure 3 et, pour plus de détails, les références [RI7, A18].

2.1.3 Validations et exemples de résultats

Cas limite du cylindre homogène:

Dans le cas d'une couche unique on a $H_{b,n}^{(L)} = H_{a,n}^{(L)} = D_n^1\left(m_L x_L\right)$. Pour une particule de paramètre de taille $x_L = x$, placée dans un milieu d'indice $m_{ext} = m$ avec $\mu_L = \mu_{ext}$, l'expression Eq. (5.24) devient :

$$b_{nI} = \frac{J_n(x)}{H_n^{(1)}(x)}\frac{m\dfrac{J_n'(mx)}{J_n(mx)} - \dfrac{J_n'(x)}{J_n(x)}}{m_L\dfrac{J_n'(mx)}{J_n(mx)} - \dfrac{H_n'^{(1)}(mx)}{H_n^{(1)}(mx)}} \tag{2.36}$$

Expression que l'on peut remettre sous la forme :

$$b_{nI} = \frac{J_n(mx)J_n'(x) - mJ_n'(mx)J_n(x)}{J_n(mx)H_n^{(1)'}(x) - mJ_n'(mx)H_n^{(1)}(x)} \tag{2.37}$$

qui est strictement identique à celle obtenue dans le cas du cylindre homogène. On trouve le même accord pour a_{nII} (§ 5.1.1)

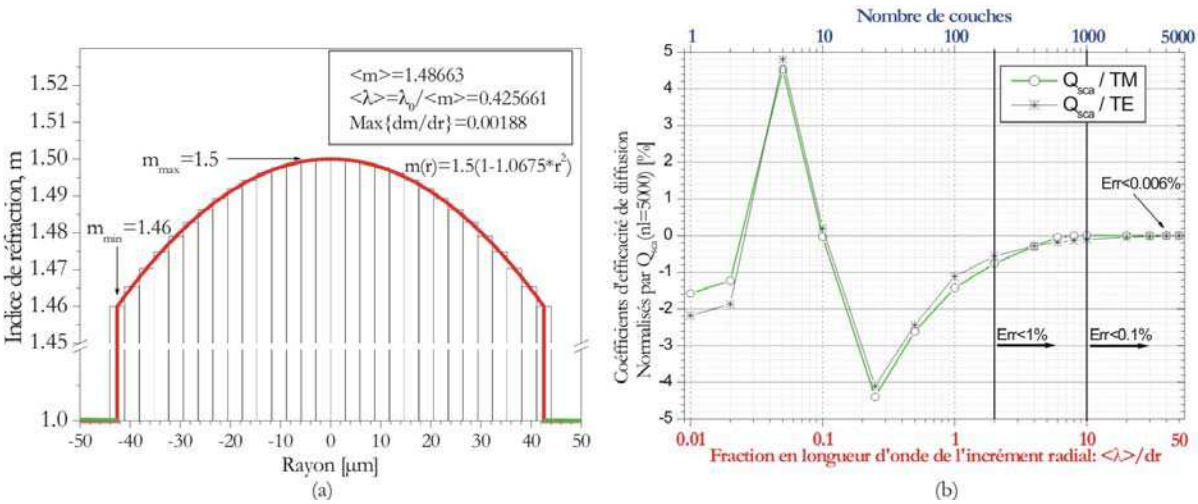

Figure 4 Diffusion par une fibre optique à gradient radial d'indice : a) Profil d'indice et b) Simulation de l'influence de la discrétisation du profil d'indice sur l'évolution relative des coefficients d'efficacité de diffusion (cas limite : L=5000).

Comparaison avec la sphère stratifiée

Intuitivement, on peut penser que la diffusion dans le plan d'un cylindre multicouche devrait être assez similaire à celle d'une sphère de même diamètre et de même profil d'indice. En fait, ce n'est pas vraiment le cas [4]… Cependant, du point de vue analytique, on peut établir des correspondances entre les harmoniques sphériques et cylindriques et au final, entre les fonctions de Ricatti-Bessel utilisées pour la sphère et les fonctions de Bessel cylindriques utilisées pour le cylindre. Cette démarche [RI7] conduit aux analogies suivantes :

$$\begin{array}{lccccccccc} \textit{Sphère} & \psi_n & \chi_n & \xi_n & D_n^1 = \dfrac{\psi_n'}{\psi_n} & D_n^2 = \dfrac{\chi_n'}{\chi_n} & D_n^3 = \dfrac{\xi_n'}{\xi_n} & D_n^{(0)} = \dfrac{\psi_n}{\chi_n} & D_n^{(x)} = \dfrac{\psi_n}{\chi_n} \\ & \downarrow & \downarrow & \downarrow & \downarrow & \downarrow & \downarrow & \downarrow & \downarrow \\ \textit{Cylindre} & J_n & Y_n & H_n^{(1)} & \dfrac{J_n'}{J_n} & \dfrac{Y_n'}{Y_n} & \dfrac{H_n^{(1)'}}{H_n^{(1)}} & \dfrac{J_n}{H_n^{(1)}} & \dfrac{J_n}{Y_n} \end{array} \tag{2.38}$$

Les relations (2.38) permettent de montrer [RI7] que les expressions des coefficients de diffusion externe TM et TE du cylindre multicouche sont formellement identiques à celles obtenues pour la sphère multicouche. Ceci valide, d'un point de vue formel, les expressions déduites dans le paragraphe § 2.1.1.

Exemples de résultats numériques

Ce modèle a été implémenté en Fortran. Ses prédictions ont été comparées à celles obtenues pour un cylindre homogène [2, 6] et les quelques résultats disponibles dans la littérature, pour des cylindres multicouches de petit paramètre de taille [7, 8]. L'accord avec ces derniers résultats n'était que partiel [RI7]. Ceci peut s'expliquer par des paramètres de calcul erronés. Par ailleurs, les auteurs de la référence [7], avec qui j'ai pris contact, m'ont clairement indiqué que leur algorithme est instable. De plus, on constate plusieurs erreurs (typographiques ?) dans les équations de la référence [8]. Aussi, malgré les nombreuses validations

analytiques de notre modèle, ces dernières remarques motivent en partie les travaux expérimentaux actuellement en cours (voir le paragraphe § 4.3.4).

La Figure 4 b) permet de juger de la stabilité numérique des algorithmes que nous avons développé. Elle simule l'évolution *relative* des deux coefficients d'efficacité de diffusion d'une fibre optique multimode « Corning », dont le profil d'indice est donné par la Figure 4 a). Ces cœfficients sont tracés en fonction : du nombre de couches utilisées pour discrétiser le profil d'indice ($L = 2 \to 5000$) et de la fraction de la longueur d'onde locale de l'incrément radial, $d\lambda / dr / = 2 \to 50$. On remarque que ces coefficients convergent rapidement vers une même valeur (i.e. $L = 5000$) et que, pour un incrément en $\lambda/10$, la différence est de moins de 0.1% (e.g. visuellement on ne constate plus aucune différence dans la forme des diagrammes de diffusion).
La stabilité de notre *modèle discret* permet donc de simuler les propriétés de diffusion de cylindres à *profil d'indice* continu (à condition que $d\lambda / dr > 10$).

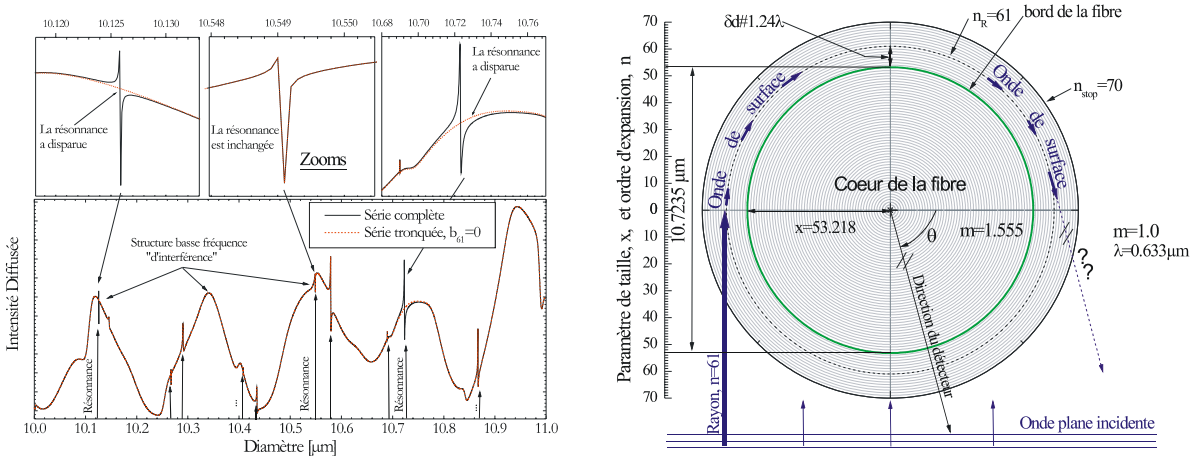

Figure 5 a) Simulation de l'intensité diffusée par une *fibre de verre-E homogène* lorsque tous les termes d'expansion des champs sont pris en compte et lorsque seul le terme b_{61} est annulé ; b) Schéma de principe sur les « *ondes de surface* » : le bord externe d'une fibre de diamètre D=10.7235µm est tracé en gras et l'*ordre d'expansion* est schématisé par la *stratification en grisé.*

La Figure 5 illustre *la complexité des mécanismes de diffusion* et l'intérêt de développer des modèles électromagnétiques. La Figure 5 a) simule l'intensité diffusée par une fibre de verre-E (m=1.555, D=10,10.0005…11µm) dans la direction $\theta = 162.5°$, lorsqu'elle est éclairée par une onde plane de polarisation perpendiculaire, avec λ=0.6328. Deux cas sont considérés: *i*) lorsque les champs diffusés sont calculés de façon habituelle, Eqs. (2.34) et (2.32), en sommant les différents termes de l'expansion, n = 1, 2…, n_{stop} et *ii*) lorsque la sommation est effectuée en posant arbitrairement comme égal à zéro le terme b_{61} = 0.0 + 0.0*i*. Cette procédure [4], introduite par Chylek et al. [9], permet «d'évaluer» la contribution des différents termes d'expansion au champ total diffusé. On peut constater que :

- Dans les deux cas l'intensité diffusée est modulée par une basse fréquence que nous attribuons à l'interférence entre les différents modes de diffusion classiques : réflexion spéculaire (*p* = 0), réflexions internes multiples (p = 2, 3…, voir le § 2.4.1)... On parle *généralement* de « Résonances Morphologico-Dépendantes(MDRs) »

- A ces MDRs se superpose une structure de résonances beaucoup plus fine. Cette dernière se caractérise par des variations brutales de l'intensité diffusée. La largeur de ces résonances est de l'ordre de

quelques nanomètres à quelques dizaines de nanomètres… Pour certains diamètres, et notamment D=10.7235, ces résonances ont disparu de la courbe d'intensité calculée avec la série « tronquée » (i.e. b_{61} = 0.0 + 0.0i). D'après le principe de l'approximation localisée, tel qu'il est schématisé par la Figure 5 b), le terme b_{61} correspond à un « rayon » dont le paramètre d'impact se situerait à près de 1.24 λ (i.e. 780*nm*) de la surface externe d'une fibre de diamètre D=10.7235. Selon l'optique géométrique, il ne devrait donc pas interagir avec la fibre. En fait, tout se passe comme si l'onde associée au cœfficient b_{61} avait orbité autour de la fibre avant d'être diffusée par celle-ci dans la direction $\theta = 162.5°$ … Avec le modèle multicouche, on peut montrer que ces *résonances, ou ondes de surface* [10], sont relativement peu sensibles à la présence d'un gradient d'indice au centre de la fibre mais, qu'en revanche, elles sont très sensibles à l'indice du milieu extérieur [4]… Ces résultats sont très intéressants du point de vue métrologique et notamment, pour la caractérisation du cladding de fibres optiques (§ 4.3.4).

D'autres exemples d'applications du modèle de diffusion par un cylindre multicouche sont présentés dans les paragraphes : §3.1.3, §3.1.4 et §4.3.4,

2.2 Théorie de Lorenz-Mie généralisée : sphère homogène et multicouche

Le traitement rigoureux du problème de la diffusion d'une onde plane harmonique par une sphère homogène, isotrope, à matériel local et linéaire (diffuseur de Mie), a été effectué par L. Lorenz [11], G. Mie [12], puis il a été reformulé par P. Debye [13], voir la Figure 6 a). Ce travail théorique est désormais connu sous le nom de « Théorie de Lorenz-Mie (LMT) ». Une présentation concise de cette théorie a été faite par Stratton [14], Kerker [15], Van de Hulst [5], Bohren et Huffman [2], Barber et Hill [1].

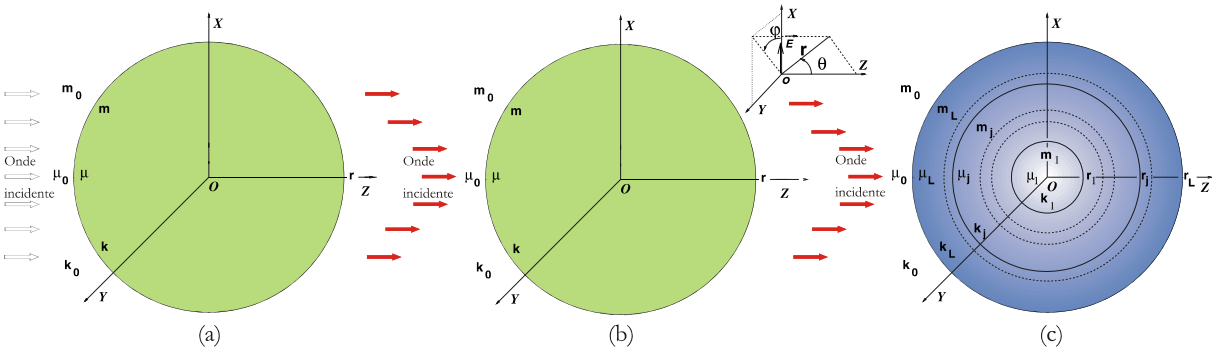

Figure 6 Problèmes traités par la théorie de Lorenz-Mie, a) Classique : onde plane/sphère homogène (LMT); b) Généralisée aux ondes de forme arbitraire et c) Généralisée aux ondes de forme arbitraire et sphères multicouches (GLMT).

Avec l'avènement du Laser et son emploi de plus en plus fréquent pour caractériser individuellement les particules, la LMT a atteint une de ses limites fondamentales : l'hypothèse d'éclairement uniforme[6] des particules, voir la Figure 6 b). Cette hypothèse restrictive a été levée par G. Gouesbet et al. [16-18], dans les années 80-90, par le développement de la Théorie de Lorenz-Mie Généralisée (GLMT). Cette généra-

[6] Les faisceaux laser, qui peuvent être fortement focalisés, engendrent de forts gradients d'intensité sur la surface des particules.

sation permet de calculer la diffusion électromagnétique d'un faisceau de forme arbitraire par une sphère homogène, voir également les contributions de Barton [19, 20].
J'ai étendu le formalisme de la GLMT au cas où la particule n'est plus simplement homogène mais présente un profil radial d'indice [RI2, A2], Figure 6 c). Cette « extension » de la GLMT permet de modéliser les propriétés de diffusion de la lumière de différentes particules bicouches ou multicouches, voir la Figure 2.

La démarche suivie pour résoudre ce problème est présentée de manière succincte dans ce qui suit, pour plus de détails, voir la référence [RI2] et la reproduction de l'article [A2].

2.2.1 Théorie et méthode numérique

Le faisceau incident sur la particule est considéré comme monochromatique et linéairement polarisé, de pulsation ω avec une dépendance temporelle en $e^{i\omega t}$. Dans le formalisme de la GLMT [17], on utilise la formulation de Bromwich pour obtenir des solutions particulières des équations de Maxwell dans le système de coordonnées (r,θ,φ), voir la Figure 6 b). Ces solutions correspondent aux champs : Transverse Magnétique (TM, i.e. $H_r = 0$); et Transerve Electrique (TE, , i.e. $E_r = 0$). $H_r = 0$ et $H_r = 0$ sont respectivement les composantes radiales des champs magnétique et électrique. Ces solutions sont générées par les Potentiels Scalaires de Bromwich (PSB), avec U_{TM} et U_{TE} pour les champs TM et TE. Elles satisfont la même équation différentielle partielle, avec pour le vecteur d'onde $k = \omega\sqrt{\mu\varepsilon}$:

$$\frac{\partial^2 U}{\partial r^2} + k^2 U + \frac{1}{r^2 \sin\theta}\frac{\partial}{\partial\theta}\sin\theta\frac{\partial U}{\partial\theta} + \frac{1}{r^2\sin^2\theta}\frac{\partial^2 U}{\partial\varphi^2} = 0 \tag{1.39}$$

De même que pour la théorie de Lorenz-Mie onde-plane, cette équation est résolue avec une méthode de séparation des variables : $U(r,\theta,\varphi) = rR(kr)\Theta(\theta)\Phi(\varphi)$. Ceci nécessite de résoudre l'équation de Bessel en coordonnées sphériques (variable radiale, *r*). Les solutions de cette dernière équation sont des combinaisons linéaires de différentes fonctions de Ricatti-Bessel : $\psi_n(kr)$, $\xi_n(k_0 r)$ et $\chi_n(kr)$. Comme pour le cylindre multicouche (§ 2.1.1), les combinaisons linéaires sont construites en respectant deux conditions milites: décroissance des champs en $1/r$ quand $r \to \infty$ et champs de dimension finie quand $r \to 0$.

Pour l'onde incidente, les potentiels scalaires de Bromwich (PSP) s'écrivent [17] :

$$\begin{aligned} U_{TM}^i &= \frac{E_0}{k_0}\sum_{n=1}^{\infty}\sum_{m=-n}^{+n} c_n^{pw} g_{n,TM}^m \psi_n(k_0 r) P_n^{|m|}(\cos\theta) e^{im\varphi} \\ U_{TE}^i &= \frac{H_0}{k_0}\sum_{n=1}^{\infty}\sum_{m=-n}^{+n} c_n^{pw} g_{n,TE}^m \psi_n(k_0 r) P_n^{|m|}(\cos\theta) e^{im\varphi} \end{aligned} \tag{1.40}$$

Les $P_n^{|m|}(\cos\theta)$ sont les polynômes de Legendre associés et les c_n^{pw}, des coefficients de normalisation liés aux ondes planes. Les $g_{n,TM}^m$ et $g_{n,TE}^m$ sont des coefficients complexes qui décrivent les caractéristiques du faisceau incident [17]. Ils sont propres à la GLMT et peuvent être calculés de différentes façon : quadratures, séries infinies et l'approximation localisée [21].

Pour les champs diffusés, les BSP sont de la forme :

$$\begin{aligned} U_{TM}^s &= \frac{-E_0}{k_0}\sum_{n=1}^{\infty}\sum_{m=-n}^{+n} c_n^{pw} A_n^m \xi_n(k_0 r) P_n^{|m|}(\cos\theta) e^{im\varphi} \\ U_{TE}^s &= \frac{-H_0}{k_0}\sum_{n=1}^{\infty}\sum_{m=-n}^{+n} c_n^{pw} B_n^m \xi_n(k_0 r) P_n^{|m|}(\cos\theta) e^{im\varphi} \end{aligned} \tag{1.41}$$

Où les A_n^m et B_n^m sont les coefficients de diffusion externe d'une sphère multicouche éclairée par un faisceau décrit par les $g_{n,TM}^m$ et $g_{n,TE}^m$.

Pour les champs internes, les BSP s'écrivent [RI2,A2]:

$$\begin{aligned} U_{jTM} &= \frac{-k_{j+1}E_0}{k_j^2}\sum_{n=1}^{\infty}\sum_{m=-n}^{+n} c_n^{pw}\left[c_{jn}^m\psi_n\left(k_j r\right)+e_{jn}^m\chi_n\left(k_j r\right)\right]P_n^{|m|}\left(\cos\theta\right)e^{im\varphi} \\ U_{jTM} &= \frac{k_{j+1}E_0}{k_j^2}\sum_{n=1}^{\infty}\sum_{m=-n}^{+n} c_n^{pw}\left[d_{jn}^m\psi_n\left(k_j r\right)+f_{jn}^m\chi_n\left(k_j r\right)\right]P_n^{|m|}\left(\cos\theta\right)e^{im\varphi} \end{aligned} \tag{2.42}$$

où les $c_{jn}^m, d_{jn}^m, e_{jn}^m, f_{jn}^m$ sont les coefficients de diffusion interne d'une sphère multicouche éclairée par un faisceau décrit par les $g_{n,TM}^m$ et $g_{n,TE}^m$.

A partir des expressions des BSP pour les champs incidents, diffusés et internes, ont peut obtenir les expressions des champs électrique et magnétique avec, par exemple, pour les champs incidents (i.e. « faisceau ») :

$$\begin{aligned} E_r^i &= k_0 E_0\sum_{n=1}^{\infty}\sum_{m=-n}^{+n} c_n^{pw} g_{n,TM}^m\left[\psi_n''\left(k_0 r\right)+\psi_n\left(k_0 r\right)\right]P_n^{|m|}\left(\cos\theta\right)e^{im\varphi} \\ E_\theta^i &= \frac{E_0}{r}\sum_{n=1}^{\infty}\sum_{m=-n}^{+n} c_n^{pw}\left[g_{n,TM}^m\psi_n'\left(k_0 r\right)\tau_n^{|m|}\left(\cos\theta\right)+mg_{n,TE}^m\psi_n\left(k_0 r\right)\pi_n^{|m|}\left(\cos\theta\right)\right]e^{im\varphi} \\ E_\varphi^i &= \frac{iE_0}{r}\sum_{n=1}^{\infty}\sum_{m=-n}^{+n} c_n^{pw}\left[mg_{n,TM}^m\psi_n'\left(k_0 r\right)\pi_n^{|m|}\left(\cos\theta\right)+g_{n,TE}^m\psi_n\left(k_0 r\right)\tau_n^{|m|}\left(\cos\theta\right)\right]e^{im\varphi} \end{aligned} \tag{1.43}$$

$$\begin{aligned} H_r^i &= k_0 H_0\sum_{n=1}^{\infty}\sum_{m=-n}^{+n} c_n^{pw} g_{n,TE}^m\left[\psi_n''\left(k_0 r\right)+\psi_n\left(k_0 r\right)\right]P_n^{|m|}\left(\cos\theta\right)e^{im\varphi} \\ H_\theta^i &= \frac{-H_0}{r}\sum_{n=1}^{\infty}\sum_{m=-n}^{+n} c_n^{pw}\left[mg_{n,TM}^m\psi_n\left(k_0 r\right)\pi_n^{|m|}\left(\cos\theta\right)-g_{n,TE}^m\psi_n'\left(k_0 r\right)\tau_n^{|m|}\left(\cos\theta\right)\right]e^{im\varphi} \\ H_\varphi^i &= \frac{-iH_0}{r}\sum_{n=1}^{\infty}\sum_{m=-n}^{+n} c_n^{pw}\left[g_{n,TM}^m\psi_n\left(k_0 r\right)\tau_n^{|m|}\left(\cos\theta\right)-mg_{n,TE}^m\psi_n'\left(k_0 r\right)\pi_n^{|m|}\left(\cos\theta\right)\right]e^{im\varphi} \end{aligned} \tag{1.44}$$

Les $\pi_n^{|m|}\left(\cos\theta\right)$ et $\tau_n^{|m|}\left(\cos\theta\right)$ sont les fonctions de Legendre généralisées [17].

Au final, en utilisant l'algorithme récursif (§ 2.1.1) et en écrivant les conditions de continuité des composantes tangentielles des champs à la traversée de chaque couche, on obtient les expressions suivantes pour les coefficients de diffusion externes [A2] :

$$\begin{aligned} A_n^m &= g_{n,TM}^m\frac{M_L\psi_n\left(M_L x_L\right)H_n\left(x_L\right)-U_L\psi_n'\left(M_L x_L\right)}{M_L\xi_n\left(M_L x_L\right)H_n\left(x_L\right)-U_L\xi_n'\left(M_L r\right)} \\ B_n^m &= g_{n,TM}^m\frac{U_L\psi_n\left(M_L x_L\right)K_n\left(x_L\right)-M_L\psi_n'\left(M_L r\right)}{U_L\xi_n\left(M_L x_L\right)K_n\left(x_L\right)-M_L\xi_n'\left(M_L x_L\right)} \end{aligned} \tag{1.45}$$

Les H_n et K_n sont des fonctions récurrentes sur les champs internes (tout comme les fonctions $H_{b,n}^L$ et $H_{a,n}^L$ obtenues dans le paragraphe § 2.1.1). M_L et U_L correspondent à l'indice relatif et la perméabilité magnétique de la dernière couche.

L'expression (1.45) est remarquable dans le sens où, la deuxième partie du membre de droite correspond aux coefficients de diffusion externe d'une particule multicouche éclairée par une onde plane. Dans le cadre de la GLMT, ces coefficients sont donc simplement égaux au produit des coefficients de forme du faisceau et des coefficients externes obtenus pour une sphère multicouche éclairée par une onde plane :

$$\begin{aligned} A_n^m &= g_{n,TM}^m A_n \\ B_n^m &= g_{n,TM}^m B_n \end{aligned} \tag{1.46}$$

En pratique, ce résultat théorique [A2] entraîne que toutes les expressions analytiques et codes de calcul développés en *GLMT/sphère homogène* peuvent être simplement étendus au cas *GLMT/sphère multicouche* en utilisant un algorithme de calcul des A_n, B_n en onde plane et par une multiplication terme à terme des

termes d'expansion des champs. A titre d'exemple, dans le champ lointain, les fonctions d'amplitude d'une sphère multicouche éclairée par un faisceau de forme arbitraire, s'écrivent ainsi:

$$S_1 = \sum_{n=1}^{\infty}\sum_{m=-n}^{+n}\frac{2n+1}{n(n+1)}\left[mA_n g_{n,TM}^m \pi_n^{|m|}(\cos\theta) + iB_n g_{n,TE}^m \tau_n^{|m|}(\cos\theta)\right]\exp[im\varphi]$$
$$S_2 = \sum_{n=1}^{\infty}\sum_{m=-n}^{+n}\frac{2n+1}{n(n+1)}\left[A_n g_{n,TM}^m \tau_n^{|m|}(\cos\theta) + imB_n g_{n,TE}^m \pi_n^{|m|}(\cos\theta)\right]\exp[im\varphi] \quad (2.47)$$

2.2.2 Exemples de résultats numériques

En guise d'illustration des simulations rendues possibles grâce à ces travaux théortiques, la Figure 7 a) montre l'évolution de l'intensité du pic de diffraction (θ=0°) produit par une particule qui se déplace transversalement dans un faisceau gaussien, de diamètre au col : $2\omega_0$=20µm. Cette particule de 80 µm de diamètre est homogène, avec un indice de m=1.39, 1.40 et 1.41 ; ou à gradient linéaire d'indice, avec : m(r)=1.39…1.41 et m(r)=1.41…1.39 (L=1000). On constate que la focalisation du faisceau entraîne l'apparition de pics d'intensité dus à la diffraction (pics latéraux) et à la réfraction (pic central). Le pic central montre une sensibilité marquée à l'indice de la particule et à la présence d'un gradient interne. Ce phénomène est utilisé dans le cadre de l'ACI « Vitama » (§ 8.5.1).

La Figure 7 b) montre l'évolution du coefficient de pression de radiation transversale exercée par un faisceau laser focalisé ($2\omega_0 = 20\mu m$) sur une particule bicouche (sphérule dans l'eau, $m_1 = 1$, $m_2/m_3 = 1.2$, D=10µm). On constate que, pour cette particule, il existe deux positions latérales stables ($C_{pr,X} < 0$) (e.g. pour les particules homogènes il n'en existe qu'une seule).

Pour plus de détails sur ce modèle et ses applications, voir la reproduction des Articles [A2] et [A5], les paragraphes §4.1.1 (biophysique) et § 4.2.2 (combustion).

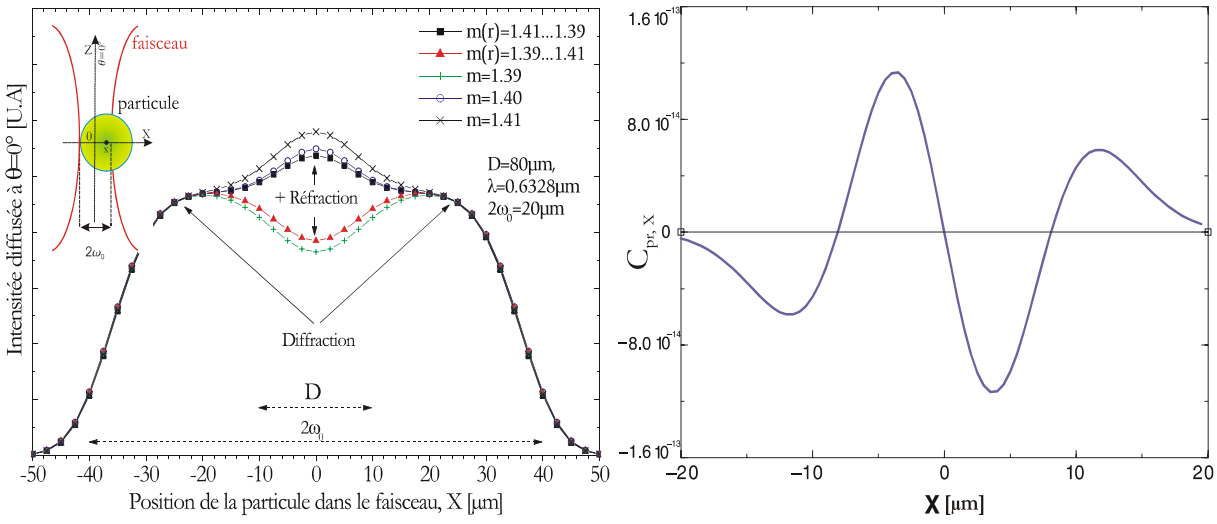

(a) (b)

Figure 7 GLMT/*sphère multicouche* : a) Evolution de l'intensité diffusée à θ=0°, par des particules homogènes ou à gradient linéaire d'indice, en fonction de leur position par rapport à l'axe d'un faisceau laser focalisé ; b) Coefficient de pression de radiation transverse exercée par un faisceau laser sur une sphérule (cf. reproduction de 'article [A2]).

2.3 Décomposition de Debye : sphère et cylindre homogènes

Debye a reformulé en 1909 [13] le problème de la diffusion dite de « Mie ». Il découle de ces travaux que l'on peut réécrire les expressions obtenues avec la LMT sous la forme de contributions liées à l'existence d'ondes partiellement réfléchies et partiellement transmises par la particule. Du fait de la géométrie du problème, ces ondes sont nécessairement sphériques pour une sphère et cylindriques pour un cylindre éclairé sous incidence normale. On distingue les ondes, diffusées par la particule, de celles qui se propagent à l'intérieur de cette dernière. Ceci amène à l'introduction, comme avec l'optique géométrique (voir le paragraphe § 2.4.1), de coefficients de «réflexion» et de «transmission » pour ces ondes partielles.

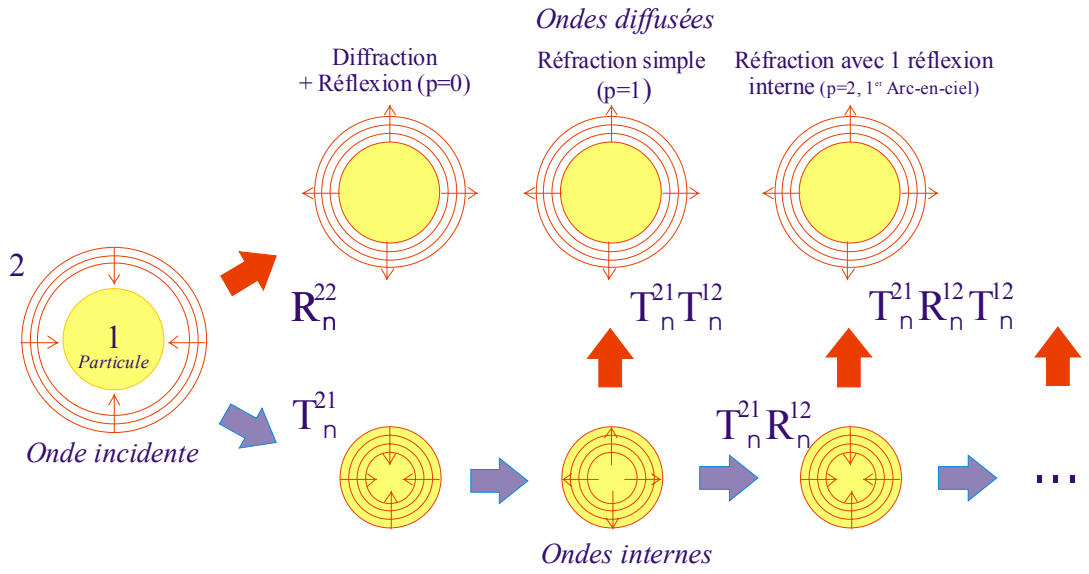

Figure 8 Décomposition de Debye : le champ incident et le champ diffusé sont décomposés en ondes partielles ayant subi p réflexions sur l'interface particule/milieu extérieur.

La Figure 8 présente un schéma d'interprétation de la méthode de décomposition de Debye, telle qu'elle a été reformulée par Hovenac et Lock [22] (voir également la référence [23]). La particule est associée au milieu 1 et le milieu extérieur, au milieu 2, avec:

- $R_n^{(22)}$: Coefficient de «réflexion» de l'onde incidente partiellement « réfléchie » (réflexion spéculaire et diffraction) vers le milieu extérieur
- $T_n^{(21)}$: Coefficient de transmission des ondes externes partielles vers l'intérieur de la particule. Une partie de l'onde incidente est donc transmise à l'intérieur de la particule.
- $R_n^{(11)}$: Coefficient de « réflexion » des ondes partielles internes sur la surface interne de la particule.
- $T_n^{(12)}$: Coefficient de transmission des ondes partielles internes vers le milieu extérieur.

.Les expressions des coefficients des séries de Debye sont données en annexe, voir le paragraphe §5.2.

Pour l'onde partielle p et l'ordre d'expansion n, les coefficients de diffusion externe s'écrivent :

$$\left.\begin{matrix} a_n(p) \\ b_n(p) \end{matrix}\right\} = \frac{1}{2}\begin{cases} 1-R_n^{(22)} \\ -T_n^{(21)}\left(R_n^{(11)}\right)^{p-1}T_n^{(12)} \end{cases} \quad \text{pour} \quad \begin{cases} p=0 \\ p\geq 1 \end{cases} \tag{2.48}$$

$p=0$ correspond à la diffraction et la réflexion spéculaire (indissociables !), $p=1$ à la réfraction simple, $p=2$ à l'onde partielle qui a subi une réflexion interne, $p=3$ avec deux réflexions internes, etc.

Il est important de noter qu'il existe une stricte équivalence entre les coefficients externes de diffusion de la théorie de Lorenz-Mie et ceux de la théorie de Debye (à condition que l'ordre de la décomposition $p\to\infty$, bien qu'en pratique $p\geq 100$ s'avère souvent suffisant) :

$$\begin{Bmatrix} a_n \\ b_n \end{Bmatrix}_{LMT} = \frac{1}{2}\left[1 - R_n^{(22)} - \sum_{p=1}^{\infty} T_n^{(21)} \left(R_n^{(11)}\right)^{p-1} T_n^{(12)}\right] \text{ pour } \alpha = \begin{cases} m \\ 1 \end{cases} \text{ et } \beta = \begin{cases} 1 \\ m \end{cases} \text{ et } p\to\infty \qquad (2.49)$$

Le calcul numérique direct de ces séries est relativement stable… et si l'on compare les diagrammes de diffusion obtenus avec les séries de Debye et la LMT, on trouve un très bon accord [RI8]. De petites différences apparaissent néanmoins à certains angles. En fait, les séries de Debye nécessitent la sommation complexe d'un plus grand nombre de fonctions que la LMT. Le calcul complet de ces séries est donc nécessairement plus sensible au développement du bruit numérique.

Le calcul de ces séries à été implémenter dans différents codes de calcul GLMT. Ceci, en s'appuyant sur les analogies établies dans le paragraphe § 2.2.1, entre les coefficients externes de diffusion pour un éclairement onde plane et un éclairement par un faisceau de forme arbitraire $\{A_n, B_n\} = \{g_{n,TM}^m a_n, g_{n,TE}^m b_n\}$. Ces résultats ont d'ailleurs été confirmés par des travaux récemment publiés par G. Gouesbet [24].

Ces codes de calcul ont a été utilisé pour interpréter certains mécanismes de diffusion de la lumière par des particules submillimétriques. De même, quels enseignements on peut en tirer pour les techniques classiques de granulométrie et réfractométrie optique de particules en écoulement [C38].

Le formalisme des séries de Debye a été dérivé pour le cylindre homogène [RI8], en s'appuyant sur les analogies établies dans le paragraphe §2.1.3, entre les harmoniques sphériques et cylindriques[7]. Ceci a permis d'introduire les séries de Debye dans les codes de simulation de différents systèmes de mesure (Interféromètre § 3.1.3, diffractomètre §3.1.4…)[4].

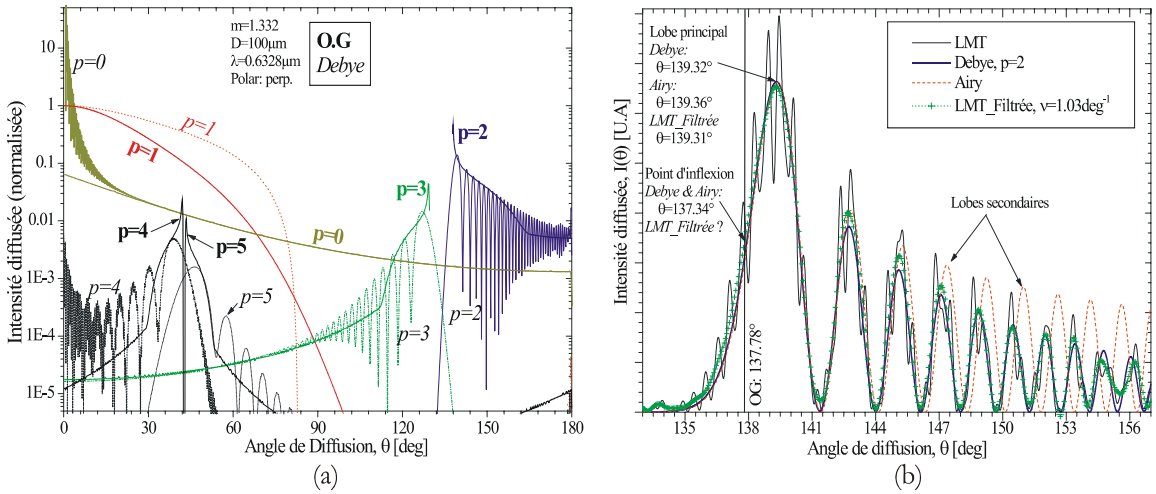

Figure 9 Décomposition de Debye : a) comparaison des diagrammes de diffusion pour les différents ordres de diffusion selon : l'optique géométrique et la décomposition de Debye ; b) diagrammes de diffusion dans la région de l'angle d'arc-en-ciel, selon : la théorie de Lorenz-Mie, la théorie de Lorenz-Mie filtrée passe-bas, la décomposition de Debye et la théorie d'Airy. Goutte d'eau de $D=100\mu m$, $\lambda=0.6328\mu m$ et de polarisation $\perp$.

[7] Nous avons suivi une démarche inverse à celle de Debye, Hovenac et Lock…

Exemples de résultats numériques :

L'optique géométrique (OG, §2.4.1) est très fréquemment utilisée pour prédire les propriétés de diffusion de la lumière de particules dont le diamètre est très grand devant la longueur d'onde, $D \gg \lambda$.
A ce titre, la Figure 9 a) compare, pour une goutte d'eau de D=100µm, les diagrammes de diffusion calculés avec l'optique géométrique et les séries de Debye. On constate ici que les prédictions de l'optique géométrique sont assez éloignées de la réalité… (e.g. la forme des «Arc-en-ciel» n'est que très grossièrement décrite, § 3.2.4). La Figure 9 b) compare les diagrammes de diffusion calculés avec la LMT, la LMT filtrée, les séries de Debye et la théorie d'Airy (Optique physique) ; dans la région du premier angle d'arc-en-ciel. Plusieurs remarques peuvent être faites :

- Les séries de Debye pour *p=2* nous donnent la composante basse fréquence du 1er arc-en-ciel. Elles permettent donc d'obtenir *directement* la forme de l'arc-en-ciel, sans structure d'ondulation.

- La théorie d'Airy donne avec une assez bonne précision la position du premier lobe et du premier point d'inflexion. Or ce sont ces deux grandeurs qui sont utilisées, à l'heure actuelle, pour déduire l'indice de réfraction des particules avec la technique de réfractométrie par angle d'arc-en-ciel «classique» [25, 26] ou globale [27] (§ 3.2.4). En revanche, la théorie d'Airy prédit très mal l'intensité relative et la position des autres lobes. A terme, cela pourrait poser de sérieux problèmes pour l'inversion des arcs-en-ciel globaux.

- Le diagramme obtenu avec la LMT filtrée passe-bas (ν*#1.03 deg⁻¹*.) est assez similaire à celui calculé avec les séries de Debye *(p=2)*. Cependant, le choix du filtre et de la fréquence de coupure est délicat. D'ailleurs, dans notre exemple, le calcul de la dérivée seconde du diagramme LMT filtrée passe-bas était trop bruité pour que l'on puisse obtenir la position du point d'inflexion [C38].

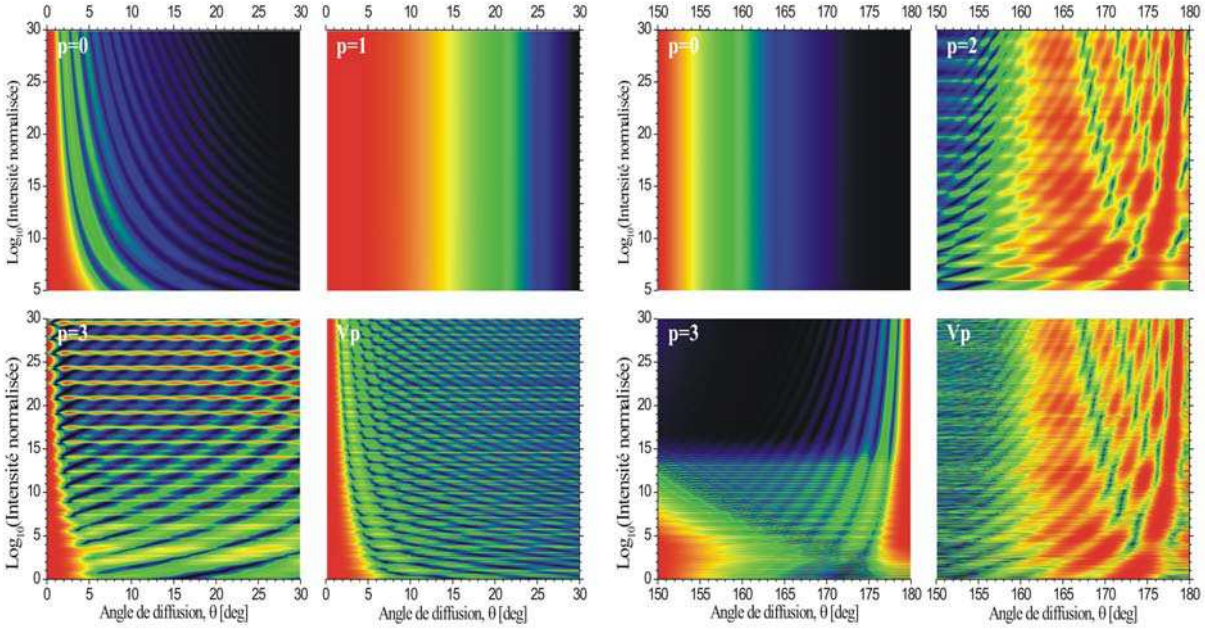

Figure 10 Décomposition de Debye : logarithme de l'intensité diffusée (vers l'avant et vers l'arrière) par une fibre de verre-E en fonction des ondes partielles prises en compte pour le calcul.

La Figure 10 présente, à droite, les diagrammes de diffusion d'une fibre de verre de renforcement, d'indice $\tilde{m} \approx 1.555 - 0.i$, dont le diamètre varie de $D=5\mu m$ à $D=30\mu m$, et pour la région angulaire $\theta = 150 - 180°$ (i.e. région du 1er angle d'arc-en-ciel). Ces diagrammes ont été calculés pour les ondes partielles : réfléchies et diffractées *(p=0)*, réfractées *(p=1)*, celles ayant subi deux réflexions internes (*p=3*) et au final, lorsque toutes les ondes partielles sont prises en compte ($\forall p$). La structure de l'arc-en-ciel appa-

raît très complexe… et elle l'est encore plus si l'on prend en compte tous les processus de diffusion ! Malgré cela, c'est dans cette région angulaire que fonctionne l'interféromètre que nous avons développé pour Saint-Gobain (§ 4.3.4).
La Figure 10 présente, à gauche, les résultats obtenus pour le domaine angulaire : $\theta = 0 - 30°$, la réflexion et la diffraction *(p=0)*, la réfraction simple *(p=1)*, la réfraction double *(p=2)* et lorsque tous les processus sont pris en compte *($\forall p$)*. Pour *p=0* on observe des «franges » brillantes et sombres qui s'apparentent à celles que prédit la théorie de la diffraction de Fraunhofer. La réfraction *(p=1)* produit un diagramme très simple, a contrario des ondes partielles (*p=3*). Lorsque que l'on somme toutes les ondes partielles ($\forall p$), on constate que le diagramme final diffère notablement de celui obtenu uniquement avec les ondes *(p=0)*. A travers cet exemple, il apparaît clairement que les ondes *(p=0)*, i.e. « la théorie de Fraunhofer », ne permettent pas de prédire correctement la figure de diffraction produite par des particules transparentes. Pour ce faire, il vaut mieux utiliser la LMT ou les premiers ordres des séries de Debye, voir par exemple le paragraphe § 3.1.4 et les références [A16] et [4].

2.4 Approximations géométrique, physique, méthode de Monte Carlo

2.4.1 Optique géométrique et particules à cœur (bicouche)

Optique géométrique

Van de Hulst [5] a fait un descriptif assez détaillé des subtilités de l'optique géométrique lorsqu'elle est appliquée au problème de la diffusion par une sphère homogène. Dans les quelques lignes qui suivent, nous nous contentons d'introduire quelques éléments et notations, auxquels les autres parties de ce manuscrit font fréquemment référence, du fait de la nature « intuitive » de l'optique géométrique.

L'optique géométrique (OG) sépare, en « rayons » réfléchis et « rayons » réfractés, la lumière diffusée par une particule (voir à ce propos le paragraphe sur les séries Debye § 2.3). Les directions de diffusion des différents rayons, voir la Figure 11, sont déterminées par les lois de Descartes. On distingue les rayons réfléchis (p=0) par la particule, des rayons simplement réfractés (p=1) et de ceux qui ont subi une réflexion interne (p=2), puis deux (p=3)… Sans absorption, cette décomposition est sans limite théorique (même si l'intensité résiduelle décroît fortement [4]). L'amplitude des différents rayons peut être calculée à l'aide des coefficients de Fresnel en amplitude. De même, la phase des différents rayons se déduit de considérations géométriques [5, 28]… On notera que :

- L'interférence des rayons entres eux (p=0, 1, 2, 3…) est à l'origine des résonances de « Mie ».
- Les rayons p=2, 3, 4… sont à l'origine du 1er , 2nd , 3ème… arc-en-ciel (bien qu'ils soient très mal décrits par l'OG)
- Les Résonances Morphologico-Dépendantes (MDRs) sont dues à l'interférence des rayons d'ordre élevé (p>1).
- Les ondes de surface et la diffraction ne sont pas décrites par l'optique géométrique.

On peut juger la qualité des prédictions de l'optique géométrique en les comparant avec celles des séries de Debye (i.e. exacts), voir la Figure 9 et le paragraphe § 2.3. En fait, les prédictions de l'OG sont plus qualitatives que quantitatives, d'où l'intérêt de développer des modèles de diffusion électromagnétique.

Particules à cœur

Les particules à cœur, ou bicouche, sont assez fréquemment rencontrées dans l'industrie et la Nature : cénosphères (résidus de combustion)[A5], particules enrobées (industrie pharmaceutique, nucléaire…), cellules biologiques, ect.

L'extension de la théorie de Lorenz-Mie Généralisée à des particules multicouches §2.2, permet de simuler très exactement les propriétés de diffusion de ces particules. Cependant, les résultats numériques de la GLMT ne sont pas toujours intuitifs… or, pour développer une méthode de détection originale de ces particules, il faut bien avoir une idée, une «intuition». Dans le cadre du stage de DEA de Damien Blondel [29], nous avons développé un modèle de diffusion de particules à cœur absorbant, basé sur l'optique géométrique. Celui-ci permet de visualiser les rayons qui impactent sur les surfaces interne et externe de ces particules, pour être ensuite diffusés dans la direction d'un détecteur. Ce type de modèle permet d'interpréter qualitativement les résultats obtenus avec la GLMT.

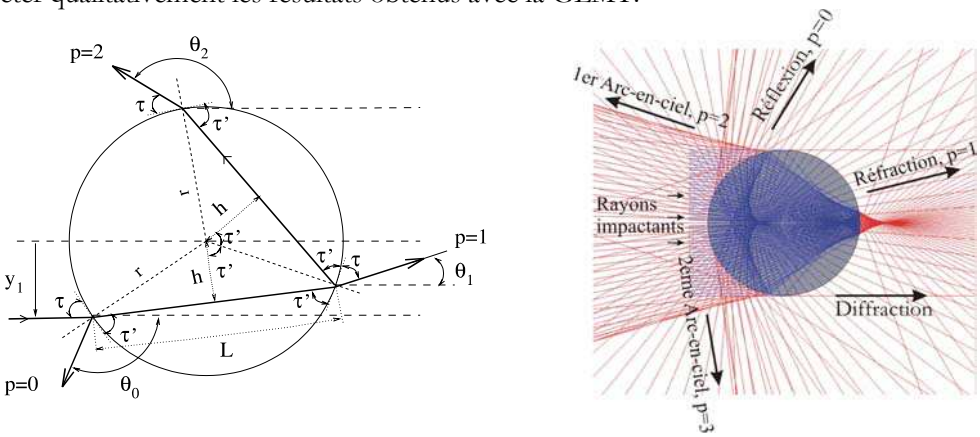

Figure 9 Diffusion de la lumière par une sphère : l'optique géométrique distingue les rayons réfléchis et réfractés par la particule

La Figure 11 a) simule les rayons lumineux diffusés dans la direction $\theta = 30 \pm 2°$, par une goutte d'eau dotée d'un cœur de carbone[8] avec pour le diamètre externe : D_{ext}=60 μm et pour le diamètre interne : D_{int}=30 μm, i.e. q= D_{int}/ D_{ext}=0.5. Le paramètre Y correspond au paramètre d'impact des rayons ou, de manière équivalente, à la position relative de la particule par rapport à un «rayon incident».

La Figure 11 b) présente l'évolution de phase des signaux lumineux diffusés par cette particule lorsqu'elle traverse une sonde phase Doppler fortement focalisée. Ce dernier calcul, obtenu avec la GLMT, montre l'existence de « plateaux de phase » : A, B, C et D, que l'on peut attribuer aux rayons a, d, g et h de la Figure 11 a), voir la reproduction de l'article [A5], Chapitre 9. .

Ces comparaisons *numériques* entre la OG et la GLMT, nous ont permis de proposer le principe d'une technique de mesure originale, basée sur la technique Dual Burst, § 3.2.1 et § 8.4.2. Celle-ci permet la mesure du diamètre externe de la particule bicouche, la détection du cœur et la mesure de son diamètre [A5]. Les possibilités de diagnostic de cette technique sont supérieures à ce que l'on trouve dans la littérature [30]. Faute de temps et de moyens, son principe n'a pas pu être validé expérimentalement. Le sujet reste donc ouvert, peut-être sera-t-il relancé dans un cadre contractuel…

[8] Modèle de cénosphère. Ce travail a été effectué dans le cadre d'une action incitative sur la combustion propre.

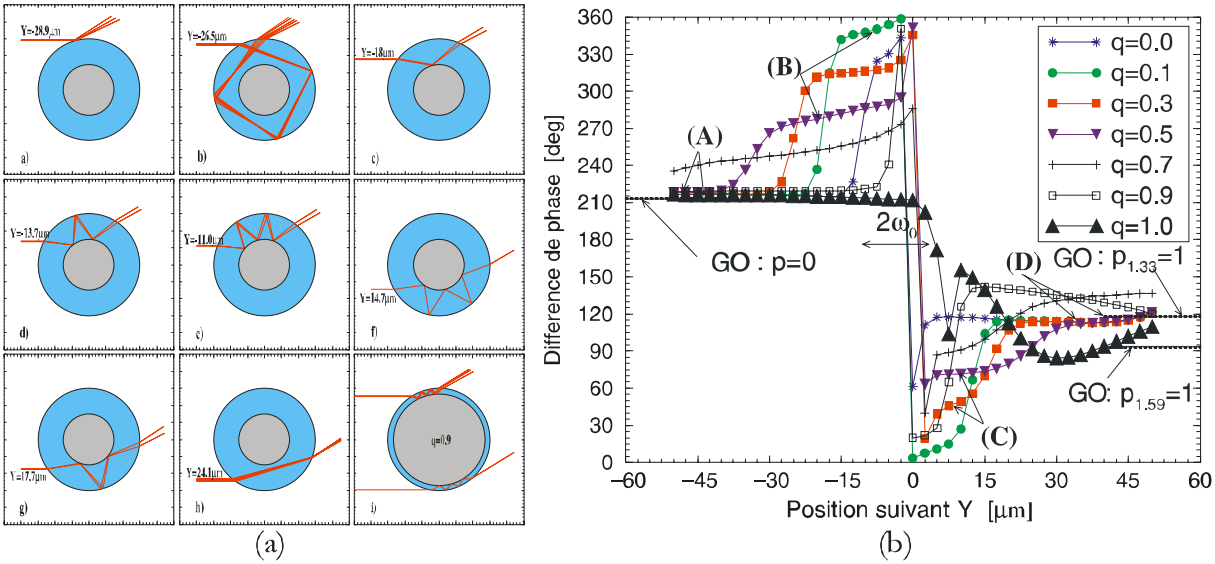

Figure 11 a) Simulation à l'aide de l'optique géométrique des rayons diffusés dans la direction $\theta = 30 \pm 2°$ par une particule bicouche. b) Simulation à l'aide de la GLMT de l'évolution de la phase des signaux Doppler produit par cette particule lorsque celle-ci traverse une sonde optique fortement focalisée (cf. reproduction de l'article [A5]).

2.4.2 Diffusion critique pour les particules homogènes

Les écoulements à bulles sont au cœur de nombreuses applications (cuves de mélange, réacteurs gaz-liquide, échangeurs à contact direct [31]…). Optiquement, une bulle peut être définie comme une particule dont l'indice de réfraction relatif au milieu environnant, $m_r = m/m'$ est inférieur à l'unité, $m_r < 1$, voir la Figure 12. Il peut donc aussi bien s'agir d'une «bulle» d'air $(m = 1)$ dans de l'eau $(m' \approx 1.332 \rightarrow m_r \approx 0.751)$ que d'une «goutte» d'eau dans une huile $(m' \approx 1.45 \rightarrow m_r \approx 0.919)$ …

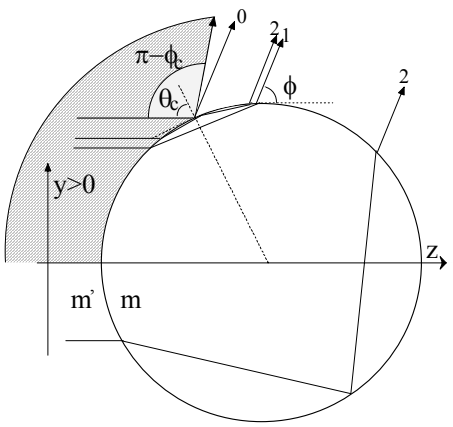

Figure 12 Géométrie du modèle de diffusion critique.

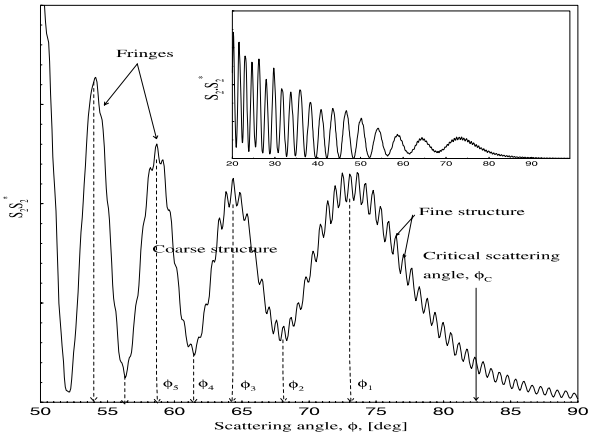

Figure 13 Diagramme de diffusion dans la région de l'angle de diffusion critique d'une bulle d'air, D=100µm dans l'eau m_r=0.751, LMT (cf. reproduction de l'article [A9]).

Les lois de la réfraction optique de Descartes indiquent qu'il existe un angle de réfraction limite pour les rayons lumineux qui se propagent d'un milieu de fort indice m' vers un milieu de faible indice m. Cet

angle « critique » conduit à une brusque transition vers la réflexion totale pour $\phi > \phi_c(m_r)$, avec $\phi_c(m_r) = 2\pi - 2\arcsin(m_r^{-1})$. La Figure 13 montre une simulation du diagramme de diffusion d'une bulle d'air dans l'eau, dans la région de l'angle de diffusion critique. On constate que près de l'angle prédit par l'optique géométrique $\phi_c(m_r) \approx 82.7°$, il existe une structure périodique, i.e. «des franges de diffusion critique». En fait, de même que pour l'arc-en-ciel [26], l'optique géométrique ne prédit pas correctement la position angulaire de la première frange brillante et la dépendance du phénomène de diffusion critique avec le diamètre de la particule. En revanche, l'OG prédit une dépendance explicite de $\phi_c(m_r)$ avec l'indice de la particule. On peut donc espérer remonter à l'indice de la particule, ou du milieu qui l'entoure, et ainsi caractériser ces différents matériaux (nature, fraction de mélange, température…)[A9, C18].

Marston et al. [32, 33] ont développé un modèle dit "d'optique physique" (« Physical Optics Approximation », POA) du phénomène de diffusion critique. Ce modèle utilise les intégrales de Fresnel pour décrire la propagation du rayonnement généré par le brusque changement d'intensité réfléchie près de l'angle critique $\phi_c(m_r)$. Seuls les rayons (p=0) sont pris en compte dans ce modèle de «diffraction». On néglige donc les contributions des rayons, ou ondes partielles, d'ordre p>0. La distribution angulaire de l'intensité de la lumière diffractée dans la région de l'angle de diffusion s'écrit [33] alors, pour $a \gg \lambda$ [9] :

$$I(\omega) = I_0 \left(\frac{a}{R}\right)^2 \frac{g(\omega)\bar{g}(\omega)}{8} \tag{2.50}$$

ω est un angle de déviation par rapport à l'angle de diffusion critique prédit par l'optique géométrique θ_c, voir la Figure 12. Ce paramètre dépend lui même des différents paramètres du problème:

$$\omega(\theta, m_r, a, \lambda) = \sin(\theta_c(m_r) - \theta)\sqrt{(a/\lambda)\cos(\theta_c(m_r))} \tag{2.51}$$

θ est l'angle de diffusion dans le plan de diffusion *(OXZ)*, I_0 est l'intensité de l'onde incidente, et *R*, la distance de la particule au point d'observation. La fonction $g\bar{g}(\omega) = [C(\omega)+1/2]^2 + [S(\omega)+1/2]^2$ est similaire à l'intégrale de Fresnel obtenue pour la diffraction en champ proche d'un front d'onde par un coin [10]. On introduit les intégrales de Fresnel en cosinus $C(\omega)$ et sinus $S(\omega)$:

$$F(\omega) = C(\omega) + iS(\omega) = \int_0^{\omega} \cos\left(\frac{\pi z^2}{2}\right) dz + i\int_0^{\omega} \sin\left(\frac{\pi z^2}{2}\right) dz \tag{2.52}$$

Rechercher la dépendance angulaire des franges de diffraction avec l'indice et le diamètre de la particule revient à déterminer les maxima et minima locaux de l'intégrale :

$$H(\alpha) = (C(\alpha)+1/2)^2 + (S(\alpha)+1/2)^2 \tag{2.53}$$

et donc, les zéros de sa dérivée :

$$(C(\alpha)+1/2)\cos\left(\frac{\pi \alpha^2}{2}\right) + (S(\alpha)+1/2)\sin\left(\frac{\pi \alpha^2}{2}\right) = 0 \tag{2.54}$$

Je n'ai pas réussi à obtenir de solutions analytiques à ce problème. Cependant, une approche numérique, un peu fine, du fait de la nature oscillante de cette intégrale, permet d'obtenir ces zéros. L'évolution de $H(\alpha)$ de même que les valeurs tabulées de ses premiers zéros sont donnés dans l'article [A8] reproduit dans le Chapitre 9.). Les zéros sont indexés par l'indice *j*. Les maxima et minima de $H(\alpha)$ correspondent aux valeurs impaires et paires de *j*. $H(\alpha)$ est équivalent à $I(\alpha)$ avec le changement de variable: $\alpha = \omega(\theta, m_r, a, \lambda)$.

[9] Pour conserver les notations de Marston, a représente ici le rayon de la particule.

La position des extremums (θ_j, i.e.: franges "brillantes" et" sombres") est obtenue par la résolution de l'équation suivante :

$$\alpha_j = \sin(\theta_c(m_r) - \theta_j)\sqrt{(a/\lambda)\theta_c(m_r)} \tag{2.55}$$

La dépendance angulaire de la frange *j*, en fonction du diamètre et de l'indice de la particule, est alors donnée par :

$$\theta_j = \frac{180}{\pi}\left[\pi - \arcsin\left(\alpha_j\sqrt{\frac{m_r\lambda/a}{\sqrt{m_r^2-1}}}\right) - 2\arcsin\left(m_r^{-1}\right)\right] \tag{2.56}$$

De cette dernière expression, il apparaît que, pour un indice donné et pour $a >> \lambda$, la position angulaire des franges de diffusion critique évolue avec le diamètre de la particule suivant une loi en $(\theta_c - \theta) \propto 1/\sqrt{a}$. Cette dépendance est plus importante que celle prédite par la théorie d'Airy de l'arc-en-ciel, pour laquelle la dépendance est en $(\theta_r - \theta) \propto 1/a^{2/3}$ (où θ_r est la position angulaire de arc-en-ciel, prédit par l'optique géométrique).

Dans le cas d'un écoulement où l'indice de réfraction des particules et du fluide est connu, le rayon de ces dernières peut être déduit de la mesure de la position angulaire d'un des extrema du diagramme de diffusion critique (d'ordre *j* connu) :

$$a_j(m_r) = \frac{\alpha_j^2\lambda m_r}{\sin^2\left[\theta_j - \pi + 2\arcsin\left(m_r^{-1}\right)\right]\sqrt{m_r^2-1}} \tag{2.57}$$

Dans le cas où l'indice des particules et/ou celui du fluide ne sont pas connus (mélange, coalescence…), il faut pouvoir obtenir la granulométrie des particules indépendamment de l'indice relatif de chaque particule. Ce problème peut être résolu en mesurant la position de deux extrema[10] dans le diagramme de diffusion, $j \equiv p$ et $j \equiv q$, avec $p < q$. En effet, après quelques manipulations mathématiques [RI5], on montre que le rayon de la particule détectée s'écrit :

$$a_{pq} = \frac{\alpha_p^2 + \alpha_q^2 - 2*\cos(\theta_q - \theta_p)\alpha_p\alpha_q}{\sin^2(\theta_q - \theta_p)} \times \frac{\lambda}{\sqrt{1 - \cos\left[\frac{\theta_p}{2} - \frac{1}{2}\arctan\left(\sin(\theta_q - \theta_p)\frac{\alpha_p}{\alpha_q - \alpha_p\cos(\theta_q - \theta_p)}\right)\right]^2}} \tag{2.58}$$

De même, on trouve l'indice de réfraction relatif de la particule:

$$m_{pq} = \left\{\sin\left[\frac{1}{2}(\pi - \theta_p) - \frac{1}{2}\arctan\left(\sin(\theta_q - \theta_p)/\left[\cos(\theta_q - \theta_p) - \frac{\alpha_q}{\alpha_p}\right]\right)\right]\right\}^{-1} \tag{2.59}$$

L'optique physique améliore de façon très significative les prédictions de l'optique géométrique. Elle permet notamment de retrouver la dépendance de la position des franges avec le diamètre. Cependant, on constate un décalage angulaire systématique avec la LMT. Ce décalage, qui n'est pas trop pénalisant pour les mesures, est vraisemblablement dû aux rayons/ondes que nous avons négligés $(p > 0)$ et/ou au phénomène de Goos-Hänchen (i.e. effet de type onde évanescente)[34]. Ce modèle a été validé expérimentalement, voir le paragraphe § 3.2.3 et la reproduction de l'article [A9].

[10] Expérimentalement, voir le paragraphe § 3.2.3, on a tout intérêt à prendre les deux premières franges brillantes, *p=1* et *q=3*, qui sont les plus facilement détectables.

2.4.3 Méthode de Monte Carlo pour les particules hétérogènes

De même que pour les particules bicouche, de nombreuses technologies mettent en jeu des particules hétérogènes dont il faut pouvoir caractériser le diamètre, la vitesse et la teneur en «hétérogénéités». Dans l'industrie chimique il s'agira, par exemple, d'optimiser les conditions de séchage et de dépôt de poudres céramique, de peintures… Dans les industries agroalimentaire et pharmaceutique, il s'agira d'optimiser les conditions de lyophilisation de différents produits (café, lait, granules…)[35, 36]. Bien souvent, ces hétérogénéités prennent la forme de petites particules en suspension dans un solvant. Il peut également s'agir d'inclusions liquides ou gazeuses dans un solide ou un liquide.

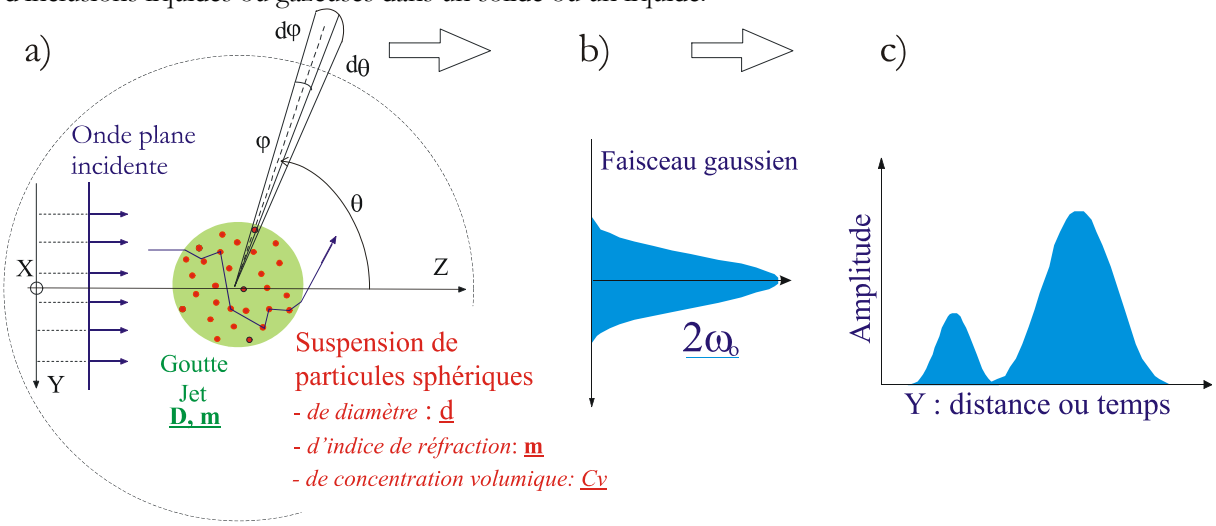

Figure 14 Diffusion de la lumière par une particule hétérogène : schéma de principe de la méthode de Monte Carlo avec faisceau incident gaussien (cf. reproduction de l'article [A8]).

En collaboration avec Jean-Luc Firpo (IUSTI), nous avons développé différents modèles de prédiction des propriétés de diffusion de la lumière par une sphère, ou un cylindre, de diamètre D et d'indice nominal m, formés à partir d'une suspension de particules de diamètre d, d'indice m' et de concentration volumique C_v. Le modèle le plus sophistiqué utilise une méthode de type Monte Carlo [A8, C20]. Il permet de simuler les effets de la *diffusion multiple* et de traiter le cas d'un éclairement par une onde plane ou un faisceau laser gaussien (pour plus de détails, voir la reproduction de l'article [A8] du Chapitre 9.). Il est à noter que Wriedt et Schuh [37] ont développé, en parallèle, un modèle assez similaire au notre.

La Figure 14 schématise l'algorithme de Monte Carlo mis au point. L'onde incidente est tout d'abord supposée plane. Elle est décomposée en rayons dont l'interaction avec la surface externe de la goutte, ou du jet, est traitée avec les lois de l'optique géométrique (en 3D), voir la Figure 14 a). La diffusion de ces rayons ou «photons», par les particules de la suspension, est traitée avec une méthode probabiliste [38]. Cette dernière est basée sur le calcul du libre parcours moyen des photons dans la suspension et d'une fonction de phase moyennée, calculée avec la LMT. Après de multiples diffusions (voir la vignette de la page *106.*), la propagation vers un détecteur virtuel, de chaque photon, est traitée avec les lois de l'optique géométrique. On suit ainsi le parcours, parfois très erratique, de centaines de milliers de photons.
Pour prendre en compte la distribution d'intensité d'un faisceau laser incident, on pondère l'intensité de chaque photon qui parvient au détecteur, par une fonction gaussienne, Figure 14 b). En décalant spatialement cette fonction gaussienne, on peut simuler les propriétés de diffusion d'une particule hétérogène dont la surface est balayée par un faisceau laser, Figure 14 c).

A titre d'exemple, la Figure 15 présente les diagrammes de diffusion obtenus pour un jet capillaire, de diamètre D=110µm, composé de billes de latex (d=3.3µm, m=1.6) en suspension dans de l'eau (m=1.332). La concentration volumique en billes de latex varie de C_v=0% à C_v=7.5%. Clairement, la présence de particules en suspension, les effets de la diffusion multiple, conduisent à une disparition du phénomène d'arc-en-ciel et à une forte décroissance de l'intensité diffusée vers l'avant. La diffusion multiple tend ici à produire une diffusion plus isotrope. Les photographies présentées à droite de la Figure 15 sont celles d'un jet dont la concentration en suspension est égale à C_v=0% et C_v=1.25%. Les particules de la suspension favorisent la diffusion des photons hors du plan de diffusion (YZ), i.e. la tâche laiteuse formée par le faisceau laser s'allonge suivant l'axe du jet).

En fait, dans notre modèle, les étapes b) et c) servent à simuler la réponse de la technique Dual Burst lors de la caractérisation simultanée de la vitesse, de la taille et de la concentration en suspension de gouttes et de jets, voir à ce propos le paragraphe § 3.2.1 et la Figure 31.

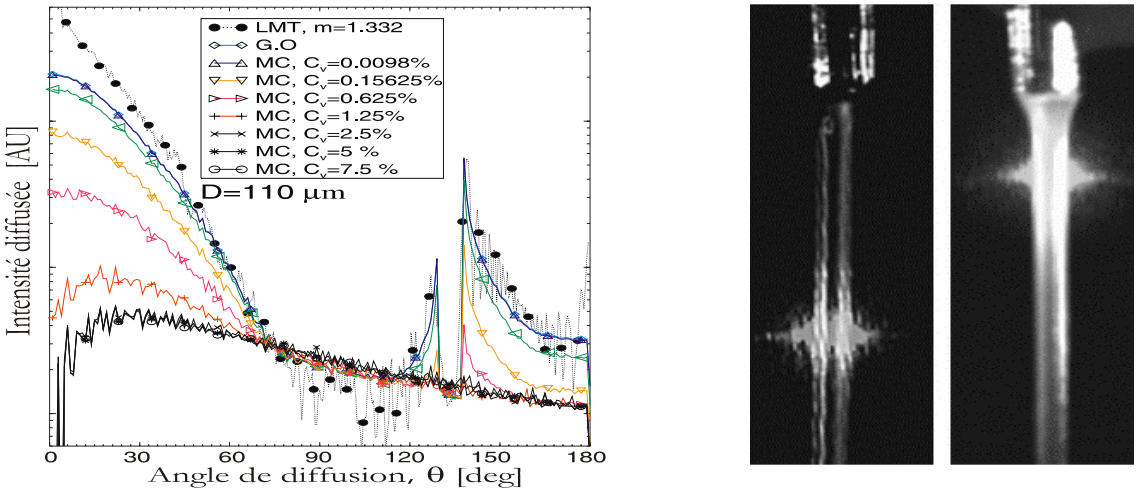

Figure 15 Diffusion de la lumière par un jet hétérogène avec, à gauche : diagrammes de diffusion obtenus avec la méthode de Monte Carlo, pour différentes concentrations en suspensions; à droite : photographie d'un jet de D=110µm lorsque la concentration en suspension augmente de C_v=0% à C_v=1.25% (cf. reproduction de l'article [A8]).

2.4.4 Modèle statistique pour les particules irrégulières

Les particules en écoulement n'ont pas toujours un état de surface « parfait » (i.e. à l'échelle des longueurs d'onde du visible, $\lambda = 0.35 - 0.75 \mu m$). Ceci est particulièrement vrai pour les particules solides, a contrario des particules liquides ou gazeuses (i.e. tension superficielle) [C40]. Du fait de la complexité mathématique du problème, il existe assez peu d'outils pour prédire les propriétés de diffusion de particules irrégulières dont le paramètre de taille est important ($\alpha > 10$)[39, 40].

En 1990, Pierre Drossart a publié [41] un modèle physique permettant de prédire très simplement les propriétés de diffusion de la lumière de particules irrégulières. Fondamentalement, ce modèle pose comme hypothèse que les irrégularités de surface n'induisent qu'un déphasage aléatoire, α_n et β_n, des deux composantes du champ électromagnétique diffusé. Pour une particule qui s'écarte peu de la sphéricité, les effets des irrégularités de surface peuvent donc être pris en compte avec la Théorie de Lorenz-Mie (TLM), en introduisant simplement des termes de déphasage aléatoire $e^{i\alpha_n}$ et $e^{i\beta_n}$:

$$S_1(\theta)=\sum_{n=1}^{\infty}\frac{2n+1}{n(n+1)}\left(a_n\pi_n(\cos\theta)+b_n\tau_n(\cos\theta)\right)e^{i\alpha_n}$$
$$S_2(\theta)=\sum_{n=1}^{\infty}\frac{2n+1}{n(n+1)}\left(b_n\pi_n(\cos\theta)+a_n\tau_n(\cos\theta)\right)e^{i\beta_n} \quad (2.60)$$

A partir de ces deux fonctions complexes, on peut déduire la moyenne temporelle et statistique de l'intensité diffusée par une particule :

$$I_1(\theta)=\left\langle S_1(\theta)\bar{S}_1(\theta)\right\rangle$$
$$I_2(\theta)=\left\langle S_2(\theta)\bar{S}_2(\theta)\right\rangle \quad (2.61)$$

Si l'on veut obtenir une forme analytique pour l'expression de $I_{1,2}(\theta)$, il faut faire une hypothèse sur la distribution statistique des irrégularités de surface. Dans le modèle de Drossart, les déphasages introduits sont indépendants et aléatoires, de distribution statistique $F(\alpha)$, avec pour $n\neq m$: $\langle\exp[i(\alpha_n-\alpha_m)]\rangle = \langle\exp[i\alpha_n]\rangle^2=\eta^2(1)$. η est la transformée de Fourier de la distribution statistique F. Dans le cas d'une distribution gaussienne des déphasages, d'écart type σ, on à : $F(\alpha)=\left(\sigma\sqrt{2\pi}\right)^{-1}\times\exp\left[-\alpha^2/\left(2\sigma^2\right)\right]$, avec $f=.\exp\left(-\sigma^2\right)$. Pour une faible valeur de l'écart type : $f\approx\left(1-\sigma^2\right)$ et, pour ce cas, on peut exprimer l'intensité diffusée par les particules irrégulières sous la forme:

$$I_1(\theta)=f\ I_1^0(\theta)\ +\ (1-f)\,I_1^{\infty}(\theta)$$
$$I_2(\theta)=f\ I_2^0(\theta)\ +\ (1-f)\ I_2^{\infty}(\theta) \quad (2.62)$$

où I_1^0 et I_2^0 correspondent aux fonctions d'intensité de la LMT «classique» (i.e. particule sphériques et ondes sphériques cohérentes). Pour les termes I_1^{∞} et I_2^{∞} on a:

$$I_1^{\infty}(\theta)=\sum_{n=1}^{\infty}\left(\frac{2n+1}{n(n+1)}\right)^2\left|a_n\pi_n(\cos\theta)+b_n\tau_n(\cos\theta)\right|^2$$
$$I_2^{\infty}(\theta)=\sum_{n=1}^{\infty}\left(\frac{2n+1}{n(n+1)}\right)^2\left|b_n\pi_n(\cos\theta)+a_n\tau_n(\cos\theta)\right|^2 \quad (2.63)$$

Ces dernières expressions correspondent à des sommations d'ondes non cohérentes. Le sens physique de f est donc celui d'un terme de cohérence partielle. Dans le modèle statistique de Drossart, l'écart type des déphasages est relié au rayon moyen (ou initial) de la particule en posant : $\sigma=(2\pi/\lambda)\rho a=\rho x$, où a est le rayon moyen de la particule, λ la longueur d'onde de la source et x le paramètre de taille. Des considérations géométriques ont conduit Petrova et Markiewicz [42] à corriger cette dernière expression en y ajoutant un terme de projection par rapport à l'angle de diffusion θ : $\sigma=\rho x\sin\theta$.

On peut apporter un second terme correcteur à cette dernière expression, en tenant compte de l'indice réel de la particule : $\sigma=m\rho x\sin\theta$. De plus, pour certains problèmes, il est important de pouvoir estimer l'écart type des fluctuations d'intensité auxquelles on peut s'attendre du fait, de « l'orientation » de la particule irrégulière, ou plus simplement, des fluctuations statistiques des irrégularités de la surface.
Le problème traité par Drossart peut être reformulé [C23] en montrant, notamment, que les déphasages induits par les irrégularités de surface peuvent être pris en compte au niveau des coefficients de diffusion externe (i.e. approximation localisée) et non plus des champs diffusés:

$$\begin{pmatrix}a_n\\b_n\end{pmatrix}_{\textit{sphère parfaite}}\rightarrow\begin{pmatrix}a_ne^{i\alpha_n}\\b_ne^{i\beta_n}\end{pmatrix}_{\textit{sphère irrégulière}} \quad (2.64)$$

Numériquement on obtient les mêmes résultats qu'avec l'approche analytique de Drossart, mais au prix de calcul donc beaucoup plus longs… car il faut sommer numériquement un grand nombre de diagrammes de diffusion. Mais cette méthode présente plusieurs avantages et notamment :

- L'obtention d'un écart-type sur l'intensité diffusée (paramètre très important pour la granulométrie optique),
- La possibilité de simuler des irrégularités de surface dont la distribution n'est pas simplement gaussienne,
- Une implémentation rapide dans différents codes de calculs qui nécessitent des intégrations particulières (e.g. interférométrie [C23]),
- A terme, de modéliser les propriétés de diffusion de particules hétérogènes par couplage avec les modèles de diffusion de particules multicouche...

A titre d'exemple, la Figure 16 a) montre une simulation du diagramme de diffusion d'une particule d'oxyde de zirconium, D=0.5 µm, pour différents états de rugosité de sa surface. Il apparaît clairement ici que les particules irrégulières diffusent plus de côté qu'une particule sphérique de même diamètre équivalant. Le paragraphe § 4.2.2 présente une application concrète de ce dernier résultat.

La Figure 16 b) simule la réponse d'un interféromètre phase Doppler à la mesure de billes de verres présentant des irrégularités de surface [C23]. Le déphasage moyen croit linéairement avec le diamètre moyen, comme pour des billes à l'état de surface parfait. En fait, les irrégularités de surface n'induisent, en moyenne, qu'un écart type sur le diamètre mesuré (i.e. élargissement de la distribution des diamètres mesurés). Dans le cas présent, cet écart-type est très significatif (il augmente avec le diamètre de la particule, à état de surface constant). Cet dernier effet à été confirmer qualitativement par des résultats expérimentaux [C23].

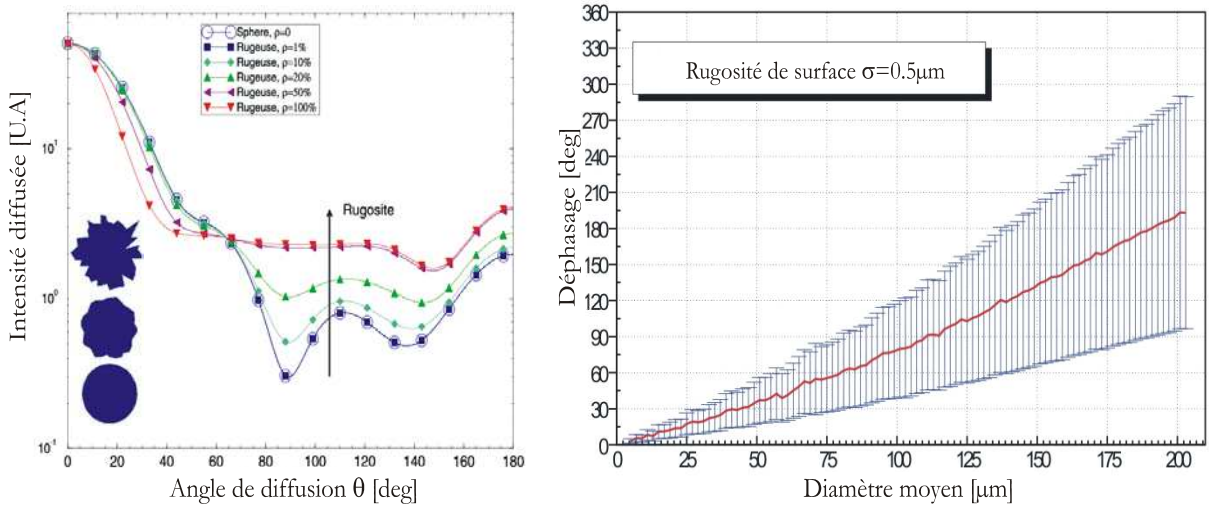

(a) (b)

Figure 16 Simulation, avec le modèle statistique, des propriétés de diffusion de particules irrégulières: a) Diagrammes de diffusion d'une particule de ZrO2, D=0.5µm, initialement sphérique, et dont la rugosité de la surface augmente ; b) Réponse d'un interféromètre phase Doppler à la mesure de billes de verres dont la surface est irrégulière.

Chapitre 3

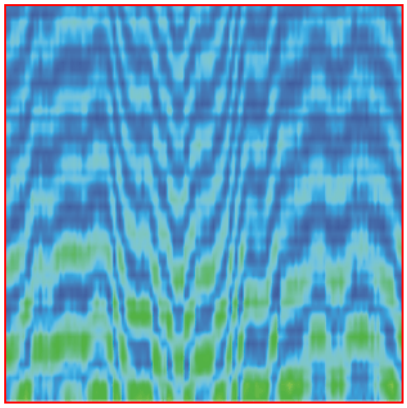

GRANULOMETRIE ET REFRACTOMETRIE DE PARTICULES EN ECOULEMENT

Ce chapitre présente, de manière succincte, les réalisés travaux sur la caractérisation du diamètre, de l'homogénéité, de la position, de la sphéricité et du matériau de particules en écoulement. Ces travaux, à dominante expérimentale, ont été essentiellement motivés par les résultats théoriques établis dans le chapitre précédant ou par une «idée» originale susceptible d'être utile, à terme, pour la caractérisation des écoulements.

3.1 Granulométrie optique

La *granulométrie* a pour objet la détermination de la *forme* et de la *distribution des diamètres* de petites particules (de quelques dizaines de nanomètres au millimètre) [C40]. Diverses disciplines scientifiques requièrent ce type de diagnostic et notamment, la *mécanique des fluides* [36]. Cette dernière impose comme contraintes supplémentaires de devoir *caractériser in situ les particules*, en *quelques micro ou millisecondes*, de déterminer *leur dynamique* et celle du *fluide* qui les transporte, sans perturber ce dernier !

Les techniques de *granulométrie optique* (ou « *laser* ») répondent en partie à ces contraintes. Cependant, a contrario des techniques de vélocimétrie laser, elles nécessitent une description précise de l'interaction lumière/particule. Ce qui nécessite de développer des modèles de diffusion sophistiqués (Chapitre 2.) et complexifie encore un peu plus le problème de la granulométrie optique de particules en écoulement.

3.1.1 Anémométrie Phase Doppler

Le sujet initial de ma thèse[11] portait sur l'élimination des effets de trajectoire auxquels sont sujets les Anémomètre Phase Doppler (PDA, [43-46]). Ces effets de trajectoire, liés à l'utilisation de faisceaux laser focalisés[12], se traduisent par une dépendance du diamètre mesuré avec la trajectoire des particules[46-48]. Le problème est que ces trajectoires ne sont pas précisément connues, même si, généralement, les écoulements ont une orientation privilégiée.

Les solutions proposées [A1, A6-7, C2, C4-5] sont basées sur l'utilisation d'une configuration optique et d'un traitement du signal particulier. Elles ont fait l'objet d'une collaboration intense avec le laboratoire du professeur F. Durst (LSTM, Université d'Erlangen-Nuremberg, Allemagne). Au final, ces travaux ont conduit au dépôt de deux brevets [B1, B2] et à la commercialisation, par la société Danoise (Dantec Dynamics [49]), d'un nouveau type de système phase Doppler «Dual Mode», voir la Figure 18 et le paragraphe § 3.2.2.

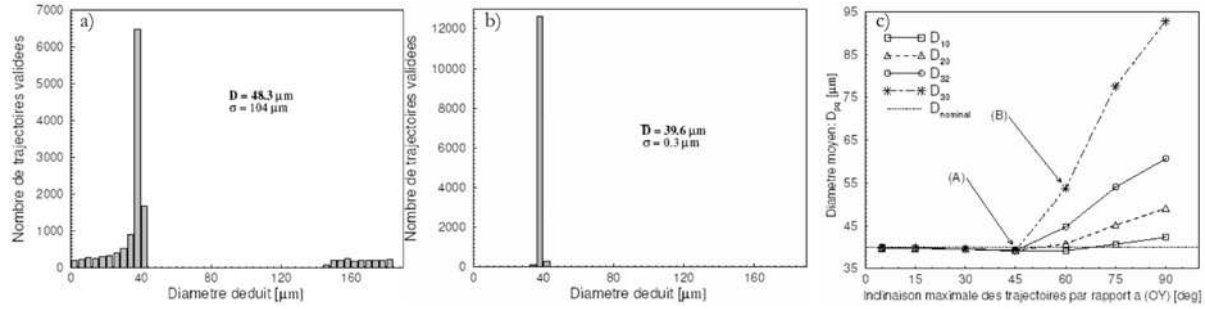

Figure 17 Simulation des histogrammes des tailles mesurées pour des gouttes d'eau de D=40µm dont la trajectoire aléatoire est inclinée de moins de 30° par rapport à l'axe Y avec : a) Un système phase Doppler classique et b) un système Dual Mode. c) Système Dual Mode : évolution des différents diamètres moyens en fonction de l'inclinaison maximale des trajectoires.

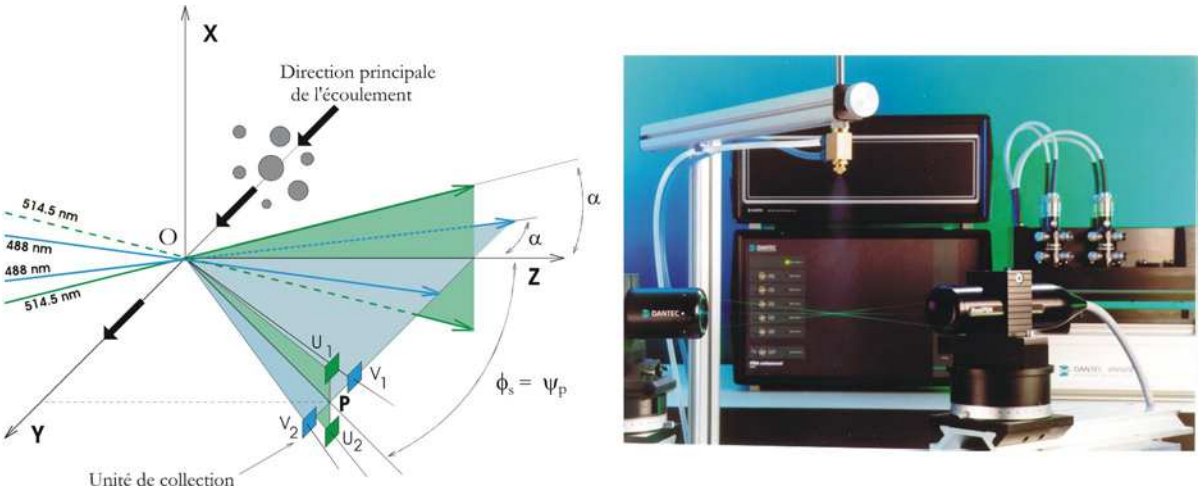

Figure 18 Schéma de principe (breveté) d'un interféromètre phase Doppler en configuration «DualMode» et photographie du système commercialisé par la société Dantec Dynamics [49].

La Figure 17 présente des résultats numériques [T1] qui ont été à l'origine du développement du système Dual Mode. Les figures a) et b) comparent la réponse d'un système phase Doppler classique et d'un système Dual Mode, lors de la mesure de gouttes d'eau (D=40 µm) dont les trajectoires aléatoires sont in-

[11] CORIA-UMR n°6614 CNRS / Université et INSA de Rouen, Nov. 1995 [T1]

[12] Ce sujet répondait à une motivation interne au laboratoire en constituant une des premières applications de la GLMT à un problème de granulométrie optique et ceci, bien avant que le partenariat avec DANTEC ne se développe.

clinées de moins de 30° de l'axe principal supposé de «l'écoulement» (Y). Le diamètre du volume de mesure est de $2\omega_0$.=80μm. La réponse du système Dual mode est quasi parfaite, alors que celle du système classique fait apparaître des diamètres près de 4 fois supérieurs à la valeur attendue (i.e. la mesure des flux sera complètement faussée).

La Figure 18 c) représente l'évolution des diamètres moyens obtenus avec un système Dual Mode, pour différentes inclinaisons des trajectoires. Pour des inclinaisons inférieures à 45°, la correction est quasi parfaite. Pour des inclinaisons supérieures, l'efficacité décroît pour s'annuler pour une inclinaison de 90°.

3.1.2 Sondes interférométriques à N-faisceaux (N>2)

L'Anémométrie Phase Doppler est la technique optique de référence pour l'étude des milieux diphasiques [C40][23]. Son domaine d'application est cependant limité du fait, notamment, de certaines contraintes sur la forme et la composition des particules (sphéricité et homogénéité parfaites, indice connu)… Elle est également limitée par des problèmes techniques (nombre de détecteurs, laser multiraies,…).

Pour remédier en partie a ces problèmes, j'ai introduit le principe d'un système phase Doppler utilisant N paires de faisceaux, incohérentes entre-elles [C24, A12], avec N>2. Ce mode de fonctionnement est bien adapté à la réalisation d'un capteur compact, miniaturisé [C15] ou à très haute résolution. Il pourrait également permettre de caractériser des particules irrégulières [C23], en se basant sur les travaux publiés par Amir Naqwi [50]. Pour plus de détails sur cette technique originale, voir la reproduction de l'article [A12] dans le Chapitre 9.

Je développe actuellement une variante de cette technique [C31, *A20*]. Elle utilise un volume de mesure formé par l'intersection de 3 faisceaux lasers coplanaires et cohérents entre eux. Classiquement, ce volume de mesure, ou sonde optique, peut être produit en focalisant le faisceau d'un laser mono raie sur un réseau de diffraction ou une cellule de Bragg [51]. La particularité ici est que l'on utilise les trois principaux ordres de diffraction $-1, 0, +1$. Dans cette configuration, les faisceaux ± 1 sont décalés en fréquence de la quantité $\pm \nu_s$ par rapport à la fréquence ν du faisceau d'ordre 0.

Les différents travaux réalisés pour décrire le comportement de cette technique d'interférométrie à trois ondes sont résumés dans ce qui suit.

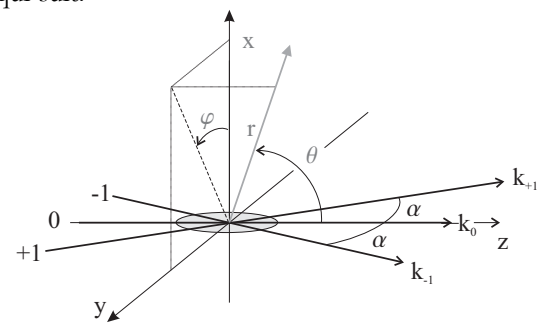

Figure 19 Géométrie du modèle à 3 faisceaux cohérents.

Modèle analytique avec ondes planes

Considérons tout d'abord les faisceaux incidents comme des ondes planes harmoniques, voir la Figure 19. Dans ce cas, le champ électrique au niveau du volume de mesure s'écrit :

$$E_T(y,z,t) = E_1 e^{j[\mathbf{k}_1.\mathbf{r}-2\pi(\nu+\nu_s)t]} + E_{-1} e^{j[\mathbf{k}_{-1}.\mathbf{r}-2\pi(\nu-\nu_s)t]} + E_0 e^{j[\mathbf{k}_0.\mathbf{r}-2\pi\nu t]} \quad (3.1)$$

La distribution de l'intensité lumineuse dans le plan *(y,z)* est calculée à l'aide du vecteur de Poynting :

$$I(y,z,t)=\frac{k}{2\mu_0\omega}\mathrm{Re}\left\{E_T E_T^*\right\} \tag{3.2}$$

Après quelques manipulations mathématiques, on trouve que la distribution d'intensité peut être reformulée sous la forme (avec $E_{-1}=E_{+1}, E_0\in\mathbb{R}$) :

$$I(y,z,t)=2E_1^2\left\{1+\cos\left[4\pi\frac{y}{\delta_2}-4\pi\nu_s t\right]\right\}+\left\{1+4E_1E_0\cos\left[2\pi\frac{y}{\delta_1}-2\pi\nu_s t\right]\cos\left[\beta z\right]\right\} \tag{3.3}$$

avec

$$\delta_1=\lambda/\sin\alpha \qquad \delta_2=\lambda/(2\sin\alpha) \qquad \beta=k(\cos\alpha-1) \tag{3.4}$$

La forme de l'équation (3.3) permet de tirer des enseignements importants sur les caractéristiques de cette sonde à trois ondes cohérentes:

- Deux réseaux de franges parallèles à l'axe optique Z s'y superposent. L'interfrange du premier est de δ_1 et celui de second de δ_2, avec $\delta_1=2\delta_2$.

- δ_2 correspond à l'interfrange d'un système classique à deux faisceaux $(-1,+1)$.

- δ_1 est l'interfrange du réseau formé par l'interférence des paires de faisceaux $(-1,0)$ et $(0,+1)$. Les franges sont parallèles à l'axe Z avec une modulation en amplitude de période : $\delta_Z=2\pi/\beta$, Figure 20 a).

- Ces deux réseaux sont modulés dans le temps, avec une fréquence $2\nu_s$ pour δ_2 et ν_s pour δ_1.

- Dans le cas le plus simple, où $E_0=E_1=E_{-1}=1$, le rapport d'amplitude des deux réseaux de franges varie entre $Min\{I(\delta_1,z,t)/I(\delta_2,z,t)\}=1/9$ et $Max\{I(\delta_1,z,t)/I(\delta_2,z,t)\}=9$.

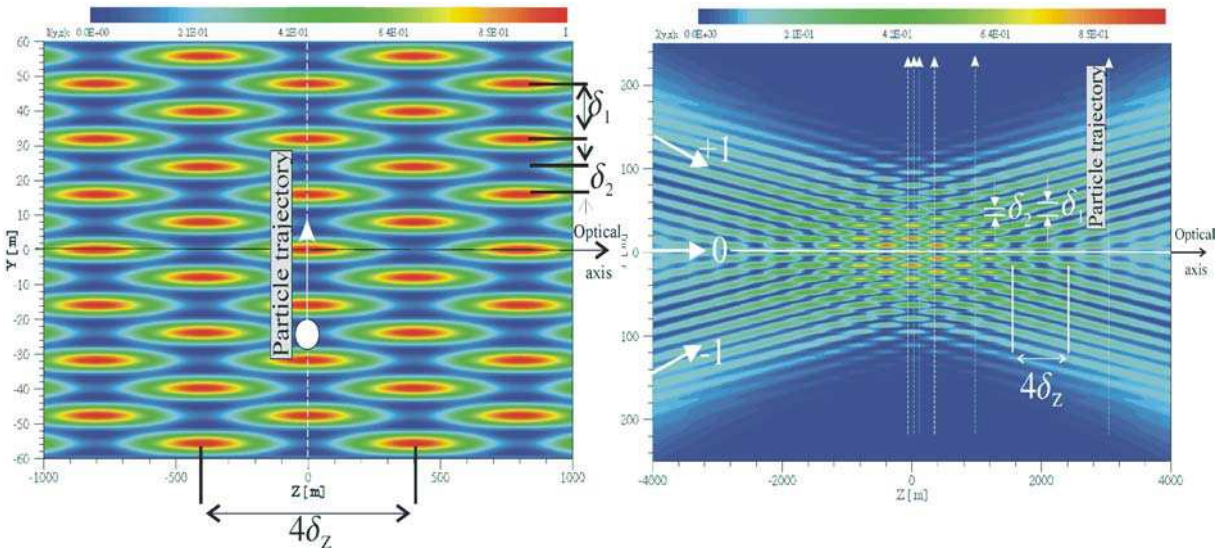

Figure 20 Distribution d'intensité, ou « champ d'interférence », dans une sonde Doppler formée par, à gauche : 3 ondes planes ; à droite : 3 faisceaux laser (TM00) de diamètre au col $2\omega_0=100\mu m$.

On considère à présent une petite particule de diamètre *D*, avec $D\ll\delta_2$, qui se déplace dans le volume de mesure, perpendiculairement aux deux réseaux de franges (i.e. suivant l'axe Y). Sa trajectoire est définie par $\{y(t)=V_y t,\ z=0\}$, voir la Figure 20 a). On suppose que l'intensité lumineuse diffusée par cette particule $I_S(y,z,t)$ est simplement proportionnelle à la distribution locale d'intensité dans le volume de mesure $I_S(y,z,t)\propto I(y,z,t)$. En posant $E_1=E_{-1}=E_0=E$, $\nu_1=V_y/\delta_1-\nu_s$ et $\nu_2=V_y/\delta_2-2\nu_s$, l'équation du signal Doppler produit par cette particule au cours de sa trajectoire est de la forme :

$$I_S(y,z,t) \propto 2E^2\left\{\frac{3}{2}+\cos(2\pi\nu_2 t)+2\cos(2\pi\nu_1 t)\cos\beta z\right\} \tag{3.5}$$

On peut rendre plus réaliste ce modèle, à faible coût, en considérant que la distribution d'intensité du volume de mesure est gaussienne[13] suivant l'axe Y: $E^2(y)=E^2(0)\exp\left[-2(y/\omega_0)^2\right]$. L'amplitude $\left|S(\nu\geq 0)\right|$ du spectre de Fourier du signal Doppler s'écrit alors :

$$\left|S(\nu\geq 0)\right| = 3G(\nu)\delta(0)+G(\nu-\nu_1)\delta(\nu-\nu_1)+2G(\nu-\nu_2)\delta(\nu-\nu_2)\left|\cos\beta z\right| \tag{3.6}$$

où $\delta(\nu)$ représente la distribution de Dirac et $\left|G(\nu)\right|$ la transformée de Fourier de la distribution d'intensité du volume de mesure $E^2(V_y t)$, avec :

$$\left|G(\nu)\right| = \left|E^2(0)\sqrt{\frac{\pi}{2}}\frac{\omega_0}{V_y}\exp\left[-\frac{1}{2}\left(\frac{\pi\omega_0\nu}{V_y}\right)^2\right]\right| \tag{3.7}$$

L'Eq. (3.6) met en évidence que $\left|S(\nu\geq 0)\right|$ présente deux pics pour $\nu \gg 0$: le premier, plus basse fréquence, est centré sur la fréquence Doppler ν_1 et son amplitude est indépendante de la position de la particule suivant l'axe Z. Le second pic, plus haute fréquence, est centré sur la fréquence Doppler ν_2 et son amplitude dépend explicitement de la position de la particule le long de l'axe optique Z. La largeur fréquentielle des deux pics est contrôlée par la fonction $\left|G(\nu)\right|$. Cette largeur ($\propto \omega_0/V_y$) décroît lorsque le temps de transit de la particule, dans le volume de mesure, augmente.

Si l'on mesure le maximum d'amplitude des deux pics de $\left|S(\nu\geq 0)\right|$, on peut calculer un rapport qui varie sur le domaine $0\leq R_\nu(z)\leq 2$ avec :

$$R_\nu(z) = \frac{Max\left\{S(\nu_2)\right\}}{Max\left\{S(\nu_1)\right\}} = 2\left|\cos\beta z\right| \tag{3.8}$$

Le principe de la technique proposée est alors trivial, il s'agit de déterminer la position de la particule le long de l'axe optique en inversant l'équation précédente :

$$z = \frac{1}{\beta}\left\{\cos^{-1}\left(\frac{1}{2}R_\nu(z)\right)\pm n\pi\right\} \tag{3.9}$$

Il est important de remarquer que cette position est déterminée modulo la distance $z=\pm n\pi/\beta$, où n est un entier naturel. La composante de vitesse de la particule suivant Y peut être également être déduite :

$$V_y = (\nu_2+2\nu_s)\delta_2 \;\equiv\; (\nu_1+\nu_s)\delta_1 \tag{3.10}$$

Modèle basé sur la théorie de Lorenz-Mie généralisée

Le modèle analytique que nous venons de développer, de type onde plane, permet d'introduire simplement le principe de la technique proposée. Cependant, une modélisation plus rigoureuse de cette dernière, requière l'utilisation de la théorie de Lorenz-Mie généralisée (§ 2.2). La GLMT permet en effet d'obtenir le champ diffusé par la particule, pour chacun des faisceaux :

$$E_\theta = \frac{iE}{kr}\exp\left[-i(kr-2\pi\nu t)\right]S_2 \qquad E_\varphi = \frac{-E}{kr}\exp\left[-i(kr-2\pi\nu t)\right]S_1 \tag{3.11}$$

Les fonctions d'amplitude de diffusion, S_1 et S_2, prennent en compte les caractéristiques des faisceaux (longueur d'onde, polarisation, diamètre et position du col par rapport à la particule…) et les propriétés de la particule (diamètre, indice complexe de réfraction, homogène ou multicouche). Dans le champ lointain, le champ diffusé s'écrit alors, dans la direction du détecteur et pour la polarisation θ :

[13] La courbure des fronts d'onde est cependant négligée

$$\left|\mathrm{S}\left(\mathbf{r},\theta,\pi/2,t\right)\right| = \frac{k}{2\pi\bar{v}\mu_0}\left[\left|E_{+1\theta}\right|^2 + \left|E_{-1\theta}\right|^2 + \left|E_{0\theta}\right|^2 + 2\,\mathrm{Re}\left\{E_{+1\theta}E_{-1\theta}^* + E_{+1\theta}E_{0\theta}^* + E_{-1\theta}E_{0\theta}^*\right\}\right] \tag{3.12}$$

Afin d'obtenir l'équation du signal Doppler produit par la particule, on peut intégrer l'Eq. (3.12) sur l'ouverture du détecteur (d'angle solide Ω) :

$$I_S\left(\mathbf{r},t\right) = \int_{\Omega}\left|\mathrm{S}\left(\mathbf{r},\theta,\pi/2,t\right)\right| d\Omega \tag{3.13}$$

Après quelques manipulations mathématiques et en introduisant les grandeurs caractéristiques d'un signal Doppler (le piédestal : P, la visibilité : V et le déphasage : Φ), l'Eq. (3.13) peut être réécrite sous la forme:

$$I\left(\mathbf{r},t\right) = P_1\left[1+V_1\cos\left(2\pi\nu_1 t+\phi_1\right)\right] + P_2\left[1+V_2\cos\left(2\pi\nu_2 t+\phi_2\right)\right] \tag{3.14}$$

avec

$$\begin{aligned}
&P_1 = \frac{k}{2\pi\bar{v}\mu_0}\left\langle\frac{1}{2}\left|E_{-1\theta}\right|^2 + \frac{1}{2}\left|E_{+1\theta}\right|^2 + \left|E_{0\theta}\right|^2\right\rangle_\Omega \qquad && P_2 = \frac{k}{2\pi\bar{v}\mu_0}\left\langle\frac{1}{2}\left|E_{-1\theta}\right|^2 + \frac{1}{2}\left|E_{+1\theta}\right|^2\right\rangle_\Omega \\
&\left\langle H_1\right\rangle_\Omega = \left\langle E_{+1\theta}E_{0\theta}^* + E_{-1\theta}E_{0\theta}^*\right\rangle_\Omega && \left\langle H_2\right\rangle_\Omega = \left\langle E_{+1\theta}E_{-1\theta}^*\right\rangle_\Omega \\
&V_1 = 2\left|\left\langle H_1\right\rangle_\Omega\right| / P_1 && V_2 = 2\left|\left\langle H_2\right\rangle_\Omega\right| / P_2 \\
&\Phi_1 = \tan^{-1}\left[-\mathrm{Im}\left(\left\langle H_1\right\rangle_\Omega\right) / \mathrm{Re}\left(\left\langle H_1\right\rangle_\Omega\right)\right] && \Phi_2 = \tan^{-1}\left[-\mathrm{Im}\left(\left\langle H_2\right\rangle_\Omega\right) / \mathrm{Re}\left(\left\langle H_2\right\rangle_\Omega\right)\right]
\end{aligned} \tag{3.15}$$

La Figure 20 a) présente la distribution d'intensité lumineuse obtenue avec l'Eq. (3.3) pour $\alpha = 2.279°$, $\lambda = 0.6328\mu m$ et $E_{+1} = E_{-1} = E_0 = 1$. Les courbes iso niveau ont été normalisées par la valeur maximale obtenue dans le plan d'interférence (YZ). Conformément à nos remarques sur l'Eq. (3.3), on constate que les franges sont effectivement modulées en amplitude suivant l'axe Y et l'axe Z, avec $\delta_1 = 2\delta_2 \approx 15.91\mu m$ et $4\delta_Z \approx 800\mu m$. La Figure 20 b) montre la distribution d'intensité simulée avec la GLMT, dans le cas de faisceaux laser gaussiens, avec un diamètre au col de $2\omega_0 = 200\mu m$, la polarisation parallèle ($\varphi = \pi/2$), un angle de collection de $\theta = 180°$, une gouttelette d'eau (m=1.332, D=0.1μm). Dans cette figure, les effets de la distribution d'intensité et de la divergence des faisceaux sont manifestes…

La Figure 21 présente l'évolution du rapport $R_\nu(z)$ pour différentes positions de la gouttelette suivant l'axe Z, calculée avec l'Eq. (3.8) et la GLMT. Dans le cas d'une onde plane, $R_\nu(z)$ évolue exactement de la façon prédite par le modèle analytique: fonction périodique $2\delta_Z = 400\mu m$ bornée par les valeurs $\approx 1/9$ et ≈ 2.0. Pour des faisceaux gaussiens, on constate que plus ils sont focalisés et plus le désaccord avec le modèle analytique croît (e.g. $R_\nu(z)$ dépasse le maximum théorique de ≈ 2.0).

Prise en compte de la divergence des faisceaux dans le modèle analytique

Ce dernier effet est imputable à la divergence des faisceaux. Il peut être pris en compte dans le modèle analytique en introduisant certains termes "phénoménologiques", soit pour l'intervalle $0 \le z \le \delta_Z$:

$$R_\nu(z) = \beta_1\cos^{\beta_3}\left(\beta_2 z\right) \tag{3.16}$$

Les constantes β_1, β_2, β_3 peuvent être déduites d'une simple régression sur l'évolution numérique prédite par la GLMT pour $R_\nu(z)$. La position de la particule est alors déduite de :

$$z_m = \frac{1}{\beta_2}\cos^{-1}\left(\frac{R_\nu(z)}{\beta_1}\right)^{1/\beta_3} \tag{3.17}$$

La Figure 21 présente une simulation de la réponse d'un système Doppler laser qui utiliserait cette technique à 3-faisceaux cohérents. La position de la particule z_m est déduite de l'Eq. (3.17) et de l'analyse de la transformée de Fourier de signaux simulés par GLMT. Pour rendre plus réaliste cette simulation, un

bruit aléatoire gaussien a été ajouté aux signaux GLMT (*SNR[14]=10 dB).* Pour chaque valeur de la position nominale z, le passage de 500 gouttelettes a été simulé. Ceci permet d'obtenir une estimation de l'écart type induit par le bruit sur «la mesure» de z_m. Ces résultats sont tracés pour deux valeurs de l'angle d'intersection des faisceaux : $\alpha = 1.24°$ et $2.56°$ et pour l'intervalle $z \in [0.45\delta_z, 0.95\delta_z]$ [15] (où la sensibilité de $R_v(z)$ à la position des particules est maximale). Ces calculs montrent qu'avec cette technique la dynamique sur les distances mesurables serait respectivement de $\approx 400\mu m$ et $25\mu m$ pour une résolution de l'ordre de $\sigma_{Z_m} \approx \pm 12\mu m$ et $\pm 1\mu m$.

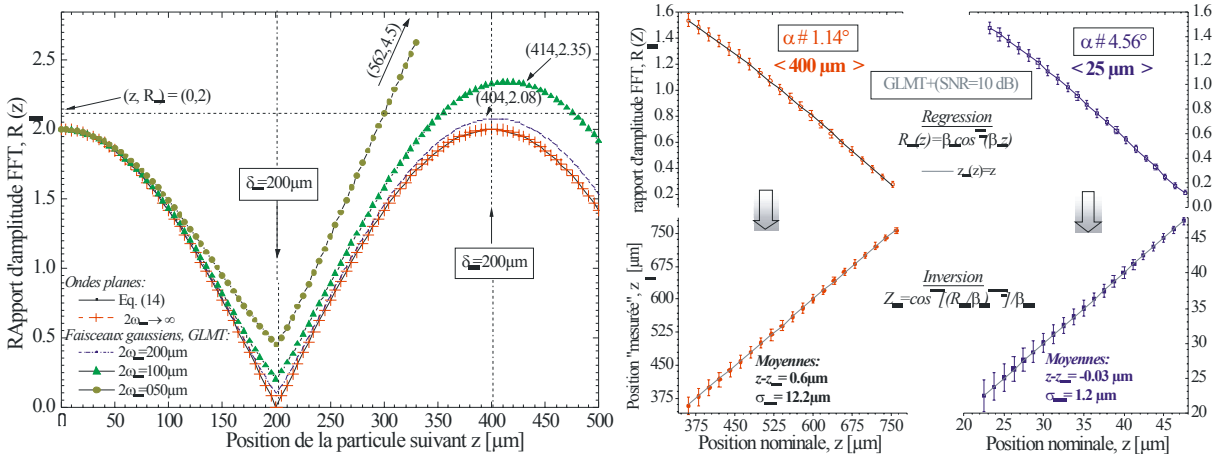

Figure 21 Interférométrie Doppler laser à 3-faisceaux cohérents avec, à gauche : comparaison de l'évolution du rapport d'amplitude $R(z)$ selon le modèle analytique (sans correction des effets de la divergence) et le modèle GLMT ; à droite : simulation d'une «mesure» de la position d'une particule suivant l'axe optique (avec bruit gaussien et modèle analytique corrigé des effets de la divergence).

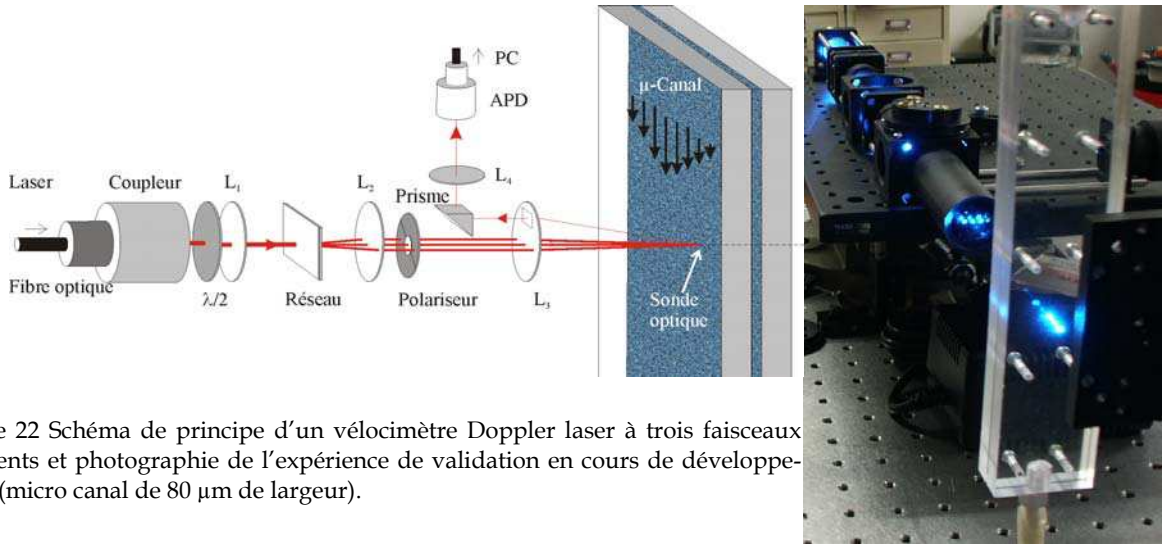

Figure 22 Schéma de principe d'un vélocimètre Doppler laser à trois faisceaux cohérents et photographie de l'expérience de validation en cours de développement (micro canal de 80 µm de largeur).

Conclusions préliminaires sur cette technique:

Elle permet de mesurer, avec un système Doppler laser à peine modifié : la vitesse et la position des particules le long de l'axe optique. De ce fait, elle pourrait être utilisée pour mesurer les *profils de vitesse* dans les *couches limites* ou dans les *micro-écoulements*, *sans avoir à déplacer l'optique*. Elle permet également d'étendre la

[14] Ce rapport signal sur bruit semble élevé, mais les signaux simulés apparaissent déjà très bruités [C35].
[15] Expérimentalement cela revient à utiliser, de manière classique, un filtrage spatial au niveau de l'optique de collection. Cette solution permet d'éliminer le problème d'indétermination sur z_m lié à la périodicité de $R_v(z)$.

dynamique des systèmes Phase Doppler (§4.3.3 et Figure 29)… Pour plus de détails sur les limites et avantages de cette technique, voir les références [C35, A20].

La Figure 22 présente un système, en cours de validation, pour mesurer les profils de vitesse dans un micro canal de 80µm de largeur.

3.1.3 L'interférométrie Phase Doppler et la mesure de fibres

Il semble que les seules études antérieures à la notre, sur l'adaptation du principe de l'interférométrie Phase Doppler à la mesure de fibres, soient celles de Mignon et al. [52-54], et de Schaub et al. [55]. Mignon a utilisé l'optique géométrique pour inverser ses mesures, avec toutes les limitations que cela implique (§2.4.1). Schaub et al. ont utilisé la théorie de Lorenz-Mie, mais leur système de mesure était particulièrement encombrement et de résolution très limitée.

Dans le cadre de la thèse d'Anne Lenoble [4], et d'études contractuelles avec le groupe Saint-Gobain (§8.4.2), nous avons développé un interféromètre optimisé pour la mesure, en ligne, de fibres de verre utilisées pour les applications de renfort (§ 4.3.3). Les fibres de renfort se caractérisent par des diamètres relativement faibles (D=5-30µm), un indice très élevé ($m \approx 1.555$) qui dépend des conditions de fibrage, des vitesses de défilement importantes (jusqu'à V_f=50 m/s), etc.

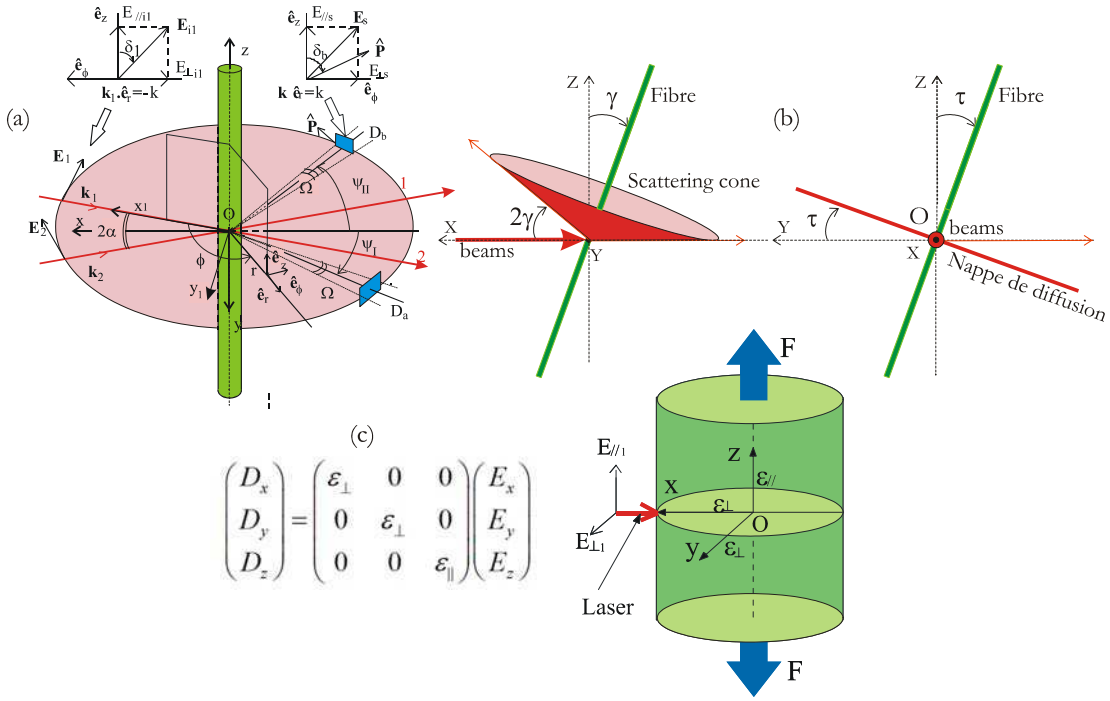

Figure 23 Géométries des différents modèles mis au point pour simuler la réponse de l'interféromètre et du diffractomètre : a) Position et forme des détecteurs, polarisation… ; b) Angles d'inclinaisons de la fibre et c) La nature tensorielle de la permittivité électrique de la fibre (biréfringence uniaxe), cf. reproduction de l'article [A13].

La réponse de ce système a été modélisé, voir la Figure 23. Le modèle prend en compte des paramètres classiques comme l'angle d'intersection ou l'état de polarisation des faisceaux incidents, la forme et l'ouverture angulaire des détecteurs… et des effets moins classiques, comme l'inclinaison de la fibre par rapport au plan des faisceaux laser, voir la Figure 23 b) et la Figure 24 b), la biréfringence uniaxe induite

par la tension de fibrage, voir la Figure 23 c) ; la dépendance de l'indice de réfraction avec les conditions de fibrage (trempage) ou la température, voir la Figure 24 b) ; la présence de fibres creuses (bulles de gaz) ou à gradient radial d'indice…

- Expérimentalement, un système de mesure complet a été mis au point : optique, électronique et logiciel (voir la Figure 25, la Figure 46 et la Figure 57). Cet interféromètre peut être utilisé en laboratoire comme sur site industriel. Sa résolution sur les diamètres est typiquement de $\sigma_D \approx 0.35\mu m$ pour $D = 7 - 42\mu m$ et un taux d'acquisition supérieur à 50 000 mesures/s, voir la Figure 28. Il permet par ailleurs de mesurer la tension de fibrage [A17] et, dans certaines conditions, de détecter les fibres creuses et les contraintes de torsion exercées sur une fibre [C25]. Pour plus de détails sur les caractéristiques de ce système, voir la reproduction de l'article [A13] et les références [C25, A17] [4].

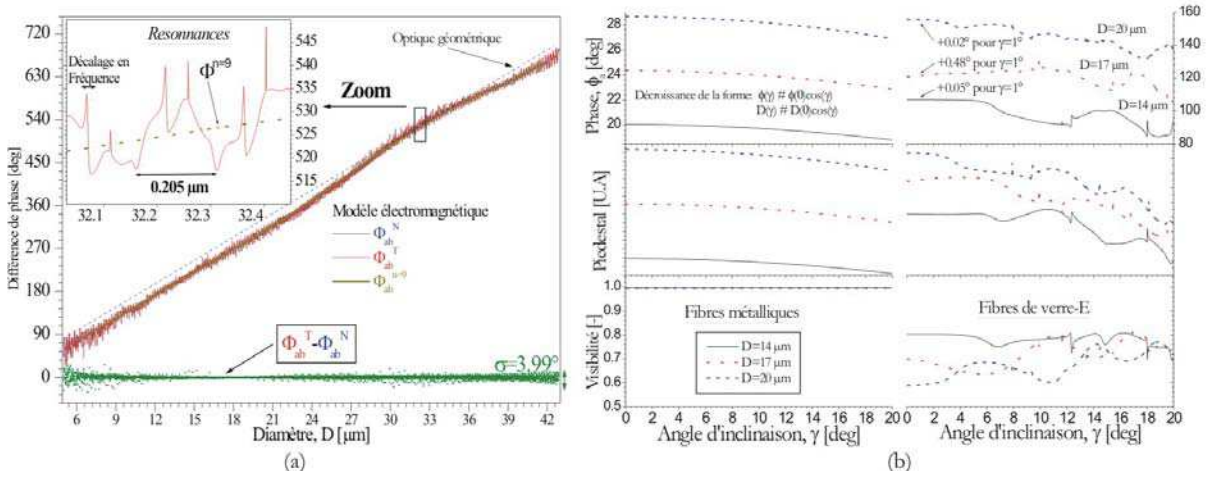

Figure 24 Exemples de modélisations de la réponse de l'interféromètre : a) simulation de sa réponse théorique lorsque l'on prend en compte (T), ou non (N), la dépendance de l'indice avec le taux de refroidissement (trempage); b) Effets de l'angle d'inclinaison γ, d'une fibre métallique et d'une fibre de verre-E, sur les paramètres caractéristiques des signaux Doppler.

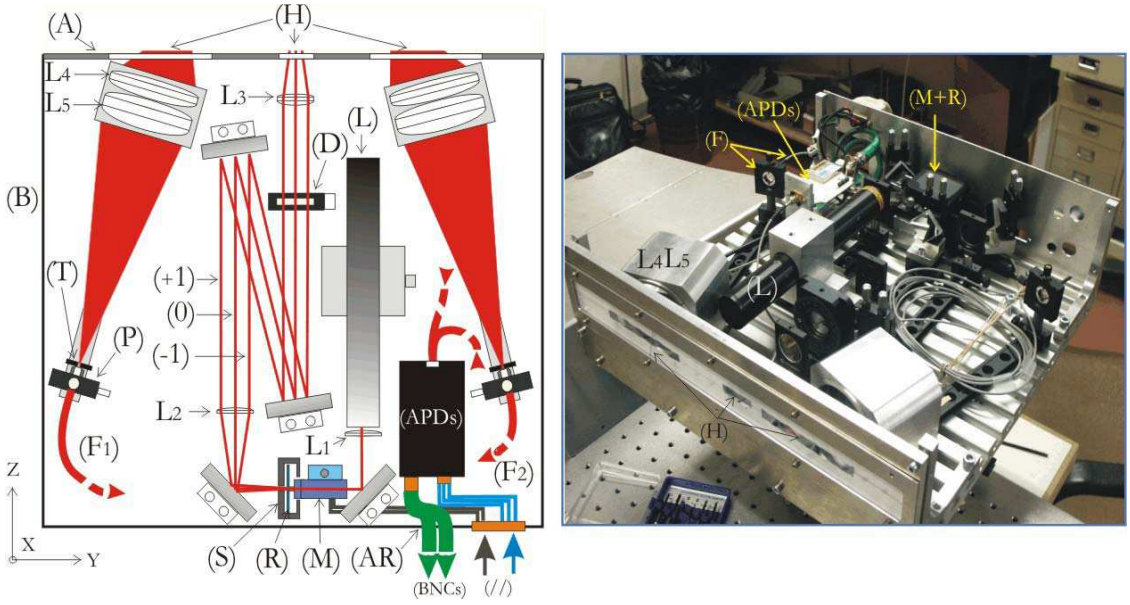

Figure 25 Schéma de principe de la tête optique de l'interféromètre rétro diffusion FIBS: (L) Laser HeNe 2.5 mW, (M-R) Moteur et Réseau de diffraction par transmission, (D) lame ½ onde, (L_3) lentille de focalisation des faisceaux, (H) Hublots ; L_3-L_4 lentilles de collection de la lumière rétro diffusée par la fibre, ($F_{1,2}$) fibres optiques et (APD) diodes photo avalanche (cf. reproduction de l'article [A13]).

3.1.4 Diffractométrie haute résolution

Dans la littérature, on trouve de nombreux travaux sur la granulométrie par diffraction laser, de fibres métalliques ou absorbantes, ou d'un ensemble de particules transparentes ou non (suspension, pulvérisation de gouttes, …). Dans le cas des fibres notamment, la plupart de ces travaux utilisent la théorie de Fraunhofer pour inverser les diagrammes de diffraction [56-58]. Souvent parce que celle-ci est rapide d'emploi (i.e. inversion des mesures en temps réel) et, dans certains cas, parce qu'elle permet de prédire *relativement* simplement la diffusion par des particules de forme complexe (particules irrégulières, cristaux [59],…). Pour une particule transparente, fortement symétrique (sphère, cylindre, ellipsoïde...), de fortes non linéarités apparaissent dans les diagrammes de diffusion/diffraction du fait des Résonances Morphologiques Dépendantes (MDRs) et des ondes de surface [60]. Ces phénomènes de résonance ne sont pas prédits par la théorie de Fraunhofer et expérimentalement, ils ne sont pas observés pour les particules absorbantes (les résonances internes sont fortement atténuées), les particules irrégulières (les ondes internes sont déphasées « aléatoirement ») ou un nuage de particules (i.e. les contributions des résonances sont moyennées du fait de la dispersion des diamètres).

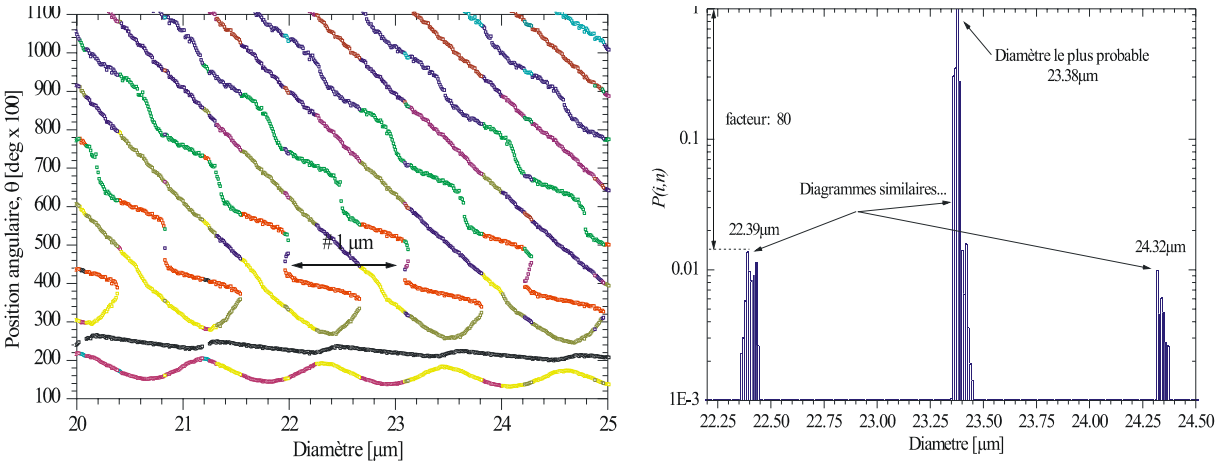

Figure 26 Diffractométrie haute résolution : a) Evolution de la position angulaire des extrema du diagramme de diffraction de fibres de verre-E ; b) Estimateur de corrélation entre un diagramme expérimental et théorique. Le maximum détermine le diamètre le plus probable pour la fibre mesurée, cf. reproduction de l'article [A16].

Dans le cadre de la thèse d'Anne Lenoble [4], nous avons mis au point un diffractomètre haute résolution et une méthode originale d'inversion des diagrammes de diffraction [C36, C37, A16]. Ce système de mesure permet d'enregistrer des rafales de 32000 diagrammes de diffraction à une cadence qui peut atteindre 43 kHz, voir la Figure 27 et la Figure 56.

La méthode d'inversion repose sur le calcul d'un estimateur de corrélation $P(i,n)$ entre les diagrammes expérimentaux (E) et des abaques théoriques (T). Ces derniers sont construits, une fois pour toutes, par extraction de la position angulaire des minima (-) et maxima (+) des diagrammes théoriques calculés avec la Théorie de Lorenz-Mie et en prenant en compte les effets optiques propres aux fibres de renforcement (§ 3.1.3). Pour une fibre de diamètre donné $D_E(n)$, l'estimateur de corrélation est maximal pour le diagramme théorique (i.e. diamètre $D_T(i)$) qui rend le mieux compte du nombre et de la position relative des extrema du diagramme expérimental en cours de traitement :

$$D_E(n) = D_T\left(i / Max\left\{P(i,n), i = 1,2\cdots n_T\right\}\right) \tag{3.18}$$

$$P(i,n)=\Delta K(i,n)\prod_{j_T^+=1}^{k_T^+}\prod_{j_E^+=1}^{k_E^+}\Delta P^+\left(i,n,j_T^+,j_E^+\right)\prod_{j_T^-=1}^{k_T^-}\prod_{j_E^-=1}^{k_E^-}\Delta P^+\left(i,n,j_T^-,j_E^-\right) \tag{3.19}$$

$\Delta K(i,n)$ et $\Delta P^{\pm}\left(i,n,j_T^{\pm},j_E^{\pm}\right)$ sont des estimateurs de corrélation sur le nombre et les positions relatives des extrema.

La Figure 26 a) présente l'évolution théorique de la position angulaire des extrema du diagramme de diffraction d'une fibre de verre-E. Ces évolutions sont déduites de l'analyse de figures du même type que celles présentées par la Figure 10. On constate que les diagrammes présentent une forte périodicité. En fait, c'est cette quasi-périodicité qui rend si ardu l'inversion des diagrammes de diffraction. Cependant, comme le montre la Figure 26 b), l'estimateur $P(i,n)$ permet de déterminer correctement le diamètre de la fibre détectée.

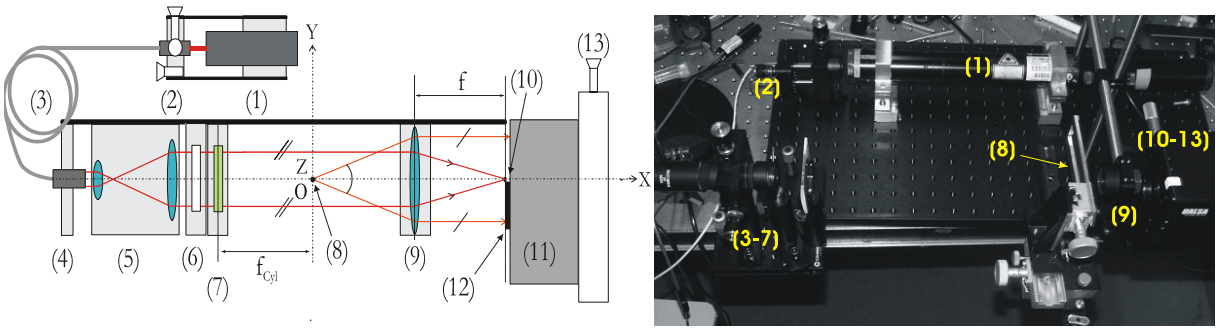

Figure 27 Schéma de principe et photographie du diffractomètre haute résolution : (1) laser HeNe 10mW ; (2-4) Coupleurs et fibre optique monomode ; (5) Agrandisseur de faisceau ; (6) Lame ½ onde ; (7) Lentille cylindrique de focale f_{cyl}=300mm; (8) Point objet ; (9) Lentille de Fourier de focale f=50mm ; (10) Point de focalisation du faisceau direct ; (11-12) Caméra et capteur CCD ; (13) Déplacement micrométrique de la caméra.

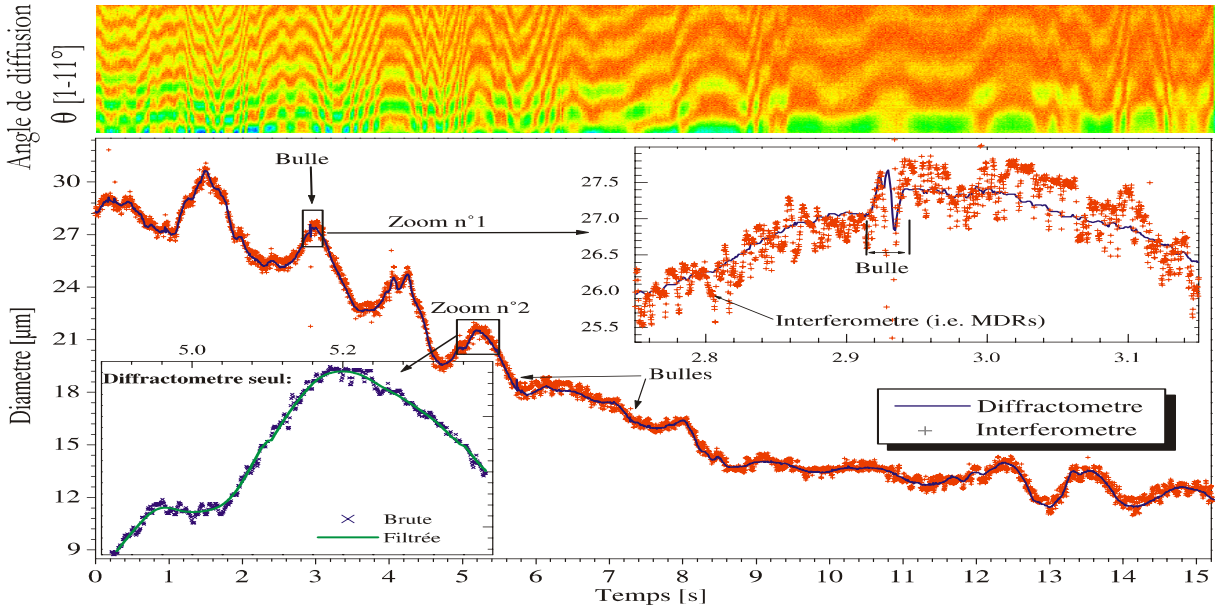

Figure 28 Diagrammes de diffraction expérimentaux (en fausses couleurs) et résultat de leur analyse avec la méthode d'inversion probabiliste. La réponse simultanée de l'interféromètre est également présentée (vitesse de fibrage : $V_f \approx 5 \rightarrow 40 m/s$), cf. reproduction de l'article [A16].

La Figure 28 présente les diagrammes enregistrés lorsque le procédé de fibrage du verre est soumis à une rampe croissante de vitesse : $V_f \approx 5 \rightarrow 40 m/s$ (§ 4.3.3). Le résultat de l'analyse de ces diagrammes expérimentaux est comparé à la réponse de l'interféromètre (§ 3.1.3). La réponse de l'interféromètre met en évidence les contributions des MDRs. La procédure d'inversion actuelle de l'interféromètre ne permet pas de déconvoluer ces contributions, contrairement à l'algorithme d'inversion du diffractomètre. Pour cette expérience, la différence entre les diamètres moyens obtenus avec ces deux systèmes est de moins de 80 nm… On peut montrer que la résolution de ce diffractomètre est typiquement de $\sigma_D \approx 20nm$ pour des fibres en cours de production et des diamètres dans la plage $D = 7 - .\ 42\mu m$. En fait, cette résolution est près de 100 fois supérieure à celle obtenue par d'autres auteurs, dans les mêmes conditions [56-58].

Ce diffractomètre haute résolution permet également de détecter les fibres creuses et *d'estimer* l'indice de réfraction des fibres. Il est important de noter que la méthode d'inversion peut être utilisée pour d'autres types de particules que les cylindres ou d'autres phénomènes optiques (cf. Arc-en-ciel, § 3.2.4). Pour plus de détails, voir la reproduction de l'article [A16] dans le Chapitre 9. et la référence [4].

3.2 Réfractométrie de particules en écoulement

La caractérisation simultanée de la *vitesse* et de la *taille* des particules est fondamentale pour étudier les écoulements diphasiques. La mesure simultanée de l'indice de réfraction des particules pourrait être tout aussi fondamentale. En effet, l'*indice* d'une particule est caractéristique de sa composition (*matériau*, *fraction de mélange*, *densité*…) et de sa *température*. La mesure de l'indice de réfraction devrait donc permettre une amélioration significative de nos capacités de diagnostics de différents phénomènes et systèmes: mélange turbulent, coalescence de gouttes, évaporation, combustion diphasique, séchage, fluidisation polyphasique, les écoulements *multiphasiques*…

Aucun système de mesure actuel, commercial ou prototype de laboratoire, n'est capable de mesurer ces trois grandeurs de façon simultanée. Il existe cependant des techniques *couplées* qui répondent partiellement à cet objectif. La technique de l'angle d'arc-en-ciel en est un exemple. Cette dernière, encore en développement, permet de mesurer le diamètre et l'indice de particules individuelles [61-63] ou d'un ensemble de particules [27]. Cependant, pour pouvoir mesurer les vitesses, les flux, la concentration en particules, elle doit être couplée avec un vélocimètre Doppler laser. Ce qui alourdit considérablement le dispositif de mesure. Il en est de même pour les techniques utilisant la Fluorescence Induite par Laser (LIF). Ces dernières nécessitent en plus de charger en molécules fluorescentes les *particules* à analyser, ce qui n'est pas toujours possible ou souhaitable (i.e. tension superficielle, évaporation, pollution…). Les mesures d'intensité nécessitent par ailleurs des calibrations assez fastidieuses [64], bien que des progrès significatifs semblent avoir été récemment réalisés dans ce domaine [65].

3.2.1 La Technique Dual Bursts (DBT) : faisceaux laser fortement focalisés

La focalisation des faisceaux laser pose généralement problème en granulométrie optique (§3.1.1), car elle produit des gradients d'intensité sur la surface des particules, des fronts d'onde courbes. Cependant, j'ai developpé le concept d'une technique originale qui tire avantage de ces gradients : la technique « Dual Bursts» (DBT) [A4].

Le principe de cette technique est le suivant :

- Deux faisceaux sont utilisés pour former un volume de mesure dont les dimensions latérales sont inférieures à celles des particules à mesurer, voir la Figure 29. Pour un détecteur placé vers l'avant, chaque particule transparente qui traverse la sonde optique produit deux signaux Doppler : l'un est dû à la lumière réfléchie par la particule et l'autre, à la lumière réfractée par cette dernière. La phase du signal réfléchi est très peu sensible à la nature du matériau de la particule, elle nous donne accès à son diamètre D_0. La phase du signal réfracté est sensible à la taille D_1 de la particule, mais aussi à la partie réelle de son indice de réfraction, m.

De la mesure de ces deux phases ont peut donc déduire le diamètre et la partie réelle de l'indice de la particule (i.e. caractéristique de son matériau), voir la reproduction de l'article [A4] dans le Chapitre 9.

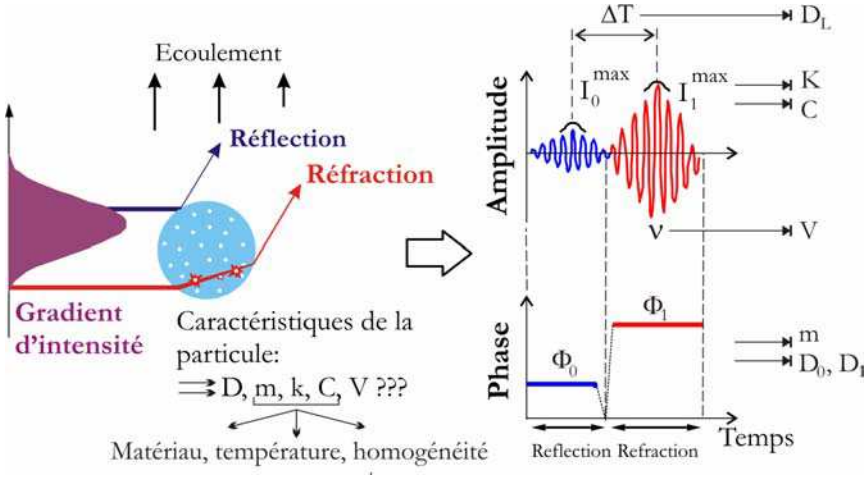

Figure 29 Schéma de principe de la Technique Dual Bursts : mesure simultanée de la vitesse, du diamètre et de l'indice complexe de réfraction (ou de la teneur en hétérogénéités) d'une particule en écoulement.

- Les signaux Doppler sont également modulés en fréquence. Classiquement, c'est de la mesure de cette fréquence ν que l'on déduit la composante V de la vitesse de la particule, voir la Figure 29.

- Les signaux Doppler sont également décalés dans le temps, ΔT. La mesure de cette grandeur permet de déduire la taille de la particule à grande échelle, $D_L = V/\nu$ [66]. La comparaison des trois mesures du diamètre : $D_0 \equiv D_1 \equiv D_L$, permet de caractériser l'état de sphéricité de la particule et d'étendre la dynamique sur les tailles mesurables. En effet, D_L n'est pas soumis à l'indétermination à 2π près et constitue une mesure à grande échelle du diamètre, contrairement à D_0 et D_1 qui sont des mesures très locales, voir la Figure 29.

Le décalage temporel des signaux résulte de la focalisation des faisceaux laser et de la différence entre la position des paramètres d'impact de la réfection et de la réfraction. Nous avons récemment monter que ce décale peut également être induit par un filtrage spatial. Dans ce dernier cas, le principe de la technique Dual Burst s'approche de celui de la technique de « Shadographie Doppler » [67] ; et il semble que nous devrions pouvoir caractériser le diamètre de particules irrégulières [RC21].

- Contrairement au signal réfléchi, le signal réfracté est très sensible à la partie imaginaire de l'indice de la particule (absorption) ou à sa teneur en hétérogénéités. De ce fait, le rapport d'intensité de ces deux signaux nous donne accès à l'absorptivité du matériau de la particule, K [C10, A4], ou à sa concentration en hétérogénéités, C_v. Dans ce dernier cas, il s'agit d'extinction qui peut être modélisée par une loi de Beer-

Lambert ou mieux, une Méthode de type Monté Carlo (§ 2.4.3) [C10-20, A8], voir la reproduction de l'article [A8] dans le Chapitre 9. Ces diagnostics sont basés sur une mesure d'un rapport d'intensité. Ils ne nécessitent donc pas de calibration, ce qui élimine les problèmes liés à la dérive du gain des détecteurs, l'encrassement des accès optiques, la turbulence du milieu environnant la particule détectée…
La mesure de la partie imaginaire de l'indice $k = \lambda / 4\pi K$, permet les mêmes types de diagnostics que la mesure de la partie réelle de l'indice, m . En effet, k , dépend également de la nature du matériau et de sa température. Cette mesure est cependant complémentaire par bien des aspects de la mesure de m .

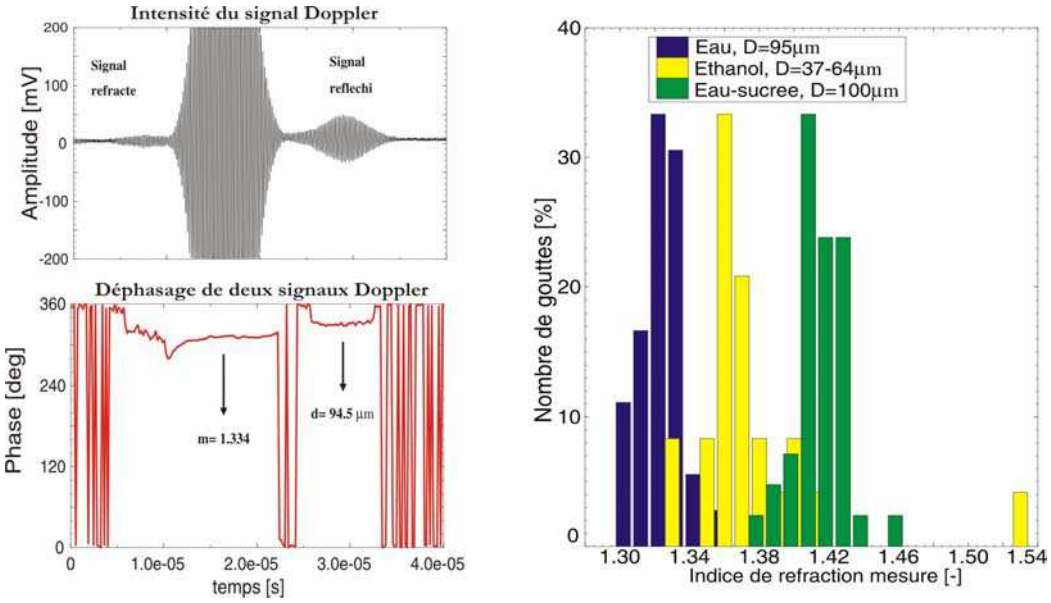

Figure 30 Technique Dual Bursts avec, à gauche : le signal Doppler produit par une goutte d'eau en écoulement (D=95µm) et le résultat de l'analyse temps fréquence de sa phase; à droite : histogramme des indices mesurés pour des gouttes d'eau, d'éthanol et d'eau sucrée (cf. reproduction de l'article [A4]).

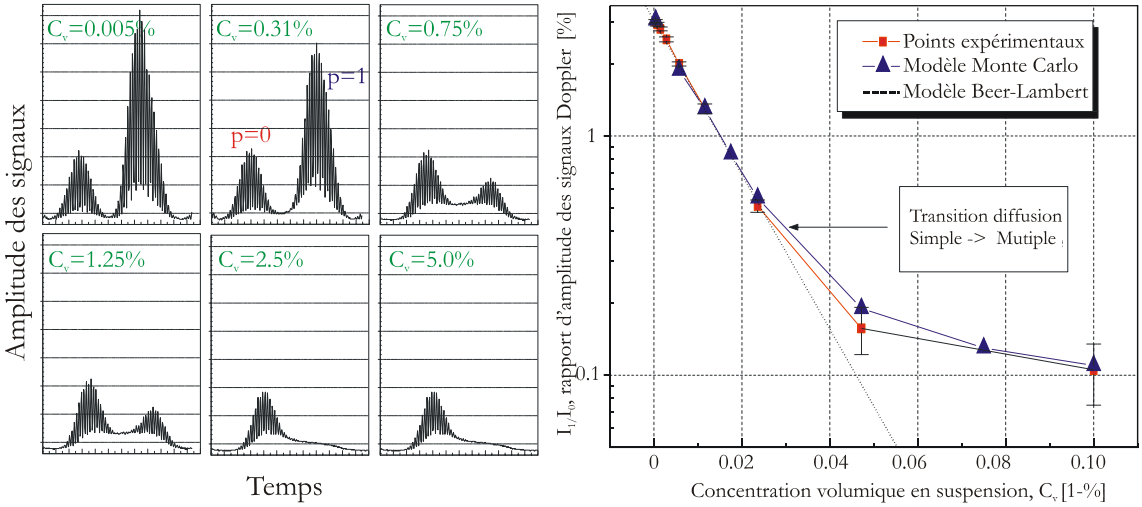

Figure 31 Technique Dual Bursts pour la caractérisation de particules hétérogènes avec, à gauche : signaux Doppler produits par un jet liquide constitué d'une suspension aqueuse de particules de latex, de concentration C_v; à droite : comparaison du rapport d'intensité de signaux expérimentaux et simulés (cf. reproduction de l'article [A8]).

- Lorsque l'hétérogénéité des particules est de symétrie sphérique (particule bicouche) 3 ou 4 signaux Doppler sont émis par celles-ci. Nous avons montré que l'analyse de la phase de ces différents signaux

permet de déterminer le diamètre externe de la particule mais aussi son diamètre interne, ou de détecter la présence d'un gradient interne §2.4.1, [A5].

Au final, la technique DBT pourrait présenter d'autres potentialités concernant la caractérisation de particules cylindriques, de particules irrégulières et la mesure d'un signal de fluorescence auto calibré… Les possibilités offertes par cette technique *originale* sont multiples. C'est d'ailleurs à ce titre qu'elle est au cœur de l'ACI « Pollution Non-Pollution » VITAMA (§ 8.4.2). Ce projet de recherche, que je dirige, vise au développement d'un système de mesure capable de caractériser de manière simultanée la **Vi**tesse, la **Ta**ille et le **Ma**tériau de particules en écoulement.

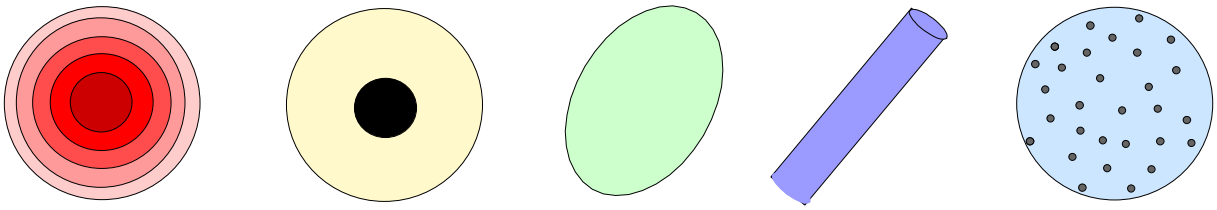

Figure 32 Particules susceptibles d'être caractérisées, à terme, avec la technique Dual Bursts.

3.2.2 L'Anémométrie Phase Doppler en configuration Dual Mode (DM)

L'interférométrie phase Doppler «classique» peut également permettre de mesurer la partie réelle de l'indice m. Pour ce faire, Naqwi et Durst [68] ont proposé d'utiliser deux optiques de collection. On mesure ainsi deux déphasages. Selon l'optique géométrique, ces déphasages sont des fonctions assez complexes de l'indice, en revanche ils sont simplement proportionnels au diamètre de la particule détectée, voir l'Eq. (3.21). Le rapport de ces deux déphasages est donc indépendant du diamètre de la particule détectée. De la connaissance théorique de l'évolution de ce rapport avec l'indice, et de sa mesure, on peut déduire l'indice de la particule. Une fois ce dernier déterminé, le diamètre est calculé à l'aide d'un des deux déphasages mesurés. Malheureusement, cette configuration optique souffre de plusieurs problèmes importants : une faible sensibilité à l'indice, une sensibilité marquée aux effets de trajectoires (§ 3.1.1) et un encombrement difficilement compatible avec l'étude d'écoulements complexes.

J'ai proposé une amélioration significative de cette technique [RI1, T1, C13]. Elle repose sur l'utilisation d'une configuration optique de type « Dual Mode » (§ 3.1.1). Cette dernière est en effet très peu sensible aux effets de trajectoire et elle permet de mesurer directement un rapport de phase à partir d'une seule optique de collection, d'où un encombrement réduit et des réglages facilités. Elle est également plus sensible à l'indice que les configurations optiques classiques.

Dans le cas d'une géométrie Dual Mode, la phase du signal produit par une particule réfractante, de diamètre D et d'indice m, est donnée par l'Eq. (3.20) pour la géométrie Plane (détecteurs V_1 et V_2 de la Figure 18) et par l'Eq. (3.21), pour la géométrie Standard (détecteurs U_1 et U_2, de la Figure 18) :

$$\phi_{P\pm} = \frac{2\pi m D}{\lambda_p} \frac{\sin\alpha \sin\left(\phi - \psi_p\right)}{\sqrt{2\left[1+\cos\alpha\cos\left(\phi\pm\psi_p\right)\right]\left[1+m^2-m\sqrt{2\left[1+\cos\alpha\cos\left(\phi\pm\psi_p\right)\right]}\right]}} \tag{3.20}$$

$$\phi_{S\pm} = \frac{\pm 2\pi m D}{\lambda_S} \frac{\sin\alpha \sin\psi_S}{\sqrt{2\left[1+\cos\alpha\cos\psi_S\cos\phi\right]\left[1+m^2-m\sqrt{2\left[1+\cos\alpha\cos\psi_S\cos\phi\right]}\right]}} \tag{3.21}$$

Le signe $\pm$ différencie la position des détecteurs élémentaires (placés derrière une même lentille de collection) par rapport à l'angle d'élévation moyen ψ ou hors axe ϕ. α est l'angle entre les faisceaux de longueur d'onde λ_P et λ_S. Ces équations montrent clairement que le rapport des déphasages est indépendant du diamètre des particules :

$$R(m) = \frac{2\phi_S}{\phi_+ - \phi_+} \qquad \forall D \tag{3.22}$$

L'équation (3.22) ne semble pas pouvoir être résolue analytiquement. Cependant, numériquement, on peut montrer que, selon l'optique géométrique, $R(m)$ décroît de manière monotone avec l'indice (sensibilité maximale pour les faibles indices)[69].

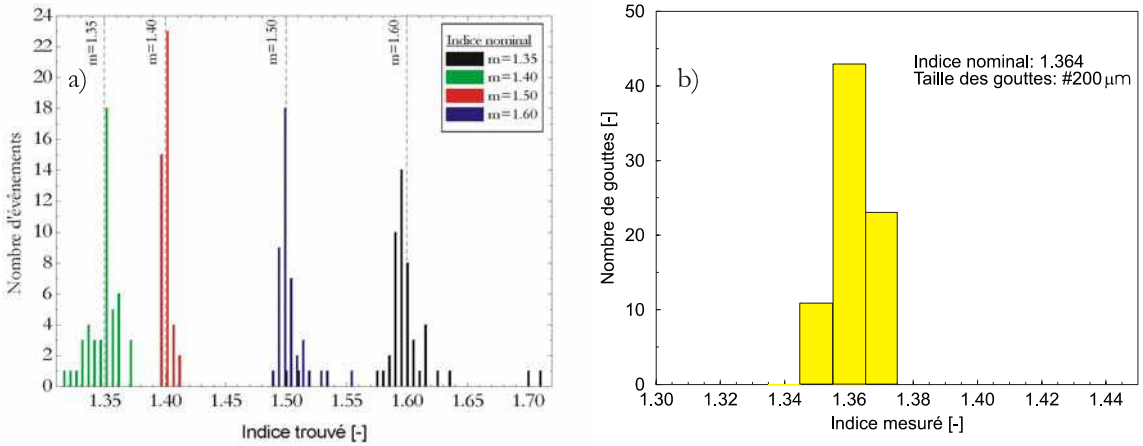

Figure 33 a) Simulation de la réponse d'un système Dual Mode à la mesure de particules composées de différents matériaux et b) Exemple de mesure d'indice sur un jet mono disperse de gouttes d'éthanol.

La Figure 33 a) simule la mesure de l'indice de différentes particules $(D = 50-300\mu m)$ avec une optique Dual Mode classique [49]. Les indices nominaux sont de $m = 1.35$ (alcools…), $m = 1.40$ (plastiques, polymères, essences,…), $m = 1.50$ (huiles lourdes, verres,….) et $m = 1.60$ (liquides d'indice, latex,...). Ces simulations ont été réalisées avec un code de calcul basé sur la GLMT et, pour simuler un bruit de mesure, en introduisant une erreur aléatoire sur les phases calculées (d'écart type : $\pm 5°$)[69]. Les distributions simulées sont distinctes. Ce système serait donc capable de différencier ces différents types de gouttes et particules dans un écoulement.

La Figure 33 b) montre un résultat expérimental *préliminaire* [T1]. Il s'agit de la distribution d'indice mesurée pour des gouttes d'éthanol pur, $m \approx 1.364$ et $D = 200\mu m$. La distribution est centrée sur la valeur attendue ($m \approx 1.362$) avec une largeur à mi-hauteur de $\approx \pm 0.008$. Cette dernière valeur définie la résolution de la technique proposée. Cette dernière est faible au regard de celle d'un réfractomètre de laboratoire ($\approx \pm 0.0001$). Mais il s'agit ici d'une mesure réalisée sur des gouttes en vol, en quelques microsecondes, et dont on a également déterminé le diamètre et la vitesse !

Toujours à titre d'exemple, la Figure 34 montre quelques résultats expérimentaux obtenus lors de l'étude de l'interaction entre deux pulvérisations : l'une d'eau pure et l'autre, d'éthanol pur. On s'attend à

ce que les zones de coalescence soient caractérisées par la présence de gouttes dont l'indice est intermédiaire entre celui de l'eau $m = 1.332$ et celui de l'éthanol $m = 1.364$.
Pour la zone d'écoulement considérée ici [T1, C13], on observe effectivement la présence de gouttes d'indice intermédiaire[16], Figure 34 b), même si la résolution de ce premier système est encore un peu faible.

En guise de conclusion, nous dirons que la technique Dual Mode n'a pas les mêmes potentialités que la technique Dual Bursts, §3.2.1. Sa résolution est encore trop faible pour certaines applications, bien-qu'elle soit déjà suffisante pour différencier des particules composées de matériaux assez différents (i.e. densités). De plus, la technique Dual Mode pourrait être rapidement implantée sur un système commercial déjà existant [49], avec tous les avantages que cela implique du point de vue de son intégration, de son l'industrialisation et de sa diffusion rapide dans la communauté… C'est pourquoi, dans le cadre de l'ACI-VITAMA (§ 8.4.2), nous travaillons également à l'amélioration de la résolution de cette technique.

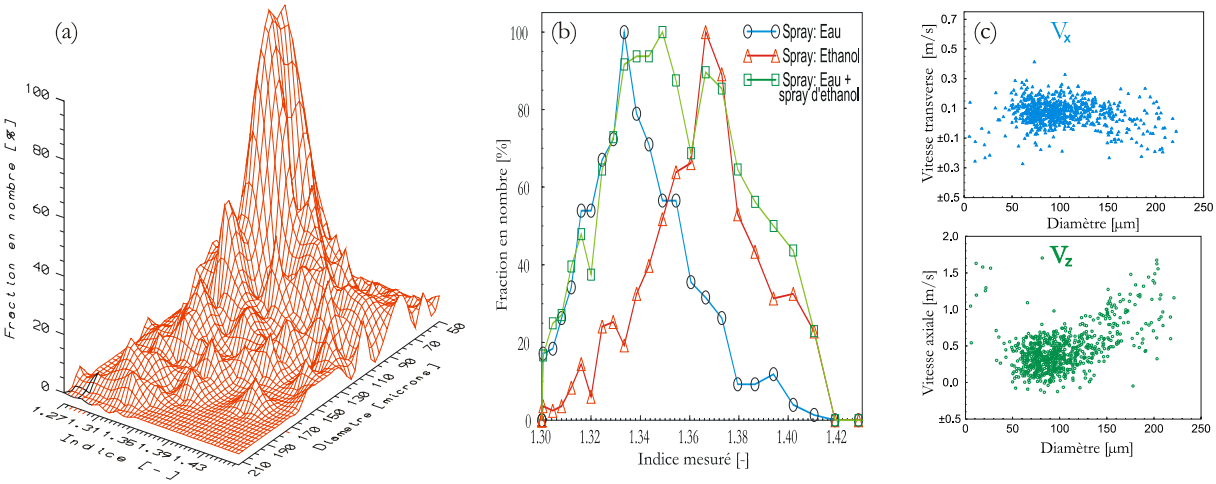

Figure 34 Résultats expérimentaux *préliminaires* sur l'étude de l'interaction entre deux pulvérisations: eau et éthanol : a) Distribution diamètre/indice, b) distribution des indices pour des diamètres entre D=50-200µm et c) corrélations diamètre/vitesses.

[16] Le pic de la distribution correspond à des gouttes dont la fraction de mélange est égale à Y=0.31 (i.e. coalescence)

3.2.3 Méthode basée sur l'analyse de la diffusion critique

Le paragraphe § 2.4.2 expose le principe de cette technique de mesure simultanée de l'indice et du diamètre de «bulles» en écoulement, par analyse de la diffusion critique [C17-18, A9].

La Figure 35 présente un schéma de principe du dispositif expérimental mis en oeuvre pour valider le principe de cette technique et le modèle asymptotique de diffusion critique (§ 2.4.2). Fondamentalement, le système optique se réduit à un laser de faible puissance, quelques lentilles et une caméra CCD. Un goniomètre de précision est cependant nécessaire pour calibrer angulairement la caméra. L'écoulement diphasique, confiné dans une cuve spectrométrique, est produit par diffusion d'air à travers un poreux immergé dans un liquide (eau, éthanol et huile silicone). La Figure 35 présente également le diagramme de diffusion critique enregistré pour une bulle l'air dans de l'éthanol. L'analyse de la position angulaire des deux premières franges brillantes et les équations du modèle de diffusion critique (§2.4.2) permettent de déterminer le diamètre et l'indice de la particule détectée : $D = 83\mu m$ et $m = 1.361$; pour plus de détails voir la reproduction de l'article [A9] dans le Chapitre 9.

Les résultats obtenus avec ce dispositif expérimental nous ont permis d'obtenir différents résultats. Cependant, à ce jour, fautes de moyens, cette technique n'a pas pu être testée sur un écoulement «réel». Pourtant, même dans son état actuel, elle n'a pas d'équivalent. De plus, elle pourrait très vraisemblablement être étendue à la caractérisation simultanée d'un ensemble de «bulles», par extrapolation du principe de la technique de l'angle d'arc-en-ciel global (§ 3.2.4).

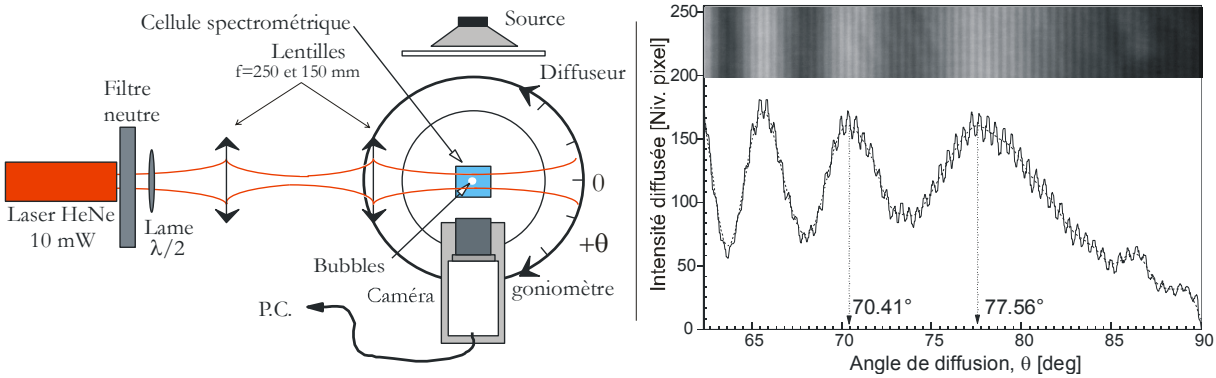

Figure 35 Schéma de principe du dispositif expérimental d'analyse de la diffusion critique et exemple du diagramme de diffusion critique produit par une bulle d'air en écoulement dans de l'éthanol (cf. reproduction de l'article [A9]).

3.2.4 Méthode basée sur le phénomène d'arc-en-ciel

Nous développons actuellement [70] une méthode de caractérisation du diamètre et de l'indice de particules en écoulement, basée sur l'analyse des caractéristiques du diagramme de diffusion dans la région de l'angle d'arc-en-ciel. Cette approche est complémentaire à celle des techniques ponctuelles ou temporelles (i.e. Phase Doppler), de par sa nature intégrale : spatiale et instantanée (i.e. Diffractométrie). Dans ce qui suit, nous présentons les modèles et la technique d'inversion développés, ainsi que quelques résultats expérimentaux types.

Arc-en-ciel produit par une particule individuelle

Le phénomène d'arc-en-ciel est lié à l'existence d'un angle de déviation limite, d'une caustique, pour les rayons lumineux qui ont subit une réflexion interne (p=2), Figure 11. Selon l'optique géométrique, le premier arc-en-ciel produit par une particule individuelle, sphérique, est localisé précisément à l'angle de diffusion θ_{rg} :

$$\theta_{rg} = 2\tau_{rg} - \cos^{-1}\left(\cos\tau_{rg}/m\right) \quad avec \quad \sin\tau_{rg} = \sqrt{\left(m^2-1\right)/3} \tag{3.23}$$

Cette équation indique que θ_{rg} ne semble dépendre que de l'indice de la particule[17].

Young, Fresnel et Airy ont développé une théorie ondulatoire du phénomène d'arc-en-ciel. Cette dernière, qui est désormais connue sous le nom de théorie d'Airy, décrit l'arc-en-ciel comme un phénomène de diffraction, dans le champ lointain, du front d'onde associé aux rayons à l'origine de l'arc-en-ciel géométrique. Pour de petits angles de déviation par rapport à θ_{rg}, ce front d'onde est de forme cubique [71].

Nous ne détaillerons pas davantage les bases physiques et mathématiques de cette théorie, qui à fait l'objet de nombreux travaux et publications. On remarquera cependant que la démarche suivie par Marston, pour développer une approximation d'optique physique (POA) du phénomène de diffusion critique (§ 3.2.3), est très similaire à celle de la théorie d'Airy.

La théorie d'Airy permet de prédire la dépendance de l'intensité lumineuse diffusée, par une particule sphérique isolée, au voisinage de θ_{rg} [72]:

$$I(\theta) = \frac{cE_0^2}{8\pi\lambda^2R^2}\left(\frac{3\lambda D^2}{16h}\right)^{2/3}\left(\int_0^\infty \cos\left[\frac{\pi}{2}\left(z\eta-\eta^3\right)\right]d\eta\right)^2 \tag{3.24}$$

Où, de manière équivalente à la POA, η est une variable d'intégration :

$$\eta = v\left(4h/\lambda D^2\right)^{1/3} \tag{3.25}$$

avec $v = D\left(\cos\tau-\cos\tau_{rg}\right)/2$ et $h^{-1} = \tan\tau_{rg}\sin^2\tau_{rg}$, R, étant la distance au point d'observation et $z(\theta)$, un angle de déviation à la position de l'arc-en-ciel géométrique :

$$z = \left(\theta-\theta_{rg}\right)\left(\frac{16D^2}{h\lambda^2}\right)^{1/3} \tag{3.26}$$

L'équation (3.24) est la représentation intégrale de la fonction d'Airy[18] [73, 74], avec :

$$\int_0^\infty \cos\left[\frac{\pi}{2}\left(z\eta-\eta^3\right)\right]d\eta = \int_0^\infty \cos\left[\frac{\pi}{2}\eta^3 - \frac{\pi z}{2}\eta\right]d\eta = \left(\frac{2\pi^2}{3}\right)^{1/3} Ai\left[-\left(\frac{\pi^2}{12}\right)^{1/3} z\right] \tag{3.27}$$

La distribution d'intensité au voisinage de l'angle d'arc-en-ciel θ_{rg} est donc proportionnelle à :

$$I(\theta,m,D,\lambda) \propto \frac{E_0^2}{h^{1/3}(m)}\left(\frac{\pi D}{\lambda}\right)^{4/3} Ai^2\left[-\left(\frac{\pi^2}{12}\right)^{1/3} z\right] \tag{3.28}$$

La théorie d'Airy permet d'améliorer de manière très significative la description de l'arc-en-ciel. L'équation (3.28) montre, par exemple, que les caractéristiques de l'arc-en-ciel ne dépendent pas seulement de l'indice des particules, mais également de leur diamètre (i.e. du paramètre de taille, dépendance en $D^{4/3}$). Cette théorie permet également d'effectuer des calculs rapides (comparé à la LMT), ce qui est un facteur non négligeable pour l'inversion de données expérimentales. Cependant, la qualité des prédictions

[17] Pour une goutte d'eau, m ∝ 1.332 pour λ=0.5 μm et T=20°C, nous avons $\theta_{rg} = 137.8°$. Les couleurs de l'arc-en-ciel viennent de la dépendance de l'indice avec la longeur d'onde (dispersion).

[18] Cette intégrale a été nommée par Airy : « Rainbow Integral »

de la théorie d'Airy décroît assez rapidement à mesure que l'on s'éloigne de l'angle d'arc-en-ciel prédit par l'optique géométrique, Figure 8. En fait, la théorie d'Airy tend à minimiser la décroissance de l'intensité et la fréquence angulaire des arcs d'ordres élevés (lobes) ; et ceci, d'autant plus que la particule est petite. Il est également important de noter que, numériquement, les séries de Debye prédisent une dépendance de l'intensité de l'arc-en-ciel en $I \propto D^{\gamma}$ avec $\gamma = 2.34013 \approx 7/3$ [70]. A l'heure actuelle, et après vérification de nos calculs, nous n'avons pas d'explication précise concernant cette différence notable avec la théorie d'Airy (les références [5, 10, 72, 75] ne s'accordent d'ailleurs pas sur ce point). Aussi, dans ce qui suit, de façon pragmatique, nous avons choisi de reformuler l'Eq. (3.28) sous la forme :

$$I(\theta,m,D,\lambda) \propto \frac{E_0^2}{h^{1/3}(m)}\left(\frac{\pi D}{\lambda}\right)^{7/3} Ai^2\left[-\left(\frac{\pi^2}{12}\right)^{1/3} z\right] \tag{3.29}$$

Cette formulation donne de très bons résultats, voir la Figure 8 et la Figure 36.

Roth et al. [25, 61, 76] semblent avoir été les premiers à avoir utilisé le phénomène d'arc-en-ciel, et la théorie d'Airy, pour caractériser expérimentalement des particules individuelles en écoulement. Van Beeck [26, 77] et Sankar et al. [78] ont également été des précurseurs dans ce domaine. L'analyse de l'arc-en-ciel produit par une particule individuelle permet, en théorie, d'obtenir la corrélation entre sa taille et son indice (matériau, composition, température). Cependant, en situation réelle, cet arc-en-ciel est fortement perturbé par la présence des autres particules. De ce fait, il est difficile à analyser.

Arc-en-ciel produit par un ensemble de particules

Les arcs-en-ciel observés dans la Nature sont produits par un ensemble de gouttes : nuage, pluie... Si la concentration en particules est faible, au sens de la diffusion simple (§ 2.4.3), on peut sommer de manière incohérente les arcs-en-ciel produits par chacune des particules diffusantes :

$$\langle I(\theta)\rangle = \int_{x=D_{\min}}^{x=D_{\max}} \int_{y=m_{\min}}^{y=m_{\max}} I(\theta,x,y,\lambda) f(x,y) dxdy \tag{3.30}$$

Où $f(D,m)$ est la fonction de répartition des diamètres (bornés par les valeurs $D_{\min}, D_{\max}$) et des indices de réfraction (bornés par les valeurs $m_{\min}, m_{\max}$), des particules qui forment l'arc-en-ciel.

Inversion du diagramme d'arc-en-ciel :

Pour caractériser un ensemble de particules, à partir de l'analyse du diagramme de diffusion $\langle I(\theta)\rangle$ (qualifié de « global » par Van Beeck [27]), il faut pouvoir déterminer le noyau de l'intégrale de l'Eq. (3.30) : $f(D,m)$ et ses bornes $D_{\min}, D_{\max}, m_{\min}, m_{\max}$. Ceci requière le développement d'une méthode d'inversion qui nécessite de poser certaines hypothèses simplificatrices :

- Dans certaines situations physiques, on pourra supposer qu'il existe une fonction de corrélation entre les tailles et les indices (e.g. décroissance de la température des particules en $\Delta T \propto D^2$), les variables *D* et *m* ne sont plus indépendantes :

$$\langle I(\theta)\rangle = \int_{x=D_{\min}}^{x=D_{\max}} I(\theta,m(x),x)_{\lambda} f(x) dx \tag{3.31}$$

- Dans d'autres situations physiques, on pourra supposer que les variations d'indice sont nulles ou négligeables (i.e. écoulement diphasique isotherme), ce qui simplifie considérablement le noyau de l'intégrale :

$$\langle I(\theta)\rangle = \int_{x=D_{\min}}^{x=D_{\max}} I(\theta,x)_{m,\lambda}\, f(x)dx \qquad (3.32)$$

- Dans des situations encore plus simples, on pourra également faire certaines hypothèses sur la forme ou le nombre de modes de la distribution des tailles et/ou des indices. Dans le cas d'un écoulement diphasique isotherme où la répartition des tailles des particules suit une distribution de type Normale (i.e.: pilote de lit fluidisé… voir le § 4.4), l'équation (3.30) se réduit alors à :

$$\langle I(\theta)\rangle = \frac{1}{\sigma_D\sqrt{2\pi}} \int_{x=D_{\min}}^{x=D_{\max}} I(\theta,x)_{m,\lambda} \exp\left[-\frac{(x-\bar{D})^2}{2\sigma_D{}^2}\right]dx \qquad (3.33)$$

Dans ce dernier cas, la méthode d'inversion à mettre en œuvre doit seulement permettre de déterminer 3 paramètres : *i)* le diamètre moyen des particules $\bar{D}$, *ii)* l'écart type des diamètres σ_D et *iii)* l'indice moyen *m*. Classiquement [36], les bornes de l'intégrale peuvent généralement être imposées arbitrairement, ou non : $\{D_{\min}, D_{\max}\} = \bar{D} \pm 3\sigma_D$. ¨

Nous avons développé différents codes de calcul de l'arc-en-ciel produit par un nuage de particules, basés sur la théorie d'Airy, les séries de Debye et la Théorie de Lorenz-Mie. La Figure 36 permet de comparer les prédictions de la théorie d'Airy et des séries de Debye, ainsi que l'influence de différents paramètres sur la forme de l'Arc-en-ciel. De manière très synthétique nous dirons que, pour une distribution granulométrique de forme donnée :

- les variations de l'indice moyen entraînent un décalage angulaire, « une translation », de l'arc-en-ciel.
- les variations de l'écart type jouent sur l'atténuation, la perte de contraste, plus ou moins forte, des lobes d'ordres élevés,
- les variations du diamètre moyen contrôlent l'étalement angulaire, « la compression/dilatation », du diagramme d'arc-en-ciel.

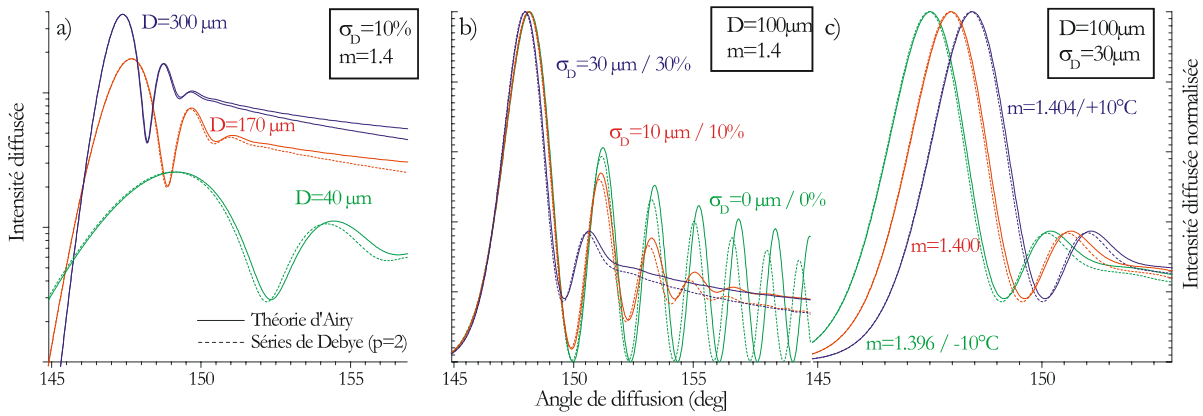

Figure 36 Influence sur l'arc-en-ciel produit par différentes distributions granulométriques (i.e. loi normale) de particules : a) du diamètre moyen, pour un écart-type de 10% et un indice constant (m=1.51); b) de l'écart type des diamètre, pour un diamètre moyen et un indice constants; c) d'une variation d'indice/température, pour un diamètre moyen et un écart type constants, λ=0.6328µm.

Partant de ces dernières remarques, nous avons mis au point un dispositif expérimental, un logiciel d'acquisition et d'inversion des signaux d'Arc-en-ciel [70]. La méthode d'inversion, encore très imparfaite,

est, dans son principe, assez proche de celle développée pour inverser les diagrammes de diffraction (§ 3.1.4).

Exemple de résultats expérimentaux

La Figure 37 présente un schéma du montage réalisé. Il se compose essentiellement d'un laser HeNe fibré, de 10mW, d'un agrandisseur de faisceau utilisé pour contrôler les dimensions du volume de mesure (avec le filtrage spatial P_3, les dimensions du volume de mesure sont de l'ordre de $1cm^3$), quelques lentilles utilisées en configuration de Fourier ($f_1=f_2=100mm$, $f_3=75mm$), d'une caméra CCD matricielle : 1024*1024 pixels 12 bits, d'une carte d'acquisition numérique et d'un PC. Le logiciel développé : GRAS, voir la Figure 61, permet de piloter intégralement la caméra (synchronisation externe, intégration, gain…) et intègre les fonctions d'inversion basées sur la théorie d'Airy et les séries de Debye.

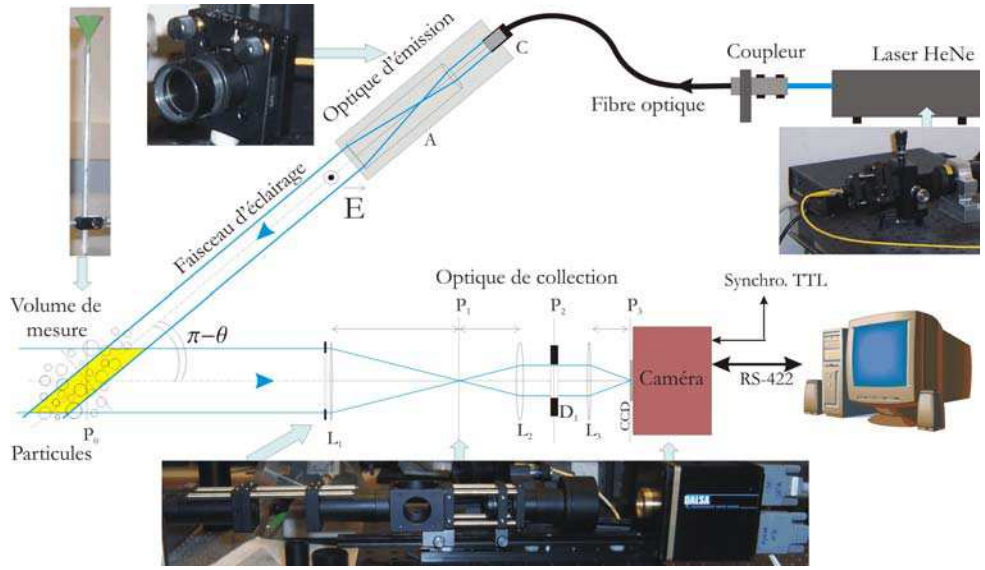

Figure 37 Schéma de principe et photographies du dispositif expérimental d'étude du phénomène d'arc-en-ciel.

A titre d'exemple, la Figure 38 montre : *i)* une photographie type d'un arc-en-ciel produit par un jet de billes de verre à température ambiante et *ii)* une comparaison du profil d'intensité expérimental avec ceux prédits par la théorie d'Airy et les séries de Debye. On constate que l'accord est globalement bon, surtout pour les positions angulaires des maxima et minima. En revanche, sur les bords du profil (points A et E), les variations d'intensité diffèrent notablement entre la théorie et l'expérience. Cet écart s'explique par le fait que le système optique est sujet à un phénomène de vignettage. En fait, le montage de Fourier nous permet de conserver les angles mais pas l'intensité relative. Nous avions déjà observé ce phénomène avec le montage de diffraction (§ 3.1.4). L'effet est cependant plus prononcé avec l'arc-en-ciel, du fait de l'éclairement hors axe.

La Figure 39 montre le résultat de l'analyse de l'arc-en-ciel de la Figure 38, en terme de granulométrie des billes de verre. Ce résultat a été obtenu en recherchant les paramètres de l'Eq. (3.33) qui minimisent l'écart entre les positions angulaires des extrema du profil théorique et du profil expérimental. Le résultat est présenté sous la forme d'une distribution Normale, qui est comparée à une mesure obtenue avec un diffractomètre commercial.

L'accord entre les deux systèmes est bon, avec : $\bar{D}_{diffrac.} = 95\mu m$, $D(50\%)_{diffrac.} = 92.5\mu m$ et $\bar{D}_{GRAS} = 92\mu m$; $\sigma_{D,diffrac.} = 14\mu m$ et $\sigma_{D,GRAS} = 11\mu m$. Cet accord à été trouvé pour une valeur de l'indice des billes de m=1.503, qui est tout à fait compatible avec les spécifications du fournisseur (m=1.5-1.51). Des résultats comparables ont été trouvé pour des échantillons de billes de verre de différents diamètres moyens et écarts type [70].

Il est à noter que la distribution brute restituée par le diffractomètre fait apparaître de très petites particules (D<50µm) qui ne peuvent pas être physiquement présentes dans le jet.

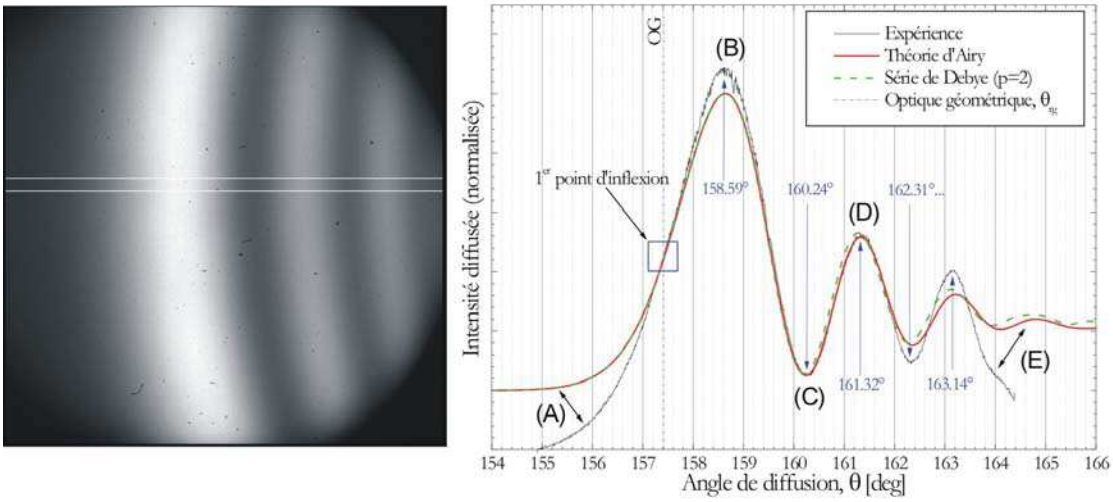

Figure 38 Photographie d'un arc-en-ciel produit par un jet de billes de verre ($D = 92 \pm 11\mu m$) et comparaison de son profil d'intensité avec la théorie.

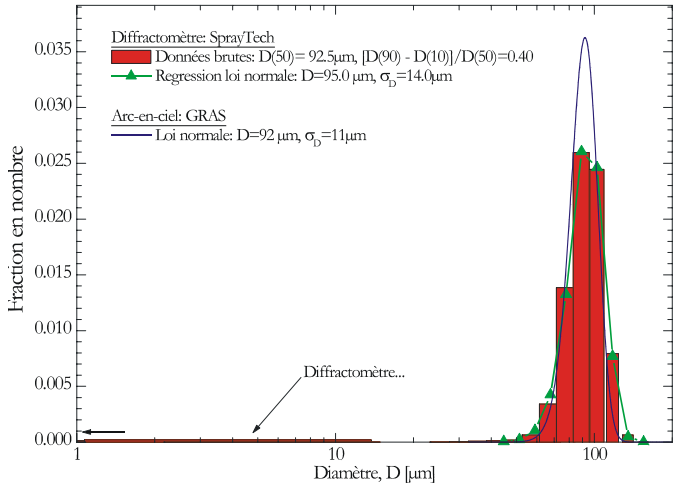

Figure 39 Comparaison de l'analyse granulométrique d'un jet de billes de verre : arc-en-ciel (GRAS) et diffractométrie (système SprayTech [71]). Nous avons choisi de normaliser l'intégrale des distributions à 1.

En guise de conclusion sur ces premiers travaux, nous dirons que les résultats obtenus sont déjà très encourageants. L'analyse de l'arc-en-ciel global permet d'obtenir une caractérisation statistique instantanée des particules (diamètre et indice) même si, dans notre cas, nous nous sommes limités à des particules d'indice fixé. A l'avenir, nous devrons automatiser la technique d'inversion et réduire le nombre d'hypothèses simplificatrices (i.e. forme de la distribution, corrélation taille-indice). Pour ce faire, il faudra

nécessairement augmenter le nombre de points de mesure *fiables,* en éliminant les effets de vignettage et/ou en utilisant d'autres effets (dispersion, polarisation).

Dans l'état actuel de nos réflexions, la principale limite de cette technique semble être la difficulté prévisible concernant la mesure *absolue* de la concentration en particules, C_v, qui est un paramètre fondamental pour l'étude des écoulements.

Chapitre 4

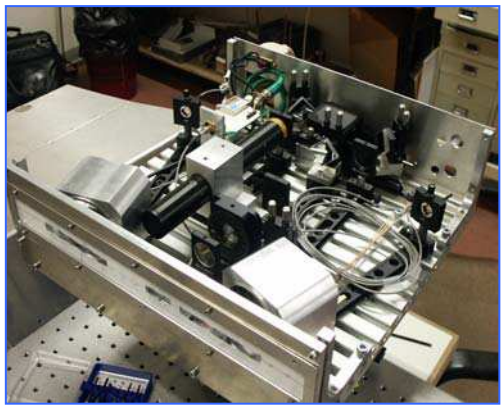

COLLABORATIONS & APPLICATIONS

Ce chapitre dresse un bilan des travaux réalisés dans le cadre de collaborations universitaires et de partenariats industriels, généralement interdisciplinaires ou « multi-physique ».

4.1 Biophysique

4.1.1 Pression de radiation et pincettes optiques

Les photons véhiculent une certaine quantité de mouvement. Par pression de radiation, un faisceau laser peut donc piéger, déplacer et mettre en rotation une particule [18, 20, 79].
Les physiciens ont développé différents outils à destination des biologistes et, notamment, les pincettes optiques («optical tweezers»). Ces dernières permettent de manipuler par pression de radiation les cellules biologiques, sans risque de les détruire [80].

Le travail sur l'extension de la GLMT aux sphères multicouches (§2.2) a permis de réaliser différentes simulations sur : *i)* le comportement des pincettes optiques lorsque la particule est creuse ou lorsqu'elle est composée d'un noyau ; *ii)* les forces nécessaires (pico Newton) à la déformation mécanique de membranes cellulaires [C9][81, 82].

La Figure 7 b) présente un exemple du calcul de l'évolution du coefficient pression de radiation transverse exercée par un faisceau laser sur une vésicule.

4.1.2 Caractérisation optique des globules rouges

Il existe différents types d'hématies (globules rouges). Certaines sont sphériques mais, pour un sujet sain, la plupart d'entre elles ont une forme ellipsoïdale dont la longueur des axes est typiquement de 7.5µm et 1.8 µm. Ces cellules sont transportées à travers tous le corps par le plasma. Elles fixent et libèrent l'oxygène par une réaction d'oxydation/réduction d'une macromolécule, l'hémoglobine, $Hb + O_2 \rightleftarrows HbO_2$.
La salinité du plasma, ou «pression osmotique », influence fortement les caractéristiques des hématies et

principalement leur volume et leur rapport d'aspect. Une pathologie conduisant à une forte pression osmotique induit un gonflement de ces cellules. Ce phénomène réduit la déformabilité des hématies et donc, leur capacité à se faufiler à travers les capillaires sanguins. Il entraîne également une augmentation critique de la viscosité du sang.

La détection de certaines pathologies sanguines nécessite de pouvoir caractériser rapidement les cellules contenues dans un échantillon sanguin: en volume et en nombre (≈hématocrite), en forme, et en taux d'oxygénation. Les systèmes d'analyse les plus évolués, optiques, comptent les cellules une par une, à partir d'un échantillon préalablement *dilué* et placé dans *une cellule de Taylor-Couette* (afin d'orienter les hématies). De sorte qu'il existe actuellement une demande de la communauté médicale pour des outils rapides d'analyse, globale et non destructive, d'échantillons sanguins non préparés.

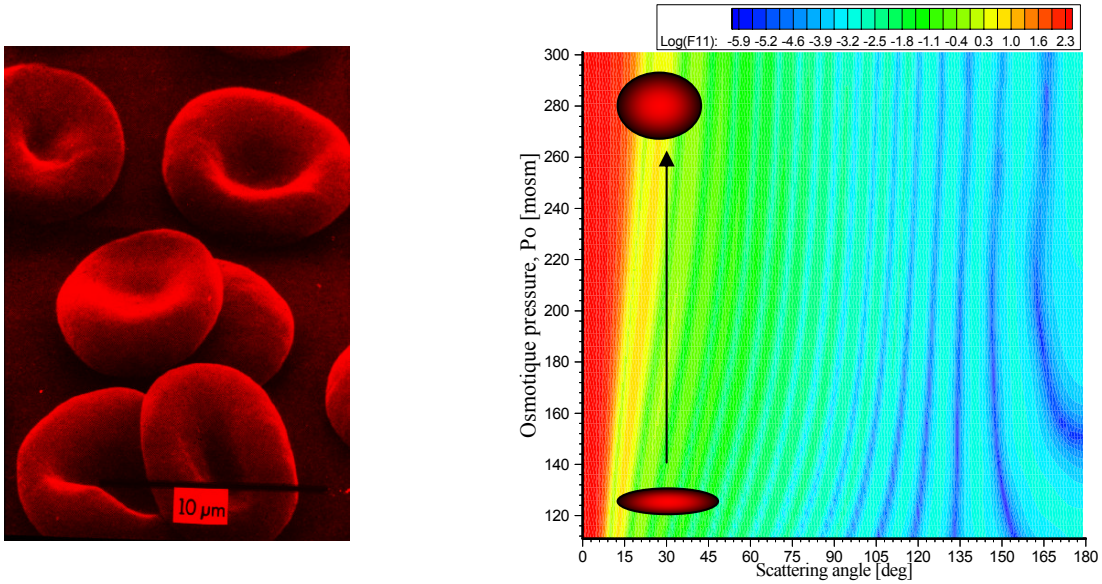

Figure 40 Caractérisation optique de globules rouges : photographie électronique et calcul de l'évolution de l'état de polarisation linéaire de la lumière diffusée par un échantillon d'hématies orientées, cf. reproduction de l'article [A15].

Suite à une demande de collaboration d'une équipe polonaise (§ 8.5.2), j'ai été amené à travailler sur la modélisation des propriétés optiques d'échantillons sanguins. Mes collègues souhaitaient mettre au point une méthode de diagnostic optique, la moins intrusive possible, du taux d'oxygénation des hématies et de la pression osmotique d'un échantillon sanguin. Mais ils ne disposaient pas d'un modèle de diffusion satisfaisant (i.e. diffraction anormale [83]).

J'ai tout d'abord développé un modèle «biophysique», en synthétisant les rares données expérimentales disponibles dans la littérature [84]. Ce dernier permet de simuler les caractéristiques physiques des hématies (volume, rapports d'aspects, densité, absorptivité spectrale…) en fonction des paramètres physiologiques (taux d'oxygénation, hématocrite, pression osmotique…). En suite, pour calculer les propriétés de diffusion de la lumière des hématies, j'ai adapté à notre problème la méthode de la T-Matrice et les codes de calculs développés par Mischenko et al. [40, 85, 86]. Ce travail a permis de concevoir un code de simulation des caractéristiques optiques d'une cellule ellipsoïdale d'orientation quelconque, ou d'un échantillon sanguin d'épaisseur optique faible (hypothèse de diffusion simple[19]), en fonction des paramètres physiologiques [C28, C33, A15], voir la reproduction de l'article [A15] dans le Chapitre 9.

[19] Nous aurions pu facilement lever cette hypothèse en utilisant les modèles de type Monte Carlo (2.4.3) et en remplaçant les particules de latex par des globules rouges…

Ces travaux ont permis d'établir que : *i)* le taux d'oxygénation peut être déduit des différences d'absorptivité spectrale de l'hémoglobine et de l'hémoglobine oxydée [87] ; et que *ii)* l'état de polarisation linéaire de la lumière diffusée par l'échantillon est très sensible à la pression osmotique (forme et indice de réfaction des globules). Malheureusement, l'état de polarisation de la lumière diffusée est également *fortement* sensible à l'orientation spatiale des cellules dans l'échantillon… Ce dernier résultat a considérablement réduit les chances de pouvoir caractériser un échantillon non préparé (sans cisaillement de l'écoulement).

Au terme de cette première collaboration, l'équipe polonaise dispose désormais d'outils de simulation adéquats. Notre collaboration a été renouvelée en 2005, sur un sujet un peu différent (§ 8.5.2).

4.2 Combustion

4.2.1 Moteur à combustion interne et choc thermique

Dans le cadre d'un programme d'échange européen[20] et d'un stage doctoral (§ 8.3.2), des modèles et des codes de calcul ont donc été élaborés afin de prédire les profils radiaux de température et de concentration de gouttes en combustion, ainsi que leurs propriétés de diffusion de la lumière [RI6].

La Figure 41 a) montre, par exemple, l'évolution simulée du profil d'indice (i.e. température) d'une goutte de décane, $D = 50\mu m$, en fonction de son temps de séjour dans une chambre de combustion. La Figure 41 b) simule la réponse d'un système phase Doppler lors de la mesure de ces gouttes, pour différents diamètres et temps de séjours. Cette figure indique notamment que, pour les gouttes de $D = 50\mu m$, le fait de négliger les gradients internes de température, lors de l'inversion des mesures de déphasage, induit une erreur de près de 20% sur les diamètres mesurés… Les calculs de flux seront donc entachés d'une erreur importante.

Cette étude à permis de rechercher des configurations optiques moins sensibleas aux gradients internes et d'autres, capables d'estimer l'indice de gouttes multi composants (fraction de mélange, température [88]).

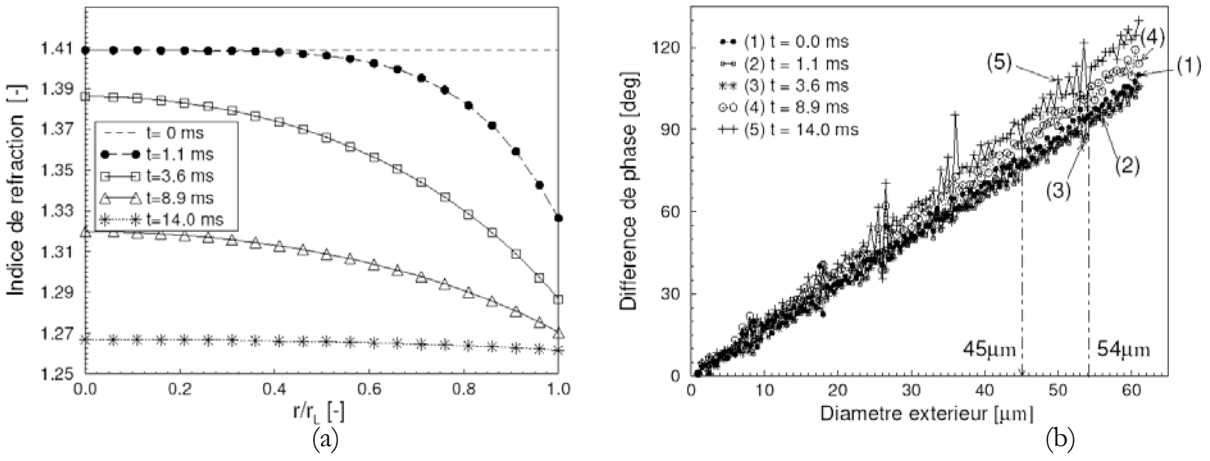

Figure 41 a) Evolution temporelle du profil d'indice (i.e. température) d'une goutte de décane passant instantanément des CNTPs à des conditions de combustion T=2000K, P=10 bars, D=50µm ; b) Réponse d'un interféromètre phase Doppler à la mesure de ces gouttes pour différents diamètres et temps de séjours dans la chambre de combustion (cf. reproduction de l'article [A5]).

[20] Alain Berlemont, CORIA-UMR CNRS 6614, Rouen

4.2.2 Moteur fusée et atomisation secondaire

Dans le cadre du GDR «moteur-fusée», j'ai participé à un projet de recherche sur les phénomènes d'atomisation secondaire sur le banc cryogénique « Mascotte » de l'ONERA (§ 8.4.2). Ma contribution, théorique et numérique, s'inscrivait dans le cadre d'une campagne de mesure de la vitesse de glissement entre la phase fluide (hydrogène gazeux) et la phase liquide (dard d'oxygène liquide), i.e. des nombres de Weber. Cette campagne posait différents problèmes métrologiques et notamment : *i)* la détection simultanée, avec un vélocimètre Doppler laser, des traceurs du fluide (ZrO_2 et MgO) et des gouttes d'oxygène liquide (LOx) ; *ii)* la distinction de ces deux types de particules.

Les traceurs du fluide sont de taille submicronique, $d \le 0.5\mu m$, alors que le diamètre des gouttes de LOx peut atteindre $D \approx 100\mu m$. En faisant l'hypothèse que les particules diffusent proportionnellement à leur surface, il vient que la gamme des diamètres des particules détectables n'excède pas, avec vélocimètre Doppler laser classique : $D_{\max} / D_{\min} \sim 50$. A priori, on ne peut donc pas caractériser simultanément les deux phases. Cependant, on peut montrer (§2.4.4) qu'en modifiant la forme des détecteurs et en plaçant l'optique de détection vers $\theta = 110 - 130°$, la dynamique en intensité des signaux Doppler produits par les deux phases est considérablement réduite du fait de la différence de sphéricité entre les traceurs du fluide et les gouttes de LOx, voir la Figure 16 et le §2.4.4.

Pour distinguer les particules des deux phases, la solution mise en place consiste à utiliser le rapport d'état de polarisation de la lumière diffusée par les particules. En effet, les particules sphériques (LOx) conservent l'état de polarisation de l'onde incidente, ce qui n'est pas le cas des particules irrégulières (traceurs du fluide).

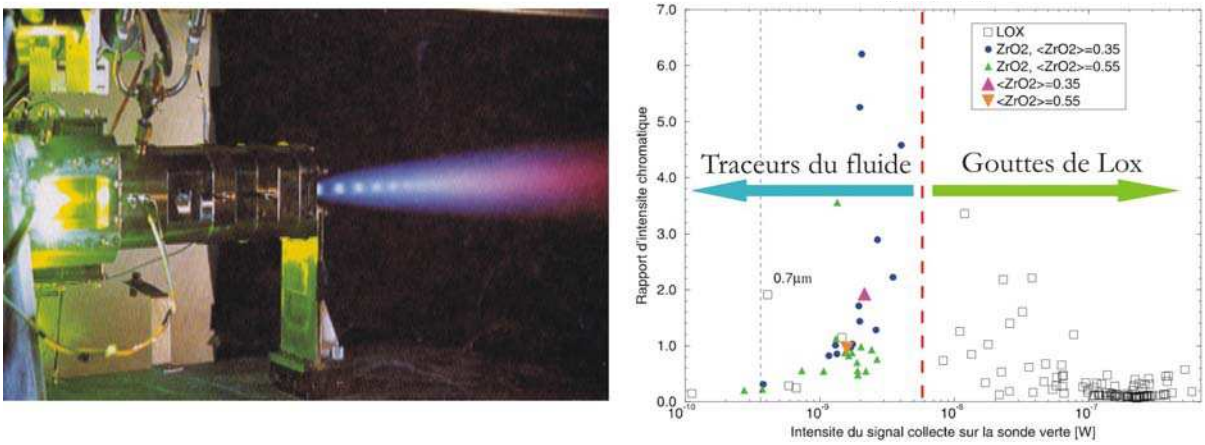

Figure 42 Photographie du banc cryogénique « Mascotte » de l'ONERA et simulation de la réponse du vélocimètre optimisé pour la détection simultanée des deux phases.

La Figure 42 montre une photographie de la tuyère du banc «Mascotte» et un résultat numérique type. La méthode de mesure et de séparation des deux phases conduit à tracer la réponse du vélocimétrie Doppler dans le plan : {intensité des signaux Doppler - rapport d'intensité chromatique ($\approx$ polarisation ici)}. Ce calcul a été obtenu pour des gouttes de LOx $(D \approx 0.7 - 100\mu m)$ et des traceurs en oxyde de zirconium $(d \approx 0.25 - 0.7\mu m)$. On constate que, pour cette configuration optique [RC6-7], non seulement on peut détecter simultanément les deux types de particules mais on peut également les séparer (i.e. ligne rouge). La vitesse de glissement entre les deux phases peut donc être mesurée.

Ces résultats numériques ont été utilisés par Pierre Gicquel et ses collègues, de l'ONERA, pour réaliser une campagne de mesures sur l'atomisation secondaire du dard liquide, à froid et en combustion [C23, A10].

4.3 Instabilités hydrodynamiques et systèmes thermiques

4.3.1 Instabilités thermo solutales et étangs solaires

Les étangs solaires font l'objet de nombreuses recherches dans la mesure où, à terme, ils devraient permettre la production durable et écologique d'électricité, ainsi que le dessalement en grande quantité d'eaux saumâtres. Il s'agit en fait de bassins dont le fond absorbe le rayonnement solaire (matériau absorbant + échangeur). L'eau chaude[21] ainsi produite peut actionner une turbine, voir la Figure 43. Un des points clé de cette technologie réside dans le remplissage du bassin : une couche d'eau saline surmontée d'une couche d'eau douce.[22] La couche saline sert à la fois de réservoir calorique (stockage et inertie thermique) et à retarder le déclenchement de la convection. La couche d'eau douce isole et protège la couche saline de la convection à l'interface air/eau, des intempéries.

Pour ces systèmes énergétiques, la stabilité de la stratification eau saline/eau douce est donc fondamentale. Elle dépend tout particulièrement de la zone à gradient de concentration, ou «interface», qui sépare les couches initialement homogènes.

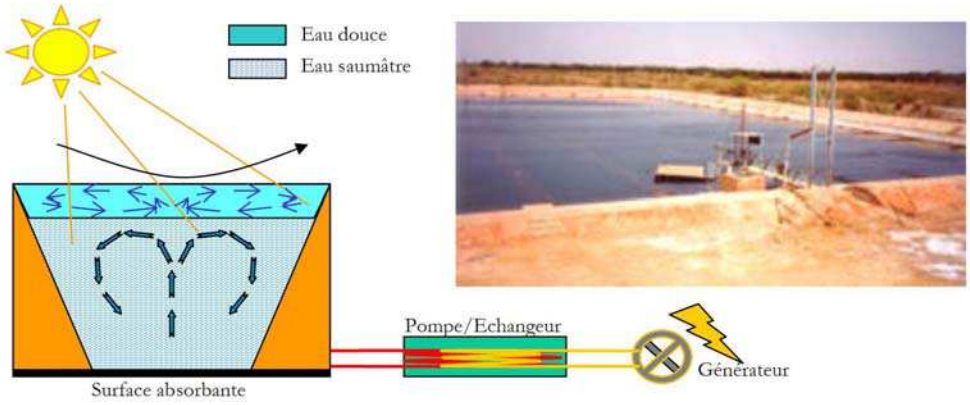

Figure 43 Schéma de principe et photographie d'un étang solaire utilisé pour la production d'électricité.

Dans le cadre d'une collaboration soutenue par le CNRS et son équivalent tunisien (DGRST), j'ai travaillé sur cette thématique de recherche et, plus particulièrement, sur la caractérisation optique de la dynamique d'écoulements stratifiés modèles, de petites dimensions (voir la Figure 44). Le système de Vélocimétrie par Images de particules mis au point (c.f. Figure 60), de même que la bouche thermique, ont permis d'obtenir les champs de vitesse dans l'ensemble de la cuve et au niveau de l'interface. Nous avons ainsi pu montrer que, lorsque le chauffage est mis en place, des cellules convectives contrarotatives apparaissent assez rapidement dans les deux couches homogènes. Elles sont co-rotatives d'une couche à l'autre et elles induisent un cisaillement important au niveau des bords inférieur et supérieur de l'interface. Ce phénomène, couplé à la diffusion massique du sel, induit une érosion hydrodynamique de l'interface et le développement d'une instabilité de type Kelvin-Helmholtz. A long terme, ces effets combinés conduisent à la destruction de la stratification, pour plus de détails voir les références [C32, C39].

Au terme de cette collaboration, l'ENIT possède désormais les outils expérimentaux nécessaires à la compréhension détaillée de ces mécanismes de déstabilisation, et à la validation des modèles de simulation de ces systèmes. Nous recherchons actuellement un support financier pour poursuivre cette collaboration.

[21] Près de 80°C avec le chlorure du sodium et le climat tunisien…
[22] Profondeur : plusieurs mètres ; surface du bassin : quelques dizaines de mètres carré à quelques dizaines d'hectares.

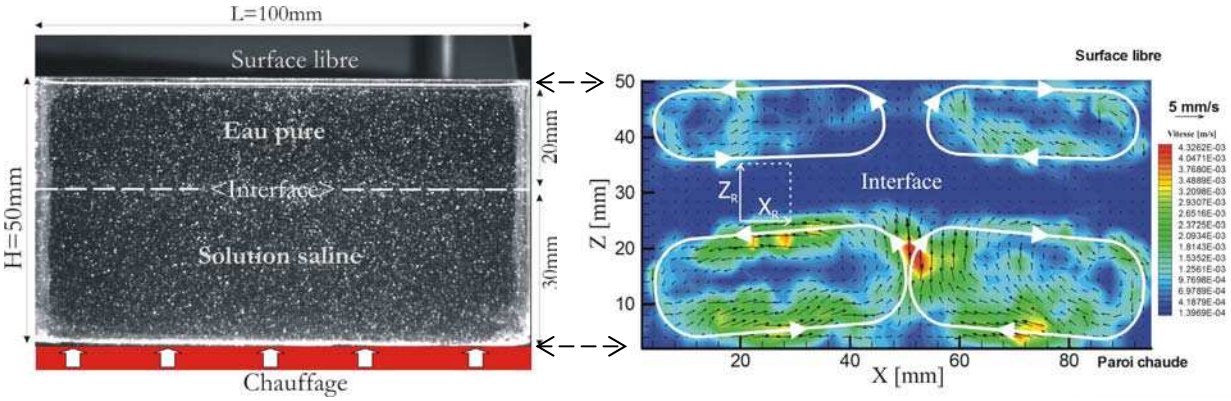

Figure 44 Etude expérimentale des mécanismes de déstabilisation d'un écoulement stratifié : photographie de la cuve d'expérimentation et champ de vitesse instantanée mesuré après 5 mn de chauffage (température imposée, T= 60°).

4.3.2 Instabilités de jets capillaires homogènes et bicouche

Dans le cadre de collaborations internes et financées, des études ont été conduites sur la stabilité de jets capillaires, qu'ils soient homogènes (une seule phase) [C8] ou bicouche (a cœur, diphasiques) [C26, A11]. L'étude des mécanismes de déstabilisation de ces écoulements est fondamentale pour certains procédés industriels (e.g. génération de particules calibrées homogènes ou enrobées) et, de manière plus fondamentale, pour améliorer notre compréhension des phénomènes d'atomisation. Les méthodes optiques mises en place pour caractériser la stabilité de ces jets axisymétriques sont du même type que celles utilisées pour la caractérisation des fibres de renfort (§4.3.3) et des fibres optiques (§ 4.3.4).

Pour les jets homogènes, l'analyse des séries expérimentales a été réalisée à l'aide des outils de la « Dynamique des Systèmes», par Christophe Letellier[23]. Pour les jets forcés, les portraits de phase ont mis en évidence des dynamiques différentes pour les différentes perturbations qui se développent le long du jet [C8][89].

Pour l'étude de la stabilité d'un jet bicouche, un modèle, unidimensionnel et non linéaire, a été développé dans le cadre d'une collaboration avec Stefan Radev (§ 8.5.2). Ce travail a mis en évidence la forte sensibilité des mécanismes de formation des gouttes satellite au rapport des tensions superficielles des deux fluides, voir la reproduction de l'article [A11] dans le Chapitre 9. Nous projettons de poursuivre cette étude par des expériences basées sur l'analyse des diagrammes de diffusion (§4.3.4).

4.3.3 Etude des conditions de stabilité d'un procédé de fibrage du verre à haute température

Dans le cadre de contrats d'étude avec les groupes Saint-Gobain Recherche et Saint-Gobain Vetrotex (§ 8.4.2), nous avons d'étudié les conditions de stabilité d'un procédé de fibrage du verre à haute température [A12-14, A17, C25, C31, C36-35]. Les fibres de verre produites sont utilisées pour renforcer les propriétés mécaniques de différents matériaux [90], voir la Figure 45. La stabilisation de ce procédé industriel est cruciale en terme de qualité du produit final, de productivité et de réduction de la quantité de déchets verriers générés (c'est d'ailleurs à ce titre que l'ADEME[24] a cofinancé la bourse de thèse de M[elle] Lenoble [4]). D'un point de vue académique, l'étude de ce procédé est intéressante de par la multiplicité des phénomènes physiques mis en jeux (chimie, thermodynamique, rayonnement d'un milieu semi transparent,

[23] CORIA, UMR n°6614 CNRS-Université de Rouen
[24] Agence De l'Environnement et de la Maîtrise de l'Energie

instabilités hydrodynamiques et contraintes mécaniques, diffusion électromagnétique…), tout en restant compatible avec des études en laboratoire, voir la Figure 46.

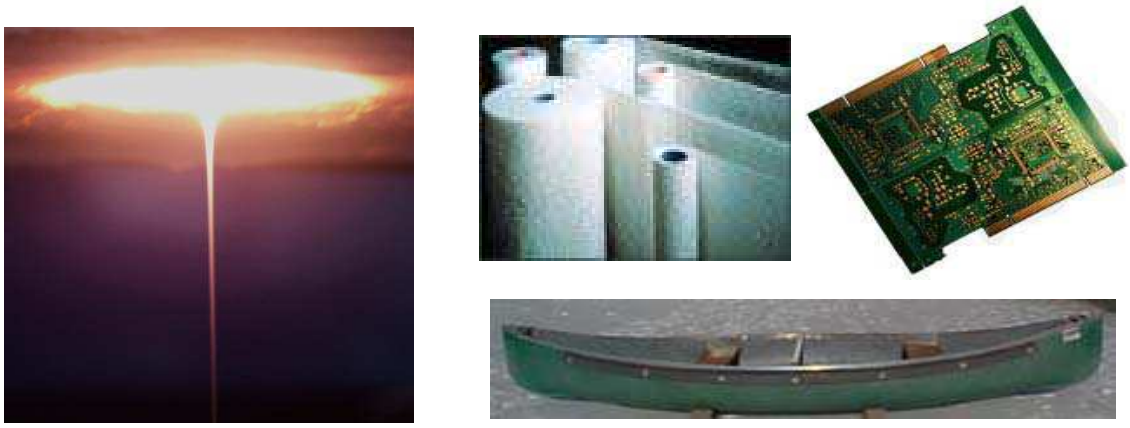

Figure 45 Photographie d'un jet de verre à haute température à l'origine de la formation d'une fibre de verre utilisée pour les applications de renfort : textile, cartes électroniques, objets moulés…

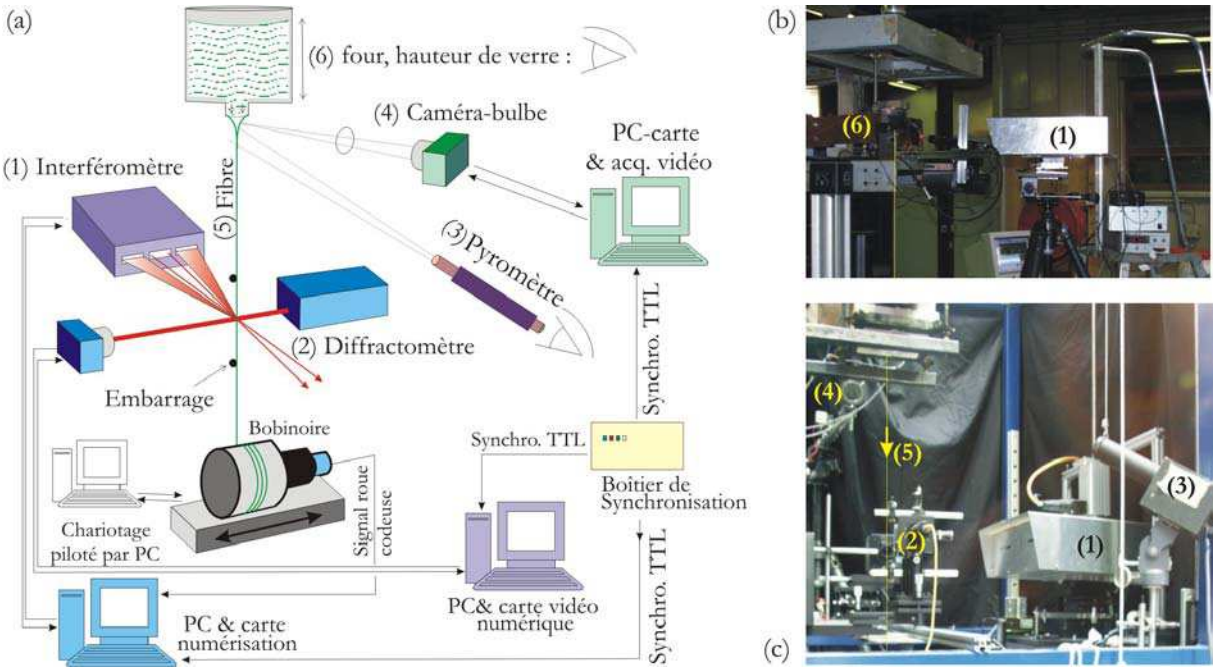

Figure 46 Schéma de principe et photographies du dispositif expérimental mis en œuvre pour étudier la stabilité d'un procédé de fibrage du verre à haute température .

Ces travaux ont abouti au développement :

- De modèles de diffusion de la lumière par différentes «fibres». Ceux-ci prennent en compte des effets comme : la biréfringence uniaxe induite par la tension de fibrage, l'inclinaison de la fibre, la dépendance de l'indice de réfraction avec les conditions de refroidissement (i.e. trempage [91]), l'existence de fibres creuses…, voir les paragraphes : § 2.1, § 3.1.3 et § 3.1.4.

- D'un interféromètre phase Doppler [A12-13, A17] et d'un diffractomètre haute résolution [A16] capables de mesurer en temps réel l'évolution du diamètre d'une fibre en cours de production, voir les paragraphes §3.1.3 et §3.1.4, la Figure 28, la Figure 56 et la Figure 57.

- D'un modèle hydrodynamique du procédé de fibrage. Ce modèle résout les équations de bilan pour un jet visqueux à haute température (modèle radiatif), 1D et axisymétrique, Figure 47 a):

$$\begin{cases} \dfrac{\partial S}{\partial t} + Sw = 0 \\ \rho\left[\dfrac{\partial wS}{\partial t} + \dfrac{\partial w^2 S}{\partial z}\right] = \dfrac{\partial}{\partial z}\left(3S\mu\dfrac{\partial w}{\partial t} + \sigma\sqrt{\pi S}\right) - 2\sqrt{\pi S\tau_a} + \rho gS \\ \rho C_p\left[\dfrac{\partial TS}{\partial t} + \dfrac{\partial TwS}{\partial z}\right] = \lambda_{air}\pi Nu\left(T_a - T\right) + 2\sqrt{\pi}S\varepsilon\tilde{\sigma}\left(T^{*4} - T^4\right) + 3\mu S\left(\dfrac{\partial w}{\partial z}\right)^2 + \lambda\dfrac{\partial}{\partial z}\left(\dfrac{S\partial T}{\partial z}\right) - \dfrac{\partial\left(Sq_z^r\right)}{\partial z} \end{cases} \quad (4.1)$$

où z, t et g représentent la coordonnée axiale, le temps et la constante de gravité; S et w, la section et la vitesse axiale du jet ; ρ, μ, τ_a, C_p, ε, σ et λ, la masse volumique, la viscosité dynamique, la tension superficielle, la chaleur spécifique, l'émissivité globale, la tension superficielle et la conductivité thermique du verre en fusion ; λ_a et T_a la conductivité thermique et la température de l'air ambiant ; Nu, le nombre de Nusselt; q_z^r, un terme d'échange thermique et T et T*, la température locale du jet et la température radiative du milieu ambiant (pour plus de détails sur ce modèle, et notamment les relations de fermeture et les équations adimentionnalisées, voir les références [4] et [C31]).

Ce modèle prédit l'évolution du profil axiale de température du jet, son profil de contraction et de tension... pour des régimes stationnaires et instationnaires.

A titre d'exemple, la Figure 47 b) compare, pour le profil de température du jet de verre, les prédictions de différents codes de calculs et des points expérimentaux obtenus par spectroscopie Brillouin [92]. Les résultats de notre modèle (IUSTI- Modfid) sont en bon accord avec les résultats expérimentaux (erreur estimée ±5° [92]). Notre modèle a également été utilisé pour simuler l'évolution du diamètre des fibres lorsque le procédé est soumis à une rampe de vitesse, une perturbation radiative ou convective [C31][93].

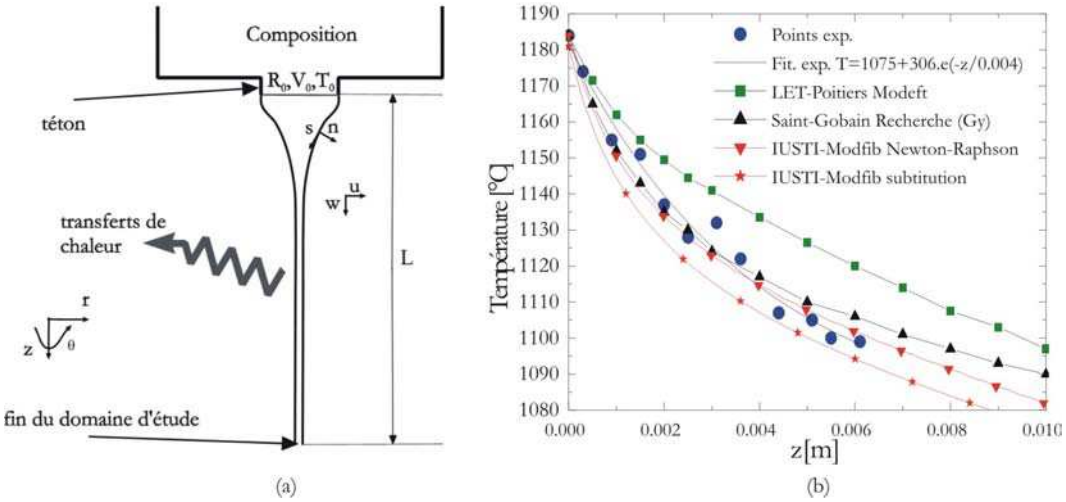

Figure 47 Etude de la stabilité d'un procédé de fibrage du verre: a) géométrie du modèle hydrodynamique de l'écoulement de verre, b) Comparaison du profil de température du jet de verre : points expérimentaux et résultats numériques

- Des études de stabilité sur une filière mono téton. La Figure 46 présente un schéma de principe et des photographies du dispositif expérimental mis en oeuvre. Il se compose d'un four à induction à haute température et d'une armoire de commande (prêtés par Saint-Gobain Vetrotex), d'un bobinoir muni d'un dispositif de chariotage, d'une mesure de température de fibrage par pyrométrie optique, d'un système d'imagerie du jet de verre en sortie de four (bulbe), de l'interféromètre et du diffractomètre. Ces systèmes de mesure et de contrôle sont synchronisés entre eux.

Cette expérience a permis de montrer que la stabilité du procédé est maximale pour des températures de fibrage de $T_0 = 1145-1175°C$ et des fibres dont le diamètre est inférieur à $D \approx 15\mu m$. Cependant, même dans ces conditions, le diamètre de la fibre produite fluctue périodiquement avec une amplitude moyenne de l'ordre de $\sigma_D / \bar{D} \approx 1.8\%$ (avec $d\sigma_D / dt \approx 1.9\mu m/s$ et $d\sigma_D / dL \approx 0.07\mu m/m$, pour $V_f = 20m/s$), voir la Figure 48 a). La fréquence des oscillations du diamètre croît avec la température de fibrage: $\nu_{osc.} \approx 0.5 \rightarrow 0.9Hz$ pour $T_0 = 1145-1250°C$.

Selon Pearson et al [94], ces oscillations résulteraient du développement d'instabilités inertielles le long du jet. Si l'on positionne nos points expérimentaux dans le diagramme de stabilité[25] construit par ces auteurs, Figure 48 b), on constate que nos points expérimentaux sont effectivement positionnés dans la région stable de ce diagramme. De plus, les points qui correspondent à une stabilité maximale sont bien ceux qui sont les plus éloignés de la ligne de transition *instable* → *stable*.

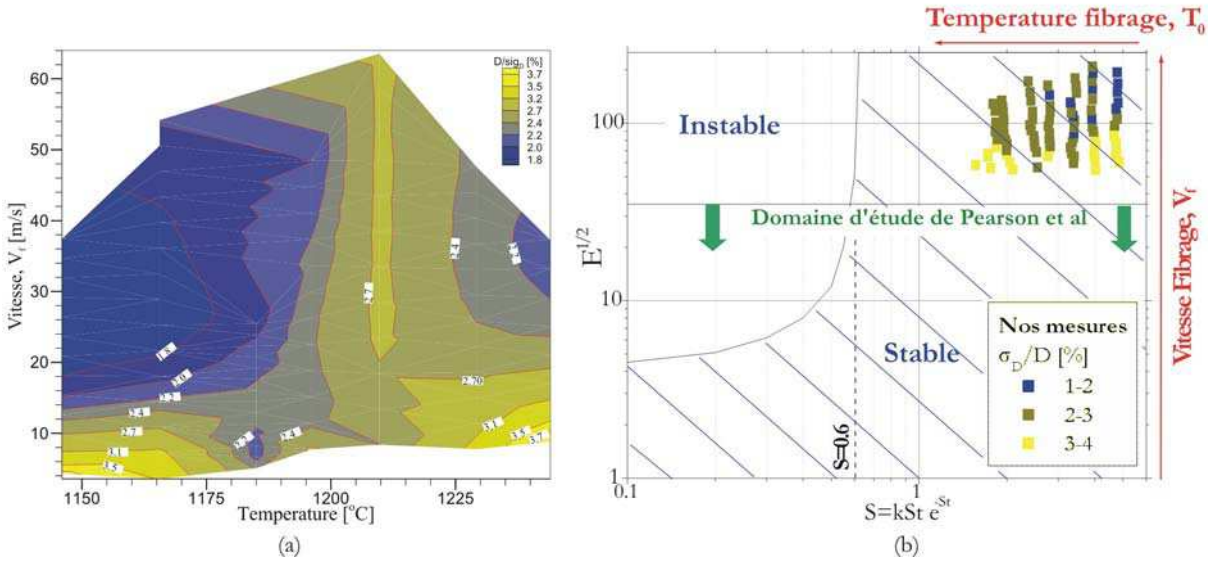

Figure 48 a) Carte expérimentale du taux de stabilité du diamètre de la fibre en fonction de la température et de la vitesse de fibrage et b) Positions de nos points expérimentaux dans le diagramme de Stabilité de Pearson.

Au terme cette étude (§8.4.2), l'interféromètre a été cédé à Saint-Gobain Vetrotex. Le groupe Saint-Gobain dispose désormais des données expérimentales, des moyens numériques et techniques, nécessaires à l'optimisation de ce procédé de fibrage. Pour plus de détails sur ces travaux, le lecteur est invité à consulter le manuscrit de thèse d'Anne Lenoble [4].

[25] Ce diagramme découle d'une analyse linéaire de stabilité des équations de bilan du procédé (dont la loi de viscosité a été fortement simplifiée). Un paramètre de stabilité S est défini. Lorsque ce dernier est S>0.6, l'amplitude des fluctuations du diamètre du jet augmente en se propageant le long du jet. Pour S<0.6, elles sont rapidement atténuées. En fait, S est un paramètre assez complexe, qui dépend *notamment* du nombre de Stanton (St) et du rapport de la vitesse de fibrage et de la vitesse débitante du jet, E.

4.3.4 Caractérisation de fibres optiques et de gradients thermiques en micro fluidique

Fibres optiques

Les fibres optiques sont utilisées dans de nombreuses applications de haute technologie. Leur procédé de fabrication est assez similaire à celui des fibres de renfort (§4.3.3). Il se distingue cependant de ce dernier par la qualité et le nombre des contrôles nécessaires à la production de fibres *de qualité optique*. Ces fibres sont généralement dotées d'un cœur en silice, enrobé d'une matrice polymère, « le cladding », puis d'une gaine de protection. Le cœur de silice, dans lequel se propage la lumière, est d'indice homogène ou, mieux encore, à gradient radial d'indice. Le diamètre du coeur, tout comme son indice de réfraction ou celui du cladding, influencent fortement les propriétés de transmission des fibres optiques. En cours de production, il faut donc pouvoir contrôler avec précision ces paramètres.

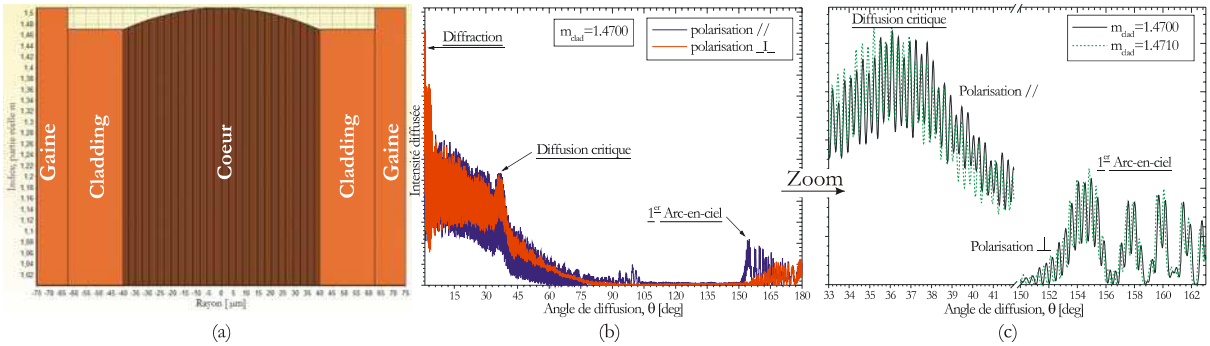

(a) (b) (c)

Figure 49 Simulation des propriétés de diffusion d'une fibres optique multimode : a) Profil d'indice simulé ; b) Diagrammes complets pour un cladding d'indice m=1.4700 ; c) Zoom sur les diagrammes dans la région de la diffusion critique et de l'arc-en-ciel, pour deux valeurs de l'indice du cladding.

Dans le cadre d'une étude contractuelle avec la société CERSA MCI (§ 8.4.2), j'ai conçu un logiciel de simulation des propriétés de diffusion de différentes fibres optiques, voir la Figure 58. Mon expertise dans le domaine de la diffusion de la lumière et de la caractérisation optique de particules, a permis d'éclaircir un certains nombres de points. A terme, cette étude, toujours en cours, devrait contribuer au développement d'un capteur optique intégré.

A titre d'exemple, la Figure 49 présente une simulation des diagrammes de diffusion d'une fibre optique multimode, pour deux valeurs de l'indice de réfraction du cladding. Le profil d'indice simulé est donné par la Figure 49 a). La Figure 49 b) et la Figure 49 c) montrent très clairement que cette variation d'indice induit un déphasage, ou une variation de fréquence, de la structure d'ondulation de la diffusion critique et du premier arc-en-ciel. Expérimentalement, on peut donc espérer détecter cette variation de propriété du cladding, à partir de l'analyse de ces déphasages.

Gradients thermiques en micro fluidique

La «miro fluidique» est un domaine en plein essor. Dans le cadre d'une collaboration avec David Brutin (IUSTI), nous réalisons actuellement une expérience dont le but est : de valider[26] le modèle de diffusion par un cylindre multicouche (§ 2.1) et de caractériser les flux de chaleur pariétaux dans des micro écoulements. L'écoulement est constitué par un fluide chaud (dodécane) qui s'écoule à l'intérieur d'un ca-

[26] Même si nous sommes confiants dans la validité de notre modèle et de nos codes… le manque de données expérimentales reste problématique pour la communauté (§ 2.1.3).

pillaire en verre, de petite section (rayon interne : R_1=10-150µm). Dans cette configuration, on s'attend ainsi à ce que la convection naturelle sur la face externe du capillaire induise des gradients thermiques radiaux dans le fluide et le verre, un refroidissement du fluide.

Des simulations hydrodynamiques réalisées avec Fluent montrent que les gradients radiaux sont faibles, voir la Figure 50 a). Cependant, les simulations électromagnétiques montrent que ceux-ci sont suffisants pour entraîner une modification de la structure du premier arc-en-ciel, voir la Figure 50 b).

A terme, nous espérons pouvoir déduire, de l'analyse de signaux d'arc-en-ciel expérimentaux, la forme des profils de température et donc, les flux thermiques.

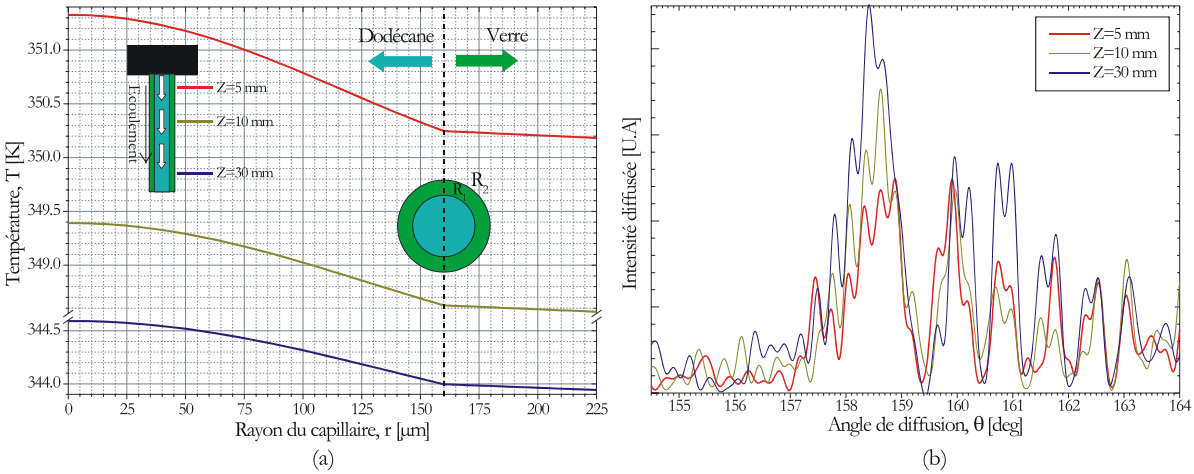

Figure 50 a) Simulation du profil de température d'un capillaire pour différentes distances au point d'injection du liquide chaud ; b) Simulations des diagrammes d'arc-en-ciel correspondants.

4.4 Fluidisation gaz-solides

Le procédé de fluidisation permet une accélération et le contrôle facilité d'un certain nombre de processus d'échange de chaleur et de masse, de réactions physico-chimiques [95-97]. De ce fait, les réacteurs à lit fluidisé, ou lit fluidisé circulant, sont largement répandus dans l'industrie.

Depuis plusieurs années maintenant, l'IUSTI développe, en partenariat avec différents industriels (EDF, CNIM, BP…), des études expérimentales sur l'hydrodynamique des écoulements en Lit Fluidisé Circulant (LFC) [98, 99], de même que des modélisations Eulérienne-Lagrangienne de ces écoulements [100]. Ma contribution à cette thématique de recherche est essentiellement expérimentale.

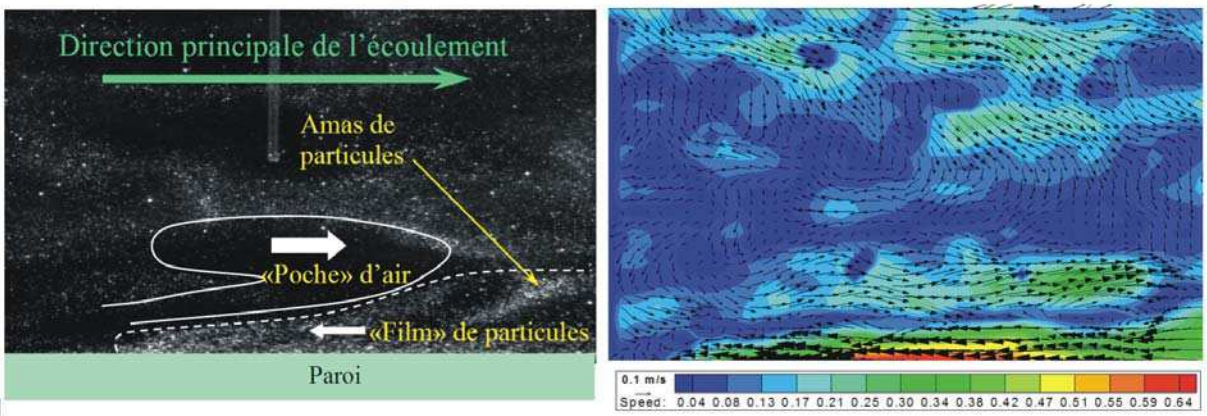

Figure 51 Image tomographique de la distribution des solides dans une colonne de fluidisation et champ de vitesse instantanée obtenu par PIV.

4.4.1 Champs dynamiques obtenus vélocimétrie par images de particules (PIV)

Les écoulements LFC sont très turbulents. L'écart type de la vitesse de la phase dispersée est pratiquement toujours supérieure à sa valeur moyenne, $\sigma_V / \overline{V} > 100\%$, voir la vignette de la page 96. Cependant, dans la partie diluée de l'écoulement, on peut observer quelques structures de faible cohérence spatiale et temporelle : amas et films de particules, poches d'air (bulles), tourbillons,… Ces hétérogénéités dans la distribution des solides font l'objet de nombreuses études car elles influencent les mécanismes réactifs (combustion, réduction des polluants) et de transfert (espèces, thermiques)[97]. Par ailleurs, les codes de calcul Eulérien-Eulérien ont par beaucoup de mal à rendre compte de l'existence de phénomènes méso échelle[27], ce qui est problématique du point de vue fondamental mais aussi industriel.

Il est impossible de décrire correctement ces structures spatio-temporelles à partir de données strictement ponctuelles (Anémométrie Phase Doppler [99]). Pour remédier à ce problème, lors de ma première année à l'IUSTI, j'ai développé un système complet de Vélocimétrie par Images de Particules (PIV). Ce système permet d'obtenir de 25 à 180 champs de vitesse par seconde [A14, C14, C19]. Il utilise aussi bien un laser continu qu'un laser YAG double impulsion et différents types de caméras vidéo. Un logiciel d'acquisition et de traitement des images PIV [55] a également été conçu, voir la Figure 60 et le paragraphe § 4.3.1.

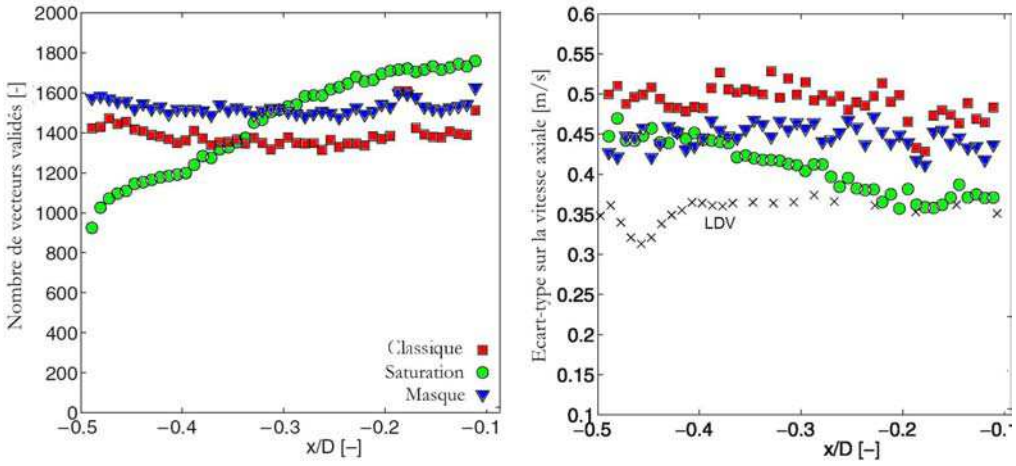

Figure 52 Comparaison des taux de validation des vecteurs vitesse et des profils de fluctuation de la vitesse axiale. x est la distance à la paroi avec D=100 mm.

Les variations spatiales de la fraction volumique en particules sont très importantes dans les écoulements LFC et ceci, même dans la zone diluée. Dans le cadre du stage doctoral de Claus Ibsen (§ 8.3.1), nous avons développé une méthode originale qui limite les effets de ces variations de concentration sur les mesures PIV [A14]. Celle-ci repose sur la création de masques dont la densité optique varie spatialement de manière inverse à la distribution d'intensité des images tomographiques (PIV). En intercalant un de ces masques entre l'écoulement et l'objectif de la caméra, le taux de validation s'en trouve considérablement amélioré, de même que les statistiques sur les vitesses. A titre indicatif, la Figure 52 compare les taux de validation des vecteurs vitesses et les profils de fluctuation de la vitesse axiale dans un LFC, lorsque l'on utilise, ou non, un masque optique. Avec cette méthode le taux de validation des vecteurs vitesses augmente de près de 10% et il devient pratiquement constant sur tout le profil (avec un système PIV classique, le taux de validation varie de près de 50%). L'écart type de la vitesse axiale semble également plus

[27] Quelques millimètres à quelques dizaines de centimètres

proche de celui obtenu avec un système LDV, bien qu'un écart perciste (ce qui n'est pas le cas pour la vitesse moyenne [A14]). On peut attribuer cette différence à la taille des mailles de calcul utilisées et au nombre d'échantillons limités (au plus ≈ 1600).

La Figure 51 présente un exemple de champ de la vitesse instantanée, obtenu dans la zone diluée de la colonne de fluidisation de $2m \times 0.2m \times 0.2m$ de l'IUSTI [98]. On observe différentes structures cohérentes : amas de particules (billes de verre, $D = 60 \pm 10\mu m$) et poches d'air, la présence d'un film de particules en chute rapide près de la paroi [C14]... L'analyse des tomographies laser (distribution spatiale des solides) et des champs de vitesse associés, permet de caractériser spatialement ces structures.

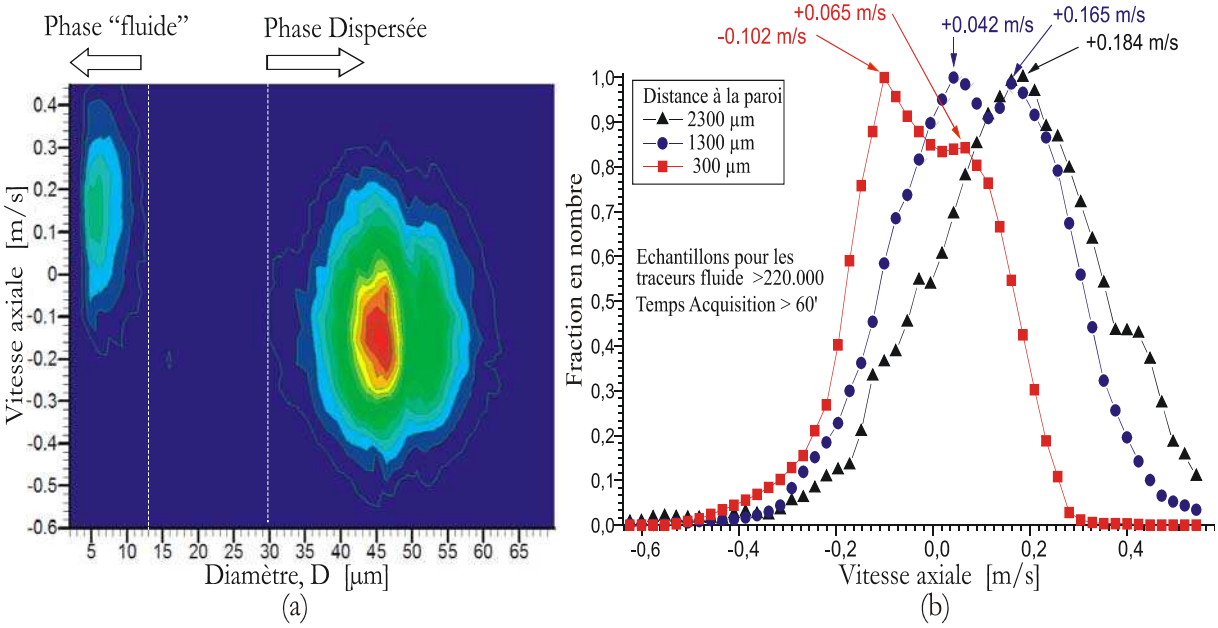

Figure 53 Mesure de la vitesse de glissement dans un LFC : a) Exemple de corrélation taille-vitesse obtenue par anémométrie phase Doppler ; b) Distributions de la vitesse des traceurs du fluide pour trois distances à la paroi (dans le film de particules).

4.4.2 Vitesse de glissement et vitesse eulérienne

La différence locale de vitesse entre la phase dispersée et la phase fluide est un paramètre fondamental des écoulements diphasiques et multiphasiques. Malheureusement, la mesure de cette « vitesse de glissement » n'est pas aisée. Cette mesure nécessite d'ensemencer le gaz en microparticules qui suivent parfaitement les différentes échelles de la turbulence du fluide [101] (§ 8.3.2). Or, dans les écoulements LFC, du fait de la zone dense, des nombreuses parois et des problèmes d'électricité statique, on ne peut pas utiliser les traceurs classiques (gouttelettes d'eau, d'huile, oxydes métalliques…). Une autre difficulté réside dans le fait que le système de mesure (optique) doit pouvoir détecter de manière simultanée les traceurs du fluide et la phase dispersée (voir à ce sujet le paragraphe § 4.2.2).

Pour palier à ces problèmes, nous avons développé un protocole expérimental utilisant un ensemencement du fluide en microballons de très faible densité (60 kg/m³) et en microbilles de verre [101]. La caractérisation simultanée de la dynamique locale des deux phases est obtenue avec un système phase Doppler.

La Figure 53 a) présente, à titre d'exemple, une corrélation taille-vitesse mesurée près d'une paroi de la colonne de fluidisation de $2m \times 0.2m \times 0.2m$. Les deux phases sont séparées par leur diamètre. On peut donc calculer la vitesse de glissement ou la distribution de la vitesse axiale du fluide (voir la Figure 53 b). Cette dernière figure montre que la distribution de la vitesse axiale du fluide devient bimodale à mesure que l'on s'approche de la paroi. On peut penser que la nature intermittente du film de particules est à l'origine de ce phénomène, voir la Figure 54. En effet, il existe au moins deux vitesses limites pour le fluide : la première, positive à nulle en moyenne, correspond à sa vitesse en l'absence du film de particules (écoulement dilué & condition de glissement nul); la seconde, négative en moyenne, correspond à sa vitesse lorsqu'il est entraîné par le film de particules (écoulement dense, traînée).

Dans le cadre d'une collaboration avec l'université de Chalmers, et du stage doctoral de Tobias Bergenblock (§ 8.3.1), nous avons montré que les vitesses moyennes obtenues avec un système phase Doppler sont sujettes à un biais statistique du fait de la nature dispersée de la phase solide et de l'échantillonnage aléatoire du système de mesure. Cependant, ce biais peut être en partie éliminé en post traitant les données brutes. En effet, en pondérant la vitesse instantanée des amas de particules, par leur masse, ont peut calculer une vitesse moyenne de la phase dispersée qui correspond mieux à celle restituée par les modèles Eulériens [C41, A21].

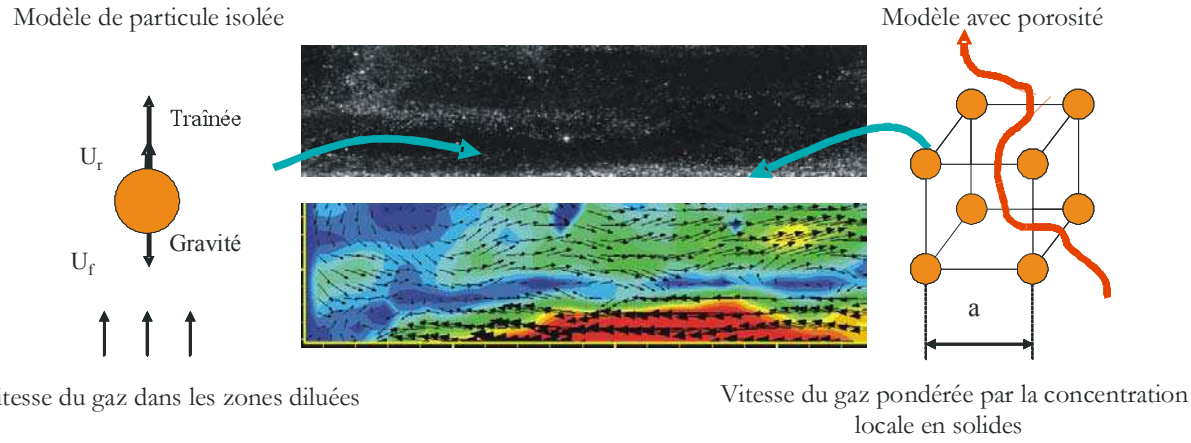

Figure 54 Les champs PIV permettent d'interpréter l'aspect bimodal des distributions de vitesse du fluide près de la paroi : il provient vraisemblablement de la nature intermittente du film de particules.

4.4.3 Plateforme de fluidisation

En 2000, nous avons démarré la construction d'une plate-forme de fluidisation (§ 8.4.2). Je suis co-responsable scientifique du projet avec Lounès Tadrist, mais d'autres chercheurs participent de manière active à ce projet et notamment : Christophe Sierra, René Ocelli, Robert Santini et Ouamar Rahli. Cette plateforme dispose de différents moyens de calcul (calculateurs parallèles) et moyens expérimentaux : pilote atmosphérique de grandes dimensions (colonne de $5m \times 0.5m \times 0.5m$, voir la Figure 55), un pilote sous pression (15 bars, colonne de $1m \times 0.1m \times 0.1m$), différents systèmes de diagnostics optiques et de traitement des poudres.

Cette plateforme constitue un outil unique au niveau national. Elle doit nous permettre d'étudier, entre autres choses, les facteurs d'échelles et les effets de la pression sur la fluidisation, de développer des partenariats industriels.

Figure 55 Photographies du pilote LFC atmosphérique de la plate-forme de fluidisation développée à l'IUSTI.

Chapitre 5

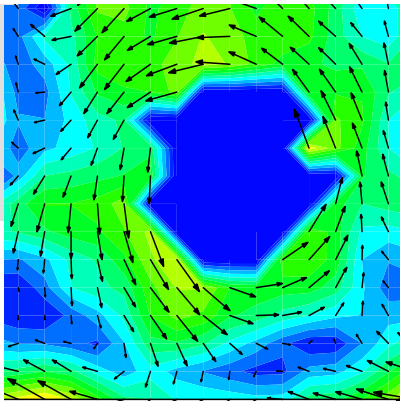

ANNEXE

5.1 Cylindre Multicouche

5.1.1 Expressions des champs TE

Pour le cas d'un champ électrique incident orienté perpendicularité à l'axe z, onde Transversale Electrique (TE), on procède de manière identique au cas d'une onde incidente TM (voir le paragraphe §2.1.2) :

- Champ incident sur la surface externe :

$$\begin{aligned}\mathbf{E}_{TE}^{i} &= -i\sum_{n=-\infty}^{\infty} E_n \mathbf{M}_n^{(1)} \\ \mathbf{H}_{TE}^{i} &= \frac{k_{ext}}{\omega\mu_{ext}}\sum_{n=-\infty}^{\infty} E_n \mathbf{N}_n^{(1)}\end{aligned} \tag{5.1}$$

Soit à la surface de la particule et en remplaçant par les composantes des harmoniques cylindriques :

$$\begin{aligned}E_z^i\left(m_{ext}x_L\right) &= H_\varphi^i\left(m_{ext}x_L\right) = 0 \\ H_z^i\left(m_{ext}x_L\right) &= \frac{\left(k_{ext}\right)^2}{\omega\mu_{ext}}\sum_{n=-\infty}^{\infty} E_n J_n\left(m_{ext}x_L\right) \\ E_\varphi^i\left(m_{ext}x_L\right) &= ik_{ext}\sum_{n=-\infty}^{\infty} E_n J_n'\left(m_{ext}x_L\right)\end{aligned} \tag{5.2}$$

- Champs diffusés:

$$\begin{aligned}\mathbf{E}_{TE}^{s} &= i\sum_{n=-\infty}^{\infty} E_n a_{nII} \mathbf{M}_n^{(3)} \\ \mathbf{H}_{TE}^{s} &= -\frac{k_{ext}}{\omega\mu_{ext}}\sum_{n=-\infty}^{\infty} E_n a_{nII} \mathbf{N}_n^{(3)}\end{aligned} \tag{5.3}$$

Soit à la surface de la particule et en remplaçant par les composantes des harmoniques cylindriques :

$$\begin{aligned}E_z^s &= H_\varphi^s = 0 \\ H_z^s &= -\frac{\left(k_{ext}\right)^2}{\omega\mu_{ext}}\sum_{n=-\infty}^{\infty} E_n a_{nII} H_n^{(1)}\left(m_{ext}x_L\right) \\ E_\varphi^s &= -ik_{ext}\sum_{n=-\infty}^{\infty} E_n a_{nII} H_n^{(1)'}\left(m_{ext}x_L\right)\end{aligned} \tag{5.4}$$

- Champs internes :

$$\begin{aligned}\mathbf{E}_{TM}^{(j)} &= \sum_{n=-\infty}^{\infty} E_n \left[d_n^{(j)} \mathbf{M}_n^{(1)} - f_n^{(j)} \mathbf{M}_n^{(2)} \right] \\ \mathbf{H}_{TM}^{(j)} &= \frac{ik_{ext}}{\omega \mu_{ext}} \sum_{n=-\infty}^{\infty} E_n \left[d_n^{(j)} \mathbf{N}_n^{(1)} - f_n^{(j)} \mathbf{N}_n^{(2)} \right]\end{aligned} \tag{5.5}$$

La condition de « dimension finie » des champs impose pour la première couche : $f_n^{(1)} = 0$.
Soit pour les champs internes à la couche j et en remplaçant par les composantes des harmoniques cylindriques :

$$\begin{aligned}E_{n,z}^{(j)} &= H_{n,\varphi}^{(j)} = 0 \\ \mathrm{H}_{n,z}^{(j)} &= \frac{k_j}{\omega \mu_j} \sum_{n=-\infty}^{\infty} E_n \left[d_n^{(j)} J_n\left(m_j x_j\right) - f_n^{(j)} Y_n\left(m_j x_j\right) \right] \\ E_{n,\varphi}^{(j)} &= k_j \sum_{n=-\infty}^{\infty} E_n \left[d_n^{(j)} J_n^{'}\left(m_j x_j\right) - f_n^{(j)} Y_n^{'}\left(m_j x_j\right) \right]\end{aligned} \tag{5.6}$$

Avec pour la dernière couche :

$$\begin{aligned}E_{n,z}^{(L)} &= H_{n,\varphi}^{(L)} = 0 \\ \mathrm{H}_{n,z}^{(L)} &= \frac{\left(k_L\right)^2}{\omega \mu_L} \sum_{n=-\infty}^{\infty} E_n \left[d_n^{(L)} J_n\left(m_L x_L\right) - f_n^{(L)} Y_n\left(m_L x_L\right) \right] \\ E_{n,\varphi}^{(L)} &= ik_L \sum_{n=-\infty}^{\infty} E_n \left[d_n^{(L)} J_n^{'}\left(m_L x_L\right) - f_n^{(L)} Y_n^{'}\left(m_L x_L\right) \right]\end{aligned} \tag{5.7}$$

-Coefficients de diffusion externe TE :
Les conditions de continuité entre la surface j-1 et j permettent d'introduire le quotient des coefficients de diffusion interne (avec $A_n^{(1)} = 0$) :

$$\mathrm{A}_n^{(j)} = \frac{f_n^{(j)}}{d_n^{(j)}} \tag{5.8}$$

et la fonction ou le « quotient intermédiaire » $H_{a,n}^{(j)}$:

$$H_{a,n}^{(j)} = \frac{J_n^{'}\left(m_j x_j\right) - A_n^{(j)} Y_n^{'}\left(m_j x_j\right)}{J_n\left(m_j x_j\right) - A_n^{(j)} Y_n\left(m_j x_j\right)} \tag{5.9}$$

On obtient ainsi la forme récurrente de $A_n^{(j)}$:

$$A_n^{(j)} = \frac{m_j \mu_{j-1} J_n\left(m_j x_{j-1}\right) H_{a,n}^{(j-1)} - m_{j-1} \mu_j J_n^{'}\left(m_j x_{j-1}\right)}{m_j \mu_{j-1} Y_n\left(m_j x_{j-1}\right) H_{a,n}^{(j-1)} - m_{j-1} \mu_j Y_n^{'}\left(m_j x_{j-1}\right)} \tag{5.10}$$

Au final, on obtient l'expression du coefficient de diffusion externe pour une onde TE, a_{nII} :

$$a_{nII} = \frac{m_{ext} \mu_L J_n\left(m_{ext} x_L\right) H_{a,n}^{L}\left(m_L x_L\right) - m_L \mu_{ext} J_n^{'}\left(m_{ext} x_L\right)}{m_{ext} \mu_L H_n^{(1)}\left(m_{ext} x_L\right) H_{a,n}^{L}\left(m_L x_L\right) - m_L \mu_{ext} H_n^{(1)'}\left(m_{ext} x_L\right)} \tag{5.11}$$

5.1.2 Reformulations analytiques

Reformulation analytique n°1

Nous introduisons les trois dérivées logarithmiques suivantes (voir le paragraphe §2.1.2):

$$D_n^{(1)}(\rho) = \frac{J_n^{'}(\rho)}{J_n(\rho)}, \quad D_n^{(2)}(\rho) = \frac{Y_n^{'}(\rho)}{Y_n(\rho)}, \quad D_n^{(3)}(\rho) = \frac{H_n^{(1)'}(\rho)}{H_n^{(1)}(\rho)} \tag{5.12}$$

Ainsi que les deux nouveaux rapports de fonctions de Bessel suivants :

$$D_n^{(0)}(\rho)=\frac{J_n(\rho)}{H_n^{(1)}(\rho)},\quad D_n^{(x)}(\rho)=\frac{J_n(\rho)}{Y_n(\rho)} \tag{5.13}$$

- On cherche à présent à faire apparaître ces dérivées et ces rapports dans les équations précédentes. Pour les champs TM par exemple, on peut reformuler l'Eq. (2.24):

$$B_n^{(j)}=\frac{J_n\left(m_j x_{j-1}\right)}{Y_n\left(m_j x_{j-1}\right)}\frac{m_{j-1}\mu_j H_{b,n}^{(j-1)}-m_j\mu_{j-1}\dfrac{J_n^{'}\left(m_j x_{j-1}\right)}{J_n\left(m_j x_{j-1}\right)}}{m_{j-1}\mu_j H_{b,n}^{(j-1)}-m_j\mu_{j-1}\dfrac{Y_n^{'}\left(m_j x_{j-1}\right)}{Y_n\left(m_j x_{j-1}\right)}} \tag{5.14}$$

Ce qui peut se récrire sous la forme :

$$B_n^{(j)}=D_n^{(x)}\left(m_j x_{j-1}\right)\frac{m_{j-1}\mu_j H_{b,n}^{(j-1)}-m_j\mu_{j-1}D_n^{(1)}\left(m_j x_{j-1}\right)}{m_{j-1}\mu_j H_{b,n}^{(j-1)}-m_j\mu_{j-1}D_n^{(2)}\left(m_j x_{j-1}\right)} \tag{5.15}$$

En procédant de même pour $A_n^{(j)}$ on obtient:

$$A_n^{(j)}=D_n^{(x)}\left(m_j x_{j-1}\right)\frac{m_j\mu_{j-1}H_{a,n}^{(j-1)}-m_{j-1}\mu_j D_n^{(1)}\left(m_j x_{j-1}\right)}{m_j\mu_{j-1}H_{a,n}^{(j-1)}-m_{j-1}\mu_j D_n^{(2)}\left(m_j x_{j-1}\right)} \tag{5.16}$$

- Pour le rapport $H_{b,n}^{(j)}$, nous partons de la forme brute :

$$H_{b,n}^{(j)}=\frac{J_n^{'}\left(m_j x_j\right)-B_n^{(j)}Y_n^{'}\left(m_j x_j\right)}{J_n\left(m_j x_j\right)-B_n^{(j)}Y_n\left(m_j x_j\right)} \tag{5.17}$$

On cherche à faire apparaître les dérivées (5.12) et les rapports (5.13):

$$H_{b,n}^{(j)}=\frac{J_n^{'}\left(m_j x_j\right)}{J_n\left(m_j x_j\right)-B_n^{(j)}Y_n\left(m_j x_j\right)}-\frac{B_n^{(j)}Y_n^{'}\left(m_j x_j\right)}{J_n\left(m_j x_j\right)-B_n^{(j)}Y_n\left(m_j x_j\right)} \tag{5.18}$$

$$H_{b,n}^{(j)}=\frac{J_n\left(m_j x_j\right)}{Y_n\left(m_j x_j\right)}\frac{\dfrac{J_n^{'}\left(m_j x_j\right)}{J_n\left(m_j x_j\right)}}{\dfrac{J_n\left(m_j x_j\right)}{Y_n\left(m_j x_j\right)}-B_n^{(j)}}-\frac{B_n^{(j)}\dfrac{Y_n^{'}\left(m_j x_j\right)}{Y_n\left(m_j x_j\right)}}{\dfrac{J_n\left(m_j x_j\right)}{Y_n\left(m_j x_j\right)}-B_n^{(j)}} \tag{5.19}$$

Au final on obtient pour les deux coefficients :

$$H_{b,n}^{(j)}=D_n^{(x)}\left(m_j x_j\right)\frac{D_n^{(1)}\left(m_j x_j\right)}{D_n^{(x)}\left(m_j x_j\right)-B_n^{(j)}}-\frac{D_n^{(2)}\left(m_j x_j\right)B_n^{(j)}}{D_n^{(x)}\left(m_j x_j\right)-B_n^{(j)}} \tag{5.20}$$

$$H_{a,n}^{(j)}=D_n^{(x)}\left(m_j x_j\right)\frac{D_n^{(1)}\left(m_j x_j\right)}{D_n^{(x)}\left(m_j x_j\right)-A_n^{(j)}}-\frac{D_n^{(2)}\left(m_j x_j\right)A_n^{(j)}}{D_n^{(x)}\left(m_j x_j\right)-A_n^{(j)}} \tag{5.21}$$

En procédant de même avec l'expression du coefficient de diffusion externe donnée par l'Eq. (2.30), on obtient :

$$b_{nI}=\frac{J_n\left(m_{ext}x_L\right)}{H_n^{(1)}\left(m_{ext}x_L\right)}\frac{m_L\mu_L H_{b,n}^{(L)}-m_{ext}\mu_{ext}\dfrac{J_n^{'}\left(m_{ext}x_L\right)}{J_n\left(m_{ext}x_L\right)}}{m_L\mu_L H_{b,n}^{(L)}-m_{ext}\mu_{ext}\dfrac{H_n^{(1)'}\left(m_{ext}x_L\right)}{H_n^{(1)}\left(m_{ext}x_L\right)}} \tag{5.22}$$

Soit au final :

$$a_{nII}=D_n^{(0)}\left(m_{ext}x_L\right)\frac{m_{ext}\mu_L H_{b,n}^{(L)}-m_L\mu_{ext}D_n^{(1)}\left(m_{ext}x_L\right)}{m_{ext}\mu_L H_{b,n}^{(L)}-m_L\mu_{ext}D_n^{(3)}\left(m_{ext}x_L\right)} \tag{5.23}$$

$$b_{nI} = D_n^{(0)}\left(m_{ext}x_L\right)\frac{m_L\mu_{ext}H_{b,n}^{(L)} - m_{ext}\mu_L D_n^{(1)}\left(m_{ext}x_L\right)}{m_L\mu_{ext}H_{b,n}^{(L)} - m_{ext}\mu_L D_n^{(3)}\left(m_{ext}x_L\right)} \tag{5.24}$$

Cette formulation est *formellement* identique à celle obtenue pour la sphère multicouches [2,3] en faisant les correspondances données par l'Eq. (2.38) avec $\mu_j = 1, j = 1\ldots L+1$ et $m_{ext} = 1$. .

L'implémentation de ces récurrences a mis en évidence une instabilité du calcul du rapport $D_n^{(x)}$ et ceci, même pour des particules de faible diamètre et quelques dizaines de couches. Dans le paragraphe suivant, nous reformulons les équations précédentes en transposant la modification introduite par Wu et al. [102] pour une sphère multicouches.

Reformulation analytique n°2 :

L'instabilité du calcul de $D_n^{(x)}$ peut être éliminée en calculant le rapport de cette fonction pour deux arguments très proches. On essaie donc de faire apparaître, dans les expressions précédentes, un rapport de fonctions $D_n^{(x)}$:

$$H_{b,n}^{(j)} = \frac{\dfrac{J_n'\left(m_jx_j\right)}{J_n\left(m_jx_j\right)} - B_n^{(j)}\dfrac{Y_n'\left(m_jx_j\right)}{J_n\left(m_jx_j\right)}}{1 - B_n^{(j)}\dfrac{Y_n\left(m_jx_j\right)}{J_n\left(m\ x_j\right)}} \tag{5.25}$$

On introduit le changement de variable :

$$\beta_n^{(j)} = B_n^{(j)}\frac{Y_n\left(m_jx_j\right)}{J_n\left(m_jx_j\right)} \tag{5.26}$$

En appliquant ce changement de variable à l'équation (5.25) on obtient :

$$H_{b,n}^{(j)} = \frac{\dfrac{J_n'\left(m_jx_j\right)}{J_n\left(m_jx_j\right)} - \beta_n^{(j)}\dfrac{J_n\left(m_jx_j\right)}{Y_n\left(m_jx_j\right)}\dfrac{Y_n'\left(m_jx_j\right)}{J_n\left(m_jx_j\right)}}{1 - \beta_n^{(j-1)}} \tag{5.27}$$

et au final :

$$H_{b,n}^{(j)} = \frac{D_n^{(1)}\left(m_jx_j\right) - \beta_n^{(j)}D_n^{(2)}\left(m_jx_j\right)}{1 - \beta_n^{(j)}} \tag{5.28}$$

Dans cette équation, le rapport $D_n^{(x)}$ a été éliminé implicitement. On opère de même pour la fonction $\beta_n^{(j)}$:

$$\beta_n^{(j)} = \frac{Y_n\left(m_jx_j\right)}{J_n\left(m_jx_j\right)}\frac{J_n\left(m_jx_{j-1}\right)}{Y_n\left(m_jx_{j-1}\right)}\frac{m_{j-1}\mu_jH_{b,n}^{(j-1)} - m_j\mu_{j-1}\dfrac{J_n'\left(m_jx_{j-1}\right)}{J_n\left(m_jx_{j-1}\right)}}{m_{j-1}\mu_jH_{b,n}^{(j-1)} - m_j\mu_{j-1}\dfrac{Y_n'\left(m_jx_{j-1}\right)}{Y_n\left(m_jx_{j-1}\right)}} \tag{5.29}$$

On introduit alors le rapport de deux fonctions $D_n^{(x)}$ à travers la nouvelle fonction $R_n^{(j)}$:

$$R_n^{(j)} = \frac{Y_n\left(m_jx_j\right)}{J_n\left(m_jx_j\right)}\frac{J_n\left(m_jx_{j-1}\right)}{Y_n\left(m_jx_{j-1}\right)} = \frac{D_n^{(x)}\left(m_jx_{j-1}\right)}{D_n^{(x)}\left(m_jx_j\right)} \tag{5.30}$$

Au final on obtient :

$$\beta_n^{(j)} = R_n^{(j)}\frac{m_{j-1}\mu_jH_{b,n}^{(j-1)} - m_j\mu_{j-1}D_n^{(1)}\left(m_jx_{j-1}\right)}{m_{j-1}\mu_jH_{b,n}^{(j-1)} - m_j\mu_{j-1}D_n^{(2)}\left(m_jx_{j-1}\right)} \tag{5.31}$$

$$H_{a,n}^{(j)} = \frac{D_n^{(1)}\left(m_jx_j\right) - \alpha_n^{(j)}D_n^{(2)}\left(m_jx_j\right)}{1 - \alpha_n^{(j)}} \tag{5.32}$$

$$\alpha_n^{(j)} = R_n^{(j)} \frac{m_j \mu_{j-1} H_{a,n}^{(j-1)} - m_{j-1} \mu_j D_n^{(1)}\left(m_j x_{j-1}\right)}{m_j \mu_{j-1} H_{a,n}^{(j-1)} - m_{j-1} \mu_j D_n^{(2)}\left(m_j x_{j-1}\right)} \tag{5.33}$$

5.1.3 Calculs des dérivées logarithmiques et rapports

Dérivée : $D_n^{(1)}$

Cette dérivée est calculée par récurrence descendante à partir de la relation suivante :

$$D_n^{(1)}(\rho) = \frac{n}{\rho} - \frac{1}{D_{n+1}^{(1)}(\rho) + \frac{n+1}{\rho}} \tag{5.34}$$

avec $n = n_{\max}, n_{\max} - 1 \ldots 0$. Pour la valeur initiale on pose : $D_{n=\max}^{(1)}(\rho) = 0 + 0i$, avec :

$$n_{\max} = Max\left(n_{stop}, \left|m_j x_j\right| + 15, j = 1 \ldots L\right) \tag{5.35}$$

L'argument ρ peut prendre les deux séries de valeurs suivantes :

$$\begin{aligned} &\rho = m_j x_{j-1}, \text{ j=2…L+1} \\ &\rho = m_j x_j, \quad \text{j=1…L} \end{aligned} \tag{5.36}$$

Dérivées : $D_n^{(2)}, D_n^{(3)}$

$D_n^{(2)}$ et $D_n^{(3)}$ sont calculées par récurrence ascendante à partir de la relation ($n = 0,1,\cdots n_{stop} - 1$):

$$D_{n+1}^{(p)}(\rho) = \frac{1}{n/\rho - D_n^{(p)}(\rho)} - \frac{n+1}{\rho} \tag{5.37}$$

Dans le cas de $D_n^{(2)}$ ces calculs sont effectués pour chaque couche $\left(\rho = m_j x_j\right)$ et avec comme valeur initiale :

$$D_0^{(2)}(\rho) = \frac{Y_0'(\rho)}{Y_0(\rho)} = \frac{-Y_1(\rho)}{Y_0(\rho)} \tag{5.38}$$

Dans le cas de $D_n^{(3)}$ ces calculs sont effectués uniquement pour l'interface externe $\left(\rho = m_{ext} x_L\right)$ et avec comme valeur initiale :

$$D_{n=0}^{(3)}\left(m_{ext} x_L\right) = \frac{H_0'^{(1)}\left(m_{ext} x_L\right)}{H_0\left(m_{ext} x_L\right)} = -\frac{J_1\left(m_{ext} x_L\right) + iY_1\left(m_{ext} x_L\right)}{J_0\left(m_{ext} x_L\right) + iY_0\left(m_{ext} x_L\right)} \tag{5.39}$$

En pratique, les fonctions de Bessel J_0, J_1, Y_0 et Y_1 sont calculées à l'aide des routines proposées la référence [74]. Des détails sur les relations de récurrence entre les fonctions de Bessel et leurs dérivées sont disponibles dans les références [2, 73] .

Rapport : $D_n^{(0)}$

Ce rapport de fonctions de Bessel peut être calculé à partir de la relation de récurrence ascendante :

$$D_{n+1}^{(0)}(\rho) = D_n^{(0)}(\rho) \frac{n/\rho - D_n^{(1)}(\rho)}{n/\rho - D_n^{(3)}(\rho)} \tag{5.40}$$

Il est calculé uniquement pour l'interface externe $\left(\rho = m_{ext} x_L\right)$ à partir de la valeur initiale :

$$D_{n=0}^{(0)}\left(m_{ext} x_L\right) = \frac{J_0\left(m_{ext} x_L\right)}{H_0^{(1)}\left(m_{ext} x_L\right)} = \frac{J_0\left(m_{ext} x_L\right)}{J_0\left(m_{ext} x_L\right) + iY_0\left(m_{ext} x_L\right)} \tag{5.41}$$

Rapport : $R_n^{(j)}$

En remplaçant les dérivées à l'ordre n+1 en fonction de leur valeur à l'ordre n, $R_n^{(j)}$ peut se calculer par récurrence ascendante avec $n = 1,\ldots n_{stop} - 1$ et $j = 2,3,\ldots,L$:

$$R_{n+1}^{(j)} = R_n^{(j)} \frac{\left[\frac{n}{m_j x_{j-1}} - D_n^{(1)}\left(m_j x_{j-1}\right)\right]\left[\frac{n}{m_j x_j} - D_n^{(2)}\left(m_j x_j\right)\right]}{\left[\frac{n}{m_j x_{j-1}} - D_n^{(2)}\left(m_j x_{j-1}\right)\right]\left[\frac{n}{m_j x_j} - D_n^{(1)}\left(m_j x_j\right)\right]} \tag{5.42}$$

Avec comme valeurs initiales ($n = 0$, $j = 2,3,\ldots,L$):

$$R_0^{(j)} = \frac{D_0^{(x)}\left(m_j x_{j-1}\right)}{D_{n=0}^{(x)}\left(m_j x_j\right)} = \frac{J_0\left(m_j x_{j-1}\right) Y_0\left(m_j x_j\right)}{Y_0\left(m_j x_{j-1}\right) J_0\left(m_j x_j\right)} \tag{5.43}$$

Récurrence

Toutes les dérivées logarithmiques et autres rapports des fonctions de Bessel cylindriques sont calculés au préalable. Les coefficients externes de diffusion peuvent alors être déterminés par récurrence ascendante :

- Etape n°1/ Couche n°1/Initialisation de la récurrence :

$$\alpha_n^{(1)} = \beta_n^{(1)} = 0.0 + i0.0 \tag{5.44}$$

$$H_{a,n}^{(1)} = H_{b,n}^{(1)} = D_n^{(1)}\left(m_1 x_1\right) \tag{5.45}$$

- Etape n°2/ Couche n°2:

$$\alpha_n^{(2)} = R_n^{(2)} \frac{m_2\mu_1 H_{a,n}^{(1)} - m_1\mu_2 D_n^{(1)}\left(m_2 x_1\right)}{m_2\mu_1 H_{a,n}^{(1)} - m_1\mu_2 D_n^{(2)}\left(m_2 x_1\right)} \qquad \beta_n^{(2)} = R_n^{(2)} \frac{m_1\mu_2 H_{b,n}^{(1)} - m_2\mu_1 D_n^{(1)}\left(m_2 x_1\right)}{m_1\mu_2 H_{b,n}^{(1)} - m_2\mu_1 D_n^{(2)}\left(m_2 x_1\right)} \tag{5.46}$$

$$H_{a,n}^{(2)} = \frac{D_n^{(1)}\left(m_2 x_2\right) - \alpha_n^{(2)} D_n^{(2)}\left(m_2 x_2\right)}{1 - \beta_n^{(2)}} \qquad H_{b,n}^{(2)} = \frac{D_n^{(1)}\left(m_2 x_2\right) - \beta_n^{(2)} D_n^{(2)}\left(m_2 x_2\right)}{1 - \beta_n^{(2)}} \tag{5.47}$$

…

- Etape n°j/ Couche n°j:

$$\alpha_n^{(j)} = R_n^{(j)} \frac{m_j\mu_{j-1} H_{a,n}^{j-1} - m_{j-1}\mu_j D_n^{(1)}\left(m_j x_{j-1}\right)}{m_j\mu_{j-1} H_{a,n}^{j-1} - m_{j-1}\mu_j D_n^{(2)}\left(m_j x_{j-1}\right)} \qquad \beta_n^{(j)} = R_n^{(j)} \frac{m_{j-1}\mu_j H_{b,n}^{j-1} - m_j\mu_{j-1} D_n^{(1)}\left(m_j x_{j-1}\right)}{m_{j-1}\mu_j H_{b,n}^{j-1} - m_j\mu_{j-1} D_n^{(2)}\left(m_j x_{j-1}\right)} \tag{5.48}$$

$$H_{a,n}^{j} = \frac{D_n^{(1)}\left(m_j x_j\right) - \alpha_n^{(j)} D_n^{(2)}\left(m_j x_j\right)}{1 - \alpha_n^{(j)}} \qquad H_{b,n}^{j} = \frac{D_n^{(1)}\left(m_j x_j\right) - \beta_n^{(j)} D_n^{(2)}\left(m_j x_j\right)}{1 - \beta_n^{(j)}} \tag{5.49}$$

…

- Dernière étape/ Etape n°L/ Couche n°L:

$$\alpha_n^{(L)} = R_n^{(j)} \frac{m_L\mu_{L-1} H_{a,n}^{L-1} - m_{L-1}\mu_L D_n^{(1)}\left(m_L x_{L-1}\right)}{m_L\mu_{L-1} H_{a,n}^{L-1} - m_{L-1}\mu_L D_n^{(2)}\left(m_L x_{L-1}\right)} \qquad \beta_n^{(L)} = R_n^{(j)} \frac{m_{L-1}\mu_L H_{b,n}^{L-1} - m_L\mu_{L-1} D_n^{(1)}\left(m_L x_{L-1}\right)}{m_{L-1}\mu_L H_{b,n}^{L-1} - m_L\mu_{L-1} D_n^{(2)}\left(m_L x_{L-1}\right)} \tag{5.50}$$

$$H_{a,n}^{(L)} = \frac{D_n^{(1)}\left(m_L x_L\right) - A_n^{(L)} D_n^{(2)}\left(m_L x_L\right)}{1 - A_n^{(L)}} \qquad H_{b,n}^{(L)} = \frac{D_n^{(1)}\left(m_L x_L\right) - B_n^{(L)} D_n^{(2)}\left(m_L x_L\right)}{1 - B_n^{(L)}} \tag{5.51}$$

Les Eqs (5.23) et (5.24), et la détermination des fonctions $H_{a,n}^{(L)}$ et $H_{b,n}^{(L)}$, permettent de déterminer les deux coefficients de diffusion externe : a_{nII} et b_{nI} .

5.2 Calcul numérique des séries de Debye

La décomposition de Debye (§ 2.3) nous permet d'obtenir les coefficients de transmission et de réflexion des ondes partielles qui s'écrivent pour la sphère [22], voir également la la Figure 8:

$$R_n^{(22)} = \frac{\alpha H_n'^{(1)}(x) H_n^{(2)}(y) - \beta H_n^{(1)}(x) H_n'^{(2)}(y)}{D_n(x,y)} \tag{5.52}$$

$$R_n^{(11)} = \frac{\alpha H_n'^{(1)}(x) H_n^{(1)}(y) - \beta H_n^{(1)}(x) H_n'^{(1)}(y)}{D_n(x,y)} \tag{5.53}$$

$$T_n^{(21)} = -\frac{2i(m_1/m_2)}{D_n(x,y)} \tag{5.54}$$

$$T_n^{(12)} = -\frac{2i}{D_n(x,y)} = \frac{T_n^{(21)}}{(m_1/m_2)} \tag{5.55}$$

avec

$$D_n(x,y) = -\alpha H_n'^{(1)}(x) H_n^{(2)}(y) + \beta H_n^{(1)}(x) H_n'^{(2)}(y) \tag{5.56}$$

$$x = \frac{\pi d}{\lambda} = kr \qquad y = \left(\frac{m_1}{m_2}\right) x = mkr \tag{5.57}$$

Les fonctions de Hankel, qui sont souvent symbolisées par les lettres grecs «Xi» et «Dzêta» : $H_n^{(1)}(z) = \xi_n(z)$ et $H_n^{(2)}(z) = \zeta_n(z)$ [73] avec $z = x$ ou $z = y$, peuvent être explicitées comme suit :

$$\begin{aligned} H_n^{(1)}(z) &= \psi_n(z) + i\chi_n(z) = z\left[j_n(z) + iy_n(z)\right] \\ H_n^{(2)}(z) &= \psi_n(z) - i\chi_n(z) = z\left[j_n(z) - iy_n(z)\right] \end{aligned} \tag{5.58}$$

$j_n(z), y_n(z)$ sont les fonctions de Bessel sphériques du premier et second ordre (ou fonctions sphériques de Bessel et de Neumann) avec $z \in \mathbb{C}$, $n \in \mathbb{N}$. Elles sont reliées aux fonctions de Ricatti-Bessel par :

$$\psi_n(z) = zj_n(z) \qquad \chi_n(z) = zy_n(z) \tag{5.59}$$

Avec la loi de récurrence suivante pour les dérivées des fonctions de Ricatti-Bessel :

$$B_n'(z) = B_{n-1}(z) + \frac{n}{z} B_n(z) \tag{5.60}$$

On obtient :

$$\begin{aligned} H_n'^{(1)}(z) &= H_{n-1}^{(1)}(z) + \frac{n}{z} H_n^{(1)}(z) \\ H_n'^{(2)}(z) &= H_{n-1}^{(2)}(z) + \frac{n}{z} H_n^{(2)}(z) \end{aligned} \tag{5.61}$$

Au final, les coefficients de diffusion externe des différents ordres de la décomposition de Debye sont donnés par l'Eq. (2.48).

Dans l'équivalence donnée par l'Eq. (2.49), entre les coefficients des séries de Debye et ceux de la théorie de la Lorenz-Mie, ces derniers sont de la forme :

$$\begin{aligned} a_n &= \frac{m\psi_n(y)\psi_n'(x) - \psi_n(x)\psi_n'(y)}{m\psi_n(y)H_n'^{(1)} - H_n^{(1)}\psi_n'(y)} \\ b_n &= \frac{\psi_n(y)\psi_n'(x) - m\psi_n(x)\psi_n'(y)}{\psi_n(y)H_n'^{(1)} - mH_n^{(1)}\psi_n'(y)} \end{aligned} \tag{5.62}$$

5.3 Copies d'écrans des logiciels développés

Les pages 89 à 94 présentent des copies d'écrans de différentes applications Windows développés sous DELPHI :

Figure 56 Copies d'écrans du logiciel d'acquisition et de traitement du diffractomètre haute résolution (HI-REDI)

Figure 57 Copies d'écrans du logiciel d'acquisition et de traitement de l'interféromètre FIBS 3.0, développé pour Saint-Gobain et la mesure de fibres de renfort en cours de production.

Figure 58 Copies d'écrans du logiciel de simulation des propriétés de diffusion de la lumière de fibres optiques à saut ou gradient d'indice: DELFI v1.0, développé pour CERSA-MCI.

Figure 59 Copies d'écrans du logiciel de simulation des propriétés de diffusion de la lumière de particules sphériques : DELPI v. 1.0. Les autres types de particules ne sont pas encore disponibles dans cette version de démonstration développée pour l'Ecole d'Automne d'Oléron (§8.3.3).

Figure 60 Copies d'écrans du logiciel de calcul des champs de vitesse par PIV : PIVO 2.0. Ce logiciel a été utilisé pour l'étude des écoulements en lit fluidisé circulant, les instabilités solutales et différentes collaborations (ENIT, CEMAGREF, Saint-Gobain Conception Verrière…)

Figure 61 Copies d'écrans du logiciel d'acquisition et de traitement de l'arc-en-ciel, GRAS v2.0, pour la caractérisation simultanée de la distribution des diamètres et des indices d'un ensemble de particules en écoulement.

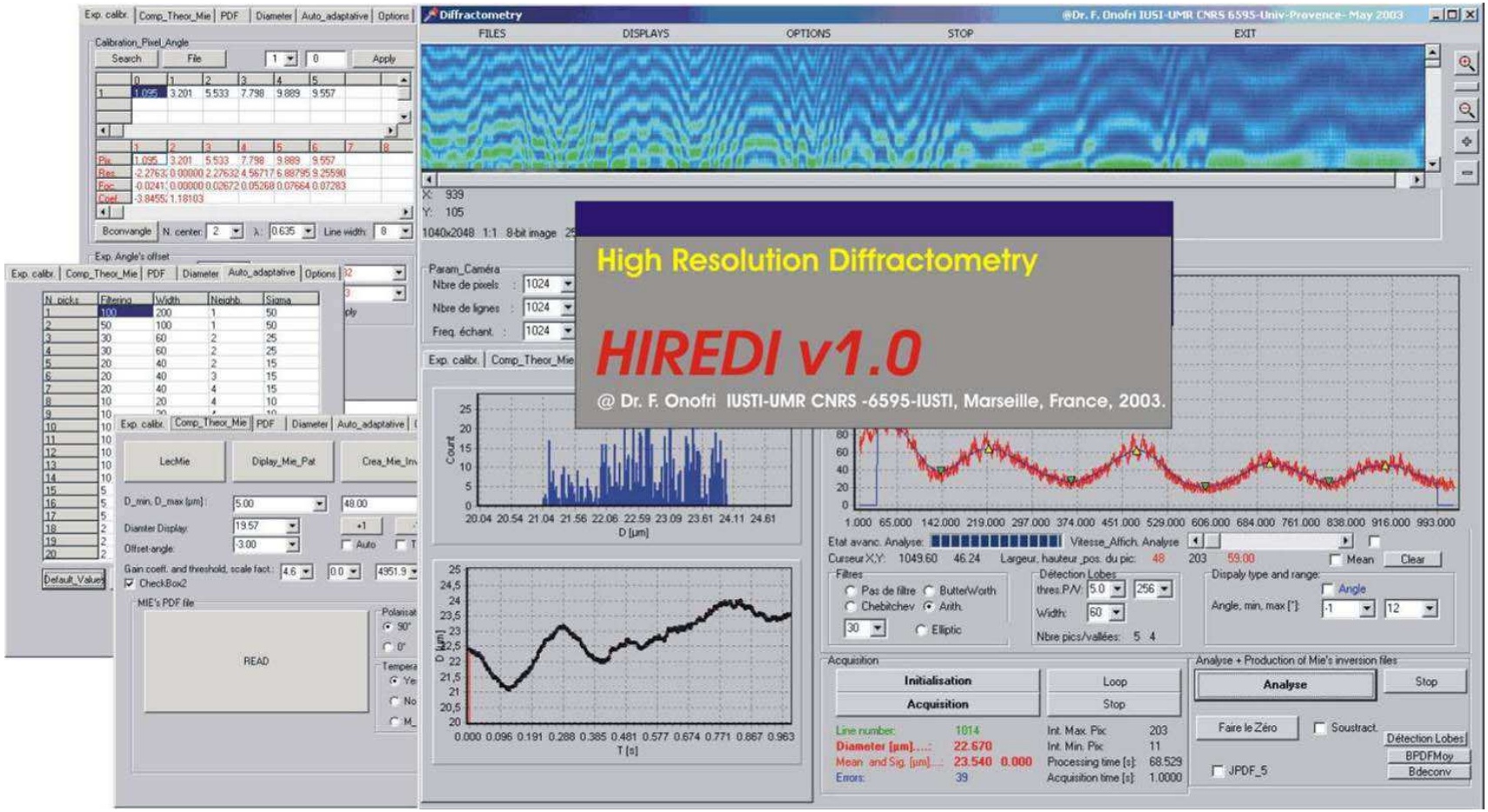

Figure 56 Copies d'écrans du logiciel d'acquisition et de traitement du diffractomètre haute résolution (HIREDI)

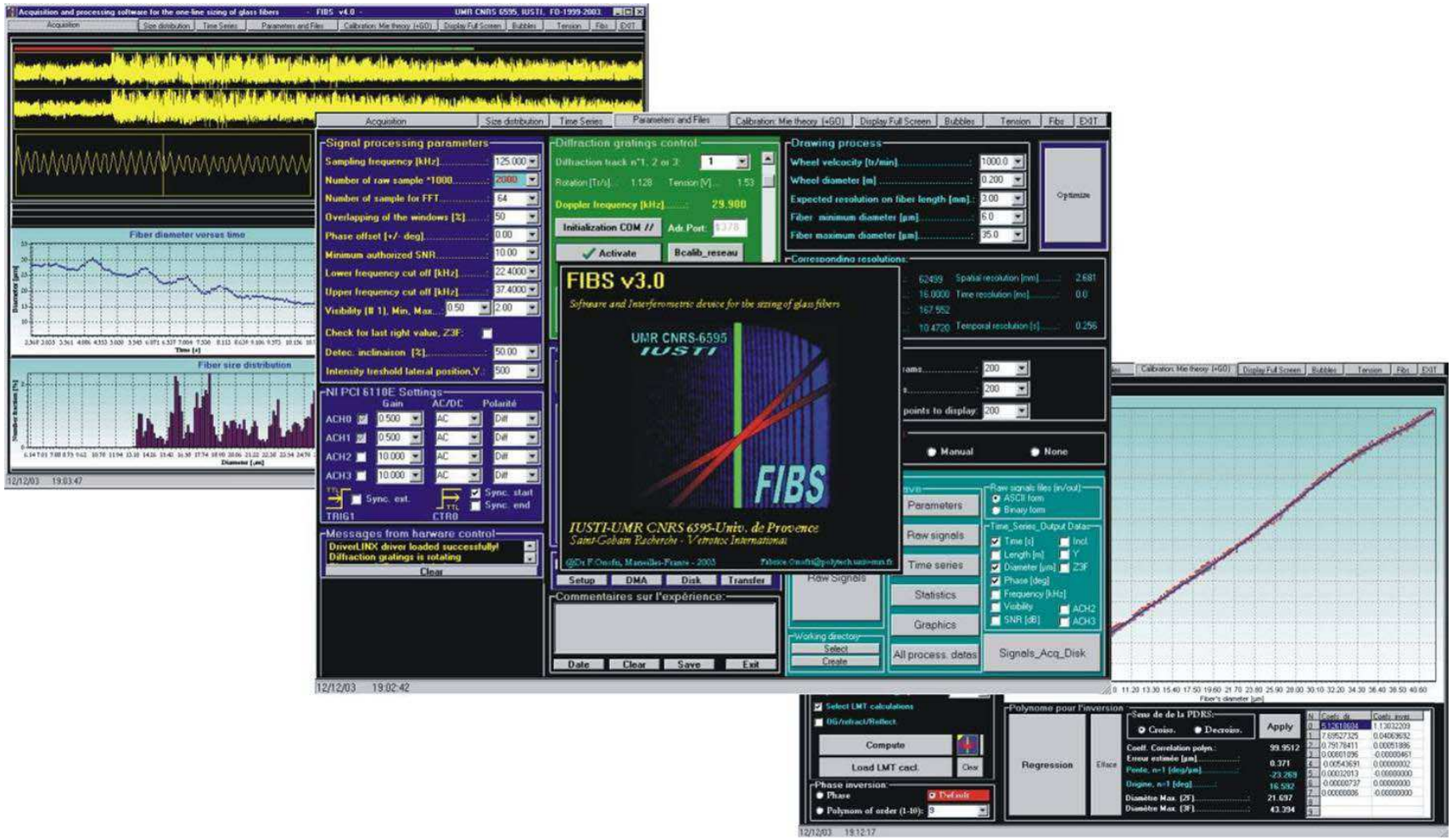

Figure 57 Copies d'écrans du logiciel d'acquisition et de traitement de l'interféromètre FIBS 3.0, développé pour Saint-Gobain et la mesure de fibres de renfort en cours de production.

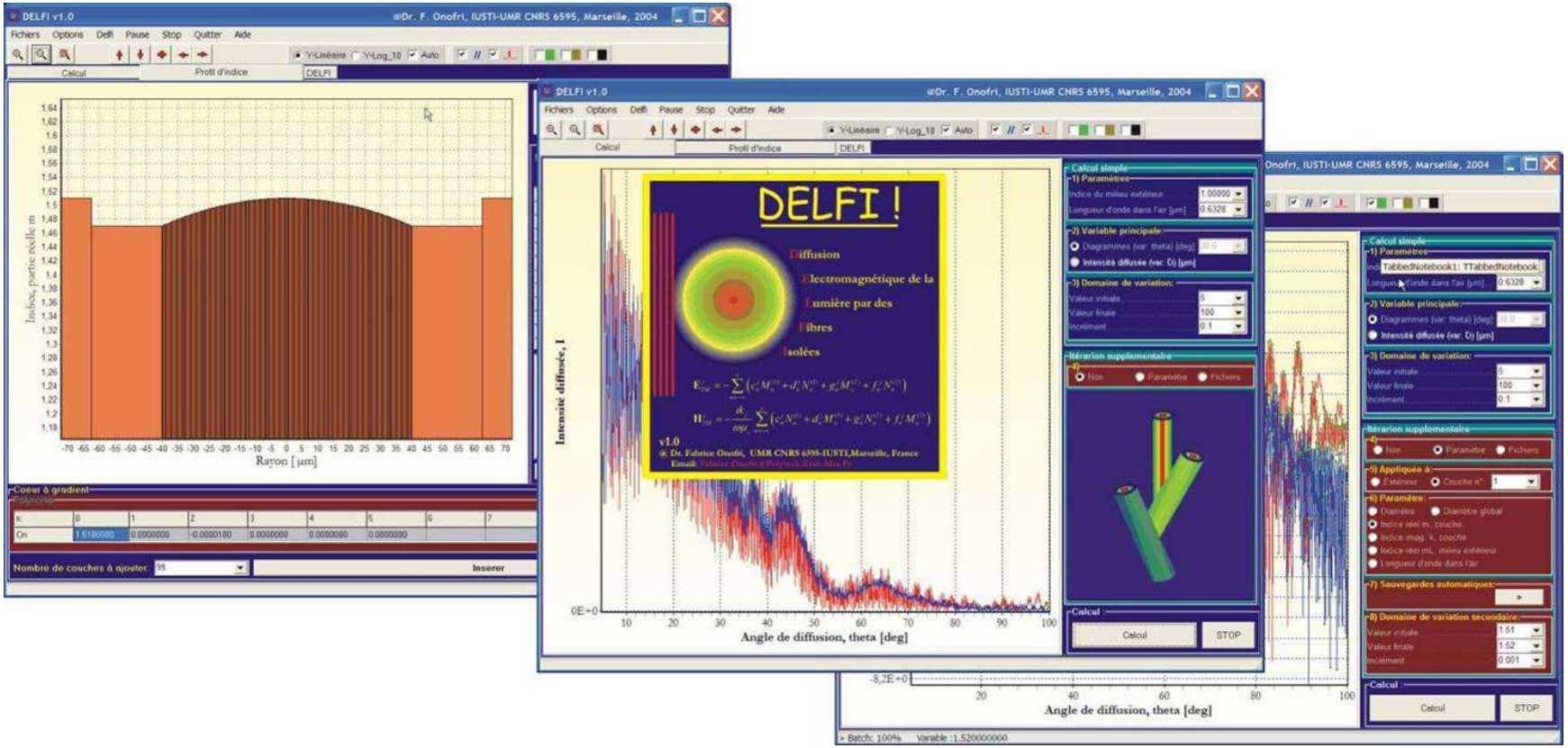

Figure 58 Copies d'écrans du logiciel de simulation des propriétés de diffusion de la lumière de fibres optiques à saut ou gradient d'indice: DELFI v1.0, développé pour CERSA-MCI.

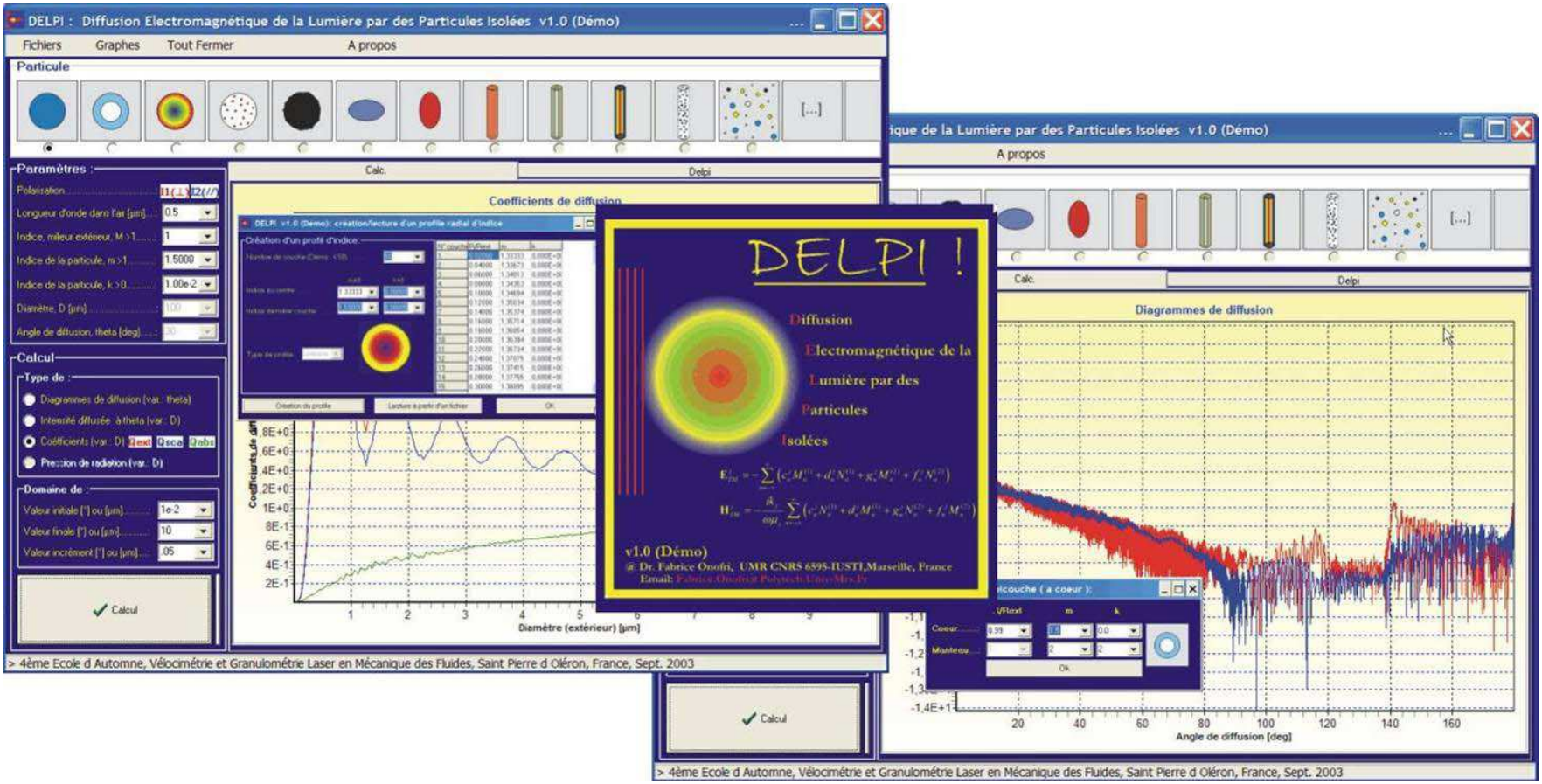

Figure 59 Copies d'écrans du logiciel de simulation des propriétés de diffusion de la lumière de particules sphériques : DELPI v. 1.0. Les autres types de particules ne sont pas encore disponibles dans cette version de démonstration développée pour l'Ecole d'Automne d'Oléron (§8.3.3).

Figure 60 Copies d'écrans du logiciel de calcul des champs de vitesse par PIV : PIVO 2.0. Ce logiciel a été utilisé pour l'étude des écoulements en lit fluidisé circulant, les instabilités solutales et différentes collaborations (ENIT, CEMAGREF, Saint-Gobain Conception Verrière…)

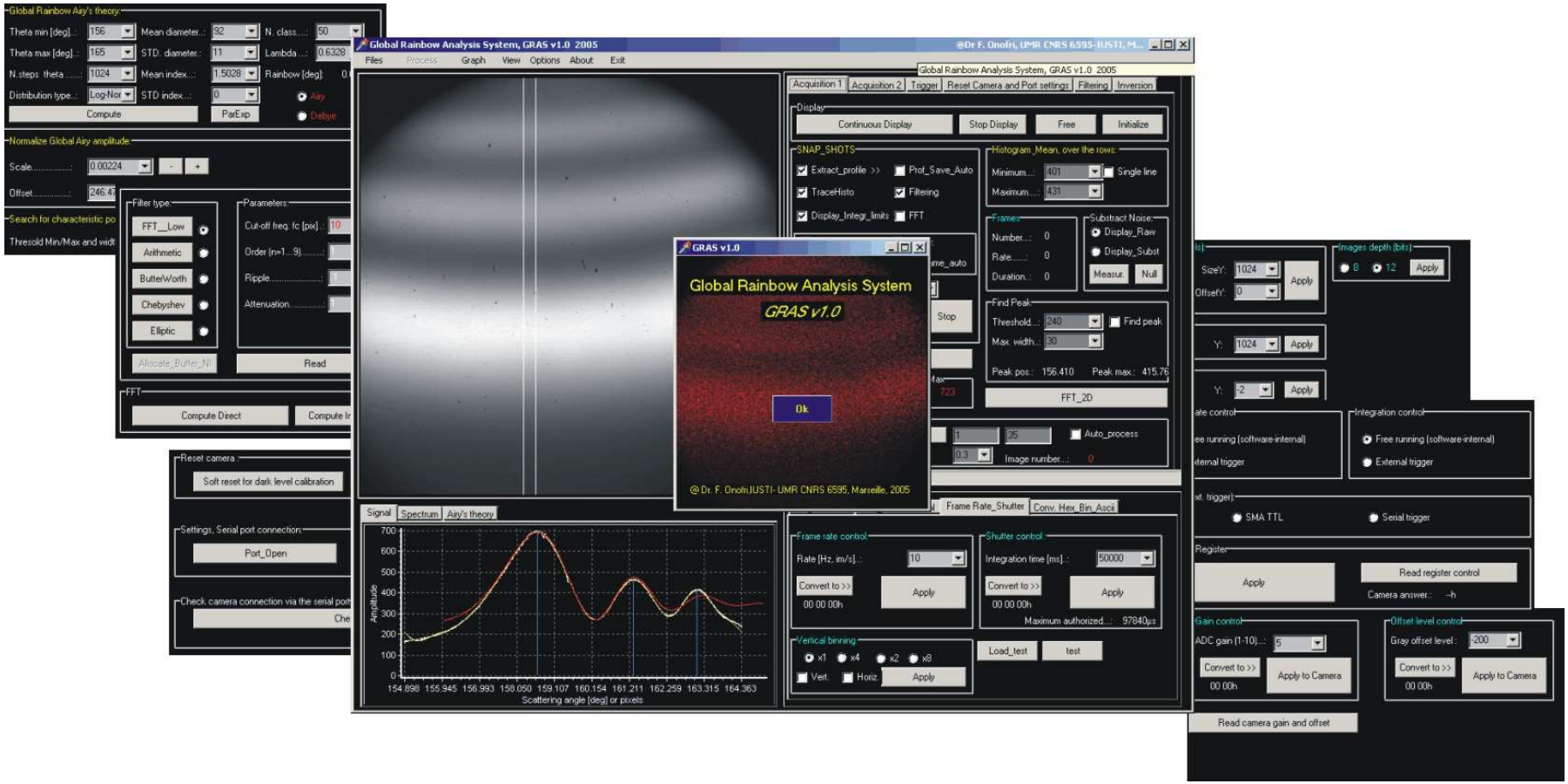

Figure 61 Copies d'écrans du logiciel d'acquisition et de traitement de l'arc-en-ciel, GRAS v2.0, pour la caractérisation simultanée de la distribution des diamètres et des indices d'un ensemble de particules en écoulement.

Chapitre 6

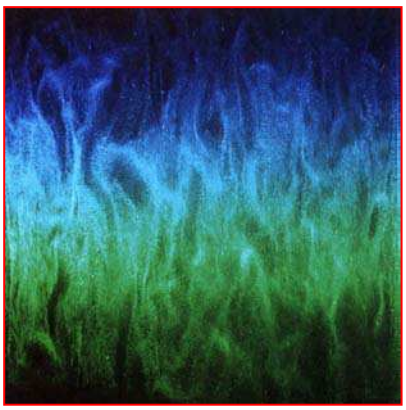

CONCLUSIONS & PERSPECTIVES

6.1 Conclusions

Au terme de ce mémoire d'Habilitation à Diriger des Recherches, il convient de conclure brièvement sur mes *activités de recherche*, *d'encadrement et de gestion de projets*, de *transferts technologiques*.

i) Les points forts de mon activité de recherche sont la *modélisation de la diffusion électromagnétique* de la lumière par des particules en écoulement (Chapitre 2), *la granulométrie optique* (au sens large, Chapitre 3) et *l'étude expérimentale*, au moyen de l'outil optique, de différents systèmes *fluides, diphasiques et multiphasiques* (Chapitres 3 & 4). J'ai développé différentes théories électromagnétiques et modèles asymptotiques pour simuler les propriétés de diffusion de la lumière de *particules homogènes (gouttes, bulles, fibres)* (§2.1-2.4), *stratifiées (suite à un choc thermique, un gradient de composition)* (§2.1 & 2.2), *hétérogènes (i.e. suspension, inclusions)* (§ 2.4.3) *irrégulières* (§ 2.4.3-2.4.4, 4.1.2). Ces développements théoriques ont donné lieu à un certains nombre de publications (§ 8.2), de même qu'au *développement du principe de techniques optiques originales* pour la *caractérisation des écoulements* (vitesse, taille et matériau) : technique dual burst, technique dual mode, diffractométrie haute résolution, réfractométrie par diffusion critique et arc-en-ciel, interférométrie Doppler laser à 3 faisceaux cohérents…, Chapitre 3. Ces travaux m'ont valu une certaine «reconnaissance scientifique», comme l'atteste ma participation à différents *conseils* ou *comités* scientifiques (§8.5).

ii) Certains travaux ont été réalisés en *collaboration* avec d'autres équipes de recherche, dans le cadre de *projets nationaux* et de *collaborations internationales* financées (§ 8.4.2), ou à l'occasion de l'*encadrement* de doctorants ou stagiaires de DEA (§ 8.3). Parmi ces travaux on citera, par exemple, la modélisation de

l'hydrodynamique d'un jet à haute température et des mécanismes de déstabilisation des jets capillaires, la modélisation des propriétés de diffusion d'échantillons sanguins ou encore, l'étude expérimentale de certaines instabilités thermo solutales...

iii) Les *transferts technologiques* ont pris une place relativement importante dans mes activités. D'une part, parce qu'ils valorisent très concrètement *mes compétences* et mes travaux, et d'autre part, parce qu'ils sont nécessaires au *financement* de mes travaux de recherche à caractère plus *fondamental*. Cette activité de *valorisation* a donné lieu à différents *partenariats industriels* qui ont pris la forme de *contrats* de recherche et de *consultance* (§8.4.2, 8.4.3), de *bourses* d'étudiants, de *brevets* (§ 3.1.1) et de *publications* (§ 8.2). Son caractère *pluridisciplinaire* apparaît dans les *domaines abordés* : *biophysique* (modélisation des propriétés de diffusion de globules rouges, calcul de la pression de radiation excercées sur des vésicules, §4.1) ; *combustion diphasique* (mesures de la vitesse de glissement sur un moteur-fusée cryogénique, modélisation et diagnostics de gouttes en combustion, § 4.2) ; caractérisation d'un procédé de fabrication de *fibres de renfort* (§ 4.3.3) et de *fibres optiques* (§4.3.4) ; création d'une *plate-forme de fluidisation* § 4.4) et caractérisation de *poudres* (§8.4.2) ; *instrumentation* (§ 3.1.3, 3.1.4, 3.2.1) *et logiciels scientifiques* (§ 8.2.4)…

6.2 Perspectives

A l'aune des résultats déjà obtenus et des collaborations en cours, on peut établir des *perspectives à moyen terme* sur mes activités de recherche :

i) Concernant la *modélisation* des propriétés de diffusion de la lumière de particules, il reste plusieurs problèmes ardus à traiter. Le modèle statistique (§2.4.4) doit être étendu aux champs internes, afin de simuler la diffusion électromagnétique de *particules hétérogènes*. Les prédictions de ce modèle seront alors comparées à celles du modèle basé sur la méthode de Monte Carlo (§2.4.3). La prise en compte d'un éclairement par une *onde de forme arbitraire*, pour le calcul des champs diffusés par un *cylindre multicouche* (§2.2), serait également intéressante. Ce travail, qui pourrait faire l'objet d'une collaboration [6, 103], serait également profitable pour l'étude en cours sur la caractérisation des *fibres optiques* (§4.3.4, 8.4.2). Ces développements théoriques et numériques nécessiteront des *validations expérimentales*. Elles pourront probablement être obtenues avec un dispositif similaire à celui actuellement utilisé pour mesurer les *flux thermiques* dans des micro écoulements (§4.3.4). La méthode d'inversion des profils d'arc-en-ciel devra être affinée.

ii) La caractérisation simultanée de la *vitesse, de la taille et du matériau* de particules en écoulement est un sujet qui me tient à cœur et dans lequel je suis engagé dans le cadre de *l'ACI VITAMA* (§8.5.1), et d'un programme Polonium (§8.5.2). Il reste cependant beaucoup de travail. Il me faut en effet développer un *prototype* de système *Dual Burst* (§3.2.1) ainsi que les *logiciels* d'acquisition de traitement de ce système et d'un système *Dual mode* (§3.1.1, 3.2.2). Ces travaux d'*instrumentation* et d'informatique *scientifiques* seront suivis par des *validations expérimentales* sur des écoulements modèles, puis des *écoulements réels* (*lits fluidisés*, pulvérisation, …). Du point de vue expérimental, il me reste également à finaliser les expériences sur la technique de me-

sure de profils de vitesse par *interférométrie Doppler laser à 3 faisceaux cohérents* (§3.1.2) et développer un système d'anlayse de l'arc-en-ciel (§3.2.4), adpaté à la caractérisatrion d'écoulements réels du laboratoire.

En matière de recherche, établir des *perspectives à long terme* s'avère très délicat. Mes travaux sur les fibres et jets en sont d'ailleurs la parfaire illustration. En effet, c'est sous l'instigation de Saint-Gobain Recherche, à la suite d'une discussion informelle, dans un congrès, que j'ai démarré ces travaux. Une rencontre, une demande de collaboration, peuvent donc considérablement infléchir une thématique de recherche. Ceci est d'autant plus vrai que l'équipe de recherche est de taille réduite… et qu'elle doit faire face à des besoins matériels, récurrents. Quoi qu'il en soit, on peut essayer de dresser quelques perspectives à long terme sur mes activités de recherche, au regard de *sujets scientifiques* qui me semblent intéressants, *«porteurs»*, aussi bien du point de vue *scientifique* que des *applications* pour la caractérisation *d'écoulements* industriels :

i) Les techniques optiques «de champ» font très certainement partie des techniques du futur. Elles ont les avantages des techniques ponctuelles (suivi temporel, rapide, local, obtention des corrélations) et des techniques intégrales (intégration spatiale, statistique instantanée) [C40]. Elles sont d'ores et déjà en place pour ce qui concerne l'étude de la dynamique des milieux fluides avec, notamment : la Vélocimétrie par Images de Particules (PIV) et la Vélocimétrie Doppler Globale (DGV). Pour les écoulements diphasiques, multiphasiques, quelques techniques de caractérisation de la phase dispersée semblent se développer (micro imagerie [104], interférométrie par défaut de mise au point (IILIS) ou PLIF [64, 105-108], holographie digitale [109, 110]). Cependant, ces dernières sont encore au stade du développement et sont limitées à des particules transparentes (i.e. IILIS, PLIF), des particules grandes devant la longueur d'onde et des milieux d'épaisseur optique faible.

ii) La caractérisation optique des *milieux denses* est également un sujet en plein développement et ou il reste encore beaucoup de choses à faire. De nombreux outils existent déjà pour l'étude de suspensions de microparticules (diffusion dynamique de la lumière, spectroscopie par diffusion d'ondes [C40][36]). En revanche, il n'existe pratiquement aucun outil pour caractériser les écoulements où les particules sont grandes devant la longueur d'onde. Les techniques basées sur l'utilisation d'impulsions laser ultra brèves (femtosecondes) sont très prometteuses, mais elles sont également très coûteuses. Les techniques d'interférométrie et d'imagerie à faible cohérence pourraient constituer une solution alternative, intéressante.

A terme, je pense m'investir dans ces deux domaines de recherche, sur la base de mon expérience actuelle et de la montée en puissance, à Marseille et sur le Technopôle de Château Gombert, du pôle optique et mécanique-énergétique.

Chapitre 7

REFERENCES

[1] Barber, P. W. and S. C. Hill, Light scattering by particles: Computationnal methods, World scientific, Singapour (1990).
[2] Bohren, C. F. and D. R. Huffman, Absorption and Scattering of Light by Small Particles, John Wiley & Sons, New-York (1998).
[3] Wu, Z. S. and Y. P. Wang, Electromagnetic scattering from multilayered sphere: recursive algorithms, Radio Science **26**(6):1393-1401 (1991).
[4] Lenoble, A., Caractérisation optique et étude de la stabilité d'un procédé de fibrage du verre, Ph.D. thesis, Université de Provence, Marseille (France), 2004.
[5] van de Hulst, H. C., Light Scattering by Small Particles, Dover Publications, New-York (1957).
[6] Gouesbet, G. and G. Gréhan, Interaction between shaped beams and an infinite cylinder, including a discussion of gaussian beams, Part. Part. Syst. Charact. **11**:299-308 (1994).
[7] Gurwich, I., N. Shiloah, and M. Kleiman, The recursive algorithm for electromagnatic scattering by tilted infinite circular multilayered cylinder, J. of Quant. Spectr. and Rad. Transf. **63**:217-229 (1999).
[8] Wu, Z. and L. Guo, Electromagnetic scattering from a multilayered cylinder arbitrarily located in a gaussian beam, a new recursive algorithms, Progress in Electromagnatics Research **18**:317-333 (1998).
[9] Chylek, P., J.T. Kiehl, M.K.W. KO, and A. Ashkin, Surface waves in light scattering by spherical and non spherical particles
(in *Lights scattering by irregularly shaped particles*, D.W. Schuerman, Editor): 153-164, Plenum Press: N.Y., 1980.
[10] Nussenzweig, H. M., Diffraction effects in semiclassical scattering, Cambridge University Press, Cambridge (1992).
[11] Lorenz, L., Lysbevaegelsen i og uden for en hal plane lysbôlger belyst kulge, Vidensk. Selk. Skr. **6**:1-62 (1898).
[12] Mie, G., Beitrâge zur optik truber medien, speziell kolloidaler metallosungen, Ann. Phys. **25**:377-452 (1908).
[13] Debye, P., Der lichtdruck auf kugeln von beliebigem material, Ann. Phys. **30**:57-136 (1909).
[14] Stratton, J. A., Electromagnetic theory, McGraw-Hill, New-York (1941).
[15] Kerker, M., The Scattering of Light, and other Electromagnetic radiations, Academic Press, N.Y., (1969).
[16] Gouesbet, G. and G. Gréhan, Sur la généralisation de la théorie de Lorenz-Mie, J. Optique **13**:97-103 (1982).
[17] Gouesbet, G., B. Maheu, and G. Gréhan, Light scattering from a sphere arbitrarily located in a Gaussian beam, using a Bromwich formulation, J. Opt. Soc. Am. A **5**(9):1427-1443 (1988).
[18] Ren, K. F., G. Gréhan, and G. Gouesbet, Radiation Pressure forces exerted on a particle arbitrarily located in a Gaussian beam by using the GLMT, and associated resonances effects, Opt. Comm. **108**:343-353 (1994).

[19] Barton, J. P., D. R. Alexandre, and S. A. Schaub, Internal fields of a spherical particle illuminated by a tightly focused laser beam: Focal point positioning effects at resonance, J. of Appl. Phys. **65**(8):2900- (1989).
[20] Barton, J. P., D. R. Alexandre, and S. A. Schaub, Theoretical determination of net radiation force and torque for a spherical particle illuminated by a focused laser beam., J. of Appl. Phys. **66**(10):4594 - (1989).
[21] Gouesbet, G., B. Maheu, and G. Gréhan, Computations of the g_n^m coefficients in the Generalized Lorenz-Mie Theory using three different methods, Appl. Opt. **27**(23):4874-4883 (1988).
[22] Hovenac, E.A. and J.A. Lock, Assessing the contribution of surface waves and complex rays to far-field scattering by use of the Debye series, J. Opt. Soc. Am. A **9**(5):781-795 (1992).
[23] Albrecht, H. E., N. Damaschke, M. Borys, and C. Tropea, Laser Doppler and Phase Doppler Measurement Techniques, Springer, Berlin (2003).
[24] Gouesbet, G., Debye Series Formulation for Generalized Lorenz-Mie Theory with the Bromwich Method, Part. Part. Syst. Charact. **20**(6):382-386 (2004).
[25] Roth, N., K. Anders, and A. Frohn, Refractive index measurements for the correction of particle sizing methods, App. Opt. **30**(33):4960-4965 (1991).
[26] van Beeck, J. P. A., Rainbow phenomena: on development of a laser-based, non intrusive technique for measuring droplet size, temperature and velocity, Ph.D. Thesis, Technical University of Eidoven (Neederlande), 1997.
[27] van Beeck, J. P. A., T. Grosges, and M.G. De Giorgi, Global rainbow thermometry assessed by Airy and Lorenz-Mie theories and compared with phase Doppler anemometry, App. Opt. **42**(19):4016-4022 (2003).
[28] Naqwi, A. and F. Durst, Analysis of the laser light scattering interoferometric devices for the in-line diagnostic of moving particles, Appl. Opt. **32**:4003-4018 (1993).
[29] Blondel, D., Détection des particules à cœur en écoulement, cas des « cénosphères », Master thesis (DEA), Université de Rouen (France), 1995.
[30] Rheims, J., H. Dahl, T. Wriedt, and K. Bauckage, Sizing Coated spheres with Phase Doppler Anemometry, in *4th Optical particle sizing conference-Partec95*, Nurnberg (Germany), pp. 409-418, 1995.
[31] Bricard, A. and L. Tadrist, Initiation aux échangeurs thermiques à contact direct, Tec et Doc, Lavoisier, Paris (1996).
[32] Marston, P.L., Critical scattering angle by a bubble: physical optics approximation and observations, J. Opt. Soc. Am. A **69**(9):1205-1211 (1979).
[33] Langley, D. S. and P. L. Marston, Critical scattering of laser light from bubbles in water: measurements, models, and application to sizing bubbles, Appl. Opt. **7**(23) (1984).
[34] Lötsch, H.K.V., Beam displacement at total reflection: the Goos-Hänchen effect, Optick **32** (1971).
[35] Manasse, U., T. Wriedt, and K. Bauckhage, Reconstruction of real size distributions hidden in Phase Doppler Anemometry results Obtained from droplets of Inhomogeneous liquids, Part. Part. Syst. Charat. **11**:84-90 (1994).
[36] Xu, R., Particle characterization: light scattering methods, Kluwer Academic Publishers, Dordrecht (2001).
[37] Wriedt, T. and R. Schuh, The inclusion-concentration measurement of suspension droplets based on Monte Carlo ray tracing, Meas. Sci. and Tech. **13**(3):276-279 (2002).
[38] Bergougnoux, L., J. Misguesh-Ripault, J-L. Firpo, and J. André, Monte Carlo calculation of backscat-tered light intensity by suspension: comparison with experimental data, Appl. Opt **35**:1735-1741 (1996).
[39] Wriedt, T., A Review of Elastic Light Scattering Theories, Part. Part. Syst. Charact. **15**:67-74 (1996).
[40] Mishchenko, M.I., J.W. Hovenier, and L.D. Travis, Light Scattering by Non Spherical Particles: Theory, Measurements and Applications, Academic press, San Diego (1999).
[41] Drossart, P., A statistical model for the scattering by irregular particles, The Astrophysical Journal **361**:29-32 (1990).
[42] Petrova, E.V. and W.J. Markiewewicz, Light scattering by nonspherical particles: a modification of the statistical model and application to Matian Aerosols, Solar System Research **31**(5):369-376 (1997).
[43] Durst, F. and M. Zaré, Laser Doppler measurements in two-phase flows, in *Proceedings of LDA-Symposium, Copenhagen*, pp. 403-429, 1975.
[44] Bachalo, W. D. and M. J. Houser, Phase/Doppler spray analyzer for simultaneous measurements of drop size and velocity distributions, Opt. Eng. **23**:583-590 (1984).
[45] Bauckhage, K., H. H. Floegel, U. Fritsching, and R. Hiller, The Phase Doppler difference method, a new laser Doppler technique for simultaneous size and velocity measurements, Part 2: Optical particle characteristics as a base for a new diagnostic technique, Part. Part. Syst. Charact. **5**:66-71 (1988).
[46] Xu, T. H. and C. Tropea, Improving the performance of two-component Phase Doppler Anemometry, Meas. Sci. Techn. **5**:969-975 (1994).

[47] Sankar, S. V., A. Inenaga, and W. D. Bachalo, Trajectory dependent scattering in Phase Doppler interferometry: minimizing and eliminating sizing error, in *6th Int. Symp. on Appl. of Laser Tech. to Fluid Mech.*, 20-23th July, Lisbon (Portugal), pp. 1.8, 1992.
[48] Gréhan, G., G. Gouesbet, A. Naqwi, and F. Durst, Particle Trajectory Effects in Phase Doppler Systems: Computations and Experiments, Part. Part. Syst. Charact. **10**:332-338 (1993).
[49] Dantec Dynamics A/S, *Tonsbakken 16-18, P.O. Box 121, DK-2740 Skovlunde, Denmark*.
[50] Naqwi, A. A., Sizing of irregular particles using a Phase Doppler system, Part. Part. Syst. Charact. **8**:343-349 (1996).
[51] Durst, F., A. Melling, and J. H. Whitelaw, Principles and practice of laser-Doppler anemometry, Academic Press, London (1981).
[52] Mignon, H., F. Onofri, G. Gouesbet, G. Gréhan, and C. Tropea, Mesure de particules non-sphériques par Phase Doppler: cas des cylindres et des particules irrégulières, in *4ème Congrés Francophone de Vélocimétrie Laser*, 26-29 Sept. Poitier (France), pp. 1-4, 8 pages, 1994.
[53] Mignon, H., Anémométrie Phase Doppler et Particules Non Sphériques: Cas des Cylindres et des Ellipsoïdes, Ph.D. thesis, Université de Rouen, Rouen (France), 1997.
[54] Mignon, H., G. Gréhan, G. Gouesbet, T. H. Xu, and C. Tropea, Mesurement of cylindrical particles with phase Doppler anemometry, Appl. Opt. **35**(25):5180-5190 (1996).
[55] Schaub, S. A., A. A. Naqwi, and F. L. Harding, Design of a phase/Doppler light-scattering system for mesurement of small-diameter glass fibers during fiberglass manufacturing, Appl. Opt. **37**(3):573-585 (1998).
[56] Lynch, L. J. and N. Thomas, Optical Diffraction Profiles of Single Fibers, Textile reseach journal **41**:568-572 (1971).
[57] Lebrun, D., A. Belaid, C. Ozkul, K. F. Ren, and G. Gréhan, Enhancement of wire diameter measurements: comparison between Fraunhofer diffraction and Lorenz-Mie theory, Opt. Eng. **35**:946-950 (1996).
[58] Ozkul, C., D. Lebrun, D. Allano, A. Abdelghani-Idrissi, and A. Leduc, Fiber diameter measurements:comparison between Fraunhofer diffraction and Lorenz-Mie theory, Opt. Eng. **30**:1855-1861 (1991).
[59] Kaye, P.H., Spatial Light Scattering as a Means of Characterising and Classifying Non-spherical Particles, Meas. Sc. and Techn. **9**:141-149 (1998).
[60] Chylek, P., J.T. Kiehl, M.K.W. Ko, and A. Ashkin, Surface waves in light scattering by spherical and nonspherical particles (in *Lights scattering by irregularly shaped particles*, D.W. Schuerman, Editor): 153-164, Plenum Press: New-York, 1980.
[61] Roth, N., K. Anders, and A. Frohn, Simultaneous measurement of temperature and size of droplets in micrometer range, J. of Laser. Appl. **2**(1) (1991).
[62] Sankar, S. V., D. H. Buermann, and W. D. Bachalo, Simultaneaous measurements of droplets size, velocity and temperature in a swirl-stabilized spray flame, in *6th International Symposium on Application of Laser Techniques to Fluid Mechanics*, Lisbon (PORTUGAL), pp., 1992.
[63] van Beeck, J. P. A. and M. L. Riethmuller, Non intrusive measurements of temperature and size of raindrops, Appl. Opt. **34**:1633-1639 (1994).
[64] Charalampous, G., Y. Hardalupas, and A.M.K.P. Taylor, Optimisation of the Droplet Sizing Accuracy of the Combined Scattering (Mie) / Laser Induced Fluorescence (LIF) Technique, in *12th Int. Symp. on Appl. of Laser Tech. to Fluid Mech.*, 12-15th July, Lisbon (Portugal), pp. 15.6, 2004.
[65] Castanet, G., P. Lavielle, M. Lebouché, and F. Lemoine, Measurement of the temperature distribution within monodisperse combusting droplets in linear stream using two colors laser-induced fluorescence., Exp. in Fluids **35**:563-571 (2003).
[66] Hess, C. F. and G. P. Wood, The pulse Displacement technique - a single Particle Counter with a size range larger than 1000:1, in *Int. Cong. on Opt. Part. Sizing*, Yokohama (Japan), pp. 475-482, 1993.
[67] Jones, A.R., N.T. Parasram, and A. M. K. P. Taylor, Numerical simulation of the sizing performance of the shadow Doppler velocimeter (SDV), Measurement Science and Technology **13**(3):317-330 (2002).
[68] Naqwi, A., F. Durst, and X. Liu, Extended Phase-Doppler system for charaterization of Multiphase-flows, Part. Part. Syst. Charact. **8**:16-22 (1991).
[69] Bonnet, J-P., Contribution à la Caractérisation Optique Des Ecoulements Polyphasiques Dans les Lits Fluidisés Circulants, Master Thesis (DEA), IUSTI-UMR CNRS 6595-Université de Provence, Marseille, 2004.
[70] Ouedraogo, M., Arc-en-Ciel global: développement d'une technique non intrusive de mesure d'indices et de tailles, Stage Ingénieur 2ème année, Ecole de l'Air-IUSTI-UMR CNRS 6595-Université de Provence, Marseille, 2005.

[71] Malvern Instruments Ltd., *Enigma Business Park, Grovewood Road Malvern, Worcestershire, United Kingdom, WR14 1XZ,* 49-64.
[72] Watson, D., *Diffraction from raindrops (Physics lecture notes)*, *University of Rochester,* http://www.pas.rochester.edu/~dmw/phy218/Lectures.htm. 2004
[73] Abramowitz, M. and I. Stegun, Handbook of Mathematical functions with formulas, graphs and mathematical tables, Dover publications inc., New-York (1964).
[74] Chang, S. C., J.M. Jin, J. Jin, and S. Zhang, Computations of Special Functions, John Wiley & Sons, New-York (1996).
[75] Lemaitre P., Porcheron E., Nuboer A., Brun P., and Malet J. Cornet P., Vendel J., Grehan G., Développement de la réfractométrie arc-en-ciel global pour mesurer la température de gouttes en chute libre, in *9ème Congrès Francophone de Vélocimétrie Laser, 14-17 Septembre 2004*: IKV,ULB, AFVL, pp. F.2.1, 2004.
[76] Roth, N., N. Anders, and A. Frohn, *Determination of size, evaporation rate, and freezing of water droplets using light scattering and radiation pressure*. 1994
[77] van Beeck, J. P. A. and M. L. Riethmuller, *Simultaneous determination of temperature and size of droplets from rainbow using Airy theory*. 1994
[78] Sankar, S. V., K. M. Ibrahim, D. H. Buermann, M. J. Fidrich, and W. D. Bachalo, An integrated Phase Doppler/Rainbow refractometer system for simultaneous measurement of droplet size, velocity, and refractive index, in *3rd Int. Cong. on Optical Partical Sizing*, Yokohama (JAPAN), pp. 275-284, 1993.
[79] Ashkin, A., Acceleration and trapping of particles by radiation pressure, Phys. Rev. Lett. **24**(4):156-159 (1970).
[80] Liu Y., Sonek G. J., Berns M.W., and Tromberg B.J., Physiological monitoring of optically trapped cells: assessing the effects of confinement by 1064-nm laser tweezers using microfluorometry., Biophys. J. **71**:2158-2167 (1996).
[81] Polaert, H., Effets mécaniques et structures de faisceaux en théorie de Lorenz-Mie généralisée, Ph.D. thesis, Université de Rouen, Rouen (France), 1999.
[82] M. I. Angelova, B. Pouligny, G. M. Martinot-Lagarde, G. Gréhan, and G. Gouesbet., Stressing Phospholipid Membranes using Mechanical Effects of light, Progr. Colloid. Polym. Sci. **97**:293-297 (1994).
[83] Streekstra, G., A.G. Hoekstra, E.J Nijhof, and R. Heethaar, Light scattering by red blood cells in ekta-cytometry: Fraunhofer vs anomalous diffraction, App.Opt. **32**:2266-2272 (1983).
[84] Azouzi, H. El, Etude de la déformabilité des globules rouges par diffusion de la lumière- Influence des tensioactifs, Ph.D. thesis, Université de Nancy I, Nancy (France), 1995.
[85] Mishchenko, M.I., Light scattering by randomly oriented rotationnally symetric particle, J. Opt. Soc. Am. A **8**:871-882 (1991).
[86] Mishchenko, M. I. and L. D. Travis, *http://www.giss.nasa.gov/~crmim/index.html*, NASA Goddard Institut, 2004
[87] Prahl, S., *http://omlc.ogi.edu/spectra/hemoglobin/index.html*, *Oregon Medical Laser Center*. 2001
[88] Kneer, R., M. Schneider, B. Noll, and S. Wittig, Diffusion controlled evaporation of a multicomponent droplet: theoritical studies on the importance of variable liquid properties, Int. J. Heat Mass Transfer **36**(9):2403-2415 (1995).
[89] Godelle, J., Analyse non linéaire de dynamiques de jets liquides cylindriques, Ph.D. Thesis, Université de Paris VII, Paris (France), 1999.
[90] Gupta, G., Chap. 2 (in *Fiber Reinforcements for composite materials*, A.R. Bunsell, Editor): 19-71, Elsevier, 1988.
[91] Corpus, J. M. and P. K. Gupta, Diameter Dependence of the Refrective Index of Melt-Drawn Glass Fibers, J. Am. Ceram. Soc. **76**(5):1390-1392 (1993).
[92] Clementin-de-Leusse, C., Etude de fibres de verre E. Caractérisation expérimentale par spectrométrie de Brillouin et test de modèle de fribrage, Ph. D. thesis, Université de Monpellier II, France, 2000.
[93] Lenoble, A., F. Onofri, and S. Radev, Modélisation physique du procédé de fibrage des fibres de renforcement, in *Congrès Français de Thermique*, 6-9 juin, Vittel (France), pp. 139-144, 2002.
[94] Pearson, J. R. A., Y. T. Sahh, and R. D. Mhaskar, *On the Stability of Fiber Spinning of Freezing Fluids,* 31-37 %L ar-Pearson76b. 1976
[95] Yerushalmi, J., High velocity fluidized beds (in *Gas Fluidization technology, Chap.7*, D. Geldart, Editor), John & Willey: New-York, 1986.
[96] Lounge, M., (in *Experimental Techniques, in Circulating Fluidized Beds*, J.R. Grace, A.A. Avidian, and T.M. Knowlton, Editors): 312-358, Blackie Academic & Professional Press: London, 1997.
[97] Horio, M. and I. Munechika, Prediction of Cluster Size In Circulating Fluidized Beds, Journal of Chemical Engineering of Japan, **30**(4):691-697 (1997).

[98] Cattieuw, P., Etude expérimentale des écoulements gaz particules dans un lit fluidisé circulant., Ph.D thesis, Université de Provence, France, 1992.
[99] Van den Moortel, T., Analyse locale et ponctuelle des écoulements gas-particules dans un lit fluidisé circulant: étude expérimentale et modélisation de la formation des amas, Ph.D. thesis, Université de Provence, France, Marseille, 1998.
[100] Helland, E., Etude des écoulements fluide-solide dans les lits fluidisés: Simulation numérique et analyse des hétérogénéités., Ph.D. thesis, Université de Provence, Marseille (France), 2000.
[101] Bensallah, A., Développement d'un protocole expérimental pour la mesure de la vitesse de glissement dans les écoulements en Lit Fluidisé Circulant, Master thesis (DEA), Université de la Méditéranée, IUSTI UMR CNRS 6595, Marseille (France), 1998.
[102] Wu, Z. S., L. X. Guo, K. F. Ren, G. Gouesbet, and G. Gréhan, Improved algorithms for electromagnetic scattering of plane waves and shaped beams by multilayered spheres, Appl. Opt. **36**(21):5188-5198 (1997).
[103] Ren K. F., Grehan G., and Gouesbet G., Scattering of a Gaussian beam by an infinite cylinder in the framework of generalized LorenzMie theory: formulation and numerical results, JOSA A **14**(11):3014- (1997).
[104] Oxford Lasers, *http://www.oxfordlasers.com*, 2004
[105] Maeda M., Kasaka Y. A, and Kawaguchi T, Improvement of the interferometric technique for simultaneous measurement of droplets size and velocity vector field in and its application to a transient spray, Exp. Fluids **33**:125-134 (2002).
[106] Hess, F., Planar Particle Image Analyzer, in *9th Int. Symp. Appl. of Laser Tech. to Fluid Mech.*, 13-16th July, Lisbon(Portugal), pp. 18.1, 1998.
[107] Pajot O. and Mounaim-Rouselle C., Droplets sizing by interferometric method based on Mie scattering in a I.C. engine, in *9th Int. Symp. Appl. of Laser Tech. to Fluid Mech.*, 13-16th July, Lisbon(Portugal), pp. 18.2, 1998.
[108] LeGal P., Farrugia N., and Greenhalgh D. A., Laser sheet dropsizing of dense sprays, Optics and Laser Tech. **31**:75 -83 (1999).
[109] Müller, J., V. Kebbel, and W. Jüptner, Characterization of spatial particle distributions in a spray-forming process using digital holography, Meas. Sci. Technol.
15:706-710 (2004).
[110] Lebrun, D., C.E. Touil, and C. Ozkul, Methods for the deconvolution of defocused-image pairs recorded separately on two CCD cameras: application to particle sizing, App. Opt. **35**(32):6375-6381 (1996).

Chapitre 8

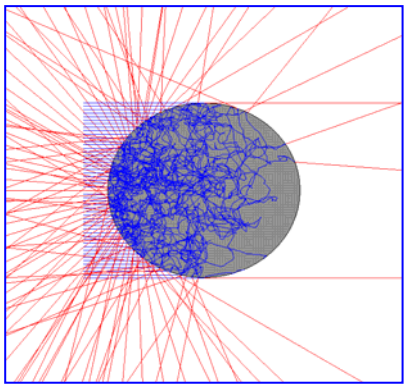

CURRICULUM ET AUTRES ACTIVITES

8.1 Curriculum vitae

Etat Civil :
Nom patronymique : ONOFRI
Prénoms : Fabrice, Roger, Angelo
Date et lieu de naissance : 27 août 1967 à Rouen
Nationalité : Française
Situation de famille : marié, deux enfants

Diplômes :
1987-90 : DEUG, Licence et Maîtrise de Physique, Université de Rouen
1990-91 : Service National (responsable d'une base de données)
1991-92 : DEA d'Aérothermochimie, UMR 6614-CORIA, Université de Rouen
1992-95 Thèse de Doctorat en Physique, option Energétique, Université de Rouen
Statut : Allocataire de Recherche (MRT)
Titre : « Prise en compte de la dimension finie des faisceaux d'éclairage en granulométrie optique : Anémométrie Phase Doppler . Diagnostics optiques des milieux diphasiques »
Directeur de Thèse : Gérard Gréhan
Label : Thèse Européenne (17 semaines en Allemagne, LSTM: Prof. F. Durst)
Mention : Très honorable avec les félicitations du jury.

Postes de recherche :
1995-96 : Attaché Temporaire d'Enseignement et de Recherche (ATER) à l'INSA de Rouen, UMR 6614-CORIA
1996-2004 : Chargé de Recherche au CNRS, section 10, en poste à Marseille à l'IUSTI-UMR n° 6595-CNRS/Université de Provence.

8.2 Publications, travaux & ouvrages

8.2.1 Articles dans des revues à comité de lecture

[A1] Aizu Y., Domnick J., Durst F., Gréhan G., **Onofri F.**, Qiu H.H., Sommerfeld M., Xu T-H and Ziema M., A new Generation of Phase Doppler Instruments for Particle Velocity, Size and Concentration Measurements, Part. and Part. Syst. Charact. **11**(1):43-54 (1994).

[A2] **Onofri F.**, Gréhan G., Gouesbet G., Electromagnetic scattering from a multilayered sphere located in an arbitrary beam, Appl. Opt. **34**(30):7113-7124 (1995).

[A3] Gréhan G, **Onofri F.**, Gouesbet G., Anémométrie Phase Doppler en milieux multiphasiques: vers de nouvelles possibilités, La Houille Blanche **1-2**:98-104 (1996).

[A4] **Onofri F.**, Girasole T., Gréhan G., Gouesbet G., Brenn G., Domnick J., Tropea C., Xu T-H., Phase-Doppler Anemometry with Dual Burst Technique for Measurement of Refractive Index and Absorption Coefficient Simultaneous with Size and Velocity, Part. and Part. Syst. Charact., **13**(2):212-224 (1996).

[A5] **Onofri F.**, Blondel D., Gréhan G., Gouesbet G., On the Optical Diagnosis and Sizing of Coated and Multilayered Particles with Phase Doppler Anemometry, Part. and Part. Syst. Charact.,**13**(2):104-111 (1996).

[A6] Tropea C., Xu T-H., **Onofri F.**, Gréhan G., Haugen P., Dual-Mode Phase Doppler Anemometer, Part. and Part. Syst. Charact. **13**(2):165-170 (1996).

[A7] Gréhan G., **Onofri F.**, Girasole T. and Gouesbet G., Measurement of Bubbles by Phase Doppler Technique and Trajectory Ambiguity, (in *Developments in Laser Techniques and Applications to Fluid Mechanics*, Adrian et al. Editors) Part III: 290-302, Springer Verlag,1996.

[A8] **Onofri F.**, Bergounoux L., Firpo J-L., Mesguish-Ripault J., Velocity, size and concentration measurements of optically inhomogeneous cylindrical and spherical particles, Appl. Opt. **38**(21):4681-4690 (1999).

[A9] **Onofri F.**, Critical Angle Refractometry: for simultaneous measurement of particles in flow size and relative refractive index, Part. and Part. Syst. Charact. **16**(3):119-127 (1999).

[A10] Gicquel P., **Onofri, F.**, Tanguy, B. and Vingert L., Travaux expérimentaux d'analyse granulométrique des ecoulements cryogeniques en combustion, Bulletin de l'Office National d Etudes et de Recherches Aerospatiales **227**:1:9 (2000)

[A11] Radev S., Kaschiev M., Koleva, M., Tadrist L., and **Onofri F.**, Numerical Analysis of the Nonlinear Instability of One-Dimensional Compound Capillary Jet, Lecture Notes in Computer Science **1988**:692-701 (2001).

[A12] **Onofri F.**, Lenoble A., Radev S., Superimposed Non Interfering Probes to extend the Phase Doppler Anemometry capabilities, Appl. Opt. **41**(18): 3590-1600 (2002).

[A13] **Onofri F.**, Lenoble A., Radev S., Bultynck H., Guering P-H., Marsault N., Interferometric sizing of single-axis birefringent glass fibres,. Part. Part. Syst. Charact. **20**(3):171-182 (2003).

[A14] Ibsen C-H., **Onofri F.**, Solberg T., Herjtager B.H., Tadrist L., Improved particle image velocimetry measurements in gas-solid flows with a dense wall layer, Meas. Sc. Technol. **14**:9-12 (2003).

[A15] Mroczka, J., Wysoczanski, D., **Onofri, F.**, Optical parameters and scattering properties of red blood cells, Optica Applicata **32**(4):691-700 (2002)

[A16] **Onofri F.**, Lenoble A., Bultynck B., Guéring P-H, High-resolution laser diffractometry for the on-line sizing of small transparent fibres, Opt. Com. **234**:183-191 (2004).

[A17] **Onofri F.**, Lenoble A., Radev S., Guering P-H, Optical measurement of the drawing tension of small glass fibres, Meas. Sci. Technol. **15**:1279-1284 (2004)

*[A18] **Onofri F.**, Brutin D., Electromagnetic scattering of a multilayered and single axis birefringent cylinder with large size parameters: theoretical, numerical and experimental results, en preparation (2005)*

*[A19] **Onofri F.**, Lenoble A., Radev S., Guering P-H, Experimental investigation of the stability of a reinforcement glass fibres drawing process, en preparation (2005)*

*[A20] **Onofri F.**, 3-Coherent Beams Phase Doppler and Laser Doppler Velocimetry Measurements Techniques, en preparation (2005)*

*[A21] T. Bergenblock, **F. Onofri**, B. Leckner, R. Occelli, L. Tadrist, Averaging of particle data from phase Doppler anemometry in unsteady two-phase flow: Validation by numerical simulation,* soumis à Int. J. of Multiphase Flow (Mars 2005)

8.2.2 Brevets

[B1] Durst F., Aizu Y., Xu T-H., Gréhan G., Gouesbet G., **Onofri F.**, Laser-Doppler-gerat sowie verfahzum betreiben eines solchen gerates, German pattent n°2153/3-93, (1993).

[B2] Durst F., Aizu Y., Xu T-H., Gréhan G., Gouesbet G., **Onofri F.**, Laser-Doppler-gerat sowie verfahzum betreiben eines solchen gerates, European patent n°94112579.1, Applicant: Invent Entwicklung Neuer Technologien GmbH (1994).

8.2.3 Congrès avec actes[28]

[C1] **Onofri F.**, Rozé C. and Gréhan G., Traitement des signaux Phase Doppler et ADL sujets aux effets de trajectoire: analyse par ondelettes, *9èmes Journées d'Etudes sur les Aérosols,* Paris, Dec., pages 81-89, 1992.

[C2] Aizu Y., Durst F., Gréhan G., **Onofri F.** and Xu T-H. , A PDA System Without Gaussian Beam Deffects*, 3rd Int. Cong. on Optical Partical Sizing* , Yokohama (Japan), pp. 461-470, 1993.

[C3] Mignon H., **Onofri F.**, Gouesbet G., Gréhan G. and Tropea C., Mesure de particules non-sphériques par Phase Doppler: cas des cylindres et des particules irrégulières*, 4ème Congrés Francophone de Vélocimétrie Laser*, Poitier (France), paper 1.4, 1994.

[C4] Tropea C., Xu T-H., **Onofri F.**, Gréhan G. and Haugen. P, Dual-Mode Phase Doppler Anemometry, *7th Int. Symp. on Appl. of Laser Tech. to Fluid Mech.*, Lisbon, July 11-14th, pages 18.31-38, 1994.

[C5] Gréhan G., **Onofri F.**, Girasole T. and Gouesbet G., Measurement of Bubbles by Phase Doppler Technique and Trajectory Ambiguity*, 7th Int. Symp. on Appl. of Laser Tech. to Fluid Mech.*, Lisbon, July 11-14, paper 18.2, 1994.

[C6] **Onofri F.**, Gréhan G., Gouesbet G., Xu T-H., Brenn G. and Tropea C., Phase-Doppler Anemometry with Dual Burst Technique for Particle Refractive Index Measurements*, 7th Int. Symp. on Appl. of Laser Tech. to Fluid Mech.*, Lisbon, July 11-14th, paper 23.2, 1994.

[C7] Pagès J.P, Corbin F., **Onofri F.**, Garo A, G. Gousbet, G. Gréhan, Réfractométrie d'arc-en-ciel: mesure de la taille et de l'indice de sphères et de cylindres multicouches*, 12èmes Journées d'Etudes sur les Aérosols*, Paris, 11-12 Dec., 1995.

[C8] Letellier C., **Onofri F.**, Maheu B., Gouesbet G. and G. Gréhan G., On the breakup of a liquid jet: Characterization of phase Doppler like time series by topology of their reconstructed state space*, 11th Europeen Conference of ILASS-Europe on Atomization and Sprays*, Partec95, Nurnberg, Germany, p. 117-122, 1995.

[C9] Ren K.F., **Onofri F.**, Gouesbet G., Gréhan G., Martinot-Lagarde G. and Pouligny B., Radiation pressure: a tool for optical measurements of pico-Newton forces, *4th Optical Particle Sizing conference-Partec95*, Nurnberg, Germany 21-23 March, pp. 87-106, 1995.

[C10] **Onofri. F.**, Gréhan G., Brenn G., Domnick J., Durst F., Tropea C., Xu T-H. The Dual Burst Technique and its application for sizing of heterogeneous particles*, 4th Opticle Partical Sizing conference-Partec95*, Nurnberg, Germany 21-23 March, pp. 60-68, 1995.

[C11] Tropea C., Xu T-H., **Onofri F.**, Gréhan G. and Haugen P., Dual-Mode Phase Doppler Anemometer, *4th Optical Particle Sizing conference-Partec95*, Nurnberg, (Germany), 21-23th March, pp. 287-296, 1995.

[C12] **Onofri F.**, Mignon H., Gouesbet G., Gréhan G. and Tropea C., Phase Doppler measurements of non spherical particles: cylindrical and multilayered particles, *4th Optical Particle Sizing conference-Partec95*, Nurnberg, Germany 21-23 March, pp. 275-284, 1995.

[C13] **Onofri F.**, Bultynck H., Gréhan G., Mesures corrélées Taille-Vitesse-Indice par Anémométrie Phase Doppler : Application à l'étude des phénomènes de coalescence et mesure de la Température de Particles , *5ème Congrès Francophone de Vélocimétrie Laser*, papier E3, 25-27 Septembre, Rouen, 1996.

[C14] **Onofri F.**, Tadrist L., Experimental analysis of spatio-temporal instabilities of the dilute gas-solids flow in a circulating fluidized bed, *6th Int. Conference on Circulating Fluidized beds*, Würzburg, Germany, August 22-27, pp. 837-842, 1999.

[28] Indifféremment, congrès avec sélection sur résumé ou article complet. Les communications ont été présentées par les personnes dont le nom est souligné.

[C15] Bultynck H., **Onofri F.**, Gréhan G., Gouesbet G., Sonde Phase Doppler Miniature : Applications aux Diagnostics en Milieux Hostiles, *5ème Congrès Francophone de Vélocimétrie Laser*, papier G1, 25-27 Septembre, Rouen, 1996.

[C16] **Onofri F.,** Tadrist L., Pantaloni J., S. Radev, Application de la Vélocimétrie Par Images et de l'Anémométrie Phase Doppler à l'Etude des Ecoulements Gaz-Solides en Lit Fluidisés Circulants, *6ème Congrès Francophone de Vélocimétrie Laser*, 22-25 Septembre, St-Louis, paper B1, 1998.

[C17] **Onofri F.**, Sur la Granulométrie et la Mesure d'Indice de Réfraction de Particules Sphériques par Analyse de la Diffusion autour de l'Angle Critique , *6ème Congrès Francophone de Vélocimétrie Laser*, 22-25 Septembre, St-Louis, papier E1, 1998.

[C18] **Onofri F.**, On the Optical Sizing and Refractive Index Measurements of Spherical Particles using the Critical Scattering Angle , *5th International Congress on Optical Particle Sizing*, 10-14th Août, Mineapolis, USA, pp. 73-76, 1998.

[C19] **Onofri F.**, Van den Moortel T., Tadrist L., Experimental analysis of spatial and temporal two-phase flows structures in Circulating Fluidized Beds using particles Images velocimetry and Phase Doppler Anemometry, *9th Int. Symp. on Appl. of Laser Tech. to Fluid Mech.*, July 13-16th, Lisbon (Portugal), paper 24.5, 1998.

[C20] **Onofri F.**, Bergounoux L., Firpo J-L., Mesguish-Ripault J., Velocity, size and concentration measurements of optically inhomogeneous cylindrical and spherical particles*, 9th Int. Symposium. on Application. of Laser Techniques to Fluid Mechanics*, 13-16th Juillet, Lisbon (Portugal), paper 9.2, 1998.

[C21] **Onofri F.,** Lenoble A., Radev S., Interférométrie Phase Doppler à sondes optiques monochromatiques non cohérentes entre elles, *7ème Congrès Francophone de Vélocimétrie Laser*, 19-22 Sept., Marseille, pages 59-66, 2000.

[C22] Gicquel P., **Onofri F.,** Tanguy, B. and Vingert L., Travaux expérimentaux d'analyse granulométrique des écoulements cryogeniques en combustion, *7ème Congrès Francophone de Vélocimétrie Laser*, 19-22 Sept., Marseille, pages 165-73, 2000.

[C23] **Onofri F.,** Etude numérique et expérimentale de la sensibilité de l'anamométrie phase Doppler à l'état de surface des particules détectées, *7ème Congrès Francophone de Vélocimétrie Laser*, 19-22 Sept., Marseille, pages 335-42, 2000.

[C24] **Onofri F.,** Lenoble A., Radev S., Superimposed monochromatic probe volumes to extend the Phase Doppler size range**,** *10th Int. Symp. on Appl. of Laser Tech. to Fluid Mech.* 10-13th july, Lisbon (Portugal), paper 20.1, 2000.

[C25] **Onofri F.,** Lenoble A., Radev S., Sizing of single fibers under torsional stress**,** *6th International Congress on Optical Particle Characterization*, 1-4th April, Brighton, UK, paper. 7, 2001.

[C26] Radev S., Kaschiev M., Koleva, M., Tadrist L., and **Onofri F.**, Effects of the velocity discontinuity on the nonlinear instability of a compound capillary jet, *Proceedings of the 9th National Congress on Theoretical and Applied Mechanics*, 19-22 Sept., Sofia(Bulagria), pp-65-69, 2001.

[C27] **Onofri F.,** Lenoble A., Bultynck H., Guering P-H. and Marsault N. Superimposed monochromatic probe volumes to extend the Phase Doppler Anemometry size. *11th Int. Symp. on Appl. of Laser Tech. to Fluid Mech.*, 8-11th july, Lisbon, session 22, 12 pages, 2002.

[C28] Wysoczanski D., Mroczka M. and **Onofri F.,** Influence of physiological conditions on optical parameters and scattering properties of red blood cells*, 11th Int. Symp. on Appl. of Laser Tech. to Fluid Mech.*, 8-11th july, Lisbon (Portugal), session 19, 11 pages, 2002.

[C29] **Onofri F.,** Lenoble A., Bultynck H., Guering P-H. and Marsault N., Diffusion de la lumière par des fibres de verre biréfringentes uniaxe et granulométrie temps réel, *8ème Congrès Francophone de Vélocimétrie Laser*, Orsay, 17-20 Sept., session TA2, 6 pages, 2002.

[C30] **Onofri F.,** Lenoble A. and Radev S. , Granulométrie optique de particules en écoulement par interférométrie Phase Doppler, *Colloque de la Société Française d'Optique Contrôles et Mesures Optiques pour l'Industrie*, 18-22 Nov St Aubin de Médoc, 8 pages, 2002.

[C31] Lenoble A., **Onofri F.** and Radev S. Modélisation physique du procédé de fibrage des fibres de renforcement. *Congrès Français de Thermique*, 3-6 juin, Vittel (France)-Elsevier, pp. 139-144, 2002.

[C32] Abdeljabar R., Safi M.J., **Onofri F.**, P.I.V Observations of the double-diffusive convection system, *Int. Conf. on Therm. Eng.: Theory and Applications*, May 31-June 4, Beirut, Lebanon, paper DD1-02, 2004

[C33] Wysoczański D., Mroczka M. and **Onofri F.**, Parametry optyczne erytrocytów w badaniach utlenowania i ciśnienia osmotycznego krwi, *Kongres Metrologii 2004*, Wroclaw, 6-9 Sept. 4 pages, 2004.

[C34] **Onofri F.,** Guering P-H. and Radev S., Light scattering properties and high-resolution diffractometry of homogeneous and non homogeneous fibres, *Proc. of the 7th Int. Cong. on Opt; Part. Charact.* Kyoto, 1-5 Aug. 2004.

[C35] **Onofri F.** and Radev S, 3-Coherent Beams Phase Doppler and Laser Doppler Velocimetry Measurements Techniques, *12th Int. Symp. on Appl. Of Laser Tech. to Fluid Mech.*, 12-15th Jul. Lisbon (Portugal), paper 25.5, 12 pages, 2004.

[C36] **Onofri F.**, Lenoble A., Guering P-H. Optical monitoring and study of the stability of a reinforcement glass fibres Drawing process, *XXth Int. Congress on Glass*, paper O-04-002, Sept. 26-Oct. 1, Kyoto (Japan), 6 pages, 2004.

[C37] **Onofri F.** and Guéring *P.-H.,* Diffusion de la lumière et diffractométrie haute résolution de fibres homogènes et à gradient radial d'indice, *9ème Congrès Francophone de Vélocimétrie Laser,* 14-17th Sept. ULB-VKI, Bruxelles, paper F.1, 8 pages, 2004.

[C38] **Onofri F.** and Bonnet J-P., Interprétation par le calcul des séries de Debye de certains mécanismes de diffusion de la lumière, *9ème Congrès Francophone de Vélocimétrie Laser,* 14-17 Sept. ULB-VKI, Bruxelles, paper D.6, 8 pages, 2004.

[C39] Abdeljabar R. and **Onofri F.** Observation par PIV des mécanismes d'instabilités convectives d'une zone inter faciale des deux couches miscibles stratifiées, *9ème Congrès Francophone de Vélocimétrie Laser,* 14-17 Sept., ULB-VKI, Bruxelles, paper D.12, 7 pages, 2004.

[C40] **Onofri F.,** Etat de l'Art de Granulométrie Laser en Mécanique des Fluides, *9ème Congrès Francophone de Vélocimétrie Laser,* 14-17 Sept., ULB-VKI, Bruxelles, paper C.F. 2, 13 pages, 2004.

[C41] Berggenblock T., Johnssson, Leckner B., **Onofri F.,** Tadrist L. Analysis of mesoscale structures in a circulating fluidized bed using phase Dopller analyser, proc. Of the *11th Conf. on Fluidization* (Eds. U. Arena et al., Eng. Conf. Int.), Ischia (Italy), paper HR9, 2004.

[C42] Hespel C., Ren K.,**Onofri F.**, Gréhan G., Etude numérique d'un granulo-vélocimétre phase Doppler à points chauds, *20ème Congrès Français sur les Aérosols*, Paris, 8-9 Dec. 2004, 8 pages.

8.2.4 Séminaires et Journées Thématiques, Rapports et Logiciels

Logiciels[29]

[L1] **Onofri F.**, Logiciel d'acquisition et traitement de signaux phase Doppler, SFO v1.0 , INSA de Rouen, Juillet 1996.

[L2] **Onofri F.**, Logiciel de Vélocimétrie par Imagerie de Particules : application à l'étude d'un Lit Fluidisé Circulant, PIVO 1.0, IUSTI-UMR 6595, Août 1997.

[L3] Firpo J-L., **Onofri F.**, Logiciel de simulation des propriétés de diffusion d'un cylindre hétérogène par la méthode de Monte Carlo, Cylindre v1.0, IUSTI-UMR 6595, Juin 1997.

[L4] **Onofri F.**, Logiciel d'acquisition et de traitement d'un diffractomètre haute résolution, HIREDI v1.0, IUSTI-UMR 6595, Juin 2003.

[L5] **Onofri F.**, Logiciel de d'acquisition et de traitement d'un interféromètre laser adapté à la mesure de fibres, FIBS v3.0, IUSTI-UMR 6595, Sept. 2004.

[L6] **Onofri F.**, Logiciel de simulation des propriétés de diffusion de particules sphériques isolées, DELPI v1.0, IUSTI-UMR 6595, Sept. 2004.

[L7] **Onofri F.**, Logiciel de simulation des propriétés de diffusion de la lumière de fibres optiques isolées, à gradients d'indice, DELFI, v2.0, IUSTI-UMR 6595, Sept. 2004.

[29] Voir les pages 89 à 93.

Rapports de contrats d'étude

[RC1] **Onofri F.**, Girasole T., Gréhan G. and Gouesbet G., Contribution of the L.E.S.P to the Optimization of the Optical design and Properties of the Dual Mode System, LESP-CORIA UNR CNRS 6614/Dantec-Invent, *rapport de contrat,* étape 1/2, 47 pages, 1994.

[RC2] **Onofri F.**, Girasole T., Gréhan G. and Gouesbet G., On the estimation of the XY cross section area of the DM-PDA, LESP/Dantec-Invent, *rapport de contrat,* final 2/2, 30 pages, 1995.

[RC3] Bultynck H., **Onofri F.** and Gréhan G., Sonde rétrodiffusion miniature, LESP/Renault-Siemens, *rapport de contrat,* étape 1/4, 10 pages, 1995.

[RC4] **Onofri F.**, Gréhan G., Etude de l'origine des taux de fluctuations de vitesse anormales observées avec le système phase Doppler Aerometrics, LESP/ EDF-LNH*, rapport de contrat,* final 1/1*,* 14 pages, 1995.

[RC5] **Onofri F.**, Garo A.., Gréhan G. and Gouesbet G., Développement d'une méthode de détection des cénosphères, *Action Incitative : Physique des phénomènes interraciaux: transferts thermiques et combustion,* LESP/DSP8, *rapport de contrat,* final 1/1, 8 pages, 1995.

[RC6] **Onofri F.**, Optimisation numérique de la configuration expérimentale à adopter lors de la campagne de mesure des champs de vitesse particulaire/fluide du foyer oxygène/hydrogène «Mascotte», IUSTI-UMR CNRS 6595/SEP-SNECMA*, rapport de contrat n°980006,* étape 1/2, 17 pages, Sept. 1998.

[RC7] **Onofri F.**, Optimisation numérique de la configuration expérimentale à adopter lors de la campagne de mesure des champs de vitesse particulaire/fluide du foyer oxygène/hydrogène «Mascotte»*,* IUSTI/SEP-SNECMA, *rapport de contrat n°980006,* final 2/2, 15 pages, Dec. 1998.

[RC8] **Onofri F.**, Etude d'un système de contrôle du diamètre d'une fibre de verre en déplacement longitudinal, IUSTI /Saint-Gobain Recherche(SGR)*, rapport de contrat n°980437,* étape 1/2, 50 pages, Jan. 1999.

[RC9] **Onofri F.**, Etude d'un système de contrôle du diamètre d'une fibre de verre en déplacement longitudinal, IUSTI/SGR*, rapport de contrat n°980437,* final 2/2, 20 pages, Mai 1999.

[RC10] **Onofri F.**, Etude sur site des fluctuations en diamètre d'une fibre de verre et des mécanismes de déstabilisation du processus de fibrage, IUSTI/ SGR*, rapport de contrat n°990437,* final 1/1*,* 36 pages, Juil. 1999.

[RC11] G. Chareyre, **Onofri F.**, B. Dalloz, Evaluation de la fraction Volatile d'un échantillon de ciment, IUSTI/CTG Italcimenti Group, *rapport de contrat n°200034,* final 1/1*,* 27 pages, Sept. 2000.

[RC12] **Onofri F.**, Lenoble A., Résultats de la campagne de mesures effectuée du 3-7 Juillet 2000 sur la filière mono téton d'Aubervilliers, IUSTI/ SGR, *rapport de contrat n°000503,* étape 1/5*,* 26 pages, Oct. 2000.

[RC13] Lenoble, **Onofri F.**, Etat de l'art de la modélisation du Fibrage du verre, IUSTI/ SGR, *rapport de contrat n°000503,* étape 2/5, 14 pages, Mars 2001

[RC14] **Onofri F.**, Lenoble, Etat d'avancement de l'interféromètre rétrodiffusion pour le contrôle des fluctuations en diamètre d'une fibre de verre en sortie de filière, IUSTI/SGR, *rapport de contrat n°000503,* étape 3/5, 39 pages, Mars 2001

[RC15] **Onofri F.**, Lenoble, L'interféromètre, la filière Vétrotex : son instrumentation et ses coûts de fonctionnement pour l'IUSTI, IUSTI/SGR, *rapport de contrat n°000503,* étape 2/5, 14 pages, Août 2001

[RC16] Lenoble A., **Onofri F.**, Code de calcul développé par l 'IUSTI pour la modélisation du procédé de fibrage du verre, IUSTI/ SGR, *rapport de contrat n°000503,* étape 5/5*,* 15 pages, Août 2001.

[RC17] **Onofri F.**, Lenoble, Etat d'avancement de l 'interféromètre FIBS : Optique, Mécanique et Logiciel, IUSTI/ SGR, *rapport de contrat n°010622,* étape 1/2*,* 17 pages, Janv. 2002.

[RC18] Lenoble A., **Onofri F.**, Dernières évolutions de l'interféromètre FIBS, *IUSTI/SGR, rapport de contrat n° 010622,* étape 2/2, 17 pages, Sept. 2002.

[RC19] **Onofri F.**, Gréhan G., Cartellier A., Benech P, Blondel D., IUSTI-CORIA-LEGI-IMEP-Dantec/FNS-DGA-CNRS*, ACI n°47 «VTAMA», rapport d'état d'avancement* n°1/4*,* 3 pages, Fev. 2004.

[RC20] **Onofri F.**, Gréhan G., Cartellier A., Benech P, Blondel D., IUSTI-CORIA-LEGI-IMEP-Dantec/FNS-DGA-CNRS, *ACI n°47 «VTAMA», rapport d'état d'avancement* n°2/4*,* 21 pages, Avril 2004.

[RC21] **Onofri F.**, Gréhan G., Cartellier A., Benech P, Blondel D., IUSTI-CORIA-LEGI-IMEP-Dantec/FNS-DGA-CNRS, *ACI n°47 «VTAMA», rapport d'état d'avancement* n°3/4*,* 3 pages, Janv. 2005.

Rapports internes

[RI1] **Onofri F.**, Gréhan G., Principe d'un PDA non sujet aux effets de trajectoire permettant la mesure simultanée de deux composantes de vitesse et du diamètre de particules d'indice de réfraction inconnu, *Rapport Interne*, LESP-UMR n°6614 CNRS – Univ. de Rouen, 5 pages, Sept. 1993.

[RI2] **Onofri F.**, Modèle de la sphère à gradient d'indice concentrique discret éclairée par un faisceau de forme arbitraire, *Rapport Interne*, LESP-UMR n°6614 CNRS-Univ. de Rouen, 40 pages, Janv. 1995.

[RI3] **Onofri F.**, On the use of "MultDiag.f" : computation of scattering diagrams for a multilayered sphere arbitrarily located in a gaussian beam, *Rapport Interne*, LESP-UMR n°6614 CNRS – Univ. de Rouen, 27 pages,1995.

[RI4] **Onofri F.**, H. Bultynck, Anémométrie à Rapport d'Intensité Chromatique (ARIC) : principe d'une technique original de mesure de la vitesse et de la hauteur de particules en écoulement dans une couche limite, rapport interne, *Rapport Interne*, LESP-UMR n°6614 CNRS – Univ. de Rouen, 25 pages, Juil. 1996.

[RI5] **Onofri F.**, Hohmann S., Wittig X. Numerical Investigation of evaporation and optical properties of fuels droplets in diesel engines conditions. Sensibility of Phase Doppler Anemometry to refractive index gradients, *Rapport Interne*, IUSTI-UMR 6595 CNRS - Univ. de Provence, Marseille, 10 pages, Dec. 1997.

[RI6] **Onofri F.**, Mesure simultanée de l'indice et du diamètre par diffusion critique : méthode d'inversion des équations de l'Approximation d'Optique Physique, *Rapport Interne*, IUSTI-UMR 6595 CNRS - Univ. de Provence, Marseille, 5 pages, Jan. 1998.

[RI7] **Onofri F.**, Modèle de diffusion d'un cylindre multicouche éclairé par une onde plane, *Rapport Interne*, IUSTI-UMR 6595 CNRS -Univ. de Provence, Marseille, 33 pages, Nov. 2002.

[RI8] **Onofri F**., Calcul des séries de Debye pour la sphère et le cylindre homogènes, *Rapport Interne*, IUSTI-UMR 6595 CNRS-Univ. de Provence, Marseille, 23 pages, Nov. 2003.

[RI9] **Onofri F**., Manuel d'utilisation du logiciel de vélocimétrie par images de particules : PIVO 2.1, *Rapport Interne*, IUSTI-UMR 6595 CNRS-Univ. de Provence, Marseille, 11 pages, Mai. 2004.

[RI10] **Onofri F**., Software and Interferometric device for the sizing of a single fibre with fix orientation: FIBS 2.1, *Rapport Interne*, IUSTI-UMR 6595 CNRS-Univ. de Provence, Marseille, 47 pages, Oct. 2004.

Séminaires et journées thématiques

[S1] **Onofri F.**, Gréhan G. et Gouesbet G., Presentation of the news tools and numerical results from LESP, *Séminaire invité dans le cadre d'une collaboration*, LSTM-Erlangen (Allemagne), Feb. 1993.

[S2] **Onofri F.**, Développements récents de l'Anémométrie Phase Doppler, *Séminaire invité,* IMFT, Toulouse, Janv. 1995.

[S3] **Onofri F.**, Mesure d'indice par Anémométrie Phase Doppler, *Séminaire invité,* Institut Von Karman, Waterloo (Belgique), Fev. 1995.

[S4] **Onofri F.** and Gréhan G., Measurements of refractive index of flying droplets with PhaseDoppler Anemometry, *11th Topical meeting*, Int. Flame Research Foundation, Biarritz, Oct. 1995.

[S5] **Onofri F.**, Optical sizing of small particles, *Séminaire invité dans le cadre d'une collaboration*, Académie des Sciences de Bulgarie, Sofia, 1998.

[S6] **Onofri F.**, Diagnostics laser en mécanique des fluides, *Séminaire invité dans le cadre d'une collaboration*, ENIT, Tunis (Tunisie), 2000.

[S7] **Onofri F.**, Sur la granulométrie haute résolution de fibres de verre en cours d'étirement, *Organisation et séminaire, 7ème Journée thématique de l'AFVL*, Meudon, Mars 2002.

[S8] **Onofri F.**, Diffusion de Mie et Interférométrie Phase Doppler à N-Faisceaux: cas des fibres étirées, *Séminaire invité, 8ème Journée thématique de l'AFVL*, Meudon, Déc. 2002.

[S9] **Onofri F.**, Etat de l'art de la granulométrie optique en mécanique des fluides, *Séminaire invité dans le cadre de la 3ème Journée FERMAT,* Toulouse, Dec. 2004.

8.2.5 Thèse

[T1] **Onofri F.**, Prise en compte de la dimension finie des faisceaux d'éclairage en granulométrie optique: Anémométrie phase Doppler- Diagnostics des milieux diphasiques, Thèse de l'Université de Rouen, Nov. 1995.

8.3 Enseignement et diffusion de l'information scientifique et technique

8.3.1 Thèses dirigées et encadrements ponctuels

Type : Encadrement d'un doctorant Allemand de l'université d'Aahren : S. Howmann, 1996
Sujet : Influence des gradients thermiques sur la caractérisation optique de gouttelettes de fuel en cours de combustion
Taux d'encadrement : 80% sur 3 mois

Type : Encadrement d'un doctorant danois de l'université d'Aalborg : C. Ibsen, 2002
Sujet : Etude des instabilités spatiales dans les écoulements en Lit fluidisé circulant
Taux d'encadrement : 80% sur 3 mois

Type : Encadrement d'un doctorant Suédois de l'université de Chalmers: T. Berggenblock
Sujet : Caractérisation expérimentale d'une vitesse Eulérienne dans les écoulement en Lit fluidisé circulant »
Taux d'encadrement : 80% sur 2 mois

Type : **Thèse de doctorat** de M^elle^ Anne Lenoble, Université de Provence, Avril 2004.
Sujet : Etude Expérimentale et Modélisation Physique d'un Procédé de Fibrage du Verre
Taux d'encadrement : 100% (dérogation obtenue pour la direction officielle)
Financement de la bourse de thèse : ADEME et Saint-Gobain Recherche

8.3.2 Encadrement de stagiaires (DEA, Ingénieurs, Maîtrise)

Type: stage de DEA, Université de Rouen : D. Blondel, 1995.
Taux et durée de l'encadrement: 100%, 6 mois.
Sujet : Détection des particules à cœur en écoulement, cas des « cénosphères ».

Type: stage de DEA, Université de Rouen : J.P. Pagès, 1995.
Taux et durée de l'encadrement: 50%, 6 mois.
Sujet : Particules avec gradient radial d'indice : simulation de l'évolution temporelle et diagnostic optique.

Type: Stage de DEA, Université de la Méditerranée : A. Bensallah, 1998.
Taux et durée de l'encadrement: 90%, 4 mois.
Sujet : Développement d'un protocole expérimental pour la mesure de la vitesse de glissement dans les écoulements en Lit Fluidisé Circulant.

Type: Stage de DEA, IUSTI-Université de Provence/Saint Gobain, 2000 : A. Deroche, 2000.
Taux et durée de l'encadrement: 100%, 6 mois.
Sujet : Etude sur site des fluctuations en diamètre d'une fibre de verre en sortie de filière et de l'origine des mécanismes de déstabilisation du processus de fibrage

Type: stage de DEA, Université d'Orsay (Paris XI)/Saint-Gobain : A. Lenoble, 2001.
Taux et durée de l'encadrement: 100%, 6 mois.
Sujet : Modes d'Instabilité d'un Procédé de Fibrage du Verre

Type: Stage de DEA, IUSTI-Université de Provence : J-P. Bonnet, 2004.
Taux et durée de l'encadrement: 90%, 5 mois.
Sujet : Amélioration du protocole expérimental pour la mesure de la vitesse de glissement dans les écoulements en Lit Fluidisé Circulant

Type: stages de 2ème année du cycle Ingénieur ou de Maîtrise
Taux et durée de l'encadrement : 100%, 2 mois.
Sujets :

- Effets de la perte de charge de la grille de fluidisation sur un lit dense : A. Rothisburger, IUSTI, 1998.
- Modélisation des propriétés de diffusion d'un jet variqueux : F. Ovofen, 1999.
- Optimisation d'un système phase doppler rétro diffusion : X. Sylvain, Ecole de l'Air, 2003.
- Mesure de la vitesse d'une surface spéculaire par thermographie infra rouge : A. Boé, IUSTI, 2004
- Extension de l'anémométrie Phase Doppler à la mesure d'indice, M. Lecart : IUSTI-Ecole de l'Air, 2004.
- Arc-en-Ciel global: développement d'une technique non intrusive de mesure d'indices et de tailles, M. Ouedrago go, IUSTI-Ecole de l'Air, 2005.

8.3.3 Participation à l'enseignement

Type: Travaux dirigés d'électricité, électrostatique et électronique, DEUG B 1ère année, Université de Rouen.
Volume horaire et statut: 24 heures de TD, vacataire, 1994.

Type: Travaux dirigés et pratiques de physique expérimentale (thermodynamique, électronique, statistiques…), DEUG A 2ème année, Université de Rouen.
Volume horaire et statut: 48 heures de TD/TP, vacataire, 1994.

Type: Travaux dirigés d'optique, Licence de Physique, Université de Rouen
Volume horaire et statut: 24 heures de TD, vacataire, 1995.

Type: Travaux pratiques d'optique, Maîtrise ès Science, Université de Rouen
Volume horaire et statut: 36 heures de TD, vacataire, 1995.

Type: Travaux pratiques de thermique, élèves ingénieurs de 3ème année, INSA de Rouen.
Volume horaire et statut: 52 heures de TP, Attaché Temporaire d'Enseignement et Recherche (ATER), 1996.

Type: Travaux pratiques sur les méthodes de mesure en Mécanique des Fluides, élèves ingénieurs de 3ème année, INSA de Rouen.
Volume horaire et statut: 52 heures de TP, ATER, 1996.

Type: Cours de Traitement du Signal et Applications à la Métrologie des Ecoulements, élèves ingénieurs de 2ème année, IUSTI, Université de Provence, 2000.
Volume horaire et statut: 10 heures de cours, vacataire.

Type: Cours de Métrologie Optique des Ecoulements, DEA de Mécanique Energétique/élèves ingénieurs de 3ème année, ENIT-Tunisie, 2001.
Volume horaire et statut: 18 heures de cours (dans le cadre d'un projet ce recherche).

Type: Cours de Métrologie Optique des Ecoulements, DEA de Mécanique Energétique/élèves ingénieurs de 3ème année et MASTER, IUSTI-UMR CNRS 6595-Université de Provence, de **1998 à 2004**
Volume horaire et statut: 12 à 18 heures de cours, vacataire.

Type: Cours sur la Diffusion de la lumière et la granulométrie optique, Ecole d'automne «Vélocimétrie et Granulométrie optique en Mécanique des Fluides», Oléron, Sep. **2003 et 2005.**
Volume horaire et statut: modules de 1h30 heures cours, *invité.*

8.4 Transferts technologiques

8.4.1 Brevets

Type: Brevet Allemand [B1], 1993
Sujet: Principe d'un granulomètre phase Doppler fonctionnant suivant une géométrie plane.

Type: Brevet Européen [B2], 1994
Sujet: Principe du système phase Doppler « Dual Mode » pour une amélioration significative des mesures de flux.
Remarque : la société Dantec Dynamics [49] exploite ce brevet, (§ 3.1.1).

Remarque pour 1998 :
Type: Demande d'ouverture d'un dossier de valorisation pour le dépôt d'un brevet CNRS
Sujet: Réfractomètre à angle d'arc-en-ciel et angle critique : « Réfractomètre à capillaire »
Conclusion du FIST: non rentable financièrement pour le CNRS, il faut chercher un partenaire industriel…

8.4.2 Contrats de recherche et projets financés

[F1] *Type :* contrat d'étude, 1994
Responsable : G. Gréhan (LESP, Rouen)
Entreprise : Dantec Measurement Technology (Danemark)
Sujet : Optimisation numérique de la géométrie Dual Mode et détermination numérique du volume d'un granulomètre Pgase Doppler : Dual Mode PDA.
Contribution personnelle: Prise en charge à 80% de l'étude et de la rédaction des rapports
Montant estimé : 150 kF H.T

[F2] *Type :* contrat d'étude, 1994
Responsable : G. Gréhan (LESP, Rouen)
Entreprise : EDF-LNH
Sujet : Etude des fluctuations du taux de turbulence enregistrés avec le système phase Doppler Aerometrics
Contribution personnelle: Prise en charge à 100% de l'étude et de la rédaction du rapport final
Montant estimé : 300 kF H.T (avec le matériel)

[F3] *Type :* Action incitative/CNRS DSP8, « Physique des phénomènes interfaciaux: transferts thermiques et combustion », 1995
Responsables : G. Gréhan - A. Garo (LESP-CORIA, Rouen)
Sujet : Détection de particules à cœur (cénosphères) et détection des particules à gradient d'indice
Contribution personnelle: Extension de la théorie de Lorenz-Mie aux particules multicouches, développement de codes de calculs, encadrement de 2 stagaires de DEA à 50% et 100%.
Support obtenu : 100 kF H.T.

[F4] *Type :* contrat d'étude, 1996
Responsable : G. Gréhan (LESP, Rouen)
Entreprise : Renault & Siemens
Sujet : Développement d'une sonde rétrodiffusion miniature permettant le suivi de la granulométrie dans un moteur à explosion
Contribution personnelle: définition des caractéristiques du premier prototype et rédaction de la première proposition d'étude.
Montant estimé : 300 kF H.T

[F5] *Type :* contrat d'étude n°980006, 1998
Responsable : **F. Onofri**
Entreprise : Société Européenne de Propulsion (SEP-SNECMA)
Cadre : GDR « Combustion dans les moteurs fusée »

Sujet : Optimisation numérique du système de mesure de la vitesse de glissement sur le banc cryogénique oxygène/hydrogène « Mascotte » de l'ONERA
Montant : 50 kF H.T.

[F6] *Type :* contrat d'étude n°980437, 1998
Responsable : **F. Onofri**
Entreprise : Saint-Gobain Recherche (SGR), Aubervilliers.
Sujet : Simulation numérique des caractéristiques d'un système optique de contrôle du diamètre d'une fibre de verre en déplacement longitudinal
Montant : 45 kF H.T.

[F7] *Type :* contrat d'étude n°990437 et bourse de DEA, 1999
Responsable : **F. Onofri**
Entreprise : Saint-Gobain Recherche (SGR)
Sujet : Etude sur site des fluctuations en diamètre d'une fibre de verre en sortie de filière
Montant : 50 kF H.T (hors indemnités)

[F8] *Type :* contrat d'étude n°000503, bourses de DEA et de thèse, 2000
Responsable : **F. Onofri**
Entreprise : Saint-Gobain Recherche (SGR)
Coninanceur des bourses : ADEME
Sujet : Développement d'un interféromètre rétrodiffusion pour l'étude des fluctuations en diamètre d'une fibre de verre en sortie de filière : application à la réduction des déchets verriers »
Montant total: 390 kF H.T. (dont 160 kF de matériels)

[F9] *Type :* contrat d'étude n°200034 et financement d'une bourse de DEA, 2000
Responsables: **F. Onofri** et B. Dalloz
Entreprise : CTG-Italcimenti
Sujet : Evaluation de la fraction Volatile d'un échantillon de ciment
Montant total: 66 kF H.T. (hors indemnités)

[F10] *Type :* projet «institutionnel», 2000
Responsables : L. Tadrist et **F. Onofri**
Financeurs : le FEDER (Europe), la Région PACA et le Conseil général des Bouches du Rhône
Sujet : Création d'une plate-forme de fluidisation
Montant total: 9.5 MF H.T.

[F11] *Type :* contrat d'étude n°010622 et financement d'un stage de DEA, 2002
Responsable : **F. Onofri**
Entreprise : Saint-Gobain Recherche et Vetrotex International
Sujet : Etude des conditions de stabilité d'un procédé de fibrage du verre
Montant total: 13.8 k€ H.T.

[F12] *Type :* Action incitative «Pollution-Non Pollution» n°47, «VITAMA», 2004
Responsable global du projet : **F. Onofri**
Financeurs : FNS, CNRS et DGA
Laboratoires et industriels participants à ce projet: CORIA-Rouen, LEGI-Grenoble, IMEP-Grenoble, Dantec-Danemark
Sujet : Caractérisation simultanée de la vitesse, de la taille et du matériau de particules en écoulement
Montant total: 125 k€ TTC (dont 55% pour l'IUSTI)

[F13] *Type :* contrat d'étude, 2005
Responsable : **F. Onofri**
Entreprise : CERSA-MCI
Sujet : Modélisation des propriétés de diffusion de fibres optiques : caractérisation des indices de réfraction.
Montant total: 3 k€ H.T.

8.4.3 Activité de consultance

[P1] *Type :* contrat de Consultant, 2000
Entreprise : Saint-Gobain Recherche, Aubervilliers
Sujet : Expertise sur la granulométrie optique de fibres homogènes

[P2] *Type :* contrat de Consultant, 2004
Entreprise : Saint-Gobain Conception Verrière, Chalon sur Saône
Sujet : Expertise sur la caractérisation optique d'écoulements modèles

[P3] *Type :* contrat de Consultant, 2004-2005
Entreprise : Saint-Gobain Vetrotex International, Chambéry.
Sujet : Expertise sur le contrôle de la stabilité d'un procédé de fibrage du verre.

8.5 Encadrement, animation et management de la recherche

8.5.1 Animation de programmes ou de projets

Direction d'équipe ou de laboratoire

Type : Responsable d'une opération de recherche, 2000-
Sujet : Diagnostics Optiques des Milieux Multiphasiques
Remarque : Je suis actuellement l'unique chercheur titulaire à émarger dans cette opération…

Type : **Responsable de l'ACI** « Pollution Non –Pollution », projet n°47, 2004-
Sujet : Caractérisation simultanée de la vitesse, de la taille et du matériau de particules en écoulement (VITAMA)
Nombre de partenaires : 4 laboratoires (IUSTI, CORIA, LEGI, IMEP) et 1 industriel (DANTEC Dynamics), soit près de 20 personnes

Participation à des conseils scientifiques et commissions, comités de lecture

Participation à des conseils scientifiques et commissions :

Membre titulaire du conseil de laboratoire de l' IUSTI UMR 6595- CNRS-Université de Provence.
D*ate :* 2000-2004-,mandat renouvelé pour la période 2004- 2008).

Membre suppléant de la commission de spécialistes de l'Université de Provence, section : 62.
Date : 1998-2001

Membre titulaire de la commission de spécialistes de l'Université de Rouen, sections: n°30, 60, 62.
Date : 2000-2004-,mandat renouvelé pour la période 2004- 2008).

Membre de sociétés savantes

Membre du conseil d'administration et trésorier de l'Association Francophone de Vélocimétrie Laser (AVFL)

Membre des Sociétés Française et Européenne d'Optique (SFO, EOS)

Comités de lecture de revues scientifiques

Particle and Particle Systems Characterization, *Wiley-VCH Verlag,* 1998-

Atomization and Sprays, *Begell House Inc.,* 1999-

Experiments in fluids, *Springer-Verlag*, 2002-

Applied Optics, *OSA-Opt. Soc. of America*, 2002-

Aerospace Science and Technology, *Elsevier*, 2002-

Journal of BioMedical Optics, *SPIE-Int. Soc. For Opt. Eng.*, 2004-

Journal of Loss Prevention in the Process Industries, *Elsevier*, 2005-

Participation à l'organisation de congrès, journées thématiques, écoles…

Président de session lors du *7th Int. Symp. on Appl. of Laser Tech. to Fluid Mech.*, Lisbon, Portugal, 11-14th Jul., 1994.

Président de session lors du *8th Int. Symp. on Appl. of Laser Tech. to Fluid Mech.*, Lisbon, Portugal, 8-11th Jul., 1996.

Président de session lors du *9th Int. Symp. on Appl. of Laser Tech. to Fluid Mech.*, Lisbon, Portugal, 13-16th Jul., 1998.

Président de session lors du *5th Int. Cong. on Optical Particle Sizing*, Minneapolis, USA, 10-14th Aug., 1998.

Membre du comité scientifique du *Int. Conf. on Optical technology and Image processing in Fluid, Thermal and Combus tion Flow-VSJ-SPIE*, Yokohama, Japon, 6-10th Dec., 1998.

Membre du comité local d'organisation du *7ème Congrès Francophone de Vélocimétrie Laser*, Marseille, 19-22 Sept., 2000.

Organisateur de la *9ème journée thématique de l'AFVL* «Granulométrie et vélocimétrie d'écoulement à basses vitesse», Meudon, Fev. 2002.

Président de session lors du *8ème Congrès Francophone de Vélocimétrie Laser*, Orsay, 17-20 Sept., 2002.

Président de session lors du *12th Int. Symp. on Appl. of Laser Tech. to Fluid Mech.*, Lisbon, Portugal, 12-15th Jul., 2004.

Membre du comité scientifique du *9ème Congrès Francophone de Vélocimétrie Laser*, Bruxelles, 14-17 Sept., 2004-

Coorganisateur de l'école d'automne *«Vélocimétrie et Granulométrie Optique en Mécanique des Fluides »*, Oléron, Sept. 2005 (Responsables : J.M. Most, F. Onofri)

8.5.2 Collaborations académiques, séjours, ou missions sur le terrain

Programme PROCOPE, 1992-1995.
Laboratoire : LSTM, Professeur F. Durst, Unversité d'Erlangen-Nuremberg, Allemagne.
Programme : PROCOPE, du Ministère des Affaires Etrangères
Responsable français : G. Gréhan.
Financeur : Ministère des Afffaires Etrangères (séjours et transport)
Sujets : Elimination des effets de trajectoire
Séjours personnels: 17 semaines

Programme AMADEUS, projet n°99006, 1998-1999.
Responsables français: L. Tadrist et **F. Onofri**
Partenaire : ITW, Prof. Linzer, Université Technique de Vienne (Autriche).
Financeur : Ministère des Afffaires Etrangères (séjours et transport)

Sujet : Lits fluidisés pressurisés et modèles du type cœur-anneau
Séjours personnels : 1 semaine

Convention d'échange CNRS-Acad. Bulgare des Sciences, projet PECO/NEI n°6617, 1999-2001.
Responsables français: **F. Onofri** et L. Tadrist
Partenaire : IMech, Pr. S. Radev, ABS, Bulgarie
Financeur : CNRS-DGRST (séjours et transport)
Sujet : Instabilité des écoulements de films de particules et jets
Séjours personnels: 3 semaines

Programme POLONIUM, projet n° 03276XD, 2001-2002.
Responsable français: **F. Onofri**
Partenaire : CEM, Prof. J. Mroczka, Université de Wroclaw (Pologne).
Financeur : Ministère des Afffaires Etrangères (séjours et transport)
Sujet : Caractérisation des propriétés de diffusion de la lumière d'échantillons sanguins
Séjours personnels : 3 semaines

Convention d'échange CNRS-Acad. Bulgare des Sciences, projet PECO/NEI n°12560, 2001-2003.
Responsables français: **F. Onofri**
Partenaire : IMech, Pr. S. Radev, ABS, Bulgarie
Financeur : CNRS-DGRST (séjours et transport)
Sujet : Instabilité des jets visqueux isothermes et non isothermes. Application au fibrage des fibres de verre.
Séjours personnels: 3 semaines

Convention d'échange CNRS-DGRST, projet n° 8684, 2000-2002.
Responsables français: **F. Onofri**
Partenaire : Laboratoire d'Energétique, Pr. M. Safi et Dr. R. Abdeljabar, ENIT (Tunisie).
Financeur : CNRS-DGRST (séjours et transport)
Sujet : Analyse par PIV des instabilités thermo solutales dans un milieu stratifié.
Séjours personnels : 3 semaines

Convention d'échange CNRS-Acad. Bulgare des Sciences, projet PECO/NEI n°16939, 2004-2005.
Responsables français: **F. Onofri**
Partenaire : IMech, Pr. S. Radev, ABS, Bulgarie
Financeur : CNRS-DGRST (séjours et transport)
Sujet : Diagnostic laser et modélisation des contraintes de torsion, des champs radiaux de température et de concentration, dans les fibres et les jets capillaires.
Séjours personnels: 1 semaine en 2004

Programme POLONIUM, projet n° 82/239590, 2005-2007
Responsable français: **F. Onofri**
Partenaire : CEM, Prof. J. Mroczka, Université de Wroclaw, Pologne.
Financeur : Ministère des Afffaires Etrangères (séjours et transport)
Sujet : Caractérisation du matériau de particules par réfractométrie Arc-en-ciel et diffusion critique
Séjours personnels : 2 semaines prévues en 2005

8.5.3 Diffusion de l'information scientifique et technique

Présentation de l'activité Diffusion de la lumière, UMR CNRS 6614-LESP
Cadre : Science en fête, 1994-1996.

Présentation de l'activité Lits fluidisés gaz-solides du laboratoire, UMR CNRS 6595-IUSTI
Cadre : Science en fête, 1997-1998.

Chapitre 9

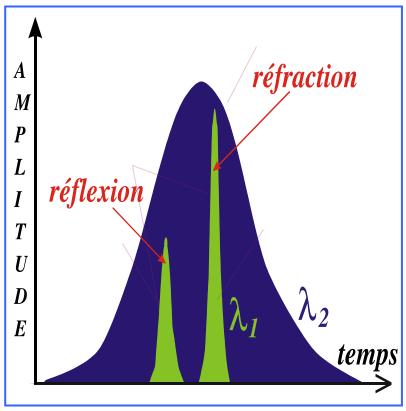

REPRODUCTIONS D'ARTICLES

Les pages qui suivent présentent les reproductions de dix articles classés par ordre chronologique :

[A2] "Electromagnetic scattering from a multilayered sphere located in an arbitrary beam"

[A4] "Phase-Doppler Anemometry with Dual Burst Technique for Measurement of Refractive Index and Absorption Coefficient Simultaneous with Size and Velocity"

[A5] "On the Optical Diagnosis and Sizing of Coated and Multilayered Particles with Phase Doppler Anemometry"

[A8] "Velocity, size and concentration measurements of optically inhomogeneous cylindrical and spherical particles"

[A9] "Critical Angle Refractometry: for simultaneous measurement of particles in flow size and relative refractive index"

[A11] "Numerical Analysis of the Nonlinear Instability of One-Dimensional Compound Capillary Jet"

[A12] "Superimposed Non Interfering Probes to extend the Phase Doppler Anemometry capabilities"

[A13] "Interferometric sizing of single-axis birefringent glass fibres"

[A15] "Optical parameters and scattering properties of red blood cells"

[A16] "High-resolution laser diffractometry for the on-line sizing of small transparent fibres

Article A2

Electromagnetic scattering from a multilayered sphere located in an arbitrary beam

F. Onofri, G. Gréhan, and G. Gouesbet

A solution is given for the problem of scattering of an arbitrary shaped beam by a multilayered sphere. Starting from Bromwich potentials and using the appropriate boundary conditions, we give expressions for the external and the internal fields. It is shown that the scattering coefficients can be generated from those established for a plane-wave illumination. Some numerical results that describe the scattering patterns and the radiation-pressure behavior when an incident Gaussian beam or a plane wave impinges on a multilayered sphere are presented.

1. Introduction

The theory of scattering of plane electromagnetic waves by spheres with isotropic and homogeneous material was first given by Lorenz[1] and Mie[2] and was further developed by Debye.[3] The theory is now referred as the Lorenz–Mie theory (LMT) and has been concisely presented by Stratton,[4] van de Hulst,[5] Kerker,[6] and Bohren and Huffman,[7] among others. During nearly one century, in spite of difficulties in the handling of numerical computations (progressively relaxed by the advent of computers and their increased efficiency and by algorithmic improvements), the LMT has been one of the most famous basic theories of the light-scattering topic.

However, with the advent of lasers and their growing use as sources for particle characterization, the LMT met one of its fundamental limitations, i.e., the assumption that the incident wave must be a plane wave. This limitation was circumvented in the eighties thanks to the advent of the generalized LMT (GLMT) that deals with the interaction between spheres and arbitrary incident beams (Refs. 8 and 9 and references therein). Although earlier developments of GLMT were concerned with the interaction between a sphere and a Gaussian beam, the case in which the incident beam is a laser sheet has been also considered.[10,11] Examples of applications are the use of radiation pressure to manipulate biological cells[12] or the analysis of the phase Doppler technique.[13,14]

Another limiting assumption of the LMT is the homogeneity of the particle material, this assumption's being shared by the GLMT. In particular, when studying two-phase phenomena in combustion, we may have to deal with nonhomogeneous particles such as heated droplets, cenospheres, or ashes.[15] In the field of biology, we may be faced with cells that are roughly spherical but nonhomogeneous, being essentially composed of a nucleus surrounded by a liquid solution and a shell.[12]

Indeed, such more complex scatterers may be investigated by the use of an extension of the LMT to multilayered spheres with many applications.[16,17] Such an extension, however, still assumes that the incident wave is a plane wave, which limits applications to the case in which the scatterer is small with respect to some characteristic dimensions of the incident beam. Recently Khaled *et al.*[18] have treated the case of light scattering by a coated sphere illuminated by an angular spectrum of plane waves used to describe a Gaussian intensity profile. This approach to describing the impinging beam has been shown[19] to be extremely time consuming and limited for practical applications.

This paper is therefore devoted to a new extension (GLMT for multilayered spheres) that allows us to deal simultaneously with arbitrary incident beams and with a class of nonhomogeneous particles. This paper is organized as follows. Section 2 introduces the Bromwich scalar potentials (BSP's) that we use to solve the problem. Section 3 defines the scattering problem and solves it, except for the set of unknown coefficients that may be determined by the use of the boundary conditions introduced in Section 4. The

The authors are with the Laboratoire d'Energétique des Systèmes et Procédés, Unité de Recherche Associée au Centre National de la Recherche Scientifique No. 230, Institut National des Sciences Appliquées de Rouen, P.O. Box 08, 76131 Mont-Saint-Aignan, France.

Received 3 June 1994; revised manuscript received 16 May 1995.
0003-6935/95/307113-12$06.00/0.

formulation is fully completed in Section 5. Section 6 is devoted to the discussion of numerical algorithms and to the presentation of exemplifying results concerning scattering diagrams and radiation pressure forces. Section 7 is a conclusion.

2. Bromwich Scalar Potentials

The incident electromagnetic beam is assumed to be monochromatic and linearly polarized, varying in time as $\exp(i\omega t)$, where ω is the angular frequency.

The Bromwich formulation enables us to obtain special solutions for Maxwell's equations in spherical coordinate systems (r, θ, φ). The general solution to Maxwell's equations is written as the sum of two special solutions with the proviso that the boundary conditions must be satisfied. These special solutions are the transverse-magnetic (TM) wave, for which $H_r = 0$, and the transverse-electric (TE) wave, for which $E_r = 0$, where H_r and E_r are the radial components of the magnetic and the electric fields respectively. They are generated by two BSP's, U_{TM} and U_{TE}, for the TM and the TE waves, respectively, for which both of them satisfy the same partial differential equation:

$$\frac{\partial^2 U}{\partial r^2} + k^2 U + \frac{1}{r^2 \sin\theta}\frac{\partial}{\partial\theta}\sin\theta\frac{\partial U}{\partial\theta} + \frac{1}{r^2\sin^2\theta}\frac{\partial^2 U}{\partial\varphi^2} = 0, \tag{1}$$

in which k is the wave number of the wave in the considered medium and is given by

$$k = \omega(\mu\epsilon)^{1/2}, \tag{2}$$

in which μ and ϵ are the permeability and the permittivity of the medium, respectively. For an $\exp(i\omega t)$ time dependence, we need to consider only BSP's of the form

$$U(r,\theta,\varphi) = \sum_{n=1}^{\infty}\sum_{m=-n}^{+n}\frac{c_n^m}{k}\begin{bmatrix}\Psi_n(kr)\\ \xi_n(kr)\end{bmatrix}P_n^{|m|}(\cos\theta)\exp(im\varphi), \tag{3}$$

which indeed are solutions of Eq. (1). The Ricatti–Bessel functions $\Psi_n(kr)$ and $\xi_n(kr)$ may be expressed as

$$\Psi_n(kr) = kr\Psi_n^{(1)}(kr), \tag{4}$$

$$\xi_n(kr) = kr\Psi_n^{(4)}(kr), \tag{5}$$

in which $\Psi_n^{(1)}(kr)$ and $\Psi_n^{(4)}(kr)$ are spherical Bessel functions given by

$$\Psi_n^{(1)}(kr) = \left(\frac{\pi}{2kr}\right)^{1/2} J_{n+1/2}(kr), \tag{6}$$

$$\Psi_n^{(4)}(kr) = \left(\frac{\pi}{2kr}\right)^{1/2} H_{n+1/2}^{(2)}(kr), \tag{7}$$

in which $J_{n+1/2}$ and $H_{n+1/2}^{(2)}$ are ordinary Bessel functions of half-integer order and Hankel functions of the second kind, respectively. In this paper, the associated Legendre polynomials $P_n^m(\cos\theta)$ are defined by

$$P_n^m(\cos\theta) = (-1)^m(\sin\theta)^m\frac{\mathrm{d}^m P_n(\cos\theta)}{(\mathrm{d}\cos\theta)^m}, \tag{8}$$

in which $P_n(\cos\theta)$ is the Legendre polynomial of order n and d is the derivative function.

From the definition of the TM and the TE waves, we have

$$H_{r,\mathrm{TM}} = E_{r,\mathrm{TE}} = 0. \tag{9}$$

Once the BSP's are known, the other field components may be obtained according to the following relations[8]:

$$E_{r,\mathrm{TM}} = \frac{\partial^2 U_{\mathrm{TM}}}{\partial r^2} + k^2 U_{\mathrm{TM}}, \tag{10}$$

$$E_{\theta,\mathrm{TM}} = \frac{1}{r}\frac{\partial^2 U_{\mathrm{TM}}}{\partial r\partial\theta}, \tag{11}$$

$$E_{\varphi,\mathrm{TM}} = \frac{1}{r\sin\theta}\frac{\partial^2 U_{\mathrm{TM}}}{\partial r\partial\varphi}, \tag{12}$$

$$H_{\theta,\mathrm{TM}} = \frac{-i\omega\epsilon}{r\sin\theta}\frac{\partial U_{\mathrm{TM}}}{\partial\varphi}, \tag{13}$$

$$H_{\varphi,\mathrm{TM}} = \frac{i\omega\epsilon}{r}\frac{\partial U_{\mathrm{TM}}}{\partial\theta}, \tag{14}$$

$$E_{\theta,\mathrm{TE}} = \frac{-i\omega\mu}{r\sin\theta}\frac{\partial U_{\mathrm{TE}}}{\partial\varphi}, \tag{15}$$

$$E_{\varphi,\mathrm{TE}} = \frac{i\omega\mu}{r}\frac{\partial U_{\mathrm{TE}}}{\partial\theta}, \tag{16}$$

$$H_{r,\mathrm{TE}} = \frac{\partial^2 U_{\mathrm{TE}}}{\partial r^2} + k^2 U_{\mathrm{TE}}, \tag{17}$$

$$H_{\theta,\mathrm{TE}} = \frac{1}{r}\frac{\partial^2 U_{\mathrm{TE}}}{\partial r\partial\theta}, \tag{18}$$

$$H_{\varphi,\mathrm{TE}} = \frac{1}{r\sin\theta}\frac{\partial^2 U_{\mathrm{TE}}}{\partial r\partial\varphi}. \tag{19}$$

3. Scattering Problem

This paper is devoted to the interaction between an arbitrary incident field and a multilayered sphere, in which the material of each layer is isotropic and homogeneous. This scattering problem is essentially solved when we know, in Eq. (3), the expansion coefficients c_n^m for the incident wave (superscript i),

the scattered wave (superscript s), and the waves inside the sphere or internal waves (subscript j for the jth layer).

A. Scatterer

The sphere is divided into L concentric layers from $j = 1$ for the core to $j = L$ for the outer layer (see Fig. 1). The jth layer has an outer diameter r_j. The material of this jth layer is characterized by magnetic and electric capacities μ_j and ϵ_j, respectively, a complex refractive index m_j, and a local wave number k_j. The external medium, denoted by a subscript 0, is assumed to be nonabsorbing.

B. Incident Wave

In the BSP expression [Eq. (3)], we have to choose the Ricatti–Bessel functions $\Psi_n(kr)$, which are the only ones to be defined at the coordinate center $r = 0$. Furthermore, the description of the incident wave in spherical coordinate systems is the same as in the GLMT, as it does not depend on whether the sphere is stratified or not. In particular, the expansion coefficients c_n^m may be expressed in terms of beam-shape coefficients (BSC's) $g_{n,\mathrm{TM}}^m$ and $g_{n,\mathrm{TE}}^m$. Then the BSP's read as[8]

$$\begin{aligned} U_{\mathrm{TM}}^i &= \frac{E_0}{k_0}\sum_{n=1}^{\infty}\sum_{m=-n}^{+n} c_n^{\mathrm{pw}} g_{n,\mathrm{TM}}^m \Psi_n(k_0 r) \\ &\quad \times P_n^{|m|}(\cos\theta)\exp(im\varphi), \\ U_{\mathrm{TE}}^i &= \frac{H_0}{k_0}\sum_{n=1}^{\infty}\sum_{m=-n}^{+n} c_n^{\mathrm{pw}} g_{n,\mathrm{TE}}^m \Psi_n(k_0 r) \\ &\quad \times P_n^{|m|}(\cos\theta)\exp(im\varphi), \end{aligned} \tag{20}$$

in which the coefficients c_n^{pw} are specific to the plane-wave case and read as

$$c_n^{\mathrm{pw}} = \frac{1}{k_0} i^{n-1}(-1)^n \frac{2n+1}{n(n+1)}. \tag{21}$$

The BSC's may be expressed in terms of quadratures according to

$$\begin{aligned} g_{n,\mathrm{TM}}^m &= \frac{(2n+1)^2}{2\pi^2 n(n+1)c_n^{\mathrm{pw}}}\frac{(n-|m|)!}{(n+|m|)!}\int_0^{\pi}\int_0^{2\pi}\int_0^{\infty}\frac{E_r^i(r,\theta,\varphi)}{E_0} \\ &\quad \times r\Psi_n^{(1)}(kr)P_n^{|m|}(\cos\theta)\exp(-im\varphi) \\ &\quad \times \sin\theta\,\mathrm{d}\theta\,\mathrm{d}\varphi\,\mathrm{d}(kr), \end{aligned} \tag{22}$$

$$\begin{aligned} g_{n,\mathrm{TE}}^m &= \frac{(2n+1)^2}{2\pi^2 n(n+1)c_n^{\mathrm{pw}}}\frac{(n-|m|)!}{(n+|m|)!}\int_0^{\pi}\int_0^{2\pi}\int_0^{\infty}\frac{H_r^i(r,\theta,\varphi)}{H_0} \\ &\quad \times r\Psi_n^{(1)}(kr)P_n^{|m|}(\cos\theta)\exp(-im\varphi) \\ &\quad \times \sin\theta\,\mathrm{d}\theta\,\mathrm{d}\varphi\,\mathrm{d}(kr). \end{aligned} \tag{23}$$

The BSC's may also be evaluated by the use of more efficient approaches: the finite-series method[20] and the localized approximation,[21] the latter's having recently receiving a rigorous formal derivation.[22,23] Between these different methods, the localized approximation is the most efficient to carry out numerical computations on desktops computers.

Applying Eqs. (9)–(19) to Eq. (20) and adding the expressions for the TM and the TE waves, we find the whole set of incident-field components:

$$\begin{aligned} E_r^i &= k_0 E_0 \sum_{n=1}^{\infty}\sum_{m=-n}^{+n} c_n^{\mathrm{pw}} g_{n,\mathrm{TM}}^m [\Psi_n''(k_0 r) + \Psi_n(k_0 r)] \\ &\quad \times P_n^{|m|}(\cos\theta)\exp(im\varphi), \end{aligned} \tag{24}$$

$$\begin{aligned} E_\theta^i &= \frac{E_0}{r}\sum_{n=1}^{\infty}\sum_{m=-n}^{+n} c_n^{\mathrm{pw}} [g_{n,\mathrm{TM}}^m \Psi_n'(k_0 r)\tau_n^{|m|}(\cos\theta) \\ &\quad + m g_{n,\mathrm{TE}}^m \Psi_n(k_0 r)\Pi_n^{|m|}(\cos\theta)]\exp(im\varphi), \end{aligned} \tag{25}$$

$$\begin{aligned} E_\varphi^i &= i\frac{E_0}{r}\sum_{n=1}^{\infty}\sum_{m=-n}^{+n} c_n^{\mathrm{pw}} [m g_{n,\mathrm{TM}}^m \Psi_n'(k_0 r)\Pi_n^{|m|}(\cos\theta) \\ &\quad + g_{n,\mathrm{TE}}^m \Psi_n(k_0 r)\tau_n^{|m|}(\cos\theta)]\exp(im\varphi), \end{aligned} \tag{26}$$

$$\begin{aligned} H_r^i &= k_0 H_0 \sum_{n=1}^{\infty}\sum_{m=-n}^{+n} c_n^{\mathrm{pw}} g_{n,\mathrm{TE}}^m [\Psi_n''(k_0 r) + \Psi_n(k_0 r)] \\ &\quad \times P_n^{|m|}(\cos\theta)\exp(im\varphi), \end{aligned} \tag{27}$$

$$\begin{aligned} H_\theta^i &= \frac{-H_0}{r}\sum_{n=1}^{\infty}\sum_{m=-n}^{+n} c_n^{\mathrm{pw}} [m g_{n,\mathrm{TM}}^m \Psi_n(k_0 r)\Pi_n^{|m|}(\cos\theta) \\ &\quad - g_{n,\mathrm{TE}}^m \Psi_n'(k_0 r)\tau_n^{|m|}(\cos\theta)]\exp(im\varphi), \end{aligned} \tag{28}$$

$$\begin{aligned} H_\varphi^i &= \frac{-iH_0}{r}\sum_{n=1}^{\infty}\sum_{m=-n}^{+n} c_n^{\mathrm{pw}} [g_{n,\mathrm{TM}}^m \Psi_n(k_0 r)\tau_n^{|m|}(\cos\theta) \\ &\quad - m g_{n,\mathrm{TE}}^m \Psi_n'(k_0 r)\Pi_n^{|m|}(\cos\theta)]\exp(im\varphi), \end{aligned} \tag{29}$$

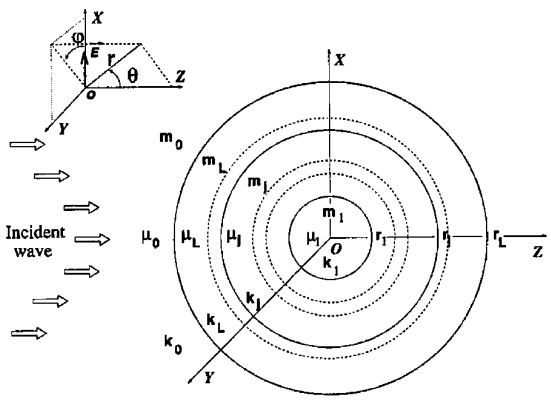

Fig. 1. Geometry of the stratified sphere.

in which the generalized Legendre functions are

$$\tau_n^k(\cos\theta) = \frac{\mathrm{d}}{\mathrm{d}\theta} P_n^k(\cos\theta) \tag{30}$$

$$\Pi_n^k(\cos\theta) = \frac{P_n^k(\cos\theta)}{\sin\theta}. \tag{31}$$

C. Scattered Wave

BSP's for the scattered wave are built by the use of the function $\xi_n(kr)$ in Eq. (3) because they are the only ones that generate an outgoing spherical wave. These BSP's may then be rewritten in the form

$$U_{\mathrm{TM}}^s = \frac{-E_0}{k_0} \sum_{n=1}^{\infty} \sum_{m=-n}^{+n} c_n^{\mathrm{pw}} A_n^m \xi_n(kr) \times P_n^{|m|}(\cos\theta)\exp(im\varphi), \tag{32}$$

$$U_{\mathrm{TE}}^s = \frac{-H_0}{k_0} \sum_{n=1}^{\infty} \sum_{m=-n}^{+n} c_n^{\mathrm{pw}} B_n^m \xi_n(kr) \times P_n^{|m|}(\cos\theta)\exp(im\varphi). \tag{33}$$

Similar to above, we apply Eqs. (9)–(19) to Eqs. (32) and (33) to obtain the scattered-field components:

$$E_r^s = -k_0 E_0 \sum_{n=1}^{\infty} \sum_{m=-n}^{+n} c_n^{\mathrm{pw}} A_n^m [\xi_n''(k_0 r) + \xi_n(k_0 r)] \times P_n^{|m|}(\cos\theta)\exp(im\varphi), \tag{34}$$

$$E_\theta^s = -\frac{E_0}{r} \sum_{n=1}^{\infty} \sum_{m=-n}^{+n} c_n^{\mathrm{pw}} [A_n^m \xi_n'(k_0 r)\tau_n^{|m|}(\cos\theta) + mB_n^m \xi_n(k_0 r)\Pi_n^{|m|}(\cos\theta)]\exp(im\varphi), \tag{35}$$

$$E_\varphi^s = -\frac{iE_0}{r} \sum_{n=1}^{\infty} \sum_{m=-n}^{+n} c_n^{\mathrm{pw}} [mA_n^m \xi_n'(k_0 r)\Pi_n^{|m|}(\cos\theta) + B_n^m \xi_n(k_0 r)\tau_n^{|m|}(\cos\theta)]\exp(im\varphi), \tag{36}$$

$$H_r^s = -k_0 H_0 \sum_{n=1}^{\infty} \sum_{m=-n}^{+n} c_n^{\mathrm{pw}} B_n^m [\xi_n''(k_0 r) + \xi_n(k_0 r)] \times P_n^{|m|}(\cos\theta)\exp(im\varphi), \tag{37}$$

$$H_\theta^s = \frac{H_0}{r} \sum_{n=1}^{\infty} \sum_{m=-n}^{+n} c_n^{\mathrm{pw}} [mA_n^m \xi_n(k_0 r)\Pi_n^{|m|}(\cos\theta) - B_n^m \xi_n'(k_0 r)\tau_n^{|m|}(\cos\theta)]\exp(im\varphi), \tag{38}$$

$$H_\varphi^s = \frac{iH_0}{r} \sum_{n=1}^{\infty} \sum_{m=-n}^{+n} c_n^{\mathrm{pw}} [A_n^m \xi_n(k_0 r)\tau_n^{|m|}(\cos\theta) - mB_n^m \xi_n'(k_0 r)\Pi_n^{|m|}(\cos\theta)]\exp(im\varphi). \tag{39}$$

D. Internal Waves

For the internal wave that corresponds to the core ($j = 1$), we must use only $\Psi_n(kr)$ in Eq. (3) as for the incident wave, $\xi_n(kr)$ not being defined for $r = 0$. Conversely, for the other internal waves ($j = 2, \ldots, L$), both $\Psi_n(kr)$ and $\xi_n(kr)$ are allowed. Therefore, BSP's for the internal waves may be rewritten as

$$U_{j\mathrm{TM}} = \frac{k_{j+1} E_0}{k_j^2} \sum_{n=1}^{\infty} \sum_{m=-n}^{+n} c_n^{\mathrm{pw}} [c_{jn}^m \Psi_n(k_j r) + e_{jn}^m \chi_n(k_j r)] \times P_n^{|m|}(\cos\theta)\exp(im\varphi),$$

$$U_{j\mathrm{TE}} = \frac{k_{j+1} H_0}{k_j^2} \sum_{n=1}^{\infty} \sum_{m=-n}^{+n} c_n^{\mathrm{pw}} [d_{jn}^m \Psi_n(k_j r) + f_{jn}^m \chi_n(k_j r)] \times P_n^{|m|}(\cos\theta)\exp(im\varphi), \tag{40}$$

in which we introduce, from future numerical considerations, the functions $\chi_n(kr)$ instead of $\xi_n(kr)$, where the functions $\chi_n(kr)$ are related to the previous Ricatti–Bessel functions by

$$\Psi_n(kr) = \xi_n(kr) - i\chi_n(kr). \tag{41}$$

Furthermore, for the core,

$$e_{1n}^m = f_{1n}^m = 0. \tag{42}$$

The internal-field components are then found to be

$$E_{jr} = k_{j+1} E_0 \sum_{n=1}^{\infty} \sum_{m=-1}^{+n} c_n^{\mathrm{pw}} [c_{jn}^m [\Psi_n''(k_j r) + \Psi_n(k_j r)] + e_{jn}^m [\chi_n''(k_j r) + \chi_n(k_j r)] P_n^{|m|}(\cos\theta)]\exp(im\varphi), \tag{43}$$

$$E_{j\theta} = \frac{E_0}{r} \frac{k_{j+1}}{k_j} \sum_{n=1}^{\infty} \sum_{m=-n}^{+n} c_n^{\mathrm{pw}} [[c_{jn}^m \Psi_n'(k_j r) + e_{jn}^m \chi_n'(k_j r)] \times \tau_n^{|m|}(\cos\theta) + m \frac{k_{j+1}\mu_j}{k_j \mu_{j+1}} [d_{jn}^m \Psi_n(k_j r) + f_{jn}^m \chi_n(k_j r)] \times \Pi_n^{|m|}(\cos\theta)]\exp(im\varphi), \tag{44}$$

$$E_{j\varphi} = \frac{iE_0}{r} \frac{k_{j+1}}{k_j} \sum_{n=1}^{\infty} \sum_{m=-n}^{+n} c_n^{\mathrm{pw}} [m[c_{jn}^m \Psi_n'(k_j r) + c_{jn}^m \chi_n'(k_j r)] \times \Pi_n^{|m|}(\cos\theta) + \frac{k_{j+1}\mu_j}{k_j \mu_{j+1}} [d_{jn}^m \Psi_n(k_j r) + f_{jn}^m \chi_n(k_j r)] \times \tau_n^{|m|}(\cos\theta)]\exp(im\varphi), \tag{45}$$

$$H_{jr} = k_{j+1} H_0 \sum_{n=1}^{\infty} \sum_{m=-n}^{+n} c_n^{\mathrm{pw}} [d_{jn}^m [\Psi_n''(k_j r) + \Psi_n(k_j r)] + f_{jn}^m [\chi_n''(k_j r) + \chi_n(k_j r)] P_n^{|m|}(\cos\theta)] \exp(im\varphi), \tag{46}$$

$$H_{j\theta} = \frac{-H_0}{r} \sum_{n=1}^{\infty} \sum_{m=-n}^{+n} c_n^{\mathrm{pw}} \left\{ m \frac{\mu_{j+1}}{\mu_j} [c_{jn}^m \Psi_n(k_j r) + e_{jn}^m \chi_n(k_j r)] \times \Pi_n^{|m|}(\cos\theta) - \frac{k_{j+1}}{k_j} [d_{jn}^m \Psi_n'(k_j r) + f_{jn}^m \chi_n'(k_j r) \times \tau_n^{|m|}(\cos\theta) \right\} \exp(im\varphi), \tag{47}$$

$$H_{j\varphi} = -\frac{iH_0}{r} \sum_{n=1}^{\infty} \sum_{m=-n}^{+n} c_n^{\mathrm{pw}} \left\{ \frac{\mu_{j+1}}{\mu_j} [c_{jn}^m \Psi_n(k_j r) + e_{jn}^m \chi_n(k_j r)] \times \tau_n^{|m|}(\cos\theta) - m \frac{k_{j+1}\mu_j}{k_j \mu_{j+1}} [d_{jn}^m \Psi_n'(k_j r) + f_{jn}^m \chi_n'(k_j r)] \times \Pi_n^{|m|}(\cos\theta) \right\} \exp(im\varphi). \tag{48}$$

BSP's and field components for the scattered and the internal waves involve sets of unknown coefficients, in particular the scattering coefficients A_n^m and B_n^m. All these coefficients may be determined by the invoking of boundary conditions.

4. Boundary Conditions

We first consider boundary conditions at the surface of the sphere, i.e., the tangential continuity of the electric and the magnetics fields at $(r = r_L)$. These conditions are expressed by

$$V_{L\theta,X}(k_L r_L) = V_{\theta,X}^i(k_0 r_L) + V_{\theta,X}^s(k_0 r_L), \tag{49}$$

in which V stands for E or H and X stands for TM or TE. Only the θ components are considered, as φ components lead to the same set of relations as θ components do, as already checked above. From the field components derived in Section 3, we then obtain, with $j = L$,

$$\frac{k_0}{k_L} [c_{Ln}^m \Psi_n'(k_L r_L) + e_{Ln}^m \chi_n'(k_L r_L)] = [g_{n,\mathrm{TM}}^m \Psi_n'(k_0 r_L) - A_n^m \xi_n'(k_0 r_L), \tag{50}$$

$$\frac{\mu_0}{\mu_L} [c_{Ln}^m \Psi_n(k_L r_L) + e_{Ln}^m \chi_n(k_L r_L)] = [g_{n,\mathrm{TM}}^m \Psi_n(k_0 r_L) - A_n^m \xi_n(k_0 r_L)], \tag{51}$$

$$\frac{\mu_L}{\mu_0} \frac{k_0^2}{k_L^2} [(d_{Ln}^m \Psi_n(k_L r_L) + f_{Ln}^m \chi_n(k_L r_L)] = [g_{n,\mathrm{TE}}^m \Psi_n(k_0 r_L) - B_n^m \xi_n(k_0 r_L)], \tag{52}$$

$$\frac{k_0}{k_L} [d_{Ln}^m \Psi_n'(k_L r_L) + f_{Ln}^m \chi_n'(k_L r_L)] = [g_{n,\mathrm{TE}}^m \Psi_n'(k_0 r_L) - B_n^m \xi_n'(k_0 r_L). \tag{53}$$

Furthermore, the internal-scattering coefficients c_{jn}^m, d_{jn}^m, e_{jn}^m, f_{jn}^m, $j = 1, \ldots, L$, are related by internal boundary conditions. We can determine them by writing the tangential continuity of the electric and the magnetic fields at the surfaces separating the jth layer and the $j - 1$th layer, $j = 2, \ldots, L$. In particular, at the surface that separates the core $(j = 1)$ and the first layer $(j = 2)$, we have

$$V_{1\theta,X}(k_1 r_1) = V_{2\theta,X}(k_2 r_1), \tag{54}$$

which, based on Eq. (42), leads to

$$\frac{k_2}{k_1} c_{1n}^m \Psi_n'(k_1 r_1) = \frac{k_3}{k_2} [c_{2n}^m \Psi_n'(k_2 r_1) + e_{2n}^m \chi_n'(k_2 r_1)], \tag{55}$$

$$\frac{\mu_2}{\mu_1} c_{1n}^m \Psi_n(k_1 r_1) = \frac{\mu_3}{\mu_2} [c_{2n}^m \Psi_n(k_2 r_1) + e_{2n}^m \chi_n(k_2 r_1)], \tag{56}$$

$$\frac{k_2^2 \mu_3}{k_1^2 \mu_2} d_{1n}^m \Psi_n(k_1 r_1) = \frac{k_2^3 \mu_2}{k_2^2 \mu_1} [d_{2n}^m \Psi_n(k_2 r_1) + f_{2n}^m \chi_n(k_2 r_1)], \tag{57}$$

$$\frac{k_2}{k_1} d_{1n}^m \Psi_n'(k_1 r_1) = \frac{k_3}{k_2} [d_{2n}^m \Psi_n'(k_2 r_1) + f_{2n}^m \chi_n'(k_2 r_1)]. \tag{58}$$

More generally, the boundary conditions between the jth layer and the $j - 1$th layer, $j = 3, \ldots, L$, are expressed as

$$V_{(j-1)\theta,X}(k_{j-1} r_{j-1}) = V_{j\theta,X}(k_j r_{j-1}), \tag{59}$$

which leads to

$$\frac{k_j}{k_{j-1}} [c_{(j-1)n}^m \Psi_n'(k_{j-1} r_{j-1}) + e_{(j-1)n}^m \chi_n'(k_{j-1} r_{j-1})] = \frac{k_{j+1}}{k_j} [c_{jn}^m \Psi_n'(k_j r_{j-1}) + e_{jn}^m \chi_n'(k_j r_{j-1})], \tag{60}$$

$$\frac{\mu_j}{\mu_{j-1}}\left[c^m_{(j-1)n}\Psi_n(k_{j-1}r_{j-1}) + e^m_{(j-1)n}\chi_n(k_{j-1}r_{j-1})\right] = \frac{\mu_{j+1}}{\mu_j}\left[c^m_{jn}\Psi_n(k_jr_{j-1}) + e^m_{jn}\chi_n(k_jr_{j-1})\right], \tag{61}$$

$$\frac{\mu_{j+1}k_j^2}{\mu_jk_{j-1}^2}\left[d^m_{(j-1)n}\Psi_n(k_{j-1}r_{j-1}) + f^m_{(j-1)n}\chi_n(k_{j-1}r_{j-1})\right] = \frac{\mu_jk_{j+1}^2}{\mu_{j-1}k_j^2}\left[d^m_{jn}\Psi_n(k_jr_{j-1}) + f^m_{jn}\chi_n(k_jr_{j-1})\right], \tag{62}$$

$$\frac{k_j}{k_{j-1}}\left[d^m_{(j-1)n}\Psi'_n(k_{j-1}r_{j-1}) + f^m_{(j-1)n}\chi'_n(k_{j-1}r_{j-1})\right] = \frac{k_{j+1}}{k_j}\left[d^m_{jn}\Psi'_n(k_jr_{j-1}) + f^m_{jn}\chi'_n(k_jr_{j-1})\right]. \tag{63}$$

5. Solving Boundary Conditions

A. Scattering Coefficients

Let us solve the set of boundary conditions to determine unknown expansion coefficients of the BSP's. To this purpose, we introduce new quantities:

$$M_j = \frac{k_{j+1}}{k_j}, \qquad U_j = \frac{\mu_{j+1}}{\mu_j}, \qquad x_j = k_jr_j, \tag{64}$$

which, for the special cases in which $j = L$ and $j = 1$, become

$$M_L = \frac{k_0}{k_L}, \quad M_1 = \frac{k_2}{k_1}, \quad U_L = \frac{\mu_0}{\mu_L}, \quad U_1 = \frac{\mu_2}{\mu_1}. \tag{65}$$

We also introduce two ratios of internal coefficients, R_{jn} and Q_{jn}, which are defined by

$$R_{jn} = -\frac{e^m_{jn}}{c^m_{jn}}, \qquad Q_{jn} = -\frac{f^m_{jn}}{d^m_{jn}}, \tag{66}$$

and lead to the following useful relations:

$$R_{(j-1)n}\frac{c^m_{(j-1)n}}{c^m_{jn}} = -\frac{e^m_{(j-1)n}}{c^m_{jn}}, \quad Q_{(j-1)n}\frac{d^m_{(j-1)n}}{d^m_{jn}} = -\frac{f^m_{(j-1)n}}{d^m_{jn}}. \tag{67}$$

The whole set of boundary conditions can then be rewritten as

$$M_1\frac{c^m_{1n}}{c^m_{2n}}\Psi'_n(x_1) = M_2[\Psi'_n(M_1x_1) - R_{2n}\chi'_n(M_1x_1)], \tag{68}$$

$$U_1\frac{c^m_{1n}}{c^m_{2n}}\Psi_n(x_1) = U_2[\Psi_n(M_1x_1) - R_{2n}\chi_n(M_1x_1)], \tag{69}$$

$$M_1^2U_2\frac{d^m_{1n}}{d^m_{2n}}\Psi_n(x_1) = M_2^2U_1[\Psi_n(M_1x_1) - Q_{2n}\chi_n(M_1x_1)], \tag{70}$$

$$M_1\frac{d^m_{1n}}{d^m_{2n}}[\Psi'_n(x_1) = M_2[\Psi'_n(M_1x_1) - Q_{2n}\mathrm{X}'_n(M_1x_1)], \tag{71}$$

$$M_{j-1}\frac{c^m_{(j-1)n}}{c^m_{jn}}\left[\Psi'_n(x_{j-1}) - R_{(j-1)n}\chi'_n(x_{j-1})\right] = M_j[\Psi'_n(M_jx_{j-1}) - R_{jn}\chi'_n(M_jx_{j-1})], \tag{72}$$

$$U_{j-1}\frac{c^m_{(j-1)n}}{c^m_{jn}}\left[\Psi_n(x_{j-1}) - R_{(j-1)n}\chi_n(x_{j-1})\right] = U_j[\Psi_n(M_jx_{j-1}) - R_{jn}\chi_n(M_jx_{j-1})], \tag{73}$$

$$M_{j-1}^2U_j\frac{d^m_{(j-1)n}}{d^m_{jn}}\left[\Psi_n(x_{j-1}) - Q_{(j-1)n}\chi_n(x_{j-1})\right] = M_j^2U_{j-1}[\Psi_n(M_jx_{j-1}) - Q_{jn}\chi_n(M_jx_{j-1})], \tag{74}$$

$$M_{j-1}\frac{d^m_{(j-1)n}}{d^m_{jn}}\left[\Psi'_n(x_{j-1}) - Q_{(j-1)n}\chi'_n(x_{j-1})\right] = M_j[\Psi'_n(M_jx_{j-1}) - Q_{jn}\chi'_n(M_jx_{j-1})], \tag{75}$$

$$M_L[\Psi'_n(x_L) - R_{Ln}\chi'_n(x_L)] = \frac{1}{c^m_{Ln}}[g^m_{n,\mathrm{TM}}\Psi'_n(M_Lx_L) - A^m_n\xi'_n(M_Lx_L)], \tag{76}$$

$$U_L[\Psi_n(x_L) - R_{Ln}\chi_n(x_L)] = \frac{1}{c^m_{Ln}}[g^m_{n,\mathrm{TM}}\Psi_n(M_Lx_L) - A^m_n\xi_n(M_Lx_L)], \tag{77}$$

$$M_L^2[\Psi_n(x_L) - Q_{Ln}\chi_n(x_L)] = \frac{U_L}{d^m_{Ln}}[g^m_{n,\mathrm{TE}}\Psi_n(M_Lx_L) - B^m_n\xi_n(M_Lx_L)], \tag{78}$$

$$M_L[\Psi'_n(x_L) - Q_{Ln}\chi'_n(x_L)] = \frac{1}{d^m_{Ln}}[g^m_{n,\mathrm{TE}}\Psi'_n(M_Lx_L) - B^m_n\xi'_n(M_Lx_L)]. \tag{79}$$

Manipulating the ratios of the above equations, e.g., Eqs. (68)/(69), (72)/(73), and (76)/(77) and introducing two new functions, $H_n(x_j)$ and $K_n(x_j)$, where

$$H_n(x_j) = \frac{\Psi'_n(x_j) - R_{jn}\chi'_n(x_j)}{\Psi_n(x_j) - R_{jn}\chi_n(x_j)}, \qquad K_n(x_j) = \frac{\Psi'_n(x_j) - Q_{jn}\chi'_n(x_j)}{\Psi_n(x_j) - Q_{jn}\chi_n(x_j)}, \tag{80}$$

we obtain two sets of recurrent relations for the determination of the scattering coefficients A^m_n and

B_n^m, which are, for A_n^m,

$$
\begin{aligned}
e_{1n}^m &= 0, \qquad R_{1n} = -\frac{e_{1n}^m}{c_{1n}^m} = 0, \qquad H_n(x_1) = \frac{\Psi_n'(x_1)}{\Psi_n(x_1)}, \\
R_{2n} &= \frac{M_1U_2\Psi_n'(x_1)\Psi_n(M_1x_1) - M_2U_1\Psi_n(x_1)\Psi_n'(M_1x_1)}{M_1U_2\Psi_n'(x_1)\chi_n(M_1x_1) - M_2U_1\Psi_n(x_1)\chi_n'(M_1x_1)}, \\
R_{jn} &= \frac{M_{j-1}U_j\Psi_n(M_jx_{j-1})H_n(x_{j-1}) - M_jU_{j-1}\Psi_n'(M_jx_{j-1})}{M_{j-1}U_j\chi_n(M_jx_{j-1})H_n(x_{j-1}) - M_jU_{j-1}\chi_n'(M_jx_{j-1})}, \\
H_n(x_j) &= \frac{\Psi_n'(x_j) - R_{jn}\chi_n'(x_j)}{\Psi_n(x_j) - R_{jn}\chi_n(x_j)}, \qquad j = 2, \ldots, L,
\end{aligned}
\tag{81}
$$

$$
A_n^m = g_{n,\mathrm{TM}}^m \frac{M_L\Psi_n(M_Lx_L)H_n(x_L) - U_L\Psi_n'(M_Lx_L)}{M_L\xi_n(M_Lx_L)H_n(x_L) - U_L\xi_n'(M_Lx_L)}, \tag{83}
$$

and for B_n^m are,

$$
\begin{aligned}
f_{1n}^m &= 0, \qquad Q_{1n} = -\frac{f_{1n}^m}{d_{1n}^m} = 0, \qquad K_n(x_1) = \frac{\Psi_n'(x_1)}{\Psi_n(x_1)}, \\
Q_{2n} &= \frac{M_2U_1\Psi_n'(x_1)\Psi_n(M_1x_1) - M_1U_2\Psi_n(x_1)\Psi_n'(M_1x_1)}{M_2U_1\Psi_n'(x_1)\chi_n(M_1x_1) - M_1U_2\Psi_n(x_1)\chi_n'(M_1x_1)}, \\
Q_{jn} &= \frac{M_jU_{j-1}\Psi_n(M_jx_{j-1})K_n(x_{j-1}) - M_{j-1}U_j\Psi_n'(M_jx_{j-1})}{M_jU_{j-1}\chi_n(M_jx_{j-1})K_n(x_{j-1}) - M_{j-1}U_j\chi_n'(M_jx_{j-1})}, \\
K_n(x_j) &= \frac{\Psi_n'(x_j) - Q_{jn}\chi_n'(x_j)}{\Psi_n(x_j) - Q_{jn}\chi_n(x_j)}, \qquad j = 2, \ldots, L,
\end{aligned}
\tag{83}
$$

$$
B_n^m = g_{n,\mathrm{TE}}^m \frac{U_L\Psi_n(M_Lx_L)K_n(x_L) - M_L\Psi_n'(M_Lx_L)}{U_L\xi_n(M_Lx_L)K_n(x_L) - M_L\xi_n'(M_Lx_L)}. \tag{84}
$$

Starting from the core of the sphere at which the two ratios of internal coefficients and the functions $H_n(x_1)$ and $K_n(x_1)$ are known, we can now use these recurrent relations to evaluate the scattering coefficients. Furthermore, Eqs. (82) and (84) may be rewritten as

$$
A_n^m = g_{n,\mathrm{TM}}^m a_n, \tag{85}
$$

$$
B_n^m = g_{n,\mathrm{TE}}^m b_n, \tag{86}
$$

where the scattering coefficients a_n and b_n are actually those which appear in the case in which the incident wave is a plane wave (see, for instance, Wu and Wang[24]). Equations (85) and (86) are also formally identical with those obtained within the framework of the GLMT for homogeneous spheres, in which a_n and b_n are the scattering coefficients of the LMT. This remark leads to two important consequences. First, from a formal point of view, all the GLMT expressions that concern external waves, i.e., scattered intensities and cross sections, including radiation-pressure cross sections, remain valid. The only difference is the change of the meaning of the scattering coefficients a_n and b_n. Second, to adapt any GLMT code to the present case under study, it is required that only the evaluation of these scattering coefficients be modified.

In particular, the scattered electrio-field components in the far-field region are

$$
E_\theta = \frac{iE_0}{k_0r}\exp(-ikr)\,\mathscr{S}_2, \tag{87}
$$

$$
E_\varphi = -\frac{E_0}{k_0r}\exp(-ikr)\,\mathscr{S}_1, \tag{88}
$$

in which the generalized amplitude functions $\mathscr{S}_1$ and $\mathscr{S}_2$ are given by

$$
\begin{aligned}
\mathscr{S}_1 = \sum_{n=1}^{\infty}\sum_{m=-n}^{+n} &\frac{2n+1}{n(n+1)} \\
&\times \left[ma_ng_{n,\mathrm{TM}}^m\Pi_n^{|m|}(\cos\theta) + ib_ng_{n,\mathrm{TE}}^m\tau_n^{|m|}(\cos\theta)\right] \\
&\times \exp(im\varphi),
\end{aligned}
\tag{89}
$$

$$\mathscr{S}_2 = \sum_{n=1}^{\infty} \sum_{m=-n}^{+n} \frac{2n+1}{n(n+1)} \times [a_n g_{n,\mathrm{TM}}^m \tau_n^{|m|}(\cos\theta) + imb_n g_{n,\mathrm{TE}}^m \Pi_n^{|m|}(\cos\theta)] \times \exp(im\varphi). \quad (90)$$

These expressions are indeed formally identical to those established within the framework of the GLMT for the homogeneous sphere.[8,9]

B. Internal-Scattering Coefficients

From Subsection 5.A, we know the scattering coefficients A_n^m and B_n^m and also all the internal coefficients ratios denoted by R_{jn} and Q_{jn}. Then, it is shown that we can evaluate the internal coefficients for each internal TM wave by using Eqs. (73) and (77) and, starting from the outer surface of the sphere, with the aid of the following recurrent relations:

$$\begin{aligned} c_{Ln}^m &= \frac{g_{n,\mathrm{TM}}^m}{U_L}\left[\frac{\Psi_n(M_L x_L) - a_n \xi_n(M_L x_L)}{\Psi_n(x_L) - R_{Ln}\chi_n(x_L)}\right], \\ e_{Ln}^m &= -R_{Ln} c_{Ln}^m, \\ c_{(j-1)n}^m &= c_{jn}^m \frac{U_j}{U_{j-1}}\left[\frac{\Psi_n(M_j x_{j-1}) - R_{jn}\chi_n(M_j x_{j-1})}{\Psi_n(x_{j-1}) - R_{(j-1)n}\chi_n(x_{j-1})}\right], \\ e_{(j-1)n}^m &= -R_{(j-1)n} c_{(j-1)n}^m, \qquad j = L, \ldots, 2. \end{aligned} \quad (91)$$

Similarly, for the internal TE waves, we start from Eqs. (74) and (78) and obtain the following recurrent relations:

$$\begin{aligned} d_{Ln}^m &= \frac{g_{n,\mathrm{TE}}^m U_L}{M_L^2}\left[\frac{\Psi_n(M_L x_L) - b_n \xi_n(M_L x_L)}{\Psi_n(x_L) - Q_{Ln}\chi_n(x_L)}\right], \\ f_{Ln}^m &= -Q_{Ln} d_{Ln}^m, \\ d_{(j-1)n}^m &= d_{jn}^m \frac{M_j^2 U_{j-1}}{M_{j-1}^2 U_j}\left[\frac{\Psi_n(M_j x_{j-1}) - Q_{jn}\chi_n(M_j x_{j-1})}{\Psi_n(x_{j-1}) - Q_{(j-1n)}\chi_n(x_{j-1})}\right], \\ f_{(j-1)n}^m &= -Q_{(j-1)n} d_{(j-1)n}^m, \qquad j = L, \ldots, 2. \end{aligned} \quad (92)$$

As we may have expected, BSC's appear in the expressions for c_{Ln}^m and d_{Ln}^m but not in the expressions for the other coefficients, as the outer layer is the only one that owns a boundary with an external surrounding space. It is then readily established that Eqs. (91) can be rewritten as

$$\begin{aligned} c_{Ln}^m &= g_{n,\mathrm{TM}}^m c_{Ln}, \\ e_{Ln}^m &= -R_{Ln} c_{Ln}^m, \\ c_{(j-1)n}^m &= c_{jn}^m c_{jn}, \\ e_{(j-1)n}^m &= -R_{(j-1)n} c_{(j-1)n}^m, \qquad j = L, \ldots, 2. \end{aligned} \quad (93)$$

in which c_{Ln} and c_{jn} are the internal coefficients for the plane-wave case, which can be established, starting from Ref. 24, as

$$c_{Ln} = \frac{1}{U_L}\left[\frac{\Psi_n(M_L x_L) - a_n \xi_n(M_L x_L)}{\Psi_n(x_L) - R_{Ln}\chi_n(x_L)}\right], \quad (94)$$

$$c_{(j-1)n} = \frac{U_j}{U_{j-1}}\left[\frac{\Psi_n(M_j x_{j-1}) - R_{jn}\chi_n(M_j x_{j-1})}{\Psi_n(x_{j-1}) - R_{(j-1)n}\chi_n(x_{j-1})}\right]. \quad (95)$$

Equations (93) furthermore show that coefficients $c_{(j-1)}^m$ can be rewritten in an iterative form:

$$c_{(j-1)n}^m = g_{n,\mathrm{TM}}^m c_{Ln} c_{(L-1)n} \cdots c_{(j+1)n} c_{jn}, \quad (96)$$

which is identical to the case of plane-wave illumination except for the appearance of a multiplicative factor $g_{n,\mathrm{TM}}^m$. Equations (92) can be easily processed in a similar way.

6. Numerical Results

This section is devoted to the discussion of the programming strategy to compute the scattering coefficients $A_n^m B_n^m$, followed by exemplifying results concerning (1) scattering diagrams and (2) radiation pressure.

A. Programming Strategy

Various programming strategies for computing the scattering coefficients of a multilayered sphere illuminated by a plane wave have been developed. In this paper we follow the technique of Wu and Wang.[24] Other strategies are possible, e.g., those developed by Bhandari[25] and Kai *et al.*[17,26] We do, however, insist that it is not the purpose of this paper to compare the advantages and the limitations of each strategy extensively. In particular, the choice of a numerical strategy to compute the scattering coefficients does not have any influence on the main part of the work presented in this paper, which is to extend the GLMT to the case of multilayered spheres.

The Riccatti–Bessel functions have asymptotic behavior, even for a reasonably sized parameter; their module can overflow the capacity of any computer. This behavior is well known from people who have worked on the homogeneous model. Nevertheless the stratified model requires a recurrent algorithm on these functions. Then great attention should be paid to overcoming any numerical source of error. For this task Eqs. (81)–(84) can be reformulated in a form compatible with their numerical calculation. Following Wu and Wang,[24] rather than directly computing the Ricatti–Bessel functions, we can introduce their logarithmic derivative and ratios, computed by recurrent relations. The logarithmic derivatives are denoted as

$$D_n^1(x) = \frac{\Psi_n'(x)}{\Psi_n(x)}, \quad D_n^2(x) = \frac{\chi_n'(x)}{\chi_n(x)}, \quad D_n^3(x) = \frac{\xi_n'(x)}{\xi_n(x)}. \quad (97)$$

The recurrent relations (81)–(84) for evaluating the

scattering coefficients A_n^m and B_n^m then become, for A_n^m,

$$e_{1n}^m = 0, \qquad R_{1n} = -\frac{e_{1n}^m}{c_{1n}^m} = 0, \qquad H_n(x_1) = D_n^1(x_1),$$

$$R_{jn} = \frac{\Psi_n(M_j x_{j-1})}{\chi_n(M_j x_{j-1})} \frac{M_{j-1}U_j H_n(x_{j-1}) - M_j U_{j-1} D_n^1(M_j x_{j-1})}{M_{j-1}U_j H_j(x_{j-1}) - M_j U_{j-1} D_n^2(M_j x_{j-1})},$$

$$H_n(x_j) = \frac{\Psi_n(x_j)}{\chi_n(x_j)} \frac{D_n^1(x_j)}{\dfrac{\Psi_n(x_j)}{\chi_n(x_j)} - R_{jn}} - \frac{R_{jn} D_n^2(x_j)}{\dfrac{\Psi_n(x_j)}{\chi_n(x_j)} - R_{jn}}, \qquad j = 2, \ldots, L, \tag{98}$$

$$A_n^m = g_{n,\mathrm{TM}}^m \frac{\Psi_n(M_L x_L)}{\xi_n(M_L x_L)} \frac{M_L H_n(x_L) - U_L D_n^1(M_j x_L)}{M_L H_n(x_L) - U_L D_n^3(M_L x_L)}, \tag{99}$$

and, for B_n^m,

$$f_{1n}^m = 0, \qquad Q_{1n} = -\frac{f_{1n}^m}{d_{1n}^m} = 0, \qquad K_n(x_1) = D_n^1(x_1),$$

$$Q_{jn} = \frac{\Psi_n(M_j x_{j-1})}{\chi_n(M_j x_{j-1})} \frac{M_j U_{j-1} K_n(x_{j-1}) - M_{j-1} U_j D_n^1(M_j x_{j-1})}{M_j U_{j-1} K_j(x_{j-1}) - M_{j-1} U_j D_n^2(M_j x_{j-1})},$$

$$K_n(x_j) = \frac{\Psi_n(x_j)}{\chi_n(x_j)} \frac{D_n^1(x_j)}{\dfrac{\Psi_n(x_j)}{\chi_n(x_j)} - Q_{jn}} - \frac{Q_{jn} D_n^2(x_j)}{\dfrac{\Psi_n(x_j)}{\chi_n(x_j)} - Q_{jn}}, \qquad j = 2, \ldots, L, \tag{100}$$

$$B_n^m = g_{n,\mathrm{TM}}^m \frac{\Psi_n(M_L x_L)}{\xi_n(M_L x_L)} \frac{U_L K_n(x_L) - M_L D_n^1(M_j x_L)}{U_L K_n(x_L) - M_L D_n^3(M_L x_L)}. \tag{101}$$

Efficient algorithms for computing the functions $D_n^1(z)$, $D_n^2(z)$, $D_n^3(z)$, $\Psi_n(z)/\chi_n(z)$, and $\Psi_n(z)/\xi_n(z)$ are available from Refs. 7 and 24. On the basis of the above algorithms, a FORTRAN subroutine has been written to compute the a_n and b_n coefficients for the stratified sphere and to incorporate them into a GLMT code. Some tests have been made for the plane-wave case, to compare with the literature, a good agreement has been found with Refs. 6, 7, 17, and 24.

B. Scattering Diagrams

Figure 2 displays scattering diagrams, in the case of an electric field's vibrating in the plane (XOZ) along (OX), for a water droplet $(m_1 = 1.33 - 0.0i)$, a carbon sphere $(m_1 = 1.6 - 0.59i)$, and a carbon sphere surrounded by a water coating with a ratio of its inner to outer radius equal to $q = 1/2$. The particle outer diameter is 10 μm. Two kinds of incident beam are considered, a plane wave and a Gaussian beam with a beam-waist diameter of 20 μm, i.e., the beam diameter is twice the outer particle diameter. The imping-

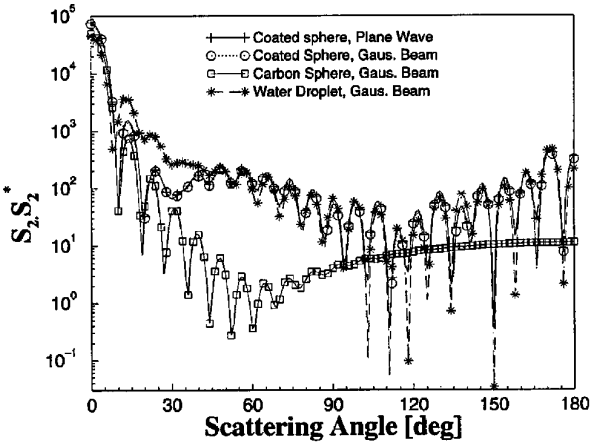

Fig. 2. Scattering diagrams for parallel polarization by a water droplet, a carbon sphere, a water-coated sphere $(q = 1/2)$ by plane-wave and Gaussian-beam illuminations: $\lambda = 0.6328$ μm, $2\omega_0 = 20$ μm, $d = 10$ μm, $X = 0$, $Y = 0$, $Z = 0$, $m_1 = 1.33 + 0.0i$, $m_2 = 1.6 - 0.59i$.

ing beams have a wavelength of 0.6328 μm. The particle center is located at the beam-waist center.

In this case the Gaussian-beam illumination coincides with the plane-wave predictions. On the other hand, coated-sphere patterns are intermediary between the two homogeneous-sphere patterns. However, for a scattering angle smaller than approximately 20°–25°, the scattering patterns of the coated particle are close to those of the homogeneous carbon-particle scattering diagram, whereas, conversely, for a scattering angle larger than 45°, they are close to the homogeneous water-droplet case. The behavior can be explained as follows:

- In the forward direction ($\theta < 20°$), the contribution of diffraction does not depend on the particle material, and the refracted contribution is due to the rays with the smallest impact parameter, i.e., to the rays impinging on the carbon core.
- For large scattering angles ($\theta > 45°$), the main contribution is due to the rays with a large impact parameter, i.e., to the rays traveling through the water coating or being reflected by this shell.

Figure 3 shows the evolution of the scattering diagrams of the coated particle in the Gaussian-beam case for three locations along the (OX) axis in the beam-waist plane, i.e., one at the beam-waist center ($X = 0$) and the two others at off-axis locations ($X = \pm 10$ μm), exhibiting the influence of the Gaussian-beam character.

Figure 4 displays scattering diagrams for parallel polarization of a multilayered sphere described by $m_j = m_1 + 0.5(m_L - m_1)(1 - \cos \pi t)$, $t = (j - 1)/(L - 1)$, $j = 1, \ldots, L$, $m_1 = 1.43 + i0.0$, $m_L = 1.33 + i0.0$, and $x_j = x_1 + (x_L - x_1)(j - 1)/(L - 1)$, where $x_1 = 0.001x_L$, $x_L = 59.4$, $L = 100$. Two kinds of incident beam are considered: (1) a plane wave and (2) a Gaussian beam with a beam-waist diameter equal to the particle outer diameter. The impinging beams have a wavelength of 0.5145 μm. The particle center is located at the beam-waist center.

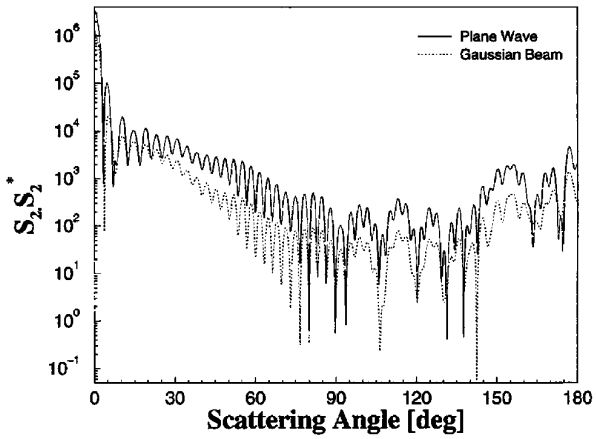

Fig. 4. Scattering diagrams for parallel polarization by a multilayered sphere: $m_j = m_1 + 0.5(m_L - m_1)[1 - \cos(\pi t)]$, $t = (j - 1)/(L - 1)$, $x_1 = 0.0001$, x_L and $x_j = x_1 + (x_L - x_1)(j - 1)/(L - 1)$, $j = 1, \ldots, L$, where $x_1 = 0.001\,x_L$, $x_L = 59.4$, $m_1 = 1.43 + i0.0$, $m_L = 1.33 + i0.0$, $L = 100$. Plane-wave and Gaussian-beam illuminations $\lambda = 0.5145$ μm. The beam-waist diameter is equal to the particle outer diameter, with $X = 0$, $Y = 0$, $Z = 0$.

For the plane-wave illumination, the scattering diagram obtained here with $L = 100$ is similar to the one obtained by Kai *et al.* in Fig. 7 of Ref. 17, with $L = 6000$. Note that the case considered here already leads to a radius increment for the stratification of less than $\lambda/10$.

C. Radiation Pressure

Figure 5 displays radiation-pressure cross section in the (OZ) direction, $C_{\mathrm{pr},Z}$ versus particle locations along (OX) in the beam-waist plane. Several two-layered particles with a carbon core and a water coating are considered ($q = 0.5, \ldots, 0.9$). The limit case of a pure water ($q = 0$) or carbon ($q = 1$) particle is also displayed (to check the results of our new GLMT code for multilayered spheres, we obtained

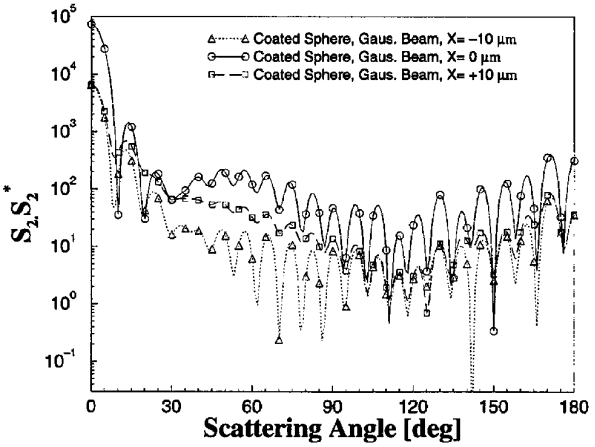

Fig. 3. Scattering diagrams for parallel polarization by a water-coated carbon sphere ($q = 1/2$) for a Gaussian-beam illumination versus its position along the (OX) axis: $\lambda = 0.6328$ μm, $2\omega_0 = 20$ μm, $d = 10$ μm, $Y = 0, Z = 0, m_1 = 1.33 + 0.0i, m_2 = 1.6 - 0.59i$.

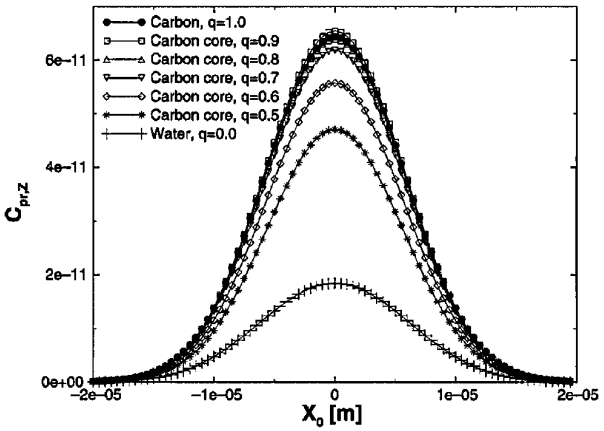

Fig. 5. Radiation-pressure cross sections $C_{\mathrm{pr},Z}$ versus particle locations along (OX) for several ratios of the water-coating radius to the carbon-core radius, with Gaussian-beam illumination. Parameters are the same as those of Fig. 3.

them by using a classical GLMT program for a homogeneous sphere[27]). The other parameters are the same as for the scattering diagrams of Figs. 2 and 3.

The scattering cross sections $C_{pr,Z}$ are maximum for $X = 0$, i.e., for a central position of the particle with respect to the beam axis. The scattering cross sections roughly increase with increasing absorbing core diameter. These behaviors can be explained as follows:

- For particles with a small absorbing core, the rays impinging on the particle with a small impact parameter are essentially refracted through the particle, giving a small amount of momentum quality to the particle in the (OZ) direction, or are reflected. Figure 2 shows that the water coating increases the backward scattering (reflection), which corresponds to a higher momentum transfer efficiency. Thus here we can distinguish two competitive effects for decreasing or increasing the radiation cross section $C_{pr,Z}$.
- For particles with a large absorbing core, the rays impinging on the particle with a small impact parameter are not refracted in forward scattering but essentially are absorbed, giving a high momentum quantity to the particle in the (OZ) direction. Furthermore, the water coating still increases the backward scattering and then the radiation pressure in the OZ direction.

The above explanation is qualitative and has to be extended more carefully in a future work. Nevertheless, it may explain why, in Fig. 5, $C_{pr,Z}$ is higher for the particle defined by $q = 0.9$ than for the carbon sphere; the thin water coating seems to enhance the radiation pressure in the OZ direction more than if it were a carbon outer surface. To ensure that it was not a numerical problem, we checked this effect by comparing the results obtained for a particle defined with $q = 0.999$ and from the pure carbon particle. Indeed the two data sets fitted very well.

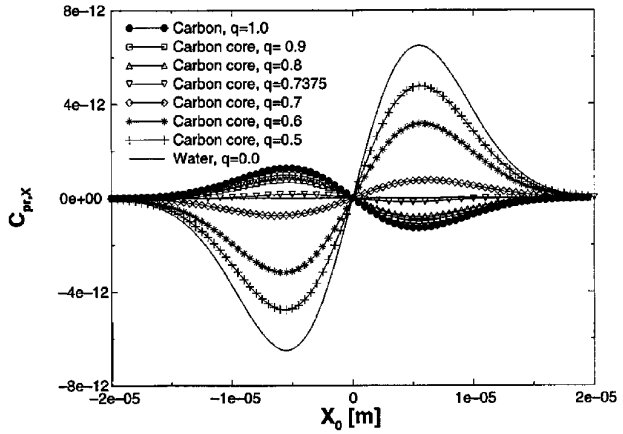

Fig. 6. Radiation-pressure cross sections $C_{pr,X}$ versus particle locations along (OX) for several ratios of the water-coating radius to the carbon-core radius with Gaussian beam illumination. Parameters are the same as those of Fig. 3.

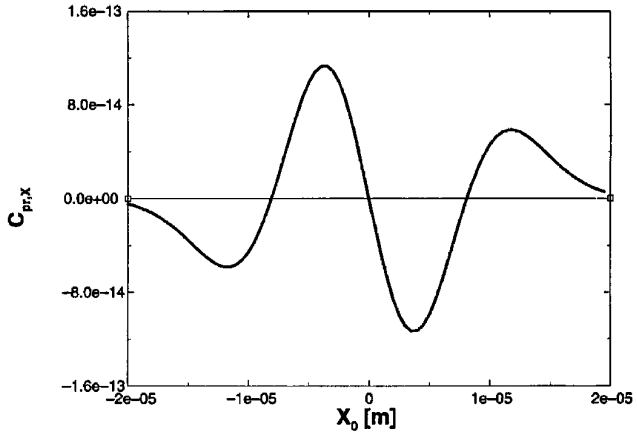

Fig. 7. Radiation-pressure cross sections $C_{pr,X}$ for a two-layered particle $(q = 0.95)$ versus its location along X with Gaussian-beam illumination. Parameters are the same as those of Fig. 3, except $m_1 = 1.0 + 0.0i$, $m_2 = 1.2 + 0.0i$.

Figure 6 displays radiation-pressure cross section $C_{pr,X}$, versus particle location along (OX) for the same conditions as above. Here the transverse radiation-pressure cross-section patterns show that, for the carbon sphere, radiation-pressure forces drive the particle out of the beam. Conversely, for a water droplet, the transverse radiation-pressure forces drive the particle to the position $X = 0$. These effects for homogeneous particles are now classical.[27,28] The radiation-pressure cross sections for the two-layered sphere are intermediary between those of the carbon and the water spheres. Thus, with $q = 0.7375$ for instance, the radiation-pressure cross-section patterns become very flat when compared with the other behaviors, i.e., there is almost no more transverse radiation-pressure effects in this direction.

Figure 7, as a last example of Gaussian-beam effects on the radiation-pressure patterns of a stratified sphere, displays radiation-pressure cross section $C_{pr,X}$ versus particle location along X for a sphere $(m = 1.2)$, with an air core $(q = 0.95)$, in air. The Gaussian beam, particle outer radius, and location are the same as in the cases studied above.

The radiation-pressure pattern is that of a reflecting particle for 2.10^{-6} m $< |X| < 4.10^{-6}$ m and corresponds to the radiation-pressure pattern of a refractive particle for -4.10^{-6} m $< X < 4.10^{-6}$ m. The beam center is highly unstable for the particle, i.e., the transverse radiation-pressure forces in the (OX) direction drive the particle out of this position. Conversely, the radiation-pressure forces tend to maintain the particle at $X = \pm 8.10^{-6}$ m, i.e., there are two symmetrical stable positions for the particle according to the radiation-pressure cross section in the (OX) direction.

7. Conclusion

We have established the theory of interaction between a multilayered sphere and an incident arbitrary beam by generalizing both (1) the theory of

interaction between a multilayered sphere and a plane wave and (2) the theory of interaction between a homogeneous sphere and an arbitrary beam (GLMT). We take the incident beam shape into account by introducing beam-shape coefficients $g_{n,X}^m$ which are identical with those of the GLMT. Exemplifying numerical results have been presented concerning (1) scattering diagrams and (2) radiation-pressure forces. It is believed that the theory will allow many applications, for instance, in the field of optical particle sizing and characterization.

References

1. L. Lorenz, "Lysbevaegelsen i og uden for en hal plane lysbôlger belyst kulge," Vidensk. Selk. Skr. **6,** 1–62 (1898).
2. G. Mie, "Beitrâge zur optik truber Medien, speziell kolloidaler Metallosungen," Ann. Phys. **25,** 377–452 (1908).
3. P. Debye, "Der Lichtdruck auf Kugeln von beliebigem Material," Ann. Phys. **30,** 57–136 (1909).
4. J. A. Stratton, *Electromagnetic Theory* (McGraw-Hill, New York, 1941).
5. H. C. van de Hulst, *Light Scattering by Small Particles* (Dover, New York, 1957).
6. M. Kerker, *The Scattering of Light, and Other Electromagnetic Radiations* (Academic, New York, 1969).
7. C. F. Bohren and D. R. Huffman, *Absorption and Scattering of Light by Small Particles* (Wiley-Interscience, New York, 1983).
8. G. Gouesbet, B. Maheu, and G. Gréhan, "Light scattering from a sphere arbitrarily located in a Gaussian beam, using a Bromwich formulation" J. Opt. Soc. Am. A **5,** 1427–1443 (1988).
9. G. Gouesbet, G. Gréhan, and B. Maheu, "Generalized Lorenz–Mie theory and applications to optical sizing," in *Combustion Measurements,* N. Chigier, ed. (Hemisphere, Washington, D.C., 1991), Chap. 10.
10. K. F. Ren, G. Gréhan, and G. Gouesbet, "Laser sheet scattering by spherical particles," Part. Part. Syst. Charact. **10,** 146–151 (1993).
11. K. F. Ren, G. Gréhan, and G. Gouesbet, "Evaluation of laser sheet beam shape coefficients in generalized Lorenz–Mie theory by using a localized approximation," J. Opt. Soc. Am. A **11,** 2072–2079 (1994).
12. M. I. Angelova, B. Pouligny, G. M. Martinot-Lagarde, G. Gréhan, and G. Gouesbet, "Stressing phospholipid membranes using mechanical effects of light," Prog. Colloid Polym. Sci. (to be published).
13. G. Gréhan, G. Gouesbet, A. Naqwi, and F. Durst, "Particle trajectory effects in phase Doppler systems: computations and experiments," Part. Part. Syst. Charact. **10,** 332–338 (1993).
14. F. Onofri, G. Gréhan, G. Gouesbet, T.-H. Xu, G. Brenn, and C. Tropea, "Phase-Doppler anemometry with dual burst technique for particle refractive index measurements," presented at the Seventh International Symposium on Applications of Laser Techniques to Fluid Mechanics, Lisbon, 11–14 July 1994.
15. M. Schneider and E. D. Hirleman, "Influence of internal refractive index gradients on size measurements of spherically symmetric particles by phase Doppler anemometry," Appl. Opt. **33,** 2379–2389 (1994).
16. A. L. Aden and M. Kerker, "Scattering of electromagnetic waves from two concentric spheres," J. Appl. Phys. **22,** 1242–1246 (1951).
17. L. Kai and P. Massoli, "Scattering of electromagnetic-plane waves by radially inhomogeneous spheres: a finely stratified sphere model," Appl. Opt. **33,** 501–511 (1994).
18. E. M. Khaled, S. C. Hill, and P. W. Barber, "Light scattering by a coated sphere illuminated by a Gaussian beam," Appl. Opt. **33,** 3308–3314 (1994).
19. J. A. Lock, "Improved Gaussian beam-scattering algorithm," Appl. Opt. **34,** 559–570 (1995).
20. G. Gouesbet, G. Gréhan, and B. Maheu, "Expressions to compute the coefficients g_n^m in the generalized Lorenz–Mie theory using finite series," J. Opt. (Paris) **19,** 35–48 (1988).
21. G. Gouesbet, G. Gréhan, and B. Maheu, "A localized interpretation to compute all the coefficients g_n^m in the generalized Lorenz–Mie theory," J. Opt. Soc. Am. A **7,** 998–1007 (1990).
22. G. Gouesbet and J. A. Lock, "Rigorous justification of the localized approximation to the beam shape coefficients in the generalized Lorenz–Mie theory. I. Off-axis beams," J. Opt. Soc. Am. A **11,** 2503–2515 (1994).
23. J. A. Lock and G. Gouesbet, "Rigorous justification of the localized approximation to the beam shape coefficients in the generalized Lorenz-Mie theory. II. On-axis beams," J. Opt. Soc. Am. A **11,** 2516–2525 (1994).
24. Z. S. Wu and Y. P. Wang, "Electromagnetic scattering for multilayered sphere: recursive algorithms," Radio Sci. **26,** 1393–1401 (1991).
25. R. Bhandari, "Scattering coefficients for a multilayered sphere: analytic expressions and algorithms," Appl. Opt. **24,** 1960–1967 (1985).
26. L. Kai, P. Massoli, and A. D'Alessio, "Studying inhomogeneities of spherical particles by light scattering," presented at the Third International Congress on Optical Partical Sizing, Yokohama, Japan, 1993.
27. K. F. Ren, G. Gréhan, and G. Gouesbet, "Radiation pressure forces exerted on a particle arbitrarily located in a Gaussian beam by using the GLMT, and associated resonances effects," Opt. Commun. **108,** 343–353 (1994).
28. A. Ashkin, "Acceleration and trapping of particles by radiation pressure," Phys. Rev. Lett. **24,** 156–159 (1970).

Article A4

Phase-Doppler Anemometry with the Dual Burst Technique for Measurement of Refractive Index and Absorption Coefficient Simultaneously with Size and Velocity

Fabrice Onofri*, Thierry Girasole*, Gérard Gréhan*, Gérard Gouesbet*, Günter Brenn, Joachim Domnick**, Tian-Hua Xu**, Cameron Tropea****

(Received: 24 August 1995)

Abstract

The principle of the dual burst technique (DBT) based on phase-Doppler anemometry (PDA) is proposed for simultaneous particle refractive index, size and velocity measurements. This technique uses the trajectory effects in PDA systems to separate the two contributions of the different scattering processes. In the case of forward scattering and refracting particles, it is shown that from the phase of the reflected contribution, the particle diameter can be deduced, whereas from the refracted contribution the particle refractive index and velocity can be obtained. Furthermore, the intensity ratio of these two scattering processes can be used for absorption measurements. Simulations based on generalized Lorenz-Mie theory and experimental tests using monodispersed droplets of different refractive indices and absorption coefficients have validated this technique.

1 Introduction

Phase-Doppler anemometry is now a well established particle sizing technique in laboratories and industries for studying two-phase flows and sprays. It can provide a particle size distribution correlated with up to three particle velocity components, with high resolution in time and space, without being intrusive. The principle, which is now about 20 years old [1–3], is that, when a particle passes through an optical measuring volume defined by the intersection of two laser beams, the phase of the light scattered by the particle carries information about the particle diameter, whereas its frequency provides information about its velocity. To collect scattered light, a scattering angle should be chosen to ensure that the phase-diameter relationship for each detector pair is linear. This condition can be met when the detectors collect light scattered by the particle mainly due to a single scattering process, i.e. reflection or first- or second-order refraction. It is well known that the scattering angle must be carefully chosen according to the particle refractive index.

As many experimental investigations in the field of two-phase flow, multiphase flow and combustion require simultaneous measurements of individual particle size, velocity and also refractive index, several systems, based on the phase-Doppler technique, have been proposed for this purpose [4, 5]. However, these systems are generally not suitable for a large measuring range of particle refractive indices. When measurements are performed in a complex flow field, e.g. in sprays, the influence of trajectory effects (TE) on refractive index measurements must also be considered [6–8]. This inevitably leads to extra receiving units for the refractive index measurements, which increases alignment requirements and costs.

Based on previous work to eliminate the TE in PDA systems [9–11], an innovative PDA technique, called the dual burst technique (DBT), is proposed in this paper for refractive index measurements, in addition to particle size and velocity measurements, using a single receiving unit [12]. A less obvious feature of the technique is that it can also provide absorption measurements.

After a short review of the newly proposed technique for TE elimination, the principle of DBT for refractive index measurements is introduced in Sections 2.1 and 2.2. Section 2.3 presents some simulation results using a program based on the generalized Lorenz-Mie theory (GLMT) [13, 14], and Section 2.4 gives some useful equations from geometrical optics (GO). Section 2.6 reports on preliminary experimental results of the DBT. In Section 2.7, these experimental results are further discussed and points for the future development of DBT are proposed. The principle of the absorption coefficient measurements is then introduced in Section 3. Section 3.1 introduces the principle and Section 3.2 presents results of numerical investigations using GLMT. The preliminary experimental results obtained with monodispersed water-ink droplets are presented in Section 3.3. Section 4 gives some concluding remarks.

2 Development of the DBT for Refractive Index Measurements

2.1 Elimination of Trajectory Effects

Recently, two PDA optical geometries and a signal processing

* Dr. *F. Onofri*, Dr. *T. Girasole*, Dr. *G. Gréhan*, Prof. *G. Gouesbet*, Laboratoire d'Energétique des Systèmes et Procédés, URA CNRS 230, CORIA, INSA de Rouen, BP 08, 76131 Mont-Saint-Aignan (France).

** Dr. *G. Brenn*, Dr. *J. Domnick*, *T.-H. Xu*, M.Sc., Prof. Dr. *C. Tropea*, Lehrstuhl für Strömungsmechanik, Universität Erlangen-Nürnberg, Cauerstr. 4, D-91058 Erlangen (Germany).

0934-0866/96/0204-0112 $10.00+.25/0

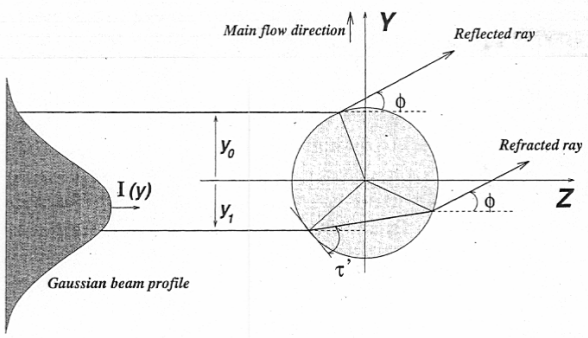

Fig. 1: Simplified scattering processes of a refractive particle in forward scattering, outside the diffraction zone.

procedure have been proposed for TE elimination. The first geometry is a planar PDA arrangement [9], and the second has been referred to as the modified standard geometry [10]. The principle used in these geometries to eliminate TE is briefly reviewed as a basis for introducing the DBT.

Referring to Figure 1, the scattering of a laser beam with a Gaussian intensity distribution from a relatively large particle is pictured. In this and for further discussions, scattering in the forward direction and refractive-dominated scattering is considered. Since the scattering angle usually exceeds 20°, diffraction can be neglected. Depending on the trajectory of the particle through the probe volume, the incident light for reflection may greatly exceed that for refraction due to the Gaussian intensity profile $I(y)$, thus altering the phase of the received light. This is the cause of the TE. For a given receiving angle, the point of the incident light impinging on the particle for the reflection (y_0) is different from the point of that for the refraction (y_1), as shown in Figure 1. Therefore, when the particle passes through the probe volume along the y axis, there will be a time delay between the intensity maxima of the reflected ray and the refracted ray. In the proposals to eliminate the TE, this time delay is used to separate the refracted light contribution from the reflected contribution. Moreover, the signal received from the refractive scattering is much larger in amplitude, allowing a positioning within the burst to ensure phase determination corresponding to refractive scattering.

The experimental illustration of this effect in the PDA technique was first used and reported by *Aizu* et al. [9], and subsequently by *Xu* and *Tropea* [10].

2.2 Principle of the DBT

In previous work on PDA, the time delay between the different scattering contributions reaching the detectors was used to suppress the TE by processing only the portion of the burst originating from refractive scattering. However, further information can be extracted by using all portions of the signal. Of the two scattering contributions, i.e. reflection ($p = 0$) and refraction ($p = 1$), only the refracted light is influenced by the material properties of the particle. The phase of the refracted light from a particle is a function of the optical set-up, particle size and particle refractive index. The phase of the reflected light is, however, only a function of optical set-up and particle size and does not depend on the particle refractive index. From the reflected burst, the particle diameter can be deduced. Knowing this diameter and the optical parameters of the phase-Doppler set-up, the particle refractive index can be determined from the phase of the refracted burst.

To use the DBT, the beam waist diameter must be reduced compared with typical values in PDA, in order to differentiate more clearly between the reflected and refracted contributions. Indeed, for a dominant refractive particle, the reflected contribution is low in amplitude compared with the refracted contribution. Therefore, any mixing between the two scattering processes must be avoided. Furthermore, with a small measuring volume, the laser power is focused on a smaller area, which also increases the intensity of the incident light and hence the signal-to-noise ratio (SNR) of the received signals.

2.3 GLMT Simulations

Numerical simulations using a phase-Doppler code based on GLMT were carried out to investigate the DBT. Water droplets were assumed to pass through a 54 μm measurement volume ($\lambda = 0.6328$ μm) of a modified standard PDA with three detectors (see Figure 2). Nevertheless, only two detectors

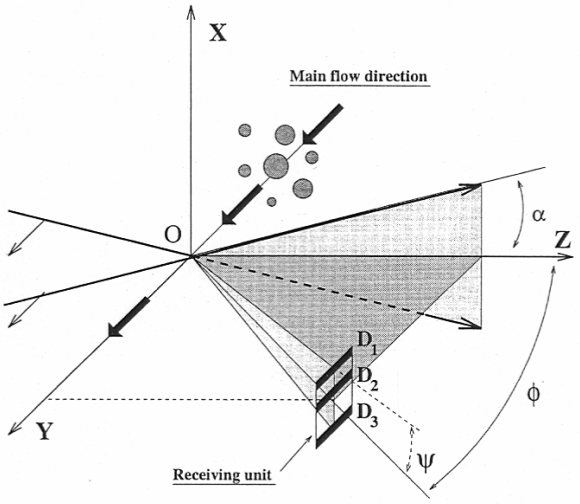

Fig. 2: Optical geometry of a modified standard PDA for implementing the DBT.

are considered for these simulations: detectors D_1 and D_3. The off-axis angle, and half-beam angle and the detector elevation angles ϕ, α, ψ^i are equal to 30°, 1.7° and ±3.69° respectively. The detector aperture shape is rectangular, with an angular aperture defined by $\delta x = \pm 0.277°$, $\delta y = \pm 2.77°$. Figure 3a displays the simulated phases when water droplets are moving along (OY) and Figure 3b displays the corresponding signal intensity.

In both Figures 3a and 3b, the two scattering processes ($p = 0$ for $Y < 0$, $p = 1$ for $Y > 0$) are evident, characterized in Figure 3a by the two plateaux of the phase evolution, and in Fig. 3b by local maxima for the signal intensity. For a 108 μm water droplet, for instance, two intensity maxima located at $y \approx -50$ μm and $y \approx 40$ μm can be distinguished. These two locations of intensity maxima correspond to two phase values in the two flat parts of the phase diagrams: $\Phi_0 \approx 269°$ and $\Phi_1 \approx 1°$ (with phase jump over 360°). Using these two phases and relations from geometrical optics (see next section), the particle diameter and refractive index are determined as 107.7 μm and 1.333, respectively. The time delay, expressed

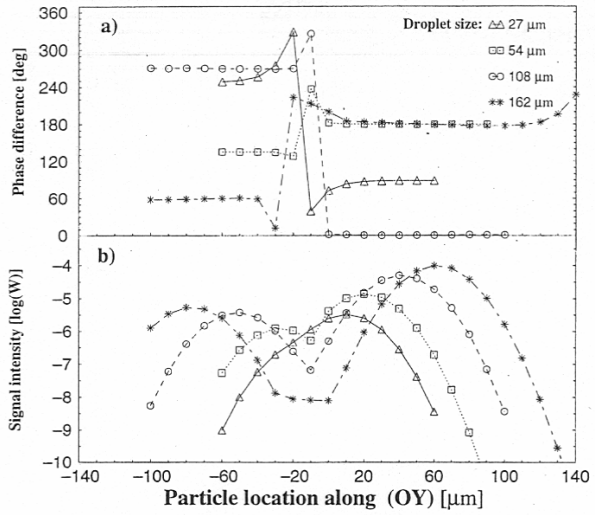

Fig 3: Dual burst technique: (a) simulated phase difference and (b) signal intensity versus droplet location and diameter. Measuring volume diameter $2\omega_0 = 54\,\mu m$, off-axis angle $\phi = 30°$, refractive index $m = 1.333$ (water droplets).

here as a spatial separation between the maxima, decreases with the particle diameter. For the 27 µm droplet, the two scattering processes are not well separated, i.e. the first intensity maximum is not clear. Furthermore, the phase difference continues to evolve in the reflected signal (as for the TE), demonstrating that there is a mixing of the scattered contributions. The diameter/refractive index deduced as above for the 27, 54 and 162 µm water droplets are 24.5 µm/1.300, 53.9 µm/1.328 and 159.9 µm/1.330, respectively.

Figure 4 displays the evolution of the simulated phase difference and the signal intensity for the 54 µm droplet when its trajectory is parallel to the fringes as in Figure 3, but at different x locations. In the phase patterns, only the mixing region evolves with the particle trajectory distance from the probe volume center. The two flat parts are independent of the particle trajectory, i.e. the DBT is free of TE for particles moving parallel to the y axis.

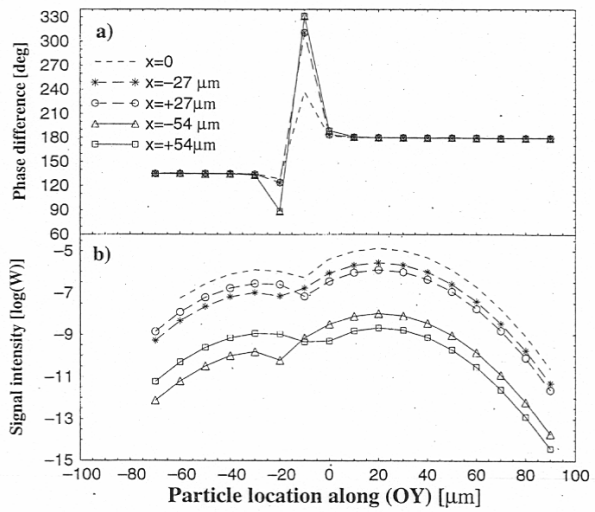

Fig. 4: DBT is free of TE: (a) simulated phase difference and (b) signal intensity versus droplet y location for different x locations. Droplet diameter $D = 54\,\mu m$, refractive index $m = 1.333$.

2.4 Analytic Formulation of Refractive Index Measurements

Detectors D_1, D_2 and D_3 are used to measure the particle size and the transverse velocity component V_{OX}. In order to obtain simultaneously the particle velocity in the direction of the main flow, a two-color PDA system has to be used.

From the signals from detectors D_1 and D_2, a phase difference Φ_p^{12} is obtained (p stands for reflection ($p = 0$) or refraction ($p = 1$)), and from D_1 and D_3 one obtains the phase difference Φ_p^{13}. Since the detector spacing between D_1 and D_2 is smaller than that between D_1 and D_3, the corresponding phase/diameter conversion factors follow: $|C_p^{13}| > |C_p^{12}|$, for $p = 0$ or $p = 1$. For a particle of diameter D and refractive index $m > 1$, we have with $C_0^{1i} < 0$ and $C_1^{1i} > 0$:

For the reflected signals:

$$(\Phi_0^{12} - 360°) = C_0^{12} \cdot D \tag{1}$$

$$(\Phi_0^{13} - 360°) - n_0 \cdot 360° = C_0^{13} \cdot D \tag{2}$$

$$n_0 = \mathrm{INT}\left\{\left[\frac{1}{360°}\left(\Phi_0^{13} - (\Phi_0^{12} - 360°)\frac{C_0^{13}}{C_0^{12}}\right) - 1\right] + 0.5\right\}. \tag{3}$$

Thus, from the phase of reflected bursts, the particle diameter D is deduced using the above expression for n_0 from

$$D = \frac{\Phi_0^{13} - 360°(n_0 + 1)}{C_0^{13}}. \tag{4}$$

For the refracted signals:

$$\Phi_1^{13} = C_1^{13} D - 360° n_1 \tag{5}$$

$$\Phi_1^{12} = C_1^{12} D \tag{6}$$

$$n_1 = \mathrm{INT}\left[\frac{1}{360°}\left(\frac{C_1^{13}}{C_1^{12}}\Phi_1^{12} - \Phi_1^{13}\right) + 0.5\right]. \tag{7}$$

The phase conversion factors C_1^{12} and C_1^{13} are both a function of the particle refractive index, hence n_1 cannot be deduced directly. To solve this problem, an approximation is made. The approximation is that the ratio C_1^{13}/C_1^{12} in Eq. (7) is only a very weak function of the refractive index and can therefore be determined independent of m for a given optical geometry. Thus, n_1 can be calculated for any one particle. One therefore obtains the quantity

$$C_1^{13} = \frac{\Phi_1^{13} + 360° n_1}{D} = f(m) \tag{8}$$

which is a function of the particle refractive index. The validity of this approximation can be briefly examined using geometrical optics.

According to *Naqwi* and *Durst* [15], the phase conversion factors for reflected light (C_0^i) and for refracted light (C_1^i) can be expressed for a point detector as a function of the off-axis angle ϕ, the half-beam angle α, the elevation angle ψ^i and the real particle refractive index m in the following form (note that the sign convention for the two scattering processes are

reversed compared with *Naqwi* and *Durst* [15]):

$$C_0^i = -\frac{u^i}{\sqrt{2(1-v^i)}} \tag{9}$$

$$C_1^i = \frac{mu^i}{\sqrt{2(1+v^i)[1+m^2-m\sqrt{2(1+v^i)}]}} \tag{10}$$

with

$$\begin{cases} u^i = k \sin\alpha \sin\psi^i \\ v^i = \cos\alpha \cos\psi^i \cos\phi \end{cases} \tag{11}$$

where $i = 1, 2, 3$ stands for the detector considered, and $k = 2\pi/\lambda$ for the wavenumber. For phase difference measurements, the useful parameters are (with $p = 0, 1$)

$$C_p^{1j} = C_p^1 - C_p^j, \quad j = 2, 3. \tag{12}$$

Thus, the particle refractive index can be deduced by reversing Eq. (10) with Eq. (12), yielding

$$m = \frac{\sqrt{2(1+v^1)} + \sqrt{2(1+v^1) - 4w}}{2w} \tag{13}$$

with

$$\begin{cases} w = 1 - \dfrac{2(u^1)^2}{(1+v^1)(C_1^{13})^2} \\ C_1^{13} = \dfrac{\Phi_1^{13} + n_1\ 360°}{D} \end{cases} \tag{14}$$

To verify that C_1^{13}/C_1^{12} is a very weak function of m, this ratio was computed using Eq. (10) for the PDA geometry used for the GLMT simulations. The results are shown in Figure 5 and the PDA geometry is given in Table 1. The dependence of C_1^{13}/C_1^{12} on the particle refractive index is extremely weak (less than 1% over a wide range). This influence on the computation of the discrete parameter n_1 can thus be neglected.

2.5 Considerations Concerning the Expected Sensitivity

Knowing the basic formulations to extract the particle refractive index and diameter from the measured phase

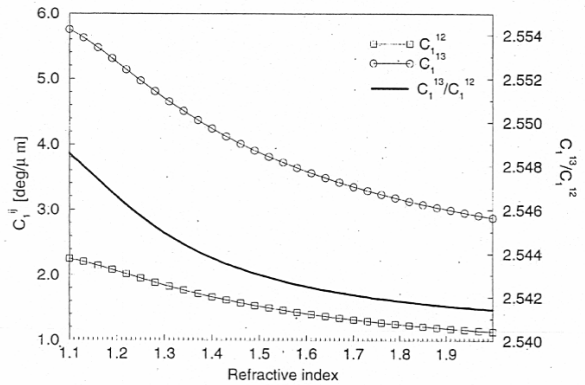

Fig. 5: Evolution of the phase conversion factors of the refracted light and their ratio versus particle refractive index.

Table 1: PDA set-up used for refractive index measurements with the DBT.

Wavelength	632.8 nm	Detector aperture (rectangular) height	2.77°
Half-beam angle	1.7°		
Polarization	Orthog.	Detector width	.277°
Off-axis angle	30°	Beam waist	54 μm
Elevation angle D_1	+3.69°	Elevation angle D_3	−3.69°

difference, a compromise must be found for the PDA optical parameters. The main conditions were selected:

- The intensity ratio between the two scattering processes has to be close to unity for easy signal processing.
- The phase sensitivity to the particle refractive index has to be maximized.
- The size and refractive index dynamic range has to be maximized.

The intensity ratio between the scattering processes is essentially a function of the off-axis angle, as demonstrated in Figure 6, where the intensity of reflected and refracted light versus the scattering angle is predicted by geometric optics for parallel and perpendicular polarization, and for $m = 1.33$, 1.34 and 1.35. In forward scattering $p = 0$ and $p = 1$ both exist. Nevertheless, differences between the reflected and refracted light for parallel polarization are much larger than for perpendicular polarization. The perpendicular polarization is therefore more suitable for the DBT.

The phase conversion factors depend on the refractive index, according to Eq. (10), but also on α, ψ, ϕ and λ. Nevertheless, we are interested in the phase sensitivity to the refractive index expressed by (dC_1^{13}/dm). In Eq. (10), the half-beam angle α and the elevation angle ψ^i play an equivalent role in the approximation of small angles. Their product can therefore be considered as the significant parameter. Figure 7a shows the evolution of the calculated conversion factor C_1 versus the particle refractive index m for $\alpha \cdot \psi = 6.27°°$, with ϕ as a parameter.

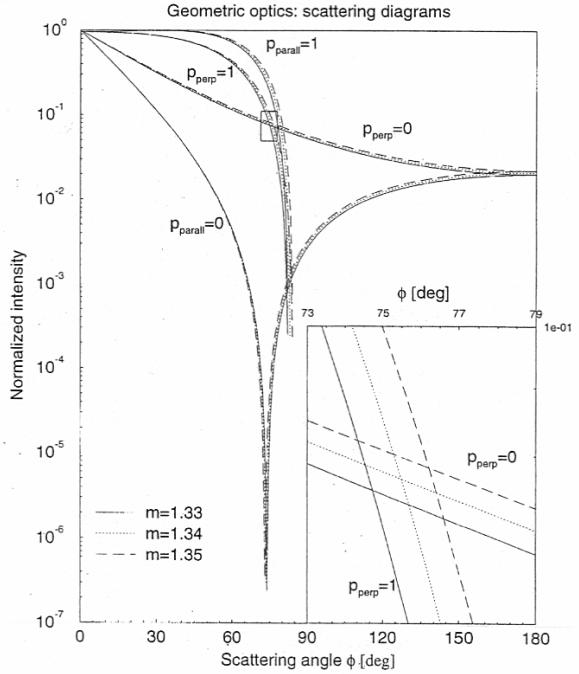

Fig. 6: Scattered intensity by reflection ($p = 0$) and refraction ($p = 1$), for $m = 1.33$, 1.34 and 1.35, calculated using geometric optics.

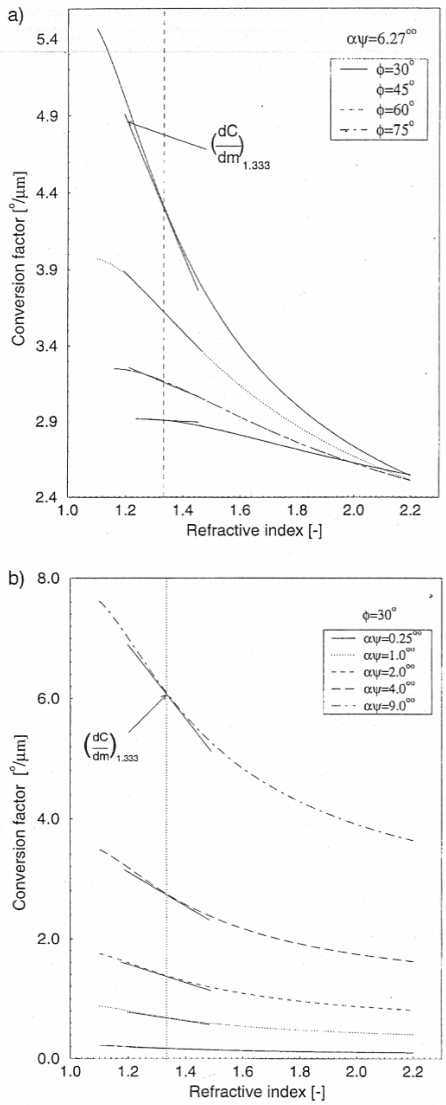

Fig. 7: (a) Evolution of the phase conversion factor C_1^{13} versus the particle refractive index and the off-axis angle for $\alpha\psi = 6.27°°$. (b) Evolution of the phase conversion factor C_1^{13} versus the particle refractive index and the product of the half-beam angle and the detector elevation angle for $\phi = 30°$. The wavelength is $\lambda = 0.6328\,\mu m$.

Figure 7b shows the conversion factor C_1^{13} as a function of m, for $\phi = 30°$ with the product $\alpha \cdot \psi$ as a parameter. The wavelength has the constant value $\lambda = 0.6328\,\mu m$.

For given m, the slope $(dC_1^{13}/dm)_m$ is an increasing function of $\alpha \cdot \psi$. Conversely, for a constant value of the parameter, it is a decreasing function of the particle refractive index. The off-axis angle also plays an important role in the phase sensitivity to the refractive index.

As an example of the quantification of this sensitivity for $\phi = 30°$, $\alpha = 1.7°$, $\psi = 3.69°$, and a particle diameter of $100\,\mu m$, a calculation yields that ϕ_1^{13} varies by 10° for a change in refractive index from $m = 1.33$ to 1.34.

2.6 Experimental Investigations

The PDA geometry used in the experiments was the same as in the GLMT simulations, except that the detector aperture shape was circular with a cone half-angle equal to 2.77°. The particle stream was directed in the negative y direction, in contrast to the illustration in Figure 2. Monodispersed droplets were used for the tests. Water ($m = 1.333$), ethanol ($m = 1.361$) and a sugar-water solution (45% sucrose by weight, $m = 1.410$), were used for achieving different particle refractive indices. The nominal sizes of the droplets, according to the set-up of the droplet generator, were 95–98 μm for water, 89–91, 100 and 125 μm for the sugar-water solution and 25–34, 38–45 and 54–64 μm for ethanol. The bursts were stored in a digital oscilloscope and read out to a PC. A zero-crossing procedure and a cross-spectral density algorithm with sliding window [16, 17] were used to compute the phase difference between the burst coming from the two detectors D_1 and D_3. A shift frequency of 5 MHz was applied to the laser beams to obtain a sufficient number of cycles in the signal bursts for signal processing.

As an example of typical dual bursts, Figure 8 shows three signals produced by D_1 and the measured phase evolution between signals of the two channels. They were produced by (a) a 25 μm ethanol droplet, (b) a 75 μm ethanol droplet and (c) a 95 μm water droplet, passing through the measuring volume along (OY). For the large particles (b) and (c), the phase diagrams show two flat zones, separated by a transition zone with a phase jump. These zones correspond to two maxima in the signal amplitude: the refracted burst (with the higher amplitude) and the reflected burst (with the lower amplitude). By measuring the phase difference around these maxima, and using Eqs. (9)–(14) with $n_0 = n_1 = 2$, the droplet size/refractive index deduced are 74.2 μm/1.354 and 93.8 μm/1.316.

In Figure 8a, a separation of the bursts due to the two scattering processes is observed but not as clear as in Figures 8b and 8c. In the phase difference curve, the transition between the two flat parts is smoother compared with cases (b) and (c) and the flatness of the curve in the reflection-dominated part is reduced. In this case, the droplet size is too small, compared with the beam waist diameter, to avoid mixing of the two scattering processes. In other words, the Gaussian intensity profile with the 54 μm waist diameter is too smooth to separate the two contributions with a sufficient time delay. This phenomenon has already been predicted by simulation in Figure 3, where the behaviour of the 27 μm droplet is equivalent to case (a) in Figure 8. Thus, for this droplet size (about half of the probe volume size) and obviously for smaller droplets, the problem is where to extract the phase information for the reflection process in the signal burst in order to obtain the best accuracy, and how to find the required position during signal processing. This is an open problem. Nevertheless, some solutions are possible, for example to make an estimate of the time delay between the maxima of the two contributions, thus enabling the right position in the reflected burst to be found according to the amplitude maximum of the burst [18]. In the current experimental investigations, when the reflected burst from a small particle could not be detected from its amplitude due to the mixing of the two contributions, the phase difference for the reflection was measured at the position where $d^2\Phi_0^{13}/dt^2 = 0$. Using this method, the droplet size/refractive index for case (a) were estimated as 25 μm/1.358. Measurements were carried out for different droplet sizes. The accuracy of the size measurements with the DBT can thus be checked over a wide size range. With the DBT, reflected bursts yield the particle diameter directly. Figure 9 displays the measured diameters from the reflected burst versus the nominal droplet diameter according to the monodispersed droplet generator. Good agreement

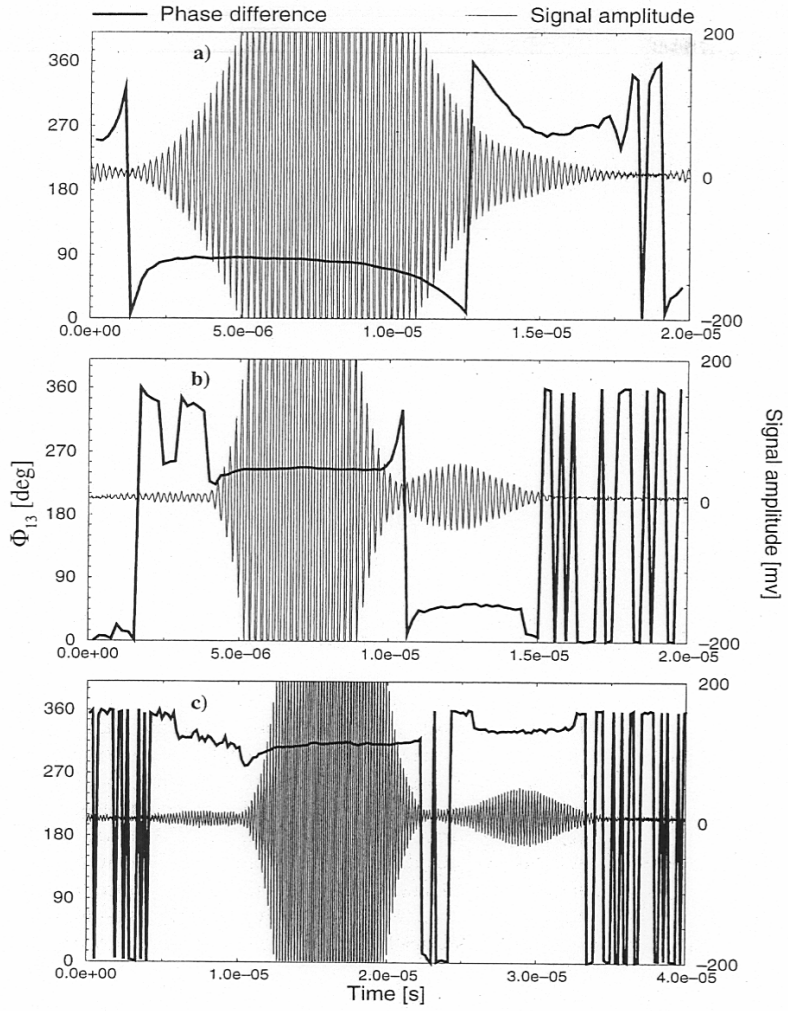

Fig. 8: Dual burst technique: typical experimentally recorded signals with their computed phase evolutions for (a) a 25 µm ethanol droplet, (b) a 75 µm ethanol droplet and (c) a 95 µm water droplet.

(within 10%) is found for large particles, even for particles larger than twice the probe volume diameter. For small droplets (below 50 µm), the diameter estimation is not as good. This point will be discussed later.

In the present experiments, the particle refractive index is known beforehand. Thus, the droplet diameter can be deduced from the refracted bursts. Figure 10 shows a comparison of the droplet diameters obtained from the reflected burst and from the refracted burst. The consistency of the information extracted from the two scattering processes is clear: droplet diameters measured from the refracted light and the reflected light agree with an accuracy of better than 10% over all the sizes. Note that here for small particles (below 50 µm), the agreement is much better than in Figure 9. It may be doubtful whether the nominal diameters of the small droplets are very accurate, because in the operation of the TSI-3450 droplet generator for producing very small droplets, the flow-rate/operating pressure took a long time to become stable, while the operating frequency range in which droplets are monodispersed depends strongly on the flow-rate. Simultaneous measurements of droplet diameter and refractive index are displayed in Figure 11. In this plot, six groups can be distinguished, as given in Table 2. The results of the measurements of groups A60, S100 and W95 are concentrated around the expected value for size and refractive index. The mean refractive index and the standard deviation of the measurements are given in Table 2.

For groups A30 and A40, the results fluctuate strongly, leading to unreliable refractive index measurements. The errors may be due to the low SNR and the selection of the portion of the signal for phase estimation.

The errors in measurements of groups A30 and A40 are much higher than those of group A60. Apart from the reasons described above, errors also arose because the distance between droplets was too small in this case. The reflected light from one droplet was thus mixed with the refracted light from another droplet behind it. This was clearly seen in the recorded signals (and partially in Figure 8a). For the measurements of group S125, a discussion is given in the next section. Figure 12 plots

Table 2: Summary of results of refractive index measurements.

Group	Material	Nominal diameter (µm)	Mean refractive index, m	Standard deviation of m
A30	Ethanol	25–34	1.382	0.0636
A40	Ethanol	38–45	1.382	0.0441
A60	Ethanol	54–64	1.360	0.0147
S100	Sugar-water	100	1.407	0.0146
S125	Sugar-water	125	1.378	0.0168
W95	Water	95–98	1.331	0.0112

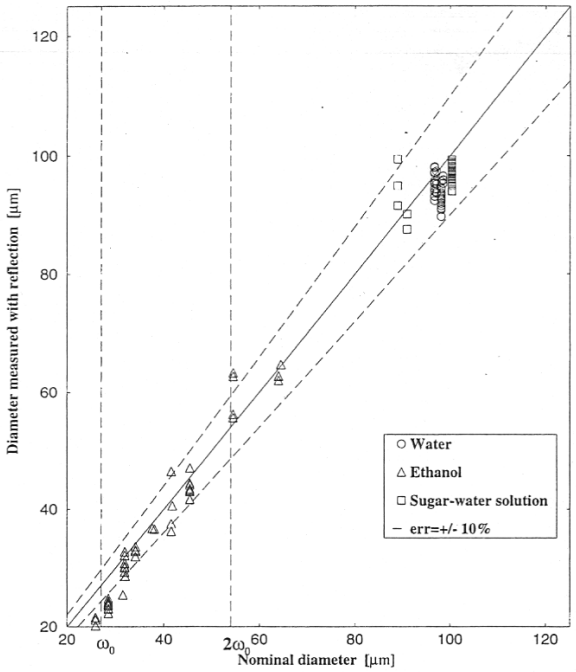

Fig. 9: Size measurements with the reflected contribution.

the data of group W95, groups A40 and A60, and group S100 as a histogram.

2.7 Discussion

From conventional PDA, it is well known that the receiving aperture size and shape are of great importance to obtain accurate size measurements [19]. The aperture size influences the signal intensity directly, whereas the aperture shape mainly determines the signal visibility. In DBT, the influence of this last parameter is even more important, because an unsuitable receiving aperture shape may lead to non-linearity of the calibration curve, especially for large particle sizes, and the tolerance to this deviation for a satisfactory refractive index measurement is much smaller than that for a size measurement. Figure 13 displays the simulated phase and signal evolution for a sugar-water droplet of 125 µm diameter for different receiving

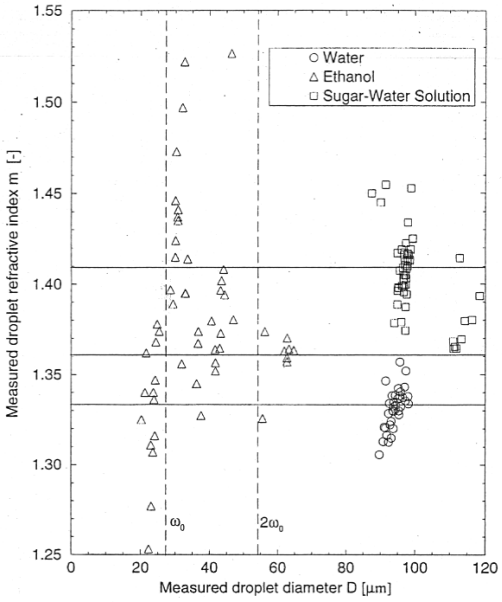

Fig. 11: Dual burst technique: measured refractive index versus the corresponding measured droplet diameter.

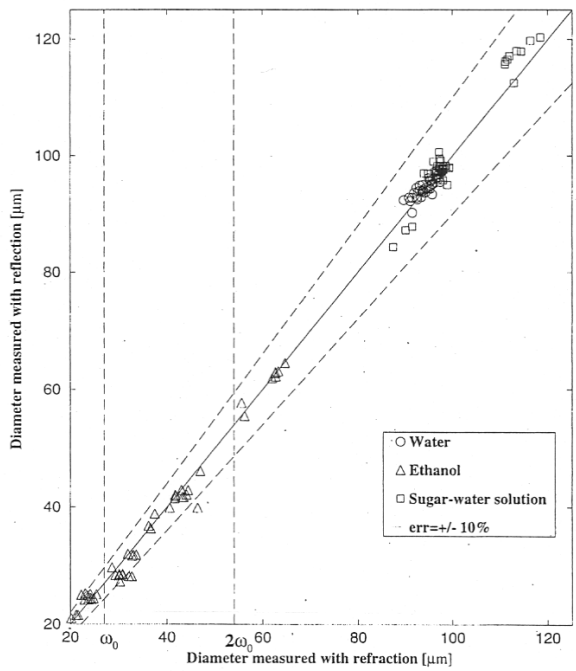

Fig. 10: Measured sizes using the reflected contribution versus the measured sizes using the refracted contribution.

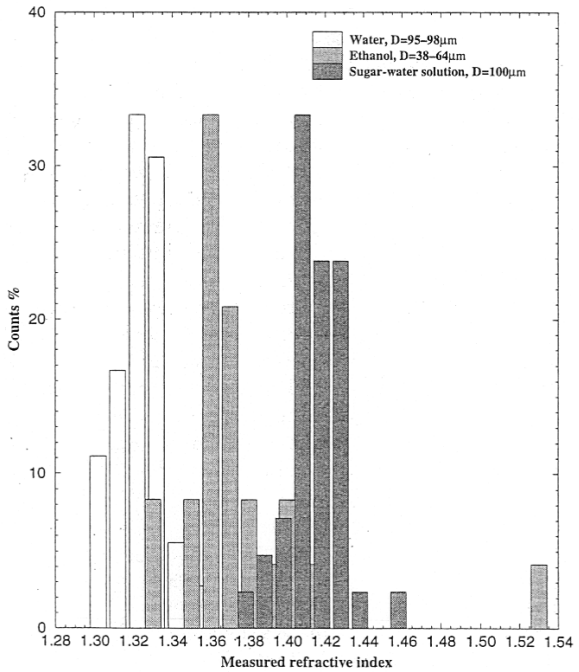

Fig. 12: Distribution of measured refractive index in groups W95, A40–A60 and S100.

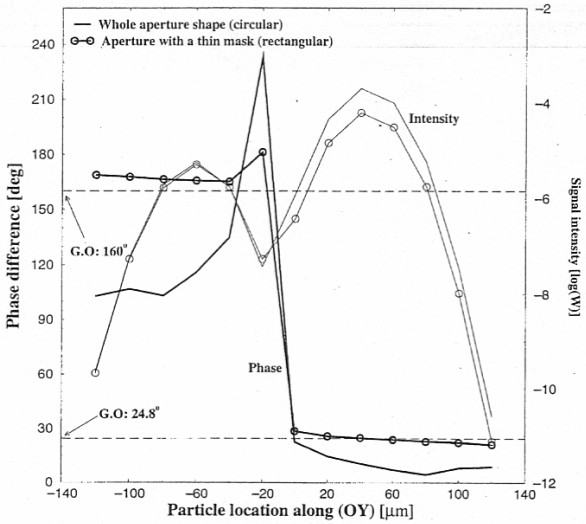

Fig. 13: Influence of the detector aperture shape. GLMT simulations for a 125 μm sugar-water droplet.

apertures. The experimental conditions for group S125 in Figure 11 were used, with the exception that the receiving apertures were replaced by narrow rectangular apertures ($\delta x = \pm 0.277°$, $\delta y = \pm 2.77°$). According to GO, the phases in this case should be 160.0° and 24.8° (with a jump of 360°) for reflection and refraction, respectively. From GLMT simulations for the rectangular aperture, using the phases around the intensity maxima, the droplet size/refractive index are predicted to be 125.4 μm/1.413. With the exact optical parameters of group S125, however, including the circular receiving aperture, the results were 115.9 μm/1.363. Regardless of the exact value, this simulation predicted that the use of a circular aperture will result in a negative error in the refractive index measurement. Very good agreement is found with the measured diameter and refractive index for the corresponding particles in Figure 11 and Table 2.

Note that in Figure 13, although the area of the circular receiving aperture is eight times larger than the rectangular aperture, the signal intensities of the reflected contribution in both cases are about the same.

As shown in Figure 8, the cross-spectral density algorithm with sliding window can be successfully used in DBT to trace the phase difference evolution. The question is, however, where to extract the phase information for the reflection process in the signal burst to obtain the best accuracy for small particles and how to find the required position during signal processing.

For each particle passing through the measuring volume, the phase of the corresponding burst can be analyzed continuously by the DBT signal processor. With the present electronics/computer, it is already possible to implement such a kind of signal processor. The main advantage is that, by tracing the phase evolution inside the dual bursts with DBT, some of the particle non-homogeneities (e.g. cenospheres) can be recognized [20–22].

3 Absorption Coefficient Measurements

3.1 Principle

Further information on the scattering particles can be deduced from the signals when the ratio of the two intensity maxima is considered. This ratio contains information on the absorption coefficient of the particle, as one of the bursts is produced by reflection and the other by refraction, and is therefore influenced by the absorption in the particle.

The principle of this extension of the DBT is explained briefly. The scattered intensity from refraction can be approximated by an exponential function of the particle diameter and absorption coefficient, which reads for the maxima

$$I_{1,K}^{max} = I_{1,0}^{max} \cdot e^{-KL} \tag{15}$$

where $I_{1,K}^{max}$ is the collected maximum of the refracted rays for a given absorbing particle and $I_{1,0}^{max}$ is the collected maximum intensity of the same particle but without absorption. K is the absorption coefficient related to the complex part k of the particle refractive index by $k = K \cdot \lambda/4\pi$. L is the optical path of the refracted rays through the particle, which can be expressed as a product of particle diameter D and a constant A which is to be determined, $L = A \cdot D$. Generally, from the previous relation it is straightforward to deduce that by measuring $I_{1,K}^{max}$, absorption measurements can be performed if the terms $I_{1,0}^{max}$ and A are known. Nevertheless, this requires calibration experiments, as at least $I_{1,0}^{max}$ is a function of the laser power, the optics alignment, the gain of detectors, etc.

In the case of the DBT, the values of $I_{1,K}^{max}$ and I_0^{max}, the corresponding maximum of the scattered light by reflection, are provided. This second term can be used as a reference value. Thus, the problem is reduced to finding an expression relating the maximum of the reflected and refracted light intensity and the constant A, for a given particle and for a given PDA configuration.

For large particles ($D \gg \lambda$), it can be shown that without absorption, the intensity ratio of reflected light and refracted light is a function of the scattering angle and the polarization of the incident light. This ratio does not depend on the particle diameter. Let $B = \ln(I_{1,0}^{max}/I_0^{max})$. Then, the absorption coefficient is

$$K = \frac{-1}{A \cdot D}\left[\ln\left(\frac{I_{1,K}^{max}}{I_0^{max}}\right) - B\right]. \tag{16}$$

According to this equation, only the ratio $I_{1,K}^{max}/I_0^{max}$ and the particle diameter D are to be measured in order to determine experimentally the absorption coefficient with the DBT. The constants A and B can be computed using GLMT or GO.

The constant A can be considered as the non-dimensional optical path of the refracted rays through the particle. Thus, GO gives

$$A = sin(\tau') \tag{17}$$

where τ' is defined in Figure 1 as a function of the particle refractive index and the scattering angle (± off-axis angle) [23].

3.2 GLMT Simulations

A PDA geometry with the same parameters as in Table 1 was used to simulate absorption measurements with the DBT; however, the off-axis angle here is 60°. This last parameter was increased to obtain a compromise between the sensitivity of the ratio $\ln(I_{1,0}^{max}/I_0^{max})$ to particle absorption and the corresponding dynamic range. The total laser power for the computations is 46 mW. The particles considered are droplets of a water-ink solution, for which the complex refractive index has been found

Table 3: Complex refractive index data used for the water-ink solutions [24].

Concentration of ink in water (wt.%)	Complex refractive index ($\lambda = 0.488\,\mu m$) at $T = 20°C$
0	$1.336 - i\,0.0$
2	$1.337 - i\,0.78 \cdot 10^{-4}$
4	$1.337 - i\,6.43 \cdot 10^{-4}$
7	$1.338 - i\,9.03 \cdot 10^{-4}$
12	$1.34 - i\,1.28 \cdot 10^{-3}$
25	$1.34 - i\,2.49 \cdot 10^{-3}$

by *Manasse* et al. [24], and is reported in Table 3. In this table, the complex refractive index is given versus the weight percentage of ink in water.

In order to simulate absorption measurements, simulations using GLMT for three droplet diameters, D = (a) 54, (b) 108 and (c) 216 μm, and different concentrations of ink, 0, 2, 4, 7, 12 and 25%, were performed. The droplet trajectory in the probe volume is along (OY). In Figure 14, the evolution of the signal intensity from D_1 and the phase difference between D_1 and D_3 are presented versus the particle location along (OY), with $X = Z = 0$.

The distinction between the reflective ($Y < 0$) and refractive ($Y > 0$) processes is clearly apparent. The effect of the absorption is to decrease the maximum of the refracted light, as expected. Refracted light becomes very weak after 25% of ink by weight is reached, i.e. $k = 2.5 \cdot 10^{-3}$. The reflected light intensity is almost constant, as assumed previously. The absorption seems to have almost no influence on the phase difference around the signal maximum, except of course for large absorption and large particles, for which the refractive process has almost totally disappeared, leading to signals with low SNR.

In order to verify the validity of Eq. (16), the following relation is plotted in Figure 15:

$$\ln\left(\frac{I_{1,K}^{max}}{I_0^{max}}\right) = f(KD) \tag{18}$$

where $I_{1,K}^{max}/I_0^{max}$ is deduced from Figures 14a, 14c and 14e by fitting a three-point exponential to the maximum of the reflected peak I_0^{max}, and to that of the refracted peak $I_{1,K}^{max}$. Note that the function $f(KD)$, according to Eq. (16), is expected to be of the form $f(KD) = B - A \cdot KD$.

From Figure 15 it is clear that the relation is linear in spite of some fluctuations for small values of KD. If we make a linear regression over the whole set of data, the slope of f is found to be equal to -0.6898 ($= A$), and the intercept is 0.8289 ($= B$).

In Figure 16, the results of the inversion of Eq. (16) using coefficients A and B deduced from Figure 15 are shown. Thus each intensity ratio and the reflected phase from Figure 14 were used to simulate measurements. In Figure 16,

- For $k \leq 7.8 \cdot 10^{-4}$, the intensity ratio evolves linearly except for the small particle ($D = 54\,\mu m$). This could be expected, as the linear regression in Figure 15, does not fit this group of values very well.
- For $7.8 \cdot 10^{-4} < k \leq 1.28 \cdot 10^{-3}$, k is determined with an accuracy of better than 10% for particles between 54 and 216 μm.
- For $1.28 \cdot 10^{-3} < k \leq 2.49 \cdot 10^{-3}$, k is also correctly estimated except for the largest particle ($D = 216\,\mu m$). This last case can be easily explained, as the collected refracted light intensity from this particle is extremely weak (see Figure 14). Thus, any uncertainty in its determination induces large deviations from the expected value. This phenomenon is a common limiting point of any absorption measurement technique.

3.3 Experimental Results

The PDA geometry used for this preliminary test is identical with that described in Table 1, except that the off-axis angle has been set to 60° in order to increase the available absorption range and the intensity of the reflected contribution (see Figure 6). The experimental procedure used was similar to that for refractive index measurements. Monodispersed droplets with different water-ink concentrations were produced by a drop-on-demand generator.

As an example, Figure 17 presents typical signal bursts recorded during the experiments for water droplets of 87 μm nominal diameter. These signals were digitally filtered in order to suppress the Doppler frequency and to make the signal intensity maxima clearly apparent.

Figure 18 presents the histograms obtained using both of the two scattering processes to deduce the size of droplets of a 16% ink solution, with a nominal size of 87 μm.

The two histograms are centered around the expected value. Nevertheless, the standard deviation of the size measurements based on the refracted process is much greater than that for the reflected process. This may be attributed to the weakness of the refracted contributions for this ink concentration, which leads to a low SNR and errors in the phase estimation. Another reason may be the influence on the physical heterogeneity of the ink solutions. Further experimental tests will be made in the future to investigate this effect.

Figure 19 presents (*i*) on-line absorption measurements obtained for different ink concentrations with the DBT, simultaneously with the droplet size and velocity, and (*ii*) absorption measurements with a static photometer with the solutions used to produce the droplets. Note that the photometer measurements could only be carried out up to a concentration of 2% ink in water. The values for higher concentrations were then computed by linear extrapolation, referring to Table 3, taking into account the wavelength of $\lambda = 0.6328\,\mu m$ used for the DBT measurements.

There are some fluctuations of the absorption measurements with DBT versus the ink concentration. Nevertheless, a linear trend can be found. Furthermore, this linear evolution (linear regression over the measurements) deviates only slightly from the extrapolated line obtained with the photometer. These deviations can be explained by the wavelength used in the computations of A and B, which was different from the wavelength used in the experiments.

4 Conclusions

The principle of an innovative technique, the phase-Doppler method with the dual burst technique (DBT), has been examined. Using this technique, a phase-Doppler anemometer (PDA) with a single receiving optics can be used to perform refractive index or absorption coefficient measurements simultaneously with particle size and velocity. The results from preliminary experimental investigations and simulations are promising. The different ink solutions in Figure 19 could

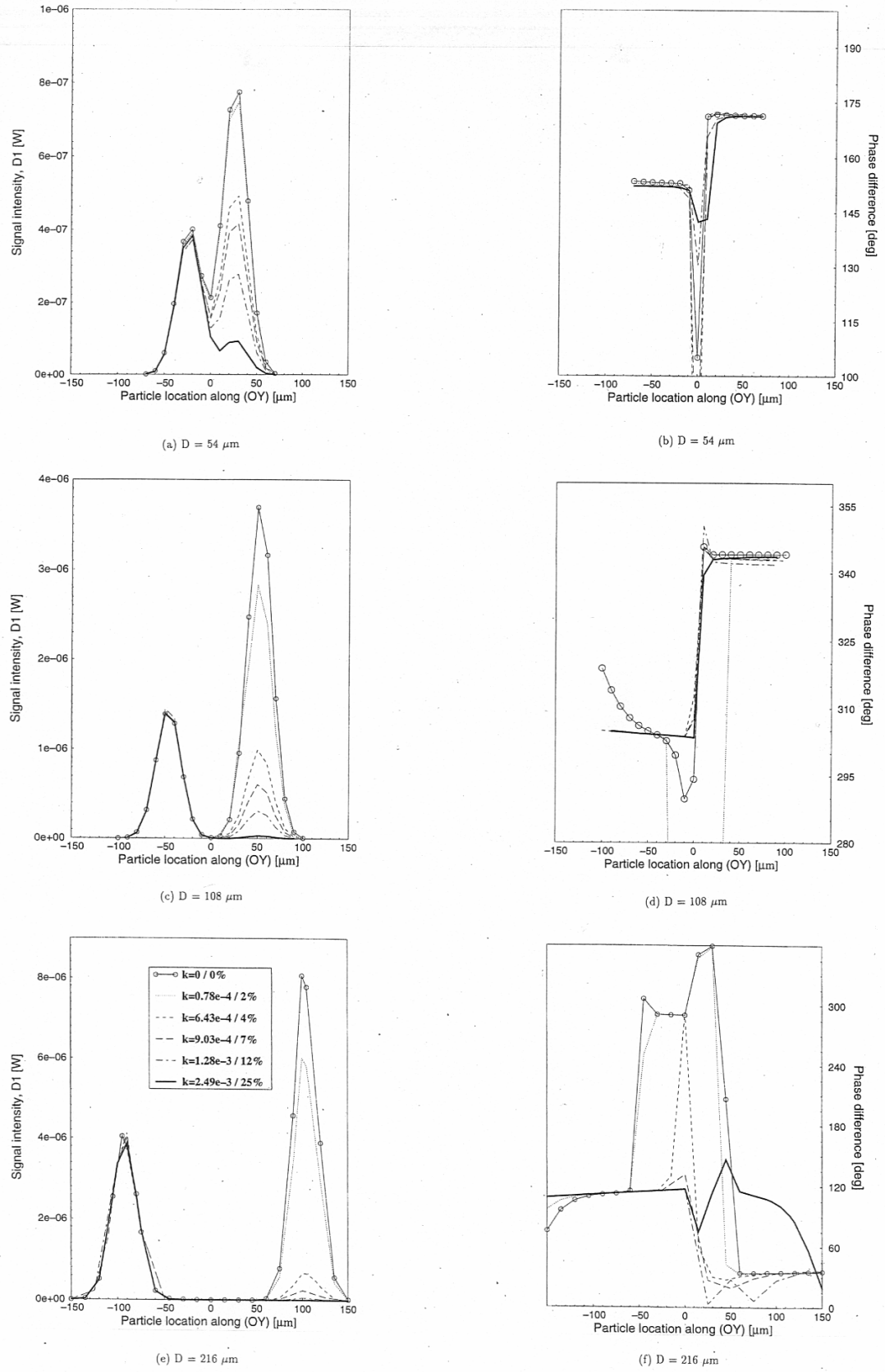

(a) D = 54 μm (b) D = 54 μm

(c) D = 108 μm (d) D = 108 μm

(e) D = 216 μm (f) D = 216 μm

Fig. 14: Evolution of the signal intensity and phase difference for three droplet diameters and six values for the complex part of the refractive index. Droplet trajectory along (OY).

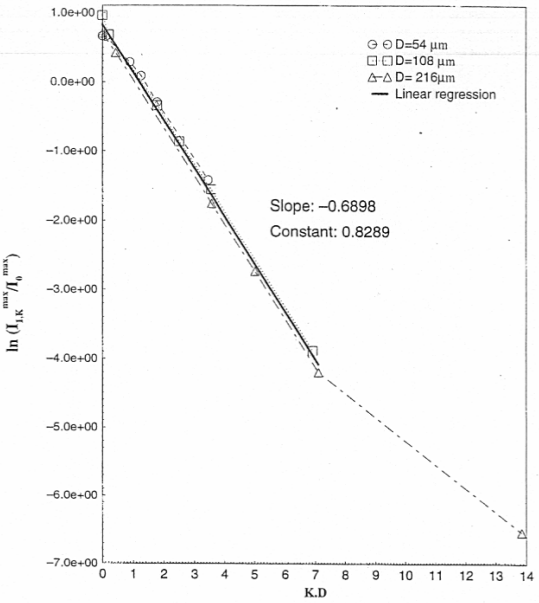

Fig. 15: Evolution of the logarithm of the ratio between the maximum of the refracted and reflected contributions versus the product of the particle diameter and absorption.

clearly be distinguished on the basis of measurements of the quantity $\ln(I_{1,K}^{max}/I_0^{max})$. It should be mentioned that, in order to compensate for effects of different x locations of the droplet trajectory parallel to the y axis, the arithmetic mean of $\ln(I_{1,K}^{max}/I_0^{max})$ from the two photodetectors D_1 and D_3 is used for the measurements. It could be shown theoretically that this method totally eliminates the influence of different droplet trajectories. For treating droplets with trajectories which are not parallel to the y axis, however, there is still more work to be done. As mentioned previously, a physically heterogeneous water-ink solution has been examined. However, in order to make a comparison with the GLMT simulations, an optically homogeneous solution would be more appropriate. This may be the source of observed discrepancies.

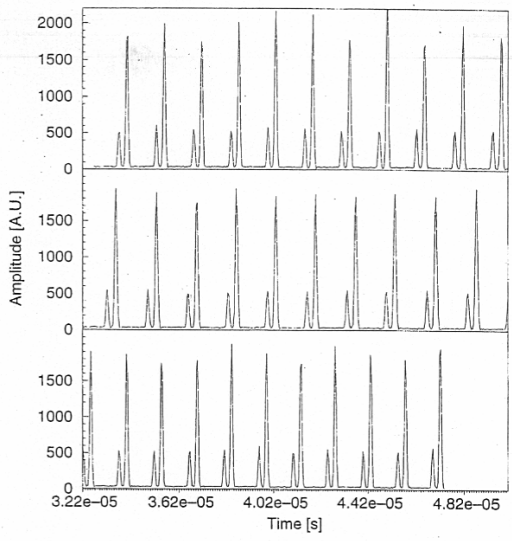

Fig. 17: Typical signal bursts recorded experimentally for water droplets of 87 µm in diameter. These signals were low-pass filtered to suppress the Doppler frequency.

The next steps will be to design an optimized DBT system based on the points discussed in this paper. This will include also considerations of the receiving aperture shape. As shown in this paper, the optimization of the DBT for refractive index or absorption coefficient measurements leads to different arrangements.

5 Acknowledgements

The authors are grateful to the Commission of the European

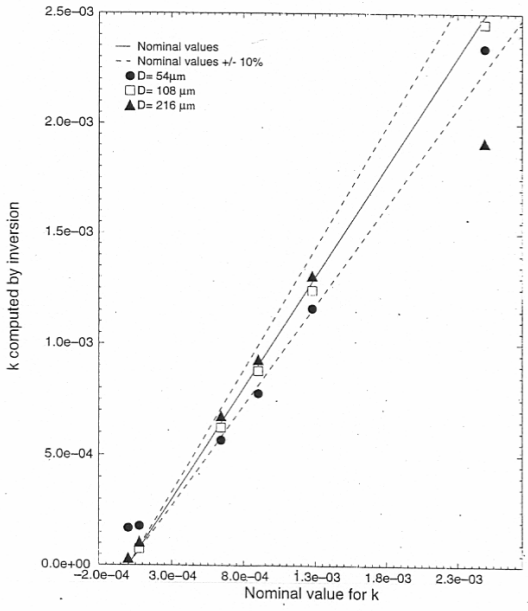

Fig. 16: Derived value for the imaginary part of the particle refractive index versus the nominal value, with the particle diameter as parameter.

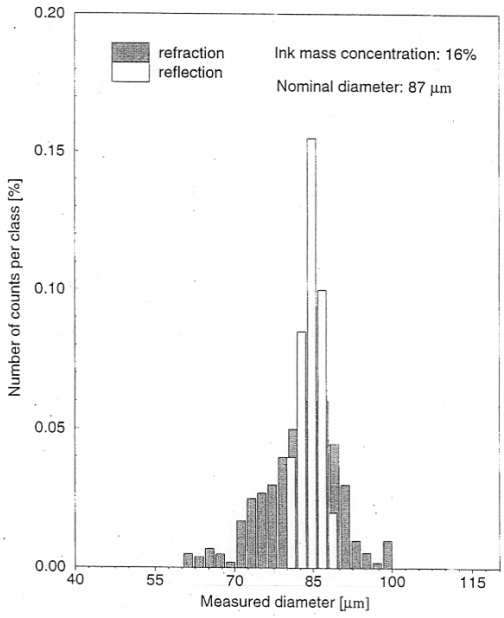

Fig. 18: Size histograms obtained with the reflected and refracted bursts of nominal monodispersed water-ink droplets (16% of ink) with 87 µm diameter.

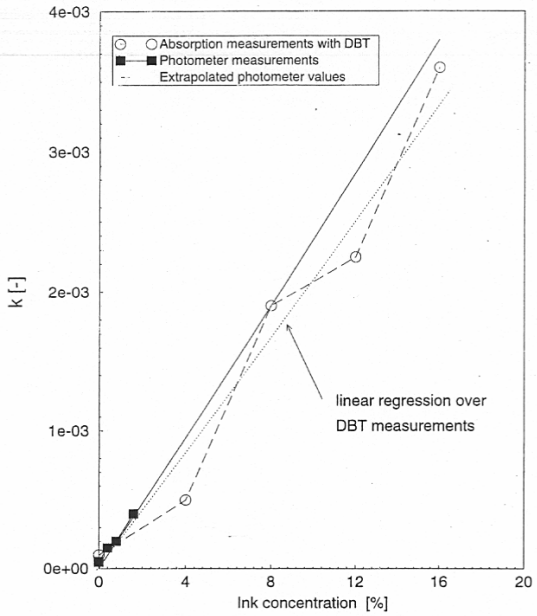

Fig. 19: Comparison of the imaginary part of the water-ink droplet refractive index measured with DBT and with a static photometer. The nominal droplet diameter is 87 µm.

Communities, the French government (program PROCOPE), the German Ministry of Research and Technology (BMFT, now BMBF) and the Deutsche Forschungsgemeinschaft (DFG) for providing financial support for this work.

6 Symbols and Abbreviations

A	constant
B	ratio of maximum intensities of refracted light and reflected light without absorption
C	phase/diameter conversion factor
D	particle diameter
I	light intensity
k	wavenumber $2\pi/\lambda$
k	imaginary part of the refractive index
K	absorption coefficient
L	optical path length
m	real part of the refractive index
n_0, n_1	integer numbers (phase jump over 2π)
p	scattering order
T	temperature
V	velocity component
x, y, z	cartesian coordinates
α	half-beam angle
δx, δy	aperture half-angles
λ	wavelength of light
τ'	angle between refracted ray and surface tangent
ϕ	off-axis angle of detectors
Φ	phase shift
ψ	elevation angle of detector
ω_0	radius of beam waist

Sub- and superscripts

0, 1	scattering order
12, 13	detector pairs
i, j	sub- and superscripts for detector numbers
perp	perpendicular
parall	parallel

7 References

[1] *F. Durst, M. Zaré:* Laser Doppler measurements in two-phase flows. Proc. LDA-Symposium, Copenhagen, 1975 pp. 403–429.

[2] *W. D. Bachalo, M. J. Houser:* Phase/Doppler spray analyzer for simultaneous measurements of drop size and velocity distributions. Opt. Eng. *23* (1984) 583–590.

[3] *M. Saffman, P. Buchhave, H. Tanger:* Simultaneous measurement of size, concentration and velocity of spherical particles by a laser Doppler method, in *Adrian, Durao, Durst, Mishina, Whitelaw* (eds.): Laser Anemometry in Fluid Mechanics-II LADOAN-Lisbon, 85–104, 1984.

[4] *A. Naqwi, F. Durst, X. Liu:* Two optical methods for simultaneous measurement of particle size, velocity, and refractive index. Appl. Opt. *30* (1991) 4949–4959.

[5] *S. V. Sankar, K. M. Ibrahim, D. H. Buermann, M. J. Fidrich, W. D. Bachalo:* An integrated phase Doppler/rainbow refractometer system for simultaneous measurement of droplet size, velocity, and refractive index. Proc. 3rd Int. Congr. Optical Particle Sizing, Yokohama (Japan) 1993, pp. 275–284.

[6] *S. V. Sankar, A. Inenaga, W. D. Bachalo:* Trajectory dependent scattering in phase Doppler interferometry: minimizing and eliminating sizing error. Proc. Sixth Int. Symp. on Application of Laser Techniques to Fluid Mechanics, Lisbon (Portugal), paper 12–2, 1992.

[7] *G. Gréhan, G. Gouesbet, A. Naqwi, F. Durst:* On elimination of the trajectory effects in phase-Doppler systems. Proc. 5th Europ. Symp. Particle Characterization (PARTEC 92), Nürnberg, 1992, pp. 309–318.

[8] *F. Onofri, C. Rozé, G. Gréhan:* Traitement des signaux phase Doppler et ADL sujets aux effets de trajectoire: analyse par ondelettes. In 9èmes Journées d'Etudes sur les Aérosols (Paris), December 8–9 1992, pp. 81–89.

[9] *Y. Aizu, F. Durst, G. Gréhan, F. Onofri, T.-H, Xu:* PDA system without Gaussian beam defects. Proc. 3rd Int. Congr. Optical Particle Sizing, Yokohama (Japan), 1993. pp. 461–470.

[10] *T.-H. Xu, C. Tropea:* Improving performance of 2D phase-Doppler anemometers. Meas. Sci. Technol. *5* (1994) 969–975.

[11] *G. Gréhan, F. Onofri, T. Girasole, G. Gouesbet:* Measurement of bubbles by phase-Doppler technique and trajectory ambiguity. Proc. 7th Int. Symp. on Applications of Laser Techniques to Fluid Mechanics, Lisbon, 1994, pp. 18.21–28.

[12] *F. Onofri, G. Gréhan, G. Gouesbet, T.-H. Xu, G. Brenn, C. Tropea:* Phase-Doppler anemometry with dual burst technique for particle refractive index measurements. Proc. 7th Int. Symp. on Applications of Laser Techniques to Fluid Mechanics, Lisbon, 1994, pp. 21.41–48.

[13] *G. Gouesbet, G. Gréhan, B. Maheu:* Generalized Lorenz-Mie theory and applications to optical sizing, in *N. Chigier* (ed.): Combustion measurements. Hemisphere Publishing Corporation, 1991, pp. 339–384.

[14] *Gréhan, G. Gouesbet, A. Naqwi, F. Durst:* Particle trajectory effects in phase-Doppler systems: Computations and experiments. Part. Part. Syst. Charact. *10* (1993) 332–338.

[15] *A. Naqwi, F. Durst:* Light scattering applied to LDA and PDA measurements, part 1: Theory and numerical treatments. Part. Part. Syst. Charact. *8* (1991) 245–258.

[16] *J. Domnick, H. Ertel, C. Tropea:* Processing of phase/Doppler signals using the cross-spectral density function. Proc. 4th Int. Symp. on Applications of Laser Techniques to Fluid Mechanics, Lisbon (Portugal), paper 3.8, 1998.

[17] *F. Onofri:* Méthodes de suivi de phase appliquées à la détection des effets de trajectoire dans les granulo-vélocimètres phase Doppler, 1993. Rapport Interne LESP URA-CNRS 230, 15 pp.

[18] *C. F. Hess, G. P. Wood:* Laser technique to measure particle size and velocity in high density applications. Proc. Sixth Int. Symp. on Application of Laser Techniques to Fluid Mechanics, Lisbon, 1992, paper 15–6.
[19] *A. Naqwi, F. Durst:* Constraint on the size and shape of the receiving aperture in a phase/Doppler system. Part. Part. Syst. Charact. *7* (1990) 113–115.
[20] *F. Onofri, H. Mignon, G. Gouesbet, G. Gréhan:* On the extension of phase-Doppler anemometry to the sizing of spherical multilayered particles and cylindrical particles. Proc. 4th Int. Congr. Optical Particle Sizing (PARTEC 95), Nürnberg (Germany), 1995, pp. 275–284.
[21] *F. Onofri:* Prise en compte des Dimensions Finies des Faisceaux d'Eclairage en Granulométrie Optique: Anémométrie Phase Doppler–Diagnostics des aux milieux Diphasiques. PhD thesis, University of Rouen, France, October 1995.
[22] *F. Onofri, D. Blondel, G. Gréhan, G. Gouesbet:* On the optical diagnosis and sizing of coated and multilayered particles with phase Doppler anemometry. Part. Part. Syst. Charac. *13* (1996) 104–111.
[23] *H. C. van de Hulst:* Light Scattering by Small Particles. Dover Publications Inc., New York 1957.
[24] *U. Manasse, T. Wriedt, K. Bauckhage:* Phase-Doppler sizing of optically absorbing liquids droplets: Comparison between Mie theory and experiment. Part. Part. Syst. Charact. *9* (1992) 176–185.

Article A5

On the Optical Diagnosis and Sizing of Spherical Coated and Multilayered Particles with Phase-Doppler Anemometry

Fabrice Onofri, Damien Blondel, Gérard Gréhan, Gérard Gouesbet*

(Received: 24 August 1995)

Abstract

After having recalled basic theoretical results concerning the extension of generalized Lorenz-Mie theory to the case of multilayered spheres, results connected with phase-Doppler anemometry are considered, showing the influence of Gaussian beam intensity profiles on the light scattering properties of these particles. Particular emphasis is placed on the case of water-coated carbon core particles, for which the possibility of obtaining simultaneous size measurements of the core and outer diameters is discussed. The sensitivity of the technique to particles with a refractive index profile is also considered, showing that this technique is more sensitive to changes in the average refractive index of the particles than to refractive index profiles, such as produced by high pressure and temperature stresses, at least for the studied geometry.

1 Introduction

Optical sizing of optically inhomogeneous particles is a field of current interest [1, 2]. The present paper deals with the restricted case of spherical particles in which inhomogeneity exhibits a radial symmetry.

There exists a large literature devoted to the study of the scattering properties of coated particles following earlier pioneering works [3–5]. The earlier work was essentially devoted to meteorological problems or to the propagation of radar waves, and consequently were mainly restricted to particles with small size parameters. One current research interest is in coated and multilayered particles [4, 6–9] in connection with the development of optical techniques to investigated multiphase flows, spray combustion, etc., in laboratories or industry [10–12]. In such cases, focused laser beams are generally used and particles cannot be considered as small with respect to the light wavelength or to the beam radial dimension. Typical examples of coated and multilayered particles encountered in various field are, for instance

- **In combustion and spray drying:**

Cenosphere particles, which are produced during the combustion of some heavy fuels and which constitute a source of pollution [13, 14]. In the earlier stage of their formation process, they appear as liquid particles with a carbon core.

Droplets under a high temperature stress and/or with a strong evaporation rate for which a refractive index profile may occur [10, 15].

- **In biology:**

Microencapsulated particles which have pharmaceutical applications [16].

Cells, for which optical tweezers based on radiation pressure forces are under development [17–19]. Such cells may be modelled as simple coated particles, including the shell and the nucleus [20], or as multilayered particles.

Several approaches have already been developed to extend optical sizing techniques for such particles and in particular phase-Doppler anemometry (PDA) [11, 15, 21]. Nevertheless, as far as we are aware, such studies were carried out under the assumption of plane wave illumination with the restricted aim of reducing the influence of particle inhomogeneities on outer diameter size measurements.

Regarding the success of PDA for optical particle sizing of spherical homogeneous particles, in academic research and for industrial development, the approach developed in this paper is essentially based on this technique. Our aim is to obtain relevant information on particle inhomogeneities by taking advantage of non-uniform illumination of the particles [12, 22].

The theoretical analysis relies on the extension of the generalized Lorenz-Mie theory (GLMT) [23, 24] to the case of multilayered particles [9].

The paper is organized as follows. Section 2 recalls some basic features of the GLMT extended to the case of multilayered particles. Section 3 discusses diagnosis and measurements from scattering diagrams and PDA signals from particles with an absorbing core. Section 4 considers the influence of refractive index profiles, created inside droplets by high pressure and high temperature stresses, on size measurements by using a classical PDA system. Section 5 is a conclusion with perspectives.

2 GLMT and Multilayered Particles

One fundamental theoretical step in extending PDA or other optical techniques to the characterization of coated and multilayered particles is the description of the interaction between a shaped beam and a multilayered particle. When compared with the Lorenz-Mie Theory (LMT) framework, GLMT [23, 24] introduces two new sets of coefficients, the so-called beam shape coefficients $g_{n,TE}^{m}$ and $g_{n,TM}^{m}$, describing the incident beam in a partial wave representation. In the far field, the generalized

* Dr. *F. Onofri*, *D. Blondel*, Dr. *G. Gréhan*, Prof. *G. Gouesbet*, Laboratoire d'Energétique des Systèmes et Procédés, INSA de ROUEN, URA CNRS 230-CORIA, BP08, 76131 Mont-Saint-Aignan Cédex (France).

0934-0866/96/0204-0104 $10.00+.25/0

scattering amplitudes S_1 and S_2 are then given by the following expressions:

$$S_1 = \sum_{n=1}^{\infty} \sum_{m=-n}^{+n} \frac{2n+1}{n(n+1)} [m a_n g_{n,TM}^m \pi_n^{|m|}(\cos\theta) + i b_n g_{n,TE}^m \tau_n^{|m|}(\cos\theta)] \exp(im\varphi) \quad (1)$$

$$S_2 = \sum_{n=1}^{\infty} \sum_{m=-n}^{+n} \frac{2n+1}{n(n+1)} [a_n g_{n,TM}^m \tau_n^{|m|}(\cos\theta) + im b_n g_{n,TE}^m \pi_n^{|m|}(\cos\theta)] \exp(im\varphi) \quad (2)$$

where a_n and b_n are the classical scattering coefficients of LMT which depend on the particle diameter, the complex refractive index of the particle material and the wavelength of the illuminating light. The scattering geometry is taken into account by the harmonic functions $\exp(im\varphi)$ and by the Legendre functions $\pi_n^{|m|}$ and $\tau_n^{|m|}$, which involve the azimuthal angle φ and the scattering angle θ [23, 24].

When a multilayered sphere is considered, boundary conditions must be written (*i*) at the frontiers of consecutive internal layers, then involving internal fields, and (*ii*) at the frontier of the outer layer, then involving the external field and the internal field in this layer, leading to an iterative problem. There, each layer is defined by its complex refractive index m_j, its magnetic permeability μ_φ and its outer size parameter $x_j = 2\pi r_j/\lambda$, from $j = 1$ for the core to $j = L$ for the outer layer while we have $j = 0$ for the external medium (Figure 1).

Using the GLMT formalism, it can be shown [9] that the scattering coefficients of a multilayered sphere illuminated by an arbitrary shaped beam can be rewritten simply in the following form:

$$A_n^m = g_{n,TM}^m A_n \quad (3)$$

$$B_n^m = g_{n,TE}^m B_n \quad (4)$$

where A_n and B_n designate the scattering coefficients of the multilayered sphere for a plane wave illumination, reading

$$A_n = \frac{M_L \Psi_n(M_L x_L) H_n(x_L) - U_L \Psi_n'(M_L x_L)}{M_L \xi_n(M_L x_L) H_n(x_L) - U_L \xi_n'(M_L x_L)} \quad (5)$$

$$B_n = \frac{U_L \Psi_n(M_L x_L) K_n(x_L) - M_L \Psi_n'(M_L x_L)}{U_L \xi_n(M_L x_L) K_n(x_L) - M_L \xi_n'(M_L x_L)} \quad (6)$$

where Ψ_n, ξ_n, and Ψ_n', ξ_n' are Ricatti–Bessel functions and the corresponding derivative, respectively, with $M_L = m_0/m_L$ and $U_L = \mu_{\gtrless}/\mu_\Lambda$ [9]. Functions $H_n(x_L)$ and $K_n(x_L)$ are deduced from recursive algorithms starting from the core of the sphere to its outer layer [9, 25].

As a consequence, GLMT codes for homogeneous spheres can readily be extended to the multilayer case by changing the subroutine which computes the scattering coefficients to a new one established for the case under study. Such subroutines are available from the literature. Let us also mention that light scattering by a coated sphere illuminated with Gaussian beam, described by using an angular spectrum of plane waves, has been considered by *Khaled* et al. [26]. Nevertheless, it has been shown that the angular spectrum approach to the beam description is several orders of magnitude more time consuming [27] than the localized approximation we use in GLMT. A code based on GLMT has been modified to simulate the response of a PDA device when multilayered particles are under study. The next sections are devoted to the presentation of results obtained by using this code.

3 On the Detection of Particles with an Absorbing Core

Within the cases of coated particles ($L = 2$), one may distinguish four major subclasses:

(1) particles with an absorbing core and a transparent shell,

(2) particles with absorbing core and shell,

(3) particles with a transparent core and an absorbing shell and

(4) particles with a transparent core and shell.

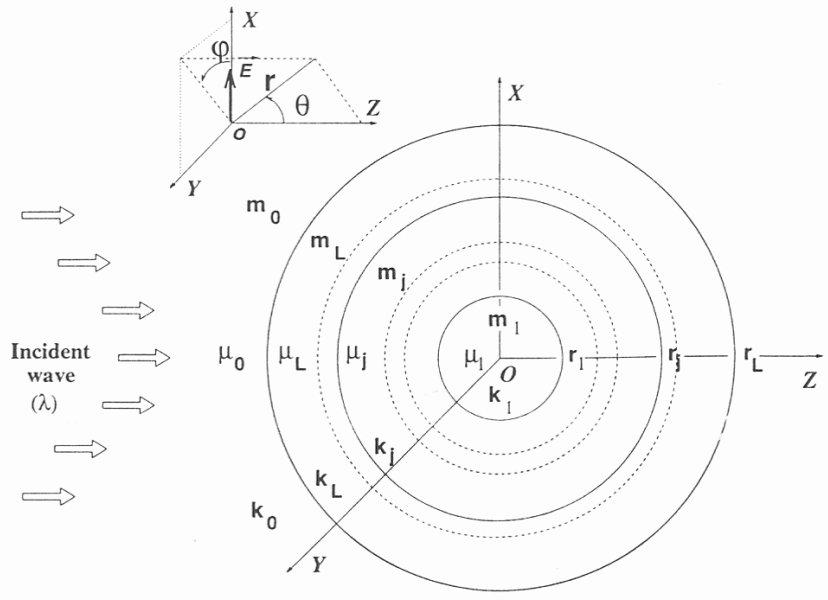

Fig. 1: Geometry of the stratified sphere theory.

While cases 1 and 2, for instance, are good models for cenospheres [13], coated oil droplets [28] or biological cells [19, 20], case 4 is a model for glass micro-balloons [21]. In the following, only case 1 is considered.

In many cases, PDA measurements are carried out for dominantly refracting homogeneous particles, leading to the usual near-forward detection at 30°. The refraction scattering process is obviously influenced by both the particle size and the particle material. In particular, the so-called dual burst technique takes advantage of this fact to measure particle refractive indices [29, 30]. In the extreme case of perfectly absorbing (reflective) particles, however, only size measurements using reflected light are allowed.

In the presence of a core inside the particle, refracted rays which normally (without any core) are scattered in direction θ (assumed to be the detector direction) may impinge on the core. The reflected rays in the detector direction, defined by an impact parameter Y_{reflec} (Figure 2), are collected whatever the core size whereas, for the refracted rays, there exists a size maximum limit for the core radius h which can be deduced from simple geometrical considerations. In Figure 2, these refracted rays are defined by the impact parameter Y_{refrac}. The evolution of the maximum core radius versus the scattering angle, with the refractive index of the shell material as a parameter, is displayed in Figure 3. For a water droplet ($m = 1.333$) and a 30° scattering angle, this maximum radius is equal to 0.57 with the outer radius as unity, i.e. there is no interaction with the core when the core diameter is smaller than 57% of the outer particle diameter.

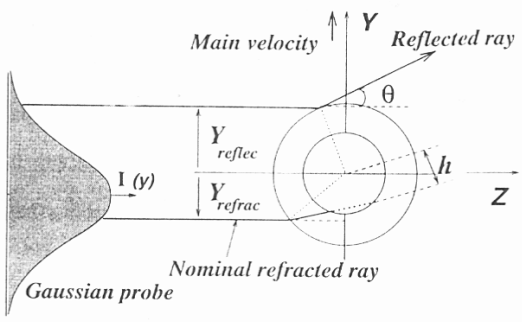

Fig. 2: Scheme of the path of the main rays (refracted and reflected) scattered in direction θ by a coated particle. Note that the corresponding refracted ray impinges on the core only when the core radius is larger than h.

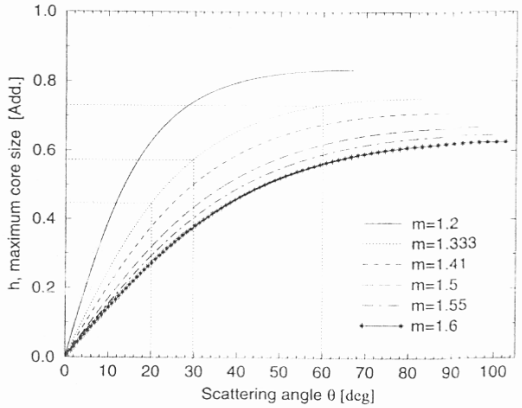

Fig. 3: Evolution of the maximum core radius versus the scattering angle, for which the refracted ray in the scattering direction θ is not blocked. The refractive index of the particle shell is the parameter.

3.1 Scattering Diagrams

GLMT for multilayered spheres enables us to obtain scattering diagrams for multilayered particles and then to discuss more deeply the previous comments based on simple geometrical considerations. Figure 4(a) presents the scattering diagrams for parallel polarization of a water-coated carbon core illuminated by a plane wave, for various ratios of the particle outer radius ($r_2 = 30\,\mu m$) over the core radius, $q = r_1/r_2$. The incident light wavelength is $\lambda = 0.6328\,\mu m$ and the refractive indices are $m_1 = 1.59 - i0.66$ and $m_2 = 1.333$.

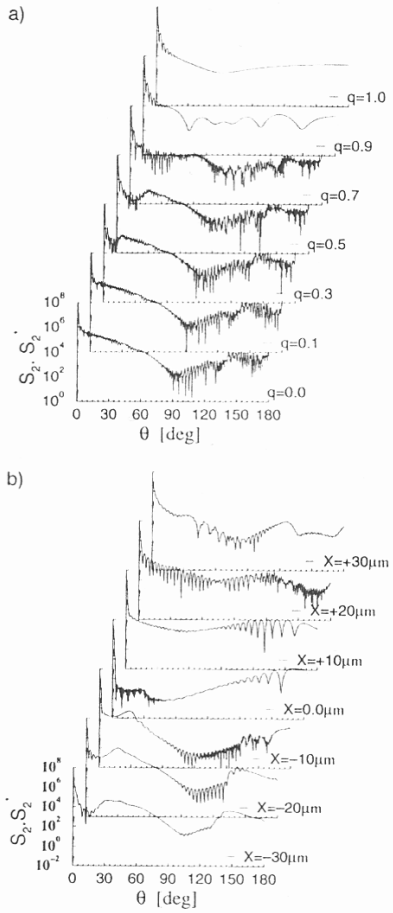

Fig. 4: Scattering diagrams for parallel polarization of water-coated carbon core spheres ($L = 2$): $m_1 = 1.59 - i0.66$, $m_2 = 1.333$, $\lambda = 0.6328\,\mu m$, $r_2 = 30\,\mu m$, (a) plane illumination versus parameters $q = 0, \ldots, 1.0$, (b) Gaussian beam illumination with $2\omega_0 = 20\,\mu m$, versus the particle location: $Z = Y = 0$, $X = -30, \ldots, +30\,\mu m$, $q = 0.5$.

For $q < 0.3$, no significant difference in the scattering patterns is observed excepted a slight decrease of the intensity for $\theta < 15°$, which may be attributed to the absorption/reflection through the particle of the refracted rays having a small impact parameter.

For $q = 0.5 - 0.7$, this last feature extends up to 30/60°, which corresponds to $h = 0.57/0.77$.

For $q = 0.9 - 1.0$, the high-frequency oscillations in the scattering diagrams, which are usually attributed to interference phenomena between different scattering orders, are no longer present. The scattering diagrams become typical of those observed for an absorbing/reflecting particle.

The influence of a Gaussian beam illumination on the scattering pattern of the same particle as above with $q = 0.5$ is considered in Figure 4(b) for parallel polarization. The beam waist diameter is 20 μm and the particle location along the OX axis in the beam waist plane (see Figure 1) is the parameter.

For $X < 0$, the refraction process is amplified [29, 30]. The scattering intensity in near forward directions ($\theta < 15°/30°$) decreases in a similar way as for $q < 0.3$ in Figure 4(a). The refracted rays with small impact parameters are more and more deviated/absorbed.

For $X = 0$, the laser beam which is smaller in diameter than the particle absorbing core appears to be significantly absorbed/deviated in forward directions. Outside the diffraction zone ($\theta > 5°$), there is a strong decrease in the scattered light intensity.

For $X > 0$, the reflected process is amplified [29, 30].

From Figure 4(a) and (b) it is clear that the presence of an absorbing core has a strong influence on the scattering pattern of a particle, particularly significant in the forward region. The strong decay in scattered intensity, observed in this region in Figure 4(b), when the particle is at the beam waist center, indicates that focused laser beams enhance this phenomenon and thus amplify the signature of the presence of a core. Core characterization from scattering diagrams should therefore be easier with laser beams which act as local probes.

3.2 PDA Signals and Coated Particles

The signature of the previously discussed particles with phase-Doppler anemometry is now considered. The evolution of the signal intensity and phase difference of simulated PDA signals, is considered in Figure 5(a) and (b), respectively, when particles travel through the center of the optical probe volume parallel to the fringes as in a modified standard PDA geometry [29, 31] (as sketched in Figure 2). The optical parameters are identical with those used by *Gréhan* et al. [32]. The off-axis angle is set to 30° and the beam diameter has been reduced to 20 μm. According to geometrical optics (GO) [33], these parameters lead to a slope in the phase-diameter relationship for the detector pair ($D1$, $D3$) of 1.96°/μm for refraction ($p = 1$) and −2.45°/μm for reflection ($p = 0$).

The intensity evolutions of the phase Doppler signals are different depending on the particle considered. For the water droplet (q = 0) and the carbon particle (q = 1), the signal intensity presents two maxima. For the water droplet, the reflection maximum occurs for $Y \approx -30$ μm whereas the refraction is maximum for $Y \approx 25$ μm. The same pattern essentially occurs for the carbon particle except that the refracted signal is extremely weak owing to the absorption. When there is a core inside the particles, additional intensity maxima occur. They have intermediate positions between those of the external reflection and refraction. For $q = 0.3$, there are four maxima occurring at $Y \approx -30$, −10, 10 and 23 μm, referred as (A), (B), (C) and (D), respectively in Figure 5(a). These positions evolve with the particle core size. For the second maximum with $Y < 0$, for instance, which is referred as (B) in Figure 5(a), the position becomes closer to the position of the maximum for the reflection as q increases. More precisely, for $q = 0.1$, 0.3, 0.5, 0.7, 0.9, the position evolves from $Y \approx 0$ μm to ≈ -10, −15, −23, −27 μm, respectively.

The signal phase evolution (Figure 5(b)) also depends on the particles considered. For the water droplet and the carbon particles, two flat parts in the phase diagrams are observed. They can be attributed to reflection for $Y < 0$ and to refraction

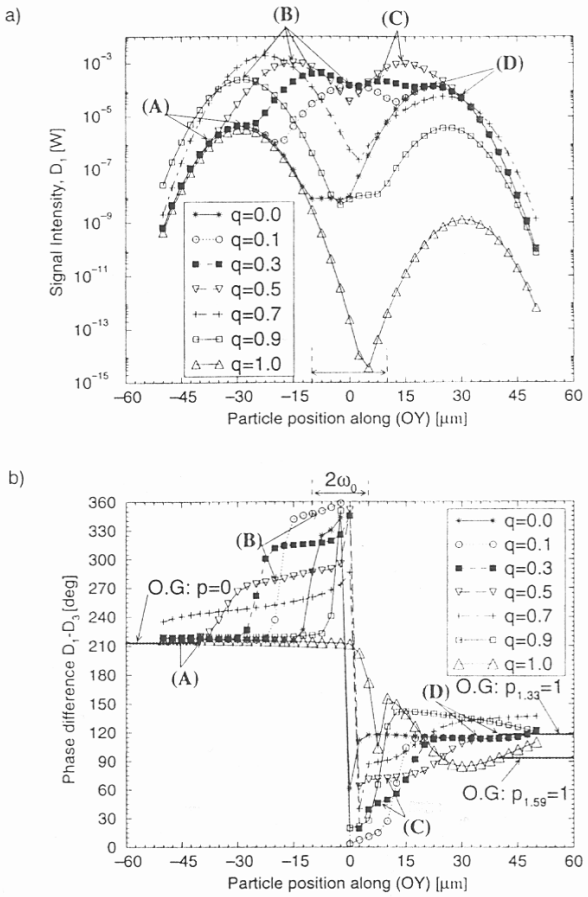

Fig. 5: Simulated PDA signals produced by water-coated carbon spheres for various values of $q(= r_2/r_1)$, with $r_2 = 30$ μm, $2\omega_0 = 20$ μm, $\lambda = 0.6328$ μm: (a) signal intensity; (b) phase difference.

for $Y > 0$. Let us note the agreement between phase differences predicted by GLMT and those predicted by GO which are represented in the figure as segments on the edges.

When there is a core inside the particles, additional flat parts in the phase diagrams occur. As an example, for the particle defined by $q = 0.5$, four flat parts are present in the phase diagram, with labels (A) for $Y < -40$ μm with $\phi_{13} \approx 217°$, (B) for $Y = (-27, -3)$ μm with $\phi_{13} \approx 270 - 290°$, (C) for $Y = (5, 17)$ μm with $\phi_{13} \approx 72°$ and (D) for $Y > 30$ μm with $\phi_{13} \approx 112°$. The level of some of these phases also depends on the particle considered. For instance, the height of the flat part (B) decreases monotically when q increases, whereas its length increases with increase in q. The phase for flat parts (A) and (B) is above 180° whereas for flat parts (C) and (D) it is below 180°. In fact, the phase sign for the former is negative, thus leading in Figure 5(b) to a phase (ϕ_{13}) reading of ($360 - \phi_{13}$).

In order to improve the understanding of the previous results, we can track, using simple geometrical optics considerations, the path of different rays scattered in the detector direction. This is displayed in Figure 6, for a single detector location at $\theta = 30°$ with an aperture of $\Delta\theta = \pm 4.39$ in the off-axis plane. The previously discussed particle with $q = 0.5$ is considered in cases (a)–(h) and the particle with $q = 0.9$ in case (i).

Cases (a)–(h) correspond to all collected rays ordered according to their impact parameter. The series actually represents different scattering processes acting when the particle crosses

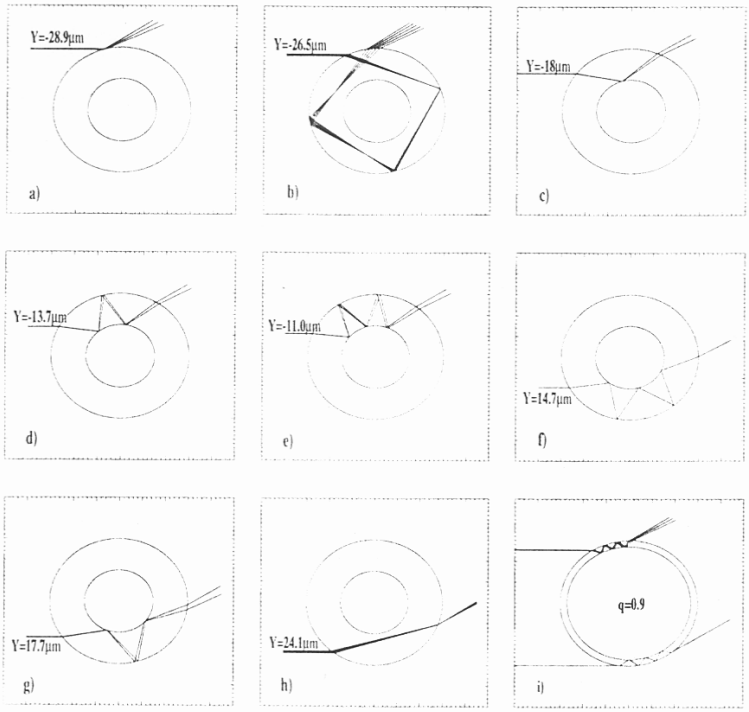

Fig. 6: Ray tracings of scattered rays in direction $\theta = 30°$ by a coated particle defined by $m_1 = 1.333$, $m_2 = 1.59 - 0.66i$, $r_2 = 30\,\mu m$, with $q = 0.5$ for (a)–(h) and $q = 0.9$ for (i). The detector aperture is in the off-axis plane with $\theta = 30 \pm 4.39°$. Cases (a)–(h) are ordered to simulate a particle trajectory along (OY) as in a PDA modified standard geometry.

the probe volume along (OY), as in a PDA modified standard geometry (see Figure 2).

In Figure 6(a), the external reflection on the shell is clearly apparent. This scattering mechanism occurs first. The impact parameter of the rays ($Y = -28.9\,\mu m$) corresponds to the middle of the transition zone between the flat parts (A) and (B) in Figure 5.

This scattering mechanism picks up information on the outer particle diameter via a reflective mechanism.

In Figure 6(b), a fourth internal reflection appears. The intensity generated by the corresponding rays may be very weak compared with those of case (a) [34]. The beam intensity profile cannot increase this contribution significantly owing to the proximity of the impact parameter with the one of external reflection (Figure 6(a)).

In Figure 6(c), (d) and (e), internal reflections with one, two and three interactions with the core occur. The impact parameters of these rays correspond in Figure 5(a) to an intensity maximum and in Figure 5(b) to the middle of the flat part with label (B). The slight evolution of the slope of this flat part may be attributed to a slow transition between the three types of internal reflection weighted by the beam intensity profile ($2\omega_0 = 20\,\mu m$).

These scattering processes pick up information on the core size via a reflective mechanism.

In Figure 6(f) and (g), the rays follow the same kind of path as in the three previous cases, but with positive impact parameters. These impact parameters correspond in Figure 5(a) to a signal maximum and in Figure 5(b) to the end of the flat part (C).

These scattering processes pick up information on the core size via a reflective mechanism.

In Figure 6(h), simple refraction occurs. The reduced critical distance h is 0.57 for the refractive index of water at a scattering angle of 30°. Since $q = 0.5$ is smaller than h in the present case, the refracted rays do not impinge on the core. In Figure 5(a), this case does not correspond to a significant signal maximum. In Figure 5(b) it corresponds to a transition zone from flat part (C) to flat part (D).

This scattering process picks up information on the particle outer diameter via a refractive mechanism.

Based on the previous comments, it is possible to interpret the successive parts (A), (B), (C) and (D) observed in Figure 5 in terms of diameter by using the phase conversion factor corresponding to the PDA geometry. In Table 1, the deduced diameters are summarized for each coated particle.

The value of the particle outer diameter deduced from flat part (A) is good, except when $q = 0.9$. From flat part (B), the core size determination is very encouraging, except maybe for $q = 0.1$. The signal intensity for the corresponding phenomenon ensures good detectability; see Figure 5(a). From flat part (C), the core size determination is also good except for $q = 0.9$. The signal intensity also ensures good detectability of this scattering mechanism. From flat part (D), the outer particle diameter can also be deduced with good accuracy, except for $q = 0.7$ and 0.9 ($h > q$). There, the signal intensity is

Table 1: Comparison between nominal size values and those deduced from the flat parts in the phase diagrams of phase-Doppler signals. The outer particle radius is $r_2 = 30\,\mu m$.

Nominal value		Flat (A)	Flat (B)	Flat (C)	Flat (D)
$q = D_1/D_2$	D_1 (µm)	$Y<0$, (µm) D_2	$Y<0$, D_1	$Y>0$, D_1	$Y>0$, D_2
0.1	6.0	58.0	2.0	4.5	57.3
0.3	18.0	58.0	18.3	20.0	57.3
0.5	30.0	58.0	31.9	29.6	57.3
0.7	42.0	58.0	44.9	37.0	67.9 (–)
0.9	54.0	50.9 (–)	57.4	8.85 (–)	67.9 (–)

nevertheless extremely weak, limiting the possibility of extracting simultaneously this size information with that deduced from flat part (B) or (C). Note in Figure 6(i) that the water shell for $q = 0.9$ seems to induce a "wave guide effect".

Finally, to conclude this section, we emphasize that there exists a possibility with PDA of extracting simultaneous information on the core and outer size of coated particles, by taking advantage of the influence of an illuminating intensity profile. Future work will be necessary to reveal the best optical parameters for signal detectability and phase linearity. Associated experimental investigations are under development.

4 PDA and Multilayered Particles

4.1 Effect of Temperature and Evaporation on Particle Refractive Index

Refractive index profiles inside particles may occur during a heating or drying process due to a temperature or concentration gradient. Such a phenomenon depends on the thermal properties of particles, the initial conditions and the conditions imposed by the external medium.

As an example, Figure 7 shows the evolution of the refractive index profile inside a droplet of decane versus its normalized radius, with time as a parameter. These profiles were obtained by using a condition limit code for an initial droplet diameter of 50 µm and a droplet initial temperature of $T_0 = 300$ K. In Figure 7(a), the temperature and pressure of the external medium is 2000 K and 10 bar, respectively. Large evolutions of the refractive index profiles and of the average values are observed versus time. In Figure 7(b) the external temperature and pressure are set to 400 K and 1 bar, respectively. The refractive index profiles are flat, but the evolution of the average refractive index is significant.

Actually, numerical computations of the scattering coefficients A_n and B_n for a multilayered sphere are in practice only feasible in limited domains, as extensively described by *Kai and Massoli* [10]. According to these authors, the maximum number of layers for a 60 µm diameter particle is typically about 10. Therefore, from now on, we must keep this limitation in mind. As an example, Figure 8 presents the ways of discretization, introduced to approach the previous refractive index profiles in 12 steps, applied to the case corresponding to time $t = 1.1$ ms in Figure 7(a). They are denoted "profile (I)" and "profile (II)". The latter more finely discretizes the outer part of the particle by considering a single average value of the refractive index for $D < 0.46$, whereas the former is more homogeneous.

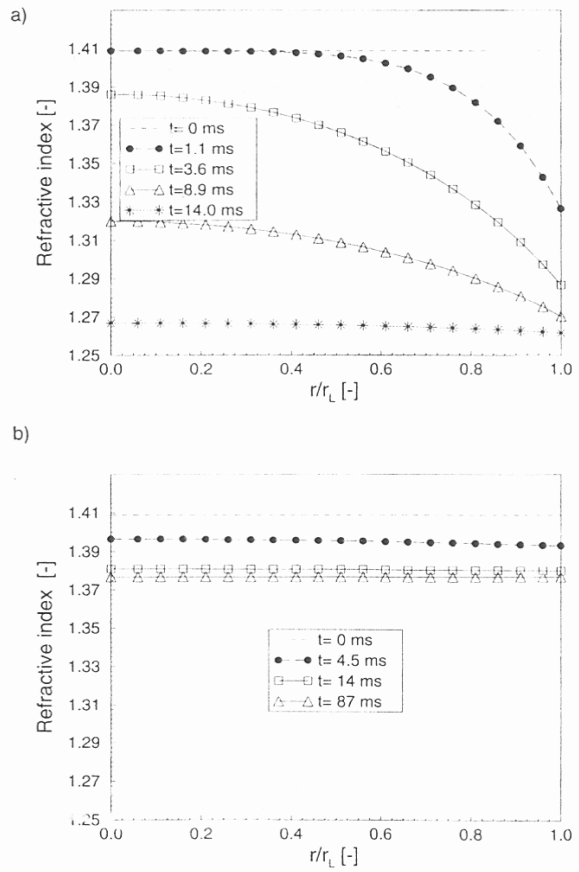

Fig. 7: Temporal evolution of the internal refractive index field for a 50 µm diameter decane droplet during two droplet-heating scenarios predicted using a conducting-limit model: (a) heating and evaporating take place in a high-temperature and -pressure environment, $T_\infty = 2000$ K, $P = 10$ bar; (b) in a low-temperature and -pressure environment, $T_\infty = 400$ K, $P = 1$ bar. The initial droplet temperature is $T_0 = 300$ K.

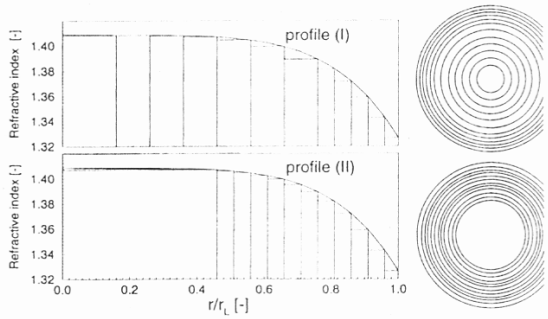

Fig. 8: Discretization of the refractive index profiles in 12 steps. The case for $t = 1.1$ ms is considered with two discretizations: profile (I) and profile (II).

4.2 Evolution of the Phase-Diameter Relationship

Figure 9 presents the phase-diameter relationship computed for the previous PDA geometry and the discretization "profile (I)". The beam waist diameter has been increased to 500 µm in

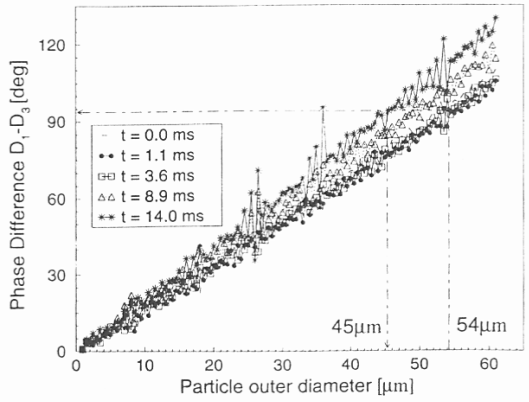

Fig. 9: Phase-diameter relationship for the various refractive index profiles inside droplets of decane considered in Figure 7(a).

order to decrease Gaussian beam effects on particle inhomogeneity effects. In Figure 9 each case from Figure 7(a) is considered.

According to Figure 9, the influence of refractive index profiles on the phase-diameter relationship is weak. For instance, the curves for cases corresponding to $t = 0$ and $t = 1.1$ ms are nearly the same. Nevertheless, significant differences occur for the curves corresponding to $t = 0$ and $t = 14.0$ ms, for which the difference in the average refractive index is the largest. The considered classical PDA geometry seems to be more sensitive to a change in the particle average refractive index than to the existence of refractive index profiles like those displayed in Figure 7(a). In this case, a particle of 54 µm diameter can be erroneously measured as a 45 µm diameter particle. The increase of oscillation amplitudes in the phase-diameter relationship with time, i.e. with decreasing refractive index, may be attributed to a relative decrease in refracted intensity for this scattering angle compared to reflection. Therefore, the refraction mechanism, which in the present case is the dominant scattering mechanism assumed for size determination, is more disturbed by reflection, leading to increased interferences.

The influence of the discretization of the refractive index profiles can be evaluated from Figure 10, where the phase-diameter relationship corresponding to the refractive index profile $t = 1.1$ ms is presented for the discretizations: "profile (I)" and "profile (II)". The two curves are almost the same and

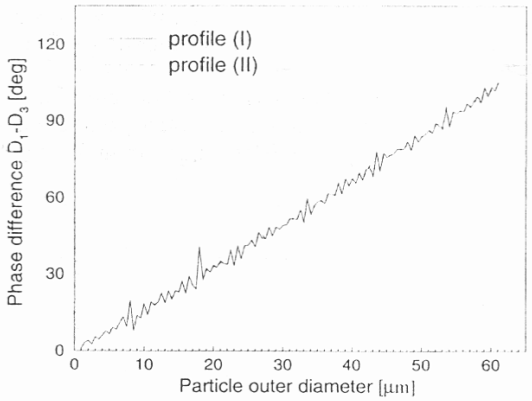

Fig. 10: Comparison of the influence on the phase-diameter relationship of the two ways to discretize the refractive index profile corresponding to $t = 1.1$ ms.

actually cannot be distinguished. The measured phase difference for this scattering angle seems not to be sensitive to the internal particle material. Note from Figure 3 that for $m = 1.41$ and 1.33, h evolves from ≈ 0.5 to 0.56, which correspond in Figure 8 to a region where the refractive index profile is almost flat. This explains why the influence of the way of discretizing the refractive index profiles seem not to be significant, at least for the conventional geometry considered here.

5 Conclusion

A new numerical tool to investigate light scattering by multilayered spheres illuminated by arbitrarily shaped beams has been briefly introduced. Its application to phase-Doppler anemometry (PDA) for the case of water-coated carbon spheres has been considered by using focused laser beams, therefore extending the principle of the dual burst technique. Information on the core and outer particle diameters seems to be reachable by carefully analyzing the temporal structure of individual phase-Doppler signals.

The influence of refractive index profiles inside droplets, induced by temperature and pressure stresses, on PDA phase-diameter relationships was investigated. It was shown that the simulated conventional PDA geometry appears to be more sensitive to variations in the absolute value of the refractive index than in the refractive index profile.

6 Acknowledgements

The authors are grateful to Professor *Wittig's* team of the University of Karlsruhe, Germany, and more particularly to Mr. *Willmann* and Dr. *R. Kneer* for providing the refractive index profiles [35].

7 Symbols and Abbreviations

A_n, B_n	scattering coefficients for multilayered spheres and plane wave illumination
GLMT	Generalized Lorenz-Mie Theory
$H_n(x_L)$, $K_n(x_L)$	recursive functions
L	number of layers
LMT	Lorenz-Mie Theory
M_L	ratio of refractive indices: m_0/m_L
PDA	Phase-Doppler Anemometry
S_1, S_2	generalized scattering amplitudes, perpendicular and parallel polarizations, respectively
U_L	ratio of magnetic permeabilities: μ_0/μ_L
a_n, b_n	scattering coefficients for homogeneous spheres and plane wave illumination
$g^m_{n,TE}$, $g^m_{n,TM}$	beam shape coefficients for transverse electric waves and transverse magnetic waves, respectively
h	maximum core size before interaction with simple refracted rays
m_i	refractive index of the *ith* layer
q	ratio of the inner particle radius to outer particle radius for coated particles
r_j	radius of the *jth* layer
x_j	size parameter of the *jth* layer
Ψ_n, ξ_n	Ricatti-Bessel functions
λ	incident wavelength
ω_0	beam waist radius
μ_i	magnetic permeability of the *ith* layer
φ	azimuthal angle
$\tau_n^{\|m\|}$, $\pi_n^{\|m\|}$	generalized Legendre functions
θ	scattering angle

8 References

[1] *U. Manasse, T. Wriedt, K. Bauckhage:* Optimization of PDA parameters for sizing of optically inhomogeneous liquid droplets. Proc. 3rd Int. Congr. on Optical Particle Sizing, Yokohama, Japan, 1993, pp. 453–460.

[2] *G. Brenn, J. Domnick, F. Durst, C. Tropea, T.-H. Xu, G. Gréhan, F. Onofri:* The Dual Burst Technique and its Application for Sizing of Heterogeneous Particles. Proc. 4th Optical Particle Sizing Conf. – Partec 95, Nürnberg, Germany, 1995, pp. 397–406.

[3] *A. L. Aden, M. Kerker:* Scattering of electromagnetic waves from two concentric spheres. J. Appl. Phys. *22* (1951) 1242–1246.

[4] *P. J. Wyatt:* Scattering of electromagnetic waves from inhomogeneous spherically symmetric objects. Phys. Rev. *127* (1962) 1837–1843. Errata, Phys. Rev. *134* (1964).

[5] *R. Fenn, H. Oser:* Scattering properties of concentric soot-water spheres for visible and infrared light. Appl. Opt. *4* (1965) 1504–1509.

[6] *R. Bhandari:* Scattering coefficients for a multilayered sphere: analytic expressions and algorithms. Appl. Opt. *24* (1985) 1960–1967.

[7] *D. W. Mackowski, R. A. Altenkirch, M. P. Menguc:* Internal absorption cross sections in a stratified sphere. Appl. Opt. *29* (1990) 1551–1559.

[8] *T. Kaiser, G. Schweiger:* Stable algorithm for the computation of Mie coefficients for scattered and transmitted fields of a coated sphere. Comput. Phys. *7* (1993) 682–686.

[9] *F. Onofri, G. Gréhan, G. Gouesbet:* Electromagnetic scattering from a multilayered sphere located in an arbitrary beam. Appl. Opt. *33* (1994).

[10] *L. Kai, P. Massoli:* Scattering of electromagnetic-plane waves by radially inhomogeneous spheres: a finely stratified sphere model. Appl. Opt. *33* (1994) 501–511.

[11] *J. Rheims, H. Dahl, T. Wriedt, K. Bauckhage:* Sizing coated spheres with Phase Doppler Anemometry. Proc. 4th Optical Particle Sizing Conf. – Partec 95, Nürnberg, Germany, 1995 pp. 409–418.

[12] *F. Onofri, H. Mignon, G. Gouesbet, G. Gréhan:* Phase Doppler measurements of non-spherical particles: cylindrical and multilayered particles. Proc. 4th Optical Particle Sizing Conf. – Partec 95, Nürnberg, Germany, 1995, pp. 275–284.

[13] *N. Bonno, J. Lahaye, G. Prado:* Formation of cenospheres during pyrolysis of residual fuel oils. Proc. 23rd Int. Symp. on Combustion, pp. 903–911. Combustion Institute, 1990.

[14] *S. W. Wong, A. C. Lin, H. Y. Chi:* Effects of surfactant on the evaporation, shell formation and disruptive behaviour of slurry droplet. Proc. 23rd Int. Symp. on Combustion, pp. 1391–1397. Combustion Institute, 1990.

[15] *M. Schneider, E. D. Hirleman:* Influence of internal refractive index gradients on size measurements of spherically-symmetric particles by Phase Doppler Anemometry. Appl. Opt. *33* (1994) 2379–2388.

[16] *B. H. Kaye:* Microencapsulation: The creation of synthetic fine particles with specified properties. KONA *10* (1992).

[17] *A. Ashkin:* Acceleration and trapping of particles by radiation pressure. Phys. Rev. Lett. *24* (1970) 156–159.

[18] *M. I. Angelova, B. Pouligny, G. M. Martinot-Lagarde, G. Gréhan, G. Gouesbet:* Stressing phospholipid membranes using mechanical effects of light. Prog. Colloid Polym. Sci. (to be published).

[19] *K. F. Ren, F. Onofri, G. Gouesbet, G. Gréhan, G. Martinot-Lagarde, B. Pouligny:* Radiation pressure: a tool for optical measurements of pico-newton forces. Proc. 4th Optical Particle Sizing Conf., Partec 95, Nürnberg, Germany, 1995, pp. 97–106.

[20] *A. Brunsting, P. F. Mullaney:* Light scattering from coated sphere: Model for biological cells. Appl. Opt. *11* (1972) 675–680.

[21] *S. V. Sankar, D. K. Kamemoto, W. D. Bachalo:* Sizing large hollow micro-balloons with the Phase Doppler interferometer. Part. Part. Syst. Charact. *10* (1993) 321–331.

[22] *F. Onofri:* Prise en compte des dimensions finies des faisceaux d'éclairage en granulométrie optique: Anénométrie Phase Doppler, Diagnostics des Milieux Diphasiques. PhD thesis, Université de Rouen, URA CNRS 230 (France), 1995.

[23] *G. Gouesbet, B. Maheu, G. Gréhan:* Light scattering from a sphere arbitrarily located in a Gaussian beam, using a Bromwich formulation. J.O.S.A. A. *5* (1988) 1427–1443.

[24] *G. Gouesbet, G. Gréhan, B. Maheu:* Generalized Lorenz-Mie theory and applications to optical sizing, in *N. Chigier* (ed.): Combustion Measurements. pp. 339–384. Hemisphere Publishing Corporation, 1991.

[25] *Z. S. Wu, Y. P. Wang:* Electromagnetic scattering for multilayered sphere: Recursive algorithms. Radio Science *26* (1991) 1393–1401.

[26] *E. M. Khaled, S. C. Hill, P. W. Barber:* Light scattering by a coated sphere illuminated by a Gaussian beam. Appl. Opt. *33* (1994) 3308–3314.

[27] *J. A. Lock:* An improved Gaussian beam scattering algorithm. Appl. Opt. *34* (1995) 559–570.

[28] *P. Massoli, F. Beretta, A. D. Alessio, M. Lazzaro:* Temperature and size measurement of single transparent droplets by light scattering in the forward and rainbow regions. Appl. Opt. *32* (1993) 3295–3301.

[29] *F. Onofri, G. Gréhan, G. Gouesbet, T.-H. Xu, G. Brenn, C. Tropea:* Phase-Doppler Anemometry with Dual Burst Technique for particle refractive index measurements. Proc. 7th Int. Symp. on Applications of Laser Techniques to Fluid Mechanics, Lisbon, July 11–14, 1994, paper 21.4.

[30] *F. Onofri, T. Girasole, G. Gréhan, G. Gouesbet, G. Brenn, J. Domnick, T.-H. Xu, C. Tropea:* Phase-Doppler anemometry with dual burst technique for measurement of refractive index and absorption coefficient simultaneous with size and velocity. Part. Part. Syst. Charact. *13* (1996) 112–124..

[31] *T. H. Xu, C. Tropea:* Improving the performance of two-component Phase Doppler Anemometry. Meas. Sci. Technol. *5* (1994) 969–975.

[32] *G. Gréhan, G. Gouesbet, A. Naqwi, F. Durst:* On elimination of the trajectory effects in Phase Doppler systems. Proc. 5th Europ. Symp. Particle Characterization, Partec, Nürnberg, 1992, pp. 309–318.

[33] *A. Naqwi, F. Durst:* Light scattering applied to LDA and PDA measurements, Part I: Theory and numerical treatments. Part. Part. Syst. Charact. *8* (1991) 245–258.

[34] *H. C. van de Hulst:* Light Scattering by Small Particles. Dover Publications, Inc. New York 1957.

[35] *R. Kneer, M. Schneider, B. Noll, S. Wittig:* Diffusion controlled evaporation of a multicomponent droplet: theoretical studies on the importance of variable liquid properties. Int. J. Heat Mass Transfer *36* (1995) 2403–2415.

Article A8

Size, velocity, and concentration in suspension measurements of spherical droplets and cylindrical jets

Fabrice Onofri, Laurence Bergougnoux, Jean-Luc Firpo, and Jacqueline Misguich-Ripault

The principle of an optical technique for simultaneous velocity, size, and concentration in suspension measurements of spherical droplets and cylindrical jets is proposed. This technique is based on phase Doppler anemometry working in the dual burst technique configuration. The particle size and velocity are deduced from the reflected signal phase and frequency, whereas the amplitude ratio between the refracted and the reflected signals is used for measuring the concentration of small scatterers inside the particles. Numerical simulations, based on geometrical optics and a Monte Carlo model, and an experimental validation test on cylindrical jets made of various suspensions, are used to validate the principle of the proposed technique. It is believed that this new technique could be useful in investigating processes in which liquid suspensions are sprayed for surface coating, drying, or combustion applications.

OCIS codes: 290.4210, 120.3180, 120.5820, 280.2490, 290.7050.

1. Introduction

Numerous industrial processes use transport powders as liquid suspensions before spraying them for surface-coating, drying, or combustion applications. Among the most important parameters suitable for controlling these processes, conventionally we find droplet size, velocity distributions, and also droplet concentration in suspension (i.e., a liquid containing small scatterers). Experimentally an optical technique such as phase Doppler anemometry (PDA), which is now a well-established particle-sizing and velocity technique for studying two-phase flows, seems to be a good candidate for obtaining the first two characteristics. Nevertheless some previous research on sizing paint sprays[1] or food-drying processes[2] has shown there are undesirable effects from the presence of scatterers inside a droplet, such as a spread in the size distributions of measured droplets or totally irrelevant size measurements for a high concentration of droplets in scatterers. Some solutions with severe limitations have been proposed for this problem: (1) collection angles in which additional scattering from scatterers is expected to be insignificant,[1] (2) near IR laser beams to reduce the size parameter of scatterers,[2] (3) off-line reconstruction algorithms and calibration experiments.[3] Measuring the droplet concentration in scatterers was beyond the scope of these contributions, which were focused on improvements in heterogeneous droplet-size measurement.

The purpose of this research is to introduce a new approach based on PDA for accurate on-line sizing of optically heterogeneous spherical and cylindrical particles in addition to measurement of the particle concentration in scatterers. For convenience we consider here only heterogeneous particles made of a liquid suspension of solid particles (scatterers) of known diameter and refractive index. Nevertheless the principle of the proposed technique could also be applied to the diagnosis of various kinds of heterogeneous particle (solid particles with small solid inclusions as well as liquid droplets with gaseous or liquid inclusions).

In Section 2 we introduce the basic principle of the proposed technique. In Section 3 we present the two models developed to evaluate the expected performance of this technique based on geometrical optics and a Monte Carlo approach. Three ways to eliminate particle trajectory effects on the concentration measurements occurring for spherical particles are proposed. In Section 4 we present the experimental

The authors are with the Institut Universitaire des Systèmes Thermiques Industriels, Unité Mixte de Recherche associée au Centre National de la Recherche Scientifique No. 6595, Université de Provence, BP 13453, Technopôle de Château-Gombert, Marseille, France. The e-mail address for F. Onofri is Onofri@iusti.univ-mrs.fr.

Received 4 January 1999; revised manuscript received 19 March 1999.

0003-6935/99/214681-10$15.00/0

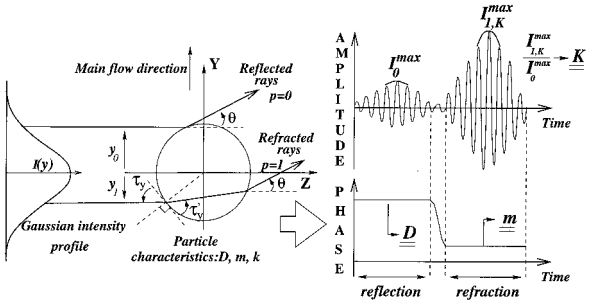

Fig. 1. Schematic of the principle of the DBT for simultaneous measurement of the complex refractive index, size, and velocity of spherical particles in flow. D, m, and K are the particle diameter, the real part of the particle material refractive index, and the particle material absorption coefficient at the laser wavelength, respectively.

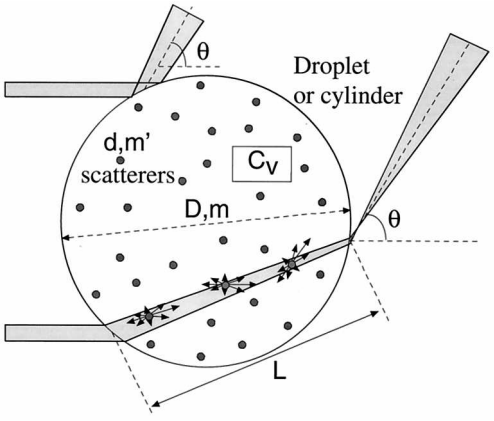

Fig. 2. Attenuation of the refracted signal, by internal scattering by small scatterers, used to deduce the suspension volume concentration C_v.

setup developed to validate the principle of this technique and the models. In Section 5 we present numerical and experimental results. Section 6 contains a discussion of the application range of this technique and of future improvements. Our conclusion is given in Section 7.

2. Principle

A. Basic Principle of the Dual Burst Technique

When PDA works in a dual burst operating mode (i.e., the optical probe volume is reduced to a size smaller than the mean particle size) two Doppler signals are detected for each particle that crosses the probe volume: a refracted and a reflected signal.[4] In such conditions the real part of the particle refractive index[5] can be deduced from the phase of the reflected signal, and the imaginary part,[6] from the amplitude ratio between the two signals. The particle diameter and velocity are deduced from the phase and the Doppler frequency of the reflected signal (see Fig. 1). In this figure, following van de Hulst notations,[7] reflected rays are referenced as rays with $p = 0$ and refracted rays as rays with $p = 1$. See the references cited by Onofri *et al.*[5,6,8] to obtain a full description of this technique including some experimental applications for particle-material recognition, particle-mixing fraction measurements, or the diagnosis of coated particles.[9]

B. Diagnosis of Heterogeneous Particles

In the PDA principle, for homogeneous particles and for a plane-wave illumination, one can easily optimize the optical setup parameters to select a dominant scattering mode,[10] mainly refraction or reflection. This step is fundamental in obtaining linear phase–diameter relationships and in limiting trajectory effects (TE's).[11,12] According to geometrical optics (GO) the rays refracted and reflected by a particle that reaches the detectors are well defined mainly according to the particle's refractive index and the detectors' location and solid aperture angle.

When the particles are no longer homogeneous, additional scattering processes occur inside the particles. The selection of a dominant scattering mode becomes almost impossible with a conventional system. One major feature of the operating mode of the dual burst technique (DBT) is that during the particle trajectory in the probe volume the different scattering processes are delayed in time owing to the successive illumination of the different impact parameters (y_0 and y_1 in Fig. 1). Thus, owing to the small size of the optical probe volume, one can expect the phase and the amplitude of the reflected signal to be unperturbed by additional internal scattering and accurate size measurements to be possible. Conversely, one can expect the initial refracted rays by the particle to be sensitive to the presence of any scatterers inside the particle (see Fig. 2). The principle of the proposed technique, for the scatterer concentration measurement, is to attribute the attenuation of the refracted signal amplitude, compared with the reflected signal, to an apparent extinction phenomenon[7] that can be related to the concentration of the scatterers inside the particle.

Intensity-measuring-based techniques are not usually considered convenient for diagnosing local structures in two-phase flows. The light intensity that is collected by the detectors is affected at the same time by the phenomenon being studied and a great many external factors (laser beam attenuation, deviation of the optical detector gain, etc.) that could vary in a complex way in time and space. A second major feature of the DBT is that the reflected and the refracted signals experience almost the same external perturbations. Thus the amplitude ratio of these two signals is almost equivalent to an on-line amplitude calibration. The reference signal, the reflected signal, is delayed in time by only a few microseconds or milliseconds, depending on droplet velocity and size. This feature leads to significant improvement in the reliability of intensity-based measurements[6] compared with the previous techniques that were developed in the 1970's to deduce the particle size from the Doppler signal's pedestal (see Ref. 13 for a detailed review).

3. Models

A. Geometrical Optics with Apparent Extinction

Assuming a suspension of low concentration inside the particle, and thus a single-scattering mode, the attenuation of the refracted rays or apparent extinction follows the Beer–Lambert law, which, for a maximum of the refracted Doppler signal, reads

$$I_{1,K}{}^{\max} = I_{1,0}{}^{\max}\exp(-KL) = I_{1,0}{}^{\max}\exp(-NC_{\text{sca}}L) = I_{1,0}{}^{\max}\exp\left(-\frac{6C_v}{\pi d^3}C_{\text{sca}}L\right), \quad (1)$$

where $I_{1,0}{}^{\max}$ is the maximum of the refracted signal when the concentration in scatterers is equal to zero. K, for absorbing particles,[6] corresponds to an absorption term (related to the refractive-index imaginary part k as $K = 4\pi k/\lambda$), which corresponds here to an apparent extinction efficiency factor,[7] $K = NC_{\text{sca}} \cdot N$ is the number of scatterers in the suspension per volume unit, and C_v corresponds to the volume concentration in scatterers. C_{sca} is the scattering cross section of individual scatterers in suspension with diameter d and real refractive index m' for wavelength λ/m, where m is the refractive index of the liquid in which the scatterers are in suspension; it is assumed to be real (although an absorption term could be taken into account). L is the path inside the particle of the refracted rays that are scattered in the detector's direction[6] with $L = D\sin(\tau_y')$. D is the particle diameter. τ_y', the angle defined in Fig. 1, depends mainly on the particle refractive index and the detector's direction θ. The validity of Eq. (1) is limited in two ways: The optical thickness of the particle must be small (typically $NC_{\text{sca}}L \leq 1$ or 2, depending on the author considered) to be in the single-scattering mode, and the term $I_{1,K}{}^{\max}$ must be due only to refracted rays that have followed a direct path through the particle without scattering by suspension. The first condition limits the refracted ray attenuation to less than ≈63–90% (see Fig. 10 in our case). Thus, because the attenuation mainly depends simultaneously on the particle and the scatterer diameters and on the suspension concentration in scatterers, the application range of this equation is expected to be severely limited. To satisfy the second condition, the optical thickness of the suspension must be small and the refracted rays must be collected into the smallest possible solid angle around the nominal refracted ray direction. Note that this last condition is better satisfied when one is considering suspensions of small scatterers[7] (compared with the laser wavelength) because the light diffracted by these scatterers is not as strongly concentrated in the forward direction as it is by scatterers with large parameters.

In Eq. (1) the amplitude of the nominal refracted rays, which cannot be obtained directly for a particle in flow, can be calculated from measuring the maximum amplitude of the reflected signal. With GO, the relationship between these two quantities can be calculated. For a point detector, if we use Fresnel's amplitude coefficients,[7] ε_1 and ε_2, and include a divergence term to account for the curvature of the particle surface, the interrelation is

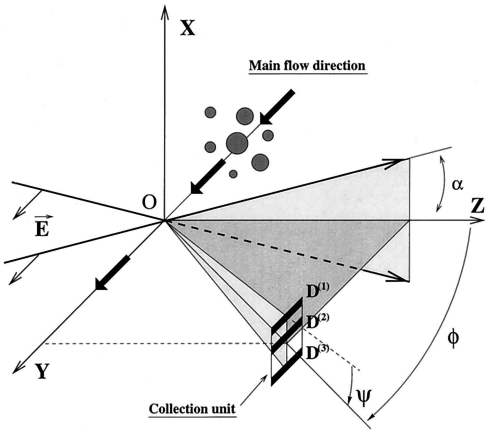

Fig. 3. Phase Doppler modified standard geometry. Three detectors $D^{(i)}$ are considered with i = 1–3. The polarization of the laser beams is parallel. (The electric vector **E** is parallel to *OY*.)

$$\frac{I_{1,0}{}^{\max}}{I_0{}^{\max}} = \frac{\varepsilon_1{}^2}{\varepsilon_0{}^2}\frac{\tan(\tau_y')}{\tan(\tau_y') - \tan(\tau_y)}. \quad (2)$$

Thus, with Eqs. (1) and (2), the particle concentration in small scatterers can be deduced, provided that we know the size and relative refractive index of the scatterers, from

$$C_v = -\frac{\pi d^3}{6D\sin(\tau_y')C_{\text{sca}}}\left\{\ln\left(\frac{I_{1,K}{}^{\max}}{I_0{}^{\max}}\right) - \ln\left[\frac{\varepsilon_1{}^2}{\varepsilon_0{}^2}\frac{\tan(\tau_y')}{\tan(\tau_y') - \tan(\tau_y)}\right]\right\}. \quad (3)$$

B. Correction for Trajectory Effects on the Amplitude Ratio

In the so-called modified standard (see Fig. 3) or planar phase Doppler geometries (see Refs. 8, 14, and 15, for a detailed review), TE's have negligible effects on phase and thus on diameter measurements when the particles move along the expected main direction.[8] But the ratio of the refracted to the reflected signal amplitude changes significantly with particle locations perpendicularly to the expected main direction[6] (these TE's occur for positions along the *OX* axis in the case of a modified standard geometry) (see Fig. 3, where α, ϕ, and ψ are the so-called half-beam, off-axis, and elevation angles). In the following the correction for these TE's is discussed.

Let us consider that, for a modified standard geometry (that we recommend for use with the DBT and spherical particles when possible), the intensity profile in the optical probe volume along the *OX* axis is of the form

$$I(x) = I(0)\exp[-2(x/\omega_x)^2], \quad (4)$$

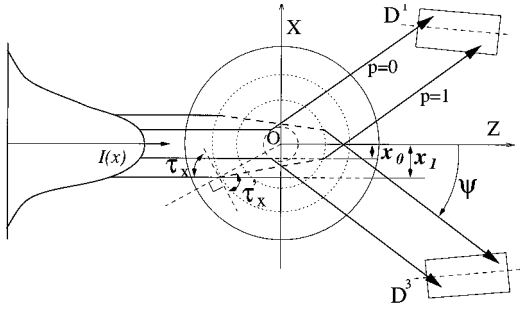

Fig. 4. For a modified standard geometry two symmetrical detectors can be used to eliminate trajectory effects on the signal amplitude ratio occurring for spherical particles, depending on their position along the *OX* axis.

where ω_x is the radius of the laser beam waist (almost equivalent to the probe volume diameter) in the *OX* direction and $I(0)$ is the maximum probe volume intensity along the beams' axis. If we assume a collection unit with two symmetrical detectors [superscript (i), with $i = 1$ and 3; see Fig. 3], the amplitude of the low-pass filtered Doppler signals for refraction and reflection are

$$I_{1,K}^{(i)}(x) = I(0)g^{(i)}I_{1,K}^{\max}\exp[-2(x \pm x_1)^2/\omega_x^2], \quad (5)$$

$$I_0^{(i)}(x) = I(0)g^{(i)}I_0^{\max}\exp[-2(x \pm x_0)^2/\omega_x^2], \quad (6)$$

where $\pm$ indicates that in Eq. (5) the sign is positive for detector 3 and negative for detector 1 and in Eq. (6) negative for detector 3 and positive for detector 1 (see Fig. 4). The term $g^{(i)}$ corresponds to the electronic gain of each detector, which is expected to be linear. The terms x_1 and x_0 are the lateral impact parameters defined in Fig. 4 with $x_1 = D\cos(\tau_x)$ and $x_0 = D\cos(\psi/2)$, where τ_x is deduced by solving the transcendental equation

$$\psi = 2\tau_x - 2\cos^{-1}[\cos(\tau_x)/m]. \quad (7)$$

We assume here that the variation of the Fresnel coefficients with the particle trajectory is negligible because, in conventional PDA systems, the displacement of the particle in the optical probe volume is small compared with the distance between the detectors and the optical probe volume. To obtain expressions independent of the gain of each detector and the laser beam intensity, we can calculate the ratio of the maximum amplitude $R^{(i)}$ of the refracted and the reflected signal for each detector:

$$R^{(i)}(x) = \frac{I_{1,K}^{\max}}{I_0^{\max}}\exp\{-2[(x \pm x_1)^2 - (x \pm x_0)^2]/\omega_x^2\}. \quad (8)$$

Now we sum the logarithm of the amplitude ratio measured from each detector:

$$\frac{\ln[R^{(1)}] + \ln[R^{(3)}]}{2} = \ln\left[\frac{I_{1,K}^{\max}}{I_0^{\max}}\right] - 2\left[\frac{x_1^2 - x_0^2}{\omega_x^2}\right]. \quad (9)$$

Finally, for the particle-volume concentration in scatterers, we found an expression independent of the particle position along the *OX* axis:

$$C_v = \frac{-\pi d^3}{6D\sin(\tau_y')C_{\text{sca}}}\left(\frac{\ln[R^{(1)}] + \ln[R^{(3)}]}{2} - \ln\left[\frac{\varepsilon_0^2}{\varepsilon_1^2}\frac{\tan(\tau_y')}{\tan(\tau_y') - \tan(\tau_y)}\right] + 2\left\{\frac{[\cos^2(\tau_x) - \cos^2(\psi/2)]D^2}{\omega_x^2}\right\}\right). \quad (10)$$

Finally, three ways to eliminate trajectory effects on the amplitude ratio can be identified:

(1) When the logarithm of the amplitude ratio of the refracted to the reflected signal from two symmetrical detectors (as they are usually in common PDA systems) is summed, Eq. (10) can be used to deduce the particle concentration in suspension directly whatever the particle position along the *OX* axis, the gain of each detector (provided that it is linear), and the attenuation of the laser beams.

(2) When the amplitude ratio of the refracted to the reflected signal from a single detector located in the scattering plane ($\psi = 0$) is used, provided that the detector aperture along *OX* can be considered small, the last term in Eq. (10) (i.e., the correction term for TE) is equal to zero ($\tau_x = \tau_x' = \pi/2, x_1 = x_0 = 0, R^{(1)} = R^{(3)}$). Equation (10) is equivalent to Eq. (3) and the particle concentration in suspension can be deduced simply from Eq. (3).

(3) When $\omega_x \to \infty$, the correction term in Eq. (10) vanishes. This condition is equivalent to using an elliptical probe volume (a longer axis along *OX*) rather than the usual Gaussian probe volume. This can be done by using laser sheets to form the probe volume.[8] In such conditions Eq. (10) is equivalent to Eq. (3) and the scatterer concentration can be deduced simply from measuring the particle diameter D from the phase of the reflected signal and the amplitude ratio $I_{1,K}^{\max}/I_0^{\max}$ (from a single detector).

C. Monte Carlo Model and Multiple Scattering

When the concentration of scatterers increases inside the particle, multiple scattering may become a dominant phenomenon and the Beer–Lambert approach developed above is expected to decline. Thus, to take this effect into account, a Monte Carlo[16] approach has been developed. This approach has been developed to predict the scattering properties of a slab, a cylindrical (with infinite length) particle, and a spherical particle composed of a liquid suspension of small scatterers. Owing to experimental considerations (see Section 4) and to save space, the model described here is only for a cylindrical particle and a planar geometry. (In Fig. 3 the jet axis is along *OY*, its trajectory is along *OX*, and the elevation angle ψ is almost equivalent to a scattering angle, $\phi = 0$.)

To describe the suspension, we consider a collection of randomly distributed scatterers inside the particle.

Table 1. Optical Characteristics of Various Latex Suspensions[a]

Parameters	Latex Particles' Diameter d (μm)				
	0.06	0.35	0.61	1.6	3.3
N (m^{-3})	6.97×10^{20}	4.26×10^{18}	7.90×10^{17}	4.46×10^{16}	5.09×10^{15}
C_{sca} (m^2)	2.74×10^{-18}	3.17×10^{-15}	3.27×10^{-13}	7.36×10^{-12}	1.68×10^{-11}
Q_{sca}	9.70×10^{-4}	0.0329	1.12	3.66	1.97
$\tilde{l}$ (m)	827	74	3.9	3.1	12
K (m^{-1})	1.91×10^{3}	1.35×10^{4}	2.85×10^{5}	3.28×10^{5}	8.55×10^{4}

[a] N, number of polystyrene particles with diameter d and per unit volume; C_{sca}, scattering cross section of the considered particles; $Q_{sca} = 4C_{sca}/\pi d,^2$ the corresponding scattering cross-section coefficient; $\tilde{l}$, mean free path for a ray between two scattering processes; K, apparent extinction coefficient. The parameters are determined for the laser wavelength λ/m' and for a volume concentration of $C_v = 10\%$.

Thus the mean free path $\tilde{l}$ for a ray (a pencil of light[7]) between two scatterers is given by $\tilde{l} = 1/NC_{sca}$. Table 1 gives an overview of the evolution of this last parameter with the scatterers' size. The probability density when a ray goes a distance l between two scatterers is $P(l) = \exp(-l/\tilde{l})/\tilde{l}$. The simulation procedure is then divided into four steps:

(1) The scattering diagram of one scatterer inside the suspension is calculated by use of the Lorenz–Mie theory with parameters λ/m, m', d and for a particular polarization. A monodisperse size distribution is assumed here for the scatterers. (A polydisperse size distribution could also be taken into account.) A look-up table of the probability for an incident ray to be scattered in the direction ψ is then created.

(2) Along the OX axis from $-D/2$ to $D/2$ more than n_i impact parameters are defined and the paths of the corresponding rays impinging on the particle are followed until they leave the particle, or until they experience n_r internal reflections with the particle–air interface. Fresnel's coefficients are used to calculate the intensity of reflected and refracted rays at the particle interface for a particular polarization. After a path l given by the probability density $P(l)$ the ray is scattered by a scatterer in the direction deduced from the look-up table. For each impact parameter, we consider more than n_p rays to obtain a representative sample. At this step the particle (with internal scatterers) scattering diagram is obtained for $n_i n_r n_p$ initial rays.

(3) A table is created with ray-impact parameters as inputs and the scattering directions, the number of collisions, the total path length of each ray, etc. as outputs. This table is used to provide various subsequent statistical and integrated quantities. In the present case a rectangular aperture is simulated for the PDA detectors by integration of the intensity of the different rays across the defined solid aperture angles. The half-angle α between the two laser beams is also taken into account by adding the collected rays at the two equivalent scattering angles (for the planar geometry $\psi \pm \alpha$).

(4) To simulate the Gaussian intensity profile in the probe volume and a particle trajectory along the OX axis, the intensity of each ray collected by the detector is weighted by a sliding Gaussian function. Each signal is then fitted by a Gaussian interpolating function to find its maximum.

4. Experimental Setup and Procedure

For precise control of the suspension concentration and the experimental facilities, tests of the proposed technique were carried out on cylindrical jets (one circular cross section) rather than spherical particles. Note that the principle of absorption measurements of flying droplets has been validated previously.[6] In addition, it has been shown that PDA can be used with no particular problem to size small[17] or large[8] cylindrical particles with axes perpendicular to the beam planes. The only modification necessary is the use of planar geometry for the optical setup.

In the experimental setup the jet was fixed. To simulate a particle trajectory, and thus produce the required two signals, a rotating mirror was used to shift the probe volume (see Fig. 5). The trajectory radius described by the probe volume was sufficiently large to ensure that the particle trajectory deviation was less than 0.05° from the direction perpendicular to the fringes. The raw Doppler signal output from a one-component Aerometrics, Inc.[18] system (based on a 10-mW He–Ne laser) was stored in an 8-bit digital oscilloscope and read out to a PC for further analysis (see Fig. 8). To reduce the solid detector angles a mask was placed in front of the receiving aperture. The optical parameters of the phase Doppler system are summarized in Table 2.

The cylindrical jet was made of suspensions of spherical polystyrene particles in water (latex). The initial solutions, with 10% volume concentration, from Bangs Laboratories, Inc.[19] were diluted with distilled and microfiltered water to obtain solutions of lower concentrations. Five latex particle sizes were used, $d = 0.06, 0.35, 0.61, 1.60, 3.30$ μm. Polystyrene has a refractive index of 1.588 for $\lambda = 0.6328$ μm. In an ambient temperature its relative refractive index to water is 1.192. Owing to the latex density, $\rho = 1.050$ g/ml, and agglomerating internal forces, solutions were put in an ultrasonic system before use. To produce the jet, the liquid suspensions were ejected from a syringe through a needle with known internal diameter (see Fig. 6). The length of the needles was a least 100 times their diameter, which was expected to be sufficient to obtain a fully developed flow at the needle output. The

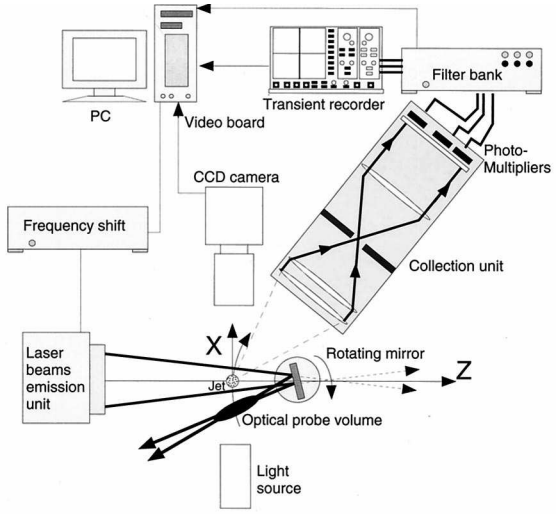

Fig. 5. Schematic of the experimental setup.

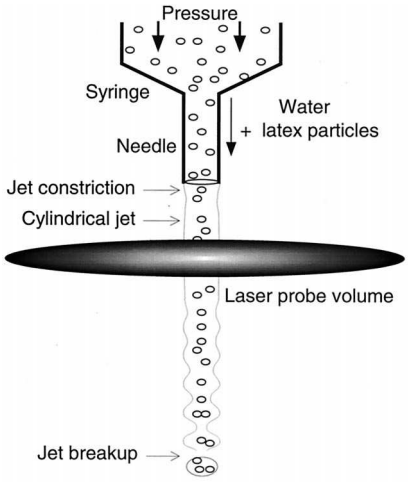

Fig. 6. Outline of the region under study along the jet axis.

stability and the diameter of the liquid jet were controlled and measured with a classical video imaging and acquisition board system. Figure 7 presents typical experimental Doppler signals obtained with this setup from detector 1. The cylindrical jet diameter was measured at 120 μm and was made of a mixture of 0.35-μm latex particles. From Figs. 7(a) to 7(f) the volume concentration varies, C_v = 0.049, 0.31, 0.75, 1.25, 2.5, and 5%. In Fig. 7(a) the reflected signal is shown at left and the refracted signal is shown at right. As expected, for all concentrations, the amplitude of the reflected signal remains almost constant, whereas at the same time a strong decay is observed for the amplitude of the refracted signal. Note also the appearance of a plateau between the two signals as the concentration in suspension increases. The refracted signal is almost unobservable for concentrations of more than 2.5% in volume.

5. Numerical and Experimental Results

The Monte Carlo simulation procedure was used in Fig. 8 to calculate the scattered-light intensity by a 110-μm cylindrical jet, which is collected by detector 3 versus the elevation angle ψ (here strictly equivalent to a scattering angle, ψ = θ, since the half-beam angle α is set to zero here). Different suspension concentrations are considered in this figure for d = 0.35 μm. The calculations are performed for an incident Gaussian beam (the jet axis is perpendicular to the beam axis and the scattering plane) with a 54-μm diameter, n_i = 5000, n_r = 7, n_p = 500. Several interesting features may be noted in this figure:

(1) The total scattered intensity seems to decrease as the suspension increases. In fact, the rays that are scattered by the suspension out of the scattering plane (*OXZ*) have little chance of being scattered later in the scattering plane and then of being collected by the detector. The finite beam dimension and the cylindrical shape of the jet also amplify this effect significantly, since scattered rays tend more

Table 2. Optical particles of the Phase Doppler System used in the Experiment and for the Numerical Simulations

Laser wavelength, λ (μm)		0.6328
Laser power (mW)		10
Beam-waist diameter, 2 ω_0 (μm)		52
Half-beam angle, α (deg)		2.27
Polarization		Perpendicular
Detectors	Mean elevation angle, ψ deg	Off-axis angle, ϕ deg
1	54.0	0
2	55.3	0
3	58.2	0
Detectors angular width, δψ [°]		Detectors angular height, δϕ [°]
0.57		0.57

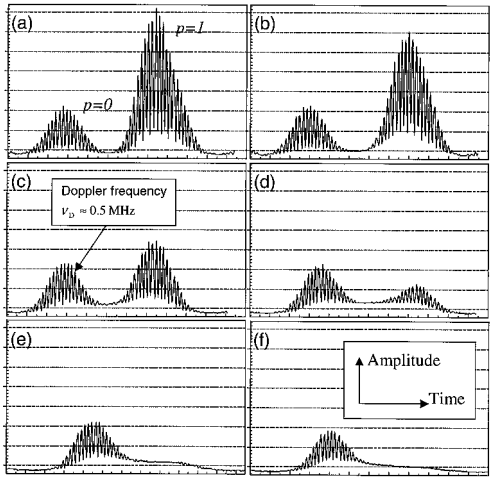

Fig. 7. Typical raw Doppler signals recorded for a 120-μm liquid jet with various concentrations in suspension: The C_v is = (a) 0.0049%, (b) 0.31%, (c) 0.75%, (d) 1.25%, (e) 2.5%, and (f) 5%. The suspension is a mixture of 0.35-μm spherical polystyrene particles in water (latex).

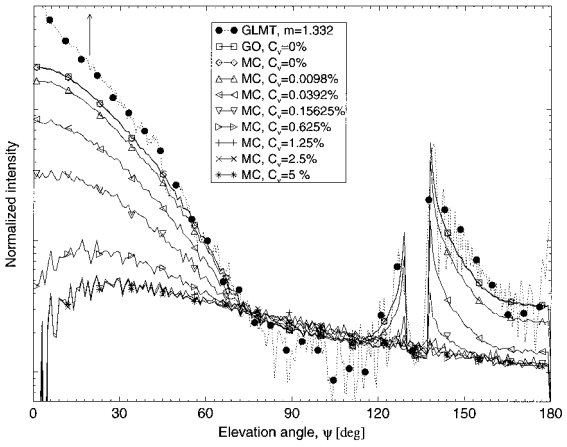

Fig. 8. Monte Carlo simulations for the light intensity that is scattered in the *OXZ* plane by a 110-μm cylindrical particle with an axis along *OY*; various scatterer concentrations, $d = 0.35$ μm, $n_i = 5000$, $n_r = 7$, $n_p = 500$.

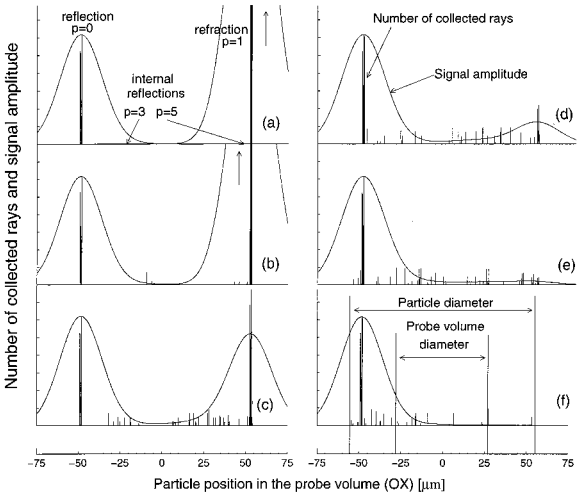

Fig. 9. Monte Carlo simulations for the evolution of the low-pass filtered amplitude of the phase Doppler signals versus the particle trajectory in the optical probe volume and for various scatterers concentrations: C_v is (a) 0%, (b) 0.0125%, (c) 1.25%, (d) 2.5%, (e) 5%, (f) 10%. $D = 110$ μm, $d = 0.35$ μm, $n_i = 3000$, $n_r = 7$, $n_p = 50$.

and more to propagate along the jet axis. For a plane-wave illumination this phenomenon would not be visible.

(2) The scattered intensity varies in different ways with increased suspension concentration, depending on the scattering angle considered: strong attenuation in the forward ($\psi \leq 30°$) and rainbow ($120° \leq \psi \leq 150°$) regions and small attenuation for $60° \leq \psi \leq 120°$. Thus, from a practical point of view, to increase the sensitivity of the proposed technique to small concentrations, it is better to collect the scattered light in the forward region or in the rainbow region. Conversely, to extend the dynamic range to higher concentrations, it is better to collect the scattered light sideways. Note that these remarks are partial because, to optimize the proposed technique, the absolute value of the refracted to the reflected signal amplitude as well as the linearity of the phase diameter relationship must also be considered.

(3) For the pure water droplet there is qualitative agreement between the generalized Lorenz–Mie theory (the Lorenz–Mie theory for Gaussian beam[12,20] illumination), GO, and Monte Carlo predictions. The proposed models do not take into account diffraction effects and the phase of the scattered rays. Thus major discrepancies occur conventionally in the pure forward, backward, and rainbow regions. They also underestimate the ripple structure of the scattering diagram predicted by the Lorenz–Mie theory, which is classically attributed to interference and resonance phenomena.

The Monte Carlo simulation is used in Fig. 9 to simulate the evolution of the Doppler signals when the jet travels through the probe volume. For a better understanding, we have limited the number of rays in this calculation, i.e., $n_i = 3000$, $n_r = 7$, $n_p = 50$. The detector considered here is detector 3; other optical parameters are equivalent to those used in Fig. 7. The vertical bars correspond to the collected rays before the application of the Gaussian sliding window and the continuous curves to the signal amplitude that is obtained later. The evolution of the amplitude ratio of the reflected and the refracted signal is in qualitative agreement with that observed from Fig. 7. The refracted signal attenuation is nevertheless stronger than the one observed in Fig. 7. This can be simply explained from Fig. 8 by the lower elevation angle of detector 1 compared with detector 3.

In Fig. 10 the evolution of the amplitude ratio versus the jet concentration in suspension, which is predicted by Eq. (3) and the Monte Carlo model, is compared with experimental results for detector 1. The diameter of the latex particles is 3.3 μm, and the diameter measured for the jet is 120 μm. For low concentrations ($C_v < 2.5\%$) the amplitude ratio decreases exponentially with increasing concentration (linear-logarithm scale). After a transition zone ($2.5 < C_v < 5\%$) the decay is significantly reduced for $C_v > 5\%$. Error bars on experimental results represent the standard deviation measured on the amplitude ratio of more than 1000 signals. Predictions from Eq. (3) are in good agreement with experimental data for $C_v < 2.5\%$ (which corresponds to an optical thickness of $NC_{sca}L < 1.8$ and a refracted signal attenuation of 84%). As expected, this equation is valid only for particles of small optical thickness, although the value obtained here is rather high. The qualitative agreement found by comparing Figs. 7 and 9 is confirmed here quantitatively and has been observed for all experiments. The Monte Carlo approach is valid over all the concentrations and the particle diameter considered here.

Figure 11 presents the evolution of the amplitude ratio between the refracted and the reflected sig-

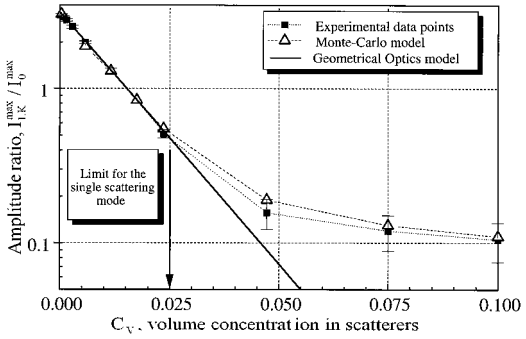

Fig. 10. Comparison of the Monte Carlo and the geometric model predictions with experimental data for the evolution of the amplitude ratio with increasing scatterer concentrations. $D = 120$ μm, $d = 0.35$ μm.

nals measured for a 120-μm jet with increasing volume concentration. Five scatterer diameters are considered. In all cases the evolution is linear up to and including a given concentration. This limit concentration depends strongly on the scatterer sizes: more than 10% for the scatterers of 0.06 μm and ≈1.25% for the scatterers of 1.6 μm. This linear evolution corresponds to an exponential decay of the refracted signal amplitude, in agreement with the law predicted by the GO model, assuming a dominant single-scattering process for particles of small optical thickness. The evolution of the slopes is also in qualitative agreement with the apparent extinction coefficients K calculated in Table 1 (for a concentration of 10% in volume). For higher concentrations the decrease in the amplitude ratio is reduced. Thus the sensitivity at high concentrations is more limited. In all cases, except for the smallest scatterers, the amplitude ratio seems to tend to a limit value. This limit can probably be attributed to the resolution limit of our experimental setup, which is a function of the detectors' sensitivity, the level of digitization, and the signal-processing efficiency for extracting the refracted signal amplitude from signals with low signal-to-noise ratios [see Figs. 7(e) and 7(f)].

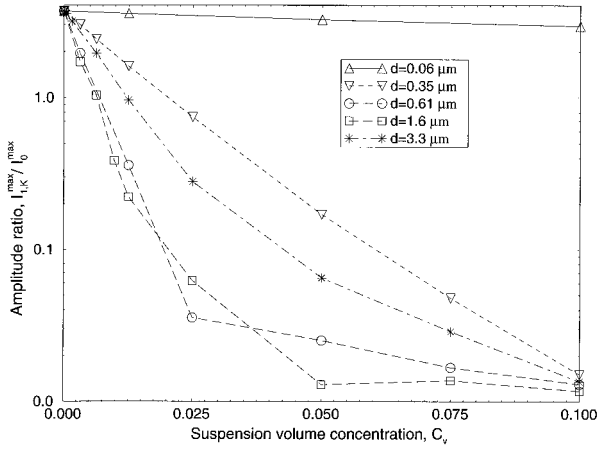

Fig. 11. Experimental evolution for the amplitude ratio versus the suspension concentration. Five scatterer sizes are considered. $D = 120$ μm, detector 3.

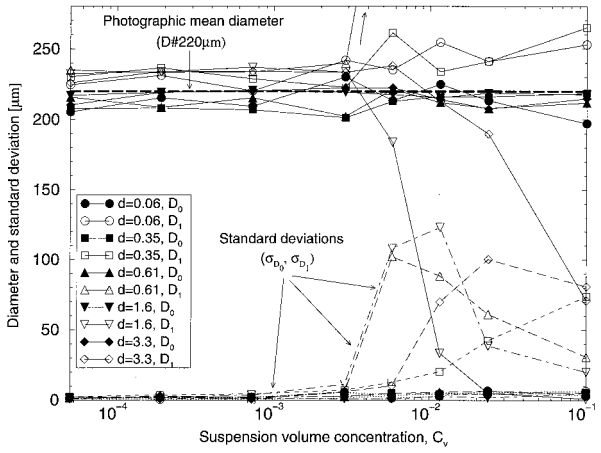

Fig. 12. Comparison between size measurements obtained from the reflected signals (diameter deduced, D_0) and the refracted signals (diameter deduced, D_1). The expected diameter is $D \approx 220$ μm.

According to the principle of the proposed technique, a significant improvement in the size measurements of heterogeneous particles is expected with the DBT, because it avoids the detectors' collecting simultaneously the light that is reflected by the particle and the light that is refracted by the particle and scattered by the suspension. To illustrate this feature, Fig. 12 presents a comparison between the measured diameter, for a jet of 220 μm, from the phase of the refracted signals and from the phase of the reflected signals. Various scatterer sizes and concentrations are considered. The evolution of the corresponding standard deviations is also plotted. For this jet diameter the reflected signals provide size measurements with deviations of less than 3% for all concentrations (0–10%). For the refracted signals this low deviation is obtained only for concentrations of less than 0.2%; it goes as high as ≈10–50% for concentrations of more than ≈0.75%. Note that the standard deviation obtained with the refracted signals would be higher if phase measurements were not limited in the 0 and 2π range. This last effect limits artificially the amplitude of the largest standard-deviation error. (The refracted signal phase oscillates randomly in a fixed range.) When the phase oscillates around zero, the measured particle diameter tends to zero (in Fig. 12, $d = 1.6$ and 3.3 μm); when it oscillates around 2π, the measured diameter reaches the maximum diameter authorized by the phase–diameter relationship (in Fig. 12, $d = 0.61$ μm). (The mean diameter measured from the refracted signals goes as high as ≈600 μm.)

6. Discussion

A. Optical Parameters and Measurement Range

For the experimental setup we chose the optical parameters mainly to obtain an optical probe volume

with a sharp intensity profile and a good compromise between the sensitivity and the dynamic range on particle-size and scatterer-concentration measurements. The reduction of the probe volume diameter leads to a better separation between the two signals and to a reduction of internal scattering effects on the phase of the reflected signals. Unfortunately, this also leads to a decrease in the particle transit time in the probe volume (and then the accuracy on phase determination) and an increase in the need for an accurate correction of trajectory effects. For detectors located in the near-forward direction (i.e., rays $p = 1$ and $p = 0$ mainly collected), a compromise is found when the probe volume diameter is approximately one-half of the minimum particle diameter.[6] Intensity-measuring-based techniques are limited in resolution and dynamic range by the digitization of the signal amplitude (an 8-bit oscilloscope was used here) and by the dynamic range of the optical detectors, so that the optical parameters are optimized to obtain a nominal amplitude ratio that is not too high and a moderate refracted signal attenuation with increasing concentration in scatterers.

The evolution of the amplitude ratio, for a given suspension concentration and particle size, depends strongly on the collection angle (through distance L). Figure 8 shows a qualitative overview of this dependence. One simple solution for increasing the sensitivity of the proposed technique to particles of small optical thickness is, for example, to collect the scattered light in the rainbow angle region. Some preliminary simulations for $\psi \approx 139°$ and a parallel polarization not reported here have shown that the reflected and the refracted signals have approximately the same amplitude for a pure water jet and that the refracted signal attenuation, with increasing concentration in scatterers, is four times as high as that obtained in Fig. 10.

The laser wavelength also plays an important role, through the factor C_{sca}, on the sensitivity and the dynamic range of the proposed technique. For the diagnosis of particles with a large optical thickness (large size and/or suspension concentration) the laser wavelength can be increased to decrease the factor C_{sca}. This well-known feature has been used for particle-size improvements by Manasse *et al.*[2] Similarly, several laser wavelengths may be used to obtain an estimation of the scatterer sizes in addition to their concentration since C_{sca} depends on both of these parameters (provided that the scatterers' size is of the order of magnitude of the laser wavelength). This procedure would be only an extrapolation of the so-called multiwavelength extinction technique that has already been developed for aerosol or spray concentration measurements.

B. Signal Processing

With a classical PDA setup, as well as for the refracted and reflected signals obtained with the DBT, the Doppler signals have the following form[10]:

$$S(t) = P_S[1 + V \cos(2\pi v_D t + \phi)], \qquad (11)$$

where P_s, V, v_D, ϕ are, respectively, the signal pedestal, visibility, frequency, and phase. From all these terms only P_s cannot be clearly attributed to an interference phenomenon. The scatterers inside the suspension induce some perturbations on the scattered ray coherence and thus on the signal visibility and phase. Thus the amplitude of high-pass filtered Doppler signals, $S(t) = P_S V \cos(\omega t + \phi)$, which is classically used for Doppler signal processing, may be sensitive to the scatterer concentration through the pedestal and the visibility (which is a complex parameter). Consequently, and also for a better comparison with model predictions, the amplitude ratio was calculated from the signal pedestal by use of the raw output signals from the PDA system rather than the filtered and the logarithm amplified signals.

7. Conclusion

The principle of an optical technique for simultaneous velocity, size, and concentration in suspension measurements of spherical droplets and cylindrical jets has been proposed. It is based on PDA working in the DBT configuration. Two models have been developed to evaluate its application range and sensitivity. An experimental test on cylindrical jets of various suspension concentrations has demonstrated the applicability of this technique. Several solutions that extend the dynamic range or sensibility of this technique have been proposed. It is believed that this new technique could be a useful tool for investigating processes in which liquid suspensions are sprayed for surface-coating, drying, or combustion applications.

References

1. J. Domnick, A. Lindenthal, C. Tropea, and T-H. Xu, "Application of PDA in paint sprays," Atomization Sprays **4,** 273–279 (1994).
2. U. Manasse, T. Wriedt, and K. Bauchhage, "Optimization of PDA parameters for sizing of optically inhomogeneous liquid droplets," in *Proceedings of the Third Optical Particle Sizing Conference*, M. Maeda, ed. (Keio University, Yokohama, 1993), pp. 453–460.
3. U. Manasse, T. Wriedt, and K. Bauchhage, "Reconstruction of real size distributions hidden in PDA results obtained from droplets of inhomogeneous liquids," Part. Part. Syst. Charact. **11,** 84–90 (1994).
4. C. F. Hess and G. P. Wood, "The pulse displacement technique: a single particle counter with a size range larger thant 1000:1," in *Proceedings of the Third Optical Particle Sizing Conference*, M. Maeda, ed. (Keio University, Yokohama, 1993), pp. 475–482.
5. F. Onofri, G. Gréhan, G. Gouesbet, T-H. Xu, G. Brenn, and C. Tropea, "Phase Doppler anemometry with Dual Burst Technique for Particle Refractive Index Measurements," in *Proceedings of the Seventh International Symposium on Applications of Laser Techniques to Fluid Mechanics*, F. Durão, ed. (Instituto Superior Técnico, Lisbon, 1994), pp. 24.1–24.9.
6. F. Onofri, T. Girasole, G. Gréhan, G. Gouesbet, G. Brenn, J. Domnick, C. Tropea, and T-H. Xu, "Phase Doppler anemometry with dual-burst technique for measurement of the refractive index and the absorption coefficient simultaneously with size and velocity," Part. Part. Syst. Charact. **13,** 112–124 (1996).

7. H. C. van de Hulst, *Light Scattering by Small Particles* (Dover, New York, 1957), Chaps. 4 and 12.
8. F. Onofri, "Prise en compte de la dimension finie des faisceaux d'éclairage en granulométrie optique: anémométrie phase Doppler diagnostics des écoulements diphasiques," Ph.D. dissertation (Université de Rouen, Rouen, France, 1995).
9. F. Onofri, D. Blondel, G. Gréhan, and G. Gouesbet, "On the optical diagnosis and sizing of coated and multilayered particles with phase Doppler anemometry," Part. Part. Syst. Charact. **13,** 104–111 (1996).
10. A. Naqwi and F. Durst, "Light scattering applied to LDA and PDA measurements, Part 1: theory and numerical treatments," Part. Part. Syst. Charact. **8,** 245–258 (1988).
11. S. V. Sankar, A. Inenaga, and W. D. Bachalo, "Trajectory dependent scattering in phase Doppler interferometry: minimizing and minimizing sizing error," in *Proceedings of the Sixth Symposium on International Applications of Laser Techniques to Fluid Mechanics*, F. Durão, ed. (Instituto Superior Técnico, Lisbon, 1994), pp. 12.2–12.10.
12. G. Gréhan, G. Gouesbet, A. Naqwi, and F. Durst, "Particle trajectory effects in phase Doppler systems: computations and experiments," Part. Part. Syst. Charact. **10,** 332–338 (1993).
13. D. Holve and S. A. Self, "Optical particle sizing for *in situ* measurements," Appl. Opt. **18,** 1632–1652 (1979).
14. T-H. Xu and C. Tropea, "Improving performance of a 2D phase Doppler anemometer," Meas. Sci. Technol. **5,** 969–975 (1994).
15. Y. Aizu, F. Durst, G. Gréhan, F. Onofri and T-H. Xu, "A PDA system without Gaussian beam defects," in *Proceedings of the Third Optical Particle Sizing Conference*, M. Maeda, ed. (Keio University, Yokohama, 1993), pp. 461–470.
16. L. Bergougnoux, J. Misguesh-Ripault, J.-L. Firpo, and J. André, "Monte Carlo calculation of backscattered light intensity by suspension: comparison with experimental data," Appl. Opt. **35,** 1735–1741 (1996).
17. H. Mignon, G. Gréhan, and C. Tropéa, "Measurement of cylindrical particles with phase Doppler anemometry," Appl. Opt. **35,** 5180–5187 (1996).
18. Aerometrics, Inc, 550 Del Rey Ave., Sunnyvale, Calif. 94086.
19. Bangs Laboratories, Inc., 9025 Technology Drive, Fishers, Ind. 46038-2886.
20. G. Gouesbet, G. Gréhan, and B. Maheu, "Light scattering from a sphere arbitrarily located in a Gaussian beam, using a Bromwhich formulation," J. Opt. Soc. Am. **5,** 1427–1443 (1988).

Article A9

Part. Part. Syst. Charact. *16* (1999) 1–9

Critical Angle Refractometry for Simultaneous Measurement of Particles in Flow: Size and Relative Refractive Index

Fabrice Onofri*

(Received: 27 October 1998; resubmitted: 27 January 1999)

Abstract

The principle of the optical technique critical angle refractometry, used to determine the size and refractive index of spherical particles (with relative refractive index below unity) in liquid flows, was investigated. This technique is based on the observation of the particle scattering pattern around the critical angle. Similarly to the recent technique developed for rainbow scattering pattern analysis for droplet temperature and size measurements, it is shown that the relative particle refractive index ($m_r < 1$) and size can be determined from the position of the primary diffraction fringe and from the angular spacing between two fringes. Explicit equations for refractive index and particle size measurement were derived from the first-order term of the physical optics approximation. An experimental validation test and numerical computations based on the Lorenz-Mie theory were used to validate the principle of the proposed technique and to estimate its sensitivity, which was shown to be of the same order as that of the rainbow technique. This technique is considered to be useful for various applications in liquid multiphase flows where the particles size and material are to be characterized.

1 Introduction

The experimental characterization or investigation of multiphase flows essentially requires the determination of three kinds of data giving access to: (*i*) the flow dynamics (velocities of the different phases, velocity fluctuations, vortices, number flux of the particles, etc.), (*ii*) the disperse phase size, shape, concentration and mass flux and (*iii*) material properties of the different phases (particle material recognition, particle and fluid temperature, chemical composition, etc.). Optical techniques, or laser techniques, are largely used to obtain these various properties as they are mainly non-intrusive, well adapted to the diagnosis of reactive flows and, in most cases, highly resolved in time and/or space. For disperse phase characterization, which we only consider here, and for the determination of parameters (*i*) and (*ii*), the optical techniques used are essentially based on elastic or quasi-elastic light scattering properties whereas material or physico-chemical property investigations (*iii*) are mainly based on inelastic light scattering properties. Thus the simultaneous determination of the disperse phase extrinsic and intrinsic properties requires multiple, complex and hence costly experiments.

These last remarks may explain the increasing number of research work on the development of laser diagnosis techniques, based on elastic light scattering, providing simultaneously the three kinds of parameters for the disperse phase. All this work is based on the measurement of the particle refractive index, which is a natural marker of particle material properties. Up to now, three methods have been successfully proposed to measure the refractive index and size of spherical flowing particles with sizes in the micrometric range:

- *Rainbow Angle Refractometry: Roth* et al. [1] proposed in 1989 the use of the position of the rainbow to deduce the refractive index of spherical droplets. This technique, known as rainbow angle refractometry, has more recently been extended to perform additional size measurements [2–4] and also velocity and size measurements combined with a phase Doppler anemometer [5]. This technique has been applied, for instance, to the analysis of droplet combustion [5, 6] and liquid jets instability [7].
- *Phase Doppler Anemometry:* in 1989 *Naqwi* et al. [8] proposed, followed by *Brenn* et al. [9] the use of an extended phase Doppler anemometer (EPDA) to perform simultaneous measurements of particle velocity, size and refractive index. The reduction of the sensitivity of this technique owing to the so-called "trajectory effects" and its applicability for confined flows have been greatly improved by the development of dual mode phase Doppler anemometer (DM-PDA) for refractive index measurements [10]. *Onofri* et al. [11] proposed in 1994 the use a dual burst technique (DBT) to obtain the same parameters with in addition the possibility of measuring the imaginary part of the particle refractive index (i.e. absorption, which may be useful for droplet evaporation studies, and material recognition) [12] or the measurement of coated [13] and heterogeneous particles [14]. These techniques have been applied to particle material recognition [11–14] and the study of spray interaction [9, 10].

* Dr. *F. Onofri*, IUSTI-CNRS UMR 6595-Université de Provence, Technopôle de Château-Gombert, 5 rue Enrico Fermi, 13008 Marseille (France).

0721-3115/99/1–9 $17.50+.50/0

– *Polarization ratio: Massoli* et al. [15] proposed in 1990 the use of the polarization ratio (measurement of the scattered light intensity for two perpendicular polarizations) to obtain the particle refractive index and size. This technique has been used for burning oil droplet temperature measurements. It is mainly limited to small particles ($D < 20\,\mu m$), whereas the rainbow and the phase Doppler techniques (except the extended system) are recommended for large particles ($D > 20\,\mu m$).

All of these techniques have been proposed for the diagnosis of spherical particles with a refractive index higher than that of the surrounding flow (i.e. liquid or solid particles in gas). Nevertheless, for some applications, and particularly in liquid flows, the particles may have a relative refractive index below unity. In this last case, one may predict that the techniques based on phase Doppler anemometry and the polarization ratio will be applicable, although no experimental data or simulations have verified this assumption yet, whereas the rainbow refractometry technique, which is the most sensitive to particle refractive index, is clearly not applicable for this kind of particle.

In this work, the principle of an optical technique for the simultaneous size and refractive index measurement of spherical particles in flows, with a relative index below unity, was investigated. This technique, referenced here as critical angle refractometry (CAR), is based on the analysis of the critical scattering pattern produced by a single particle illuminated by a laser beam. This technique could be useful for particles in flow characterization with possible applications for size distribution measurements, material recognition or the study of coalescent phenomena in liquid/liquid systems. The paper is organized as follows. Section 2 recalls some basic features of the critical scattering of light by spherical particles. The physical optics approximation (POA) introduced by *Marston* and *Kingsbury* [16, 17] is developed to obtain analytical expressions to predict the dependence of the angular position of the diffraction fringes on particles size and refractive index. Section 3 compares predictions from POA and from the Lorenz-Mie Theory (LMT). Section 4 describes the optical set-up used to validate the principle of CAR and presents the experimental results obtained. Section 5 is a conclusion.

2 Scattering of Light by a Spherical Particle Near the Critical Angle

From Descartes' refraction optics laws, we know that in the case of light rays passing from a medium of higher refractive index (m') to a medium with a lower refractive index (m, relative refractive index $m_r = m/m' < 1$), there exist an angle of incidence $\phi_c(m_r) = \arcsin(m_r^{-1})$, leading to an abrupt transition to total reflection for $\phi > \phi_c(m_r)$. In the case of light rays incident on a spherical particle, with radius a and with refractive index m, located in a liquid flow with refractive index m' with $m_r = m/m' < 1$ (these particles are commonly referred to as "bubbles"), the same phenomenon occurs but for a curved surface [19], giving rise, near the so-called "critical angle", to a complex scattering pattern, Figure 1, presents the typical scattering pattern that is produced, in the critical angle region, by an air bubble in water ($m_r = 0.751$) with a diameter $D = 100\,\mu m$. Numerical calculations with the Lorenz-Mie Theory have been performed for the parallel polarization and an incident plane with a wavelength of λ. This scattering diagram is characterized by strong oscillations: a coarse structure (large fringes) superimposed on a fine

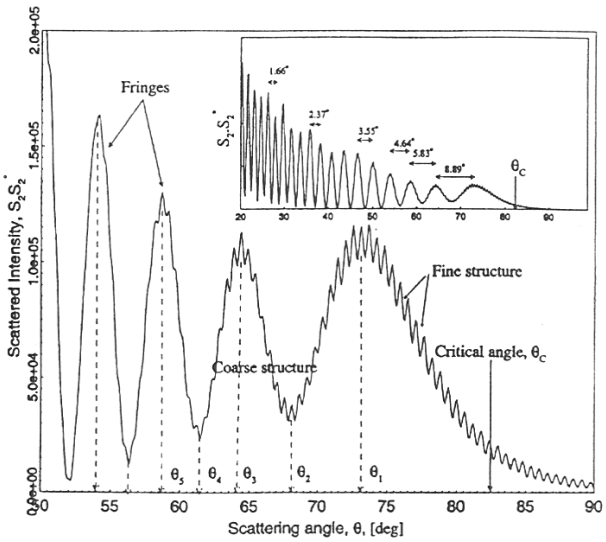

Fig. 1: Lorenz-Mie theory for scattering near the critical angle by a 100 μm diameter air bubble in water, $m_r = 0.751$.

structure (small amplitude and high-frequency fringes). This pattern is qualitatively very similar to that observed in the rainbow angle region [3].

Note in Figure 1 that there exists a shift of several degrees between the location of the first maximum in the scattering pattern (from right to left) and the critical angle location predicted by geometrical optics, $\theta_c(m_r) = \pi - 2\phi_c(m_r)$.

Numerous efforts have been made to propose models giving more insight than the exact solution provided by the Lorenz-Mie theory (LMT) into the roles of parameters such as a, m_r and λ in the production of the aforementioned scattering structures [16–22]. *Marston* and *Kingsbury* [16, 17] developed a so-called "physical optics approximation" (POA) where the contribution from surface reflection is treated by a procedure similar to Airy's theory of the rainbow: a Kirchhoff-type approximation is applied to the amplitude distribution along a virtual reflected wavefront. The reflection contribution ($p = 0$ in the *Van de Hulst* [23] terminology) is approximated as a step function: this "edge reflectivity" [21] gives rise to an angular distribution of scattered intensity similar to a Fresnel straight-edge pattern, which accounts for the diffraction fringes of low angular frequency. Similarly to the corresponding phenomena observed for the rainbow phenomenon, the fine structure is shown [17] to be unrelated to the critical scattering and is concerned with an interference phenomenon occurring between near-side and far-side refracted rays (rays with $p = 2$ of opposite impact parameters ($x > 0$ and $x < 0$ as illustrated in Figure 2).

In the following, to obtain analytical expressions for the coarse structure dependence on particle size and relative refractive index, we neglect contributions from internal reflections ($p > 1$) and direct transmission ($p = 1$). Thus, for $a \gg \lambda$, the angular distribution of the coarse structure is as follows [16]:

$$I(\omega) = I_0 \left(\frac{a}{R}\right)^2 \frac{g(\omega)\bar{g}(\omega)}{8} \tag{1}$$

where ω is the lateral angular displacement of the observation point from the critical angle predicted by geometrical optics (GO),

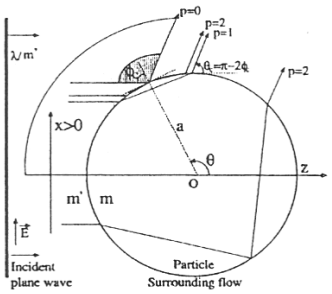

Fig. 2: Reflection and refraction of rays near the critical angle that are scattered at angle θ by a spherical particle with relative refractive index below unity ($m_r < 1$).

θ_c, and depends on the various parameters of the scattering problem:

$$\omega(\theta, m_r, a, \lambda) = \sin(\theta_x(m_r) - \theta)\sqrt{(a/\lambda)\cos(\theta_c(m_r))}. \quad (2)$$

θ is the scattering angle considered in the scattering plane ((OXZ)), see Figure 2), I_0 is the incident intensity and R is the observation distance from the particle center. The function $g\bar{g}(\omega) = [C(\omega) + 1/2]^2 + [S(\omega) + 1/2]^2$ is similar in form to the well-known Fresnel (near-field) diffraction by a straight edge [24]. It is used to predict the far-field intensity of a particle because of the abrupt variation in amplitude of the virtual wave front near the critical angle and because of the curvature of this wave front [17, 22]. $C(\omega)$ and $S(\omega)$ are Fresnel's cosine and sine integrals, defined as

$$F(\omega) = C(\omega) + iS(\omega) = \int_0^{\omega} \cos\left(\frac{\pi z^2}{2}\right)\mathrm{d}z + \mathrm{i}\int_0^{\omega} \sin\left(\frac{\pi z^2}{2}\right)\mathrm{d}z. \quad (3)$$

Determining the dependence of the angular position and spacing of the diffraction fringes with respect to the particle radius and relative refractive index is equivalent to looking for the extremum of the following general function:

$$H(\alpha) = (C(\alpha) + 1/2)^2 + (S(\alpha) + 1/2)^2 \quad (4)$$

and then looking for the solutions of its derivative:

$$(C(\alpha) + 1/2)\cos\left(\frac{\pi\alpha^2}{2}\right) + (S(\alpha) + 1/2)\sin\left(\frac{\pi\alpha^2}{2}\right) = 0. \quad (5)$$

No exact solutions have been found for Eq. (5) so a classical numerical iterative procedure has been used to find them. Figure 3 shows the evolution of $H(\alpha)$. Table 1 gives tabulated solutions found for Eq. (5). They are ordered with the index j, with maximum occurring for odd values of j and minimum for even values of j. $H(\alpha)$ being equivalent to $I(\omega)$ with the change of variable $\alpha = \omega(0, m_r, a, \lambda)$, the locations of the extrema (θ_j, i.e. bright and dark diffraction fringes) of the function $I(\theta)$, versus the particle radius a and relative refractive index m_r, can be deduced by solving the following equation:

$$\alpha_j = \sin(\theta_c(m_r) - \theta_j)\sqrt{(a/\lambda)\cos(\theta_c(m_r))}. \quad (6)$$

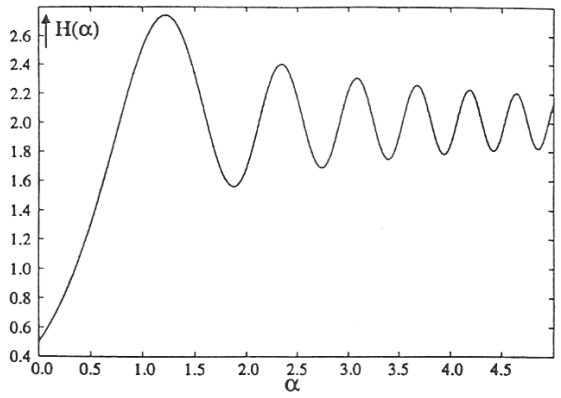

Fig. 3: Evolution of Fresnel's integral based function, $H(\alpha)$.

Table 1: Tabulated solutions of function $H(\alpha)$.

j	Location of the jth extremum, α_j
1st	1.2171982507
2nd	1.8725190624
3rd	2.3448538242
4th	2.7390080864
5th	3.0881958234
6th	3.3913355077
7th	3.6741104772

The dependence of the angular location (in degrees) of the jth fringe versus the particle diameter and relative refractive index is then found to be given by

$$\theta_j = \frac{180}{\pi}\left[\pi - \arcsin\left(\alpha_j\sqrt{\frac{m_r\lambda/a}{\sqrt{m_r^2 - 1}}}\right) - 2\arcsin(m_r^{-1})\right]. \quad (7)$$

For a fixed refractive index and for $a \gg \lambda$, the angular deviation from the critical angle of the diffraction fringes versus the particle radius evolves as $(\theta_c - \theta) \propto 1/\sqrt{a}$. This dependence on size is stronger than that predicted by Airy's theory for the rainbow phenomenon and an equivalent particle: $(\theta_r - \theta) \propto 1/a^{2/3}$ (θ_r is the angle predicted by geometrical optics for the rainbow angle). For a flow and particles of known refractive index, the particle radius can be determined by measuring the location of any extrema in the critical scattering pattern (provided that we know its numbering order, j):

$$a_j(m_r) = \frac{\alpha_j^2\lambda m_r}{\sin^2[\theta_j - \pi + 2\arcsin(m_r^{-1})]\sqrt{m_r^2 - 1}} \quad (8)$$

a is denoted here as $a_j(m_r)$ as it is relative to the jth fringe and to a fixed relative refractive index. It comes out also from Eq. (8) that several estimations of the particle diameter can be performed by measuring the angular positions of several fringes.

To avoid the dependence of the radius estimation on a prior knowledge of the local flow refractive index and particle refractive index, the positions of at least two fringes, $j = p$ and $j = q$ (with $p < q$), have to be measured (experimentally it may be convenient to use the first two bright fringes, i.e. $p = 1$ and $q = 3$). Finally, after some rearranging [25], the particle size and relative refrac-

tive index can be determined simultaneously, from the first-order term of the POA with the following expressions:

$$a_{pq} = \frac{\alpha_p^2 + \alpha_q^2 - 2^* \cos(\theta_q - \theta_p)\alpha_p\alpha_q}{\sin^2(\theta_q - \theta_p)} \times \frac{\lambda}{\sqrt{1 - \cos\left[\frac{\theta_p}{2} - \frac{1}{2}\arctan\left(\sin(\theta_q - \theta_p)\frac{\alpha_p}{\alpha_q - \alpha_p\cos(\theta_q - \theta_p)}\right)\right]^2}} \quad (9)$$

$$m_{pq} = \frac{1}{\sin\left[\frac{1}{2}(\pi - \theta_p) - \frac{1}{2}\arctan\left(\frac{\sin(\theta_q - \theta_p)}{\cos(\theta_q - \theta_p) - \frac{\alpha_q}{\alpha_p}}\right)\right]}. \quad (10)$$

3 Lorenz-Mie Theory Predictions and Comparison with the Diffraction Model

3.1 Lorenz-Mie Theory Predictions

Figure 4 presents the scattering pattern in the critical angle region that is predicted by the Lorenz-Mie Theory, for a spherical particle with $m_r = 0.751$ (which may correspond to an air bubble ($m = 1$) in water ($m' = 1.332$)), versus its diameter. Note that throughout the numerical study the wavelength is set to $\lambda = 0.6328\,\mu m$ and the electric vector to be parallel to the scattering plane (parallel polarization), the contrast of the critical scattering pattern being maximum for this polarization. When the particle size increases, the position of the different maximum tends asymptotically to a limit angle (which is significantly different from the critical angle predicted by geometrical optics, θ_c). The asymptotic evolution is close to that predicted by Eq. (7): $(\theta_c - \theta) \propto 1/\sqrt{a}$ (see Figure 8). When the particle size decreases, apart from the scattering pattern decreasing in intensity, we can see that the fringe widths increase drastically. The critical scattering pattern is also shifted further and further away from θ_c in the forward direction. From a metrological point of view, we may conclude from this evolution that the investigation of two-phase flows with large particles size distributions (particularly for small particles with diameter $D < 100\,\mu m$) requires the observation of a large angular domain (at least 30° for particles between 50 and 200 μm), which may introduce difficulties in determining accurately the position of the fringes on such a wide angular range.

Lorenz-Mie calculations are used in Figures 5 and 6 to illustrate the strong dependence of the angular position of the first diffraction bright fringes on the relative particle refractive index m_r. In Figure 5, the particle diameter and refractive index are fixed at $D = 100\,\mu m$ and $m = 1$. The refractive index of the surrounding medium m' evolves slightly from 1.335 to 1.3157 ($m_r = 0.751$–0.760). For this refractive index range, the effect of the decreasing relative refractive index on the critical scattering pattern is an almost linear shift of the whole pattern in the forward direction. For this particle size and relative refractive index range the sensitivity of the position of the first critical fringe is about 75° for $\Delta m = 1$, whereas for the rainbow angle the corresponding sensitivity is 140° for an equivalent particle, i.e. water droplet in air).

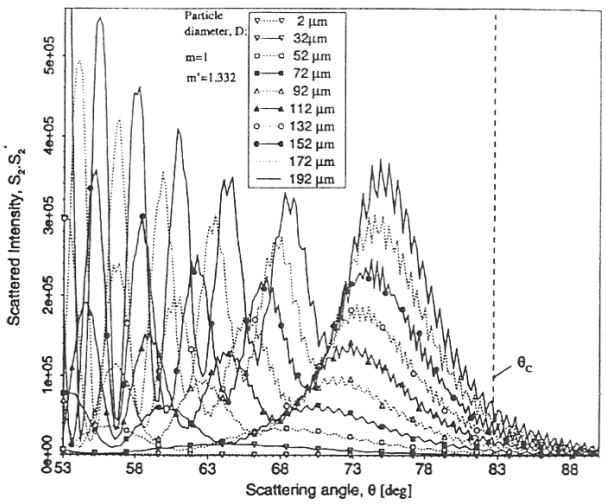

Fig. 4: Lorenz-Mie theory for the evolution of the critical scattering pattern versus the particle diameter, $m_r = 0.751$.

In Figure 6 the particle diameter is also fixed at $D = 100\,\mu m$. The relative refractive index m_r evolves in a large range, from 0.67 to 0.979. Figures 6(a) and (b) correspond, for instance, to an air bubble in water or in oil ($m' = 1.5$), Figure 6(c) corresponds to a water droplet in oil and Figure 6(d) and (e) correspond to a glycerine ($m' = 1.41$) droplet in oil and in a fuel ($m' = 1.44$), respectively. As already mentioned regarding Figure 5, the critical scattering pattern is extremely sensitive to the particle relative index. For the considered refractive index range, θ_1 evolves from $\approx 87.4°$ to $\approx 4.02°$. This evolution is strongly nonlinear for $m_r \geq 0.75$. The sensitivity of the critical angle to the particle size and relative index is maximum when $m_r \to 1$ (see Figure 10). The intensities of the first fringes also increase drastically as the relative refractive index increases (the intensity scale in Figure 6(e) has been increased by a factor of 100 compared with other cases). The shape of the critical scattering pattern is also greatly modified as $m_r \to 1$. In case Figure 6(e), for which the relative refractive index is close to unity, the critical scattering pattern and the diffraction lobe merge.

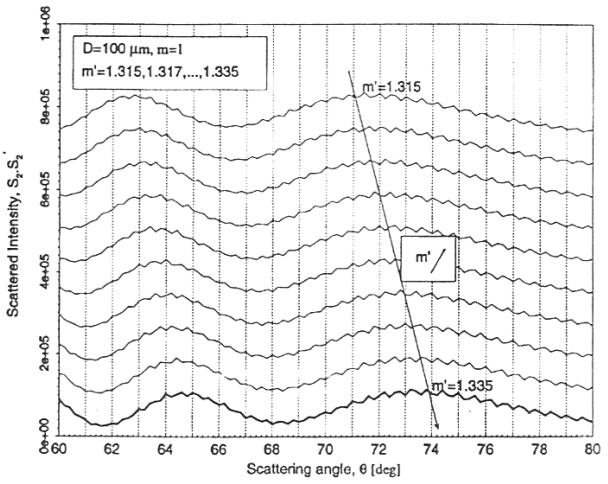

Fig. 5: Lorenz-Mie theory for the evolution of the critical scattering pattern versus a small variation of the relative particle refractive index, $D = 100\,\mu m$.

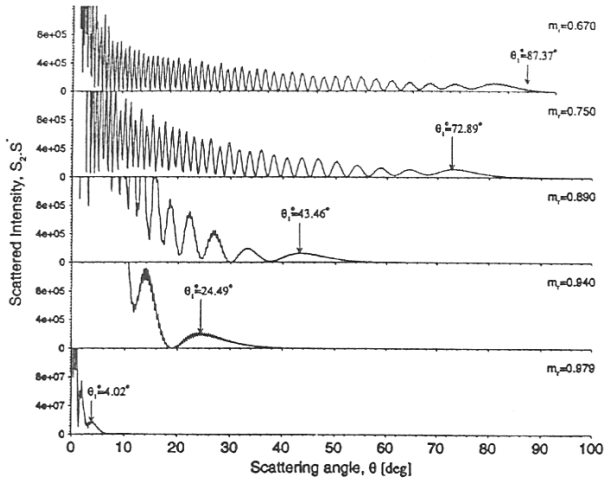

Fig. 6: Lorenz-Mie theory for the evolution of the critical scattering pattern versus a large variation of the relative particle refractive index, $D = 100\,\mu m$. Cases (a) and (b) correspond to an air ($m = 1$) bubble in oil ($m' = 1.5$) and in water ($m' = 1.332$), cases (c) and (d) to a glycerine ($m = 1.41$ droplet in oil and water and case (e) to a glycerine droplet in a liquid fuel ($m = 1.44$).

It may be thought from Figure 1 that the critical scattering pattern has a periodic component. The existence of a periodicity would be an interesting feature, from an experimental point of view, as it would facilitate the critical angle signal detection and filtering (to remove the fine structure). However, this is not the case. Figure 7 presents the amplitude of the Fourier transform of the critical scattering pattern obtained in Figure 1, for $\theta = 20 - 100°$. The spectrum exhibits weak peaks (related to high-order fringes) with their related harmonics. The angular frequency of the first fringe is lost in the contribution of the signal continuous component. The contribution to the spectrum of the fine structure is also not clear. The lower visibility of the diffraction fringes and the disappearance of the fine structure for high-order fringes ($j \geq 5$) probably explain why the spectrum does not exhibits clear peaks such as those observed in the rainbow scattering pattern [3].

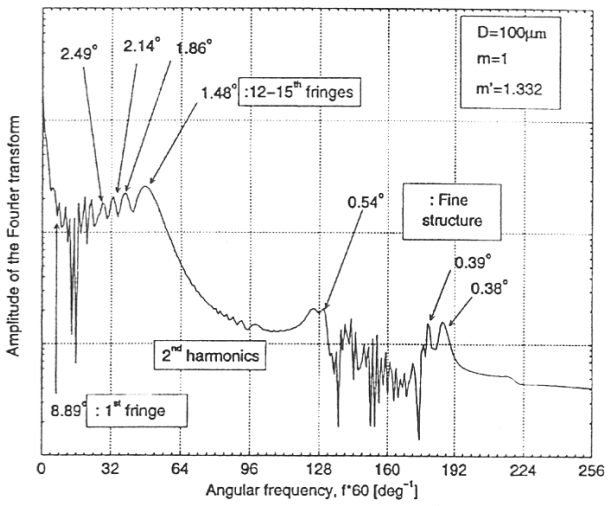

Fig. 7: Angular frequency spectrum of the critical scattering signal of Figure 1.

3.2 Comparisons Between LMT and POA Predictions

In order to compare predictions from Eq. (7) and LMT for the coarse structure dependence on the particle size, the evolution of the angular position of the first fringe was calculated, for both approaches, versus the particle diameter and with the relative refractive index as a parameter. A low-pass filtering procedure was applied to LMT predictions to remove the fine structure. For a better comparison, owing to the large range of variation of θ_1, Figure 8 presents the evolution of $(\theta_1 - \delta\theta_1)$ rather than θ_1, where $\delta\theta_1$ corresponds to the particular angular shift introduced for each relative refractive index. Qualitative agreement is found between the diffraction model and LMT predictions. Careful examination of this figure shows nevertheless that POA underestimates θ_1 for particles with diameter $D \geq 100\,\mu m$. For particles with diameter $D < 100\,\mu m$, three typical cases can be distinguished according to the considered relative refractive index range:

(i) $0.751 \geq m_r \geq 0.667$ (this relative refractive index range corresponds typically to gas bubbles in liquids (i.e. $m_r(air/water) = 1/1.332$, $m_r(air/oil) = 1/1.5$: POA predictions are significantly improved when the particle diameter decreases. This may be attributed to a better validation, as the particle radius curvature decreases, of the basic edge reflectivity assumption made in the diffraction model (note that for the rainbow angle the validity of Airy's theory decreases with decreasing particle size [4]). From Fresnel's coefficients it can be easily shown that a decreasing relative refractive index increases the contribution of reflected light ($p = 0$) to the total particle scattering compared with the contribution from other scattering processes ($p < 1$) which improved, for this refractive index range, our choice to consider only the first-order term of the POA.

(ii) $0.945 > m_r \geq 0.888$ (this relative refractive index range corresponds typically to liquid or solid particles in liquids, i.e. $m_r(glycerine/oil) = 1.41/1.5$, $m_r(water/oil) = 1.332/1.5$): the discrepancy between the two approaches decreases more slowly with decreasing particle diameter. The increasing contribution to the total scattering of refracted and internally reflected rays is assumed to be responsible for this effect.

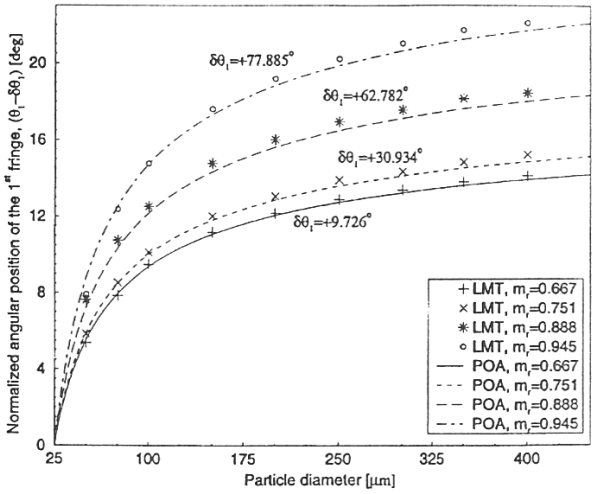

Fig. 8: Lorenz-Mie theory and physical optics approximation predictions for the first diffraction fringe maximum location versus the particle diameter. The particle refractive index is fixed ($m = 1$) and the liquid flow refractive index (m') acts as a parameter.

(iii) $1 \geq m_r \geq 0.945$ (this relative refractive index range corresponds typically to liquid or solid particles in liquids with close relative refractive indexes (i.e. m_r(*fuel/oil*): 1.44/1.5): the discrepancy is significant and POA overestimates the angular position of the first fringes. This discrepancy may be attributed to the so-called "anomalous diffraction" (see *Van de Hulst* [23]) which occurs for particles with relative index close to unity ($m_r \rightarrow 1$). In this case it is known that the interference between the diffracted light and the reflected/transmitted light becomes a dominant phenomenon (see Figure 6).

Figure 9 compares predictions from Eq. (7) and LMT for the evolution of the position of the first two bright fringes, θ_1 and θ_3, and the angular spacing, $\Delta\theta_{31} = \theta_3 - \theta_1$, versus the refractive index of the surrounding medium m' with $m = 1$. We calculated 21 and 200 data points for the POA and LMT curves, respectively. The particle diameter is fixed at 75 and 150 µm. The small oscillations observed with LMT come from the fine structure of the critical scattering pattern (see Figure 1) which was not totally, and then successfully, removed by the filtering procedure. For the considered refractive index range, the position of the first two fringes increases almost linearly with decreasing relative particle refractive index. POA and LMT give almost the same slope for all the corresponding cases so that we can conclude that the diffraction model gives a correct estimation for the evolution of θ_1 and θ_3 with the relative refractive index. Nevertheless, an angular shift of about 1° is observed between POA and LMT predictions and for both particle sizes. This discrepancy is also evident from the evolution of the angular spacing, $\Delta\theta_{31}$.

Figure 10 compares both predictions for an extremely large range of variation of m_r and for five particle sizes. Region (A) corresponds to gas bubbles in common liquids. In this case, as already mentioned with regard to Figure 9, the angular position of the first diffraction fringe evolves almost "linearly" with m_r. POA predictions are slightly shifted from those of LMT. Region (B) corresponds to liquid or solid particles in liquids (or solids). In this case, the discrepancy between POA and LMT predictions increases significantly as $m_r \rightarrow 1$ when, at the same time, the critical angle sensitivity to the relative refractive index increases.

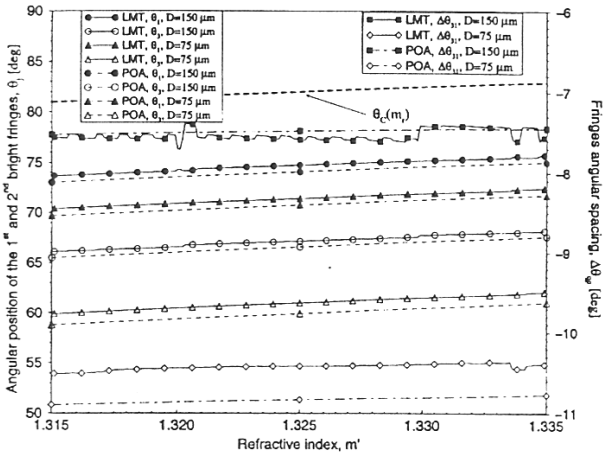

Fig. 9: Comparison of the Lorenz-Mie theory and the physical optics approximation for the location of the first two diffraction fringe maximum and the corresponding angular spacing versus the inverse of the refractive index (m'/m). This figure has been partly deduced from Figure 5.

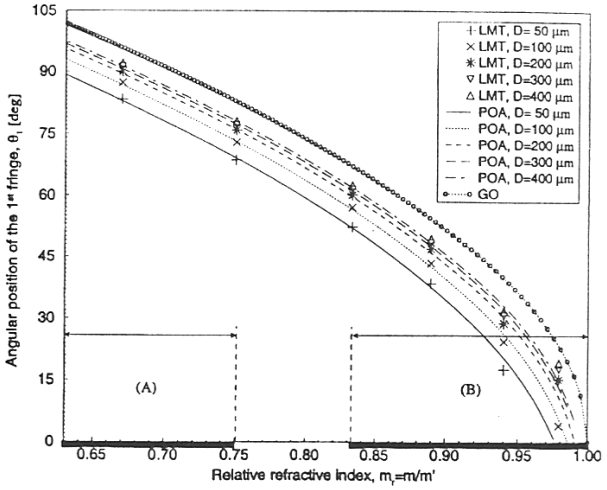

Fig. 10: Comparison of the Lorenz-Mie theory and the physical optics approximation for the location of the first diffraction fringe maximum versus a large variation of the particle relative refractive index (m/m'). Five particle diameters are considered. This figure has been partly deduced from Figure 6.

3.3 Discussion

The CAR sensitivity to the relative particle refractive index is of the same order as (slightly inferior to) that obtain with the rainbow technique, whereas for the particle size its sensitivity is higher (but nevertheless comparable). It is thought that this technique could be useful for various applications in liquid multiphase flows where the particle size and material are to be characterized. This technique could be an alternative to or be used in combination with existing techniques such as those based on phase Doppler anemometry [8–12], which are known to provide reliable size and velocity measurements but a weak resolution in refractive index measurements. One major difference with PDA for size measurement is in the nonlinearity of the function $\theta = f(D)$ (Figure 8), which may induce an increasing measurement error with increasing particle size, if the absolute uncertainty in the angle measurement is assumed to be constant. This could be considered as a limiting point compared with PDA, which uses a linear phase-diameter relationship. However, this also means that the CAR is more adapted to size fluctuation measurements and thus for applications where an extreme precision on size measurement is required.

From the numerical simulations we may conclude that if the first-order term of the POA ($p = 0$) accounts well for the roles of parameters such as a, m_r and λ in the coarse structure of the critical scattering pattern, it may not be with sufficient precision for applications requiring extreme accuracy on particles size and refractive index determination. From a practical point of view and to improve this model, two solutions may be adopted:

(i) To take into account contributions from refracted rays through the particles ($p = 1$) and those which have experienced one internal reflection ($p = 2$). Nevertheless, this approach would lead to complex expressions without analytical solutions [25] and decreases the interest of the POA compared with the use of direct LMT or complex angular momentum theory (CAM) [22] calculations, for an hypothetical enhancement of the predictions (physical effects such

as the Goos-Hänchen [26] effect will still not be taken into account).

(ii) To use LMT predictions to create a look-up table in order to correct the angular shift which is observed with the POA predictions, at least for the two first fringes. For a given refractive index range ($m_r \leq 0.751$), this could be done only versus the particle size as from Figures 9 and 10 it appears that the angular shift is very weakly dependent on the relative refractive index. In all cases, the procedure for the size and refractive estimation would be, for instance, (a) to use Eq. (8) to obtain a first estimation of the particle diameter by assuming a mean relative refractive index, (b) to look up in the table the correction introduced by LMT to the POA predictions for the corresponding size, (c) to use this new estimation of the particle diameter to estimate the particle refractive index from Eq. (10), (d) to iterate operations (b)–(d) to obtain the correct particle diameter and relative refractive index by using a convergence criterion. Note that a similar procedure has been used by *Corbin* et al. [27] for the rainbow technique.

4 Experimental Validation

4.1 Optical Set up and Procedure

Figure 11 illustrates the apparatus used to validate the principle of the proposed technique. Rising air bubbles were produced by injecting air into a porous medium immersed in a spectrophotometric cell (40 × 40 × 120 mm) filled with a liquid, i.e. demineralized water ($m' = 1.332$), ethanol ($m' = 1.364$) or a silicone oil ($m' = 1.458$). The incident light was produced by a 10 mW horizontally polarized helium-neon laser, $\lambda = 0.6328/m'$ μm. Before entering the cell the laser beam was collimated with two lenses. The beam waist diameter at the measurement point was approximately 410 μm. The laser beam polarization angle and its intensity were controlled with a half-wavelength plate and a variable neutral density filter. The scattering pattern was recorded with a Jai M30 video camera which allows 360 images per second in a 752 × 66 pixels format. The video signal was directed to a video board for digitization and for processing on a personal computer. The camera lens was focused at infinity. It had a focal length of 50 mm with $f/d = 1.6$ so that angle of view was limited in water, ethanol and the silicone oil to 28.6°, 27.67° and 22.73°, respectively. A macro lens was also used to measure the size (referred to here as the "photographic diameter") of the rising bubbles from their image obtained under backscattering illumination (white light source and a diffuser). The cell and the camera were placed on a rotating plate to which a precise goniometer was attached. This set-up was found very convenient to take into account, for each liquid, refraction effects at the viewing window. During the calibration procedure a mirror was immersed in the cell at the measurement point location. The laser beam deflection was measured with the goniometer and the camera in order to calibrate the camera angle view scale. To match the bubble positions with the optical probe volume, defined by the laser beam waist location and the camera lens object plane, the cell was moved with micro displacements to scan most of the photospectrometric cell volume. During the experiments the camera shutter was used to adjust the camera time exposure.

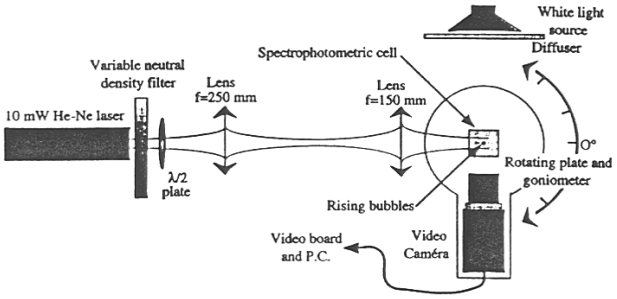

Fig. 11: Top view of the optical set-up used to validate the principle of the critical angle refractometry.

4.2 Preliminary Experimental Results

Figure 12 shows three typical images recorded near the critical angle of rising bubbles with different sizes and relative refractive indices: (a) air bubble in water, $D = 115$ μm, $m' = 1.332$; (b) air bubble in ethanol, $D = 130$ μm, $m' = 1.364$; (c) air bubble in silicone oil, $D = 88$ μm, $m' = 1.458$. These nominal refractive indices were measured, at ambient temperature, with a classical Abbé refractometer. The diameter reported here is the photographic diameter (it cannot be considered as an absolute reference owing to the difficulties in identifying bubble edges with the imaging system).

The previous images have been corrected (with a resampling algorithm) for refraction effects at the glass/air interface so that the scale given at the bottom of these figures indicates the true scattering angles. In all three cases the coarse structure is present (broad vertical light and darks bands) in addition to the superimposed fine-structure lines. Reflections on glass cell walls and on other bubbles are responsible for the background noise.

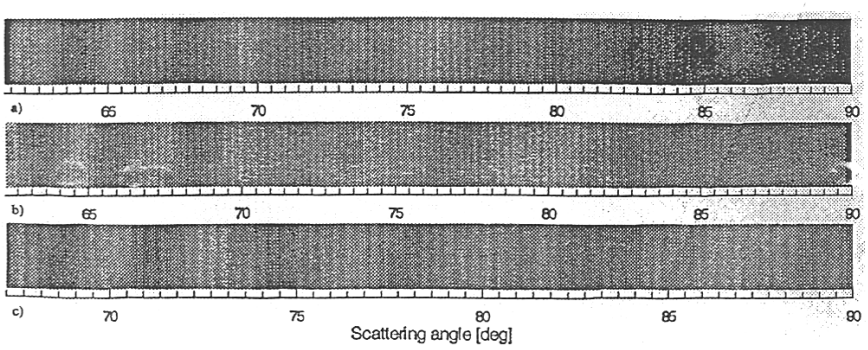

Fig. 12: Images of the scattering pattern observed in the critical angle region for a rising (*a*) air bubble in water, $D = 115$ μm, $m' = 1.332$, (*b*) air bubble in ethanol, $D = 130$ μm, $m' = 1.364$ and (*c*) air bubble in silicone oil, $D = 88$ μm, $m' = 1.458$. The angular scale indicates the true scattering angles.

Figures 13–15 show the intensity profiles corresponding to the images from Figure 12. They have been obtained by adding the video signal from all of the 66 camera lines. This procedure is commonly used to improve the signal-to-noise ratio. The average curves correspond to the evolution of the intensity profiles when a Fourier filter smoothing algorithm is applied (window width $\approx 2°$.

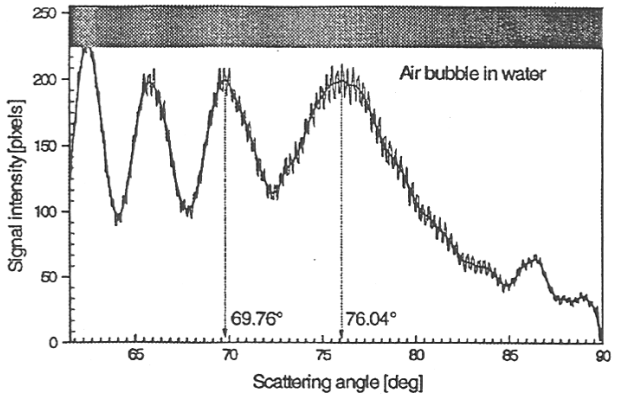

Fig. 13: Intensity profile of the scattering pattern corresponding to case (*a*) in Figure 12. The average curve corresponds to the intensity profile when a Fourier filter smoothing algorithm is used to remove the fine structure (window width $\approx 2°$).

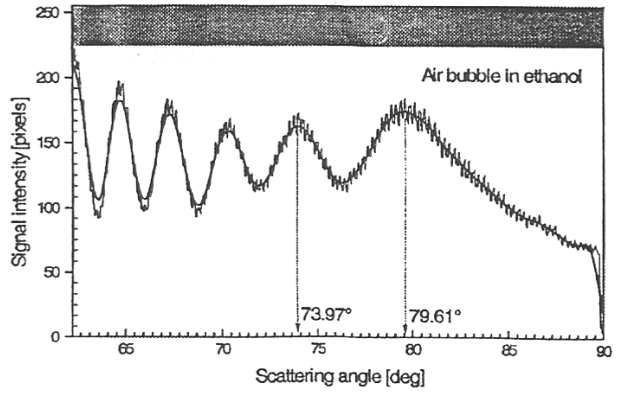

Fig. 14: As Figure 13 for case (b) in Figure 12.

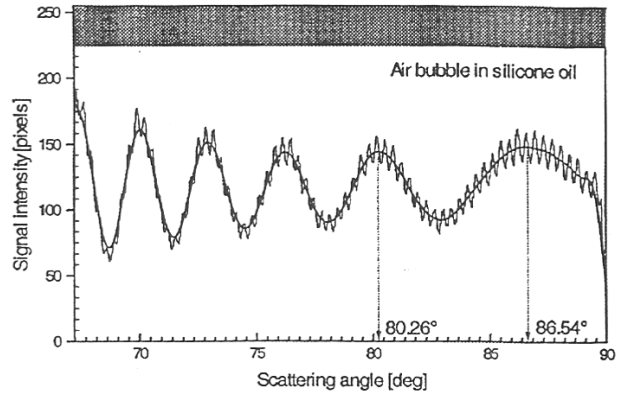

Fig. 15: As Figure 13 for case (c) in Figure 12.

Table 2: Summary of the experimental data and results obtained for the different bubbles.

	Water	Ethanol	Silicone oil
Photographic diameter (μm)	115	130	88
Nominal refractive index, m'	1.332	1.364	1.458
Position of the 1st bright diffraction fringe, $\phi_1(°)$	76.04	78.45	85.9
Position of the 2nd bright diffraction fringe, $\phi_3(°)$	69.76	71.85	78.35
Diameter with Eq. (8), ϕ_1 and m' (μm)	105.9	122.5	90.5
Diameter with Eq. (8), ϕ_3 and m' (μm)	105.2	123.8	92.7
Diameter with Eq. (9), ϕ_1 and ϕ_3 (μm) only	104.5	125.2	95.0
Refractive index m' with Eq. (10), ϕ_1 and ϕ_3 only	1.3324	1.3633	1.4558

Finally, from the filtered intensity profiles the position of the first two bright diffraction fringes (ϕ_1 and ϕ_3) can be measured. Table 2 gives the values obtained for the bubble diameter and relative refractive index when Eqs (8), (9) and (10) are used with the measured values for ϕ_3 and ϕ_1. Good agreement is found between the photographic diameter and those deduced from the critical scattering pattern analysis and the POA. The deviation between the different values is less than 10, 5 and 8% for the water, ethanol and silicone oil bubbles, respectively. For refractive index measurements the deviation from the Abbé refractometer measurements is less than 0.03, 0.05 and 0.2%, respectively, which is already sufficient for most applications requiring particle material recognition. Results obtained with LMT are not reported here and will be the subject of a future publication.

5 Conclusion

The principle of an optical technique for determining the size and relative refractive index of spherical particles in flows (with particle relative refractive index below unity), by observing their scattering pattern around the critical angle, was investigated. It is thought that this technique, referenced here as critical angle refractometry, could be useful for the characterization of the size and material of spherical particles in flow size and material, and more particularly in applications requiring high precision in the determination of these parameters.

6 Acknowledgments

The author is grateful to the French National Center for Scientific Research (CNRS) and the Bulgarian Academy of Sciences for providing partial financial support for this work.

7 Symbols and Abbreviations

CAR	Critical angle refractometry
$C(x)$, $S(x)$	Fresnel's integrals
D	particle diameter
$H(\alpha)$	function describing the diffraction angular pattern versus the dimensionless parameter α
GO	geometrical optics

LMT	Lorenz-Mie theory
POA	Physical optics approximation
$S_2.S_2^*$	scattered light intensity for parallel polarization
a	particle radius
i	complex number
j, p, q	index of the jth, pth, qth diffraction fringes observed in the critical scattering pattern
m	refractive index of the particle material for the laser wavelength
m'	refractive index of the surrounding medium for the laser wavelength
m_r	particle refractive index relative, $m_r = m/m'$
α_j	solutions of function $H(\alpha)$
λ	laser wavelength in air
θ	scattering angle
θ_c	critical angle position predicted geometrical optics
θ_r	rainbow angle position predicted by geometrical optics
θ_j	angular position of the jth diffraction fringe

8 References

[1] *N. Roth, K. Anders, A. Frohn:* Simultaneous measurement of temperature and size of droplets in the micrometer range. Proc. 7th Int. Congress on Optical Methods in Flow and Particle Diagnosis, ICALEO 88, LIA, Sunnyvale, CA, Vol. 67, 1988, pp. 294–304.

[2] *P. Massoli, F. Berena, A. D'Alessio, M. Lazzaro:* Temperature and size measurement of single transparent droplets by light scattering in the forward and rainbow regions. Appl. Opt. *32* (1993) 3295–3301.

[3] *J. P. A. J. Van Beeck., M. L. Riethmuller:* Non intrusive measurements of temperature and size of single falling raindrops. Appl. Opt. *34* (1995) 1633–1639.

[4] *J. P. A. J. Van Beeck:* Rainbow phenomena: on development of a laser-based, non intrusive technique for measuring droplet size, temperature and velocity. PhD Thesis, Technical University of Eindhoven (Netherlands). 1997.

[5] *S. V. Sankar, K M. Ibrahim, D. H. Buermann, M. J. Fidrich, U. D. Bachalo:* An integrated phase Doppler/rainbow refractometer system for simultaneous measurement of droplet size, velocity, and refractive index. Proc. 3rd Int. Congress on Optical Particle Sizing, Yokohama (Japan), 1993, pp. 275–284.

[6] *M. Schneider, F. D. Hirleman, H. Saleheen, D. Q. Chowdhury, S. C. Hill:* Rainbow and radially-inhomogeneous. Proc. 3rd Int. Congress on Optical Particle Sizing, Yokohama (Japan), 1993, pp. 323–326.

[7] *X. Han, K. F. Ren, Z. Wu, F. Corbin, G. Gouesbet, G. Gréthan:* Characterization of initial disturbances in liquid jet by rainbow sizing. Appl. Opt., to be published 1998.

[8] *A. Naqwi, F. Durst, X. Liu:* Extended phase-Doppler system for characterization of multiphase-flows. Part. Part. Syst. Charact. *8* (1991) 16–22.

[9] *G. Brenn, J. Domnick, F. Durst, C. Tropea, T-H. Xu:* Investigation of polydisperse spray interaction using an extended phase Doppler anemometer. Proc. 7th Int. Symp. On Applications of Laser Technique to Fluid Mechanics, 1994, Lisbon (Portugal), paper 21.

[10] *F. Onofri:* Prise en compte de la dimension finie des faisceaux d'éclairage en granulométrie optique: anémométrie phase Doppler-diagnostic des millieux diphasiques. PhD Thesis, University of Rouen (France), 1995.

[11] *F. Onofri, G. Gréhan, G. Gouesbet, T-H. Xu, C. Brenn, C. Tropea:* Phase-Doppler anemometry with dual burst technique for particle refractive index measurements. Proc. 7th Int. Symp. on Applications of Laser Techniques to Fluid Mechanics, Lisbon (Portugal), 1994, paper 21.4.

[12] *F. Onofri, T. Girasole, G. Gréhan, G. Gouesbet, G. Brenin, J. Dominick, C. Tropea, T-H. Xu:* Phase-Doppler anemometry with dual burst technique for measurement of refractive index and absorption coefficient simultaneously with size and velocity. Part. Part. Syst. Charact. *13* (1996), 212–224.

[13] *F. Onofri, L. Bergounoux, J-L. Firpo, J. Misguish-Ripault:* Velocity, size and concentration measurements of optically inhomogeneous cylindrical and spherical particles. Proc 9th Int. Symp. on Applications of Laser Techniques to Fluid Mechanics, Lisbon (Portugal), 1998, paper 9.2.

[14] *F. Onofri, D. Blondel, G. Gréhan, G. Gouesbet:* On the optical diagnosis and sizing of coated and multi-layered particles with phase Doppler anemometry. Part. Part. Syst. Charact. *13* (1996) 104–111.

[15] *P. Massoli, F. Berreta, A D'Allessio:* Single droplet size, velocity, and optical characteristics by the polarization properties of the scattered light. Appl. Opt. *28* (1990) 1200–1208.

[16] *P. L. Marston:* Critical scattering angle by a bubble: physical optics approximation and observations. J. Opt. Soc. Am., *69* (1979), 1205–1211.

[17] *P. L. Marston, D. L. Kingsbury:* Scattering by a bubble in water near the critical angle: interference effects. J. Opt. Soc. Am. *71* (1981), 358–361.

[18] *D. S. Langley, P. L. Marston:* Critical scattering of laser light from bubbles in water: measurements, models, and application to sizing bubbles. Appl. Opt. *23* (1984) ??? pages.

[19] *G. E. Davis:* Scattering of light by an air bubble in water. J. Opt. Soc. Am., *45* (1955) 572–581.

[20] *N. Fiedler-Ferrari:* Espalhamento de Mie na vizinhanca do angulo critico, PhD Thesis, University of São Paulo (Brazil), 1983.

[21] *N. Fiedler-Ferrari, H. M. Nussenzweig:* Mie scattering near the critical angle. Part Charact. *4* (1987) 147–150.

[22] *H. M. Nussenzweig:* Diffraction Effects in Semiclassical Scattering. Cambridge University Press, Cambridge, 1992.

[23] *H. C. Van de Hulst:* Light Scattering by Small Particles. Dover Publications Inc., New York 1957, Chapt. 11 and 12.

[24] *G. R. Fowles:* Introduction to modern Optics. Holt, New York 1975.

[25] *F. Onofri:* Personal communication, RAC 1097, UMR CNRS 6595-IUSTI, 1997.

[26] *H. K. V. Lötsch:* Beam displacement at total reflection: the Goos-Hänchen effect. Opt. *32* (1971).

[27] *F. Corbin, A. Caro, G. Gouesbet, G. Gréhan:* Réfractométrie d' arc-en-ciel: application au diagnostic des gouttes avec gradient d'indice. Proc. 5ème Cong. Francophone de Vélocimétrie Laser, Rouen (France), 1996, paper El.

Article A11

Numerical Analysis of the Nonlinear Instability of One-Dimensional Compound Capillary Jet

St. Radev[1], M. Kaschiev[2], M. Koleva[2], L. Tadrist[3], and F. Onofri[3]

[1] Institute of Mechanics, Bulgarian Academy of Sciences
Acad. G.Bonchev str. Bl.4, 1113 Sofia, Bulgaria
stradev@sradev1.imbm.bas.bg
[2] Institute of Mathematics and Informatics, Bulgarian Academy of Sciences
Acad. G.Bonchev str. Bl.8, 1113 Sofia, Bulgaria
{kaschievd,mkoleva}@math.bas.bg
[3] Institut Universitaire des Systemes Thermiqus Industriels
Universite de Provence, Technopole de Chateau Gombert
5, rue Enrico Fermi, 13453 Marseille Cedex 13, France
{ltadrist,onofri}@iusti.univ-mrs.fr

Abstract. The nonlinear instability of a compound jet consisting of a liquid core and immiscible coaxial liquid layer is studied. The equations of motion for both liquids (phases) are used in one-dimensional (1-D) approximation similar to that known for one-layer jet.A numerical method is proposed for calculation the radiuses of both interfaces and axial velocities of the core and outer layer. The method is tested for determining the typical forms of compound jet disintegration.

1 Introduction

The compound jet generation principles and a qualitative description of the hydrodynamic of the jet have been given by Hertz and Hermanrud [1]. In their experiments they observed three different types of compound jet instability, namely capillary, sinuous and varicose instability depending on the jet velocity. The present paper is restricted to the analysis of the capillary instability only. The latter manifests itself into disintegration of the jet into drops of different configurations and sizes.

The first models developed to study this kind of compound jet instability are based on the one–dimensional approximation of the Navier-Stokes equations. Based on this approximation in Radev and Shkadov [2] a linear analysis of the jet instability is performed which reveals three different break-up regimes, namely breaking as a single jet, breaking of the core and disintegration by meeting of the interfaces. (Further on for brevity these regimes will be referred as First, Second and Third break-up regimes, respectively). Similar analysis is proposed by Sanz and Meseguer [3].

As it could be expected the above linear models are well suited to the initial evolution of the perturbations along the jet but failed to predict the final break-up configuration, which is strongly controlled by the nonlinear effects. The latter

L. Vulkov, J. Waśniewski, and P. Yalamov (Eds.): NAA 2000, LNCS 1988, pp. 692–701, 2001.

are taken into account in Epikhin et al.[4] and Radev et al. [5] in which the jet flow is assumed of uniform velocity profile and approximated by one–dimensional equations of motion. The disturbances are considered periodical in space of a given wave length, whose amplitude increases in time. The analysis in Epikhin et al. [4] is made by a decomposition of the disturbances in a Fourier series with unknown amplitudes, while in Radev et al. [5] a spline-difference numerical method is proposed. The experimental observations that the jet break-up gives rise of both main and satellite drops are confirmed numerically as well. Moreover it is shown that the satellites for the First disintegration regime are formed from the core liquid only and are entrained by the layer flow. In the Second regime the compound satellite drops appear consisting of a core and concentric layer formed from the jet core and surrounding layer respectively.

For completeness it should be mentioned that 2-D models of the compound jet instability are proposed in Tchavdarov and Radev[6] and Tchavdarov et al. [7]. In the former a linear analysis is performed while the latter is concerned with a direct numerical simulation.

The present paper deals with the nonlinear instability of a one-dimensional compound jet. A numerical method is proposed for calculating the evolution in time of both the interface radiuses and core and layer velocities. It allows accounting for a stepwise profile of the undisturbed velocity. The method is illustrated by the typical disintegration forms of the jet.

2 Statement of the Problem

The compound jet shown in Fig. 1 consists of an axisymmetrical liquid core of (undisturbed) radius H_1 and density ρ_1 and a surrounding coaxial layer of another immiscible liquid of outer radius H_2 and density ρ_2 . Both liquids are assumed incompressible and nonviscous. Hereafter the subscript $j = 1$ is set for the core, whereas $j = 2$ is used for the layer.

The jet flow is related to a cylindrical coordinate system (r, z), whose z – axis is directed along the jet axis. By using H_* and U_* as respectively linear and velocity scales the 1-D equations of motion of the jet could be written in the following nondimensional form (for more details see Radev and Shkadov (1985)[2])

$$\frac{\partial u_j}{\partial t} + u_j \frac{\partial u_j}{\partial z} = -\frac{\partial p_j}{\partial z} , \quad j = 1, 2, \tag{1}$$

where the axial velocities $u_j = u_j(t, z)$ and the pressures $p_j = p_j(t, z)$ are unknown functions of the time and axial coordinate.

Partial differential equations for the unknown radiuses $r = h_j(t, z)$ of the inner and outer interfaces are derived from the mass-conservation equation written simultaneously for the core and layer

$$\frac{\partial h_1}{\partial t} + u_1 \frac{\partial h_1}{\partial z} + \frac{1}{2} h_1 \frac{\partial u_1}{\partial z} = 0 , \tag{2}$$

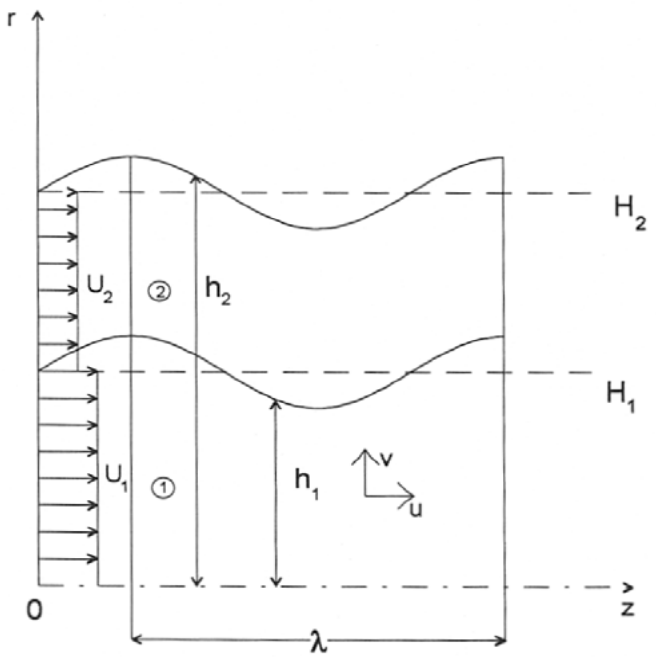

Fig. 1. Compound jet section of length λ related to a cylindrical coordinate system. The undisturbed core and jet are assumed of constant radiuses (H_1 and H_2 respectively) and of uniform axial velocities (U_1 and U_2), the latter allowing for a velocity jump (discontinuity) $\Delta U = U_1 - U_2 > 0$; λ stands for the wave length of the imposed disturbances

$$\frac{\partial h_2}{\partial t}+u_2\frac{\partial h_2}{\partial z}+\frac{1}{2}\left[1-\left(\frac{h_1}{h_2}\right)^2\right]h_2\frac{\partial u_2}{\partial z}+\frac{1}{2}\frac{h_1}{h_2}h_1\frac{\partial u_1}{\partial z}+(u_1-u_2)\frac{h_1}{h_2}\frac{\partial h_1}{\partial z}=0\,. \quad (3)$$

The pressure terms in eq. (1) are given in the form

$$p_j=\frac{\rho_2}{\rho_j}p_{j+1}+\sigma_j\kappa_j\,, \quad j=1,2, \quad (4)$$

where κ_j are the mean curvature of the interfaces

$$\kappa_j=\left[1+\left(\frac{\partial h_j}{\partial z}\right)^2\right]^{-1/2}\left\{\frac{1}{h_j}-\left[1+\left(\frac{\partial h_j}{\partial z}\right)^2\right]^{-1}\frac{\partial^2 h_j}{\partial z^2}\right\}\,, \quad (5)$$

while $\sigma_j = T_j/(\rho_j H_* U_*^2)$ denote the corresponding inverse Weber numbers related to the inner and outer surface tensions T_j.

In the absence of gravity it is convenient to seek spatially periodical solutions of the above system of partial differential equations, that is

$$\begin{aligned} &h_j(t,z+\lambda)=h_j(t,z), \qquad u_j(t,z+\lambda)=u_j(t,z),\\ &\frac{\partial h_j}{\partial z}(t,z+\lambda)=\frac{\partial h_j}{\partial z}(t,z), \quad \frac{\partial u_j}{\partial z}(t,z+\lambda)=\frac{\partial u_j}{\partial z}(t,z), \quad (6)\\ &\frac{\partial^2 h_j}{\partial z^2}(t,z+\lambda)=\frac{\partial^2 h_j}{\partial z^2}(t,z), \end{aligned}$$

where λ represents the wave length.

3 Linear Instability Analysis of a Compound Jet

In the context of the linear instability analysis the jet flow is decomposed into a steady and nonsteady (disturbed) part. In the steady case the system (1)-(5) allows a simple solution of the form

$$h_j(t,z)=H_j\,, \qquad u_j(t,z)=U_j\,, \quad (7)$$

representing a compound jet of constant radiuses and uniform axial velocities of the core and coaxial layer.

The perturbed flow is given in the form

$$h_j(t,z)=H_j+\tilde{h}_j(t,z), \quad u_j(t,z)=U_j+\tilde{u}_j(t,z), \quad p_j(t,z)=P_j+\tilde{p}_j(t,z) \quad (8)$$

assuming that the nonlinear terms in respect to the disturbances are small enough to be neglected. The solution of the linearized boundary value problem (1)-(8) appears in an analytical form

$$(\tilde{h}_j,\tilde{u}_j,\tilde{p}_j)(t,z)=(\bar{h}_j,\bar{u}_j,\bar{p}_j)\exp[i\alpha(z-ct)], \quad (9)$$

where $\alpha = 2\pi/\lambda$ is a given wave number while the complex amplitudes $\bar{h}_j, \bar{u}_j, \bar{p}_j$ and complex phase velocity of the perturbations

$$c=\frac{\omega}{\alpha}+i\frac{q}{\alpha} \quad (10)$$

are unknown. In equation (10) ω denotes the angular frequency, while $c_r = \omega/\alpha$ stands for the phase velocity and $\alpha c_i = q$ - for the growth rate of the disturbances. The complex phase velocity and the wave number are connected in the following (usually called dispersion) equation

$$\begin{aligned} &(U_1-c)^4-2(U_1-U_2)(U_1-c)^3+\\ &\left[(U_1-U_2)^2+\tfrac{1}{2}\sigma_2(1-\delta^2)(1-\alpha^2)+A_1\right](U_1-c)^2-\\ &2A_1(U_1-U_2)(U_1-c)+\\ &\left[A_1(U_1-U_2)^2+\tfrac{1}{4}\sigma_1\sigma_2\delta^{-1}(1-\delta^2)(1-\delta^2\alpha^2)(1-\alpha^2)\right]=0\,, \end{aligned} \quad (11)$$

where

$$A_1 = \frac{1}{2}\left[\sigma_1\delta^{-1}(1-\delta^2\alpha^2) + \sigma_2\delta^2\frac{\rho_2}{\rho_1}(1-\alpha^2)\right] . \qquad (12)$$

In principle the initial conditions for the system (1)-(5) should satisfy the equation (6), otherwise they could be chosen arbitrary. However from a physical point of view it will be of interest to have a possibility to study the evolution of initially small disturbances up to the break-up point. Following the linear instability theory in Radev and Shkadov [2] the form of the jet perturbations of sufficiently small amplitudes is derived from the linearized equations (1)-(5). Below on we briefly present some details concerning the linear instability analysis of a compound jet, which will be used in the formulation of initial conditions for the equations (1)-(5) fitted to the linear solution. For our further considerations we will need some details concerning the solutions of the dispersion equation.

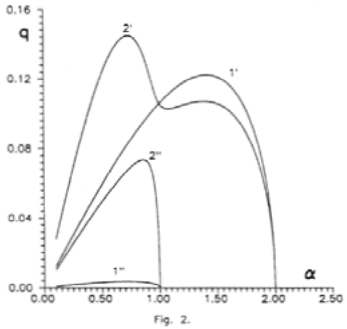

Fig. 2.

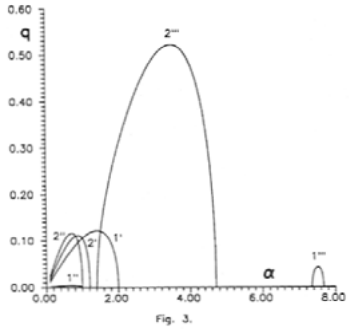

Fig. 3.

Fig. 2. Amplification rate of the disturbances versus wave number α at a zero undisturbed velocity jump. $\Delta U = 0, \sigma_1 = 0.015, \delta = 0.5, \rho_2/\rho_1 = 1$; Curves $1'$ and $1''$: $\sigma_1/\sigma_2 = 100$, $2'$ and $2''$: $\sigma_1/\sigma_2 = 0.1$. The superscript $'$ and $''$ above denote the first and second linear modes respectively. The maximum growth rate within the curve $1'$ is controlled by the inner surface tension. When the outer surface tension increases this maximum moves into the range of the long waves (curve $2'$)

Fig. 3. The effect of the undisturbed velocity jump on the growth rate. $\Delta U = 0.5, \sigma_1 = 0.015, \delta = 0.5, \rho_2/\rho_1 = 1$. Curves $1'$, $1''$ and $1'''$: $\sigma_1/\sigma_2 = 100$, $2'$, $2''$ and $2'''$: $\sigma_1/\sigma_2 = 0.1$. The superscripts $'$, $''$ and $'''$ above denote the first, second and third linear modes respectively. In the interval of the very short waves a third mode is burned (curve $1'''$). When the outer surface tension increases this mode moves into the range of the long waves with the highest growth rate inside it (curve $2'''$). Simultaneously the second mode (curve $2''$) tends to move above the first mode (curve $2'$) at the begining of long wave interval

This is an algebraic equation of fourth order for calculating the complex phase velocity c as a function of the wave number at given values of the nondimensional parameters $\sigma_j, U_j, \delta = H_1/H_2, \rho_0 = \rho_2/\rho_1$. After determining the complex phase velocity the unknown complex amplitudes $\bar{h}_j, \bar{u}_j$ could be found from the linearized equations (1)-(8) provided that the value of one of these amplitudes is given.

In the particular case when the undisturbed velocity profile is uniform in the both phases ($U_1 = U_2$) eq. (11) is reduced to a biquadratic equation. It is easily seen that in general this equation has two pairs of complex conjugate roots: the first one is defined within the wave number interval $0 < \alpha < \delta^{-1}$, while the second - in $0 < \alpha < 1$. The two branches (further on called modes) with positive imaginary parts c_i define two families of disturbances which grow with amplification rates equal to $q = \alpha c_i$ and propagate with one and the same phase velocity $c_r = U_1$. In Fig. 2 the "$q - \alpha$" curves for both modes are illustrated for two characteristic values of the ratio σ_2/σ_1 of the surface tensions. If as usually we assume that in natural conditions the jet is disintegrated by the disturbances of a higher amplification rate then in Fig. 2 they correspond to the maximum of "$q - \alpha$" curve related to the first mode. However in the case of $\sigma_2/\sigma_1 >> 1$ this maximum (q_I^*) is attached to the wave number close to the Rayleigh one $\alpha^* \approx \sqrt{2}/2$ and is controlled by the outer surface tension. In the case $\sigma_2/\sigma_1 << 1$ the maximum (q_I^*) moves to the range of the shorter waves ($\alpha^{**} \approx \sqrt{2}/2\delta$) being controlled by the inner interface.

The "$q - \alpha$" curves in the case of a stepwise velocity profile are shown in Fig. 3 for a given value of the velocity jump $\Delta U = U_1 - U_2 > 0$. The main difference in respect to the case of a continuous velocity profile manifests itself in the appearance in the range of the short waves of a new unstable mode, resulting in a third family of growing disturbances. The maximum growth rate of the disturbances q_{III}^* and the corresponding wave number α^{***} depends on the value of the velocity jump ΔU: when the latter increases the maximum growth rate increases as well, while the wave number α^{***} moves into the direction of the longer waves. Looking at Fig. 3 it should be mentioned that at sufficiently high values of ΔU the maximum growth rate corresponding to the second mode (q_{II}^*) may become higher than to the first mode (q_I^*)).

Coming back to the nonlinear boundary-value problem (1)-(6), it is quit natural to apply equations (8) and (9) as initial conditions for this problem. It is important to note that in the conditions (8) and (9) one of the complex amplitudes say $\bar{h}_j$ must be considered as an additional input parameter of the nonlinear problem. It will be denoted by $\bar{h}_{j0}$ to point out that this is the initial amplitude of the corresponding interface radius at time $t = 0$. As far as the complex phase velocity is explicitly involved in the linearized form of equations (1)-(5) (not written in the paper) the number of the selected mode will act as a second input parameter in the initial conditions (8) and (9).

4 Numerical Method

In order to eliminate the disturbance translation along the jet axis it is convenient to introduce new independent variables (ξ, τ) and new dependent variables (w_j, Π_j) as follows

$$\xi = \alpha z - \omega t, \quad \tau = \alpha\sqrt{\sigma_*}t, \quad 0 \le \xi \le 2\pi. \tag{13}$$

$$u_j = U_j + \sqrt{\sigma_*}w_j, \quad \Pi_j = \sigma_*^{-1}p_j. \tag{14}$$

In these expresstions $\omega = \alpha c_\tau$ and σ_* stands for σ_2 (or σ_1).

Following [8], for solving the nonlinear boundary value problem (1)-(6), written in new variables, we use the Continuous Analog of Newton Method (CANM). A finite difference method of second order for discretization the obtained CANM problem is applied. All results, shown in figures, are obtained using the Crank-Nikolson difference scheme with steps $h_\xi = \pi/200, h_\tau = 0.01$. The CAMN needs 2-3 iterations to solve the problem in each layer $\tau_k = kh_\tau$.

The jet disintegration time τ_b is determined when one of the following conditions is satisfied

$$\min_\xi h_1(\tau_b, \xi) \le 10^{-2}, \quad or \quad \min_\xi (h_2(\tau_b, \xi) - h_1(\tau_b, \xi)) \le 10^{-2}.$$

5 Results and Discussion

Due to the fact that the above described problem appears as multiparametric one, it is rather difficult to illustrate the effect of all entering parameters. For that we will limit our discussion to the case of zero velocity jump ΔU. In these conditions the jet instability is mainly controlled by the ratio σ_1/σ_2 of the surface tensions, whose effect will be analysied below. The values of the remaining nondimensional parameters will be fixed as follows:

$$\sigma_1 = 0.015, \delta = 0.5, \rho_2/\rho_1 = 1, h_{20} = 0.01. \tag{15}$$

Moreover we will concentrate our attention to the cases when the jet is initially excited by the perturbations (8) and (9) related to the first mode of the dispersion equation. In general the calculations will be performed for the wave number of the highest amplification rate. The effect of the second and third mode remains to be studied additionally.

5.1 Compound Jet Disintegration at $\sigma_1/\sigma_2 \ll 1$

In this case the jet instability is controlled by the outer surface tension. The jet disintegration behaves like one-layer jet break-up, as shown in Fig.4, whose parameters correspond to the curve $2'$ in Fig.2. The resulting main and satellite drops are compound as well and consist of a core and concentric layer formed by the inner and outer liquid respectively.

5.2 Compound Jet Disintegration at $\sigma_1/\sigma_2 \gg 1$

When the inner surface tension prevaluates the jet instability appears as a core disintegration resulting into main and satellite drop, which after breaking are entrained by the surrounding liquid. This disintegration regime of the compound jet is demonstrated in Fig.5, whose parameters correspond to curve $1'$ in Fig.2. It should be mentioned that after the core break-up the jet still remains continuous up to the breaking of the outer interface. However this break-up regime is out of the scope of our model.

5.3 Compound Jet Disintegration at $\rho_2 < \rho_1$

A new type of jet disintegration appears if in the range $\sigma_1/\sigma_2 \ll 1$ the density of the outer liquid is decreased below the density of the core. As shown in Fig.6 the minimum distance between the interfaces becomes zero, while the inner interface is still far from the jet axis. This form of a jet disintegration is admissible in the numerical experiments only if $\rho_2 < \rho_1$. However in contrast to the disintegration regimes shown in Fig.4 and Fig.5, this in Fig.6 remains to be demonstrated experimentally.

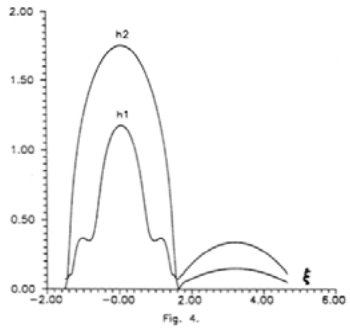

Fig. 4.

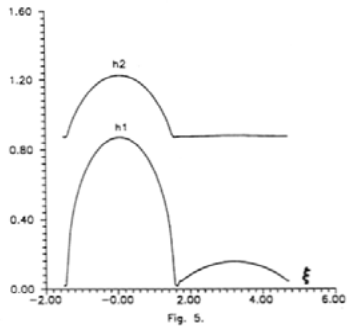

Fig. 5.

Fig. 4. Compound jet break-up as one-layer jet. $\sigma_1/\sigma_2 = 0.1, \alpha = 0.707, \Delta U = 0, \tau_b = 8.24$. The remaining input parameters are given in (15). The jet is amplified by the corresponding first mode (curve $2'$ in Fig.2). Both interfaces break-up simultaneously at the same points forming one main and one satellite compound drop within one wave length

Fig. 5. Compound jet disintegration due to the core break-up. $\sigma_1/\sigma_2 = 100, \alpha = 1.41, \Delta U = 0, \tau_b = 0.41$. The remaining input parameters are given in (15). The jet is amplified by the corresponding first mode (curve $1'$ in Fig.2). The core breaks-up the first while the layer still exists as a coherent portion. The main and satellite drops detached from the core are entrained by outer flow

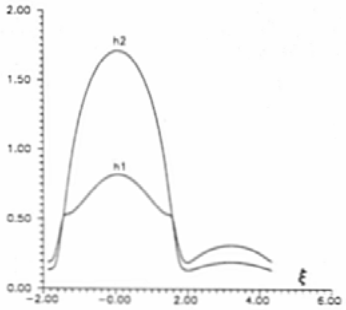

Fig. 6. Compound jet disintegration due to the meeting of the interfaces. $\sigma_1/\sigma_2 = 0.1, \alpha = 0.73, \tau_b = 9.06, \rho_2/\rho_1 = 0.5$ The values of σ_1, δ and h_{20} are given in (15). The jet is amplified by the corresponding first mode. The outer interface approaches the inner one faster than the latter reaches the jet axis

6 Conclusion

The nonlinear instability of a compound jet is studied as a solution of initially small disturbances up to the jet desintegration. It is shown that the nonlinear effects significantly affect the final stages of the jet desintegration. The type of the latter as well as the type of satellite formation is mainly controlled by the ratio of the inner and outer surface tensions. The numerical method developed on the basis of one-dimensional equations of motion accounts for discontinuity (jump) of the velocity in both phases. However the effect of the velocity jump on the jet instability remains to be studied separately.

References

1. Hertz, C. H., Hermanrud, B.: A liquid compound jet, J. Fluid Mech., **131** (1983) 271–287
2. Radev, S. P., Shkadov, V.Ya.: On the stability of two–layer capillary jets, Theor. and Appl. Mech., Bulg. Acad. Sci., **3** (1985) 68–75 (in russian)
3. Sanz, A., Meseguer, J.: One-dimensional linear analysis of the compound jet, J. Fluid Mech., **159** (1985) 55–68
4. Epikhin, V. E., Radev, S. P., Shkadov, V.Ya.: Instability and break–up of two-layer capillary jets, Izv. AN SSSR, Mech. Jidkosti I Gaza, **3** (1987) 29–35 (in russian)
5. Radev, S. P., Boyadjiev, T. L., Puzynin, I. V.: Numerical study of the nonlinear instability of a two–layer capillary jet, JINR Communications P5-86-699, Dubna, 1986 (in russian)
6. Radev, S., Tchavdarov, B.,: Linear capillary instability of compound jets, Int. J. Multiphase Flow, **14** (1988) 67–79

7. Tchavdarov, B., Radev, S., Minev, P.: Numerical analysis of compoud jet disintegration, Comput. Methods Appl. Mech. Engrg., **118** (1994) 121–132
8. St. Radev, M. Koleva, M. Kaschiev, L. Tadrist, Initial Perturbation Effects on the Instability of a Viscous Capillary Jet, Recent Advances in Numerical Methods and Applications, Proc. of 4th Int. Conf. Num. Meth. Appl., 1998, Sofia, Bulgaria, (ed. O. Iliev, M. Kaschiev, S. Margenov, Bl. Sendov, P. Vassilevski), pp.774-882, World Scientific Publ.

Article A12

Superimposed noninterfering probes to extend the capabilities of phase Doppler anemometry

Fabrice Onofri, Anne Lenoble, and Stefan Radev

We propose using multiple superimposed noninterfering probes (SNIPs) of the same wavelength but different beam angles to extend the capabilities of phase Doppler anemometry. When a particle is moving in a SNIP the Doppler signals that are produced exhibit multiple Doppler frequencies and phase shifts. The resolution of the measurements of particle size (i.e., by fringe spacing and Doppler frequency) increases with beam angle. Then, with the solution proposed, even with only two detectors several measurements of size can be obtained for the same particle with increasing resolution if we consider higher frequencies in the signal. Several optical solutions to produce SNIPs as well as a signal-processing algorithm to treat the multiple-frequency Doppler signals are proposed. Experimental validations of the sizing of spherical and cylindrical particles demonstrate the applicability of this technique for particle measurement. We believe that this new technique can be of great interest when high resolution of size, velocity, and even refractive index is required.

OCIS codes: 120.3180, 280.3340, 290.5850, 030.1640, 120.0120, 280.2490.

1. Introduction

Phase Doppler anemometry[1–4] (PDA) is now a well-established interferometric technique for measurement of particle size and velocity in two-phase flows. Two types of model are used to explain the working principle of this technique. The first model, usually referred to as the scattered fields addition model, is a rigorous approach based on exact calculation of the interference field produced on the aperture of a photodetector by the net field scattered by a particle located at the crossing of two laser beams. The particle-scattering properties as well as the optical parameters of the PDA geometry are taken into account through intensive calculations that use either geometrical optics or the Lorenz–Mie theory.[5,6]

The second model, called the heuristic fringe model, was introduced to explain the basis of laser Doppler anemometry (LDA); see Ref. 7 and 8. Afterward it was used to explain the principle of PDA, as this technique is an extension of LDA. In the heuristic fringe model it is considered that at the crossing of two incident coherent laser beams there exists a fringe pattern whose characteristics depend only on the properties (mainly wavelength and crossing angle) of the laser beams. The particle is assumed to be perfectly spherical and to act as a microspherical lens that projects the probe volume fringe pattern onto the aperture of the photodetector [Fig. 1(a)]. In the paraxial approximation the spherical particle's focal length is $f \approx mR/[2(m-1)]$ (we restrict our analysis to the refracted rays), where R, m, and λ are the radius and the relative refractive index of the particle and the laser wavelength, respectively. In the probe volume the fringe pattern is defined by fringe spacing $i_v = \lambda/[2\sin(\alpha)]$, where α is the beam's half-angle. For a projection plane located a distance L from the particle's focal point the projected fringe spacing is $i_p = i_v L/f$. For two identical point detectors D^1 and D^2 that are symmetrical to the Oz axis with elevation angles $\psi^1 = -\psi^2 = \psi$, the distance between the detectors is $l^{12} = L\tan(2\psi)$. When the particle crosses the probe volume fringes with a velocity component V_x along the Ox axis the signal output from the two detectors exhibits the same heterodyne Doppler frequency, namely, ν. LDA uses this feature to deduce from the measurement of this Doppler frequency[8] the particle velocity component $V_x = \nu i_v$. The Doppler signals emerging from the two detectors are phase shifted in relation to each other by the

F. Onofri (Fabrice.Onofri@polytech.univ-mrs.fr) and A. Lenoble are with the Institut Universitaire des Systèmes Thermiques Industriels, Unité Mixte de Recherche No. 6595, Centre National de la Recherche Scientifique, Université de Procence, Technopôle de Château-Gombert, 13453 Marseille cedex 18, France. S. Radev is with the Institute of Mechanics and Bio-Mechanics, Bulgarian Academy of Sciences, ul. "Acad. G. Bonchev" block 4, 1113 Sofia, Bulgaria.

Received 31 May 2001; revised manuscript received 29 January 2002.

0003-6935/02/183590-11$15.00/0

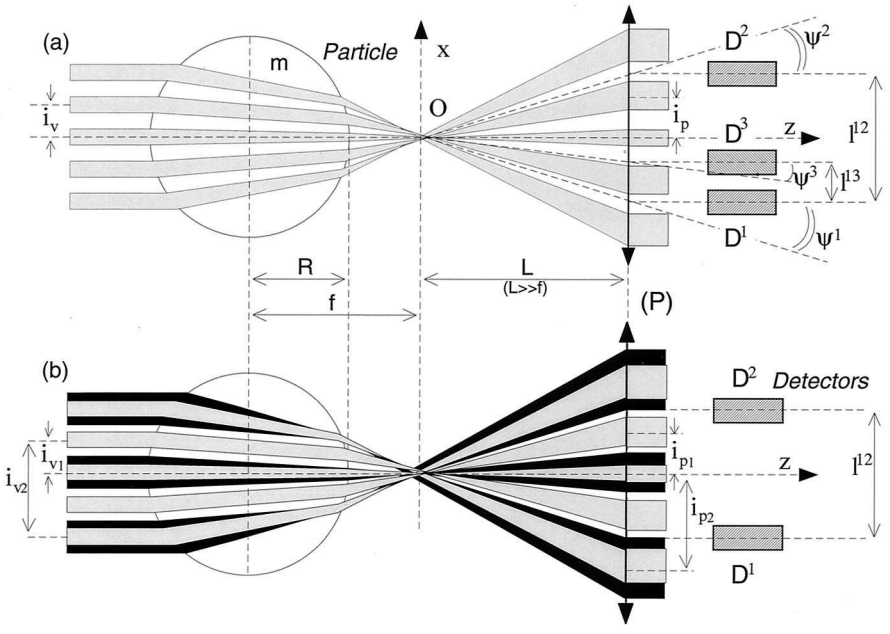

Fig. 1. Schematics of (a) PDA and (b) SNIP PDA techniques according to the heuristic fringe model.

quantity $\Delta\phi^{12} = 2\pi(l^{12}/i_p) = 2\pi\,(fl^{12}/i_vL)$. The measurement of this phase shift is used by PDA to deduce the particle diameter. A phase-diameter conversion factor $C^{12} = \Delta\phi^{12}/2R$ is usually defined by

$$C^{12} \approx \frac{\pi}{\lambda}\frac{m}{m-1}\,\alpha\psi[\mathrm{rad}/\mu\mathrm{m}]. \tag{1}$$

Expression (1) is limited to the paraxial approximation ($\psi \ll 1$), and it does not take into account many effects such as diffraction, polarization, and internal reflections inside the particle as well as the off-axis location of the detectors. Nevertheless this simple expression gives a good estimation of the dependence of C^{12} on parameters ψ, α, and m. We found by comparison with the predictions of a geometrical optics interference model that C^{12} is estimated to a greater accuracy than 2.5% for the parameter ranges $\alpha, \psi \in [0\text{–}5°]$ and $m \in [1.1\text{–}1.7]$. One important point to note is that the beam's half-angle and the elevation angle are equivalent in expression (1). This interesting property forms the basis of the proposed technique, which is detailed below.

By using expression (1), one can simply deduce particle diameter D from measurement of phase shift $\Delta\phi^{12}$, where $D = \Delta\phi^{12}/C^{12}$. More precisely, because of the 2π ambiguity in any measurement of phase shift $\Delta\phi^{12}$, the particle diameter reads as $D = (\Delta\phi^{12} + 2n\pi)/C^{12}$, where n is a natural integer that remains to be determined. To determine n, classic PDA systems use a third detector, D^3. This additional detector permits the measurement of two phase shifts, namely, $\Delta\phi^{12}$ and $\Delta\phi^{13}$, for each particle. The elevation angle of detector D^3 is chosen from the condition $C^{12}/C^{13} \approx 3$ (i.e., $l^{12}/l^{13} \approx 3$). With this well-known solution, reasonable accuracy can be maintained in particle-size determination without severe reduction of the dynamics of the measurable size range.

Here we propose an alternative solution to obviate the need for a third detector. It consists in using multiple superimposed probe volumes with different fringe spacings (i.e., beam half-angles). Figure 1(b) is a schematic of the proposed technique, although for clarity only two probes, with fringe spacings i_{v1} and i_{v2}, are superimposed in this figure. In this case the particle still acts as a projection system, but now the fringe pattern projected onto the detectors is the result of the superimposition of two fringe patterns with fringe spacing i_{p1} and i_{p2}, as shown in Fig. 1(b). When the particle crosses this probe volume the signal output from detectors D^1 and D^2 exhibits multiple frequencies and a multiple-phase-shift structure. Lower Doppler frequency corresponds to larger fringe spacing, which leads to a smaller phase-diameter conversion factor ${C_{v1}}^{12}$, which ensures the size range dynamics of the system; see expression (1). Higher Doppler frequency corresponds to smaller fringe spacing and thus to a higher conversion factor ${C_{v2}}^{12}$, which ensures the resolution of the system for particle-size determination. Two key issues in this technique have to be considered: first, the way to avoid mutual interference in each pair of laser beams that is used to produce the probe volumes, and second, the signal-processing scheme for treating experimental signals. Reflecting the first issues this technique is referred to subsequently as the superimposed noninterfering probes (SNIP) PDA.

This paper is organized as follows: In Section 2 we review various possibilities and conditions for producing SNIP PDA probe volumes. In Section 3 we present the signal-processing scheme developed to recover the multiple phase shifts and Doppler frequencies from SNIP PDA signals. In Section 4 we

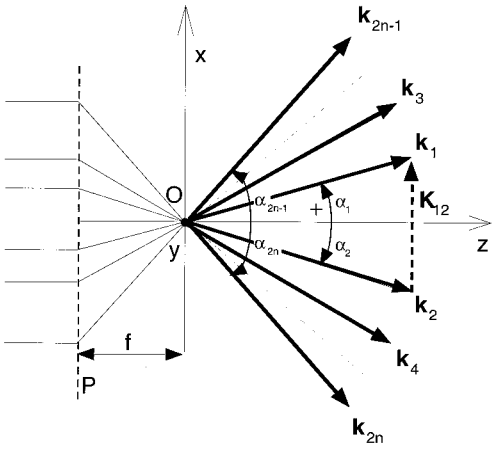

Fig. 2. Coordinate system *Oxyz* at the beam crossing.

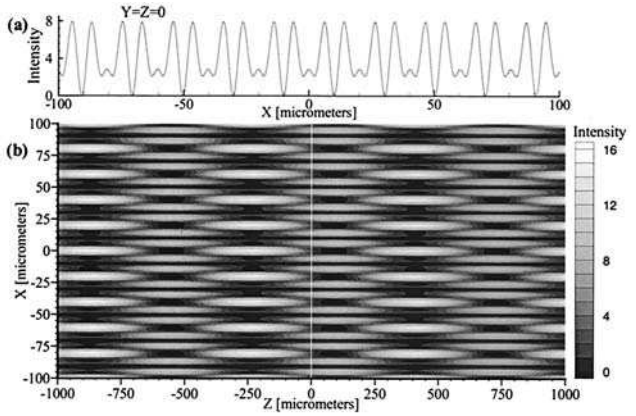

Fig. 3. (a) Calculation of the fringe intensity profile along *Ox* for $z = y = 0$. (b) Fringe intensity pattern in the *Oxy* plane when two coherent pairs of beams are superimposed with $i_p/i_q = 3$.

present the experimental setups and results that we carried out to demonstrate the applicability of the proposed technique. Section 5 contains a discussion of the most interesting features of SNIP PDA compared with those of some classic systems, including perspectives for future improvements.

2. Methods for Obtaining Noninterfering Superimposed Probes

A. Superimposition of Multiple Coherent Pairs of Beams

We are interested in calculating the interference field produced by the superimposition of N pairs of coherent beams that propagate in the *Oxz* plane and cross at point *O*, as shown in Fig. 2. To simplify this analysis we treat the beams as coherent harmonic and linearly polarized plane waves, each in the same polarization state, so the expression for the electric field vector that corresponds to beam n is reduced to

$$\mathbf{E}_n(\mathbf{r}, t) = \mathbf{E}_0 \exp[-j(\mathbf{k}_n \cdot \mathbf{r} + \varphi_n)]\exp(-j2\pi\nu t), \quad (2)$$

where $\mathbf{r}$ is the position vector in the coordinate system *Oxyz* and $\mathbf{k}_n$, φ_n, and ν are the wave vector, the phase, and the frequency, respectively, of beam n, see Fig. 2. Wave vectors with $n = 2l - 1$ and $m = 2l$ ($l \geq 1$) are symmetrical with respect to the *Oz* axis. The angle between wave vectors $\mathbf{k}_n$ and reference direction *Oz* is denoted α_n. The net field amplitude is a sum of all of the component fields, and the resultant field intensity is proportional to the time average (over a period much longer than $1/\nu$) of the squared modulus of the total amplitude:

$$\langle I(\mathbf{r})\rangle \propto \left\langle \left| \sum_{n=1}^{2N} E_n \right|^2 \right\rangle = \left\langle \sum_{m=1}^{2N} E_m \sum_{n=1}^{2N} E_n^* \right\rangle. \quad (3)$$

Using relation (3) yields the field intensity within the probe volume where $\mathbf{K}_{nm} = \mathbf{k}_n - \mathbf{k}_m$ and $\varphi_{nm} = \varphi_n - \varphi_m$:

$$\langle I(\mathbf{r})\rangle \propto 2E_0^2 \left[N + \sum_{n=1}^{2N} \sum_{m>n}^{2N} \cos(\mathbf{K}_{nm} \cdot \mathbf{r} + \varphi_{nm}) \right]. \quad (4)$$

The general expression for the scalar product $\mathbf{K}_{nm} \cdot \mathbf{r}$ reads as

$$\mathbf{K}_{nm} \cdot \mathbf{r} = \frac{2\pi}{\lambda} \begin{bmatrix} \cos(\alpha_n) & -\cos(\alpha_m) \\ \sin(\alpha_n) & -\sin(\alpha_m) \end{bmatrix} \begin{pmatrix} z \\ x \end{pmatrix}. \quad (5)$$

The phase delay between beams n and m, φ_{nm}, is compared to the reference plane (P) a distance f from the coordinate system's center *O*, where all beams are considered to be in phase. Then

$$\varphi_{nm} = \frac{2\pi f}{\lambda} [1/\cos(\alpha_n) - 1/\cos(\alpha_m)]. \quad (6)$$

In relation (4) the cosine term corresponds formally to the classic fringe pattern observed in a PDA probe volume when two coherent beams cross each other. For symmetrical beams with respect to *Oz* the scalar product in Eq. (5) is only a function of x (i.e. $n = m - 1$). In this case, as in classic PDA probes, the fringes are parallel to *Oz*. In the other case (i.e., $n \neq m - 1$) the scalar product in relation (4) depends on both x and z, so the fringe pattern is expected to be much more complex than the one observed for a classic LDA–PDA system. Figure 3 illustrates this behavior when expressions (4)–(6) are used to compute the fringe pattern produced by the interference of two coherent pairs of beams ($2N = 4$) for $\lambda = 0.6328$ μm and $f = 0.5$ m, with beam half-angles $\alpha_1 = -\alpha_2 = \alpha_3/3 = -\alpha_4/3 = 0.9°$. In Fig. 3(b) the contour levels show that the fringes are still parallel to *Oz* but with an unusual amplitude modulation along this axis. In Fig. 3(a) the fringe intensity profile $I(x, 0, 0)$ is plotted; it corresponds to the vertical white line in Fig. 3(b). From our simulations, not reported here, it appears that the fringe pattern depends strongly on the ratio of beam angles α_1/α_3 as well as on phase delay φ_{nm}. The latter tends to shift the whole fringe pattern along *Oz*.

Thus interference between nonsymmetrical beams with respect to *Oz* induces a complex fringe pattern whose use in the usual LDA–PDA applications previously seemed to be awkward.

B. Superimposition of Multiple Incoherent Pairs of Beams

We are interested in calculating the interference field pattern produced by the superimposition of N pairs of symmetrical beams with respect to Oz that originate from the same laser source but with a time delay $(n-1)\tau$. For the nth pair of coherent beams the general expressions for the electric field vectors, (E_{2n-1} and E_{2n}), where $\varphi_{2n-1} = \varphi_{2n}$, read as

$$\begin{aligned}\mathbf{E}_{2n-1}(\mathbf{r}, t) &= \mathbf{E}_0 \exp[-j(\mathbf{k}_{2n-1}\cdot\mathbf{r} + \varphi_{2n})] \\ &\quad \times \exp\{-j2\pi\nu[t-(n-1)\tau]\}, \\ \mathbf{E}_{2n}(\mathbf{r}, t) &= \mathbf{E}_0 \exp[-j(\mathbf{k}_{2n}\cdot\mathbf{r} + \varphi_{2n})] \\ &\quad \times \exp\{-j2\pi\nu[t-(n-1)\tau]\}. \end{aligned} \quad (7)$$

Two fields, $\mathbf{E}_n$ and $\mathbf{E}_m$, are phase shifted in relation to each other by the quantity $\Lambda_{nm} = 2\pi\nu N_{nm}\tau$, provided that $m > n$, where for odd values of $(m-n)$ the number of time delays N_{nm} is equal to $(m-n-1)/2$ and for even values it is equal to $(m-n)/2$. In stationary conditions the time-averaged intensity at the beam crossing (over a period much longer than $1/\nu$) has the general form

$$\langle I(\mathbf{r})\rangle \propto 2E_0^2\left[N + \sum_{n=1}^{2N}\sum_{m>n}^{2N} |\gamma_{nm}(N_{nm}\tau)| \times \cos(\mathbf{K}_{nm}\cdot\mathbf{r} + \varphi_{nm} + \Lambda_{nm})\right]. \quad (8)$$

A time-dependent function $|\gamma_{nm}(t)|$ is introduced here to take into account the temporal limited-laser-source coherence. This function is classically known as the degree of coherence or the coherence function of the laser source.[9] It is a function of time delay $N_{nm}\tau$ between the two beams n and m. For a quasi-monochromatic source ($\Delta\nu/\nu \ll 1$) and beams of equal intensity, the coherence function is equal to the fringe contrast function $|\gamma(t)| = (I_{\max} - I_{\min})/(I_{\max} + I_{\min})$, where $I_{\max}$ and $I_{\min}$ are the local intensity extrema of the fringes observed at the beam's crossing. Typically, the coherence function decreases exponentially with the time delay,[10] $|\gamma(t)| \sim \exp(-\nu t)$ and a coherence time τ_c and a coherence length L_c are usually defined as $|\gamma(\tau_c)| = 1/e$ and $L_c = c\tau_c$. c is the speed of light in the medium. For a laser source the evolution of $|\gamma_{nm}(t)|$ is more complex. Classic lasers used in PDA–LDA operate simultaneously in more than one longitudinal mode. If the modes have random phases, the coherence function (i.e., the Fourier transform of a few spectral lines separated by $\Delta\nu = c/L_0$, where L_0 is the laser cavity length), has successive maxima and minima with a temporal periodicity of L_0/c and a spatial periodicity such that $L_c \approx L_0$ (see Section 4 below).

Note that, if all the initial pairs of beams are successively delayed in time with respect to one another from the laser coherence time ($\tau = \tau_c$), in expression (8) all the interference terms that correspond to nonsymmetrical pairs of beams vanish (i.e., $|\gamma_{nm}(t)| = 0$ if $n \neq m-1$ and $|\gamma_{nm}(t)| = 1$ if $n = m-1$). Finally the average intensity at the beam crossing reduces to

$$\langle I(\mathbf{r})\rangle \propto 2E_0^2\left\{N + \sum_{n=1}^{N}\cos[\mathbf{K}_{(2n-1)2n}\cdot\mathbf{r}]\right\}. \quad (9)$$

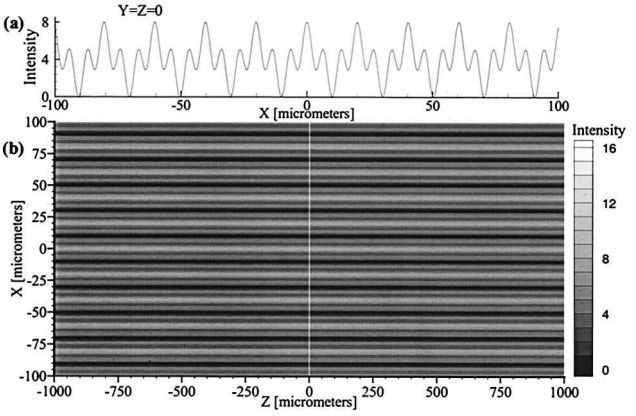

Fig. 4. The same as in Figs. 3(a) and 3(b) but for two incoherent pairs of beams superimposed.

The net fringe pattern reduces simply to the addition or the superimposition of the fringe pattern produced by each pair of symmetrical beams. Figure 4 shows the fringe patterns obtained for the same parameters as in Fig. 3 but for two mutually incoherent pairs of beams. The fringes are now parallel and without amplitude dependency along Oz; the multiple-frequency structure of the SNIP is now clear.

C. Superimposition of Cross-Polarized Coherent Pairs of Beams

For only two crossed linearly polarized pairs of coherent beams (i.e., $n = 1, 2$) the general expression for the electric field vectors of the pair n of symmetrical beams (E_{2n-1} and E_{2n}) is

$$\begin{aligned}\mathbf{E}_{2n-1}(\mathbf{r}, t) &= \mathbf{E}_0\begin{pmatrix}\cos\delta_n \\ \sin\delta_n\end{pmatrix}\exp[-j(\mathbf{k}_{2n-1}\cdot\mathbf{r} + \varphi_{2n})] \\ &\quad \times \exp(-j2\pi\nu_n t), \\ \mathbf{E}_{2n}(\mathbf{r}, t) &= \mathbf{E}_0\begin{pmatrix}\cos\delta_n \\ \sin\delta_n\end{pmatrix}\exp[-j(\mathbf{k}_{2n}\cdot\mathbf{r} + \varphi_{2n})] \\ &\quad \times \exp(-j2\pi\nu_n t), \end{aligned} \quad (10)$$

where δ_n is the angle of the electric field vectors of the pair of beams n with Oy. For 2 cross-polarized SNIP, $|\delta_1 - \delta_2| = \pi/2$. In this case the average intensity at the beam crossing reduces to

$$\langle I(\mathbf{r})\rangle = 2E_0^2\left[N + \sum_{n=1}^{2}\cos(\mathbf{K}_{(2n-1)2n}\cdot\mathbf{r})\right]. \quad (11)$$

Like the solution in Subsection 2.B, the net fringe pattern is equal to the superimposition of the fringe patterns produced by both pairs of symmetrical beams.

3. Signal Processing

The signal-processing scheme used here to recover the multiple Doppler frequencies and the corresponding phase shifts is based on the calculation of cross-spectral density[11] (CSD) as a function of time series $S^1(t)$, $S^2(t)$ that comes from detectors D^1 and D^2 when a particle is inside the probe volume. The signal output from each detector is considered to be linear with respect to the intensity of light collected by the detectors.

As a first step we consider the SNIP PDA signals as multiple-frequency and multiply phase-shifted signals of infinite duration and without low-frequency amplitude modulation. Note that in fact this type of perfect signal is not too different from the experimental signals observed for fixed particles in the probe volume (see Fig. 11 below) or for liquid jets or fibers moving along the Oz axis.[12,13] The SNIP is assumed to be composed of n mutually noninterfering pairs of beams with beams' half-angle α_n, so for each detector the high-pass filtered SNIP PDA signals reduce to $S^{1,2}(t) \propto \Sigma_{n=1}^{N} \cos(2\pi\nu_n t + \phi_n{}^{1,2})$, where ν_n is the Doppler frequency that is due to the beams' frequency shift and $\phi_n{}^{1,2}$ is the signal phase shift, which depends on both the particle-scattering properties (size, refractive index, and shape) and the optical setup of the PDA system. For $\nu > 0$ the Fourier transforms of these signals are reduced to $S^{1,2}(\nu) = \Sigma_{n=1}^{N} \delta(\nu - \nu_n)\exp(-j\phi_n{}^{1,2})$, where $\delta(\nu - \nu_n)$ is the Dirac delta function. The CSD function reads as

$$S^1(\nu)S^2(\nu)^* = |G^{12}(\nu)|\exp[-j\theta^{12}(\nu)] = \sum_{n=1}^{N} \delta^2(\nu - \nu_n)\exp(-j\Delta\phi_n{}^{12}). \quad (12)$$

From Eq. (12) it follows that CSD modulus spectrum $|G^{12}(\nu)|$ is composed of N Dirac functions, each of which identifies a Doppler frequency $\nu = \nu_n$ presented in the SNIP PDA signals. For each of these frequencies the phase-shift difference between the two signals can be determined in the CSD phase spectrum $\theta^{12}(\nu)$ through $\Delta\phi_n{}^{12} = \phi_n{}^1 - \phi_n{}^2 = \theta^{12}(\nu_n)$.

A more general form for a SNIP PDA signal is

$$S(t) = \sum_{n=1}^{N} P_n[1 + V_n \cos(2\pi\nu_n t + \phi_n)], \quad (13)$$

where, as in any classic phase Doppler system, P_n and V_n are the signal pedestal and visibility, respectively.[14] These functions depend on a large number of parameters: the particle-scattering properties, the detector aperture's collection angle and shape, particle trajectory in the probe volume, etc. A good approximation for the evolution of P_n is given by $P_n = I_0 \exp[-\pi(t/\tau_0)^2]$, assuming the same Gaussian intensity distribution for all SNIPs and that the particles are small compared with the probe volume with trajectories not too far from the probe volume's center. Transit time τ_0 depends on all the parameters cited above. It is nevertheless independent of the pair of beams that we consider here. However, the signal's visibility can depend strongly on the beam's half-angle and therefore on the SNIP. Thus for $n = 1 \ldots N$ SNIP the CSD of the high-pass filtered SNIP PDA signals is given for $\nu > 0$ as

$$|G^{12}(\nu)|\exp[-j\theta^{12}(\nu)] = \frac{I_0{}^2\tau_0{}^2}{4} \sum_{n=1}^{N} \left(V_n \exp\{-\pi[(\nu - \nu_n)\tau_0]^2\}\exp(-j\phi_n{}^1)\right) \times \sum_{n=1}^{N} \left(V_n \exp\{-\pi[(\nu - \nu_n)\tau_0]^2\}\exp(+j\phi_n{}^2)\right). \quad (14)$$

Let $\bar{\nu} = (\nu_n + \nu_m)/2$ and $\Delta\nu = (\nu_m - \nu_n)/2$, then Eq. (14) can be rewritten as

$$|G^{12}(\nu)|\exp[-j\theta^{12}(\nu)] = \frac{I_0{}^2\tau_0{}^2}{4} \sum_{n=1}^{N} \sum_{m>n}^{N} [V_n{}^2 \exp(-2\pi\tau_0{}^2 \times (\nu - \nu_n)^2 \exp(-j\Delta\phi_n{}^{12}) + 2V_nV_m \exp\{-2\pi\tau_0{}^2 \times [(\nu - \bar{\nu}_{nm})^2 + (\Delta\nu_{nm})^2]\}\exp[-j(\phi_n{}^1 + \phi_m{}^2)])]. \quad (15)$$

The first term on the right-hand side of Eq. (15) indicates that in the CSD modulus spectrum the Doppler frequencies are identified as Gaussian peaks with a frequency bandwidth controlled by transit time τ_0. At the maximum of these peaks, $\nu = \nu_n$, the signal's phase-shift difference can be directly determined from the phase of the CSD function as $\Delta\phi_n{}^{12} = \theta^{12}(\nu_n)$. The second term may be considered a perturbation of the first term. When the Doppler frequencies of the pair of beams n and m tend to overlap $[(\Delta\nu_{nm})^2 \to 0]$, the phase-shift differences of the two signals cannot be so simply related to the phase of the CSD function.

Figure 5(a) shows two SNIP PDA signals simulated for $n = 5$ superimposed probe volumes. In this example, instead of imposing a particle velocity, a particle size, and a fringe spacing, we directly impose $\tau_0 = 150$ μs, $V_n = 1$, $\nu_n/\nu_1 = n$, and $\Delta\phi^{12}(\nu_n)/\Delta\phi^{12}(\nu_1) = n$, with $\nu_1 = 20$ kHz and $\Delta\phi^{12}(\nu_1) = 20°$, so the Doppler frequencies and the phase shifts are in the range 20–320 kHz and 20°–320°, respectively. Figure 5(b) shows a zoom of a part of Fig. 5(a). For Fig. 5(c), white noise has been added to the previous signals (with a signal-to-noise ratio of 5 dB). The CSD phase spectra and moduli of these noise-added signals are shown in Fig. 6. These spectra were computed with the same software that we used for our research described below in the experimental part of this paper to treat experimental signals. In the modulus spectrum the five Doppler frequencies can easily be identified by large peaks. In the phase spectrum the corresponding phase shifts are identified as plateaus. By using a three-point Gaussian fit for the modulus peaks and a linear fit for the phase spectrum,[11] we determined the Doppler frequencies and phase shifts. They were found to be in good agreement with the nominal values, as shown in Figs. 6(a) and 6(b). One important point to note here is that the relative error of the phase-shift estimation decreases as we consider higher Doppler frequencies; for $n = 1 \ldots 5$ we found successive shifts of 3.5%, 1.0%, 0.65%, 0.5%, and 0.28%. To some extent this

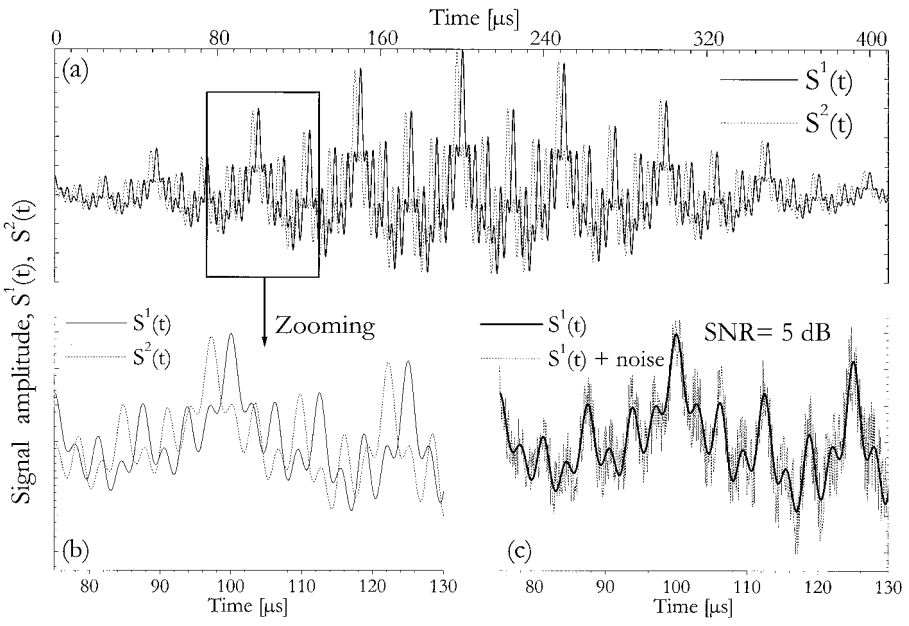

Fig. 5. High-pass filtered signals simulated for $n = 5$ SNIPs with $\nu_n/\nu_1 = \Delta\phi^{12}(\nu_n)/\Delta\phi^{12}(\nu_1) = n$, where $\nu_1 = 20$ kHz and $\Delta\phi^{12}(\nu_1) = 20°$: (a) complete signals, (b) zoom of (a), (c) signals with white noise added (SNR, signal-to-noise ratio).

fact justifies the acceptability of the present technique.

In the working principle of the SNIP PDA technique the two successive Doppler frequencies ν_n and ν_m in the signal are assumed to be clearly distinct, in as much as in the opposite case there is no difference between the two phase-diameter conversion factors. Nevertheless, as the Doppler frequencies are proportional to one component of the particle velocity, it follows that, when the particle velocity decreases, the two frequencies tend to overlap. In such a case it could become increasingly more difficult to distinguish between the two frequencies and as a consequence to extract the two phase shifts. In classic PDA systems the laser beams are frequency shifted by use of Bragg cells or by rotation of the transmission gratings.[8] Within the framework of the heuristic fringe model this well-known solution tends to impose a velocity shift on the probe volume fringes. In this case the sign of the direction of motion of the

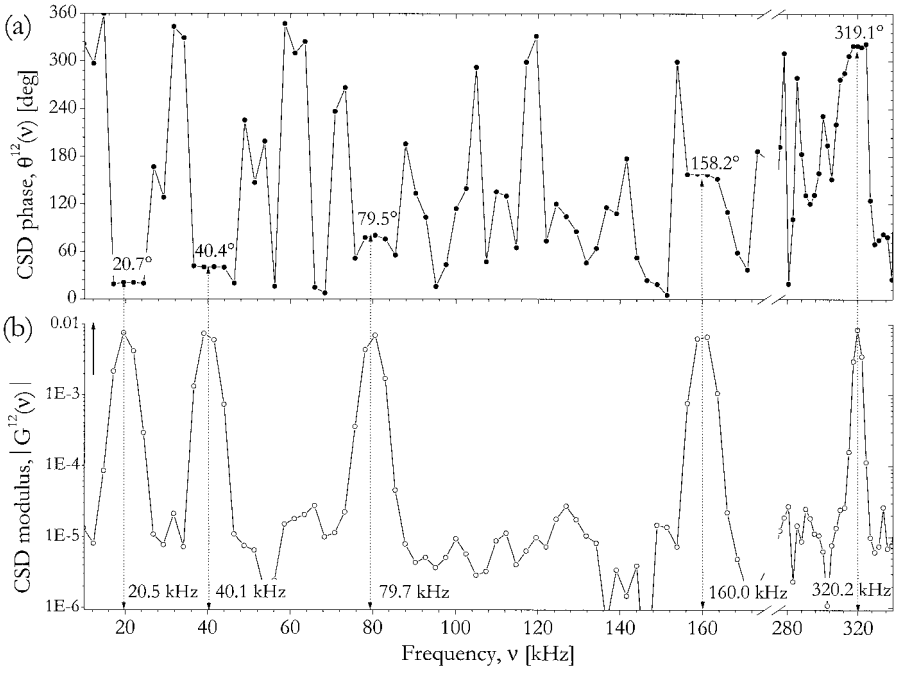

Fig. 6. (a) Phase and (b) modulus spectra of the CSD of signals from Fig. 5 with noise added.

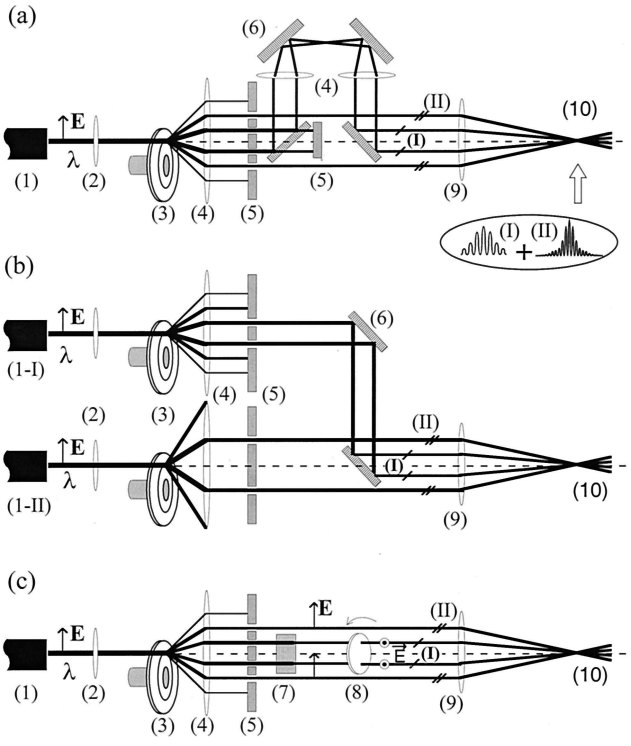

Fig. 7. Optical setups to produce a SNIP: (a) system (A) with a retardation line, (b) system (B) with two independent laser sources, (c) system (C) with cross-polarized probes. (1) He–Ne laser, (2) focusing lens, (3) transmission diffraction gratings, (4) collimating lens, (5) beam stop, (6) mirrors, (7) neutral-density filter, (8) half-wave retardation plate, (9) transmitting lens, and (10) SNIPs.

particle can be determined and motionless particles located in the probe volume can be characterized.[8] The SNIP PDA technique may also take advantage of this solution, but the laser beam's frequency shift must be different for each pair of beams. This solution is not so restricting, as is demonstrated in what follows.

4. Experimental Validation

A. Optical Setups to Produce Superimposed Noninterfering Probes

On the basis of the considerations above, three systems for producing SNIP volumes were tested with two types of reception unit. Note that in the present study the laser wavelength is always $\lambda = 0.6328$ μm.

1. System (A): Single Laser Source with a Retardation Line

System (A) [Fig. 7(a)] takes advantage of the limited coherence time of a 2.5-mW He–Ne laser with cavity length $L_0 = 200$ mm to produce two pairs of beams, labeled I and II in what follows. The laser beam output is focused onto a rotating transmission diffraction grating. The diffracted beams are then collimated with a spherical lens. A beam stop is used to stop all the diffracted beams that are not of order ±1 or ±2. A beam splitter separates beams ±1 into two pairs of beams. One pair is directed to a beam stop and the other one is directed to a retardation line, which controls the additional path length L and maintains the beam divergence (two lenses of equal focal length are used for this purpose). At the output of the retardation line the two beams (i.e., pair I) are redirected to be parallel to the two beams ±2 (i.e., pair II). A transmission lens is then used to focus the four laser beams and to produce the SNIP volume. The frequency shift of the two pairs of beams is controlled through the transmission diffraction grating's rotating velocity.[8]

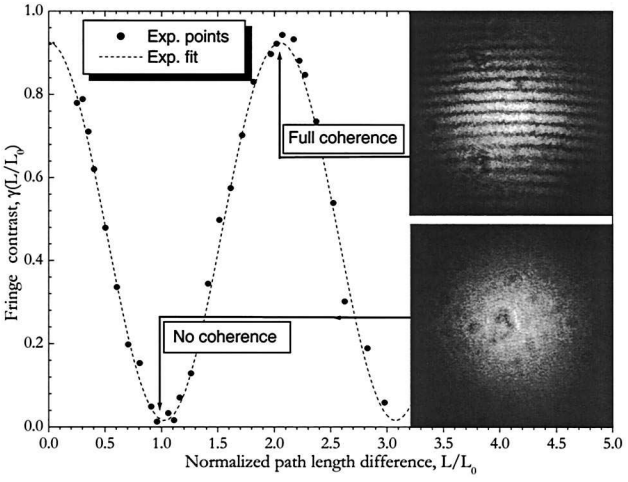

Fig. 8. Measurement with system (A) of the coherence length of a 2.5-mW He–Ne laser with a cavity length of $L_c = 200$ mm and $\lambda = 0.6328$ μm.

One can also use this setup to determine the laser's coherence length and so distance L. For this purpose we blocked one beam from each pair such that in the probe volume only the closest beams from each pair interfere ($n = 1$ and $m = 3$). The probe volume fringe pattern (*Oxy* plane) was then projected on to a screen by a microscope objective and recorded with a CCD camera. Thus the coherence function of the laser source could be deduced from measurement of the fringe contrast versus normalized distance L/L_c. On the right-hand side of Fig. 8 two recorded fringe patterns are shown that correspond to a maximum coherence ($|\gamma_{13}(L/L_c \sim 2)| \sim 0.93$) and a minimum coherence ($|\gamma_{13}(L/L_c \sim 1)| \sim 0.01$). Note that here we did not find exactly the theoretically expected values for the extrema of the coherence function (i.e., $|\gamma_{13}^{\max}| = 1$ and $|\gamma_{13}^{\min}| = 0$). In our opinion this discrepancy is caused by difficulty in measuring precisely the contrast of the probe volume fringes. On the left-hand side of Fig. 8 the second maximum has almost the same amplitude as the first one, which means that this laser operates with only two longitudinal modes. Finally we can conclude here that, as expected, the coherence length of this laser is almost equal to the laser's cavity length. Then, in

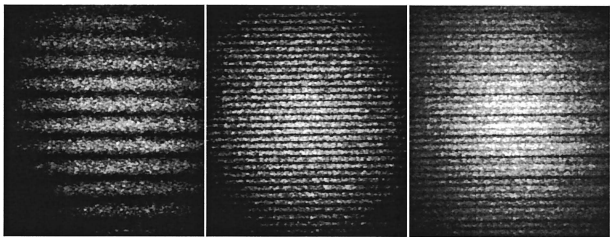

Fig. 9. Image of the projection (*Oxy* plane) of the fringe pattern of system (B). The pair of beams I (left) and II (middle) is shown individually. Right, the two pairs of beams are superimposed.

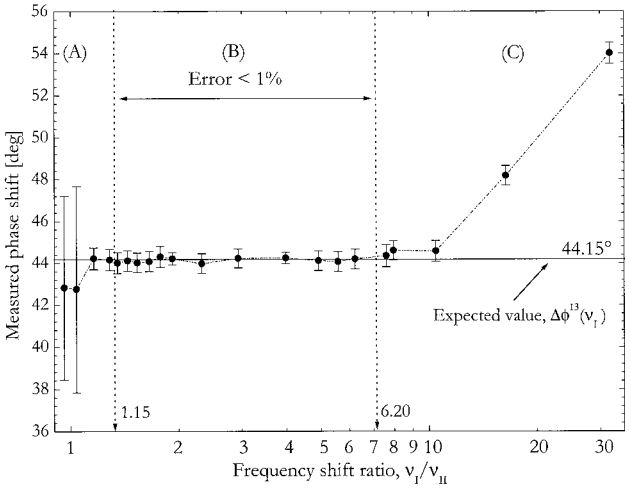

Fig. 10. Evolution of the phase-shift difference measured for small copper fibers fixed in the SNIP volume of system (B) versus the ratio of the frequency shifts of the two pairs of beams.

what follows, the retardation line of system A is set to fulfill the condition $L = L_c = 200$ mm.

2. *System (B): Two Independent Laser Sources*

A second optical system [Fig. 7(b)] was developed by utilization of two different laser sources and two rotating transmission diffraction gratings. For this purpose the beam output from two He–Ne lasers (2.5 and 10 mW) was focused onto two different transmission diffraction gratings. In both cases the diffracted beams of order ± 1 (i.e., pairs of beams I and II) were aligned by a single transmission lens to be parallel and focused at the same location. Figure 9 shows images of the projected fringe patterns obtained as described above. On the left and in the middle of Fig. 9 the fringe patterns of beam pair *I* and *II*, respectively, are shown individually. The fringe spacing ratio is ≈ 3. At the right in Fig. 9 the corresponding superimposed fringe pattern is shown. There no evidence of any interference between the two pairs of beams.

One can also use this setup to estimate the effect of the overlap of the two SNIP frequency shifts on the phase-shift estimation. In Fig. 10 the phase-shift measurement for a copper fiber is presented as it relates to the ratio between the frequency shifts of the two pairs of beams. In this experiment one frequency shift ($\nu_{II} \approx 159$ kHz) was kept essentially constant, whereas the other one was varied to yield a frequency shift ratio ν_I/ν_{II} in the range 0.96–32. The expected phase shift is $\Delta\phi_{\nu II}{}^{12} \approx 44.6°$. For a frequency shift ratio in the range 1.15–6.2 [zone (B) in Fig. 10] there is almost no effect from overlap of the

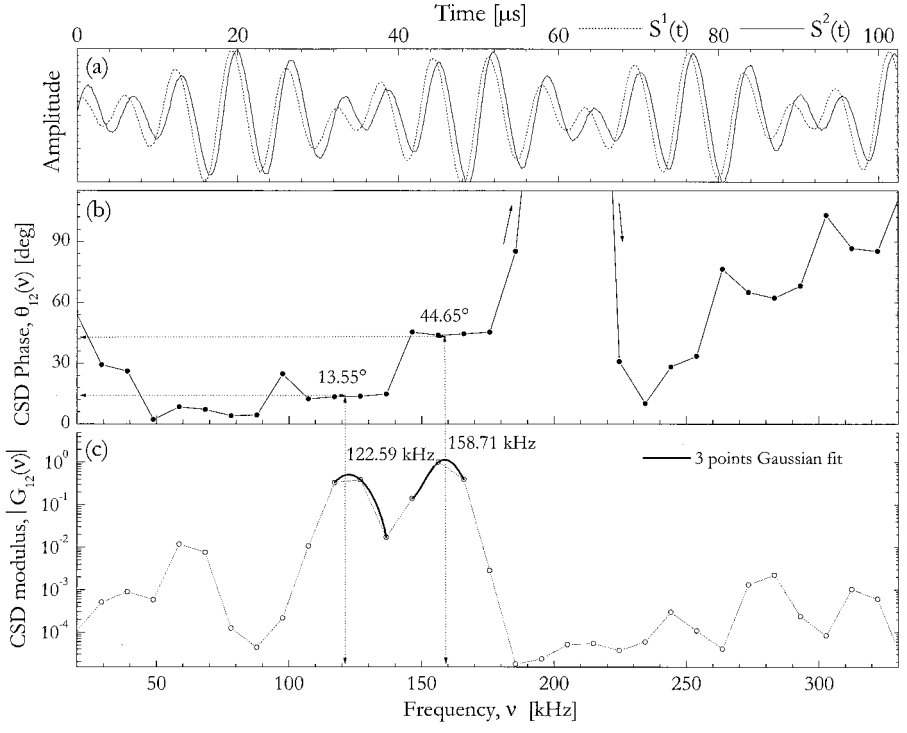

Fig. 11. (a) Typical experimental SNIP signals obtained for Fig. 10 when the frequency shift ratio is 1.3, (b) corresponding CSD phase, (c) CSD modulus spectrum.

two frequencies. The deviation of the phase-shift measurements is less than 1%. Nevertheless, for a frequency ratio below 1.2 [zone (A)] and above 6.2 [zone (C)] the error increases drastically. For zone (A) the errors clearly come from difficulty in distinguishing between the two frequencies presented in the signal, whereas for zone (C) the errors may be attributed to decreasing quality of signal digitization as the frequency shift increases. Figure 11(a) shows a typical signal recorded during this experiment as well as the CSD spectra [Figs. 11(b) and 11(c) for $\nu_I/\nu_{II} \approx 1.3$. Even if the two peaks of the CSD modulus begin to overlap, they can nevertheless be clearly distinguished from each other. In the CSD phase spectrum the corresponding phase shifts can be clearly identified by two plateaus. Note that the high quality (high signal-to-noise ratio) of the two SNIP signals presented in Fig. 11(a) always appears when fixed fibers or fibers with a longitudinal displacement[12,13] in the probe volume are considered.

3. *System (C): Single Laser Source with a Cross-Polarized Beam Pair*

Our third experimental setup is based on the superimposition of two cross-polarized pairs of beams [Fig. 7(c)]. The output of a 10-mW linearly polarized He–Ne laser is directed onto a rotating transmission diffraction grating. The diffracted beams are collimated by a spherical lens. A beam stop is used to stop all diffracted beams except the one with orders of ± 1 and ± 3 to form the pairs of beams I and II, respectively. Note that, from the drawing requirements in Fig. 7(c), pair II is associated with the beams with diffraction order ± 2. The intensity of the diffracted beams decreases significantly relative to their diffraction order. Thus a variable neutral-density filter is used to decrease the intensity of beams ± 1 to the intensity of the other pair of beams. Afterward a single half-wave retardation plate is used to turn the polarization plane of pair of beams I by 90° with respect to the polarization plane of pair of beams II. Finally, the probe is a summation of the two cross-polarized probes of different fringe spacings and frequency shifts.

B. Particle-Size Measurements

The principle of the proposed technique was validated by sizing of both spherical glass beads and cylindrical metallic wires.

1. *Systems (A) and (B) for Sizing Flowing Glass Beads*

Figure 12 presents typical experimental results obtained by measurement of the size distribution of glass beads falling out of a vibrating tank. The glass beads (refractive index $m = 1.51$) were previously sieved to be within the nominal size range 100–160 μm. At the probe volume location the beads velocity was ~0.5 m/s. Three kinds of result are presented in this figure:

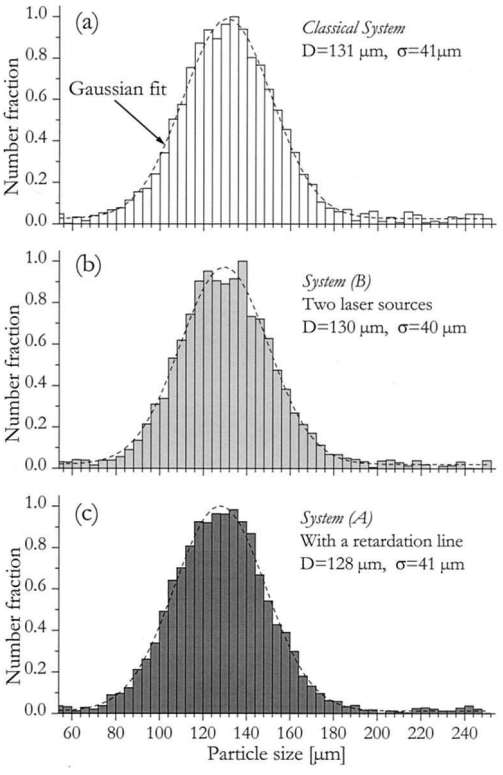

Fig. 12. Size distributions measured for glass beads falling from a vibrating tank with (a) a classic PDA and (b), (c) two SNIP PDA systems, (B), and (A).

Figure 12(a) shows the size distribution obtained with a classic phase Doppler system from Aerometrics Inc.[15] This system uses a 10-mW He–Ne laser to produce a 320-μm (at $1/e^2$) probe volume at 500 mm from the transmission lens. The beams' half-angle was set to $\alpha = 2.71°$. The collection unit was composed of three detectors of elevation angles $\psi^{1,2} = \pm 4.1°$ and $\psi^3 = \pm 1.27°$. This unit was located in the forward-scattering domain at an off-axis angle of 30°. By using the Lorenz–Mie theory (LMT) we found that the phase-shift diameter conversion factors of this system are $C^{12} \approx 1.72°/\mu m$ and $C^{13} \approx 4.97°/\mu m$.

Figure 12(b) shows the size distribution obtained by system (B) and the collection unit and the electronics of the Aerometrics system (detectors 1 and 3 only) for detection of the Doppler signals. The beams' half-angles were $\alpha_I = 0.45°/\mu m$ and $\alpha_{II} = 2.71°/\mu m$. The phase-shift diameter conversion factors of the corresponding SNIP PDA were found to be ${C_I}^{12} \approx 0.83°/\mu m$ and ${C_{12}}^{12} \approx 4.973°/\mu m$.

Figure 12(c) shows the size distribution obtained by system (A) and, as for system (B), with the collection unit and the electronics of the Aerometrics system. The beams' half-angles were $\alpha_I = 0.76°/\mu m$ and $\alpha_{II} = 1.52°/\mu m$. The phase-shift diameter conversion factors of the corresponding SNIP PDA were found to be ${C_I}^{12} \approx 1.40°$ and ${C_{II}}^{12} \approx 2.79°/\mu m$. The

probe volume diameter of the two SNIP systems was ~300 μm.

For the three cases the Doppler signals (classic and SNIP signals) were recorded by a digital oscilloscope and treated with a processing software developed by us. That hardware was required for the processing of the SNIP PDA signals, as was shown in Section 3. It was also necessary for the treatment of classic Doppler signals because we are interested here in validation of the principle of the proposed technique and not in validation of the signal-processing scheme used for the correction of trajectory effects or the probe volume's size.[16] The two last-named effects are known to have a strong influence on PDA results. This is the reason why, for a better comparison, we avoided using the Aerometrics Inc.'s software to process the classic Doppler signals. For each system the statistics were obtained for 10,000 validated samples. Figure 12 shows that there are no significant differences among the shapes and the statistical moments of the three size distributions, a result that demonstrates that use of the SNIP technique is highly appropriate for correction of the 2π ambiguity in the phase-shift estimation.

2. System (C) for the Sizing of Metallic Fibers

An emission unit based on system (C) with two single backward collection units was tested to measure small-diameter metallic fibers. The two collection units were built by us and were placed at elevation angles $\psi^1 = -\psi^2 = 170°$.[13] The probe volume was located 200 mm from the optics and had a diameter of 600 μm. The beams' half-angles were $\alpha_I = 0.45°/\mu m$ and $\alpha_{II} = 1.835°/\mu m$. The metallic fibers were made from pure copper and were fixed in the probe volume. Their nominal diameter was controlled with a precision micrometer of ±1-μm resolution. Copper has a complex refractive index in the visible domain of $m = 0.88 - 0.46j$, so the main scattering process in the near-backward direction is essentially reflection. The phase-shift diameter conversion factors of the corresponding SNIP PDA were found to be ${C_I}^{12} \approx 0.81°/\mu m$ and ${C_{II}}^{12} \approx 3.29°/\mu m$. Figure 13 compares the diameters of several fibers measured with the SNIP PDA system (statistics from 5000 samples) and the diameters measured with a micrometer. The correction for the 2π ambiguity in the phase shift, $\Delta\phi_{\nu_{II}}{}^{12}$ is sketched in this figure. Note that over the entire size range the two size measurement are in good agreement.

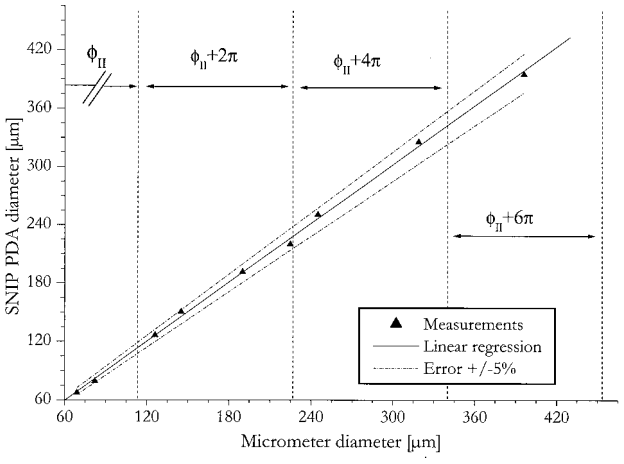

Fig. 13. Comparison of the size measurements of small copper fibers with a precision micrometer and with system (C).

5. Discussion

In this paper the concept of a superimposed noninterfering probe phase Doppler anemometry technique for particle-size measurement has been introduced by means of a heuristic model rather than by a rigorous model based on the Lorenz–Mie theory.[5,6,13,17] The reason for this is that, in the LMT framework, the scattering of super-imposed pairs of mutually incoherent beams is strictly equal to the addition of the scattering of each pair of beams taken individually. This means for instance that the phase-diameter calibration curve that corresponds to each SNIP (at each Doppler frequency) is the same as it would be if it were a single-phase Doppler probe. In our opinion LMT calculations would be interesting only when the two pairs of beams were only partially mutually incoherent. From Fig. 3, this seems to be of no practical interest. The same conclusion holds only partially for a cross-polarized pair of beams. In fact, in classic phase Doppler systems the polarization state of the laser beams is either in the scattering plane or perpendicular to the scattering plane, so the development of a particular LMT-based model to calculate the corresponding SNIP PDA calibration curves would be necessary only when irregular particles,[18] birefringent cylinders, or cylinders at oblique incidence,[13] which tend to modify the polarization state of the incoming beams, were considered. Such is not the case for homogeneous spherical particles or homogeneous cylinders at normal incidence.

For practical considerations, systems (A) and (C) seem to be most interesting for future developments. It is rather straightforward to realize system (C), which nevertheless, has a limited number of SNIPs. System (A) is thought to have great potential, provided that a laser of a shorter coherence length is used to build a compact system, which could be achieved with a laser diode or a YAG laser with a coherence length of a few tens of millimeters. Note that this kind of laser is already used in some LDA systems and could significantly reduce the bulky design of the system presented in this paper, which was the result mainly of our limited experimental facilities.

In our opinion the SNIP PDA technique may have several additional advantages when it is compared with the usual PDA technique for the following applications:

The sizing of small particles with classic PDA systems requires the use of a planar geometry in which the collection of the Doppler signals is obtained from

two separate collection units located in the near-forward scattering domain.[19] With this optical configuration and because of alignment considerations, it is almost impossible to use a third collection unit to limit the 2π ambiguity in the phase-shift measurements. If we now consider a SNIP PDA system working in a planar configuration, such as system (C), this problem can easily be solved by use of an additional pair of beams.

The size distribution of irregular particles can be determined to some extent with a classic PDA system, as was shown by Naqwi.[20] One of the main conclusions of that paper[20] is that, unlike for spherical particles, for irregular particles the probe volume; fringe spacing has a strong influence on the statistical moments of the measured size distribution. This means that the SNIP PDA technique could have great potential for the detection of irregular particles.[21]

The detection of internal constraints in glass fibers could be also an interesting use of the SNIP PDA technique. Two of the present authors have already shown theoretically[13] that the PDA technique can detect mechanically induced birefringence inside glass fibers with diameters of a few tens of micrometers. We believe that a SNIP PDA based on system (C), which allows two phase shifts, each of which corresponds to two cross-polarized pairs of beams, to be measured will be suitable for detection of the presence of one ordinary and one extraordinary refractive index inside the fiber.

Two velocity components could be obtained with the proposed technique without any requirement for use of a multiline laser, as is usually done with classic LDA–PDA systems. This requires that one of the pairs of beams in system (A), (B), or (C) be rotated 90° such that the particle velocity component along *Oy* can be determined at the same time as the particle velocity component along *Ox*. In addition, this effective low-cost solution could offer the possibility that the SNIP PDA system could be used in a dual-mode configuration for improving mass flux measurements[22] or for particle refractive-index measurements.[16]

The authors are grateful to the French National Center for Scientific Research and the Bulgarian Academy of Sciences for providing financial support for this research (project CNRS-BAS No. 6617).

References and Notes

1. F. Durst and M. Zaré, "Laser Doppler measurements in two-phase flows," in *The Accuracy of Flow Measurements by Laser Doppler Methods—Proceedings of LDA-Symposium, Copenhagen, Denmark, 1975*, P. Buchhave, J. M. Delhaye, F. Durst, W. K. George, K. Refslund, and J. H. Whitelaw, eds. (Proceedings LDA-Symposium, Skovlunde, Denmark, 1976), pp. 403–429.
2. W. D. Bachalo and M. J. Houser, "Phase/Doppler spray analyzer for simultaneous measurements of drop size and velocity distributions," Opt. Eng. **23,** 583–590 (1984).
3. K. Bauckhage, H. H. Floegel, U. Fritsching, and R. Hiller, "The phase Doppler difference method, a new laser Doppler technique for simultaneous size and velocity measurements. 2. Optical particle characteristics as a base for a new diagnostic technique," Part. Part. Syst. Charact. **5,** 66–71 (1988).
4. E. D. Hirleman, "History of development of the phase Doppler-sizing velocimeter," Part. Part. Syst. Charact. **13,** 59–67 (1996).
5. A. Naqwi and F. Durst, "Light scattering applied to LDA and PDA measurements. I. Theory and numerical treatments," Part. Part. Syst. Charact. **8,** 245–258 (1991).
6. G. Gréhan, G. Gouesbet, A. Naqwi, and F. Durst, "Particle trajectory effects in phase Doppler systems: computations and experiments," Part. Part. Syst. Charact. **10,** 332–338 (1993).
7. R. J. Adrian and R. J. Goldstein, "Analysis of a laser-Doppler anemometer," J. Phys. E **4,** 505–511 (1971).
8. F. Durst, A. Melling, and J. H. Whitelaw, *Principles and Practice of Laser-Doppler Anemometry* (Academic, London, 1981).
9. W. Lauterborn, T. Kurz, and M. Wiesenfeldt, *Optique Cohérente* (Masson, Paris, 1997).
10. S. G. Lipson, H. Lipson, and D. S. Tannhauser, *Optical Physics* (Cambridge U. Press, Cambridge, 1995).
11. J. Domnick, H. Ertel, and C. Tropea, "Processing of phase-Doppler signals using the cross-spectral density function," in *Proceedings of the Third European Symposium on Particle Characterization*, E. H. K. Leschonski, ed. (NurnbergMesse, Nurnberg, Germany, 1988), pp. 473–483.
12. F. Onofri, L. Bergounoux, J.-L. Firpo, and J. Mesguish-Ripault, "Velocity, size, and concentration measurements of optically inhomogeneous cylindrical and spherical particles," Appl. Opt. **38,** 4681–4690 (1999).
13. F. Onofri and A. Lenoble, "Sizing of single fibers under torsional stress," in *Proceedings of the Sixth International Congress on Optical Particle Characterization*, A. R. Jones, ed. (Institute of Physics, Bristol, UK, 2001), paper 7.7.
14. W. M. Farmer, "Measurement of particle size, number, density, and velocity using a laser interferometer," Appl. Opt. **11,** 2603–2609 (1972).
15. TSI Incorporated, 500 Cardigan Road, Saint Paul, Minn. 55126.
16. F. Onofri, "Prise en compte de la dimension finie des faisceaux d'éclairage en granulométrie optique: anémométrie phase Doppler—diagnostics des milieux diphasiques," Ph.D. dissertation (Université de Rouen, Rouen, France, 1995).
17. F. Onofri, G. Gréhan, and G. Gouesbet, "Electromagnetic scattering from a multilayered sphere located in an arbitrary beam," Appl. Opt. **34,** 7113–7124 (1995).
18. M. Mischenko, "Shape and Structure," in *Proceedings of the Sixth International Congress on Optical Particle Characterization*, A. R. Jones, ed. (Institute of Physics, Bristol, UK, 2001), paper 1.1.
19. A. A. Naqwi, R. P. A. Hartman, and J. C. M. Marijnissen, "Basic studies of electrohydrodynamic atomization using phase Doppler measurement technique, "Part. Part. Syst. Charact. **13,** 143–149 (1996).
20. A. Naqwi, "Sizing of irregular particles using a phase Doppler system," Part. Part. Syst. Charact. **8,** 343–349 (1996).
21. F. Onofri, "Etude numérique et expérimentale de la sensibilité de l'interfrométrie phase Doppler à l'état de surface des particles détectées," in *Proceedings of the Septième Congrés Francophone de Vélocimétrie Laser*, M. Elena, ed. (Université de Provence, Marseille, France, 2000), pp. 335–342.
22. C. Tropea, T.-H. Xu, F. Onofri, G. Gréhan, and P. Haugen, "Dual-mode phase Doppler anemometer," Part. Part. Syst. Charact. **13,** 165–170 (1995).

Interferometric Sizing of Single-Axis Birefringent Glass Fibers

Fabrice Onofri*, Anne Lenoble*, Stefan Radev, Hervé Bultynck***, Paul-Henri Guering***, Nicolas Marsault******

(Received: 30 October 2002; accepted: 13 March 2003)

Abstract

This paper deals with the on-line sizing of small diameter glass fibers (i.e. $d < 30$ μm) produced for textiles and reinforcement applications. Two models based on the Lorenz-Mie Theory are introduced to predict the basic light scattering properties and the response of a phase Doppler interferometer (PDI) to the sizing of infinite glass fibers. Among other parameters, these models take into account particular effects such as the fiber's single-axis birefringence and the fiber's refractive index dependence on its cooling rate (i.e. diameter). Both effects have a weak influence on the mean response of the PDI but a strong influence on the resonance structures of its phase-diameter relationship. Two optical set-ups were selected from a numerical optimization procedure and tested experimentally. Experimental results are presented demonstrating the validity of the models and the ability of the developed PDI set-ups to study some features of the fiber drawing-process: fluctuations of the fiber diameter when the nozzle is submitted to a convective perturbation and, when the fiber take-up velocity is modulated, the detection of hollow fibers.

Keywords: birefringence, fibers, interferometry, Lorenz-Mie theory

1 Introduction

The glass fibers used for textiles or for reinforcing plastic matrices are produced by a continuous formation process where a vertical jet is generated by a flow of molten glass through a cylindrical nozzle [1]. The jet is simultaneously cooled and attenuated under mechanical tension. The solidified jet is wound around a rotating wheel which provides the required tension. The formation process is clearly axi-symmetric. The jet, after a contraction factor of 250–500, reaches a constant diameter D for a distance from the nozzle exceeding 15 to 20 times the nozzle diameter ($D_0 \approx 2$ mm). For continuous fiber formation and a given chemical melt glass composition, the fiber diameter is mainly controlled through the adjustment of the melt glass fiberising temperature and the fiber take-up velocity V_z (imposed by the wheel rotation frequency). For commercial *E-glass* fibers, typical values for the fibersising temperature and the take-up velocity are in the range $T_0 = 1200$–$1300\,^{\circ}$C and $V_z = 10$–50 m/s. For a distance from the nozzle above ~ 500 times the nozzle diameter, the fiber temperature is only a few degrees above the ambient temperature.

In the manufacturing process, several hundred fibers are produced at the same time to form a bundle (i.e. strand). The distribution of the diameter of the fibers plays an important role in the physical performance of the final product. Thus, the ability to monitor the characteristics of small fibers is important from both manufacturing efficiency and quality control viewpoint. It is also suitable for the validation of basic models [2, 3] on the stability of the drawing process in respect to various perturbation sources: heterogeneity of the melt glass composition and temperature, fluctuations in the take-up velocity or in the hydrodynamic conditions of the drawing process (turbulence, radiative heat transfer, etc.). Consequently, there is actually a strong need for highly time-resolved measurements of the size of the fibers during the formation process.

* Dr. *F. Onofri*, Msc. *A. Lenoble*, IUSTI-UMR CNRS No. 6595, Université de Provence, Technopôle de Château-Gombert, 13453 Marseille Cedex 13 (France).
** Prof. *S. Radev*, IMECH, Bulgarian Academy of Sciences, 1113 Sofia (Bulgaria).
*** Dr. *H. Bultynck*, Dr. *P.-H. Guering*, Saint-Gobain Recherche, 93303 Aubervilliers Cedex (France).
**** Dr. *N. Marsault*, Saint-Gobain Vetrotex International, 73000 Chambéry (France).

 0934-0866/03/0506-0001 $ 17.50+.50/0

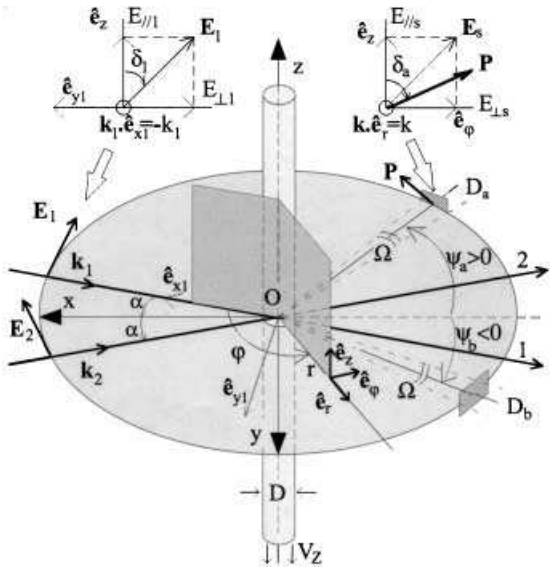

Fig. 1: Geometry for the scattering model.

The measurement methods for the diameter of the fibers currently in use in the fiberglass industry are mainly off-line techniques: weighting techniques (the mean diameter is deduced from a mass balance and the measurement of the length of the sample), air permeability experiments or scanning electron microscopy (SEM)[1]. The first two techniques give access only to average quantities whereas the last gives detailed information (shape, surface roughness and size) but on a very small scale, which limits its practical interest for the study of the stability of the process to various temporal perturbations. On-line optical techniques such as diffraction [4] or micro-video imaging techniques [2] are mostly used for basic research. Their resolution on the size of a single fiber is nevertheless limited, particularly when considering that, owing to the temperature and the dirty environment of the formation process, the receiving optics cannot be positioned close to the fiber to be measured.

It has been shown more recently [5–7] that, in the case of fibers with a circular cross-section and an isotropic material, the phase Doppler interferometric (PDI) technique has the potential to provide real-time measurements of the distribution of the diameter of single fibers. Mignon et al. [6] described the light-scattering properties of fibers using geometric optics, with special emphasis on the influence on the size measurement of the fiber's tilt angle compared with the plane of the laser beams. One limiting point in this earlier work is that, owing to the simple scattering model used, there is no prediction of the resonance structure and of the other non-linearities of the phase-diameter relationship (PDRS). Schaub et al. [7] developed a more rigorous model, based on the Lorenz-Mie theory (LMT), for the prediction of the PDI response to the sizing of infinite fibers with a possible tilt angle. Various optical configurations for the design of a PDI system dedicated to the sizing of glass fibers are also presented. This work was nevertheless mainly dedicated to the sizing of fibers used for thermal insulation. Consequently, their work does not take into account some effects characteristic of the formation process of reinforcement fibers: the high refractive index of *E-glass*, the mechanically induced birefringence of the fibers due to the high tension stress, the refractive index dependence of glass fibers on their size, etc.

In this paper, a rigorous light-scattering model and an optimization procedure taking into account all of the previously listed effects are introduced [8]. Section 2 presents the theoretical model developed to predict the basic light-scattering properties of a single fiber. Section 3 presents the model for the response of a PDI system when sizing an infinite birefringent fiber. Numerical results concerning the influence of various parameters on the PDI response are presented in Section 4. Section 5 presents the experimental set-ups and results carried out to validate the models. Section 6 gives the conclusions.

2 Scattering Model

2.1 Light Scattering by an Infinite Right Circular Homogeneous Cylinder

In the laboratory coordinate system (Oxyz), the fiber is considered as an infinite and homogeneous right circular cylinder with axis z and diameter D (see Figure 1). A local Cartesian coordinate system (Ox_1y_1z) is defined as the incident wave 1 with wavevector $\mathbf{k_1}$ propagates along (Ox_1), i.e. $\mathbf{k_1} = -k_1\mathbf{e_{x1}}$. ($Ox_1y_1z$) can be deduced from (Oxyz) by a rotation around the z-axis of the angle $-\alpha$. The incident wave is considered as a linearly polarized harmonic plane wave with frequency ν_1 and wavelength λ. The electric field vector $\mathbf{E_1}$ of the incident wave can be divided into a component $E_{\parallel}\mathbf{e}_z$ parallel to the (x_1z) plane and a component $L - E_{\perp}\mathbf{e}_{y1}$ perpendicular to the (x_1z) plane. The polarization angle of the incident electrical field is referred to the angle δ_1 between the z-axis and the direction of the incident electric field vector $\mathbf{E_1}$ that is, we write the incident field as

$$\mathbf{E}_1 = (E_{\parallel 1}\cos\delta_1\mathbf{e_z} - E_{\perp 1}\sin\delta_1\mathbf{e}_y)\exp[i(\mathbf{k}_1\cdot\mathbf{r}_1 - 2\pi\nu_1 t)]. \quad (1)$$

A cylindrical coordinate system ($Or\phi z$) is introduced where the scattering angle ϕ is the angle between the x_1-axis and the scattering direction $\mathbf{e_r}$. The scattered field, subscript s, is the sum of two perpendicular components:

$$\mathbf{E_s} = E_{\|s}\mathbf{e_z} + E_{\perp s}\mathbf{e}_{\phi}. \quad (2)$$

Following Bohren and Huffman [9], under normal incidence (the light is only scattered in the plane $z=0$) and in the far field, with $\theta = \pi - \phi$, the asymptotic expressions for the scattered field are given by

$$\begin{pmatrix} E_{\|s}(r,\theta,t) \\ E_{\perp s}(r,\theta,t) \end{pmatrix} = \exp\left[\frac{3\pi i}{4}\right]\sqrt{\frac{2}{\pi kr}} \times \begin{pmatrix} T_1 & 0 \\ 0 & T_2(\theta) \end{pmatrix} \begin{pmatrix} E_{\|1}\cos\delta_1 \\ E_{\perp 1}\sin\delta_1 \end{pmatrix} \exp[kr - 2\pi\nu_1 t]. \quad (3)$$

The two terms $T_1(\theta)$ and $T_2(\theta)$ of the amplitude scattering matrix read

$$T_1(\theta) = \sum_{n=-\infty}^{n=+\infty} b_{nI}\exp[-in\theta] = b_{0I} + 2\sum_{n=1}^{+\infty} b_{nI}\cos(n\theta).$$
$$T_2(\theta) = \sum_{n=-\infty}^{n=+\infty} a_{nII}\exp[-in\theta] = a_{0II} + 2\sum_{n=1}^{+\infty} a_{nII}\cos(n\theta). \quad (4)$$

where b_{nI} and a_{nII} are the external scattering coefficients for an infinite and homogeneous right circular cylinder and for the incident beam components $\mathbf{E}_{\|1}$ and $\mathbf{E}_{\perp 1}$, respectively. These functions, which describe the particle properties (shape, diameter and refractive index), are complex functions which require calculations of the Hankel and Bessel functions of the first kind with their derivatives [9]. It can be useful to study the degree of linear polarization of the light scattered by the fiber, particularly for the diagnosis of birefringent fibers. To do so, part of the light that is scattered by the fiber is collected by a detector composed of a collimating lens, passed through a linear polarizer, and finally focused on to a photodetector. In Figure 1 and for detector D_a, the polarizer axis **P** makes an angle δ_a with $\mathbf{e}_z$. Finally, the scattered field after the linear polarizer reads as

$$\begin{pmatrix} E_{\|s} \\ E_{\perp s} \end{pmatrix}_P = \begin{pmatrix} \cos^2\delta_a & \sin\delta_a\cos\delta_a \\ \sin\delta_a\cos\delta_a & \sin^2\delta_a \end{pmatrix} \begin{pmatrix} E_{\|s} \\ E_{\perp s} \end{pmatrix}. \quad (5)$$

The scattered energy at position (rθz), over the time duration $1/\nu_1$, may be calculated with the help of the Poynting vector:

$$\langle S_s\rangle_{1/\nu_1} = \frac{1}{2}\mathrm{Re}\{E_s \times H_s^*\}. \quad (6)$$

In a free homogeneous and non-magnetic medium with magnetic permeability μ_0, the Poynting vector reduces to

$$\langle S_s\rangle_{1/\nu_1} = \frac{1}{4\pi\mu_0\nu_1}\mathrm{Re}\{\mathrm{E_s} \times (\mathrm{k} \times \mathrm{E_s})^*\} = \frac{\mathrm{k}}{4\pi\mu_0\nu_1}\mathrm{E_s}\mathrm{E_s^*}. \quad (7)$$

2.2 Refractive Index Dependence on the Cooling Rate

There have been several reports [1, 10] that the mechanical and optical properties of the fibers depend not only on the chemical composition of the initial melt glass but also on their formation conditions and mainly on their *cooling rate*. In fact, during the drawing process, the cooling rate can be as high as $-100\,000\,^{\circ}$C/s for the smallest fibers. This phenomenon has a great influence on the structural relaxation of the fiber material.

Corpus and Gupta [10] developed a simple model to predict the refractive index dependence on the fiber's cooling rate. It is based on the following three considerations: (*i*) m depends on the fictive temperature of a glass T_f, (*ii*) T_f of a glass depends on its cooling rate q, and (*iii*) the maximum q experienced by a fiber is inversely proportional to D^2. Corpus et al. [10] found good agreement between their model and experimental data obtained for a soda-lime-silica melt of NBS-170 composition.

From this work, we derived the following analytical relation for the dependence of the refractive index of the fiber on its cooling rate (which reduces to a dependence on its diameter):

$$m(D)_T = \sqrt{\frac{\beta_T(\theta_T+2)\ln(D) + \alpha_T(\theta_T+2) - 1}{\beta_T(\theta_T-1)\ln(D) + \alpha_T(\theta_T-1) - 1}}. \quad (8)$$

To estimate the coefficients α_T, β_T and θ_T for *E-glass*, we used the experimental results of Clementin-de-Leusse [11]. A *non-linear* curve-fitting procedure was used to fit the raw data points with Eq. (8) and we have found $\alpha_T = 119.68047$, $\beta_T = -82.49331$ and $\theta_T = 3.10733$.

Figure 3 (a) shows the corresponding evolution. A strong increase in the refractive index is observed for small fibers ($D < 15$ μm), with $\Delta m = +0.0143$ over the size range $D = 5-45$ μm. Note that in this paper, owing to the high cooling rate of reinforcement fibers, the fiber is considered to be at ambient temperature at the measurement location (see Section 1). If it is not the case, the coefficients of Eq. (8) should be recalculated to take into account the bulk glass refractive index dependence on temperature.

2.3 Refractive Index Dependence on Drawing Stress

During the formation process, the fiber is subjected to a high mechanical tension, F. This tension, or drawing stress, is typically 0.497 and 0.36 g for fibers of 5 and 10 μm, respectively (i.e. a tension of 632 and 115 kg/cm^2). It can be significantly higher according to the drawing conditions and the fiber path between the nozzle and the

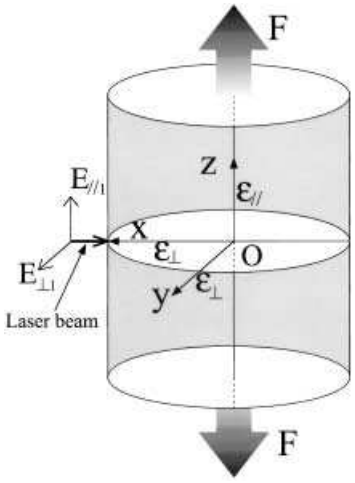

Fig. 2: Geometry for the single-axis birefringent fiber model.

rotating wheel. Under such stress, the fiber material may be birefringent. As sketched in Figure 2, it is expected to be single-axis (optical axis along the fiber axis) owing to the symmetry of the drawing process. The fiber's birefringence, which is likely to vanish when it is cut, but not completely [1], has to be taken into account to predict the light-scattering properties of the fiber during the process. Following the previous remarks the fiber material permittivity tensor is

$$\begin{pmatrix} D_x \\ D_y \\ D_z \end{pmatrix} = \begin{pmatrix} \varepsilon_\perp & 0 & 0 \\ 0 & \varepsilon_\perp & 0 \\ 0 & 0 & \varepsilon_\parallel \end{pmatrix} \begin{pmatrix} E_x \\ E_y \\ E_z \end{pmatrix} \tag{9}$$

where $\varepsilon_\perp$ and $\varepsilon_\parallel$ are the two electrical permittivity constants and D_x, D_y, D_z, the three components of the electrical displacement vector.

Neglecting absorption of glass in the visible range, the fiber's extraordinary refractive index, $m_\parallel$, and the fiber's ordinary refractive index, $m_\perp$, can be related to the electrical permittivity constants with

$$m_\perp = \sqrt{\frac{\mu\varepsilon_\perp}{\mu_0\varepsilon_0}},\ m_\parallel = \sqrt{\frac{\mu\varepsilon_\parallel}{\mu_0\varepsilon_0}}. \tag{10}$$

Assuming that the fiber birefringence $(m_\parallel - m_\perp)$ is proportional to the tension F applied to the fiber, we find that

$$m_\parallel - m_\perp = -m_\perp \sigma(T_0)\left(\frac{1.29\cdot 10^4 F}{D^2}\right) \tag{11}$$

where F is the drawing tension applied to the fiber in grams, $\sigma(T_0)$ the optical stress coefficient of the fiber material and D the diameter of the fiber in micrometers. $\sigma(T_0)$ and F depend on the formation process conditions, and mainly on the nozzle temperature, T_0, which has a strong influence on the melt glass viscosity. For the drawing of *E-glass*, with a nozzle temperature of $T_0 = 1200\,^\circ$C, the optical stress coefficient is $\sigma(T_0)\cdot 6.1\cdot 10^{-7}$ MPa^{-1}. By using Eq. (11) we find that the difference between the two refractive indices, $m_\parallel - m_\perp$, is $2.4\cdot 10^{-4}$ and $4.3\cdot 10^{-5}$ for a fiber of diameter 5 and 10 μm, respectively.

Figure 3(b) presents the evolution of the extraordinary refractive index, $m_\parallel$, versus the diameter of the fiber (i.e. tension). For this purpose, Eq. (11) was used and the fiber's tension was deduced from the measurement of the oscillation frequency of the fiber when it is perturbed during the formation process (this last procedure will be detailed in future work). In Figure 3(b) the effect of tension on the fiber refractive index is more pronounced for small fibers $(D < 15\ \mu m)$. The change in the fiber's refractive index is nevertheless small, i.e. $\Delta m_\parallel = +0.0008$ over the size range $D = 5-45$ μm. Note that here, this measured tension includes that attributed to the melt glass viscosity, the drag force, the surface tension, etc., as well in addition to that introduced by the mechanical friction of the fiber along its path up to the measuring point.

In Eq. (3), the scattered field component $E_{\parallel s}$ depends only on the external scattering coefficients b_{nI} and $E_{\perp s}$ depends only on the external scattering coefficients a_{nII}. In fact, the scattering coefficients themselves depend on the laser wavelength, the fiber size and refractive index (relative to the external medium refractive index). Therefore, to predict the scattered field by a single-axis birefringent fiber, we only have to use Eqs. (3) and (5) (if a linear polarizer is used) with b_{nI} $(\lambda, D, m = m_\parallel)$ and a_{nII} $(\lambda, D, m = m_\perp)$ (see Section 4).

3 Model for the Phase Doppler Response

To model the response of a PDI system when measuring a single-axis birefringent fiber under normal incidence, one has to compute the interference field pattern produced on the detector aperture when the fiber is located at the crossing of two TM00 laser beams, 1 and 2. It is assumed that the waist of each beam is located at the beams' crossing, with a diameter far larger than that of the fiber. These conditions being fulfilled, we can use the previous results obtained for incident plane waves [12]. The fiber is assumed to have only small displacements in the (Oxy) plane. This condition is necessary to be under the remote detector approximation (i.e. small displacements of the fiber do not change the scattering angles). It may have a high velocity along the z-axis (as usual in the drawing process). To take into account beam 2, we introduce an additional local Cartesian coordinate

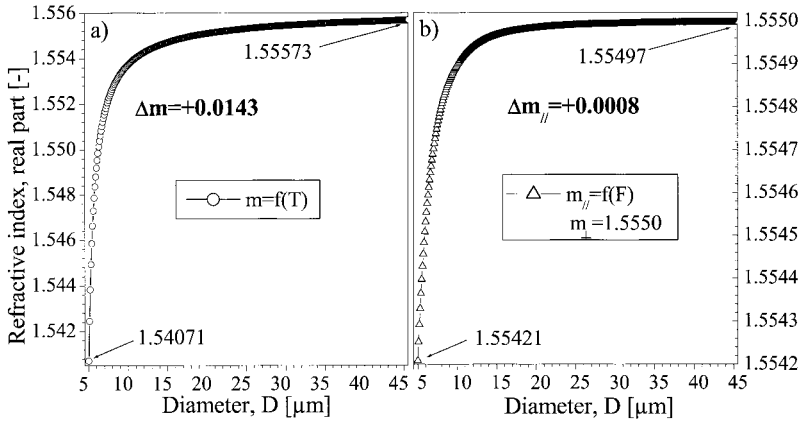

Fig. 3: Evolution of the fiber refractive index with (a) the cooling rate and (b) the mechanical tension.

system (Ox_2y_2z) as previously done for beam 1. Each beam has a given polarization angle, δ_1 and δ_2, and a given frequency ν_1 and ν_2. Note that in the principle of the PDI technique, the two laser beams are frequency shifted in relation to each other with Bragg cells or with a rotating transmission grating [13–14]. Among other features, this allows one to obtain frequency-modulated signals although the particle is fixed in the probe volume. We now consider a point detector D_a with a polarizer angle δ_a, located in the (Oxy) plane, distant by r from the fiber and positioned at elevation angle ψ_a (see Figure 1 (a)). In this configuration detector D_a is located at the following scattering angles: for beam *1*, $\theta_1 = \psi_a + \alpha$ and for beam *2*, $\theta_2 = \psi_a - \alpha$. Using Eq. (2) the scattered field collected by the detector D_a reads

$$\mathbf{E}_s(\psi_a) = [E_{\parallel s1}(\psi_a+\alpha) + E_{\parallel s2}(\psi_a-\alpha)]\mathbf{e_z} + [E_{\perp s1}\ (\psi_a+\alpha) + E_{\perp s2}(\psi_a-\alpha)]\mathbf{e}. \tag{12}$$

For the case where $\nu_1/\nu_2 \sim 1$ and with a mean frequency $\nu = (\nu_1+\nu_2)/2$, the Poynting vector reduces to

$$\mathbf{S}_s = \frac{\mathbf{k}}{2\pi\mu_0\nu}\left[|E_{\parallel s1}|^2 + |E_{\parallel s2}|^2 + |E_{\perp s1}|^2 + |E_{\perp s2}|^2 + 2\mathrm{Re}\left\{E_{\parallel s1}E^*_{\parallel s2} + E_{\perp s1}E^*_{\perp s2}\right\}\right]. \tag{13}$$

The previous expression can be reformulated in a more convenient form:

$$\mathbf{S}_s = \frac{\mathbf{k}}{4\mu_0\pi\nu}(G + \mathrm{Re}\{H\exp[-2i\pi\nu_D(t)]\}) \tag{14}$$

with

$$G = |E_{\parallel s1}|^2 + |E_{\parallel s2}|^2 + |E_{\perp s1}|^2 + |E_{\perp s2}|^2 \tag{15}$$

$$H = E_{\parallel s1}E^*_{\parallel s2} + E_{\perp s1}E^*_{\perp s2} \tag{16}$$

$$\nu_D(t) = (\mathbf{k}_1 - \mathbf{k}_2)\cdot\mathbf{r} + \nu_s = -4\pi\ \sin\ \alpha v_y(t) + \nu_s. \tag{17}$$

In Eqs. (15) and (16), expressions for the scattered-field components must be replaced by their proper expressions deduced from Eqs. (3) and (5) with, for instance, for beam *1* and detector D_a:

$$E_{\parallel s1} = \exp\left[\frac{3\pi i}{4}\right]\sqrt{\frac{2}{\pi kr}}[\cos^2\delta_a T_1(\psi_a+\alpha)E_{\parallel 1}\cos\delta_1 + \sin\delta_a\cos\delta_a T_2(\psi_a+\alpha)E_{\perp 1}\sin\delta_1]$$

$$E_{\perp s1} = \exp\left[\frac{3\pi i}{4}\right]\sqrt{\frac{2}{\pi kr}}[\sin\delta_a\cos\delta_a T_1(\psi_a+\alpha)E_{\parallel 1}\cos\delta_1 + \sin^2\delta_a T_2(\psi_a+\alpha)E_{\perp 1}\sin\delta_1]. \tag{18}$$

In Eq. (17), the scalar product $(\mathbf{k}_1 - \mathbf{k}_2)\cdot\mathbf{r}$ has been reformulated in a time-dependent form. When the fiber moves slightly in the (Oxy) plane the previous term depends on the fiber velocity component along the y-axis, $V_y(t)$. This term is responsible for a frequency shift of the collected signal, the so-called "heterodyne Doppler frequency". During the formation process, any fluctuation in the position of the fiber in respect to the y-axis may be detected from the fluctuation of ν_D.

For a physical detector, Eq. (14) has to be integrated over the receiving aperture Ω. As sketched in Figure 1, under normal illumination, the integrating angle reduces to $[\psi_a - \Omega/2,\ \psi_a + \Omega/2]$. Thus, assuming a detector with a linear aperture and with a linear response (electrical signal proportional to the intensity of the light collected), the electrical signal output from this detector is

$$I(t) = \int_{\Omega} |S_s(t)|d\psi. \tag{19}$$

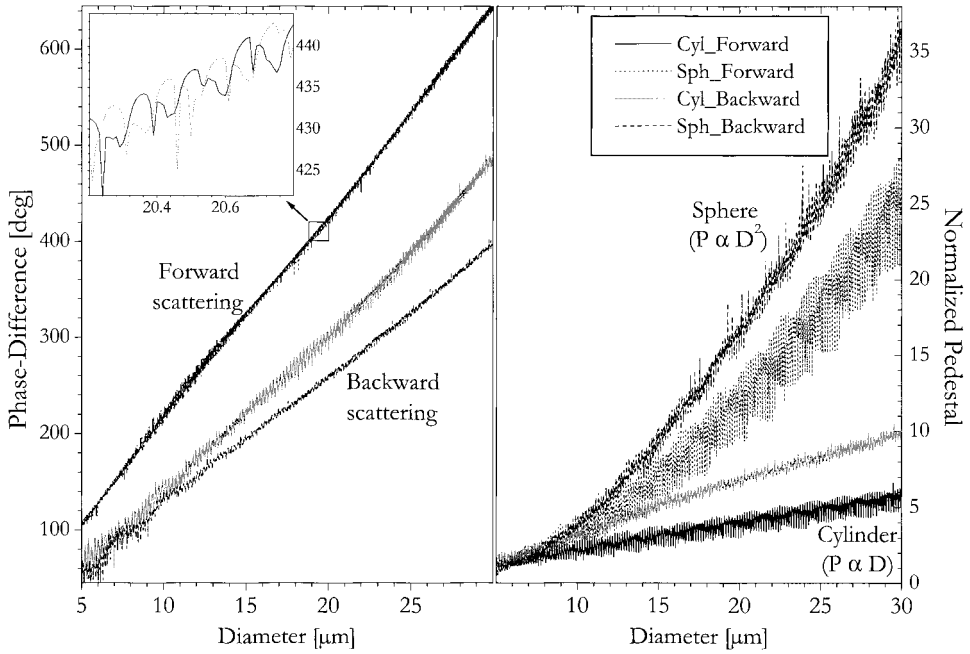

Fig. 4: Comparison of the PDRS and the pedestal calculated for cylindrical and spherical particles. Forward scattering domain, set-up (A); and backward scattering domain, set-up (D). The pedestal is given for detectors located at $\psi = 72.5^\circ$ and $\psi = 162.5^\circ$. It is normalized by the value obtained for a 5 μm particle.

Using Eq. (14) the previous expression can be reformulated in the following form [15]:

$$I(t) = \langle G \rangle_\Omega + 2\sqrt{\langle H_i \rangle_\Omega^2 + \langle H_r \rangle_\Omega^2} \times \cos\left[\tan^{-1}\left(\langle H_i \rangle_\Omega / \langle H_i \rangle_\Omega\right) - 2\pi \nu_D t\right] \quad (20)$$

where the terms in brackets mean integrated quantities over the detector-receiving aperture of the functions introduced in Eqs. (15) and (16), with

$$\langle G \rangle_\Omega = \int_\Omega G d\psi \langle H_r \rangle_\Omega = \int_\Omega \mathrm{Re}\{H\} d\psi$$

$$\langle H_i \rangle_\Omega = \int_\Omega \mathrm{Im}\{H\} d\psi. \quad (21)$$

We now introduce the new quantities *P, V,Φ,* usually known as the Doppler signal pedestal, visibility and phase, respectively, with

$$P = \langle G \rangle_\Omega / (2\pi \mu_0 \nu r) \quad (22)$$

$$V = 2\sqrt{\langle H_i \rangle_\Omega^2 + \langle H_r \rangle_\Omega^2} \,/ \langle G \rangle_\Omega \quad (23)$$

$$\Phi = \tan^{-1}(\langle H_i \rangle_\Omega + \langle H_i \rangle_\Omega). \quad (24)$$

Finally, Eq. (20) can be reformulated to obtain the equation of a phase Doppler signal:

$$I(t) = P[1 + V\cos(2\pi \nu_D t + \Phi)]. \quad (25)$$

The phase Φ in Eq. (25) is an absolute phase which, in the remote detector approximation and for plane wave illumination, depends only on the optical setup and the properties of the fiber. As an absolute phase, it cannot be measured directly. As a result, in the principle of the PDI technique, two detectors D_a and D_b or more are used to measure the phase difference between the two Doppler signals. An alternative solution is proposed in [16]. From the two detectors, subscripts *a* and *b*, positioned at elevation angles ψ_a and ψ_b, we obtain two Doppler signals: $I_a(t)$ and $I_b(t)$. The phase difference between $I_a(t)$ and $I_b(t)$, i.e. $\Phi_{ab} = \Phi_a - \Phi_b$, can be measured, for instance, with the help of the cross-spectral density function. The dependence of Φ_{ab} on the diameter of the fiber, $\Phi_{ab} = f(D)$, is usually referred as the theoretical phase-diameter relationship (PDRS). According to the principle of the PDI technique, the size of the measured particle (sphere or fiber in the present case) is deduced from the measurement of the phase difference Φ_{ab} and from the knowledge of the PDRS.

The validation of the previous models is performed in three ways. First, we compare our predictions with the predictions of a code devoted to homogeneous and inhomogeneous spherical particles [5, 15 – 18]. Figure 4 shows a comparison between the PDRS and the pedestal calculated for cylindrical and spherical particles and that for an optical set-up working in the forward scattering

domain and for an optical set-up working in the backward scattering domain. The results are in good agreement for the forward optical set-up and in rather poor agreement for the backward set-up. Consequently, in the backward scattering region, PDI codes devoted to spheres should be used carefully when they are used for cylinders even when considering normal illumination. Note that in Figure 4, for cylindrical particles, the signal pedestal increases proportionally with the particle diameter, whereas for spheres, it increases proportionally with the square of the diameter. Second, we compared our results with the results found in the literature for homogeneous fibers with a lower refractive index based on geometrical optics [5, 6] and on the Lorenz-Mie theory [7]. Perfect agreement is found between the results. Third, we made comparisons with experimental data, as will be detailed in Section 5.

4 Numerical Results

4.1 Refractive Index Dependence on the Cooling Rate

The influence of the fiber refractive index dependence on its size (i.e. the cooling rate) can be estimated from Figure 5. In this figure the theoretical PDRS is calculated for a PDI type (D) (see below for details) when Eq. (8) is used, $\Phi_{ab}^{T}(D)$ or not, $\Phi_{ab}^{N}(D)$ (constant refractive index, m = 1.5550). The difference between these two responses, $\Phi_{ab}^{T}(D) - \Phi_{ab}^{N}(D)$, is also shown. Eq. (8) introduces a change in the refractive index from 1.5407 to 1.55573 for a fiber in the size range $D = 5 - 45$ μm. In both cases the PDRS is almost linear, except for a break in the slope for diameters around $D \approx 30$ μm, which can be explained by the presence of a local minimum of the signal visibility [15]. The refractive index dependence on the fiber size seems to have no significant influence on the mean PDRS. It nevertheless has some influence on its *resonance structure:* a frequency shift (which appears to be a phase shift) is observed for small diameters $D < 12$ μm and large diameters $D > 30$ μm (see the top left corner of Figure 5). This last remark is confirmed by the evolution of the amplitude of the phase difference, $\Phi_{ab}^{T}(D) - \Phi_{ab}^{N}(D)$. For small diameters, this behavior can be understood from the sharp evolution of the refractive index up to $D = 12$ μm. For larger diameters, this can be understood by the increase of the total optical thickness of the fiber. For intermediate diameters the difference is weaker. This behavior may be attributed to the fact that, in this region, the two resonance structures appear to be almost in-phase, although they have different frequencies. For all the size range $D = 5 - 43$ μm, the standard deviation of the phase difference $\Phi_{ab}^{T}(D) - \Phi_{ab}^{N}(D)$ is 3.99°. This means that, by neglecting the refractive index dependence on the fiber cooling rate, we introduce an additional mean error of $\Delta\sigma_{ab-D}^{Lin} = 0.24$ μm to the estimation of the mean diameter of the fiber (see below for details). Observe that for this particular geometry, the resonance structure of the PDRS, which is characteristic of the morphological dependent resonances (MDRs) [9], has a frequency of about 0.205 μm/μm. This last frequency is determined from the Fourier spectrum of the PDRS, not presented here, which exhibits a large frequency peak for this particular frequency.

The influence of the fiber's axial tension on the PDRS can be estimated from Figure 6. The difference between the PDRSs is plotted when Eq. (11) is used (fiber under tension, i.e. during the formation process) and the PDRS when Eq. (11) is not used (cut fiber, i.e. off-line measurements). For this purpose, the refractive index dependence on tension presented in Figure 3 (b) is used for the size range 5 – 7 μm. Large peaks can be observed in this figure. They correspond to sharp resonances (between $+24°$ and $-45°$), which occur for different diameters and refractive indices (i.e. axial stress in the present case). The mean standard deviation between the two relationships is about 3.29°. As previously, this means that by neglecting the effect of tension on the fiber optical properties, we introduce a mean error of $\Delta\sigma_{ab-D}^{Lin} = 0.20$ μm to the estimation of the fiber's mean diameter. For the size range, $D = 5 - 43$ μm, this addition mean error is only of $\Delta\sigma_{ab-D}^{Lin} = 0.06$ μm (i.e. standard deviation in the phase: *0.94°*). Nevertheless for some particular diameters, the error can be significantly higher (up to 1.43 and −2.69 μm*)* for diameters corresponding to sharp resonances in Figure 6.

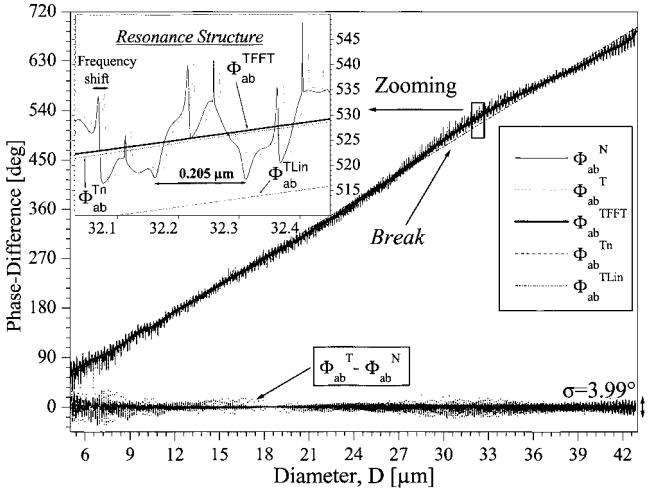

Fig. 5: Comparison of the PDRS of set-up (D) when the effect of the refractive index dependence with the cooling rate is taken into account or not.

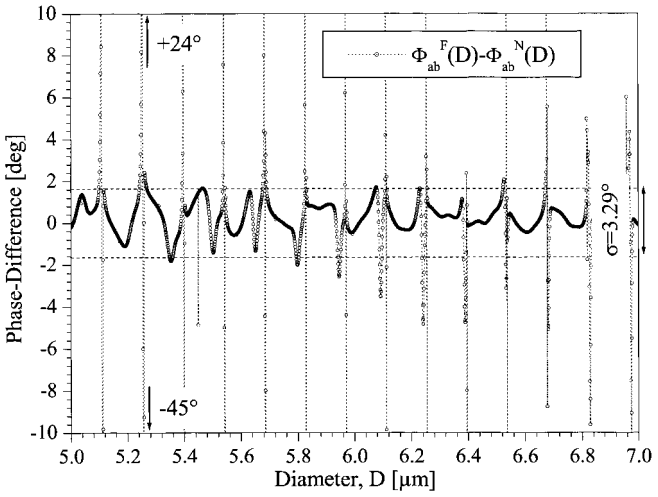

Fig. 6: Difference between the PDRS of set-up (D) when the effect of single-axis birefringence (tension) is taken into account or not.

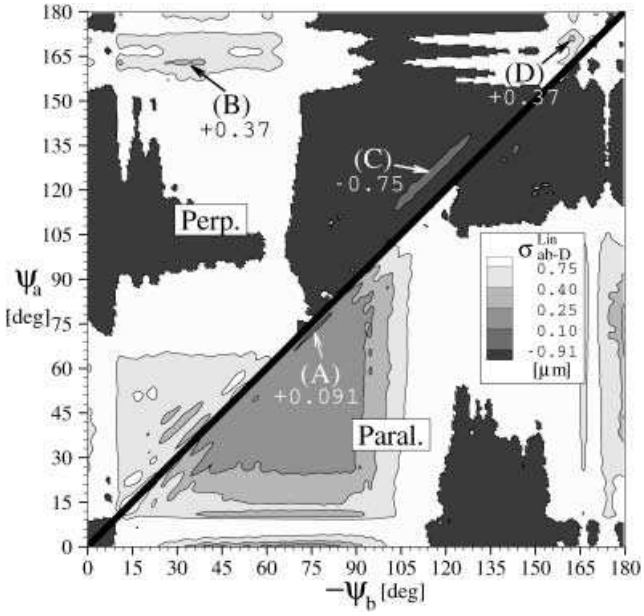

Fig. 7: Iso-level map of the estimated mean error in the fiber diameter versus the elevation angle of the two detectors and the polarization state of the incident beams. Top left corner: perpendicular to the scattering plane. Bottom right corner: parallel to the scattering plane.

4.2 Optimization of the PDI Set-up

The objective of the numerical optimization of the optical set-up of a PDI system has two key points: (*i*) the reduction of the oscillatory behavior of the PDRS, to ensure a higher accuracy in the measurement of the fiber size; and (*ii*) the reduction of the bulky design of the optical set-up to fulfil constraints imposed by the industrial environment. This optimization is clearly a multi-parameter study as the phase difference $\Phi_{ab}(D)$, and also the signal pedestal and visibility, depend on the optical parameters of the IPD, $\lambda, \delta_1, \delta_2, \alpha, \psi_a, \psi_b, \Omega, \delta_a, \delta_b$ and the properties of the fiber, D, composition, F, T_0, etc. Obviously, not all of these parameters are of the same importance, so we need to define a criterion to quantify the relative importance of each one. There are many ways to do so. In the present work, we used the following procedure:

- The phase Doppler LMT based code is used to compute the theoretical PDRS, $\Phi_{ab}(D)$, for the set of parameters under study and for a fiber within the size range $D = 5-30$ μm or $D = 5-45$ μm.
- A fitting procedure is used to obtain a one to one PDRS which fits the theoretical PDRSs. Three fitting functions were tested for this purpose: (*i*) a linear relationship with slope b and ordinate a, $\phi_{ab}^{Lin}(D) = a + bD$; (*ii*) a polynomial function of degree n with coefficients λ_q, $\phi_{ab}^{n}(\mathrm{D}) = \sum_{0}^{n} \lambda_q D^q$; (*iii*) a low-pass filtered PDRS calculated with a Fourier transform with a cut-off frequency slightly below that of the resonance structures, $\phi_{ab}^{FFT}(D) = TF^{-1}[\ TF[\Phi_{ab}(D)]^* \mid H(\nu_D - \nu_{Dcut\text{-}off}) \mid]$. Figure 5 shows a comparison between the theoretical PDRS, $\Phi_{ab}(D)$, and the fitted PDRSs, $\phi_{ab}^{FFT}(D)$, $\phi_{ab}^{n}(D)$ and $\phi_{ab}^{Lin}(\mathrm{D})$. The first two fitted PDRSs follow the large-scale fluctuations of the theoretical one whereas the linear one does not take into account such evolutions. The linearized PDRS is clearly a poor estimator of the real evolution of the theoretical PDRS. In Figure 5 the cut-off frequency is set to $\nu_{Dcut\text{-}off} = 1/0.210$.
- The standard deviation between the theoretical PDRS and the fitted ones is calculated with, for the linear fitting, $\sigma_{ab-\phi}^{Lin} = f(\Phi_{ab}(D) - \phi_{ab}^{Lin}(D))$. This standard deviation takes account of the deviation from linearity of the PDRS and also the amplitude of the resonance structure. For calculations presented in Figure 5, we found $\sigma_{ab-\phi}^{Lin} = 9.03^\circ$, $\sigma_{ab-\phi}^{n=9} = 5.60^\circ$ and $\sigma_{ab-\phi}^{FFT} = 5.51^\circ$.
- Finally, this standard deviation in the phase difference can be used to estimate the mean error in the size of the fiber that is introduced when the fitted PDRSs are used instead of the real one (i.e. we neglect the resonance structure), with for the linear fitting case $\sigma_{ab-D} = \sigma_{ab-\phi}/\mathrm{b}$. For calculations presented in Figure 5, we find $\sigma_{ab-D}^{Lin} = 0.541$ μm ($\mathrm{a} = -27.67^\circ$, $\mathrm{b} = 16.75^\circ/$μm), $\sigma_{ab-D}^{n=9} = 0.354$ μm and $\sigma_{ab-D}^{FFT} = 0.352\ \mu m$. The filtered PDRS gives the best results.

Figure 7 presents an iso-level map of the estimated mean size error σ_{ab-D}^{Lin}, for fibers in the size range 5–30 μm, versus the elevation angle of both detectors. The top left

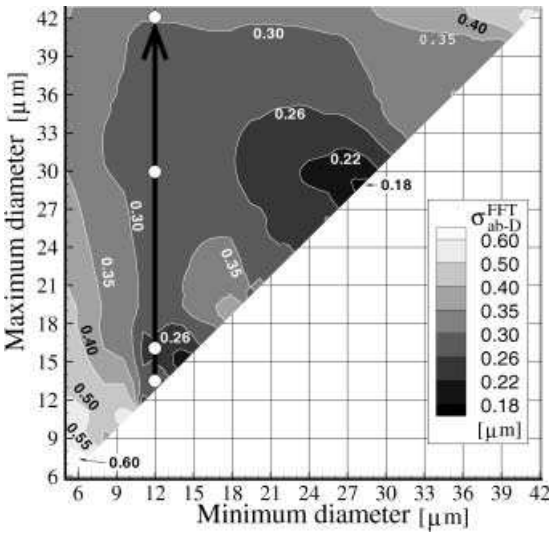

Fig. 8: Iso-level map of the estimated mean error on the fiber diameter for set-up (D) versus the boundary of the fibers size range: minimum and maximum diameter.

corner corresponds to incident beams with polarization perpendicular to the scattering plane (Oxy) and the bottom right corner corresponds to incident beams with polarization parallel to the scattering plane. In all calculations in this paper and also for the experimental set-ups, the half-beam angle is fixed at $\alpha = 1.11^\circ$, with $\lambda = 0.6328$ μm, to give a reasonable dynamic on the measured diameter. For the detector half-beam aperture, there exists an optimum aperture angle [19] which is about $\Omega/2 = 6^\circ$. Nevertheless, for experimental considerations (spherical aberrations) it is fixed here at $\Omega/2 = 5.15^\circ$.

Four zones (A – D), corresponding to a minimum size error, can be identified in this map. They correspond to four types of optical set-ups. Observe that here, for drawing considerations, the estimated error is set negative when the slope of the PDRS is negative (dominant reflective scattering process) and it is set positive when the corresponding slope is positive (dominant refractive scattering process), with:

- Set-up (A), for parallel polarization, the two detectors are located in the forward scattering region in a more or less symmetrical way with respect to the (Ox) axis, i.e. $\psi_a = 75.8^\circ$ and $\psi_b = -72.8^\circ$. In this region, the dominant scattering process is a refraction process with $\sigma^{Lin}_{ab-D} = 0.091$ μm and $b = 22.09^\circ/\mu$m.
- Set-up (B), one detector is located in the so-called rainbow regions $\psi_a = 163.0^\circ$ (refracted rays with one or two internal reflections) and the other one in the forward region $\psi_b = -33.0^\circ$ (single refraction process). For this geometry, with a bulky design, we find that $\sigma^{Lin}_{ab-D} = 0.37$ μm and $b = 19.33^\circ/\mu$m.
- Set-up (C), the two detectors are on both sides of the optical axis and more precisely in the so-called Alexander dark band (the dominant scattering process is reflection), $\psi_a = 125.61^\circ$ and $\psi_b = -115.3^\circ$. This scattering mode is "usually considered" as the least sensitive to any change in the fiber material homogeneity. Nevertheless, in addition to its bulky design, this arrangement provides the lowest accuracy in the fiber size, $\sigma^{Lin}_{ab-D} = 0.75$ μm with $b = -15.27^\circ/\mu$m.
- Set-up (D), the two detectors are on both sides of the optical axis, in the near-backward region and more particularly in the rainbows region. This optical arrangement is clearly the most compact one, $\psi_a = 162.5^\circ$ and $\psi_b = -166.7^\circ$, and provides an acceptable accuracy in the size of the fiber, $\sigma^{Lin}_{ab-D} = 0.37$ μm, $\sigma^{Lin}_{ab-D} = 0.54$ μm with $b = 16.75^\circ/\mu$m.

Owing to the resonances, the size resolution depends also on the size range considered. Figure 8 presents an iso-level map of the estimated error in the fiber diameter, σ^{FFT}_{ab-D}, for an IPD of type (D), versus the boundary of the fibers size range: minimum and maximum diameter. The maximum size range is $D = 5 - 45$ μm. As an example, the estimated mean error is $\sigma^{FFT}_{ab-D} = 0.30$, 0.26, 0.30 and 0.35 μm for a fiber whose diameter evolves in the size ranges $D = 12 - 14$, $12 - 17$, $12 - 30$ and $12 - 42$ μm, respectively.

5 Experimental Set-up and Results

5.1 Experimental Set-up

The optical set-ups (A) and (D) were tested experimentally. The output of *2.5 mW* linearly polarized helium-neon laser ($\lambda = 0.6328$ μm) is focused on to a rotating transmission diffraction grating. The diffracted beams are collimated with a spherical lens and a beam stop is used to stop all the diffracted beams with an order differing from ± 1. The two out-coming beams are collimated and focused by a transmission lens with a focal length of 400 mm. The probe volume diameter is ~ 300 μm. The use of a half-wave retardation plate and the selection of the diffraction gratings rotating velocity allow the control of the laser beam polarization and the laser beam frequency shift ν_s. The light scattered by the fiber, when it is in the probe volume, is collected by two receiving optics composed of a set of two achromatic lenses, with a collection angle $\Omega/2 = 5.15^\circ$ and a focal length of 400 mm. The collected light is focused on two multimode polymer fibers. Two pre-amplified avalanche photo diodes (APDs), with 0.1 kHz – 10 MHz bandwidth, are used for the conversion of optical signals into electrical signals. Figure 9 shows a photograph of

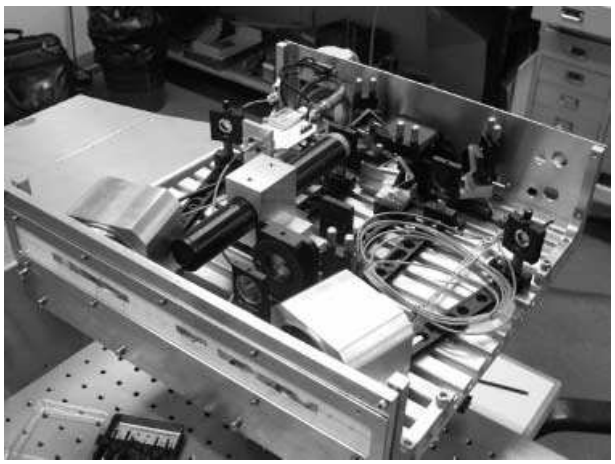

Fig. 9: Photograph of the system FIBS. All the optics and the hardware are included in the head.

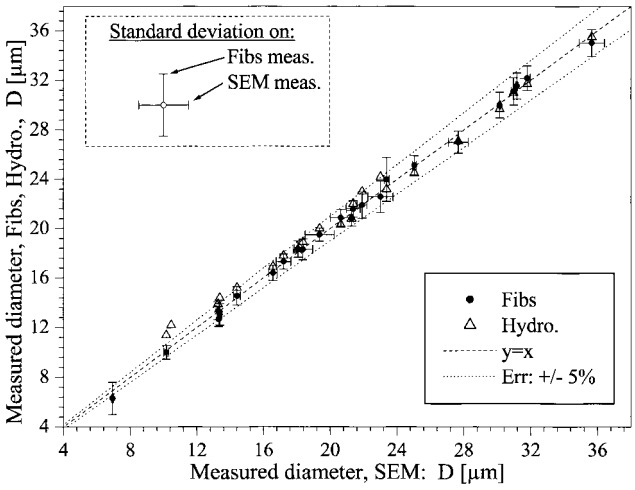

Fig. 10: Comparison between the fiber's mean diameter measured during the formation process with FIBS, and from hydrodynamic calculations, versus off-line SEM measurements on fixed fibers.

system (D), referred to further on as "FIBS". All the optics and the hardware are included in the head. This system can operate in a three-coherent beam mode (diffracted beams with an order of ± 1 and 0 are used) [20]. As a result of this configuration, close to that presented in [16], the practical size dynamic range of this PDI system is extended from $D = 5 - 22$ μm to $D = 5 - 44$ μm.

The electrical output of the two APDs is digitized with a PC data acquisition board. Data acquisition and processing software, using a sliding cross-spectral density function algorithm, were developed to measure the phase difference between the raw Doppler signals. For the results presented above, the diffraction grating velocity was set to obtain a typical frequency shift of $\nu_s \approx 250$ kHz. With a sampling acquisition rate of 1 MHz, and calculation windows of 32 samples for the CSD calculations, this ensures 38 500 measurements per second (i.e. a longitudinal resolution of 1.3 mm) for a fiber take-up velocity of 50 m/s.

Experiments were carried out on a laboratory-scale single-fiber drawing bench developed by Saint-Gobain Vetrotex Int. and also on fixed fibers.

5.2 Experimental Results

Figure 10 shows a comparison between the diameter of the fiber (measured during the drawing process under stationary conditions) with (*i*) the near-backward interferometer FIBS (over 9 min, i.e. fiber length 4 – 27 km); (*ii*) results from hydrodynamic calculations (based on the mass flow rate and the molten glass initial temperature); versus (*iii*) the size measured with a scanning electron microscope (SEM) for several samples of fibers. The raw phase-measurements obtained are converted into diameter time series with the FFT-filtered PDRS taking account of tension and the cooling rate. All the measurements are in good agreement, better than that obtained previously [8] when only the linearly fitted PDRS was used. Nearly all the measurements are in the range $\pm 5\%$ of the diameter measured with the SEM. According to the authors, the small discrepancies observed come from two major sources (*i*) some uncertainties in the calibration of the SEM and in its video image resolution and (*ii*) we are comparing punctual measurements (SEM) with mean measurements (FIBS and hydrodynamic calculations), which may differ if the process is not perfectly stable (which is usually the case for small diameters, for instance).

Figure 11 (a) presents the evolution of the diameter of the fiber, measured with FIBS, when the take-up velocity is decreased by steps from 33 down to 3 m/s. The fiber's diameter evolves inversely with the take-up velocity. The diameter of the fiber is measured continuously from 11 to 32 μm without any sign of a jump of 2π in the measured phase. This last behavior is obtained with the three-coherent beam operating mode. Figure 10 (b) presents the corresponding histogram.

Figure 12 presents the response of system (A) when the nozzle is submitted to a short convective perturbation (one blows on the nozzle). Strong fluctuations in fiber's diameter are observed. After a few seconds (i.e. more than 160 m) the fiber returns to its nominal size $D \approx 8.3$ μm, without breaking.

Figure 13 presents the response of system (A) when a hollow fiber is measured (gas bubbles were generated in the melt glass composition). A fiber with a gas core induces sharp oscillations in the measured phase differ-

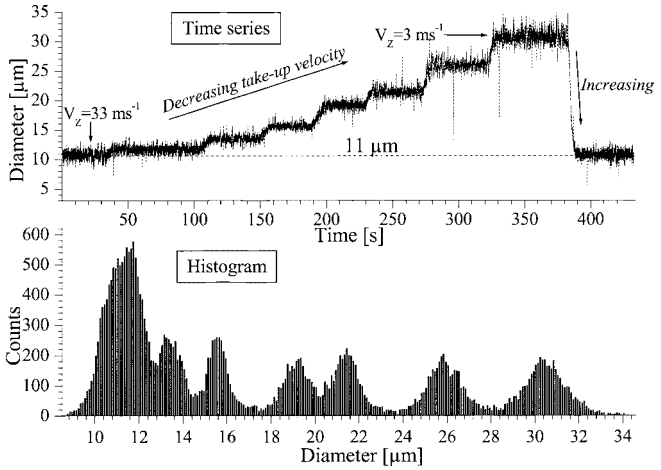

Fig. 11: Evolution of the fiber's diameter measured with FIBS when the take-up velocity is decreased by steps from 33 down to 3 m/s. (a) Time series and (b) corresponding histogram.

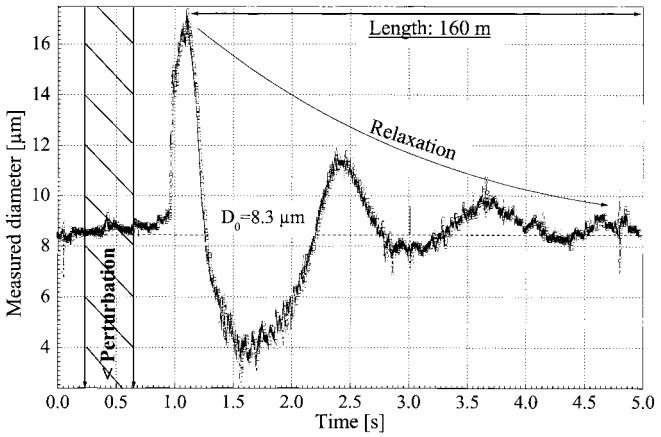

Fig. 12: Evolution of the fiber's diameter measured with set-up (A) when the nozzle is submitted to a short convective perturbation (one blows on the nozzle).

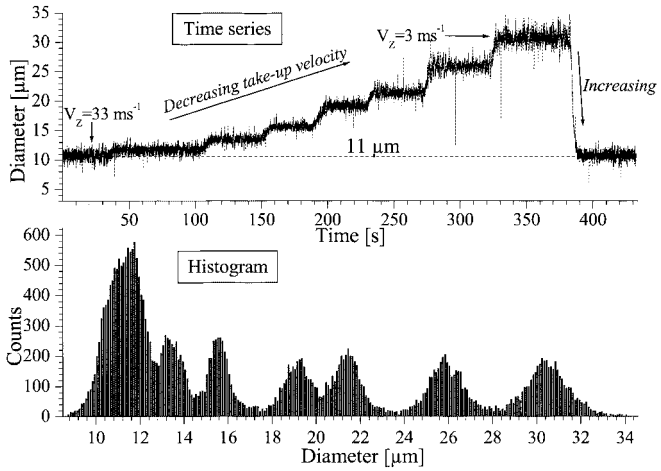

Fig. 13: Evolution of the fiber's diameter measured with set-up (A) when gas bubbles are generated in the melt glass composition (hollow fiber).

ence, which in fact cannot, for the moment, be correctly related to the fiber outer diameter. Nevertheless, these sharp oscillations are a good indicator of the presence of gas bubbles in the melt glass composition and in the rate of hollow fibers, which are important pieces of information. In Figure 13, the fiber's initial and final diameter are about $D = 8.2$ µm. From the time duration of the sharp resonances, we can estimate the length of the hollow fiber: $L \approx 2$ m for the first and $L \approx 0.6$ m for the second.

6 Conclusion

Two models based on the Lorenz-Mie theory have been introduced. They predict the basic light scattering properties and the response of a PDI to the sizing of infinite glass fibers used mainly for reinforcement applications. Among other parameters, they take into account the fiber's single-axis birefringence and the fiber's refractive index dependence on its cooling rates. Numerical results have shown that these two effects have a weak influence on the mean response of the PDI but a strong influence on the resonance structures of the PDRS (i.e. morphological dependant resonances). By neglecting the resonances, and for fibers in the size range 5 – 45 µm, the achievable resolution of the fiber size is 0.35 µm for an optical set-up working in the backward scattering region at 350 mm from the fiber. For an optical set-up working in the forward scattering region, the corresponding resolution is typically 0.09 µm. Experimental results obtained for both set-ups have demonstrated the validity of the models developed and also the ability of the PDI set-ups developed to study some features of the fiber-drawing process.
Perspectives of this work will be in the deconvolution of the resonance structures of the PDRS to increase the achievable resolution by a factor of 10 (at least).

7 Acknowledgements

The authors are grateful to ADEME (French Agency for the Environment and Energy Resources) and to CNRS (project PECO/NEI) for providing partial financial support for this work, and also to Dr. S. Schaub, who sent us data to compare the predictions of our models in the case of homogeneous fibers [8].

8 Nomenclature

D	fiber diameter
D_0	nozzle diameter
D_a, D_b	detectors

E	electrical field
F	fiber tension
P	Doppler signal pedestal
PDI	phase Doppler interferometry or interfeometer
$PDRS$	phase-diameter relationship
S_s	Poynting's vector
SEM	scanning electron microscope
T_0	melt glass initial temperature
T_f	fictive temperature
T_1, T_2	coefficients of the amplitude scattering matrix
V	Doppler signal visibility
a_{nI}, b_{nI}	external scattering coefficients
m, $m_{\parallel}$, $m_{<MQ>}$	homogeneous, extraordinary and ordinary refractive index
Φ_{ab}	theoretical PDRS including the resonance structures
$\phi_{ab}^{FFT}(D)$	PDRS fitted with a low-pass filtering procedure
$\phi_{ab}^{n}(D)$	PDRS fitted with a polynomial function or order n
$\phi_{ab}^{Lin}(D)$	PDRS fitted with a linear relationship
Ω	detector aperture angle
ψ_a, ψ_b	elevation angles
α	half-beam angles
δ_1, δ_2	incident beams polarization angles
δ_a, δ_b	polarizer angle
$\varepsilon_{\parallel}$, $\varepsilon_{\perp}$	extraordinary and ordinary electrical permittivity
λ	laser wavelength
ν_1, ν_2, ν_s	laser beam frequency and relative frequency shift
ν_D	Doppler frequency or heterodyne frequency
σ_{ab-D}^{Lin}	estimated error in the fiber diameter with $\phi_{ab}^{Lin}(D)$
σ_{ab-D}^{n}	estimated error in the fiber diameter with $\phi_{ab}^{n}(D)$
σ_{ab-D}^{FFT}	estimated error in the fiber diameter with $\phi_{ab}^{FFT}(D)$
$\sigma(T_0)$	optical stress constant at temperature T_0

9 References

[1] G. Gupta, *Fibers Reinforcements for Composite Materials.* Elsevier, New York, **1988**.

[2] L. R. Gliksman, The Dynamics of a Heated Free Jet of Variable Viscosity Liquid at Low Reynolds Numbers. *J. Basic Eng.* **1968**, *15*, 343 – 354.

[3] A. Lenoble, F. Onofri, S. Radev, Modélisation Physique du Procédé de Fibrage des Fibers de Renforcement, in *Proc. Congrés Français de Thermique*, Vittel, France, **2002**, 139 – 145.

[4] L. J. Lynch, N. Thomas, Optical Diffraction Profiles of Single Fibers. *Text. Res. J.* **1971**, *41*, 568 – 572.

[5] F. Onofri, H. Mignon, G. Gouesbet, G. Gréhan, On the Extension of Phase Doppler Anemometry to the Sizing of Spherical Multilayered Particles and Cylindrical Particles, in *4th Int. Congress on Optical Particle Sizing*, Nürnberg, Germany, **1995**, 275 – 284.

[6] H. Mignon, G. Gréhan, G. Gouesbet, T-H. Xu, C. Tropea, Measurement of Cylindrical Particles with Phase Doppler Anemometry. *Appl. Opt.* **1996**, *35*, 5180 – 5190.

[7] S. Schaub, A. Naqwi, F. L. Harding, Design of a Phase/Doppler Light-Scattering System for Measurement of Small-Diameter Glass Fibers during Fibers Glass Manufacturing. *Appl. Opt.* **1998**, *37*, 573 – 585.

[8] F. Onofri, A. Lenoble, H. Bultynck, P.-H. Guering, N. Marsault, Interferometric Sizing of Single-Axis Birefringent Glass Fibers, in *11th Int. Symposium on Applications of Laser Techniques to Fluid Mechanics*, Lisbon, Portugal, **2002**, paper 22.3.

[9] C. F. Bohren, D. R. Huffman, *Absorption and Scattering of Light by Small Particles.* Wiley, New York, **1983**.

[10] J. M. Corpus, P. K. Gupta, Diameter Dependence of the Refractive Index of Melt-Drawn Glass Fibers. *J. Am. Ceram. Soc.* **1993**, *76*, 1390 – 1392.

[11] C. Clementin-de-Leusse, *Etude de Fibers de Verre E. Caractérisation Expérimentale par Spectrométrie de Brillouin et Test de Modèle de Fribrage.* PhD Thesis, Université de Monpellier II, **2000**.

[12] G. Gouesbet, G. Gréhan, K. F. Ren, Rigorous Justification of the Cylindrical Localized Approximation to Speed Up Computations in the Generalized Lorenz-Mie Theory for Cylinders. *J. Opt. Soc. Am. A* **1998**, *15*, 511 – 523.

[13] F. Durst, A. Melling, J. H. Whitelaw, *Principles and Practice of Laser-Doppler Anemometry.* Academic Press, London, **1981**.

[14] H. E Albrecht, M. Borys, N. Damaschke, C. Tropea, *Laser Doppler and Phase Doppler Measurement Techniques.* Springer, Berlin, **2003**.

[15] A. Naqwi, F. Durst, Analysis of the Light Scattering Interferometric Devices for the In-Line Diagnosis of Moving Particles. *Appl. Opt.* **1993**, *32*, 4003 – 4018.

[16] F. Onofri, A. Lenoble, S. Radev, Superimposed Non-Interfering Probes to Extend the Phase Doppler Anemometry Capabilities. *Appl. Opt.* **2002**, *41*, 3590 – 3600.

[17] F. Onofri, D. Blondel, G. Gréhan, G. Gouesbet, On the Optical Diagnosis and Sizing of Coated and Multilayered Particles with Phase Doppler Anemometry. *Part. Part. Syst. Charact.* **1996**, *13*, 104 – 111.

[18] F. Onofri, L. Bergounoux, J.-L. Firpo, J. Mesguish-Ripault, Velocity, Size and Concentration Measurements of Optically Inhomogeneous Cylindrical and Spherical Particles. *Appl. Opt.* **1999**, *38*, 4681 – 4690.

[19] F. Onofri, A. Lenoble, S. Radev, Sizing of Single Fibers Under Torsional Stress, in *6th International Congress on Optical Particle Characterization*, Brighton, UK, **2001**, paper 7.

[20] F. Onofri, A. Lenoble, S. Radev, 3-Coherent Beams Phase Doppler Interferometry, submitted for publication in *Optics Commun.* **2002**.

Article A15

Optica Applicata, Vol. XXXII, No. 4, 2002

Optical parameters and scattering properties of red blood cells

JANUSZ MROCZKA, DARIUSZ WYSOCZAŃSKI

Wrocław University of Technology, Chair of Electronic and Photonic Metrology, Wybrzeże Wyspiańskiego 27, 50-370 Wrocław, Poland.

FABRICE ONOFRI

UMR no 6595-IUSTI, CNRS-Universite de Provence, Marseille, France.

The results of investigation of the scattering properties of red blood cells (RBC or erythrocyte) modelled as a spheroid for fixed and random orientations versus osmotic pressure and oxygenation have been presented. We investigate the scattering properties of a single RBC for fixed and random orientations *versus* the osmotic pressure and oxygenation. The final goal of this study is to determine whether it is possible to infer the previous blood characteristics from a whole blood sample under single or multiple scattering.

1. Introduction

An erythrocyte has a round shape a biconcave disc of 7.5 ± 0.3 μm in diameter and thickness of $(1.4-2.1)\pm0.4$ μm. The mean concentration of haemoglobin in an erythrocyte is $HC = 350\pm2.5$ g/l. Haemoglobin is responsible for the spectral absorption of RBCs. Under normal conditions the RBCs are oblate in shape and their volume equals $V_0 = 90$ μm^3 for the osmotic pressure $P_o = 300$ mosm (see Fig. 1a). The shape of unhealthy RBCs can significantly differ from

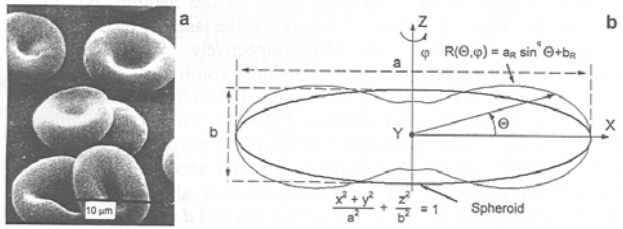

Fig. 1. View of real human RBCs for normal osmotic pressure $P_o = 300$ mosm (a). Models of RBC (b).

the one presented in the figure. It also strongly depends on the osmotic pressure. So that one can expect to diagnose RBCs oxygenation rate and the osmotic pressure from RBCs shape analysis and absorption diagnosis.

The whole blood (non-diluted and non-hemolyzed) is a disperse system in which RBCs form the major part of a dispersed phase with plasma as a dispersing medium.

In clinical haematology, there is a need for accurate and precise measurement of the RBC geometrical (size and shape) and mechanical (deformability) properties, as well as oxygenation. Haemoglobin in a RBC takes mainly two forms: an oxidised form (HbO_2, responsible for the transport of oxygen) and unoxygenated form (Hb). Haemoglobin is responsible for light absorption properties of the erythrocyte (oxygenated blood appears to be light red and non-oxydated – dark red). Thus the measurement of the RBC light absorption may be a measurement of the blood cell haemoglobin concentration and oxygenation and thus, its efficiency in oxygen transport.

There exist several clinical laboratory instruments which employ flow-cytometric methods in counting RBCs and measuring their volume distribution. Most of them use forward light scattering at one or two angles, or an electronic resistive pulse sizing method for the RBCs volume distribution measurements. There is nevertheless a need to improve the techniques which estimate the RBC geometrical properties only from effective volume measurements and give no information about the oxygenation and shape of RBCs.

There are many reports in the literature on the computation of the scattering properties of a RBC. The earlier works were based on the Lorenz–Mie theory assuming a RBC as homogenous spherical particles. Nevertheless, due to the complex shape of these particles, this approach cannot be of real practical use. Latter works were based on the assumption of an oblate form (axi-symmetric ellipsoid with symmetrical axis radius a, like $a/b > 1$) for the RBC and their optically "soft nature" [1]

$$|m-1| \ll 1,$$
$$kd|m-1| \ll 1 \tag{1}$$

where m, k, d are the RBC relative refractive index in the medium considered ($m = m_{RBC}/m_m$), the wave vector ($k = 2\pi m_m/\lambda$, where λ is the laser wavelength in free space) and an equivalent diameter of the RBC, respectively.

The previous conditions make it possible to obtain a solution of the scattering problem that is quite simple and physically obvious analytical form usually referred to as the anomalous diffraction approximation [2]–[6]. The first condition is usually fulfilled as, in the visible range, the RBCs have a proper refractive index about $m_{RBC} = 1.4$ and the surrounding medium (plasma) about $m_m = 1.335$, *i.e.*, $m = 1.4/1.335 = 1.05$. Nevertheless, the second condition is always violated. For instance, for the previous parameters with $\lambda = 0.6328$ μm and $d = 4.9$ μm, we found that $kd|m-1| = 1.6$. This introduces some limitations as regards the accuracy of this approach and it also limits the prediction of the RBC scattering properties in the

small angle range. In spite of the strong limitations of this approach it has recently been used in [7] to predict the light scattering properties of RBC with their shape approaching natural one (Fig. 1**b**) within the spherical co-ordinate system

$$R(\theta,\varphi) = a_R \sin^q\theta + b_R \tag{2}$$

where $d = (2a_R + b_R)$ is the diameter and $2b_R$ is the thickness in the centre. As typical parameters for erythrocytes they have chosen $d = 7.5$ μm, corresponding to $a_R = 3$ μm and $b_R = 0.75$ μm and the exponent is estimated at $q = 5$. They have also assumed that the osmolarity of the suspension medium causes "isovolumetric sphering" of the cell, where the case $q = 0$ corresponds to the sphere. This last hypothesis seems to be invalidated by some experimental studies [8], [9].

The T-matrix method (or extended boundary condition method) has also been previously used to compute the scattering properties of a RBC for the fixed orientation. This accurate method does not require any particular assumption on the optical parameters of the scattering particles, *i.e.*, RBC in the present case. It is nevertheless limited to simple geometrical shapes and also, due to numerical instabilities, in the maximum size parameter that can be calculated. The T-matrix method allows us to compute scattering coefficients as well as the phase function, the degree of linear or circular polarisation for arbitrary scattering angles [6], [10], [11].

2. Simulation strategy and procedure

To compute the light scattering properties of RBCs we have chosen the T-matrix method, for obtaining accurate predictions on the scattering coefficients and angular scattering dependences which are supposed to be necessary to infer statistical properties of RBC from a blood sample and not only from single RBCs. For this purpose we used the T-matrix code from [10], [11] available from the web site [12]. The RBC shape will be modelled by an oblate ellipsoid (see Fig. 1**b**) with the equation: $\frac{x2+y^2}{a^2}+\frac{z^2}{b^2}=1$, where a is a symmetrical axis. This particle has the same projection area along Z axis as the form given in Eq. (2), when $a = a_R + b_R$ and $b = b_R$. It has a comparable volume but a smaller projected surface along X or Y axes.

The haemoglobin, Hb (0% oxygenation) and HbO_2 (100% oxygenation), complex refractive index dependence on wavelength [13], [14] is presented in Fig. 2**a**. At the first sight, it appears from the figure that the major difference in the spectral absorption between Hb and HbO_2 is in the range of 600−750 nm. Nevertheless, if we consider a simple intensity ratio experiment to distinguish the two types of haemoglobin from the intensity transmission through blood samples (width L), the relevant parameter is the difference in the two spectral absorptions: $\frac{I_{Hb}}{I_{HbO_2}} = \exp[-(k_{Hb}-k_{HbO_2})L]$. Figure 2**b** presents the difference in the spectral absorption of the two types of haemoglobin. The difference in the blood sample transmission is

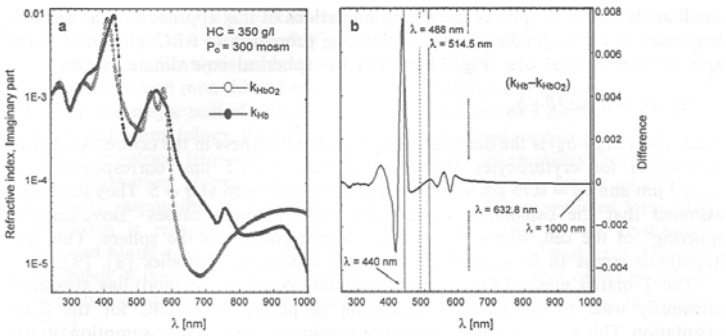

Fig. 2. Spectral absorption of RBC for oxygenated (HbO_2) and non-oxygenated haemoglobin (Hb): a − imaginary part of refractive index *vs.* wavelength, b − difference between the imaginary parts of refractive index *vs.* wavelength for non-oxygenated and oxygenated blood.

expected to be a maximum for wavelength about 380-450 nm. The refractive index inside a RBC is

$$\tilde{m}_{RBC} = m_{RBC} + ik, \tag{3}$$

m_{RBC} is expected to depend on the RBC haemoglobin concentration, the concentration being varied for different people (typical value: HC = 350 g/dm^3). The linear dependence upon HC is known [1]

$$m_{RBC}(HC) = m^0_{RBC} + \alpha HC \tag{4}$$

where for the constant we use: $\alpha = 0.0019$ g/dm^3 and $m^0_{RBC} = 1.335$.

The real part of the refractive index dependence on the wavelength is neglected. This is justified by the following arguments:

i) in the light scattering calculations we use the relative refractive index $m = m_{RBC}/m_m$ so that for some part the wavelength dependence is cancelled out,

ii) as the best of authors' knowledge, there are no reliable data in the literature on this dependence.

There are also very scarce reliable data in the literature about the RBC shape dependence on osmotic pressure, so we use the following experimental results and procedure.

The aspect ratio a/b is deduced from the experimental data [8] giving the evolution of the volume of RBCs in terms of a cylinder with the length $2b$ and radius a. Note that this way of defining the RBCs volume is common in the clinical practice.

The evolution of parameter a is deduced from a linear fit of a few pieces of experimental data on the shape of RBCs [9]. As a result, using these data we derive shape dependence on osmotic pressure for the RBCs:

$$V_{cyl}(P_o) = 339 - 1.88P_o + 0.00491P_o^2 - 4.46\cdot10^{-6}P_o^3,$$
$$a = [0.00310(P_o - 150) + 3.210],$$
$$b = \frac{V_{cyl}(P_o)}{2\pi a^2}. \tag{5}$$

In terms of volume, the RBC is equivalent to a sphere with radius $r_{sph} = \left(\frac{V_{cyl}(P_o)}{2\pi}\right)^{1/3}$. When the osmotic pressure decreases from 300 to 111 mosm the RBC geometrical aspect ratio decreases from $\xi = a/b = 3.28$ (oblate shape) to $\xi = 1.002$ (spherical shape), see Fig. 3. In the opposite case, the RBC volume

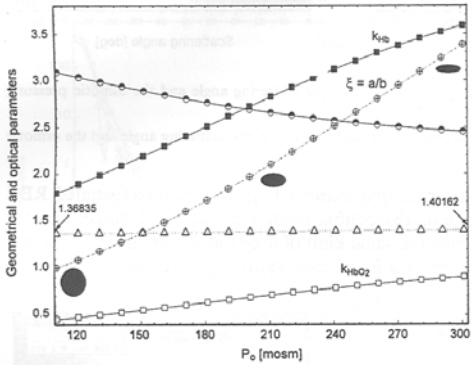

Fig. 3. Evolution of the RBC geometrical and optical properties *vs.* the osmotic pressure: ○ – spheroidal aspect ratio, $\zeta = a/b$, -○- – radius volume equivalent sphere, -△- – refractive index, real part, ■- – refractive index, imaginary part $\times 500$/Hb, -□- – refractive index, imaginary part $\times 500/HbO_2$.

increases (the equivalent sphere radius increases). This causes a dilution of the haemoglobin inside the RBC: $HC(P_0) = HC(300)V_{cyl}(300)/V_{cyl}(P_o)$ and thus a change in the RBC refractive index $m_{RBC}(HC)$ and absorption $k(P_o) = k(300)V_{cyl}(300)/V_{cyl}(P_o)$. In Figure 3 the evolution of the spectral absorption and refractive index with the osmotic pressure is given for $\lambda = 100$ nm and $HC(300) = 350$ g/l.

3. Numerical results and discussion

First, we consider the case where the RBC is in fixed orientation: the incident laser beam propagates along the RBC symmetrical axis, and we analyse the scattering in the azimuthal plane. Under such geometry, Fig. 4 presents an iso-level map for the

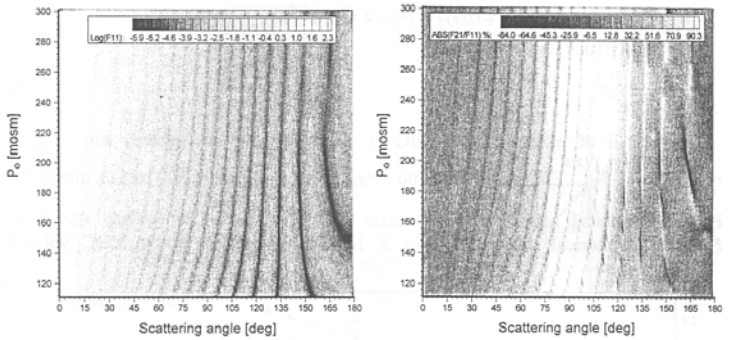

▲

Fig. 4. Iso-level map of the scattering phase function *vs.* the scattering angle and the osmotic pressure, RBC in fixed orientation.

Fig. 5. Iso-level map of the scattering degree of linear polarisation *vs.* the scattering angle and the osmotic pressure, RBC in fixed oriantation.

evolution of the phase function (scattering element F_{11}) for a non-oxygenated RBC *vs.* the osmotic pressure (change in absorption, refractive index and shape) and the scattering angle. Figure 5 presents the same kind of map but for the degree of linear polarisation of the scattered light (ratio of two scattering elements: $-F_{21}/F_{11}$).

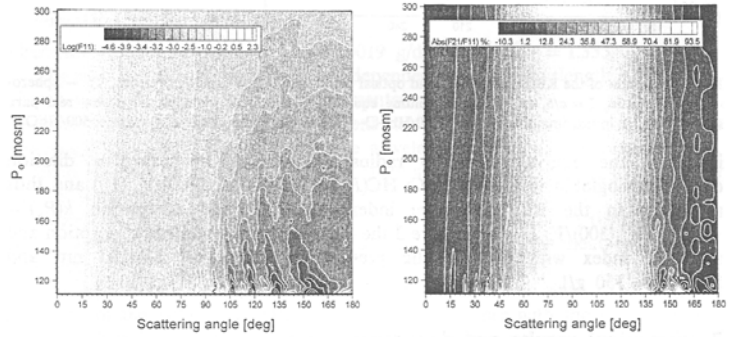

▲

Fig. 6. Iso-level map of the scattering phase function *vs.* the scattering angle and the osomotic pressure, RBC in random orientation (integration over all directions).

Fig. 7. Iso-level map of the scattering degree of linear polarisation *vs.* the scattering angle and the osmotic pressure, RBC in random orientation.

In both cases there is the evolution of the scattering elements *vs.* the osmotic pressure and obviously with the scattering angle. This dependence seems nevertheless to be weaker and weaker as the RBC osmotic pressure tends to 300 mosm (spherical shape).

We now consider the case of randomly oriented RBC. This case is expected to be of greater interest to infer RBCs properties from a whole blood sample.

Figures 6 and 7 are equivalent to Figs. 4 and 5 but for randomly oriented RBC. It appears from Fig. 6 that there is still the evolution of the phase function *vs.* the osmotic pressure, however, it is more confusing. From Fig. 7, it appears, surprisingly to some extent, that the degree of linear polarisation is no more a good parameter for the diagnosis of RBCs osmotic pressure or shape.

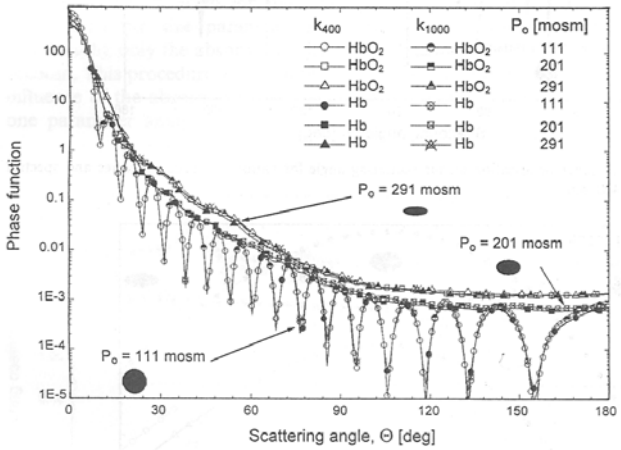

Fig. 8. Phase function *vs.* the scattering angle for various osmotic pressures, two types of spectral absorption (at 440 and 1000 nm) and for oxygenated and non-oxygenated haemoglobin.

Figures 8 and 9 show the evolution of the phase function and the degree of linear polarisation *vs.* the scattering angle for two cases of spectral absorption (corresponding to a laser wavelength of $\lambda = 440$ nm and $\lambda = 1000$ nm), for oxygenated (100%) and non oxygenated (0%) haemoglobin, and for three osmotic pressures ($P_o = 111$, 201 and 291 mosm). For low osmotic pressure the evolution of the phase function and the degree of linear polarisation are characteristic for those obtained with the Lorenz–Mie theory for spherical particles: strong resonance structures are observed. When the osmotic pressure increases, *i.e.*, the RBC geometrical aspect ratio increases, the previous evolution tends to be smoothed. In Fig. 8 increasing osmotic

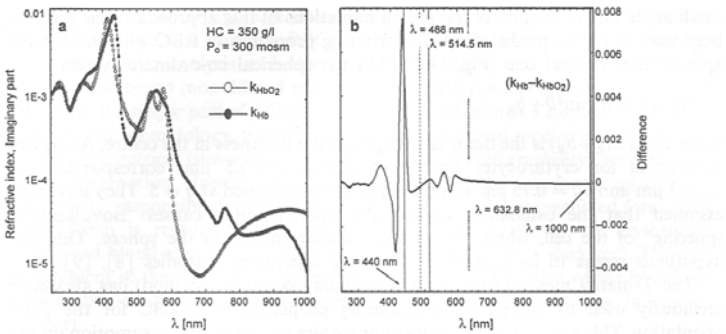

Fig. 2. Spectral absorption of RBC for oxygenated (HbO_2) and non-oxygenated haemoglobin (Hb): a – imaginary part of refractive index *vs.* wavelength, b – difference between the imaginary parts of refractive index *vs.* wavelength for non-oxygenated and oxygenated blood.

expected to be a maximum for wavelength about 380-450 nm. The refractive index inside a RBC is

$$\tilde{m}_{\mathrm{RBC}} = m_{\mathrm{RBC}} + ik, \tag{3}$$

m_{RBC} is expected to depend on the RBC haemoglobin concentration, the concentration being varied for different people (typical value: HC = 350 g/dm^3). The linear dependence upon HC is known [1]

$$m_{\mathrm{RBC}}(\mathrm{HC}) = m^{\circ}_{\mathrm{RBC}} + \alpha \mathrm{HC} \tag{4}$$

where for the constant we use: $\alpha = 0.0019$ g/dm^3 and $m^{\circ}_{\mathrm{RBC}} = 1.335$.

The real part of the refractive index dependence on the wavelength is neglected. This is justified by the following arguments:

i) in the light scattering calculations we use the relative refractive index $m = m_{\mathrm{RBC}}/m_{\mathrm{m}}$ so that for some part the wavelength dependence is cancelled out,

ii) as the best of authors' knowledge, there are no reliable data in the literature on this dependence.

There are also very scarce reliable data in the literature about the RBC shape dependence on osmotic pressure, so we use the following experimental results and procedure.

The aspect ratio a/b is deduced from the experimental data [8] giving the evolution of the volume of RBCs in terms of a cylinder with the length $2b$ and radius a. Note that this way of defining the RBCs volume is common in the clinical practice.

The evolution of parameter a is deduced from a linear fit of a few pieces of experimental data on the shape of RBCs [9]. As a result, using these data we derive shape dependence on osmotic pressure for the RBCs:

pressure from 202 to 291 induces the onset of the phase function, it has nevertheless no significant influence on the linear degree of polarisation, see Fig. 9. The influence of the spectral absorption in Figs. 8 and 9 is extremely weak, so we may have some doubt about the possibility of diagnosing the RBC oxygenation from the analyses of the phase function and the degree of linear polarisation.

Figure 10 presents the evolution of the corresponding extinction scattering coefficients Q_{ext}. For wavelength $\lambda = 1000$ nm the extinction coefficient dependence on RBC oxygenation is almost null. For $\lambda = 440$ nm this dependence is not negligible, the ratio $Q_{ext}(Hb)/Q_{ext}(HbO_2)$, k_{440} evolves about 4–5% which could be measurable, it is nevertheless not a one-to-one relation with the osmotic pressure, see the curve in Fig. 10. This behaviour can be explained based on Fig. 11, where the evolution of the scattering coefficients (extinction, scattering, and absorption) *versus* the wavelength is given for the two types of haemoglobin. Note that in these calculations the size parameter α is kept constant (independent of the laser wavelength), only the absorption coefficient dependence on wavelength is taken into account. This procedure was found to be convenient for reducing our analysis of the influence of the absorption coefficient on the scattering pattern and coefficients to one parameter analysis.

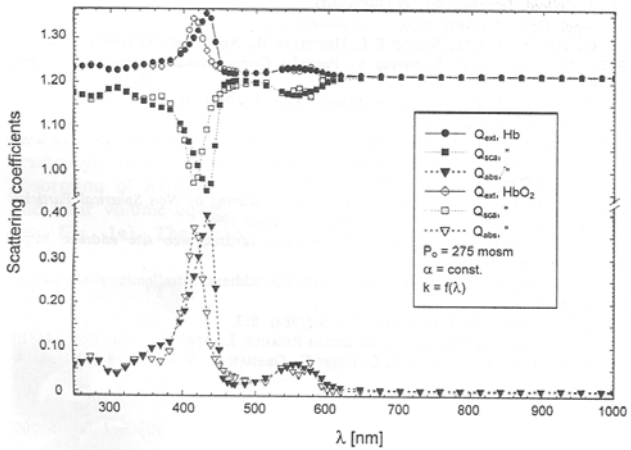

Fig. 11. Scattering coefficients (extinction, scattering and absorption) *vs.* the incident light wavelength and for oxygenated and non-oxygenated haemoglobin. Note that the RBC size parameter is taken independent of the wavelength.

It appears from Figs. 6–11 that contrary to fixed oriented RBCs the diagnosis of the osmotic pressure of randomly oriented RBC is expected to be rather difficult. The osmotic pressure has some influence on the phase function and on the extinction scattering coefficient which is not a one-to-one relation. The diagnosis of the oxygenation rate of RBCs seems to be an even more difficult task. The influence of the haemoglobin absorption on the basic scattering parameters and functions, which is rather large, seems to be too small to be detected experimentally.

4. Conclusions

Finally, one can expect that in the case of a whole blood sample with a polydisperse size distribution for RBCs and obviously under multiple scattering conditions, it would not be possible to infer reliable statistical properties of a RBC. We claim that one solution to this problem would be to fix the orientation of all RBCs present in the blood sample (as is done for a single RBC in flow-cytometric methods) under single or multiple light scattering conditions [15]–[17].

References

[1] Tycko D.H., Metz M.H., Epstein E.A., Grinbaum A., Appl. Opt. **24** (1985), 1355.
[2] Van de Hulst H.C., *Light Scattering by Small Particles*, Wiley, New York 1957.
[3] Latimer P., J. Colloid. Interface Sci. **39** (1972), 103.
[4] Latimer P., Appl. Opt. **19** (1980), 3039.
[5] Streekstra G., Hoekstra A.G., Nijhof E.J., Heethaar R., Appl. Opt. **32** (1983), 2266.
[6] Barber P.W., Hill S.C., *Light Scattering by Particles Computational Methods*, World Sci., Singapour 1990.
[7] Borovoi A.G., Naats E.I., Oppel U.G., J. Biomed. Opt. **3** (1998), 364.
[8] Fung Y.C., Microvascular Res. **5** (1972), 335.
[9] El Azouzi H., *Etude de la deformabilite des globules rouges par diffusion de la lumiere – Influence des tensioactifs*, Ph.D. Thesis, Universite de Nancy I, France 1995.
[10] Mishchenko M.I., J. Opt. Soc. Am. A **8** (1991), 871.
[11] Mishchenko M.I., Hovenier J.W., Travis L.D., *Light Scattering by Non Spherical Particles: Theory, Measurements and Applications*, Academic, San Diego 1999.
[12] Mishchenko M.I., Travis L.D., from NASA Goddard Institut, web site address: http://www.giss.nasa.gov/~crmim/index.html
[13] Prahl S., from Oregon Medical Laser Center, web site address: http://omlc.ogi.edu/spectra/hemoglobin/index.html
[14] Steinke J.M., Shepherd A.P., J. Opt. Soc. Am. **5** (1988), 813.
[15] Onofri F., Bergounoux L., Firpo J.-L., Mesguish-Ripault J., Appl. Opt. **38** (1999), 4681.
[16] Czerwiński M., Mroczka J., Girasole T., Gousbet G., Grehan G., Appl. Opt. **40** (2001), 1514.
[17] *Ibidem*, p. 1525.

Received July 5, 2002

Article A17

Available online at www.sciencedirect.com

SCIENCE DIRECT®

Optics Communications 234 (2004) 183–191

OPTICS COMMUNICATIONS

www.elsevier.com/locate/optcom

High-resolution laser diffractometry for the on-line sizing of small transparent fibres

Fabrice Onofri [a,*], Anne Lenoble [a], Hervé Bultynck [b], Paul-Henri Guéring [b]

[a] CNRS, UMR No. 6595-IUSTI, University of Provence 5 rue Enrico Fermi, Technopôle de Chateau Gombert, F-13453 Marseille Cedex 13, France

[b] Saint-Gobain Recherche, 39, quai Lucien Lefranc, B.P. 135, F-93303 Aubervilliers Cedex, France

Received 20 October 2003; received in revised form 9 February 2004; accepted 10 February 2004

Abstract

A simple and robust method for the inversion of the laser diffraction diagrams of small transparent fibres is introduced. Based on Lorenz-Mie theory (LMT) calculations and the definition of a correlation estimator, it allows the particle diameter to be determined without the classical size ambiguity problem due to morphological-dependent resonances (MDRs). Experimentally, when sizing single reinforcement glass fibres during their forming process, the typical resolution obtained is about $\sigma \approx 0.02$ μm for the size range $D = 7$–42 μm. This inversion method is thought to be also applicable for the diagnosis of other highly symmetrical and transparent particles as well as other particle characteristics.

PACS: 42.25.Fx; 42.30.Sy; 42.81.Cn; 81.05.Kf

Keywords: Laser diffractometry; Inversion; Lorenz-Mie theory; Sizing; Glass fibres

1. Introduction

The on-line sizing of small glass fibres used for reinforcement applications is necessary from both manufacturing efficiency and quality control viewpoints [1]. Highly resolved measurements (in size and time) are also suitable for the validation of hydrodynamical models [2,3] on the stability of the drawing process with respect to various perturbation sources: heterogeneity of the melt glass composition and temperature, fluctuations in the melt glass jet cooling rate (radiative heat transfer, turbulence, etc.), the take-up velocity, etc.

For a long time the laser diffractometry technique has been thought to be an appropriate tool for the on-line sizing of small glass fibres [4–6]: the optical setup is rather simple, the measurement is almost instantaneous and can be easily performed at a high frequency rate, the fibre can move in a

* Corresponding author. Tel.: +33-4-91-10-68-92; fax: +33-4-91-10-69-69.

E-mail addresses: Fabrice.Onofri@polytech.univ-mrs.fr (F. Onofri), Anne.Lenoble@polytech.univ-mrs.fr (A. Lenoble), Herve.Bultynck@saint-gobain.com (H. Bultynck), Paul-Henri.Guering@saint-gobain.com (P.-H. Guéring).

0030-4018/$ - see front matter © 2004 Elsevier B.V. All rights reserved.
doi:10.1016/j.optcom.2004.02.026

large probe volume without any influence on the measurement, etc. In fact, this technique is largely used for the sizing of a wide variety of single particles (absorbing or metallic wires, spherical or irregular particles) or clouds of particles (suspensions, two-phase flows). In most cases, the Fraunhofer theory is used for the inversion of the laser diffraction diagrams and to recover the particle size or the particle size distribution. The main interest of this theory lies in its relative simplicity when it is applied to predict the scattering properties of particles with a complex shape.

In the scattering diagram of transparent and highly symmetrical particles (spheres, cylinders, ellipsoids, etc.) strong non-linearities, or resonances, are observed (see for instance Fig. 2). Known as the morphological-dependent resonances (MDRs) [7], they are attributed to the internally reflected rays and they are not predicted by the Fraunhofer theory. Experimentally these resonances are not usually observed for absorbing particles (internal reflected rays are absorbed), for irregular particles (internal reflected rays are more or less randomly phase shifted by each other) or a cloud of polydisperse particles (the different contributions are smoothed). So that most of the work published in the literature about the inversion of laser diffraction diagrams are not relevant to our problem. The inversion of the diffraction pattern of transparent and highly symmetrical particles requires a particular treatment.

In this paper, we introduce the principle of a simple and robust method for the inversion of the laser diffraction diagrams of small transparent fibres. It allows the determination of the diameter of a single homogeneous fibre without the classical size ambiguity problem due to the above-mentioned effects. This method is thought to be easily extended for the sizing of other type of fibres (absorbing, coated, with a refractive index profile) as the inversion procedure is totally decoupled from the input parameters of the scattering model. Section 2 briefly presents the model used to predict the light scattering properties of glass reinforcement fibres; it is based on the Lorenz-Mie theory. Section 3 presents the method for the inversion of the experimental scattering diagrams. Section 4 presents some experimental results and comparisons demonstrating the robustness and efficiency of the proposed method. Section 5 is a conclusion with some perspectives for future extensions.

2. Scattering model and numerical examples

The light scattering properties of an infinite homogeneous right circular cylinder, with axis Z, illuminated under normal incidence by a time–harmonic plane wave, has been extensively discussed in [8]. In this work, the problem is treated rigorously by solving the wave equation in the circular coordinate system (r, θ, Z). A separation method (i.e. Lorenz-Mie theory) is used for that purpose. Fig. 1 sketches the drawing process as well as the scattering model geometry under study. The fibre's shape is modeled by a right circular infinite cylinder. In the drawing process the fibre orientation is fixed. Therefore, in the following, there is no need to consider the effect of the fibre's inclination. Following Bohren and Huffman [8] the electrical field scattered by the fibre, in the direction θ and in the far field $kr \gg 1$, can be split in two independent components, one parallel $E^{s}_{\parallel}(r,\theta)$ and one perpendicular $E^{s}_{\perp}(r,\theta)$ to the scattering plane (XOY)

$$\begin{pmatrix} E^{s}_{\parallel}(r,\theta) \\ E^{s}_{\perp}(r,\theta) \end{pmatrix} = \exp\left[\frac{3\pi \mathrm{i}}{4}\right]\sqrt{\frac{2}{\pi kr}}\begin{pmatrix} T_1(\theta) & 0 \\ 0 & T_2(\theta) \end{pmatrix} \times \begin{pmatrix} E^{0}_{\parallel} \\ E^{0}_{\perp} \end{pmatrix} \exp\left[\mathrm{i}(kr - 2\pi v t)\right], \quad (1)$$

where classically, $E^{0}_{\parallel}$, $E^{0}_{\perp}$ are the amplitude of the incident electrical field components, $k = 2\pi/\lambda$ is the wave number and v the incident field frequency. The two terms $T_1(\theta)$ and $T_2(\theta)$ of the amplitude scattering matrix read as

$$T_1(\theta) = \sum_{n=-\infty}^{n=+\infty} b_{n\mathrm{I}} \exp[-\mathrm{i}n\theta] = b_{0I} + 2\sum_{n=1}^{n=+\infty} b_{n\mathrm{I}} \cos(n\theta),$$
$$T_2(\theta) = \sum_{n=-\infty}^{n=+\infty} a_{n\mathrm{II}} \exp[-\mathrm{i}n\theta] = a_{0II} + 2\sum_{n=1}^{n=+\infty} a_{n\mathrm{II}} \cos(n\theta), \quad (2)$$

where $b_{n\mathrm{I}}$ and $a_{n\mathrm{II}}$ are the external scattering coefficients for a homogeneous cylinder [8] or a multilayered cylinder (coated or finely stratified) [9]. For a homogeneous cylinder these coefficients

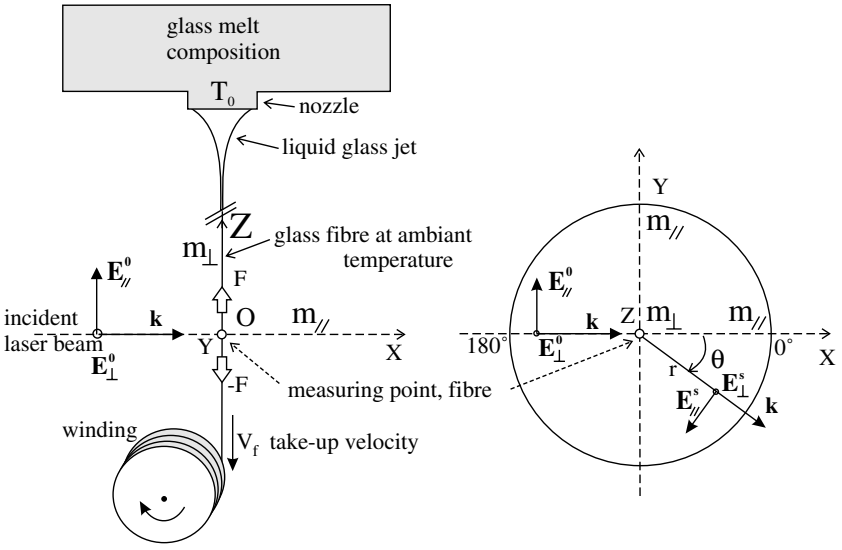

Fig. 1. Sketches of the glass fibre drawing process and the geometry of the scattering model.

takes into account the diameter D, its refractive index m (constant or radial profile), the incident wavelength λ and the external medium refractive index (equal to unity in this study).

From the calculation of the external scattering coefficients, and with the help of the Poynting's vector, the time-averaged scattering diagrams or "diffraction diagrams" (if limited to the forward region, i.e. $\theta \approx 0°$) can be calculated. For the angular intensity distribution we obtain

$$I^{s}_{\parallel}(\theta) = \left[E^{0}_{\parallel} T_1(\theta)\right]^2 \Big/ (2\pi^2 vr),$$
$$I^{s}_{\perp}(\theta) = \left[E^{0}_{\perp} T_2(\theta)\right]^2 \Big/ (2\pi^2 vr). \tag{3}$$

For the case of glass reinforcement fibres two additional effects have to be taken into account in this model: the fibre single axis-birefringence due to the drawing stress (i.e. the mechanical tension, **F**, see Fig. 1), and the effect of the glass melt cooling rate (and not simply the residual temperature [10]). Practically, both effects induce a refractive index dependence with the fibre size and the initial glass melt temperature, T_0. In fact, for the drawing stress, two refractive indexes have to be considered for the fibre: one along the fibre axis $m_{\perp}$ and one transverse to the fibre axis, $m_{\parallel}$, as sketched in Fig. 1. The reader is referred to [3,11] to obtain more details about the modeling of these effects and their influence on the scattering properties of transparent fibres. In subsequent computations these effects have been taken into account and all numerical and experimental results are given for $T_0 = 1200$ °C, $\lambda = 0.6328$ μm, perpendicular polarisation and for $m(\text{Composition}, T_0, D) \approx 1.555$ [3,11].

As an example of the increasing complexity of the scattering diagrams due to MDRs, Fig. 2 shows an iso-level map of the logarithm of the scattered intensity $\log_{10} I^{s}_{\perp}(\theta)$, on the left, for reinforcement fibres (transparent, $m \approx 1.555$), and on the right, for metallic fibres (reflecting, $m = 1.555 - 2\mathrm{i}$). The left-axis corresponds to the fibre's diameter which evolves in the range $D = 5, 5.01, \ldots, 45$ μm. The bottom-axis represents the scattering angle with $\theta = 0°, 0.01°, \ldots, 15°$. For the metallic fibres, the scattering patterns are rather simple. They exhibit only a few extremes (bright "fringes" and dark "fringes"). For the transparent fibres, a dense and high-frequency pattern seems to be superimposed to the one obtain for the metallic fibres.

The angular position of the extremes corresponding to Fig. 2 (the case of glass fibres) is plotted in Fig. 3. Note that for drawing considerations, the position of only one extreme in five is

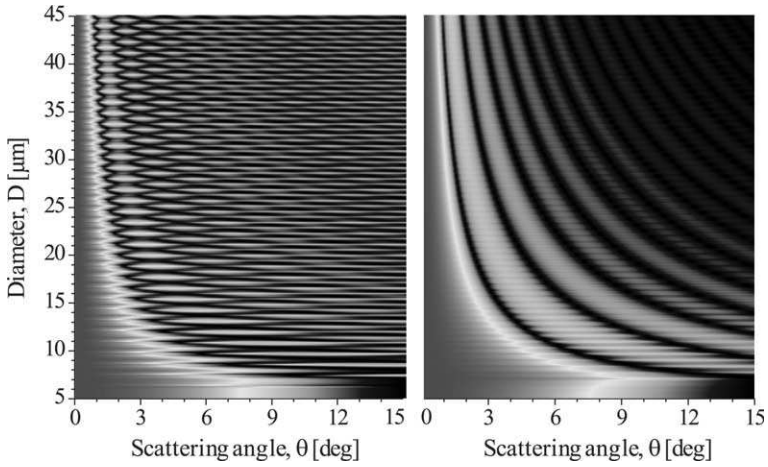

Fig. 2. Iso-level maps of the logarithm of the intensity scattered by fibres versus, bottom-axis, the scattering angle, $\theta = 0°, 0.01°, \ldots, 15°$, and left-axis, the fibre diameter $D = 5, 5.01, \ldots, 45$ μm. Left: reinforcement E-glass fibres; right: metallic fibres.

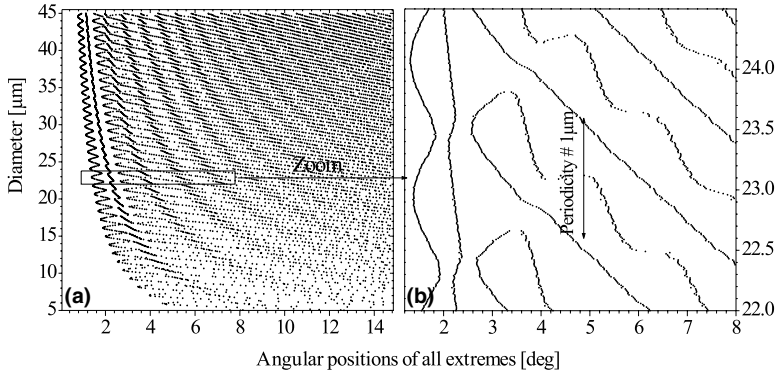

Fig. 3. Angular position of the extremes (minima and maxima) of the scattering pattern corresponding to Fig. 2 (the case of the glass fibres).

drawn in the left part of Fig. 3. These extremes have been extracted automatically with the same software as the one used in Section 4 to analyse experimental scattering diagrams. In Fig. 3, the pattern obtained exhibits periodicities with the fibre's size (~1 μm). At this step, the complexity of this pattern rends questionable the possibility of obtaining a one-to-one relation between one scattering diagram and one fibre diameter. However, minor differences exist between two "similar" scattering diagrams and the scattering pattern is not purely periodic. Hence we can expect to develop an inversion method to relate a scattering diagram to a single fibre's diameter, like the one we propose below.

3. Inversion method

We first start with the calculation of n_T theoretical scattering diagrams corresponding to the fibres size range that we expect to measure $D_T(i) = 5, 5.01, \ldots, 45$ μm, and for an angular range of $\theta = 0°, 0.01°, \ldots, 15°$. These calculations are performed only once, with the scattering model introduced above plus the refractive index dependence $m(E - \text{glass}, T_0, D, F)$ [3,11]. A lookup table is then created, summarising two kinds of properties of the scattering diagrams for each diameter (as in Fig. 3): the number of local maxima $k_T^+(i)$ and local minima $k_T^-(i)$; and the angular position of each of these extremes $\theta_T^+(i, j_T^+)$ and $\theta_T^-(i, j_T^-)$

$$D_{\mathrm{T}}(i) \to \begin{cases} \theta_{\mathrm{T}}^{+}(i, j_{\mathrm{T}}^{+}), & j_{\mathrm{T}}^{+} = 1, 2 \ldots, k_{\mathrm{T}}^{+}(i), \\ \theta_{\mathrm{T}}^{-}(i, j_{\mathrm{T}}^{-}), & j_{\mathrm{T}}^{-} = 1, 2 \ldots, k_{\mathrm{T}}^{-}(i), \end{cases} \tag{4}$$

where the superscript + stands for local maxima and the superscript − for local minima. No information on the relative intensity of the extremes is used here as, from an experimental point of view, intensity criteria were found to be unreliable.

For a given experiment, n_{E} scattering diagrams are registered in time from which the position of the extremes $\theta_{\mathrm{E}}^{-}(n, j_{\mathrm{E}}^{-})$ and $\theta_{\mathrm{E}}^{+}(n, j_{\mathrm{E}}^{+})$ can be extracted

$$D_{\mathrm{E}}(n) \to \begin{cases} \theta_{\mathrm{E}}^{+}(n, j_{\mathrm{E}}^{+}), & j_{\mathrm{E}}^{+} = 1, 2, \ldots, k_{\mathrm{E}}^{+}(n), \\ \theta_{\mathrm{E}}^{-}(n, j_{\mathrm{E}}^{-}), & j_{\mathrm{E}}^{-} = 1, 2, \ldots, k_{\mathrm{E}}^{-}(n), \end{cases} \tag{5}$$

here $D_{\mathrm{E}}(n)$ represents the size of the fibre that we want to determine, with $n = 1, 2, \ldots, n_{\mathrm{E}}$. We assume here that the temporal resolution of the acquisition system is high enough for there to be no smoothing of the scattering diagrams in time (i.e. with the fibre size). The problem is now to associate the theoretical diagram, i, with the experimental one, n, so we have $D_{\mathrm{E}}(n) \approx D_{\mathrm{T}}(i)$.

Comparing the measured diagrams and reference diagrams the absolute angular deviations between each of their maxima and minima are

$$\begin{aligned} \Delta\theta^{+}\left(i, n, j_{\mathrm{T}}^{+}, j_{\mathrm{E}}^{+}\right) &= \left|\theta_{\mathrm{T}}^{+}\left(i, j_{\mathrm{T}}^{+}\right) - \theta_{\mathrm{E}}^{+}\left(n, j_{\mathrm{E}}^{+}\right)\right|; \\ \Delta\theta^{-}\left(i, n, j_{\mathrm{T}}^{-}, j_{\mathrm{E}}^{-}\right) &= \left|\theta_{\mathrm{T}}^{-}\left(i, j_{\mathrm{T}}^{-}\right) - \theta_{\mathrm{E}}^{-}\left(n, j_{\mathrm{E}}^{-}\right)\right|. \end{aligned} \tag{6}$$

For each of these couples, a correlation estimator can be associated

$$\begin{aligned} \Delta P^{+}\left(i, n, j_{\mathrm{T}}^{+}, j_{\mathrm{E}}^{+}\right) &= \frac{\sigma_{\theta}(i)}{\Delta\theta^{+}(i, n, j_{\mathrm{T}}^{+}, j_{\mathrm{E}}^{+}) + 1}; \\ \Delta P^{-}\left(i, n, j_{\mathrm{T}}^{-}, j_{\mathrm{E}}^{-}\right) &= \frac{\sigma_{\theta}(i)}{\Delta\theta^{-}(i, n, j_{\mathrm{T}}^{-}, j_{\mathrm{E}}^{-}) + 1}, \end{aligned} \tag{7}$$

where $\sigma_{\theta}(i)$ is a control parameter which represents the maximum angular deviation to consider that a theoretical and an experimental extreme could be identical. $\Delta P^{+}(i, n, j_{\mathrm{T}}^{+}, j_{\mathrm{E}}^{+})$ and $\Delta P^{-}(i, n, j_{\mathrm{T}}^{-}, j_{\mathrm{E}}^{-})$ are maximum if the absolute angular deviations are null. They decrease linearly as the angular deviation increases.

For the case of $D_{\mathrm{E}}(n) = D_{\mathrm{T}}(i)$, the number of maxima and minima of the corresponding diagrams is be expected to be the same $k_{\mathrm{E}}^{+}(n) = k_{\mathrm{T}}^{+}(i), k_{\mathrm{E}}^{-}(n) = k_{\mathrm{T}}^{-}(i)$. Practically, these numbers may be slightly different if the experimental diagrams are noisy. Nevertheless, if they are significantly different, we may assume that $D_{\mathrm{E}}(n) \neq D_{\mathrm{T}}(i)$, so that we introduce a discrimination factor $\delta_k(i)$ like

$$\delta_k(i, n) = \begin{cases} 0, & \text{if } |k_{\mathrm{E}}^{+}(n) - k_{\mathrm{T}}^{+}(i)| > \sigma_k(i) \quad \text{or } \left|k_{\mathrm{E}}^{-}(n) - k_{\mathrm{T}}^{-}(i)\right| > \sigma_k(i), \\ 1, & \text{if } |k_{\mathrm{E}}^{+}(n) - k_{\mathrm{T}}^{+}(i)| \leqslant \sigma_k(i) \quad \text{and } \left|k_{\mathrm{E}}^{-}(n) - k_{\mathrm{T}}^{-}(i)\right| \leqslant \sigma_k(i), \end{cases} \tag{8}$$

where $\sigma_k(i)$ is a second control parameter which represents the maximum deviation, for the number of the maxima and the minima, to consider that two diagrams could be identical. During an experiment, if the fibre size evolves in a wide range, the number of corresponding extremes is expected to vary considerably (for instance $k_{\mathrm{T}}^{-} = 1$–11 for $D = 5$–42 μm). Therefore, as there are more extremes for large fibres, i.e. more information, the inversion procedure could be biased towards the upper size range. To overcome this problem, the following weighting factor is introduced:

$$\Delta K(i, n) = \frac{\delta_k(i, n)}{k_{\mathrm{T}}^{+}(i) k_{\mathrm{T}}^{-}(i) + 1} \tag{9}$$

where $\Delta K(i, n)$ is maximum for the smallest fibres and decays with the fibre size (non-linearly). It is null if the deviation in the numbers of extremes is too significant, i.e. greater than $\sigma_k(i)$.

Now we build a correlation estimator for the couple of diagrams (i, n) as the product of the previous elementary estimators

$$\begin{aligned} P(i, n) = \Delta K(i, n) &\prod_{j_{\mathrm{T}}^{+}}^{k_{\mathrm{T}}^{+}} \prod_{j_{\mathrm{E}}^{+}}^{k_{\mathrm{E}}^{+}} \Delta P^{+}\left(i, n, j_{\mathrm{T}}^{+}, j_{\mathrm{E}}^{+}\right) \\ &\times \prod_{j_{\mathrm{T}}^{-}}^{k_{\mathrm{T}}^{-}} \prod_{j_{\mathrm{E}}^{-}}^{k_{\mathrm{E}}^{-}} \Delta P^{-}\left(i, n, j_{\mathrm{T}}^{-}, j_{\mathrm{E}}^{-}\right). \end{aligned} \tag{10}$$

Finally, the measured fibre diameter, $D_{\mathrm{E}}(n)$, is considered to be equal to the theoretical diameter, $D_{\mathrm{T}}(i)$, giving the greatest correlation estimator

Table 1
Values of the control parameters used in this study

$k_T^+(i)$	1	2	3	4	5	6	7	8	9	10	11	12
$\sigma_k(i)$	1	1	1	2	2	2	3	3	3	4	4	4
$\sigma_\theta(i)$ (°)	0.5	0.35	0.25	0.25	0.15	0.15	0.15	0.10	0.10	0.10	0.10	0.10

$$D_E(n) = D_T(i/\max\{P(i,n),\ \ i = 1,2,\ldots,n_T\}). \tag{11}$$

The values of the control parameters $\sigma_k(i)$, $\sigma_\theta(i)$ depend necessarily on the fibre's diameter. For reinforcement glass fibres and the experimental setup presented below, the authors have used the values in Table 1. They are given versus the number of the maxima of the theoretical diagrams (and not the fibre size, which we want to determine).

4. Experimental validations

4.1. Setup

A schematic drawing of the high-resolution diffractometer (HIREDI) developed to validate the principle of the proposed inversion method is presented in Fig. 4. The output of a 2.5 mW He-Ne laser (1), with wavelength $\lambda = 0.6328$ μm, is coupled (2) to a single mode polarisation maintaining optical fibre (3). The optical fibre output is precisely collimated with integrated optics (4) and a laser beam expander (5). A cylindrical lens (6), with focal length $f_{cyl} = 500$ mm, is used to focus the laser beam along the reinforcement fibre's axis, Z. So that, at the measurement point (7), a laser sheet lights the fibre to be measured. This laser sheet is collimated along the Y-direction, with a large axis width of 2 mm. Its smaller axis, along Z, is located in (7), with a width of $2\omega_Z \approx 50$ μm at $1/e^2$. The light scattered by the reinforcement fibre is collected by a Fourier lens (8) with focal length $f = 50$ mm. To prevent camera saturation, the direct beam's spot (9) is focused several hundred microns from the first photo-sensitive elements of the CCD (11). The far field scattering pattern is then digitised by an 8 bits linear camera (10), with 1024 pixels (size: 10 μm × 10 μm) and a line frequency rate in the range ($f_e = 70$ Hz to 43 kHz). The camera output is digitised with an LDVS digital video board and processed with a PC. This acquisition system can perform off line or on line measurements. The off line mode is used when a high-acquisition rate is needed (up to 43 kHz) but the acquisition sequence is limited to 32 Mbytes (i.e. 32,000 diagrams at a frequency rates of 1024 Hz). In the on line acquisition mode, about 150 diagrams per second can be captured and inversed. This last acquisition rate is limited by our acquisition and inversion software which has not yet been optimised for speed. The angular resolution and range of the system is of $\Delta\theta \approx 0.01°$/pixels with $\theta = 1.50°$–$12.75°$. Note that during the calibration procedure, the angular positions of the extremes were found to be independent for the fibre position in the probe volume ($\Delta X = \Delta Y = \pm 1$ mm), i.e. there was no evidence of the influence of

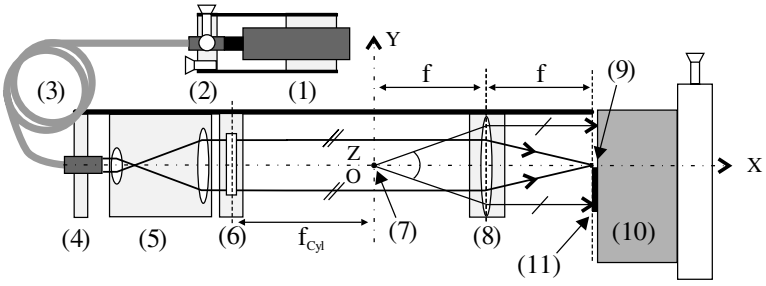

Fig. 4. High-resolution diffractometer (HIREDI): optical setup.

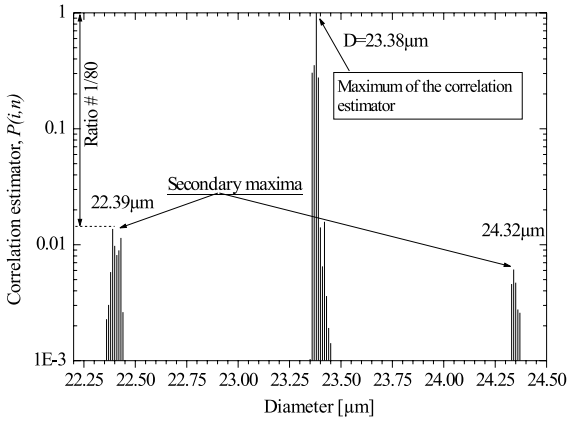

Fig. 5. Typical evolution of the correlation estimator $P(i,n)$.

the laser sheet divergence and intensity gradients [12]. So, in the following, we can use the previous scattering model, based on plane waves, for the inversion of experimental scattering diagrams.

4.2. Experimental results

Experimental validation has been carried out on a laboratory-scale single glass fibre drawing bench developed by Saint-Gobain Vetrotex Int. [3]. A typical evolution of the correlation estimator $P(i,n)$ is presented in Fig. 5. It has been extracted from the analysis of the experimental series presented in Figs. 6 and 7. It is almost null out side the considered size range. It is maximum for a fibre with diameter $D_E = D_T = 23.38$ μm. The maximum of $P(i,n)$ is much greater than its secondary maxima (ratio ≈1/80) which corresponds to fibres giving similar scattering patterns. In this example, it is clear that the correlation estimator introduced above allows the differentiation of experimental scattering patterns that are rather similar, i.e. the inversion of the contributions of the MDRs.

Fig. 6 presents a typical experimental time series of scattering diagrams recorded when the fibre take-up velocity V_f increases rapidly from 5 to 40 m/s, with $f_e = 2048$ Hz. This temporal evolution corresponds to a fibre length of ≈800 m. Three phenomena are emphasised in the zoomed figures: (a) the presence of a gas bubble in the initial glass melt composition induces the formation of a hollow fibre. These hollow fibres appear as discontinuities in the scattering diagrams so that they can be easily detected and counted; (b) fast evolutions of the scattering pattern are observed as well as (c) slower ones (i.e. fast and slow perturbations propagate along the melt glass jet during the drawing process).

Fig. 7 presents the fibre's diameter evolution corresponding to Fig. 6, obtained simultaneously with the high-resolution diffractometer and a laser interferometer operating in the backward scattering domain [11,13,14]. In this figure, the diffractometer resolution appears to be much higher than

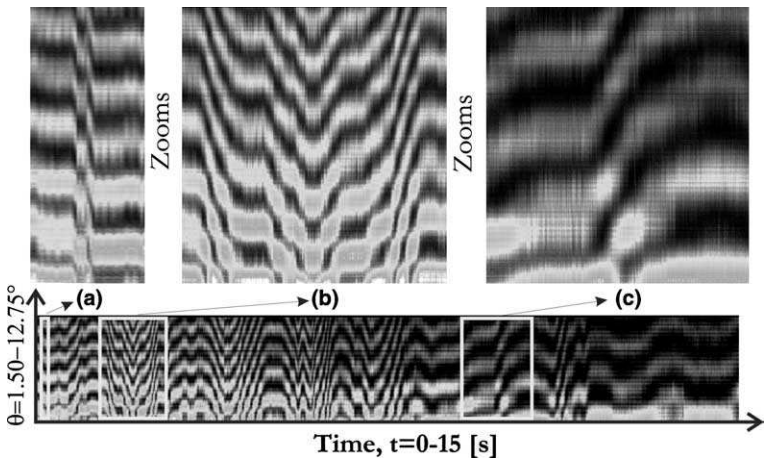

Fig. 6. Experimental scattering diagrams time series when the fibre's take-up velocity is rapidly increased (V_f = 5–40 m/s).

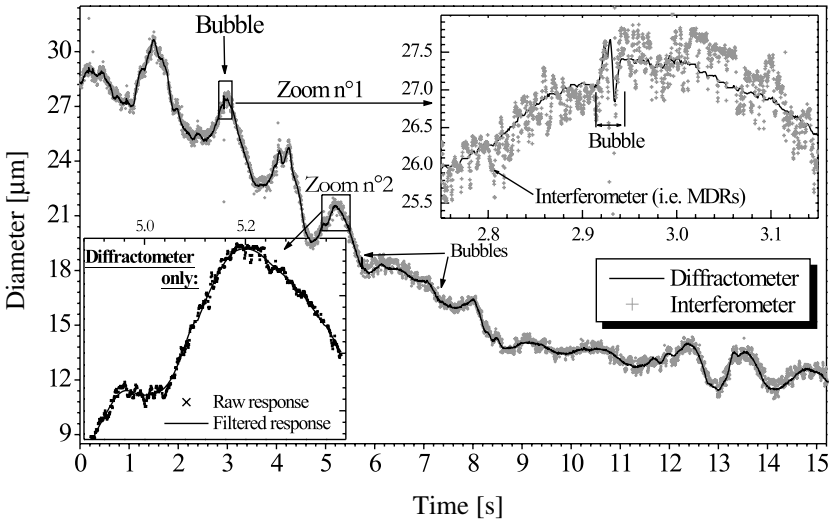

Fig. 7. Comparison between the response of the high-resolution diffractometer and that of a backward scattering interferometer, time series corresponding to Fig. 6.

the interferometer one (see zoom no. 1 in Fig. 7). This can be simply explained by the fact that the inversion of the MDRs is successful with the diffractometer (there are no diameter jumps of ~1 μm) which is not yet the case with the interferometer. For the whole diameter evolution, both systems give very similar statistics with, for the means, $\overline{D}_{\text{Diff.}} \approx 18.68$ μm and $\overline{D}_{\text{Int.}} \approx 18.76$ μm, and for the standard deviation, $\sigma(D_{\text{Diff.}}) \approx 5.94$ μm and $\sigma(D_{\text{Int.}}) \approx 6.23$ μm. So, for the whole size range considered here, $D = 11$–32 μm, the difference in the mean response of these *two independent measurement systems* is only about ~0.08 μm. For the standard deviation in the difference of both responses, the value found $\sigma(D_{\text{Int.}} - D_{\text{Diff.}}) \approx 0.29$ μm is in close agreement with the predicted limit resolution for the interferometer [11] (i.e. *this difference is mainly induced by the interferometer*). In Fig. 7, bubbles appear as sharp resonances whose occurrence can be counted for further statistics. At that time, hollow fibres are not correctly measured by both systems.

The smoothed response of the diffractometer is plotted in Fig. 7 for a restricted size evolution (see zoom no. 2). This smoothed response has been calculated by applying a sliding Fourier filter to the diffractometer raw response, with a window width of 20 samples (i.e. ≈10 ms). In this zoomed figure, the raw response appears to be slightly noisy compared to the smoothed one. This "noise" can be considered as the limit resolution of this diffractometer. By calculating the standard deviation of the amplitude of this noise, relative to the filtered response, we found $\sigma = \sigma(D_{\text{Diff.}} - \text{Filtered}\{D_{\text{Diff.}}\}) = 0.02$ μm for the whole size range considered in Fig. 7. Note that this resolution is only equal to two steps of the diameter increment used to produce the theoretical lookup table given in Eq. (4). Other experiments, not reported here, have shown that a similar resolution is obtained with this setup for the size range of interest for reinforcement glass fibres, i.e. $D \approx 7$–42 μm.

Comparison between off-line size measurements (on cut fibres) have been also performed with the diffractometer, the interferometer, and with the analysis of scanning electron microscope (SEM) images [3]. For fifteen samples in the size range $D \approx 8$–41 μm, the difference in the diffractometer and the SEM responses was found to be in the range ±1%. Despite this rather good agreement, a better agreement could be expected, for instance: ±0.1% since for a fibre with a diameter equal to $D = 20$ μm we have $\sigma/20 \approx 0.001$. Nevertheless, it must be remembered that, if SEMs have an extremely high imaging resolution, their true

"sizing" or "scaling" resolution is limited by parameters such as *the magnification's calibration*, the CCD camera resolution. So, these results are thought to be compatible with the one derived from the analysis of Fig. 6 and 7. The difference between the interferometer and the SEM response was found to be in the range ±5% [11]. This larger discrepancy is attributed to MDRs which have a strong effect on the interferometer response for a particular size.

5. Conclusion and perspectives

A simple and robust method for the inversion of the laser diffraction diagrams of transparent glass fibres has been introduced. Based on Lorenz-Mie theory calculations and the definition of a correlation estimator, it allows to determine the particle diameter without the classical size ambiguity problem due to morphological-dependent resonances. When applied to the inversion of experimental scattering diagrams recorded with a preliminary optical setup, the resolution obtained is typically of $\sigma \approx 0.02$ μm for the size range $D = 7$–42 μm.

It will be shown in a future work that this method can be easily extended to characterize hollow fibres (i.e. internal and external diameter, provided they are axi-symetrical) and fibres' refractive index when it is unknown. This method is applicable to more compact optical setups and for the diagnosis of other kinds of highly symmetrical and transparent particles.

Acknowledgements

The authors are grateful to Saint-Gobain Vetrotex and to ADEME (French Agency for Environment and Energy Resources) for providing experimental facilities and financial support for this work.

References

[1] G. Gupta, in: A.R. Bunsell (Ed.), Fibers Reinforcements for Composite Materials, Elsevier, New York, 1988.
[2] L.R. Gliksman, J. Basic Eng. 15 (1968) 343.
[3] A. Lenoble, Ph.D. Thesis, Université de Provence, Marseille, France, November 2003.
[4] L.J. Lynch, N. Thomas, Textile Res. J. 41 (1971) 568.
[5] D. Lebrun, S. Belaid, C. Ozkul, K.-F. Ren, G. Gréhan, Opt. Eng. 35 (1996) 946.
[6] C. Ozkul, D. Lebrun, D. Allano, A. Abdelghani-Idrissi, A. Leduc, Opt. Eng. 30 (1991) 1855.
[7] P. Chylek, J.T. Kiehl, M.K.W. KO, A. Ashkin, in: D.W. Schuerman (Ed.), Lights Scattering by Irregularly Shaped Particles, Plenum Press, New York, 1980.
[8] C.F. Bohren, D.R. Huffman, Absorption and Scattering of Light by Small Particles, Wiley, New York, 1998.
[9] F. Onofri, submitted for publication in C.R. Acad. Sci. Paris, Serie II b (2004).
[10] J.M. Corpus, P.K. Gupta, J. Am. Ceram. Soc. 76 (1993) 1390.
[11] F. Onofri, A. Lenoble, S. Radev, H. Bultynck, P.-H. Guering, N. Marsault, Part. Part. Syst. Charact. 20 (2003) 171.
[12] G. Gouesbet, G. Gréhan, K.F. Ren, J. Opt. Soc. Am. A 15 (1998) 511.
[13] F. Onofri, L. Bergounoux, J.-L. Firpo, J. Mesguish-Ripault, Appl. Opt. 38 (1999) 4681.
[14] F. Onofri, A. Lenoble, S. Radev, Appl. Opt. 41 (2002) 3590.

Résumé

Ce manuscrit d'habitation à diriger des recherches porte sur la caractérisation optique des écoulements multiphasiques. Il rassemble trois types de contributions. La première, traite de la modélisation des propriétés de diffusion de la lumière des particules rencontrées dans ces milieux : gouttes, bulles et fibres homogènes ; particules sphériques, fibres et jets à gradient radial d'indice, à cœur ; particules ellipsoïdales, hétérogènes ou irrégulières. Ces développements théoriques et numériques sont basés sur la théorie de Lorenz-Mie ou des modèles asymptotiques : modèle statistique, optique physique et géométrique. La deuxième partie de ce manuscrit, introduit le principe de techniques optiques originales pour la caractérisation simultanée de la vitesse, de la taille et du matériau de particules en écoulement : technique Dual Burst, Dual Mode, Interférométrie phase Doppler à 3 faisceaux cohérents, diffractométrie haute résolution, diffusion critique et arc-en-ciel. La troisième partie présente différents travaux réalisés dans le cadre de collaborations universitaires ou industrielles, sur des sujets aussi variés que la caractérisation des propriétés optiques de globules rouges, la caractérisation de système en combustion, les instabilités de jets capillaires homogènes ou à cœur ; le fibrage du verre à haute température ; les fibres optiques ; l'étude expérimentale d'instabilités thermo-solutales et de l'hydrodynamique d'écoulements gaz-solides en lit fluidisé circulant. Ce manuscrit comprend également un résumé de mes activités d'enseignement, de valorisation et de management de la recherche, ainsi que les reproductions de dix articles.

Mots clés : Ecoulements, instabilités, particules, diagnostics lasers, granulométrie, réfractométrie, interférométrie, diffractométrie, électromagnétisme, théorie de Lorenz-Mie.

Title: Optical Diagnosis of Multiphase Flows

Abstract

This habilitation manuscript deals with the optical characterization of multiphase flows. It gathers three types of contributions. The first part concerns the modelling of the light scattering properties of various particles encountered in flows: homogeneous droplets, bubbles and fibres; spherical and cylindrical particles with internal refractive index gradients or coated; ellipsoidal, heterogeneous and irregular particles. These theoretical and numerical works are established in the framework of the Lorenz-Mie theory or with physical or geometrical approximations. The second part introduces the principle of several new optical techniques for the simultaneous characterization of the velocity, the size and material of flowing particles: Dual Bursts and Dual Mode techniques, Phase Doppler interferometry with 3 coherent beams, high resolution diffractometry, rainbow and critical scattering. The third part presents several works completed in collaboration, on subjects connected with: biophysics; combustion; instabilities of capillary and viscous jets, homogeneous and coated; glass-fibre drawing, optical fibres, thermosolutal instabilities and gas-solid circulating fluidized beds flows. This manuscript includes also a summary of my activities of teaching, valorization and management of research, as well as the reproductions of ten articles.

Keywords: Multiphase flows, instability, particles, laser diagnosis, granulometry, refractometry, interferometry, diffractometry, electromagnetism, Lorenz-Mie theory